

Document downloaded from:

<http://hdl.handle.net/10251/210291>

This paper must be cited as:

Velty, A.; Corma Canós, A. (2023). Advanced zeolite and ordered mesoporous silica-based catalysts for the conversion of CO<sub>2</sub> to chemicals and fuels. *Chemical Society Reviews*. 52(5):1773-1946. <https://doi.org/10.1039/d2cs00456a>



The final publication is available at  
<https://doi.org/10.1039/d2cs00456a>

Copyright The Royal Society of Chemistry

Additional Information

# Advanced zeolites- and ordered mesoporous silica- based catalysts for the conversion of CO<sub>2</sub> to chemicals and fuels

## AUTHOR(S):

Alexandra Velty, Avelino Corma

## ADDRESS:

Instituto de Tecnología Química, Universitat Politècnica de València-Consejo Superior de Investigaciones Científicas, Avenida de los Naranjos s/n, 46022 València, Spain

## EMAIL:

acorma@itq.upv.es

## ORCID ID:

**Alexandra Velty: 0000-0002-8263-4570**

**Avelino Corma: 0000-0002-2232-3527**

A	Introduction.....	8
1	Scope.....	8
2	Zeolites.....	11
3	Ordered mesoporous silicates (OMS).....	13
4	Objectives.....	14
B	Catalytic conversion of CO <sub>2</sub> .....	16
1	Synthesis of carbonates.....	16
1.1	Synthesis of cyclic carbonates.....	17
1.1.1	Synthesis of cyclic carbonates via cycloaddition.....	18
1.1.2	Synthesis of cyclic carbonates via olefin oxidative carboxylation.....	44
1.1.3	Other routes for the preparation of cyclic carbonates.....	46
1.2	Synthesis of dialkyl carbonates.....	46
1.2.1	Introduction.....	46
1.2.2	Acid-base OMS-based catalysts for the synthesis of dialkyl carbonates.....	48
1.2.3	Zeolite-based catalysts for the synthesis of dialkyl carbonates.....	49
1.2.4	Conclusion.....	49
2	Synthesis of carbamates.....	50
2.1	Synthesis of acyclic carbamates.....	51
2.1.1	Introduction.....	51
2.1.2	Three component coupling of amine, RX and CO <sub>2</sub> for the synthesis of carbamates...51	
2.2	Synthesis of 2-oxazolidinones.....	56
2.2.1	Introduction.....	56
2.2.2	Cycloaddition of CO <sub>2</sub> with aziridine.....	57
2.3	Conclusion.....	59
3	Other formation of C-N bond.....	61
4	Synthesis of carboxylic acid.....	62
4.1	Carboxylation reaction via CO <sub>2</sub> insertion into C-M bond for the synthesis of carboxylic acid..62	
4.2	Synthesis of acetic acid.....	62

4.2.1.	Introduction .....	62
4.2.2.	Zeolite based catalysts for acetic acid synthesis.....	63
4.2.3.	Conclusion.....	67
4.3.	Synthesis of propanoic acid .....	68
4.4.	Conclusions .....	69
5	Hydrogenation of CO <sub>2</sub> .....	70
5.1.	Hydrogenation/Reduction of CO <sub>2</sub> to formic acid.....	70
5.1.1.	Introduction .....	70
5.1.2.	Zeolite-based catalysts for formic acid synthesis .....	71
5.1.1.	OMS-based catalysts for formic acid synthesis.....	73
5.1.2.	Conclusion.....	74
5.2.	Hydrogenation of CO <sub>2</sub> to methanol .....	74
5.2.1.	Introduction .....	74
5.2.2.	Thermodynamics for CO <sub>2</sub> hydrogenation to methanol.....	75
5.2.3.	Mechanism insights for CO <sub>2</sub> hydrogenation to methanol .....	76
5.2.4.	Catalysts for CO <sub>2</sub> hydrogenation to methanol.....	77
5.2.5.	Conclusion.....	86
5.3.	Catalytic methylation of aromatics with CO <sub>2</sub> /H <sub>2</sub> .....	88
5.4.	Direct conversion of CO <sub>2</sub> to dimethylether (DME).....	90
5.4.1.	Introduction .....	90
5.4.2.	Thermodynamics of direct DME synthesis.....	91
5.4.3.	Cu-based catalysts for direct DME synthesis .....	93
5.4.4.	Pd and bimetallic catalytic system for direct DME synthesis.....	104
5.4.5.	Conclusion.....	106
5.5.	CO <sub>2</sub> methanation .....	110
5.5.1.	Introduction .....	110
5.5.2.	Thermodynamics of CO <sub>2</sub> methanation .....	111
5.5.3.	Catalysts for CO <sub>2</sub> methanation.....	112
5.5.4.	Conclusion.....	129
5.6.	Hydrogenation of CO <sub>2</sub> into higher alcohols (C <sub>2+</sub> OH) .....	134
5.6.1.	Introduction .....	134
5.6.2.	Zeolite based catalysts for hydrogenation of CO <sub>2</sub> to C <sub>2+</sub> OH .....	136
5.6.3.	OMS-based catalysts for CO <sub>2</sub> hydrogenation to C <sub>2+</sub> OH.....	141
5.6.4.	Conclusion.....	141
5.7.	Hydrogenation of CO <sub>2</sub> to C <sub>2+</sub> .....	142
5.7.1.	Introduction .....	142
5.7.2.	Direct hydrogenation of CO <sub>2</sub> to fuels over bifunctional catalytic system incorporating zeolites. 145	
5.7.3.	Direct hydrogenation of CO <sub>2</sub> to olefins over bifunctional catalytic system incorporating zeolites via methanol mediated route .....	152

5.7.4.	Direct hydrogenation of CO <sub>2</sub> to aromatics over bifunctional catalytic system incorporating zeolites.....	153
5.7.5.	Conclusion.....	160
6	SYNGAS.....	164
6.1.	Catalytic reduction of CO <sub>2</sub> with hydrogen (RWGS) .....	164
6.1.1.	Introduction .....	164
6.1.2.	Mechanism .....	165
6.1.3.	Catalysts for RWGS process .....	166
6.1.4.	Conclusion.....	173
6.2.	Dry reforming of methane (DRM).....	176
6.2.1.	Introduction .....	176
6.2.2.	Thermodynamics .....	176
6.2.3.	Mechanism of dry reforming of methane .....	178
6.2.4.	Catalysts for DRM .....	178
6.3.	Dry reforming of alcohols (DR-alcohols).....	233
6.3.1.	Dry reforming of ethanol (DRE) .....	233
6.3.2.	Dry reforming of glycerol (DRG) .....	236
6.3.3.	Conclusion.....	239
7	Oxidative dehydrogenation (ODH) of alkanes with CO <sub>2</sub> .....	239
7.1.	Introduction .....	240
7.1.1.	Mechanistic insights.....	240
7.1.2.	Role of redox properties.....	241
7.1.3.	Role of lattice oxygen.....	241
7.1.4.	Role of the acid/base sites.....	242
7.1.5.	Metal oxide based catalysts for ODH of alkanes .....	242
7.2.	Styrene production by ethylbenzene (EB) ODH.....	243
7.2.1.	Zeolite-based catalysts for EB ODH .....	244
7.2.1.	OMS-based catalysts for EB ODH.....	245
7.2.2.	Conclusion.....	250
7.3.	Ethylene production by ethane ODH.....	253
7.3.1.	Introduction .....	253
7.3.2.	Zeolites based catalysts for ethane ODH.....	253
7.3.1.	OMS-based catalysts for ethane ODH .....	256
7.3.2.	Conclusion.....	262
7.3.1.	Propylene production by propane ODH .....	267
7.3.2.	Introduction .....	267
7.3.3.	Zeolites-based catalysts for propane ODH .....	268
7.3.4.	OMS-based catalysts for propane ODH .....	273
7.3.5.	Conclusion.....	276
7.4.	Isobutene production by isobutane ODH .....	281
7.4.1.	Introduction .....	281

7.4.2.	OMS- and zeolite-based catalysts for isobutane ODH .....	281
7.4.3.	Conclusion.....	283
7.5.	Conclusion.....	283
C	Electro and photocatalytic conversion of CO <sub>2</sub> .....	286
1	Electroreduction of CO <sub>2</sub> .....	286
2	Photoreduction of CO <sub>2</sub> .....	287
2.1.	Fundamentals of photocatalytic CO <sub>2</sub> reduction.....	287
2.2.	Photocatalysts for the reduction of CO <sub>2</sub> .....	290
2.2.1.	Zeolite-based catalysts for the photoreduction of CO <sub>2</sub> .....	290
2.2.2.	Conclusion.....	294
2.2.3.	OMS-based catalysts for the photoreduction of CO <sub>2</sub> .....	297
2.2.4.	Conclusion.....	301
2.2.5.	Conclusion.....	302
D	Summary and perspectives.....	304
E	References .....	311

**Abstract:** For many years, capturing, storing or sequestering CO<sub>2</sub> from concentrated emission sources or from the air has been a powerful issue in reducing atmospheric CO<sub>2</sub>. Moreover, the use of CO<sub>2</sub> as a C1 building block to mitigate CO<sub>2</sub> emissions and, at the same time, produce sustainable chemicals or fuels is a challenging and promising alternative to meet global demand for chemicals and energy. Hence, the chemical incorporation and conversion of CO<sub>2</sub> into valuable chemicals has received much attention for the last decade, since CO<sub>2</sub> is an abundant, inexpensive, nontoxic, nonflammable, and renewable one-carbon building block. Nevertheless, CO<sub>2</sub> is the most oxidized form of carbon, thermodynamically the most stable form and kinetically inert. Consequently, chemical conversion of CO<sub>2</sub> requires highly reactive, rich-energy substrates, highly stable products formed or harder reaction conditions. The use of catalysts constitutes an important tool to the development of sustainable chemistry, since catalysts increase the rate of reaction without modifying the overall standard Gibbs energy in the reaction. Therefore, special attention has been given to catalysis, and in particular to heterogeneous catalysis because of the environmentally friendly nature of its recyclable nature attributed to simple separation and recovery, as well as its applicability to continuous reactor operations. Focusing on heterogeneous catalysts, we decided to center on zeolite and ordered mesoporous materials due to their high thermal and chemical stability and versatility, which make them good candidates for the design and development of catalysts for CO<sub>2</sub> conversion. In the present review, we analyze the state of the art for the last 25 years and the potential opportunities for the zeolite and OMS (ordered mesoporous silicas) based materials to convert CO<sub>2</sub> into valuable chemicals essential for our daily lives and fuels, and to pave the way towards reducing carbon footprint. In this review, we have compiled, to the best of our knowledge, the different reactions involving catalysts based on zeolites and OMS to convert CO<sub>2</sub> into cyclic and dialkyl carbonates, acyclic carbamates, 2-oxazolidones, carboxylic acids, methanol, dimethylether, methane, higher alcohols (C<sub>2+</sub>OH), C<sub>2+</sub> (gasoline, olefins and aromatics), syngas (RWGS, Dry reforming of methane and alcohols), olefins (oxidative dehydrogenation of alkanes) and simple fuels by photoreduction. The use of advanced zeolite and OMS based materials, and the development of new processes and technologies should constitute a new impulse to boost the conversion of CO<sub>2</sub> into chemicals and fuels.

List of the abbreviations and acronyms used in this review article.

<b>Abbreviation</b>	<b>Name</b>
Ea	Activation Energy
HOMO	Highest occupied molecular orbital
LUMO	Lowest unoccupied molecular orbital
CAGR	Compound annual growth rate
CCS	Carbon capture and storage
CCU	Carbon capture and utilization
DRM	Dry reforming of methane
ODH	Oxidative dehydrogenation
RWGS	Reverse water gas shift
WGS	Water gas shift
FT	Fisher Tropsch
MTO	Methanol to olefins
MTA	Methanol to aromatics
MTP	Methanol to propylene
DR-alcohols	Dry reforming of alcohols
DRE	Dry reforming of ethanol
DRG	Dry reforming of glycerol
PtL	Power to liquid
OSM	Oxygen storage material
DMF	Dimethyl formamide
MeOH	Methanol
EtOH	Ethanol
PrOH	Propanol
DME	Dimethylether
CS	Chitosan
EB	Ethylbenzene
ST	Styrene
DEC	Diethylcarbonate
DABCO	Diazabicyclo octane
DBU	1,8-Diazabicyclo[5.4.0]undec-7-ene
TEA	Tetraethylamine
SDA	Structure directing agent
SAPO	Silicoaluminophosphate
ALPO	Aluminophosphate
MOF	Metal-organic frameworks
OMS	Ordered mesoporous silicates
TEM	Transmission Electron Microscopy
IR	Infrared
XANES	X-ray Absorption Near-Edge Structure
XPS	X-ray photoelectron spectroscopy
XRD	X-ray diffraction
BET	Brunauer, Emmett and Teller

---

TPR	Temperature-programmed reduction
TPD	Temperature programmed desorption
DRIFTS	Diffuse reflectance infrared fourier transform spectroscopy
FT	Fourier transform
DFT	Density functional theory
TON	Turn over number
TOF	Turn over frequency
STY	Space time yield
WHSV	Weight hourly space velocity
GHSV	Gas hourly space velocity
Sel.	Selectivity
TOS	Time on stream
X	Conversion
Conv.	Conversion
Ref.	Reference

---



## **A Introduction**

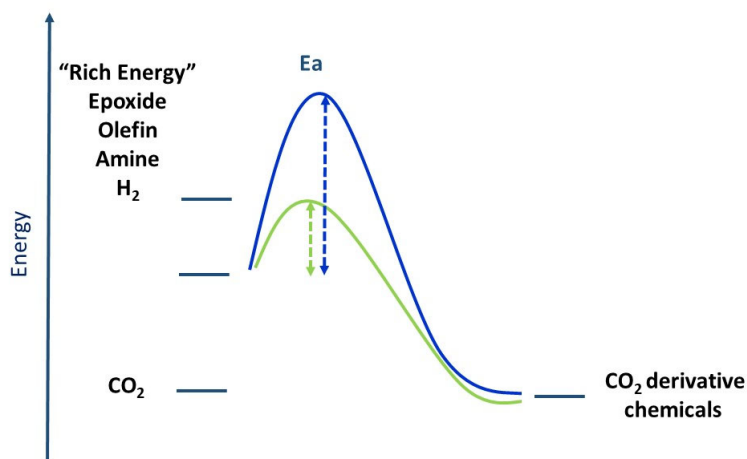
### **1 Scope**

Since 1850 and the beginning of the industrial revolution, human sources of carbon dioxide emissions into the atmosphere have grown constantly and dramatically, at a rate of almost 3% each year. The CO<sub>2</sub> emissions and population growth<sup>1</sup> can be closely linked and world population, currently 7.8 billion, is expected to reach 9.1 billion by 2050 and 11.2 billion by 2100. This population growth will mainly occur in developing countries. Then, if until now the impact of developing countries over greenhouse gas emission has been negligible, this is now increasing and will continue to do so, due to the economic development needed to reduce poverty and the actual linkage of economic development, energy consumption and use of fossil hydrocarbons as primary source of energy. However, this paradigm can be changed and, at present, large effort are being done to generate the energy on the bases of renewable sources.

The global warming is one of the main issue of the 21<sup>st</sup> century and it is principally due to CO<sub>2</sub> and methane emissions. CO<sub>2</sub> is a greenhouse gas found to be present in the atmosphere at a concentration of 418 ppm.<sup>2</sup> CO<sub>2</sub> emission are also related to the ocean acidification, climate change and species extinction. For many years, the development of capture, storage or sequestration technologies of CO<sub>2</sub> from concentrated emission sources (natural gas, industrial processing) or air, constitute powerful matters to reduce atmospheric CO<sub>2</sub>. Moreover, the capture technologies make CO<sub>2</sub> available for its use in food processing and chemical industries. Incorporate anthropogenic CO<sub>2</sub> and build chemicals is a way to pave a path towards a more sustainable and renewable carbon economy and neutrality, and constitutes a supplement to geological sequestration. Thus, our society is moving away from carbon capture and storage (CCS) to carbon capture and utilization (CCU). Consequently, the chemical incorporation and conversion of CO<sub>2</sub> into valuable chemicals has received much attention for the last decade. CO<sub>2</sub> is an abundant, inexpensive, nontoxic, nonflammable, and renewable one-carbon building block. CO<sub>2</sub> finds main purposes as green alternative to carbon monoxide and phosgene in the production of carbonates, carboxylic acids and derivatives. Nevertheless, CO<sub>2</sub> is the most oxidized form of carbon, thermodynamically the most stable form and kinetically inert. Consequently, chemical conversion of CO<sub>2</sub> requires highly reactive, rich-energy substrates, highly stable products formed or harder reaction conditions. In the context of low-carbon economy, the use of severe reaction conditions cannot be considered since the high-energy consumption also involves more CO<sub>2</sub> emissions, unless the energy will be supplied by renewables sources. Some traditional thermal processes allow the CO<sub>2</sub> incorporation into valuable products such as the synthesis of urea,<sup>3,4</sup> salicylic acid<sup>5</sup> and inorganic carbonates that

do not require the use of catalyst to be industrially applied.<sup>6–8</sup> Meanwhile, numerous catalytic transformations have been the center of several studies using organometallic complexes<sup>9</sup> and heterogeneous or homogeneous catalysts,<sup>10–13</sup> and the incorporation of CO<sub>2</sub> into chemicals such as urea derivatives, carbonates, carbamates, methanol and dimethyl-ether, alcohols, formic and carboxylic acids, alkanes, olefins and aromatics, among others, have been described.<sup>12,14–16</sup> Nevertheless, the scope and efficiency of the reported CO<sub>2</sub> transformations are narrow and have not been industrially applied due to the thermodynamic stability and kinetic inertness of CO<sub>2</sub>. Indeed, CO<sub>2</sub> transformations usually require the use of a high ratio of organometallic compounds, solvent, additives associated to the production of large amount of hazardous wastes and are generally performed under harsh reaction conditions.

In chemical processes, the use of catalysts constitutes an important tool for the development of sustainable chemistry. Indeed, catalysts increase the rate of reaction without modifying the overall standard Gibbs energy change in the reaction.<sup>17</sup> Therefore, an adequate and effective activation of substrates (CO<sub>2</sub>) allow overcoming the energy barrier of the reaction, improving the reaction rate and selectivity. Consequently, highly efficient catalysts in terms of energy, selectivity, productivity and reusability are decisive to develop sustainable and economic process (Figure 1). Thus, in accordance with green chemistry and sustainability criteria, the development of effective and robust heterogeneous catalysts is crucial (Figure 2).



**Figure 1.** Catalytic reaction of CO<sub>2</sub> with "rich energy" substrate.

Solid catalysts are attractive due to advantageous characteristics such as activity, robustness, efficiency, recovery and recycling, ease of handling that makes them economically advantageous, and environmentally friendly by minimizing waste. Focusing on heterogeneous catalysts, we will center here on ordered micro- and meso- porous materials because of the flexibility in their composition and pore structure system, they are adjustable and customizable, and high surface area. Considering ordered microporous materials for CO<sub>2</sub> conversion, metal

organic frameworks (MOFs) have exhibited catalytic activity for transforming CO<sub>2</sub> into chemicals and several compilation works have been published in the last years.<sup>16,12,18</sup> Nevertheless, chemical, thermal and mechanical stability of MOFs<sup>19,20</sup> is one of the major concerns. Indeed, chemical stability of MOFs in the presence of moisture, solvents, acids, bases, and potential coordinating anions could be limited.<sup>21</sup> At the same time, the use of severe reaction conditions such as heat, vacuum or pressure generally undermine their structural stability. All these drawbacks considerably hampers, so far, MOFs uses and applications. In contrast, zeolite (Figure 3) and ordered mesoporous materials (Figure 4) exhibit high thermal and chemical stability which makes them good candidates for the design and development of catalysts for CO<sub>2</sub> conversion. For all of the above, the present review will offer a recompilation on the state of art of the use of zeolites and ordered mesoporous materials for the conversion of CO<sub>2</sub> to chemicals and fuels.

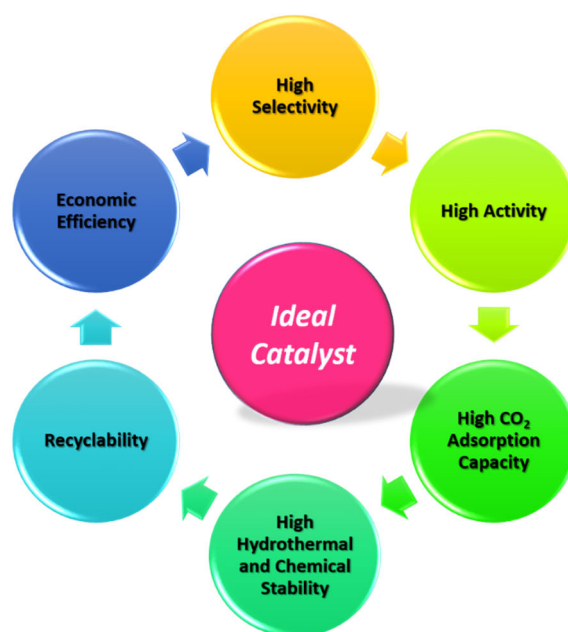


Figure 2. Properties of an ideal catalyst.

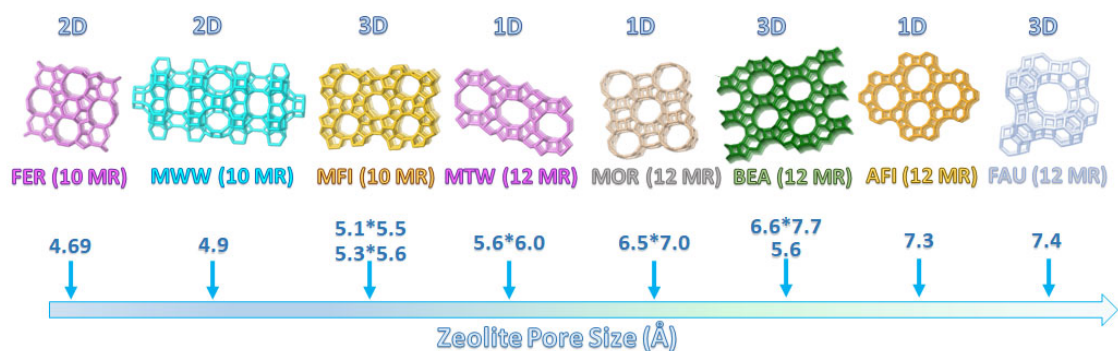
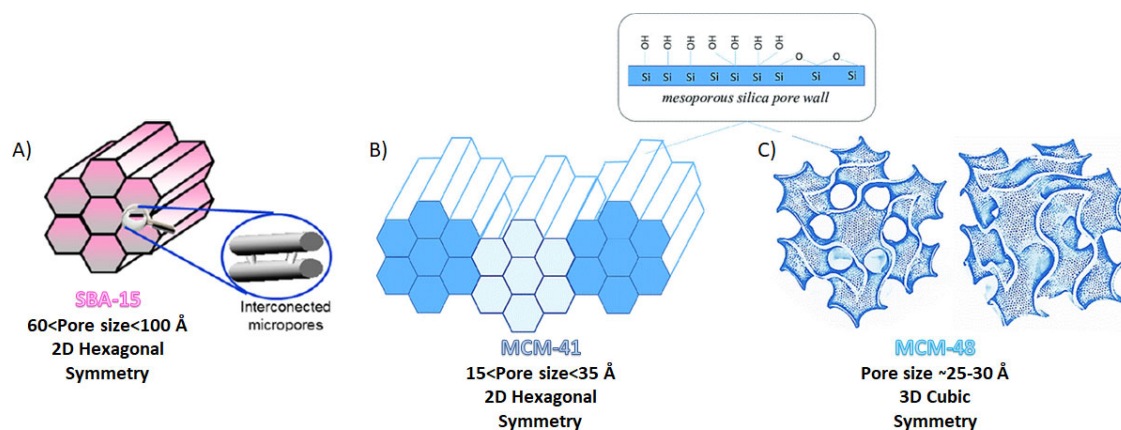


Figure 3. Main characteristics of the zeolites studied throughout this review (images are produced by 3D drawing tool in database of zeolites structures, Accessed 17 March 2022).



**Figure 4.** Main characteristics of the OMS studied throughout this review. A Reprinted with permission from ref. <sup>22</sup>, B and C Reprinted with permission from ref. <sup>23</sup>. Copyright 2019.

## 2 Zeolites

Following with ordered microporous materials, zeolites constitute the most important catalysts traditionally used in oil-refining and petrochemistry<sup>24</sup> and find numerous applications as adsorbents, ions exchangers and finally as catalysts in many chemical processes.<sup>25,26</sup> More specifically, zeolites are crystalline microporous aluminosilicates with cavities and pore topologies of molecular dimensions (Figure 4). Zeolites are characterized by their high surface areas and shape/size selectivity along with the flexibility in their chemical compositions and the ability to accommodate different metals in their frameworks, resulting in acid/base or redox properties.<sup>27</sup> Moreover, their high thermal stability makes them robust and readily reusable after regeneration stage.

The versatility in the tetrahedra assembly lead to the diversity of zeolite structure with tridimensional framework constituted by cages and channels with molecular dimensions. Up to now, 235 natural and synthetic zeolite framework types have been recognized by the International Zeolite Association (IZA) and assigned with three-letter code.<sup>28,29</sup> Zeolites are characterized by dimensions of the channels conventionally defined by the ring size of the aperture. Accordingly, zeolites are classified as small-pore ( $\leq 8$ -ring), medium-pore (10-ring), large-pore (12-ring), and extra-large-pore zeolites ( $> 12$ -ring). The microporous void space enables the access and diffusion of molecules with suitable size, shape, and polarity, well-known as shape-selectivity in zeolites. In some cases the molecular dimensions of zeolites pore systems present severe limitations for the access, formation and diffusion of large molecules. Therefore different strategies were explored to improve the diffusion, increasing the zeolite pore sizes,<sup>30-33</sup> decreasing crystal size,<sup>34-36</sup> forming single layer zeolites (delaminated) or introducing mesoporosity into the zeolite crystals.<sup>37-40</sup>

The zeolite framework is formed by corner-sharing TO<sub>4</sub> tetrahedra where T could be a metal or metalloid such as Si, Al, Fe, Ge, B, Ti, etc., while in the aluminophosphate family Al and P are

predominant. The substitution of an atom by another with lower valency such  $\text{Si}^{4+}$  with  $\text{Al}^{3+}$  or  $\text{P}^{5+}$  with  $\text{Si}^{4+}$  generates a negative charge on the framework which has to be compensated by a proton or a metallic cation that is responsible of the acid/base properties of the zeolites. Compositional and geometric factors are the main features that control the acid/base properties.

The basicity in zeolites is associated to the presence of basic framework oxygen atoms, basic sites of Lewis type, and their strength is related to the density of negative charge. Therefore, the zeolite basicity is a function of the nature of the framework atoms, the extra-framework cations nature and the zeolite structure. To modify and enhance the basic properties of zeolites two main approaches have been explored: the incorporation of alkali metal clusters and oxide/hydroxide particles or the variation of the nature of the cation framework or extra-framework with suitable physicochemical properties using low electronegativity cations such as alkali metal cations.<sup>41-44</sup>

In the same way, the partial substitution of Si atoms with Sn, Ti, or Zr introduces well-defined Lewis acid sites conferring new catalytic properties to the zeolite which are mainly governed by the metal coordination.<sup>45,46</sup>

Owing to their remarkable properties (Figure 5) such as high hydrothermal stability, adsorption, acid/base and redox properties, availability and low production cost, zeolites have been widely and successfully used as efficient catalysts, adsorbents, and ion exchangers. Zeolites can also act as host for different compounds such as single atom, metal clusters or nanoparticles,<sup>47-51</sup> molecular catalysts, organometallic species or forming composites with multifunctionalities.<sup>52,53</sup> The preparation of these advanced multifunctional materials can be performed during the zeolite synthesis, by adsorption/impregnation, ion-exchange and assembly inside the pores and cages (ship-in-a-bottle), and with or without reaction with silanol groups of the surface (covalent bond). On the bases of the versatility of zeolites in composition, structure and catalytic properties and their industrial availability, zeolites can be active players for  $\text{CO}_2$  capture and conversion.



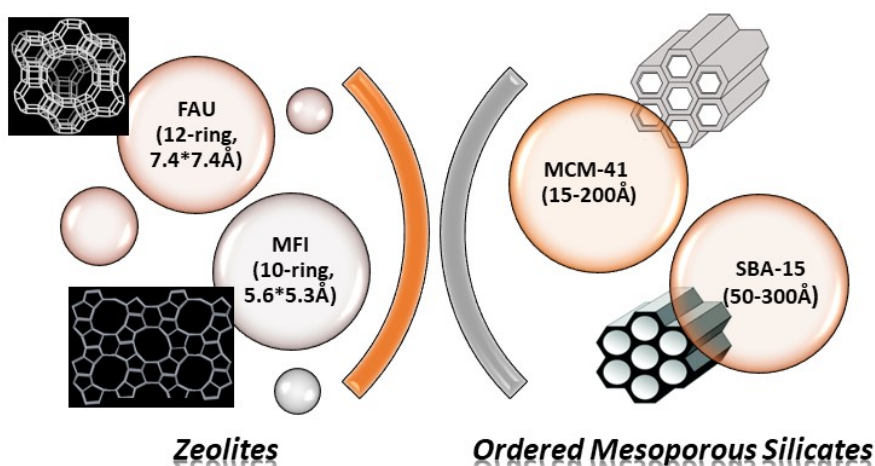
**Figure 5.** Tunable physicochemical and textural properties of zeolites and OMS.

### 3 Ordered mesoporous silicates (OMS)

To overcome the limitations of zeolite structure to the access, formation and diffusion of large molecules (kinetic diameter  $>10\text{\AA}$ ), many efforts have been made for the synthesis of mesoporous within the zeolite crystals<sup>54-57</sup> as well as for the synthesis of ordered mesoporous constructed from tetrahedral units (TO4) with different spatial orientations forming channels and cavities.<sup>58,59</sup> In 1992, a new M41S family of ordered mesoporous silicates (OMS) was successfully synthesized by Mobil Oil Cooperation such as MCM-41 (hexagonal)<sup>60</sup> and MCM-48 (cubic)<sup>61</sup> with pore diameters  $>20\text{ \AA}$ . The discovery of the new family of nanostructured mesoporous materials M41S by ExxonMobil marked a new breakthrough for the development of advanced catalysts for industrial processes.<sup>62</sup> M41S materials offer adjustable and well-defined pore sizes (15-200 $\text{\AA}$ ) with uniform shapes and ordered to some degree along micrometer length scales and amorphous silica walls. MCM-41 material is the most known, studied and used (Figure 6).<sup>63,64</sup> In 1998, the family of ordered mesoporous silicates was extended by the synthesis of Santa Barbara Amorphous (SBA) materials with larger pore size ranging between 50 and 300  $\text{\AA}$  and improved thermal, mechanical and chemical stability (Figure 6).<sup>63,65</sup>

As it occurs for zeolites, the incorporation of Al in the mesostructure modifies the acid/base properties of the material with special relevance from catalytic standpoints. In the same way, the introduction of transition metal such as Ti, Sn, V and Cr into the framework or grafted on the surface allowed preparing materials with expanded catalytic properties (Figure 5).<sup>66-69</sup>

Moreover, the ordered mesoporous silica offer great opportunities for the deposition of cluster, nanoparticles and oxide with high dispersion owing to their high surface areas and large pore dimensions avoiding pore blockage and making possible the diffusion of metal precursors. In the same way, the functionalization of the surface with organic or inorganic functional groups of ordered mesoporous materials enables the efficient immobilization of biomolecules, organocatalysts and metal-organano complexes via covalent bonding with silanol groups, conferring new physical and chemical properties.<sup>59,70,71</sup> Therefore, modified ordered mesoporous materials find applications in large variety of fields such as catalysis, host-guest chemistry, adsorption, separation, semiconductors etc.<sup>60,72–75</sup>



**Figure 6.** Examples of zeolites and OMS.

#### 4 Objectives

CO<sub>2</sub> constitutes a non-toxic and non-flammable raw material. The use of CO<sub>2</sub> as C1 building block is very attractive since provides eco-friendly process that fulfill numerous principles of “Green Chemistry”. Moreover, CO<sub>2</sub> shifts from an undesirable waste to an alternative carbon feedstock. CO<sub>2</sub> is the most oxidized form of carbon and so very stable. Consequently, chemical conversion of CO<sub>2</sub> requires highly reactive/rich-energy substrates or strong reaction conditions (Figure 1). Therefore, catalysis is key for CO<sub>2</sub> conversion and the design of suitable catalysts will allow to overcome the kinetic barriers enabling new technologies for a sustainable transition to fossil sources. Accordingly, owing the great features and customizable properties, industrial availability and thermal stability, zeolites and ordered mesoporous silicates may offer great opportunities for conversion of CO<sub>2</sub> into valuable chemicals in order to minimize, and perhaps revert, the greenhouse effect of anthropogenic CO<sub>2</sub>.<sup>76–79</sup>

Here, we present a critical review of the different reported concepts and findings on mechanism, catalytic performance, catalysts types and strategy design to the direct successful conversion of CO<sub>2</sub> into chemicals in the presence of advanced zeolites and OMS based materials. Although different reviews present CO<sub>2</sub> conversions, this review differs in presenting the potential and

versatility of zeolites and OMS and their capabilities to be engineered for preparing catalysts suitable for the development of industrial catalysts directed to manufacture of a wide range of bulk, commodity, specialties and fine chemical products, polymers and fuels. Several chemical conversions of CO<sub>2</sub> (Figure 7) for the synthesis of carbonates (cyclic and dialkyl), carbamates (acyclic and 2-oxazolidinones), carboxylic acid through different chemical reactions such as cycloaddition, carboxylation and coupling are explored. Numerous CO<sub>2</sub> conversions based on hydrogenation/reduction process for the production of MeOH, DME, C<sub>2</sub>-OH, CH<sub>4</sub>, or SYNGAS through RWGS are also reviewed. The main achievements for the production of gasoline, olefins and aromatics through CO<sub>2</sub> hydrogenation undergoing CO<sub>2</sub> modified Fischer Tropsch or methanol mediated route have been discussed taking into account several recent and very comprehensive reviews.<sup>11,80,89,81-88</sup> The dry reforming of methane and alcohols with CO<sub>2</sub> constitute other important pathways to produce SYNGAS and allow for a continuity in the production of a broad range of chemicals, commodities, specialties and fuels, currently manufactured from fossil resources. The oxidative dehydrogenation of alkanes to ensure a more sustainable and selective production of alkenes is also reviewed. Finally, the photocatalysis using zeolite and OMS-based materials for the reduction of CO<sub>2</sub> to the production of solar fuels has been examined. Considering environmental impact, economic cost and sustainability, an analysis of the different developed catalytic systems has been done based on the required reaction conditions such as temperature, pressure and catalyst efficiency and availability. From now on, in order to mitigate the effect of anthropogenic CO<sub>2</sub> emissions, considering the global situation of energy deficiency, all processes that contemplate CO<sub>2</sub> uses and conversion, especially those involving high energy consumption, must use green and renewable energy, (sun, wind, water), to be sustainable and efficient.

In Figures 7 and 8 we show the different processes reported in the present revision and which uses advanced multifunctional materials based on zeolites and OMS and which will be developed below.



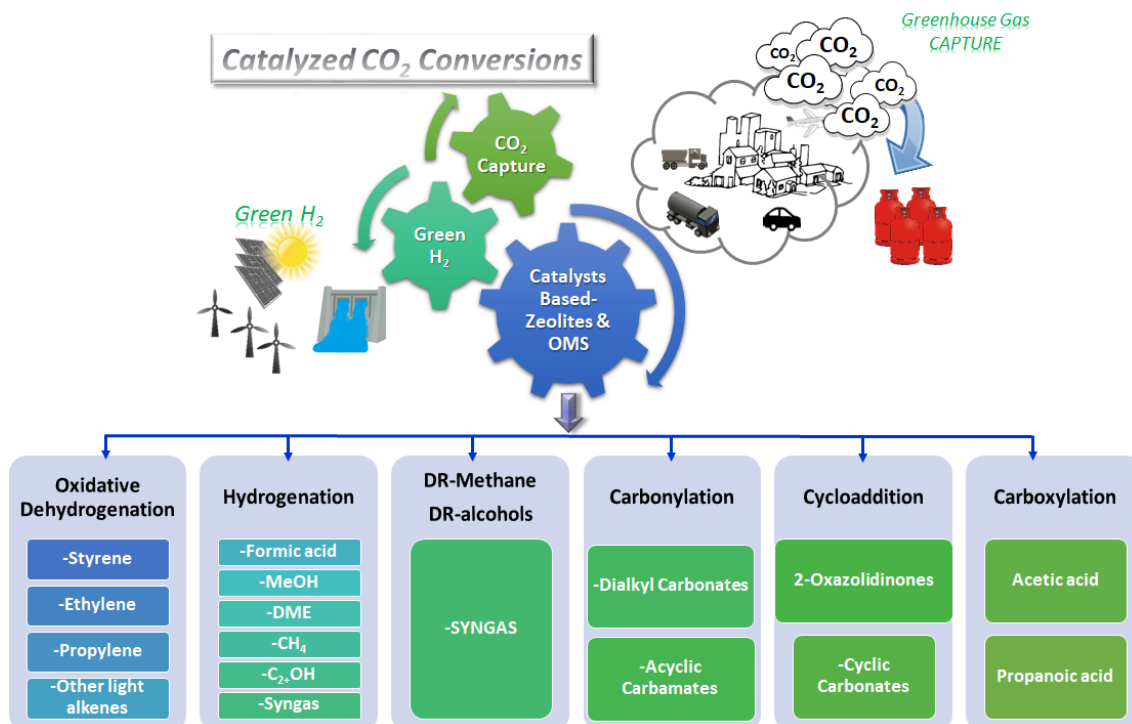


Figure 7. CO<sub>2</sub> conversion into chemicals and fuels covered in this review.

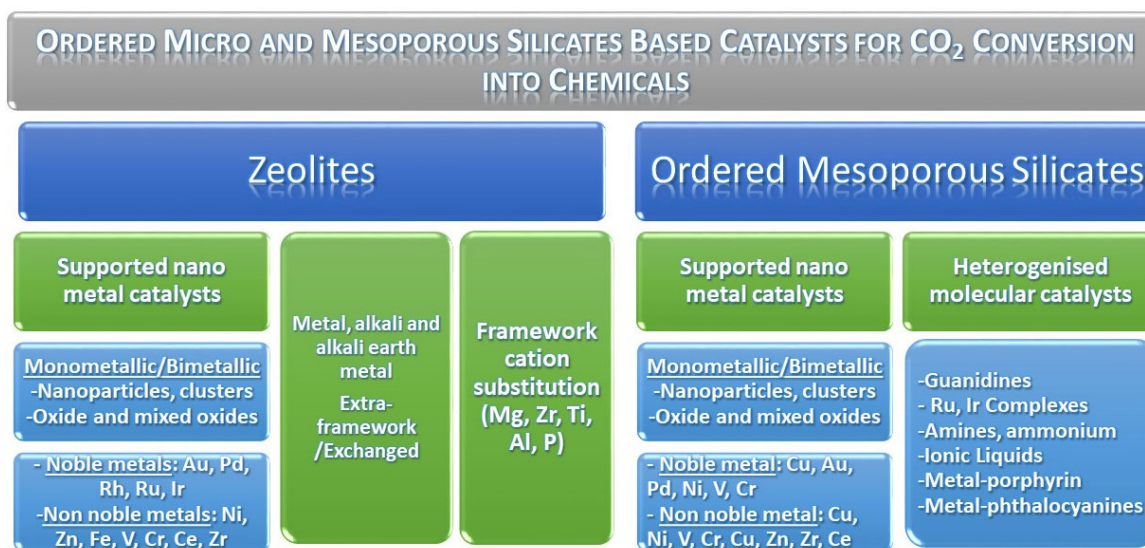


Figure 8. Zeolite- and OMS-based catalysts for the CO<sub>2</sub> conversion to chemicals and fuels covered in this review.

## B Catalytic conversion of CO<sub>2</sub>

### 1 Synthesis of carbonates

Organic carbonates constitute an important class of intermediates that can be synthesized through sustainable and environmentally-friendly process using CO<sub>2</sub> as raw materials, “the carbonyl green route”. Moreover, the synthesis of organic carbonates is an attractive, valuable and promising approach for CO<sub>2</sub> utilization since it involves 100% atom economy. Organic carbonates constitute important green raw materials for the synthesis and substitution of a large

number of toxic and/or volatile compounds such as phosgene, epoxides or cyanates, due to their especial properties as polarity and solubility, good biodegradability, harmless and chemical versatility.<sup>90-93</sup> Thus they find application in numerous fields as intermediates, fine and commodity chemicals,<sup>94</sup> solvents,<sup>95</sup> agrochemicals, monomers for polymers industry<sup>96</sup>, electrolytes for lithium ion batteries<sup>97</sup> and also lubricants (Figure 9).<sup>98-100</sup> Organic carbonates have been synthesized conventionally by reacting highly toxic and hazardous phosgene with alcohols or diols.<sup>101</sup> Every year, high amounts of organic cyclic and linear carbonates are produced for a total market of about 18 million tons per year within 80.000 tons of cyclic carbonates of which 40.000 tons per year are produced from CO<sub>2</sub>.<sup>102</sup>

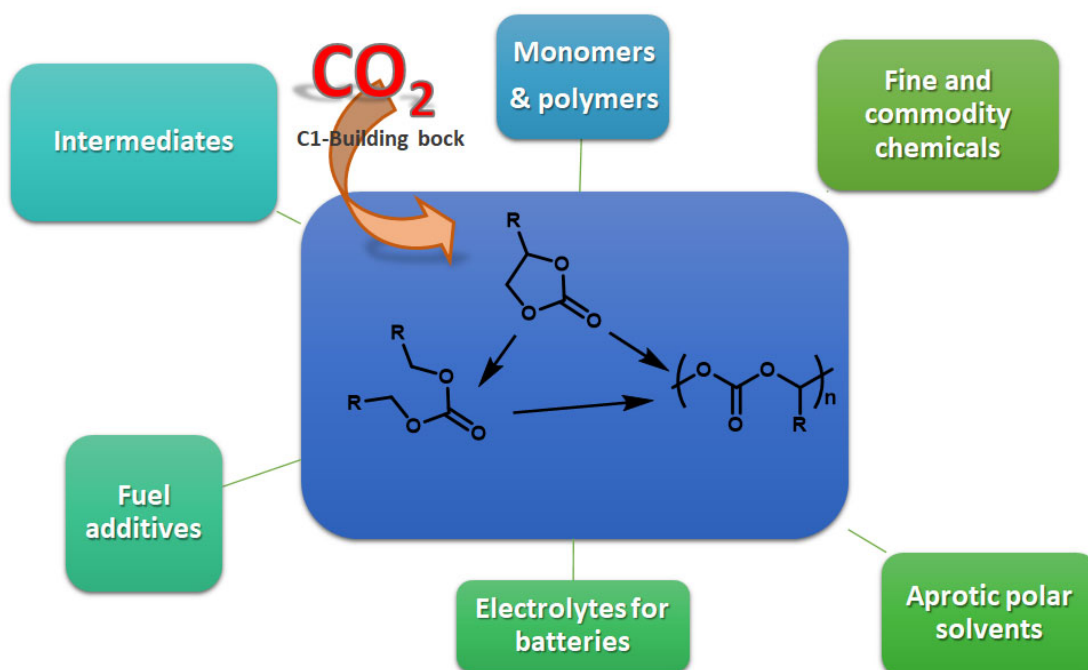
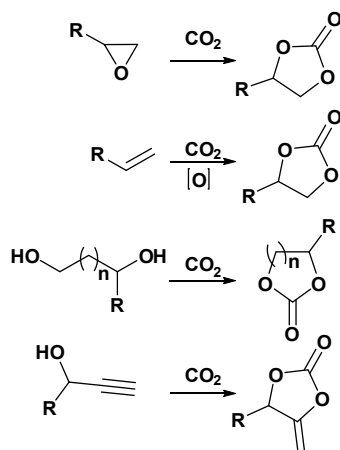


Figure 9. Carbonates applications.

### 1.1. Synthesis of cyclic carbonates

Cyclic carbonates find numerous application due to their polarity, high boiling point, low toxicity and good biodegradability. Different direct synthetic pathways from CO<sub>2</sub> can be followed to prepare cyclic carbonates from diols, epoxides, propargylic alcohols and olefins (Scheme 1).



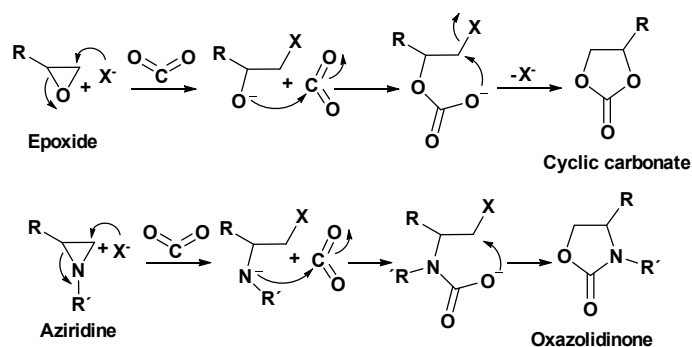
**Scheme 1.** Different pathways to the synthesis of cyclic carbonates from CO<sub>2</sub>.

### 1.1.1. Synthesis of cyclic carbonates via cycloaddition

#### a) Introduction

An attractive and important approach to convert CO<sub>2</sub> is the catalytic coupling of CO<sub>2</sub> with high-energy three-membered ring substrate or cycloaddition, especially, with epoxides and aziridines since important intermediates in the synthesis of chemicals and fine chemicals can be produced. Moreover, cycloaddition of CO<sub>2</sub> and three-membered ring molecule is 100% atom economy reaction and is environmentally friendly helping to mitigate the CO<sub>2</sub> environment impact.

Cycloaddition usually involves three steps: ring opening, CO<sub>2</sub> insertion and ring closure (Scheme 2).<sup>103–107</sup> The ring opening is accelerated by nucleophilic attack, for example, an halide, while the use of a Lewis acid or an hydrogen bond donor induce the polarization of the epoxide ring, while the use of a Lewis base favours the adsorption and activation of CO<sub>2</sub>.



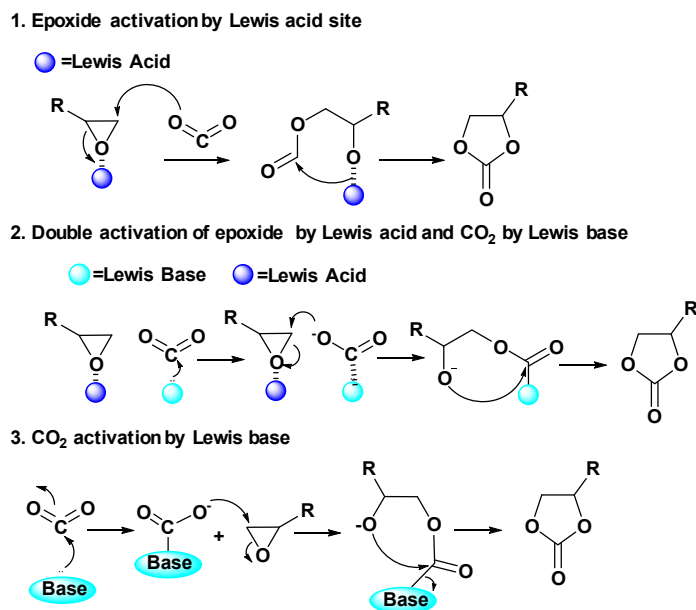
**Scheme 2.** Possible mechanism of cycloaddition for the preparation of cyclic carbonates or oxazolidinones assisted by nucleophile attack (X<sup>-</sup>).

Cyclic carbonates have conventionally been synthesized by reacting harmful reactant phosgene with diols, with the corresponding formation of hydrochloric acid.<sup>108</sup> Then, the synthesis of five-membered cyclic carbonates via cycloaddition of epoxides with CO<sub>2</sub> constitutes a straightforward, green and safe alternative to toxic reagents such as phosgene or its derivatives. Therefore, considering “green chemistry” and “atom economy” principles, cycloaddition

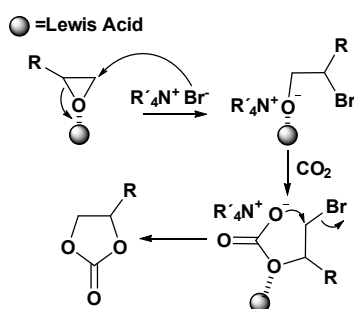
represents a very attractive process. Cyclic carbonates<sup>109</sup> are stable and find a large number of applications in chemical industry,<sup>110,111</sup> specially in polymers industry (adhesives and foams).<sup>112</sup> Moreover, a peculiarity of organic carbonates is their non-toxicity, good biodegradability and their high boiling point and high solvency making them useful aprotic polar solvents.<sup>113</sup> The preparation of carbonate constitutes a great case of CO<sub>2</sub> application as a chemical feedstock with economic and environmental benefits.

b) Reaction mechanism

The synthesis of cyclic carbonate incorporating CO<sub>2</sub> involves three steps: firstly the epoxide ring-opening (rate determining step),<sup>114</sup> followed by the CO<sub>2</sub> insertion and finally, the carbonate ring-closure.<sup>115,116</sup> Different designs of catalytic systems have been followed considering CO<sub>2</sub> and/or epoxide molecules activation. Usually, the catalytic system is composed by one or two catalytic functions consisting of a Lewis acid center for the activation of epoxide and/or CO<sub>2</sub> molecules and a Lewis base center that acts as nucleophile. [Scheme 3](#) illustrates different activation mechanisms taking into account various catalytic systems. One of them involves the use of N-based co-catalyst such as tetra-alkyl ammonium halide though this constitutes the main drawbacks from environmental and economic standpoints ([Scheme 4](#)). Homogeneous organocatalysts were developed that constitute an attractive alternative since they offer different advantages such as price, readily availability and free metal contaminants. The catalytic properties of several organocatalysts based on ammonium,<sup>117,118</sup> phosphonium,<sup>119–121</sup> and imidazolium salts,<sup>122–124</sup> as well as organic amines<sup>125</sup> have been reported. Nevertheless, organocatalysts present some drawbacks such as low activity and requirement of high loading and harder reaction conditions. Numerous group III–V transition metal complexes have been used as Lewis acid catalysts in the homogeneous and heterogeneous phases to perform cycloaddition of CO<sub>2</sub> with epoxides.<sup>126</sup> A large number of works reported the use of metal complex catalysts such as zinc<sup>107</sup> and aluminum alkyls, tin complexes,<sup>127,128</sup> organoantimony halide or alkali metal salts<sup>129</sup> in the presence of a basic co-catalyst for the preparation of cyclic carbonates. Nevertheless, despite the high catalytic activity, their use involves important limitations such as toxicity, water and air sensitivity, catalyst recycle, tedious handle and work-up, hazardous wastes production and severe reaction conditions (temperatures, CO<sub>2</sub> pressure), which prevent industrial application due to high energy and economical costs. Therefore, the interest to develop new heterogeneous and multifunctional catalysts is constant and topical, and numerous attempts have been reported in the literature.<sup>117,130</sup>



**Scheme 3.** Catalytic activation of CO<sub>2</sub> and/or epoxide for cycloaddition to afford cyclic carbonate.



**Scheme 4.** Catalytic activation of epoxide for cycloaddition to afford cyclic carbonate in the presence of co-catalyst.

c) Zeolite-based catalysts for the synthesis of cycli carbonates

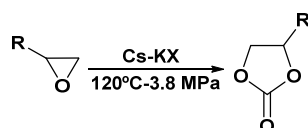
i) *Basic Zeolites*

Given that CO<sub>2</sub> is acidic and inert, the increase of catalysts basicity is required to promote CO<sub>2</sub> adsorption, activation and reactivity.<sup>131</sup> Since zeolites are well-known for their intrinsic acid catalytic properties, their use for the activation of CO<sub>2</sub> is not possible when in acidic form, and strategic modifications or functionalization are required in order to increase their basic properties. In the case of zeolites (silicoaluminates), different strategies were studied to modify the basicity,<sup>132</sup> which is associated to the presence of framework oxygen atoms, and their strength is related to the density of negative charge. Consequently, the zeolite basicity, i.e. the negative charge on oxygen atom, is a function of framework and extra-framework composition and zeolite structure, as was said before. Calculation of the average Sanderson electronegativity allows to quantitatively determine the average charge on the oxygen when the framework composition is varied.<sup>132–134</sup> To modify and enhance the basic properties of zeolites two main approaches have been explored.<sup>41–44</sup> The first consists in introducing within the pore system of

alkali metal clusters and oxide/hydroxide particles, and the second attempt to modify the intrinsic basicity of the framework oxygen varying the cation framework or the exchange of cations with low electronegativity cations such as alkali metal cations, in extraframework positions.

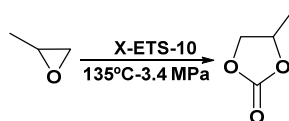
\* *Cation exchanged zeolites as catalysts for the preparation of cyclic carbonates*

The cycloaddition of CO<sub>2</sub> with various epoxides on Cs/KX zeolite through a Lewis base activation mechanism (Scheme 2, 3) has been explored. The catalytic performance of Cs/KX<sup>131,135</sup> zeolite was compared to different solid bases such as KX, Cs/Al<sub>2</sub>O<sub>3</sub> and MgO at 140°C and 2 MPa CO<sub>2</sub> pressure. For all cases the carbonates yields were low and maximum 19 % 1,3-dioxolan-2-one yield was reached in the presence of Cs/KX (Table 1, Entries 1-2; Scheme 5). This study revealed that reactivity was influenced by base strength, porosity, and Lewis acidity of the catalysts.



**Scheme 5.** Formation of cyclic carbonates in the presence of Cs-KX zeolites.

The catalytic performance of various alkali- and alkaline-earth-exchanged ETS-10 zeolites was compared for the cycloaddition to produce propylene carbonate at 135°C and 0.2 MPa CO<sub>2</sub> pressure.<sup>136,137</sup> The alkali-exchanged catalysts exhibited significantly higher activity than the alkaline-earth-exchanged catalysts. The difference in activities was found to be directly associated with the partial negative charge of the oxygen atoms in the structure, the higher the basic strength, the higher the catalytic activity, being the basic strength controlled by the electropositivity of the extra-framework cation.<sup>132</sup> Additional studies with exchanged X and ETS-10 zeolites showed that the presence of water enhanced the reaction rate owing to the enhancement of the Brønsted acidity. Adsorption of small amount of water contributed to the formation of surface OH groups and induced a better-tuned acid–base active sites required for the cycloaddition as was presented before when discussing the reaction mechanism.<sup>137</sup> Nevertheless, the carbonates yield remained low <15% (Table 1, Entries 3-4; Scheme 6), as a consequence of the usually weak basicity presented by zeolites and which is an important issue for the CO<sub>2</sub> activation.



**Scheme 6.** Formation of propylene carbonate in the presence of exchanged ETS-10 zeolites.

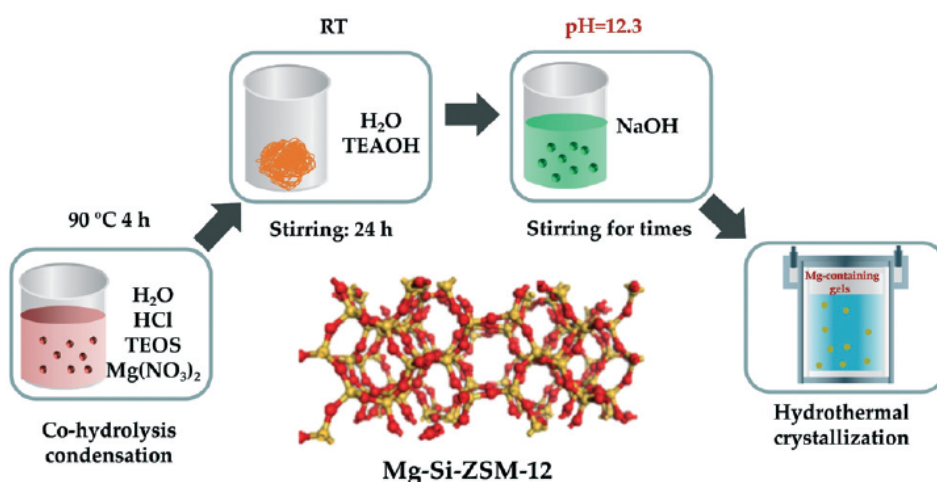
\* *Effect of the framework cation substitution in zeolites on the catalytic activity for cyclic carbonates production*

- Phosphorous framework

The introduction of phosphorous in a zeolite framework can result in materials with base properties such as SAPOs (Silicoaluminophosphate)<sup>138</sup> and ALPOs<sup>139</sup> (aluminophosphate crystalline microporous aluminophosphate materials). In line, a microporous silicoaluminophosphate SAPO-56 with AFX topology (tridimensional small pore structure with cages) was tested as catalyst for the synthesis of chloropropene carbonate. The small pore size ( $\sim 3.4 \times 3.6 \text{ \AA}$ ) is similar to the kinetic diameter of several gas molecules and specially CO<sub>2</sub>. Therefore, SAPO-56 offers special characteristics for CO<sub>2</sub> capture and/or conversion.<sup>140-142</sup> The synthesis was performed under microwave heating, and its catalytic properties due to both Brønsted and Lewis acid sites associated with Al framework atoms and OH groups were checked for the synthesis of chloropropene carbonate.<sup>143</sup> Good catalytic performance was registered for SAPO-56 synthesized under microwave, with 84.8 % chloropropene carbonate yield, at 110°C, 0.1 MPa CO<sub>2</sub> pressure, besides this sample presented lower amount of Brønsted acid sites 1.240 versus 1.701 mmol.g<sup>-1</sup> (Table 1, Entry 5). The recyclability of the samples was checked and noticeable change in the catalytic performance of both catalysts were not observed. SAPO-56 presents interesting catalytic properties and stability and is a low-cost catalyst. Nevertheless, further literature search within the patent and open literature indicated that the investigation was not pursued.

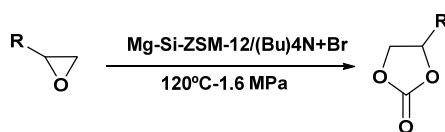
- Alkaline-earth metal ions framework

Recently, different approaches were explored for the construction of basic Al-free zeolites by the framework incorporation of metal ions with low electronegativity and so create new basic sites with improved basicity. Likewise, a family of alkaline-earth metal ions (Mg, Ca, Sr or Ba)-silicalite-1, MS-1 metallosilicate zeolites, through direct one-pot hydrothermal synthesis was reported.<sup>144</sup> In line, alkaline-earth metal framework-substituted ZSM-12 zeolites were prepared and specifically Al-free Mg-Si-ZSM-12 zeolites with unidimensional 12 member ring pores (12MR) and different Mg contents were prepared with mostly tetrahedral Mg species and stable in contact with water (Figure 10).



**Figure 10.** Preparation of Mg-framework-substituted ZSM-12 zeolites with unidimensional 12 member ring pores (12MR). Reprinted with permission from ref.<sup>145</sup>. Copyright 2019, Royal Society of Chemistry.

Accordingly, the cycloaddition of different substituted epoxides was performed in the presence of Mg-Si-ZSM-12 and a widely used efficient co-catalyst, tetrabutylammonium bromide.<sup>145</sup> The Mg-Si-ZSM-12/tetrabutylammonium bromide catalytic system exhibited high catalytic activity for the cycloaddition of CO<sub>2</sub> with various aromatic, alkyl and etheryl epoxides producing cyclic carbonates with high yield and selectivity at relatively low temperature (60-90 °C) and 0.1 MPa CO<sub>2</sub> pressure (Scheme 7). The catalytic performance of Mg-Si-ZSM-12 was compared with those of Mg-containing silicalite-1 (MgS-1) and MgO. With MgS-1 and MgO the conversion was 70 and 75 %, respectively, while the conversion was of 95 % in the presence of Mg-Si-ZSM-12 under identical reaction conditions. The higher activity was attributed to the higher strength of the basic sites Mg-Si-ZSM-12 (Table 1, Entries 6-10). A recycling test revealed the stability of styrene oxide conversion and selectivity to phenyl dioxolane over five runs. These results evidence the high efficiency of Mg-containing MTW zeolite for CO<sub>2</sub> fixation under mild conditions.



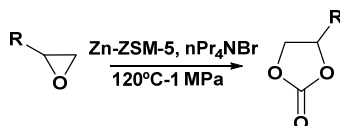
**Scheme 7.** Formation of cyclic carbonates in the presence of Mg-Si-ZSM-12/(Bu)<sub>4</sub>N<sup>+</sup>Br<sup>-</sup> catalytic system.

ii) *Effect of the presence of Lewis acid sites in zeolites on the catalytic activity for cyclic carbonates production*

A multifunctional Zn-HZSM-5 catalyst with Brønsted acidity (acid T-OT hydroxyles), Lewis acidity (non-framework Al and Zn sites) and Lewis basicity was used as catalyst in the presence of tetra-n-propylammonium bromide (nPr<sub>4</sub>NBr) for the preparation of different cyclic carbonates with high yield and selectivity at 140 °C and 3 MPa CO<sub>2</sub> pressure.<sup>146,147</sup> The high availability of active centers make possible the optimum activation of CO<sub>2</sub> over metallic center and activation of epoxides over both metal center and through hydrogen bond. Then, high catalytic activity was achieved with high yield (up to 99%) in the presence of nPr<sub>4</sub>NBr for the preparation of various



alkyl, aromatic and ether epoxides (Table 1, Entries 11-18; Scheme 8). Larger scale experiments were performed and showed the reproducibility of the process as well as one reuse of the catalyst was successfully performed. The main issue of the procedure is the use of 0.5 mol% of  $n\text{Pr}_4\text{NBr}$  and relative high  $\text{CO}_2$  pressure. However, this multifunctional heterogeneous zeolitic catalyst can be considered as a possible path to the incorporation of upgrading  $\text{CO}_2$  into valuable chemicals. Further literature search for this catalytic system within the patent and open literature indicated nevertheless that the investigation was not pursued.



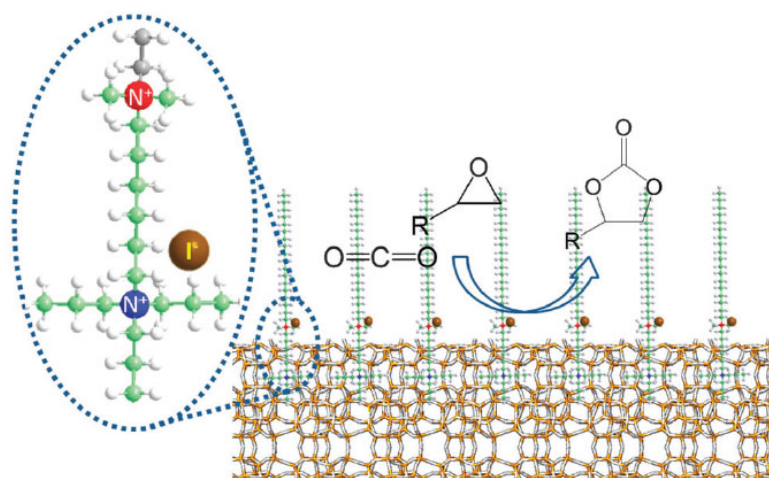
**Scheme 8.** Formation of propylene carbonate in the presence of Zn-ZSM-5 zeolites.

The catalytic performance of titanosilicate molecular sieves TS-1 and TiMCM-41 bearing Lewis acid active sites, in the presence of a N-based co-catalyst, were explored to prepare cyclic and linear carbonates by cycloaddition with  $\text{CO}_2$ , following the mechanism in Scheme 4.<sup>148,149</sup> The authors claimed a possible synergism between the catalyst and co-catalyst, being the nucleophilicity of the nitrogen atom increased by the electrophilic interaction of the  $\text{Ti}^{4+}$  with the epoxide. High yields were achieved at 120-140°C, 0.69 MPa  $\text{CO}_2$  pressure, starting from epoxides or olefins. Moreover, the reaction can occur without  $\text{CH}_2\text{Cl}_2$  as solvent. However, the reported catalytic data are low and the zeolite based catalysts cannot be considered as efficient in terms of activity and selectivity under mild reaction conditions (Table 1, Entries 19-23).

*iii) Zeolite catalysts incorporating quaternary ammonium halide for cyclic carbonates production*

Structure directing agents (SDA) play a fundamental role in the steps of nucleation and crystal growth during zeolite synthesis, and they have to be extracted or burned off from the crystallized zeolite, to make free and accessible the pore system. However, one way to take advantage of the SDA is to use it as catalyst.<sup>150,151</sup> Though, for their use as catalysts, SDA-zeolite composite materials have to present high stability against leaching and severe reaction conditions, moreover, active sites have to be accessible. Following this approach, highly efficient organic-inorganic hybrid zeolites have been prepared by halogen anion-exchange.<sup>152</sup> Indeed, instead of extracting the SDA out, lamellar MFI materials prepared with  $\text{C}_{18}\text{H}_{37}\text{Me}_2\text{N}^+(\text{CH}_2)_6\text{N}^+\text{Pr}_3\text{]Br}_2^-$  as SDA were used directly as active sites ion-exchanged with various halogen anions ( $\text{I}^-$ ,  $\text{Cl}^-$  and  $\text{Br}^-$ ) (Figure 11). As aforementioned, the use of quaternary ammonium halides have been widely used to perform the cycloaddition of  $\text{CO}_2$  with epoxide. The iodide exchange material (LMFI-I) was the most efficient catalyst for the cycloaddition of  $\text{CO}_2$  with different epoxides. The authors showed the cooperation between ammonium cations of the

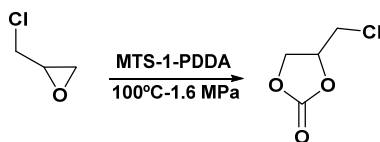
SDAs and the iodide anions to catalyze the selective cycloaddition of CO<sub>2</sub> and different epoxides without solvent and additives, at 140°C and 2 MPa CO<sub>2</sub> pressure, with conversion and selectivity up to 99 and 95%, respectively (Table 1, Entries 24-28).



**Figure 11.** Cycloaddition of epoxides and CO<sub>2</sub> over halogen anion-exchanged hybrid zeolite catalyst. Reprinted with permission from ref.<sup>152</sup>. Copyright 2014, Royal Society of Chemistry.

The cycloaddition mechanism involves approach of the epoxide molecule to the accessible ammonium cation followed by the iodide attack, leading to oxy-anion which in turn attacks the carbon dioxide to finally reach ring closure (Scheme 2). The hybrid material exhibited a good stability and reusability. The chloroethylene carbonate yield was stable around 90% for the first three runs and decreased to 79% for the fourth use, remaining the selectivity constant at 95%. This approach provides a catalyst with an interesting catalytic performance and potential.

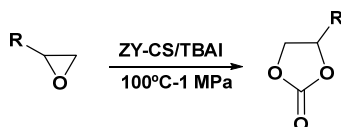
Following the same strategy, a mesoporous TS-1 zeolite (MTS-1) was prepared using polydiallyldimethylammonium chloride (PDDA) as structure directing agent (SDA). The mesoporous TS-1 zeolite incorporating the SDA offers both Lewis basic sites and Lewis acid sites associated to the presence of SDA and framework Ti species. The bifunctional catalyst exhibited good catalytic properties for the cycloaddition reaction after treatment with hydrochloric acid. The yield of chloropropene carbonate was up to 98 % at 120°C, 1.6 MPa CO<sub>2</sub> pressure for 6 h and in acetonitrile as solvent (Scheme 9). The mesoporous-TS-1 catalyst was reused for 4 runs without noticeable deactivation that was attributed to the high stability of the zeolite structure and template agents that did not diffuse out the pores. Following the same procedure, propene, styrene and isobutylene carbonates were obtained with 80, 35 and 14 yield%, respectively, showing a limited scope of the catalyst together with the necessity to use solvent (Table 1, Entries 29-32).<sup>153</sup> This materials presented limited accessibility to the active sites due to poor pore channel connectivity and low surface areas and pore volume.



**Scheme 9.** Formation of chloropropene carbonate in the presence of MTS-1-PDDA zeolite catalyst.

Recently, basic ZSM-5<sup>154</sup> zeolite with mesopores has been prepared using 1,4-diazabicyclo[2.2.2]octane as structure directing agent and the calcined sample was reacted with aqueous ammonia to provide a basic ZSM-5 with mesopores in the crystallites. The Basic-Meso-ZSM-5 exhibited higher activity than Meso-ZSM-5 for the cycloaddition in ionic liquid media. Nevertheless, the activity of Basic-Meso-ZSM-5 is low with yield close to 7 % for the synthesis of chloroethylene carbonate. The author attributed the low activity to the no-CO<sub>2</sub> activation. When, the cycloaddition was performed in the presence of N,N-dimethyl amino pyridine (DMAP), the yield increased until 80 %, and the catalytic composition was successfully used to the synthesis of different carbonates at 120°C and 0.8 MPa CO<sub>2</sub> pressure (Table 1, Entries 33-35). Nevertheless, the catalytic data of DMAP alone under the same reaction conditions were not reported.

An interesting mesoporous zeolite-chitosan composite (ZY-CS) with high thermal stability was prepared from Serbian zeolite (kinoptiolite) and chitosan (CS). Characterization study showed that ZY was uniformly dispersed in the CS matrix incorporating negatively charged sites of Al-zeolite (Si-O<sup>-</sup>) and the positively charged sites of chitosan (NH<sub>3</sub><sup>+</sup>). Furthermore ZY-CS composite presented enhanced CO<sub>2</sub> adsorption capacity due to the mesoporous structure and interaction sites, favourable to the adsorption and activation of CO<sub>2</sub>. The catalytic properties of CS and ZY-CS composite were checked for the cycloaddition reaction between CO<sub>2</sub> and epoxides in the presence of a co-catalyst TBAI (tetra-n-butylammonium iodide) to activate CO<sub>2</sub>. Moderate to low propylene carbonate yields of 61% and 32% in the presence of ZY-CS and CS were achieved, respectively after 6h of reaction time, 100°C and 1 MPa CO<sub>2</sub> pressure. While for chloropropene carbonate the yield was 99.5% (Table 1, Entries 36-38; Scheme 10).<sup>155</sup> These results indicated a reduced scope of the catalyst.

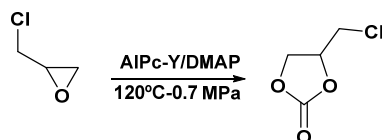


**Scheme 10.** Formation of cyclic carbonate in the presence of ZY-CS/TBAI catalyst.

*iv) Encapsulation of organometallic complexes into zeolites for cyclic carbonates production*

Other strategies to heterogenise active metal complexes consist in encapsulating the catalytic active species. Indeed, zeolites offer the possibility of coupling the shape selectivity of their pore

system (channels and cages) with the specific reactivity of metal complexes. The zeolite structure makes possible the trapping of metal complex inside the pores without bonding to the surface, named as “ship-in-a-bottle”,<sup>156</sup> and referring to zeolite encapsulated metal chelates and cluster complexes. Metal phthalocyanines were encapsulated as well in Y zeolite and their efficient catalytic activity in the presence of N-based co-catalysts (Lewis base) was reported for the synthesis of cyclic carbonates.<sup>157,158</sup> The catalytic performance of zeolite-Y-encapsulated complexes was higher than the homogeneous and silica-supported phthalocyanine complexes ones. The catalytic activity for the synthesis of chloropropene carbonate of different metal complexes were compared and followed the order Co < Ni < Cu. A study of addition of Lewis-base as co-catalyst showed the highest activity with N,N-dimethyl aminopyridine (DMAP) (mechanism [Scheme 4](#)). For the synthesis of chloropropene carbonate, the best catalytic data were achieved in the presence of AlPc-Y at 120°C (98% conversion, 100% selectivity) ([Table 1, Entries 39-40; Scheme 11](#)). It is well known that Lewis bases form coordination complexes with metal phthalocyanines and that polar solvents compete with the Lewis bases to form the complex and modify the activity.<sup>159</sup> Therefore, under optimised reaction conditions, in dichloromethane, at 120°C and 0.69 MPa CO<sub>2</sub> pressure, carbonates yields up to 98 and 93 % using epichlorohydrin and propylene oxide as epoxide, respectively, were obtained. The AlPc-Y hybrid catalyst was reused for three consecutive runs without loss of activity and selectivity. A good catalytic performance is exhibited but the tedious preparation and catalyst cost may limit its application.



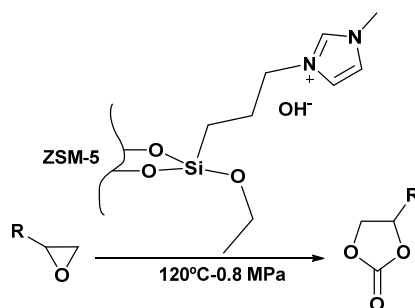
**Scheme 11.** Formation of chloropropene carbonate in the presence of AlPc-Y/DMAP catalyst.

Co and Mn supported metalloporphyrins on NaX were prepared, characterized and used as catalysts in the presence of phenyltrimethylammonium tribromide as co-catalyst for the preparation of propylene carbonate. NaX supported tetra-metalloporphyrin catalysts exhibited higher catalytic results than unsupported ones. Maximum 95.6 % PC selectivity at 94.5 % conversion, at 120°C for 5 h and 3 MPa CO<sub>2</sub> pressure was reached in the presence of Co porphyrin supported complex that could be successfully reused three times ([Table 1, Entry 41](#)).<sup>160</sup> This type of catalysts exhibits good catalytic performance however their economic cost prevents their application.

v) *Immobilization of ionic liquids into zeolites for cyclic carbonates production*

In the last twenty years, the discovery and use of ionic liquids has received much interest from the scientific community and has been the subject of numerous publications.<sup>161,162</sup> Ionic liquids (ILs) such as quaternary ammonium, phosphonium, imidazolium and pyridinium and their functionalised forms have found numerous application in organic chemistry and chemical process as catalysts or solvents. The catalytic activity of ILs and supported ILs to perform the cycloaddition of CO<sub>2</sub> and epoxides was explored and revealed the suitable catalytic properties of imidazolium based ionic liquids.<sup>163–165</sup>

The functionalization of nanocrystalline zeolite (Nano-ZSM-5) with various amines (primary, secondary, and tertiary) subsequently converted into quaternary ammonium hydroxide and basic ionic liquids was described for the synthesis of cyclic carbonates.<sup>166</sup> Catalytic results showed that in the amine based catalysts, the activity decreased in the following order: tertiary > secondary > primary amine, and the ILs-functionalized catalysts exhibited higher catalytic performance than amine-functionalized ones. Moreover, OH<sup>-</sup> based ILs exhibited better activity than HCO<sub>3</sub><sup>-</sup> and Cl<sup>-</sup>. The Basic-Nano-ZSM-5-Pr-MIM-OH exhibited the highest activity for the cycloaddition of CO<sub>2</sub> and epichlorohydrin and other aliphatic and aromatic epoxides, at 0.8 MPa CO<sub>2</sub> pressure, 120°C and 4-12 hours (Table 1, Entries 42-44; Scheme 12). The recycling study showed that catalyst structure and properties were stable for five recycles.



**Scheme 12.** Preparation of cyclic carbonate in the presence of basic-Nano-ZSM-5-Pr-MIM-OH catalyst.

The immobilization through chemical bonding of three poly-epichlorohydrin-methimidazole (polyether (PECH) imidazole) ionic liquids (PIILs) with amino, hydroxyl and carboxylic groups and the integrated co-catalyst, ZnBr<sub>2</sub>, on ZSM-5 zeolite was attempted, and their catalytic performance for cycloaddition reaction explored. The three immobilized catalysts consist of polyether macromolecular chains as the main chains and imidazole rings as the branched chains. ZSM-5-HOOC-[PECH-MIM]Cl/[ZnBr<sub>2</sub>] exhibited the best catalytic performance that was attributed to small amount of HOOC-[PECH-MIM]Cl/[ZnBr<sub>2</sub>] physically adsorbed, providing acid ability for ring opening. Therefore, propylene carbonate was synthesized at 130° C, 2.5 MPa CO<sub>2</sub> pressure, and 0.75 h, with 98.3% conversion and 97.4% selectivity. The reuse study showed that

the good catalytic activity was maintained after eight cycles (68.6% yield) (Table 1, Entry 45; Scheme 13).<sup>167</sup>

**Scheme 13.** Preparation of propylene carbonate in the presence of ZSM-5-PIIL/[ZnBr<sub>2</sub>] catalyst.

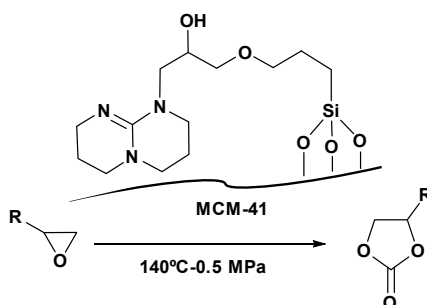
d) OMS-based catalysts for the preparation of cyclic carbonates

Mesoporous molecular sieves offer numerous opportunities as catalysts and supports due to their properties such as adjustable pore diameter, sharp pore distribution, large surface area and pore volume. Moreover, the presence of silanol groups on the surface enables chemical modifications through covalent bonding. Accordingly, much efforts have been devoted to the heterogenisation of metal organic species and organocatalysts using ordered mesoporous materials.

i) *Supported organocatalysts onto OMS for the preparation of cyclic carbonates*

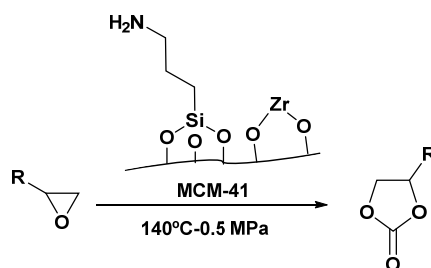
\* *Supported amine onto OMS*

Organic amines and supported ones have been reported to catalyse the cycloaddition of CO<sub>2</sub> and epoxides,<sup>168</sup> and so far, the mechanism in the presence of an organic base has not been well explored. One attempt to heterogenise guanidine MTBD (7-methyl-1,5,7-triazabicyclo[4.4.0]dec-5-ene) on MCM-41 to perform the cycloaddition of various substituted epoxides with CO<sub>2</sub> was reported.<sup>169</sup> Nevertheless, the results were lower in the presence of the heterogeneous guanidine than with the homogeneous one and long reaction time were required (70 h) for the synthesis of cyclic carbonate, at 140°C and 0.5 MPa CO<sub>2</sub> pressure (Table 1, Entries 46-51; Scheme 14). However, MCM-41-TBD showed the great advantage of solid catalysts that could be reused successfully, at least, for three recycles.



**Scheme 14.** Preparation of cyclic carbonates in the presence of MCM-41-TBD.

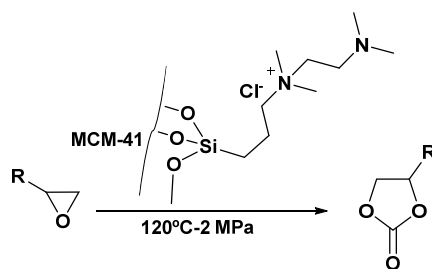
A bifunctional based MCM-41 material bearing Lewis acid and basic sites due to the presence of Zr framework and (3-aminopropyl)triethoxysilane was synthesized (APTES@ZrO<sub>2</sub>-MCM-41).<sup>170</sup> The cycloaddition of CO<sub>2</sub> and epoxide follows a mechanism of double activation through CO<sub>2</sub> activation by the amine functional group (nucleophile) and epoxide ring opening activation by Lewis acid sites through Zr atoms. The scope of the catalyst was shown through the preparation of different cyclic carbonates with yield up to 95%, in the presence of tetrabutylammonium iodide (TBAI) as co-catalyst, under 2 MPa CO<sub>2</sub> pressure, 80°C, without solvent and 3h of reaction time. Moreover, the catalyst was recycled for five runs with negligible loss of activity (Table 1, Entries 52-56; Scheme 15).



**Scheme 15.** Preparation of cyclic carbonates in the presence of APTES@ZrO<sub>2</sub>-MCM-41/TBAI.

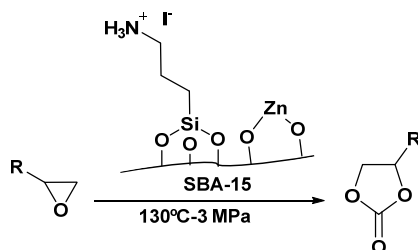
\* *Immobilization of quarternary ammonium salts onto OMS*

As aforementioned, quaternary ammonium salts exhibit high catalytic activity for the cycloaddition of epoxide and CO<sub>2</sub>. Considering the fact that silanol groups on the surface open possibilities of chemical modifications through covalent bonding, the condensations of different type of organo-silanes with OH groups were performed for the functionalisation of the mesoporous surface. Following this synthetic strategy, mesoporous molecular sieve catalysts based on alkylammonium and imizadolium (ionic liquids) have been prepared and used for the preparation of cyclic carbonates. In 2010, heterogeneous bifunctional MCM-41 catalyst with grafted quaternary ammonium salt with a terminal amino group was synthesized and used as catalyst for the preparation of cyclic carbonate by cycloaddition of CO<sub>2</sub> and epoxide followed by the transesterification with methanol to provide dimethyl carbonate. The bifunctional catalyst exhibited high catalytic activity and reusability for the preparation of numerous cyclic carbonates with yield up to 99%, at 120°C and 2 MPa CO<sub>2</sub> pressure (Table 1, Entries 57-63; Scheme 16).<sup>171</sup> This hybrid catalyst showed suitable catalytic performance with a wide scope and high reusability. The results are interesting and there is an incentive to achieve a less costly catalyst, based on this concept, for industrial applications.



**Scheme 16.** Preparation of cyclic carbonates in the presence of bifunctional MCM-41 catalyst.

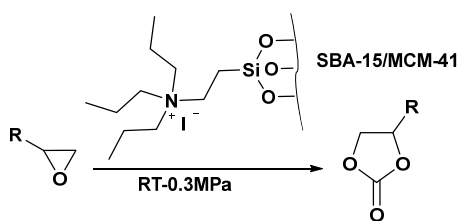
An improved bifunctional Zn/SBA-15 supported ammonium salt (NH<sub>4</sub>I-Zn/SBA-15) as single-component heterogeneous catalyst for the cycloaddition was developed. Previously, a reported Zn/SBA-15 catalyst coupled with DMF showed good catalytic properties for the cycloaddition of CO<sub>2</sub> with propylene oxide.<sup>172</sup> In the catalytic process, zinc active sites acted as Lewis acid activating epoxide and opening the ring, while DMF acted as co-catalyst to activate CO<sub>2</sub> for further conversion. However, the Zn/SBA-15/DMF catalyst presented drawbacks such as the need of a co-catalyst and leaching. Then, the new NH<sub>4</sub>I-Zn/SBA-15 composite exhibited higher catalytic performance, 93% yield and 99% selectivity for the synthesis of propylene carbonate at 130°C, 3 MPa CO<sub>2</sub> pressure and 12 h, without co-catalyst, were reached (Table 1, Entries 64-68; Scheme 17). In addition, other cyclic carbonates can be prepared and the catalyst can be easily reused with slight loss of activity after five recycles.<sup>173</sup>



**Scheme 17.** Preparation of cyclic carbonates in the presence of NH<sub>4</sub>I-Zn/SBA-15 composite.

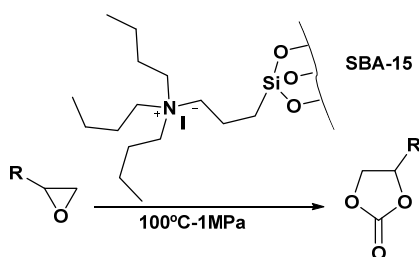
The catalytic performance of ammonium salt grafted on SBA-15 and MCM-41 materials were compared for the synthesis of styrene and hexene carbonates at room temperature, 0.3 MPa CO<sub>2</sub> pressure and without solvent.<sup>174</sup> MCM-41 catalyst exhibited higher activity than the SBA-15 catalyst. Furthermore, the recycle study showed higher recyclability of MCM-41 catalyst than SBA-15, since styrene carbonate yield was maintained for four cycles with the MCM-41 catalysts, while in the presence of SBA-15 catalyst the yield decreases after the third cycle from 86% to 20% (Table 1, Entries 69-70; Scheme 18). These materials worked under mild reaction conditions, at atmospheric pressure and room temperature, which made them interesting for a possible application in flow process.





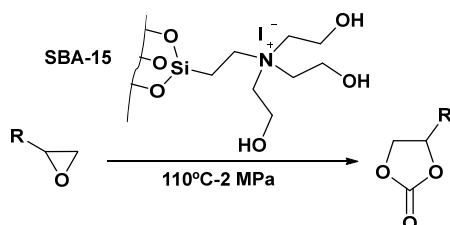
**Scheme 18.** Preparation of cyclic carbonates in the presence of ammonium salt grafted on MCM-41.

Similarly, the preparation and catalytic performance of N,N,N-tributyl-N-propylammonium iodide-functionalized on silica gel and SBA-15 was reported, and the synergetic effect of the silanol groups and tetrabutylammonium iodide salt was demonstrated.<sup>175</sup> Styrene and 1,2-buthylenecarbonates were synthesized under mild conditions, 1 MPa CO<sub>2</sub> pressure, 100°C for 4h (Table 1, Entries 71-72, Scheme 19). However, the reusability of the catalysts showed to be dependent on the nature of the support and the substrate.



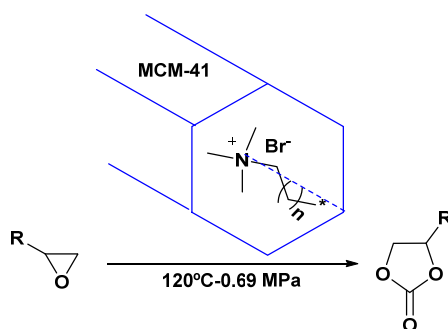
**Scheme 19.** Preparation of cyclic carbonates in the presence of N,N,N-tributyl-N-propylammonium iodide-functionalized on SBA-15.

Likewise, SBA-15-based catalyst exhibited a constant catalytic activity for five runs for 1,2-buthylenecarbonate synthesis and a constant decrease of catalytic activity for styrene carbonate synthesis. More recently, a propyl-triethanol-ammonium iodide grafted SBA-15 catalyst (TEA/SBA-15) was synthesized and successfully used in cycloaddition of CO<sub>2</sub> with epoxides at 110 °C and 2.0 MPa CO<sub>2</sub> pressure. The incorporation of OH groups introduces an important function for the activation of epoxides by the hydrogen-bonding donor group, favouring the ring opening and nucleophilic iodide attack. High yields were obtained and TEA/SBA-15 catalyst could be reused with good stability, at least for five runs, with a propylene carbonate yield, > 90%, and constant selectivity (99%) (Table 1, Entries 73-77; Scheme 20).<sup>176</sup>



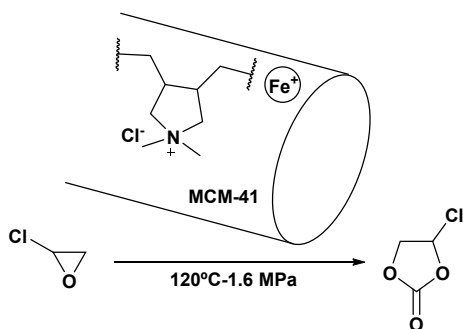
**Scheme 20.** Preparation of cyclic carbonates in the presence of propyl-triethanol-ammonium iodide SBA-15 catalyst.

The possibility of using organic templates (SDA) employed for the synthesis of micro and mesoporous materials as active sites for catalyzing the synthesis of cyclic carbonates using CO<sub>2</sub> has also been considered. Following that strategy, the as-synthesized MCM-41 with cetyltrimethyl ammonium as template showed to be an active and reusable catalyst for the synthesis of different cyclic carbonates at 120°C, 0.69 MPa CO<sub>2</sub> pressure and without solvent or co-catalyst.<sup>177</sup> Chloropropene, propene, styrene and butylene carbonates were obtained with 90-99% (Table 1, Entries 78-81; Scheme 21). MCM-41 catalyst was recycled eight times and unfortunately the catalytic activity decreased after the fifth recycle. The decrease in activity was attributed to partial loss of crystallinity (long-range ordering) of the catalyst. Interestingly, the as synthesized hybrid material offered interesting catalytic behavior under mild reaction conditions. Moreover, aryl carbamates via the reaction of amines, CO<sub>2</sub> and alkyl halides could be prepared.



**Scheme 21.** Preparation of cyclic carbonates in the presence of as-synthesized MCM-41 with cetyltrimethyl ammonium as catalyst.

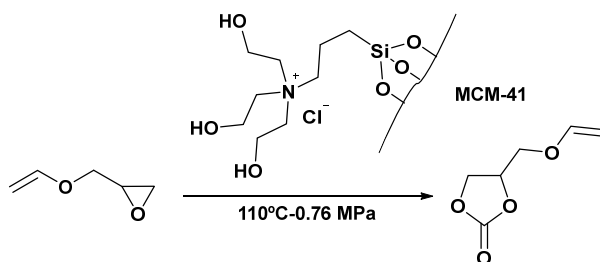
In 2020, the catalytic performance of two types of bi-functional iron doped mesoporous materials, Fe-HMS and Fe-MCM-41 containing the organic template (PDDA: Poly(diallyldimethylammonium)) was explored as catalyst for the synthesis of cyclic carbonates. The presence of PDDA and framework Fe species provide basic and acid active sites, exhibiting a synergetic effect and high catalytic activity for the cycloaddition.<sup>178</sup> CO<sub>2</sub>-TPD revealed that Fe-HMS offered more accessible basic sites and exhibited the highest activity. Moreover, Fe-HMS material showed higher stability and reusability than Fe-MCM-41. The Fe-MCM-41 deactivation was attributed to leaching of active species and low accessibility of the active site due to poor pore structure. In the presence of Fe-MCM-41 catalyst, good 79.7 yield% of chloro propene carbonate was obtained (Table 1, Entry 82; Scheme 22). Unfortunately, the catalyst showed limited reusability.



**Scheme 22.** Preparation of chloropopene carbonate in the presence of Fe-MCM-41 containing the organic template (PDDA) as catalyst.

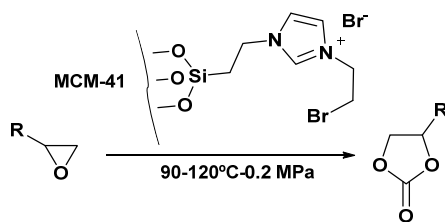
\* *Immobilization of ionic liquid onto OMS*

As was mentioned above, the catalytic activity of ionic liquids and supported ionic liquids for cycloaddition of CO<sub>2</sub> and epoxides was reported, as well as the suitable catalytic properties of imidazolium based ionic liquids.<sup>163–165</sup> Likewise, hybrid MCM-41 materials were prepared by immobilization of ionic liquids (ILs) (pyridine, triethyl (TEA), trihexyl and triethanol amine).<sup>179</sup> The study showed the effect of different parameters such as the number of active ammonium centres and steric and inductive effects, while moderate to low yield of allyl glycidyl carbonate were obtained, being highest 69.5% and 88.5% yield and selectivity, respectively, in the presence of TEA-MS41, at 110°C and 0.76 MPa CO<sub>2</sub> pressure (Table 1, Entry 83; Scheme 23).



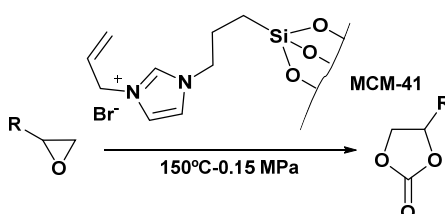
**Scheme 23.** Preparation of allyl glycidyl carbonate in the presence of propyl-triethanol ammonium chloride/MCM-41 catalyst.

More recently, the immobilization of imidazole (Imi) on MCM-41 (MCM-41-Imi/Br) and catalytic activity for cycloaddition was reported and styrene carbonate was successfully synthesized under solvent free conditions, 2 MPa CO<sub>2</sub> pressure and 90-120°C.<sup>180,181</sup> The quaternary imidazolium center activates CO<sub>2</sub> molecule providing a carbamate anion while ring opening of the epoxide occurs by bromide ion attack. A study of reusability showed a constant decrease in the conversion from 100 to 85% along four recycles (Table 1, Entries 84-88; Scheme 24). The loss in activity was attributed to the bromide ions loss.



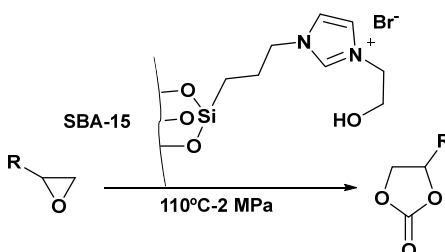
**Scheme 24.** Preparation of cyclic carbonates in the presence of MCM-41-Imi/Br catalyst.

More recently, the same group reported the preparation and catalytic activity of MCM-41 functionalized imidazolium-allyl bromide ionic liquid (MCM-41-Imi/All-Br) for the preparation of cyclic carbonates. MCM-41-Imi/All-Br exhibited moderate catalytic activity for the cycloaddition of CO<sub>2</sub> and different epoxides with yield up to 68.8 % of propylene carbonate, at 150°C and 1.5 MPa CO<sub>2</sub> pressure, without solvent. No data of reusability of the hybrid material were reported (Table 1, Entries 89-92; Scheme 25).<sup>182</sup>



**Scheme 25.** Preparation of cyclic carbonates in the presence of MCM-41-Imi/All-Br catalyst.

Similarly, 1,2,4-triazolium-based ionic liquids (TRILs) were immobilized on SBA-15 and used for cycloaddition varying catalyst and process parameters, such as functional groups, anions of the catalysts, temperature, pressure, reaction time and catalyst amount. Hydroxyl and carboxyl-functionalized 1,2,4-triazolium-based ILs immobilized on SBA-15 exhibited high catalytic performance due to synergetic effect between OH or COOH groups and the bromide anions through hydrogen bond activation of epoxide ring and nucleophilic attack, respectively. The catalyst showed good stability and could be reused over six cycles. At 110°C and 2 MPa excellent yield and selectivity were achieved (Table 1, Entries 93-98; Scheme 26).

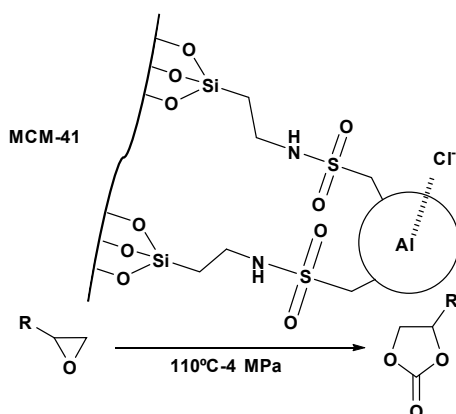


**Scheme 26.** Preparation of cyclic carbonates in the presence of TRILs/SBA-15 catalyst.

ii) *Immobilization of organometallic-complexes onto OMS for the preparation of cyclic carbonates*

Metallophthalocyanines constitute an important class of organometallic compounds with accessible cost and good chemical and thermal stability that have exhibited catalytic activity for

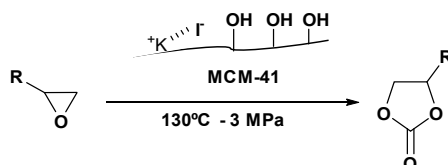
different reactions.<sup>183–185</sup> Aluminum phthalocyanine complex was covalently bonded to the MCM-41 surface and used as heterogeneous catalyst for synthesis of cyclic carbonates from carbon dioxide and epoxides at 110°C and 4 MPa CO<sub>2</sub> pressure. The immobilized phthalocyanine complex activity was based on TOF calculations and remained constant for ten recycling (Table 1, Entries 99-102; Scheme 27).<sup>186</sup>



**Scheme 27.** Preparation of cyclic carbonates in the presence of Cl-Al-Phtalocyanine/MCM-41 catalyst.

iii) *Supported salts onto OMS for the preparation of cyclic carbonates*

Alkali metal salts (Na, K, Li) have been used to perform cycloaddition of CO<sub>2</sub> with epoxide since they present some advantages such as abundance, low-cost, and non-toxicity.<sup>187</sup> In contrast, their low activity made necessary the use of co-catalyst in large amount. This together with a neutralization step were the main issues for environment and industrial perspectives.<sup>188,189</sup> Recently, an interesting low-cost supported KI/MCM-41 catalyst was prepared by the incipient wetness impregnation method. KI/MCM-41 catalyst with 35wt% loading of KI exhibited very high catalytic activity for the synthesis of various carbonates with yield up to 96%, under 3 MPa CO<sub>2</sub> pressure, 130°C and 5 hours (Table 1, Entries 103-107; Scheme 28). The catalyst was easily recovered and could be reused but a marked loss of activity was observed. In fact, the propylene carbonate yield decreased from 99.3 to 62.4 % after the fourth use.<sup>190</sup> The decrease in activity was attributed to possible adsorption of products and reagents that block accessibility to the active sites while no characterization data of the spent catalyst was performed.




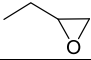
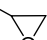
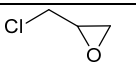
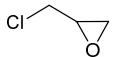
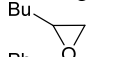
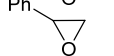
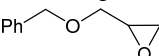
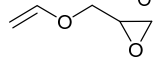

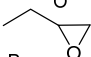
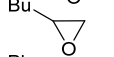
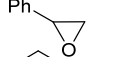
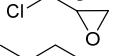
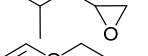
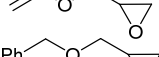
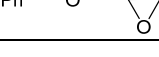
**Scheme 28.** Preparation of cyclic carbonates in the presence of KI/MCM-41 catalyst.

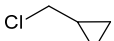
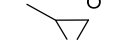
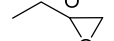
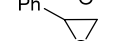
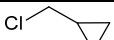
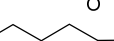
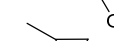
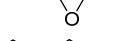
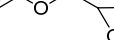
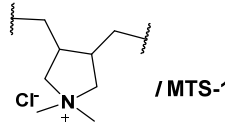
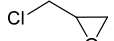
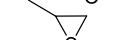
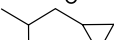
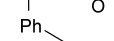
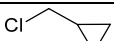
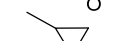
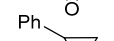
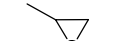
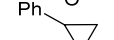
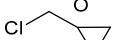
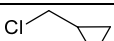

e) Conclusion

A broad variety of advanced heterogeneous catalytic systems was reported in the bibliography, and some of them exhibited high catalytic behavior with good scope for the cycloaddition of

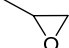
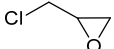
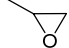
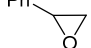
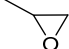
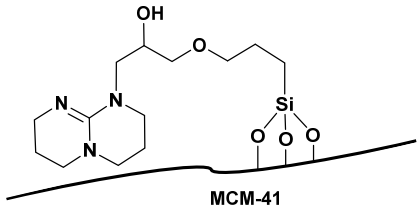
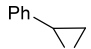
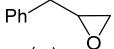
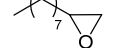
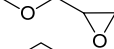

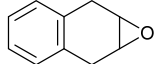

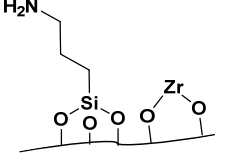
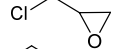
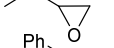
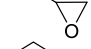
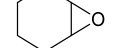
epoxides with CO<sub>2</sub>. Nevertheless, some of the reported catalysts presented one or more issues such as low stability, need of a co-catalyst, poor catalyst reusability or harsh operating conditions (high pressure and/or high temperature). Moreover, the catalyst cost remained high, especially if there is limited reusability and loss of efficiency along the runs. A catalytic system incorporating quaternary ammonium halide has shown to be efficient for the cycloaddition of CO<sub>2</sub> and epoxide. In this sense, the ability of zeolite and OMS as a host should be a reliable avenue for the development of an efficient and stable heterogeneous catalyst for CO<sub>2</sub> cycloaddition with epoxide, due to the synergistic effects of the multifunctional active sites of quaternary ammonium halide, for one side, and for example of a Lewis acid present in the zeolite or OMS structure, for the other. Accordingly, among all examples, the possibility of using ordered micro and mesoporous materials incorporating the structure directing agent (SDA) that can act as active sites for catalyzing the cycloaddition opens interesting opportunities since they moreover present high stability against leaching and hard reaction condition, and demonstrated recyclability. On the other hand, this approach lowers the cost of the catalyst which is limited to the cost of zeolite or mesoporous material synthesis, which in addition could be further calcined and used in other processes. Undoubtedly, the systematic study and understanding of the reaction mechanism, kinetics, thermodynamics, determination of reaction intermediates and active species due to the advantages of computational chemistry, and in situ and operando spectroscopy should allow a great understanding, to help rationalize experimental results and thus the design of new efficient zeolite and OMS -based catalysts and processes.

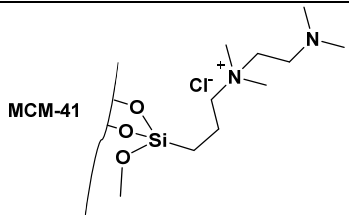

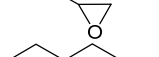
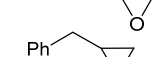
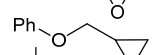
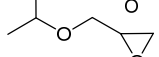
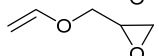
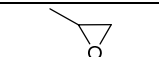
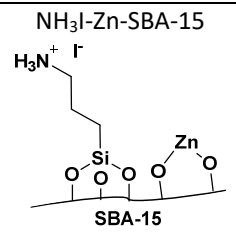

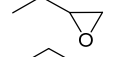
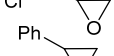
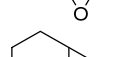

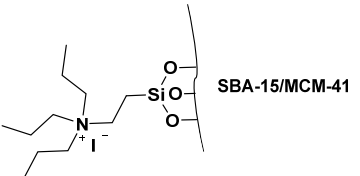
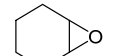
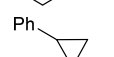
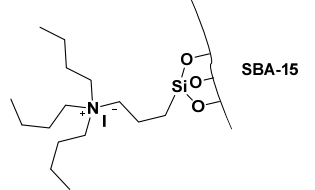
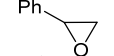
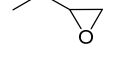
**Table 1.** Summary of the zeolite- and OMS-based catalysts performance and reaction conditions for CO<sub>2</sub> and epoxides cycloaddition.

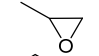
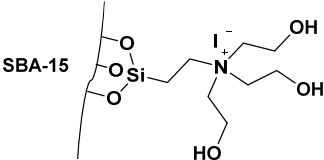
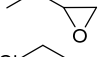
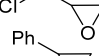
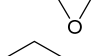

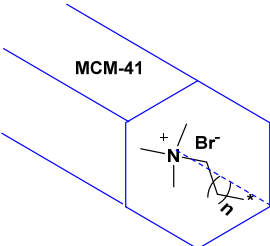
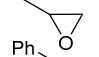
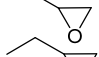
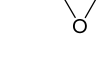
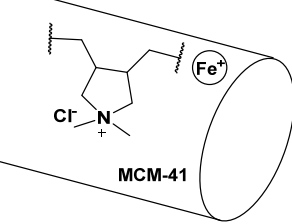
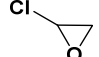
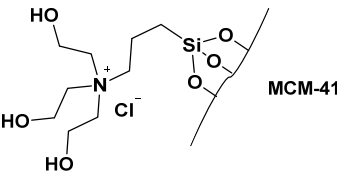
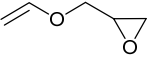
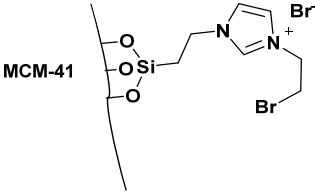
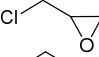
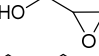
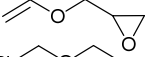
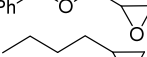
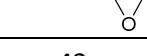
Entry	Catalysts	Conditions	Substrates	Yield/Selectivity (%)	Catalyst/Substrate	Year	Ref
<b>Zeolite-based catalysts</b>							
1	Cs-KX (zeolite)	120°C, 3.8 MPa, 3h		19%	150 mg/2g	2001	131
2				0.3%			
3	ETS-10	135°C, 3.44 MPa, 24h		14.9	1 g/20 mL	2004	136
4	Cs- ETS-10 K- ETS-10		Cs- ETS-10 K- ETS-10	13.7			
5	SAPO-56	100°C, 0.1 MPa, 4h		84.8	100 mg/18 mmol	2013	143
6	Mg-Si-ZSM-12 Co-catalyst: TBAB	60-90°C, 0.1 MPa, 9h		95/99 (60°C, 10h)	120 g/5 mol Co-catalyst: TBAB= 3 mol%	2019	145
7			92.2/96 (90°C, 9h)				
8			91.2/95 (90°C, 9h)				
9			94/99 (90°C, 9h)				
10			94/95 (90°C, 9h)				
11	Zn-ZSM-5 Co-catalyst: nPr <sub>4</sub> NBr	120°C, 1 MPa, 8h		99	50 mg/10 mmol (580 mg)	2017	147
12		87					
13		99					
14		99					
15		91					
16		98					
17		89					
18		99					

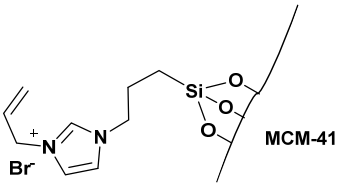
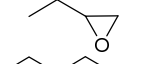
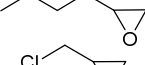

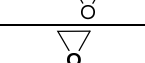
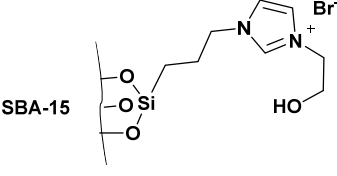
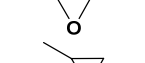
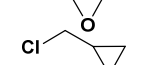
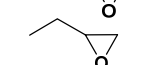
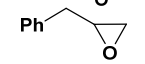
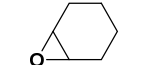

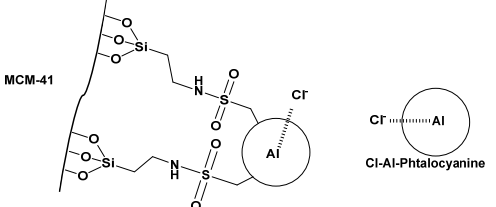
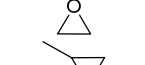
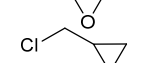
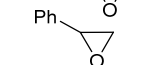
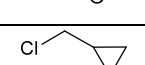
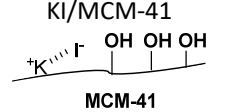
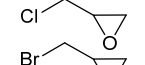
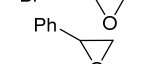
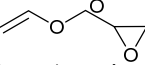
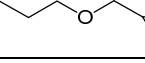

19	Ti-TS1	120°C, 0.69 MPa, 4h		85.4/92.6/790	100 mg/18 mmol Co-catalyst: DMAP= 0.0072mmol, 0.04 mol% 20 mL CH <sub>2</sub> Cl <sub>2</sub>	2003 <sup>148</sup>	
20	Ti-TS1			66.8/84.6/412			
21	Ti-TS1			76.6/70.9/354			
22	Ti-TS1			44.7/45.5/166			
23	Ti-MCM-41 (140°C)			100/82/595			
24	SDA-Zeolite LMFI-I	140°C, 2 MPa, 4h		85.6/95/TON: 589	100 mg/10 mmol	2014 <sup>152</sup>	
25				70.85/96/TON: 483			
26				97.1/97.6/TON: 652			
27				99.4/95.7/TON: 650			
28				29.5/100/TON: 193			
29	 / MTS-1	100°C, 1.6 MPa, 6h		80.8/98.3	300 mg/25.5 mmol 22 mL solvent	2018 <sup>153</sup>	
30							80.1/97.8
31							35.3/94.4
32							14.7/96.9
33	NH <sub>3</sub> -Meso-ZSM-5 Co-catalyst: DMAP	120°C, 0.8 MPa, 4h		71.6/92.1	100 mg/ 51 mmol DMAP: 10 mg	2017 <sup>154</sup>	
34				65.6/94.3			
35				75.9/95.7 (10 h)			
36	ZY-CS Co-catalyst: TBAI	100°C, 1 MPa, 6h		61	50 mg/2 mL epoxide Co-catalyst: TBAI= 45 mg	2018 <sup>155</sup>	
37				77			
38				99.5			
39	AlPc-Y Co-catalyst: DMAP	120°C, 0.69 MPa, 4h		95.7/99.3	1.66g (0.04 mol%)/18 mmol, Co-catalyst: DMAP= 0.0072 mmol, 20 mL CH <sub>2</sub> Cl <sub>2</sub>	2003 <sup>157</sup>	
40				93.1/90.9 (160°C)			



41	Co(Cl)TPP/NaX Co-catalyst: phenyl trimethylammonium tribromide (PTAT)	120°C, 3 MPa, 5h		90.4/95.6	1 g/100 mmol (9.2g) Co-catalyst: PTAT= 0.22mmol catalyst= 0.11 mmol	2014 <sup>160</sup>	
42	Basic-Nano-ZSM-5/Pr-MIM-OH	120°C, 0.8 MPa, 4h		87.5/97.1/TON:307.8	50 mg/51 mmol	2017 <sup>166</sup>	
43				88.3/99.6/TON:302			
44				78.5/97.2/TON:92			
45	PIILs-ZSM-5-ZnBr <sub>2</sub>	130°C, 2.5 MPa, 0.7 h		95.7/97.4	2.5 wt% catalyst	2018 <sup>167</sup>	
<b>OMS-based catalysts</b>							
46	 MCM-41	140°C, 0.5 MPa, 70h		90/92	0.79g/26 mmol 5 mL acetonitrile	2003 <sup>169</sup>	
47				95/97			
48				77/90			
49				79/90			
50				67/94			
51				55/92			
52	APTES@ZrO <sub>2</sub> -MCM-41	80°C, 2 MPa, 3h		97	16 wt% /0.1 mol co-catalyst: TBAI= 10 mg (0.1 mmol)	2017 <sup>170</sup>	
53	 MCM-41			93			
54				96			
55				91			
56				90			
co-catalyst: TBAI							

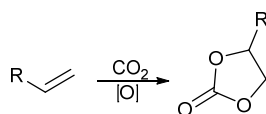
57	 <p>MCM-41</p>	120°C, 2 MPa, 6h		99/99	10wt%/30 mmol	2010 <sup>171</sup>
58				99/99		
59				90/90		
60				97/97		
61				99/99		
62				98/98		
63				99/99		
64	 <p>NH<sub>3</sub><sup>+</sup>-Zn-SBA-15 SBA-15</p>	130°C, 3 MPa, 12h		93/99	0.1g/2g	2016 <sup>173</sup>
65				88/99		
66				95/99		
67				71/99		
68				13/99		
69	 <p>SBA-15/MCM-41</p>	RT, 0.3 MPa, 24h		73	0.5g/0.22-0.4g	2017 <sup>174</sup>
70				92		
71	 <p>SBA-15</p>	100°C, 1 MPa, 4h		98/98.5	2 mol%/2 mL BO: 22.7 mmol SO: 17mmol	2018 <sup>175</sup>
72				95.1/98.1		

73	SBA-15/ $(\text{CH}_2\text{CH}_2\text{OH})_3\text{PrNI}$	110°C, 2 MPa, 3-5h		93.4/99 (4h)	200 mg/34.5 mmol	2019 <sup>176</sup>
74				91.6/99 (4h)		
75				96.3/99 (3h)		
76				85.5/99 (5h)		
77				43.6/98 (10h)		
78			MCM-41	120°C, 0.69 MPa, 3-8h		
79				90.1/100/TOF: 35 (5h)		
80				86.8/88.4/TOF: 22 (8h)		
81				86.3/91.8/TOF: 37 (5h)		
82		120°C, 1.6 MPa, 6h		79.7/96	300 mg/2 mL 22 mL Acetonitrile	2020 <sup>178</sup>
83		110°C, 0.76 MPa, 6h		61.5/88.5 TON: 63.1/TOF: 6.3	1g/40 mmol Acetonitrile	2008 <sup>179</sup>
84		90-120°C, 0.2 MPa, 4h		97/97/TOF: 23.5	300 mg/30 mmol	2013 <sup>181</sup>
85				98.3/98.3/TOF: 23.9		
86				98/98.5/TOF: 15.8		
87				96.7/100//TOF: 31.3		
88				100/100/TOF: 32.4		

89		150°C, 0.15 MPa, 8h		57.6/99.9	0.2g/12.4g	2019 <sup>182</sup>
90				13.4/97.7		
91				68.6/99.1		
92				68.8/95.4		
93		110°C, 2MPa, 2-24h		99/99	0.5mmol/50 mmol	2013 <sup>191</sup>
94				99/99		
95				99/99		
96				95/99		
97				80/99		
98				75/99		
99		110°C, 4 MPa, 2h		TOF: 415	0.1mmol/250 mmol Co-catalyst: 0.1 mmol	2002 <sup>186</sup>
100				TOF: 280		
101				TOF: 452		
102				TOF: 384		
103		130°C, 3 MPa, 5h		91.2	0.25g/20 mmol	2014 <sup>190</sup>
104				90.3		
105				94.7		
106				97.2		
107				96.5		

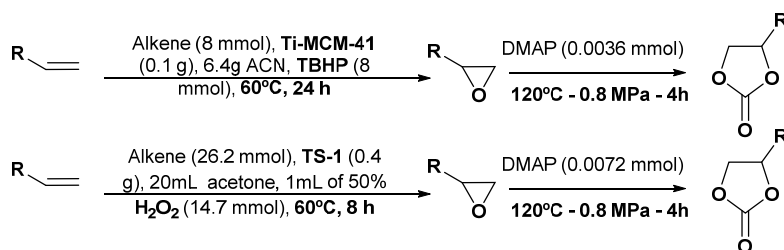
### 1.1.2. Synthesis of cyclic carbonates via olefin oxidative carboxylation

Since numerous epoxides are toxic, mutagenic and also expensive, an alternative route for the production of cyclic carbonates is the one-pot “oxidative carboxylation” of olefins and CO<sub>2</sub> (Scheme 29). In comparison to epoxide and CO<sub>2</sub> cycloaddition this synthetic approach is more economical taking into account the alkenes availability and cost. The strategies for this appealing synthetic approach are classified into two categories: two-step sequential reaction consisting of oxidation followed by carboxylation (cycloaddition), or direct oxidation and carboxylation in a single-step catalyzed by soluble catalysts, such as salen-complexes or ammonium salts<sup>192193</sup> and heterogeneous catalysts such as metal oxides.<sup>194</sup>



**Scheme 29.** Olefin oxidative carboxylation for the preparation of cyclic carbonates.

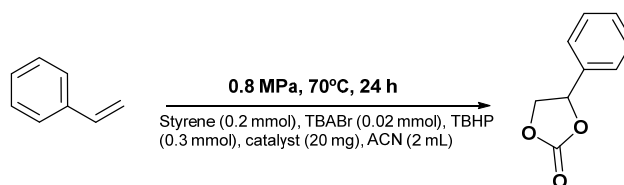
In the literature only few references relative to the direct olefin oxidative carboxylation in the presence of zeolites or ordered mesoporous silicate based catalysts were reported. The remarkable catalytic properties as oxidation catalysts of titanosilicate molecular sieves in the presence of H<sub>2</sub>O<sub>2</sub> or TBHP as oxidant have been widely reported and specifically for epoxidation of alkenes.<sup>195–198</sup> Therefore, the use of titanosilicates for the preparation cyclic carbonates through one-pot two-steps process, based on epoxidation and cyclo-addition of the synthesized epoxide and CO<sub>2</sub> constitutes an interesting strategy. Following this direction, a first attempt of direct synthesis of cyclic carbonates from alkenes in the presence H<sub>2</sub>O<sub>2</sub> or TBHP as oxidant and titanium-silicalite-1 (TS-1) and mesoporous Ti-MCM-41 was reported. The preparation of cyclic carbonate was carried out in a two-steps reaction by epoxidation at 60°C followed by cycloaddition at 120°C in the presence of DMAP as a co-catalyst (Scheme 30).



**Scheme 30.** Preparation of cyclic carbonates by olefin oxidative carboxylation.

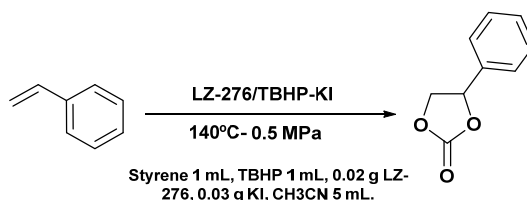
In the presence of TS-1, cyclic carbonates from allyl chloride and styrene using H<sub>2</sub>O<sub>2</sub> as oxidant could be obtained with 28% and 6%, respectively, while in the presence of Ti-MCM-41 and TBHP as oxidant, with 13 and 33%, respectively, being the total cyclic carbonate low. TiMCM-41, with larger pore diameter exhibited higher selectivity to cyclic carbonate formation than TS-1.

Recently, a class of titanium-grafted mesoporous silica catalysts was prepared starting from molecularly defined metal clusters. The organosol mixture of zero-valent Ti-clusters were impregnated onto the surface of ordered mesoporous silica molecular sieves (MCM-41 and MMM-2), that yielded dispersed non-single-site  $Ti^{(IV)}_nO_x$ -like silica-supported catalyst after calcination.<sup>199</sup> The prepared  $Ti_nO_x$ -MCM-41 catalyst was active in the oxidative carboxylation of styrene in the presence of TBABr as co-catalyst, and styrene carbonate was produced with 35.6 and 40% yield and selectivity, respectively, at 70°C, 0.8 MPa  $CO_2$  pressure, with 1.5 equivalent of TBHP (Scheme 31). The catalyst derived of zero-valent Ti-clusters impregnated on mesoporous mesophase MMM-2 silica, exhibited higher activity (67%) and selectivity (70%). These  $Ti^{(IV)}$  highly dispersed catalysts presented good results towards oxidative carboxylation and open the path to the study and development of new redox based ordered mesoporous catalysts.



**Scheme 31.** Preparation of styrene carbonate by olefin oxidative carboxylation.

Walnut-like zeolite Al-LZ-276 with Phi zeolite structure was recently prepared by hydrothermal method and without organic template and further used as catalyst for the direct preparation of styrene carbonate in the presence of TBHP as oxidant and KI as co-catalyst.<sup>200</sup> The authors proposed a two-step process with firstly styrene epoxidation catalyzed by LZ-276/TBHP-KI followed by cycloaddition catalyzed by LZ-276/KI. At 140°C and 0.5 MPa  $CO_2$  pressure, 77% styrene carbonate yield was obtained after 10h (Scheme 32). The blank control experiment demonstrated the catalytic contribution of the walnut-type zeolite catalyst, as 52% styrene carbonate yield without zeolite was achieved under the same reaction conditions. The recyclability test showed a marked deactivation of the zeolite during the four cycles with a decrease in styrene carbonate yield from 77 to 40%.



**Scheme 32.** Preparation of styrene carbonate in the presence of LZ-276/TBHP-KI catalyst.

In comparison to epoxide and  $CO_2$  cycloaddition, the oxidative carboxylation of olefin is a synthetic route more economical. However, up to now, few studies in the presence of heterogeneous catalysts, zeolites or OMS have been reported. Based on the remarkable

catalytic properties as oxidation catalysts of titanosilicate molecular sieves and the possibility of design organic-inorganic structured solid catalysts with different active sites, new efforts should focus on the development of this route to the sustainable production of carbonates.

### 1.1.3. *Other routes for the preparation of cyclic carbonates*

#### a) Direct CO<sub>2</sub> carbonylation of diols for the preparation of cyclic carbonates

The direct CO<sub>2</sub> carbonylation of diols constitutes another attractive and alternative route to produce cyclic carbonates and to mitigate CO<sub>2</sub> emissions (Scheme 1). This process also presents great thermodynamic limitations, operating at high CO<sub>2</sub> pressure and involves the production of water that induces hydrolysis of carbonates and catalyst deactivation, requiring the use of large amount of dehydrating agents. Though several works explored the opportunities for homogeneous and heterogeneous catalysts such as metal-based complexes, metallic salts, organocatalysts and ionic liquids,<sup>97</sup> we have not found reports using zeolites or OMS based catalytic system. Zeolites and OMS based catalysts should offer great opportunities owing to their ability to host different acid/base active sites of Lewis and Brønsted type that could enable both the carbonylation of diols and the elimination of water via hydration process such as nitrile, that constitutes a strategy largely adopted to shift the thermodynamic equilibrium.<sup>201</sup> In addition, control of the hydrophobic properties of the catalytic surface could be exploited to remove water and prevent deactivation of the active centers.

#### b) Reaction of CO<sub>2</sub> with propargylic alcohols for the preparation of dialkyl carbonates

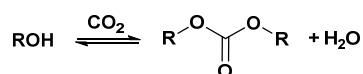
Reaction of CO<sub>2</sub> with propargylic alcohols gives alkylidene cyclic carbonates and constitutes another attractive green route (Scheme 1). Nevertheless, no reported investigations using ordered microporous or mesoporous based catalytic system were found up to our knowledge. This process present thermodynamic limitations and requires harsh reaction conditions (temperature, pressure) and the use metal-based catalysts.<sup>202</sup>

## 1.2. Synthesis of dialkyl carbonates

### 1.2.1. *Introduction*

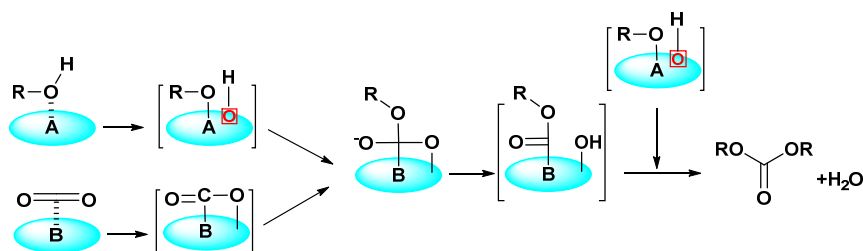
Dialkyl carbonates play an important role in our daily life and among them the most important short-chain dialkyl carbonates are diethyl (DEC) and dimethyl carbonates (DMC). The numerous properties of dialkyl carbonates such as polarity, good biodegradability, low toxicity and reactivity make them important chemical materials to produce polycarbonates, chemical intermediates, fuel additives and solvents for coating, adhesives and for batteries.<sup>90,91,203,204</sup> Dialkyl carbonates can be prepared by different phosgene free synthetic routes such as alcoholysis of urea, oxidative carbonylation of alcohols or transesterification of cyclic or dialkyl carbonates. The

interests and economic viability of each route vary in function of local resources, environmental standpoint, value and application of the dialkyl carbonates. The direct carbonylation of alcohols by reacting CO<sub>2</sub> with two equivalents of an alcohol to yield linear carbonates and water as sole side-product, constitutes a valuable and attractive alternative. This direct synthesis pathway offers a green and sustainable approach to prepare linear carbonates but very challenging because of the need to activate CO<sub>2</sub>, the unfavourable thermodynamics of the reversible process, the deactivation of the catalysts, and the hydrolysis of dialkyl carbonates formed due to the concomitant formation of water (Scheme 33). Thus, the development of effective catalytic system requires the combination of an efficient and recyclable catalyst with a dehydration system. Indirect synthesis of dialkyl carbonates from CO<sub>2</sub> can also be carried out starting from urea produced at large scale from CO<sub>2</sub>. The production of dialkyl carbonates directly from CO<sub>2</sub> requires both the activation of alcohol and the formation of alkyl species and activation of CO<sub>2</sub> molecules preferably over acidic and basic sites, respectively. A possible mechanism is proposed in Scheme 34 adapted from proposed mechanisms reported by Arbelaez et al.<sup>205</sup> and Bian et al.<sup>205</sup> In the last decades, numerous catalysts for the preparation of dialkyl carbonates such as Sn,<sup>206</sup> Ti<sup>207</sup> and Nb,<sup>208</sup> metal oxides (Ce, Zr, Cu, Fe)<sup>209–213</sup> and heteropolyoxometalate catalysts<sup>214,215</sup> have been studied. Although, numerous investigations focused on the synthesis of short-chain dialkyl carbonate from CO<sub>2</sub> in the presence of homogeneous and heterogeneous catalysts, but the numerous limitations of yields, corrosion, work-up conditions and low catalyst recyclability are still the bottlenecks of the process. The transesterification of cyclic and short-chain dialkyl carbonate constitutes a mature alternative technology to prepare more specific and long chain carbonates. Reported studies of DEC synthesis in the presence of Li, Cs, Na or K carbonates at 100°C and 5 MPa stated DEC yields up to 1.4%.<sup>216</sup> In the presence of oxides and mixtures, maximum 0.62% DEC yield in the presence of CeO<sub>2</sub><sup>212</sup> at 140°C and 5 MPa or 3.2% DEC yield in the presence of ZrO<sub>2</sub>/SiO<sub>2</sub><sup>217</sup> at 150°C and 20 MPa were reported. In the presence of alkoxide (MeOK), maximum 16.2% DEC yield at 80°C and 7.3 MPa was reported.<sup>218</sup> These data show that the preparation of dialkyl carbonate is not an easy task and that the design of new efficient and recyclable catalytic system is very challenging.



**Scheme 33.** Synthesis of dialkyl carbonate from CO<sub>2</sub>.





**Scheme 34.** Possible mechanism for the dialkyl carbonate formation by carbonylation of alcohol with CO<sub>2</sub>.

### 1.2.2. Acid-base OMS-based catalysts for the synthesis of dialkyl carbonates

The formation of linear carbonates requires both the activation of CO<sub>2</sub> and methanol molecules and ideally requires the presence of both acidic and basic sites. Therefore, the design of efficient and recyclable catalyst has been based on this acid-base catalytic mechanism. Metal metal oxides have therefore been intensively explored as catalysts for the preparation of dialkyl carbonates since they offer the possibility to combine the presence of both acid and basic active sites on the catalytic surface with tunable strength, dispersion and structure. Also, the synergetic effect between acidic and basic sites can be provided by amphiprotic oxides.<sup>209</sup> Therefore, different oxides mixtures (CeO<sub>2</sub>, ZrO<sub>2</sub>) have been employed.<sup>210,219–221</sup> As aforementioned, the basicity in zeolite and ordered mesoporous material is associated to the presence of framework oxygen atoms, Lewis basic sites, and their strength is related to the density of negative charge. Therefore, the basicity or the negative charge on oxygen atom, is a function of framework atoms, the extra-framework cations nature and the structure. To modify and enhance the basic properties different approaches can be followed such as the occlusion in the pore system of alkali metal clusters and oxide/hydroxide particles, or the modification of the intrinsic basicity of the framework oxygen, varying the cation framework or by cation-exchange of the extra-framework cations, suitably using low electronegativity cations such as alkali metal cations.<sup>41–44</sup> Following these leads, the catalytic performance of solid base materials, CeO<sub>2</sub> or exchanged alkali metal MCM-41 and Na-ZSM-12, Cs-ZSM-12 zeolites were investigated for the synthesis of diethyl carbonate in the presence of butylene oxide as a dehydrating agent. It could be expected that the high internal surface area of MCM-41 enabled high dispersion of CeO<sub>2</sub> providing higher density of basic sites. Moreover, the local environment of the exchanged alkali metal and the pore structure influenced the catalytic properties and accessibility to the active sites. At 170°C and 4.5 MPa CO<sub>2</sub> pressure, low yield and selectivity to diethyl carbonate (DEC) were achieved. The higher DEC formation was obtained in the presence 16wt% Ce-H-MCM-41 and 32 wt% Ce-Si-MCM-41 and attributed to presence of weak and strong basic sites while no DEC was observed in the presence of the alkali metal exchanged materials.<sup>222</sup>

CeO<sub>2</sub> has been widely explored for CO<sub>2</sub> conversion due to its suitable properties to activate CO<sub>2</sub> molecule.<sup>223–228</sup> Thus, numerous works have reported the high potential of CeO<sub>2</sub> for the direct synthesis of dialkyl and cyclic carbonates.<sup>219,228,229</sup> However the main limitations of CeO<sub>2</sub> is its easy deactivation by water, therefore the control of hydrophobic and hydrophilic properties of the catalytic surface can play a key role. Accordingly, the hydrophobicity of Ce/SBA-15 catalysts was varied by silylation of OH group with hexamethyldisilazane.<sup>230</sup> The catalytic behavior of the silylated samples revealed that the catalytic activity was related to the amount of moderate acid sites enabling the activation of methanol and to the hydrophobicity that allowed reducing the deactivation by water adsorption. Then, hydrophobic catalysts exhibited higher activity than hydrophilic samples. The highest 0.2% DMC yield close to equilibrium value was obtained in the presence of Ce/SBA-15-6 hydrophobic catalyst at 130°C, 12 h and 12 MPa.

### 1.2.3. Zeolite-based catalysts for the synthesis of dialkyl carbonates

In order to shift the equilibrium of the process, the effectiveness of different strategic organic and inorganic dehydrating agents have been reported such as ketals,<sup>231</sup> orthoesters,<sup>232</sup> and epoxides,<sup>233</sup> molecular sieves.<sup>234</sup> Among them ketals present different advantages such as price, availability, harmless and chemical neutrality. Alcohol and ketone react to produce a ketal and water which reversibly give back alcohol and ketone. During the dialkyl carbonates formation, advantage of the production of water could be taken to hydrolyze the acetal and produce alcohols and ketones. Accordingly, the efficient combination of CeO<sub>2</sub> and H-FAU as solid and recyclable catalyst to perform the direct diethyl carbonate (DEC) synthesis from CO<sub>2</sub> and ethanol in the presence of DEP (2,2-dimethoxy propane) as a dehydrating was described. Different zeolites with similar and optimized Si/Al close to 25 were checked but the higher DEC yield and selectivity were achieved in the presence of the FAU zeolite. Therefore, a 62% high DEC yield based on DEP was obtained at 120°C and 6.5 MPa CO<sub>2</sub> after 24h of reaction. Moreover, the stability of the catalytic system was shown over 4 cycles.<sup>235</sup> Previously, the catalytic data of the DEC synthesis in the presence of ZrO<sub>2</sub> as catalyst and 3A molecular sieve as co-catalyst showed the improved DEC yield, about 2.5-fold, induced by the presence of molecular sieve. In optimized reaction conditions, 150°C and 7 MPa and ZrO<sub>2</sub>/3A ratio of 5:2, 0.384 mmol DEC yield was obtained after 2h with 85% selectivity.

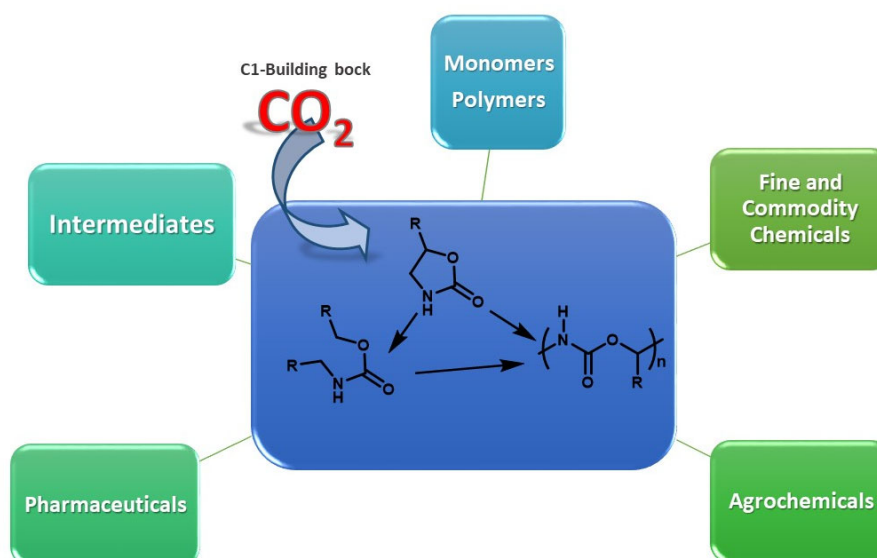
### 1.2.4. Conclusion

The direct synthesis of dialkyl carbonates is a difficult task due to thermodynamics and the reversibility of the process. Moreover, the production of water constitutes another limitation and induces a rapid deactivation of the catalysts and hydrolysis of the carbonates. Very few attempts to design and develop heterogeneous catalytic systems have been investigated and

remains a topic to be explored. Zeolites and ordered mesoporous-based catalysts, due to their versatility to accommodate different types of active sites and the possibility to control their hydrophobic properties, should be good candidates to develop active and efficient catalysts to activate both CO<sub>2</sub> and ROH molecules and remove water through chemical transformation or rapid desorption from the catalytic surface. Moreover, the development of knowledge and insights in the elucidation of catalytic species, intermediates and substrates through theoretical calculations, characterization and modeling studies should be of great value to rationalize experimental data and design new efficient and recyclable catalysts.

## 2 *Synthesis of carbamates*

Organic carbamates is an important class of chemicals that find applications in a variety of polymers (polyurethanes), agrochemicals,<sup>236,237</sup> drugs and medicines,<sup>238</sup> and intermediates of fine and commodity chemicals.<sup>239–241</sup> The carbamate group features a particular stability due to the delocalization of the non-bonding electrons on the N-atom into the carboxyl moiety. This specific stability allows improving the pharmacokinetic properties of drugs and that is the reason of the presence of this functional group in many pharmaceuticals (Figure 12).<sup>242–244</sup> As such, more than 10.000 tons of carbamates per year are used in the agriculture<sup>245</sup>. The production of carbamates currently proceeds through alcoholysis of isocyanates or aminolysis of chloroformates,<sup>246–248</sup> being the preparation of isocyanates and chloroformates issued from highly toxic and corrosive phosgene.<sup>249,250</sup> Thus the use of anthropogenic CO<sub>2</sub> as C1 source for the preparation of carbamates is very topical and numerous works have been reported.<sup>251,252</sup> Different approaches have been attempted for the production of carbamates from CO<sub>2</sub> and amines, and different substrates such as alcohols, metal alkoxide, epoxide and alkyl halides. Nevertheless, several limitations as high CO<sub>2</sub> pressure, long time of reaction, use of homogeneous catalysts, low yields and limited scope need to be improved for a successful application. Thus, the rational design and development of efficient and recyclable heterogeneous catalysts for the synthesis of carbamates from CO<sub>2</sub> is still topical.

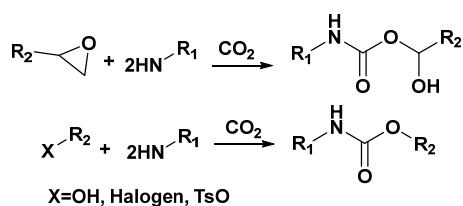


**Figure 12.** Scheme of carbamates applications.

## 2.1. Synthesis of acyclic carbamates

### 2.1.1. Introduction

As aforementioned, in the literature different pathways using  $\text{CO}_2$  as carboxyl moiety for the preparation of acyclic carbamates have been widely studied (Scheme 35). Nevertheless, the synthesis of acyclic carbamates presents thermodynamic limitations and harsh reaction conditions are generally required. Numerous catalytic systems such as metal-based catalysts (Al, Sn, Ru, Zn, Fe),<sup>253–255</sup> base (DBU)<sup>241,256,257</sup> and alkali metal salts have been described for the preparation of carbamates (Scheme 35).<sup>258,259</sup> However, few attempts involved the use of ordered microporous and mesoporous based catalysts as catalysts or as support, and only the synthesis of acyclic carbamates following the three components coupling of amine, RX and  $\text{CO}_2$  pathway has been described in the presence of these types of materials.

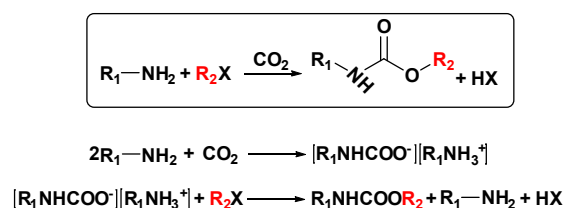


**Scheme 35.** Synthesis pathways of acyclic carbamates.

### 2.1.2. Three component coupling of amine, RX and $\text{CO}_2$ for the synthesis of carbamates

Among different possible pathways, oxidative carbonylation of amine represents a sustainable and eco-friendly pathway to produce organic carbamates ( $\text{R}_1\text{NHCO}_2\text{R}_2$ ) from  $\text{CO}_2$  (Scheme 36).  $\text{CO}_2$  and amine reaction provides a carbamate anion that after reaction with an alkyl halide yields a carbamate. In the absence of catalyst, the amine alkylation also occurs and constitutes the main side product. To minimize the undesired reaction, different catalysts have been used such

as base catalysts (DBU, alkali metal salts),<sup>260-264</sup> alkyl-onium salts<sup>265,266</sup> and metal based catalysts (Pd, Zn).<sup>263,267</sup> In the literature only few examples describing the use of OMS based catalysts was reported.



**Scheme 36.** Oxidative carbonylation of amine in the presence of alkyl halides.

a) Zeolite-based catalysts for the three component coupling of amine, RX and CO<sub>2</sub>

Zeolite-beta synthesized with tetraethylammonium bromide (TEABr) as structure directing agent (SDA) was used as catalyst for the synthesis of aryl carbamates by oxidative carbonylation of amines with CO<sub>2</sub>.<sup>268</sup> Aliphatic and aromatic carbamates were obtained with high selectivity 84-95% without solvent requirement, at 80°C and 0.34 MPa CO<sub>2</sub> pressure (Table 2, Entries 1-6). The order of reactivity with amines was the following: octylamine > cyclohexylamine > hexylamine > benzylamine > aniline > 2,4,6-trimethyl aniline, being higher the reactivity of aliphatic amines than aromatic amines. Previously, the same group reported the catalytic performance of different titanosilicate molecular sieves (TS-1, Ti-MCM-41, Ti-SBA-15) and metal phthalocyanine complexes encapsulated in zeolite-Y for the synthesis of carbamates.<sup>268,269</sup> Alkyl and aryl carbamates were synthesized with high yields >80% in the presence of TS-1, and in the case of bulky substrates like 2,4,6-trimethylaniline and cyclododecylamine, the mesoporous Ti-SBA-15 was more active than TS-1, at 80°C and 0.34 MPa CO<sub>2</sub> pressure (Table 2, Entries 7-13). Similarly, metal phthalocyanines encapsulated in Y zeolite exhibited efficient catalytic activity under the same reaction conditions, and butyl-N-phenyl carbamate was prepared with 75 yield%. Likewise, the same group described the catalytic performance of an organo-functionalized mesoporous titanosilicate (SBA-15) with adenine group for the formation of carbonates and carbamates using CO<sub>2</sub> as the raw material.<sup>207</sup> The presence of both, titanium ions (weak Lewis acid sites) and the amine moieties (the basic sites), was require to maximize the carbamates yield. Aliphatic and aromatic carbamates were prepared with high selectivity (84-85%), even without solvent, being aliphatic amines more reactive (Table 2, Entries 14-19). However, the main drawback of these methodologies is the need of a strong donor solvent like DMF.

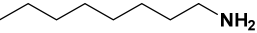
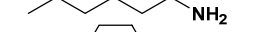
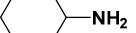
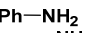
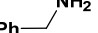
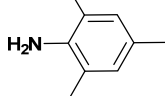
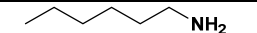
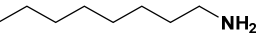
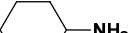
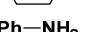

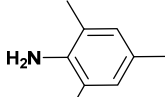
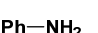
b) Ordered mesoporous based catalysts for the three component coupling of amine, RX and CO<sub>2</sub>

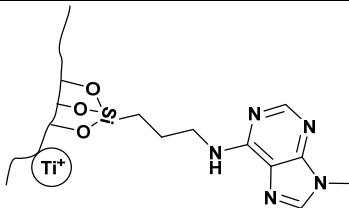
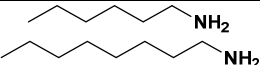
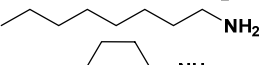
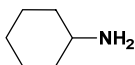
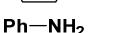
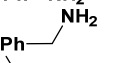
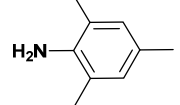
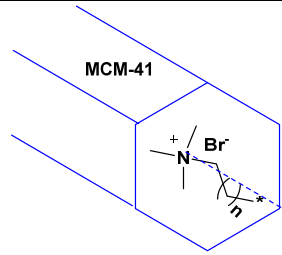
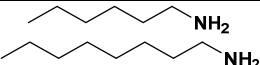
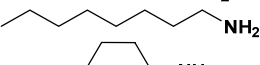
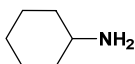
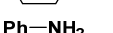
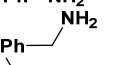
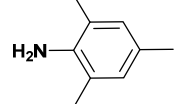
The synthesis and catalytic activity of an as-synthesized form of MCM-41 with cetyltrimethylammonium bromide as SDA for the production of carbamates was also described.<sup>177</sup> The coupling reaction of CO<sub>2</sub>, n-butyl-bromide and N-alkyl and N-aryl amines was performed with high selectivity and without solvent at 80°C and 0.34 MPa CO<sub>2</sub> pressure, nevertheless, recyclability of the MCM-41 catalyst was not explored (Table 2, Entries 20-25). The catalytic activity of the same materials was also reported for the synthesis of cyclic carbonates.

c) Conclusion

The synthesis of acyclic carbamates have been scarcely investigated in the presence of zeolites and OMS based catalysts although good yield and selectivity were reached. The recyclability of the catalysts should be further explored and reaction conditions improved for achieving potential application. This process generally requires highly active and selective homogeneous organometallic complexes and strong bases, and it is of interest to find heterogeneous alternatives. Today, it is still difficult to transfer the remarkable catalytic activity of homogeneous organometallic complexes to solid catalysts. Nevertheless, recent developments on the rational design of solid catalysts with well defined single or multi active sites, can help to synthesis of tailored made hybrid organic-inorganic structured materials containing one or the two required catalytic functions. This last could be a good direction to achieve more successful solid catalysts for the synthesis of acyclic carbamates.

**Table 2.** Summary of the different catalytic systems and reaction conditions for oxidative carboxylation of amines.

Entry	Catalysts	Conditions	Substrates	Yield/Selectivity (%)	Catalyst/Substrate	Year	Ref
1	Beta zeolite/TEABr	80°C, 0.34 MPa, 4h		91.7/91.7	150 mg/10 mmol amine / 10 mmol n-ButylBr	2005	268
2				79.9/84.2			
3				85.5/88.6			
4				45.9/86.9			
5				68.6/90			
6				20/95.2			
7	TS-1	80°C, 0.34 MPa, 3h		86.4/94.5	DMF: 10g 2 mmol amine/ 2 mmol n-ButylBr 100 mg TS-1	2004	269
8				89.5/96.5			
9				58.5/92.5			
10				89.3/96			
11				63.4/95.2			
12				54.8/97.8			
13	CuPc_Y			74.9/80	2 mmol amine/ 6 mmol n-Butyl-Br 83 mg CuPc_Y		

14		80°C, 0.34 MPa, 4h		84.9/88	10 mmol amine/ 12 mmol n-ButylBr 100 mg catalyst	2005 <sup>207</sup>
15			92.4/93.5			
16			76/83.5			
17			89/89			
18			82.2/92.8			
19		65.5/87.8				
20		80°C, 0.34 MPa, 3h		85.4/94.5	10 mmol amine/ 10 mmol n-ButylBr 150 mg catalyst	2006 <sup>177</sup>
21			90.1/90.1			
22			75.8/80.6			
23			42.7/83.7			
24			69.2/91			
25		28.4/94.8				



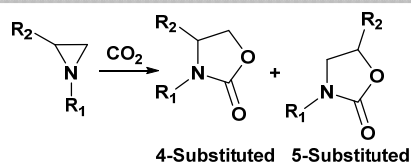
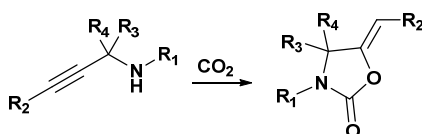
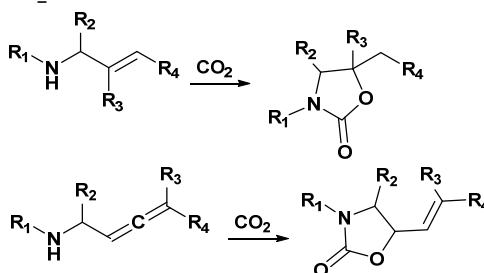
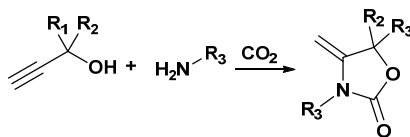
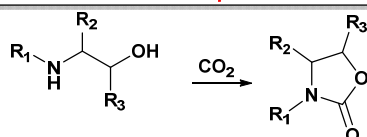
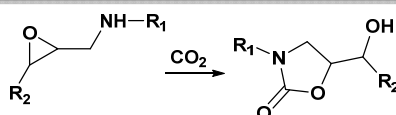
## 2.2. Synthesis of 2-oxazolidinones

### 2.2.1. Introduction

Oxazolidinones are heterocyclic compounds containing N and O in a 5-member ring with a wide scope of applications in chemical synthesis for the production of chiral auxiliaries,<sup>270</sup> agrochemicals<sup>271</sup> and pharmaceuticals, such as antidepressants<sup>272</sup> and antitumor drugs.<sup>273</sup> Moreover, 2-oxazolidinones represent a novel class of synthetic antimicrobial agents exhibiting a potent activity against Gram-positive organisms.<sup>274–277</sup> Besides, 2-oxazolidinones have found application as solvent for lithium-ion batteries<sup>278</sup> and ink-jet printing.<sup>279</sup>

Classically, 2-oxazolidinones are prepared from aminoalcohols and carbonyl group sources such as phosgene, carbonate and isocyanate.<sup>280,281</sup> Other important route of synthesis involves the reaction of epoxides with isocyanates.<sup>282,283</sup> As it was mentioned above, alternatives to the use of reactant issue from phosgene and phosgene are of great interest to avoid its toxicity, the associated production of corrosive salts and hazardous storage and handling. Therefore, the use of CO<sub>2</sub> is an environmentally friendly promising and challengeable alternative to the use of toxic, harmful and costly substrates.<sup>284,285</sup> In the last two decades, a series of CO<sub>2</sub> fixation pathways for the preparation of functionalized 2-oxazolidinones, such as cycloaddition of CO<sub>2</sub> with aziridines,<sup>284</sup> CO<sub>2</sub> fixation through cyclisation with unsaturated compounds such as propargylamines,<sup>284,286</sup> allylic and  $\alpha$ -allylic amines,<sup>287</sup> and coupling of propargylic alcohols, amines and CO<sub>2</sub>,<sup>285</sup> dehydrative condensation of  $\beta$ -amino alcohols<sup>284,288,289</sup> and condensation with epoxyamine have been explored (Scheme 37).

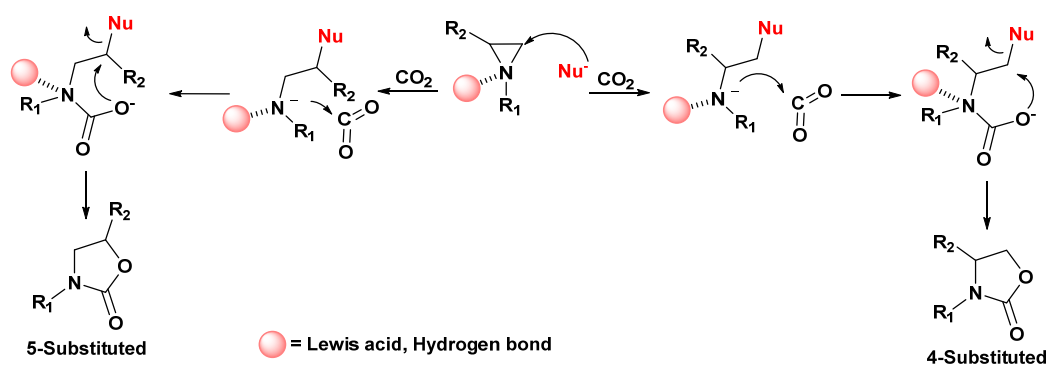
Works have been published on different synthetic routes to fix anthropogenic CO<sub>2</sub> into 2-oxazolidinones in the presence of organometallic complexes, metal salts, organocatalysts (ionic liquid, quaternary ammonium, phosphine and bases). Attempts of heterogenisation<sup>290–294</sup> of organocatalysts and organometallic complexes were explored as well as the possibilities of MOFs as catalysts.<sup>295,296</sup> Nevertheless, the use of ordered micro and mesoporous materials has been almost unexplored.

**CYCLOADDITION OF CO<sub>2</sub> TO AZIRIDINE****CYCLISATION OF UNSATURATED COMPOUNDS****\* CO<sub>2</sub> fixation to N-Substituted propargylamines****\* CO<sub>2</sub> fixation to allylic and α-allynylic amines****\* Coupling of propargylic alcohol, amine and CO<sub>2</sub>****DEHYDRATIVE CONDENSATION OF β-AMINOALCOHOLS WITH CO<sub>2</sub>****CONDENSATION OF EPOXYAMINE WITH CO<sub>2</sub>**

**Scheme 37.** CO<sub>2</sub> fixation pathways to the production of substituted 2-oxazolidinones.

### 2.2.2. Cycloaddition of CO<sub>2</sub> with aziridine

The cycloaddition of CO<sub>2</sub> with aziridine constitutes an important route to mitigate the excess emissions while preparing high value-added chemicals (Scheme 37) through the chemical fixation of CO<sub>2</sub> with 100% atom efficiency. Numerous studies have focused on the synthesis and reactivity of aziridines since they are an important tool in organic chemistry owing to the high reactivity of the ring-strain that at the same time makes them unstable.<sup>297</sup> The cycloaddition proceeds in three steps: the first and limiting step is the ring opening of N-heterocycle through nucleophilic attack, followed by the attack of the formed zwitterion to CO<sub>2</sub> molecule to provide a carbamate. The last step is the intramolecular cyclization via a nucleophilic attack (Scheme 38).

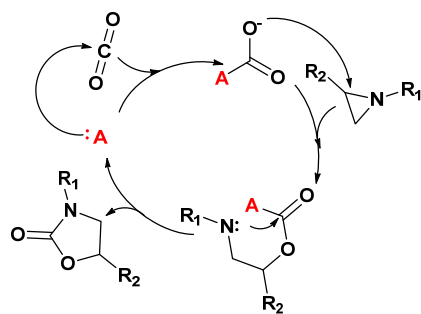


**Scheme 38.** Common cycloaddition mechanism between aziridine and CO<sub>2</sub> under aziridine ring activation and nucleophilic attack.

Though a large variety of homogeneous catalysts exhibited high catalytic performance for cycloaddition, such as ionic liquids,<sup>298,299</sup> alkali metal salts,<sup>300–303</sup> quaternary ammonium,<sup>304</sup> metal salts<sup>305</sup> and metal complexes,<sup>306–308</sup> these catalytic systems usually operate under harsh reaction conditions (high temperature and pressure). In addition to the main issues of homogeneous catalyst such as the non-recyclability, production of wastes, the described synthesis routes commonly involve expensive catalysts and limited substrate scope.<sup>309</sup> Very few works using OMS-based materials were reported and none zeolites-based. Cycloaddition of CO<sub>2</sub> with aziridine in the presence of heterogeneous catalysts is an underdeveloped synthesis route, worth to be thoroughly explored.

Due to their properties such as large pore size and high surface area, ordered mesoporous materials offer numerous possibilities to support and immobilize homogeneous catalysts. Recently, amine functionalized MCM-41 catalyst were prepared and used for the synthesis of oxazolidinones, expecting that hydrogen bonding of primary amine groups with nitrogen atom of aziridines could accelerate the ring opening of aziridines.<sup>310</sup> The hybrid catalyst exhibited high catalytic activity for the synthesis of numerous 5-aryl-2-oxazolidinones with high yield up to 98%, at 40–80°C and high 5 MPa CO<sub>2</sub> pressure. Moreover, the catalyst showed high stability and recyclability. The yield of 3-butyl-5-phenyloxazolidin-2-one was maintained for five consecutive recycles. A mechanism via zwitterions was described. The nucleophilic attack of the carbamate ion lead to the main product of reaction derived from ring-opening of the aziridine at the hindered carbon (5-substituted oxazolidinone) (Table 3, Entries 1-7).

Previously, an N-Heterocyclic carbene (NHC) functionalized MCM-41 was synthesized and used as catalyst for the cycloaddition of CO<sub>2</sub> with epoxides and aziridines (Scheme 39). The authors showed that the NHC-CO<sub>2</sub> adduct was the catalytic active species. Different oxazolidinones were obtained with excellent yield and regioselectivity, under mild reactions conditions, 100°C and 2 MPa CO<sub>2</sub> pressure (Table 3, Entries 8-11).<sup>311</sup>



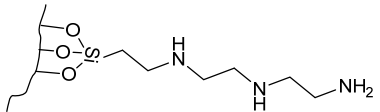
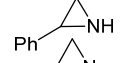
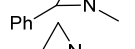
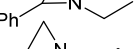
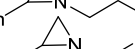
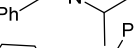
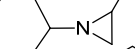

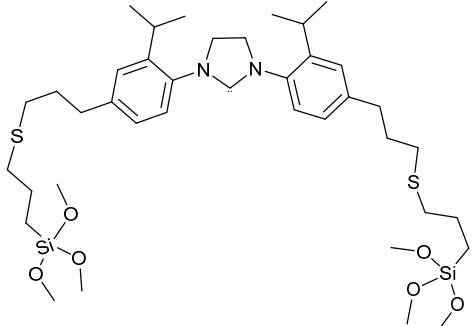
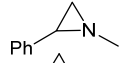
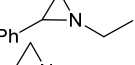
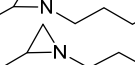
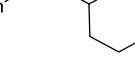
**A:** N-Heterocyclic carbene (NHC) functionalized MCM-41,  
amine functionalized MCM-41

**Scheme 39.** Catalyzed cycloaddition of aziridines with CO<sub>2</sub>.

### 2.3. Conclusion

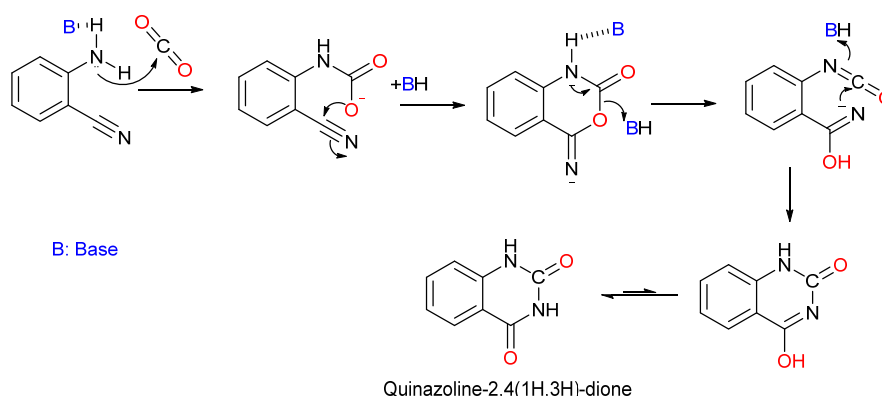
Several investigations have focused on substituting toxic carbonylating agents by inexpensive, nontoxic and accessible CO<sub>2</sub>. Nevertheless, due to the CO<sub>2</sub> inertness, the CO<sub>2</sub> fixation to produce 2-oxazolidines is a difficult task and several limitations such as moderate yields and selectivity, the use of large amount of homogeneous catalysts and harsh reaction conditions constitute impediments for the high-scale production. Therefore the design and development of efficient, selective, recyclable and economic catalyst is still challenging. Today, we have knowledge and tools for the rational design of micro and mesoporous materials that can act as molecular sieves for reactant selection, while containing well-isolated single or multiple active sites accommodated on the zeolite walls, and so accessible to reactants through their diffusion. From there, materials could be developed with regular pores and cavities, even by “ab initio” synthesis<sup>312</sup> that can control the reactant adsorption and transition-state stabilization and supplying the desired process selectivity.<sup>313</sup> Besides, kinetic, theoretical and modelling studies, are still required to a rational design of the catalysts. Then, owing to their robustness, versatility in their possibilities of functionalization, zeolites- and OMS- based catalytic systems containing multi active centers for activation of CO<sub>2</sub> molecule and others components of the different CO<sub>2</sub> fixation pathways may offer opportunities worth to be explored for the production of carbamates.

**Table 3.** Summary of the different catalytic systems and reaction conditions for CO<sub>2</sub> and aziridines cycloaddition.

Entry	Catalysts	Conditions	Substrates	Yield/Selectivity (%)		Catalyst/Substrate	Year	Ref
				5-subst./4-subst.				
1		120°C, 1.6 MPa, 6h		100/92, 95:5	25wt%/1 mmol	2014	310	
2				100/96, 96:4				
3				199/97, 99:1				
4				100/92, 99:1				
5				98/90, 98:2				
6				80/65, 91:9				
7				100/98, 99:1				
8		100°C, 2 MPa, 24h		99/95, 64:36	20 mg/2 mmol 1.5 mL CH <sub>2</sub> Cl <sub>2</sub>	2011	311	
9				99/92, 92:8				
10				99/94, 100:0				
11				83/80, 100:0				

### 3 Other formation of C-N bond

The use of CO<sub>2</sub> as C1 building block is of great interest, and as aforementioned the main issue is thermodynamic stability and kinetic inertness of CO<sub>2</sub>. The use of high-energy substrate such as epoxide and aziridine constitutes an effective strategy for the fixation of CO<sub>2</sub>, and among the active substrates, amines are good candidates for the formation of new C-N bond.<sup>252,314,315</sup> Important examples are the synthesis of urea, carbamates or oxazolidinones and polyurethanes. Quinazoline-2,4(1H,3H)-dione constitutes an important class of Nitrogen-containing heterocycles with biological activities that find a large number of applications as pharmaceuticals.<sup>316-319</sup> The synthesis of quinazoline-2,4(1H,3H)-dione derivatives starting from non-toxic, low cost and readily available substrates such as CO<sub>2</sub> and 2-aminobenzonitrile is of great interest and constitutes an environmentally friendly process with 100% atom efficiency and an alternative route to the use of toxic phosgene, carbamates,<sup>320</sup> anthranilic acids with urea,<sup>321,322</sup> potassium cyanate and chlorosulfonyl isocyanate.<sup>319</sup> A new and straightforward and, over all green synthetic route of quinazoline-2,4(1H,3H)-dione in the presence of DBU has been reported. In the presence of a base catalyst, the formation of quinazoline-2,4(1H,3H)-dione involves the nucleophilic attack of the amino group to CO<sub>2</sub>. After cyclization, aperture and new cyclization, quinazoline-2,4(1H,3H)-dione is produced (Scheme 40).



**Scheme 40.** Synthesis of quinazoline-2,4(1H,3H)-dione by carbonylation of 2-aminobenzonitrile and CO<sub>2</sub>.

The use of CO<sub>2</sub> and 2-aminobenzonitrile to the preparation of quinazoline-2,4(1H,3H)-dione is a recent synthesis pathway and has to be further explored. In fact, we have found two references using ordered micro or mesoporous materials. Recently, mesoporous basic zeolite for various transformations involving large organic molecules have been synthesized<sup>154</sup> and functionalized with primary, secondary, and tertiary amines via a post-synthetic method by covalent bonding. Accordingly, nanocrystalline zeolite (Nano-ZSM-5) functionalized with basic ionic liquids was used for the quinazoline-2,4(1H,3H)-dione synthesis. Under optimized reaction conditions, 150°C, 12h, in protic solvent (DMF), selected CO<sub>2</sub> pressure (3.5 MPa), 93.6% yield was achieved.<sup>166</sup> The same group previously reported the use of covalently amine (3-(2-(2-

aminoethylamino) ethylamino) propyltrimethoxysilane, AEPTMS) functionalized MCM-41, as efficient and recyclable catalyst for the synthesis of a variety of quinazoline-2,4(1H,3H)-dione compounds from substituted 2-aminobenzonitriles and CO<sub>2</sub> in water.<sup>323</sup> Solvent played a fundamental role and highly polar solvents were adequate to achieve high yield being the best yields achieved in DMF and water. Under optimized reaction conditions, at 130°C, 18h and 3.5MPa CO<sub>2</sub> pressure, 91% quinazoline-2,4(1H,3H)-dione yield was achieved. The successful scope of the catalyst, as well as the possibility to reuse the catalyst for five consecutive recycles was shown for various substrates.

## 4 *Synthesis of carboxylic acid*

### 4.1. Carboxylation reaction via CO<sub>2</sub> insertion into C-M bond for the synthesis of carboxylic acid

Carboxylic acids constitutes an important class of commodity chemicals with numerous application as solvents, intermediates for pharmaceuticals, flavors and fragrances and monomers for polymer productions. Carboxylic acid are usually prepared by oxidation of hydrocarbons with the exception of acetic acid that is issued from carbonylation of methanol. The production of carboxylic acid from CO<sub>2</sub> insertion into C-H bond is a green and atom economy reaction. Nevertheless, this reaction is thermodynamically unfavourable, being both endothermic and entropically disfavoured. Thus, this transformation is very challenging and the design and preparation of new catalysts to overcome this kinetic barrier is of great interest. Then, the preparation of carboxylic acids via carboxylation of alkanes by insertion of CO<sub>2</sub> into a C-metal bond is still at an early stage and offers numerous research opportunities.

### 4.2. Synthesis of acetic acid

#### 4.2.1. Introduction

Acetic acid is an important raw material in the chemical industry for the production of vinyl acetate and acetic anhydride. Acetic acid is produced by fermentation and chemical routes. Every year, 7 Mt of acetic acid are produced and 190 kt are issued from fermentation. Carbonylation of methanol, oxidation of aldehyde and oxidation of ethylene are the main chemical pathways, while the direct conversion of CO<sub>2</sub> and CH<sub>4</sub> to produce acetic acid is an attractive route to mitigate global warming and emission of greenhouse gases (Scheme 41). Using two gases with greenhouse effect, this route of acetic acid synthesis is considered green and represents an atom economy reaction. Nevertheless, the inertness of both molecules CH<sub>4</sub> and CO<sub>2</sub> makes this conversion very difficult and thermodynamically limited. Calculation of Gibbs energy showed an increase,  $\Delta G = 71.17 \text{ kJmol}^{-1}$ ,<sup>324</sup> and, the development of an efficient catalyst to overcome the kinetic barrier constitutes a great challenge.



**Scheme 41.** Direct synthesis of acetic acid from CO<sub>2</sub> and methane

Many heterogeneous catalytic systems have been developed such as Cu/Co supported on oxide,<sup>325</sup> Pd and Pt on carbon or alumina,<sup>326</sup> Pd or Rh on silica.<sup>327</sup> Nevertheless, up to now these catalysts exhibited poor selectivity, low acetic acid yield and turnover frequency, and operate at high temperature, > 425°C.

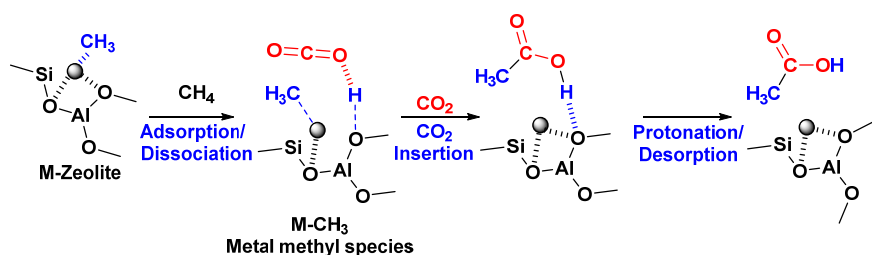
#### 4.2.2. Zeolite based catalysts for acetic acid synthesis

##### a) Zeolite-based catalysts containing Cu and Fe for acetic acid synthesis

Recently, zeolites, especially metal ion-modulated zeolites, were found to be highly active in the dissociation of the C-H bond<sup>328</sup> of methane and the C-C coupling between the methyl group (-CH<sub>3</sub>) and CO<sub>2</sub>.<sup>329</sup> Accordingly, numerous studies have focused on the activation of CH<sub>4</sub> molecules in metal exchanged zeolites.<sup>330,331</sup> Naturally, CH<sub>4</sub> is converted into methanol by the methane monooxygenase (MMO) enzymes using Cu and Fe as active metals. Two forms of monooxygenase exist, cytoplasmic (soluble) and membrane-bounded (particulate) with different active sites, a bis(m-oxo)diiron<sup>332</sup> and Cu cluster,<sup>333,334</sup> respectively, the latter catalyzing the oxygen insertion into the C-H methane bond. Different studies attributed the catalytic activity to a Cu dimer<sup>334</sup> or to a trinuclear Cu cluster.<sup>335</sup>

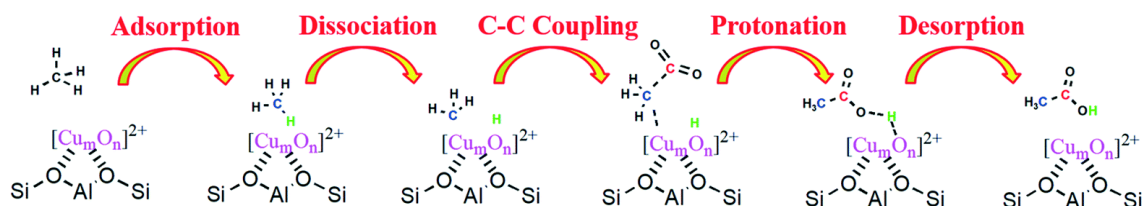
Accordingly, numerous catalytic systems based on iron and copper-oxygen species in inorganic matrices were studied for methane oxidation. One of the most promising catalysts is the copper and iron exchanged zeolites. Following these leads, different catalytic system were designed and explored to determine the nature of active Cu-clusters for the conversion of CH<sub>4</sub> into methanol. Recently,<sup>336</sup> a study of cationic species in Cu-MOR materials showed that, in contrast to other metal-modulated zeolites<sup>337,338</sup> where different cationic species are present, in Cu-MOR only homogeneous single sites are anchored. Trinuclear Cu-oxo clusters, [Cu<sub>3</sub>(μ-O)<sub>3</sub>]<sup>2+</sup>, anchored to two framework Al atoms located at the pore mouth of the 8-MR side pockets were well described. Moreover, these trinuclear Cu-oxo clusters showed to be highly stable under dry conditions. The C-H bond activation of methane molecule to methanol production has been the objective of many studies. Despite the efforts and numerous works, the nature of the active sites and the mechanism of activation of both CH<sub>4</sub> and CO<sub>2</sub> molecules and their conversion into acetic acid on metal modulated zeolites are still the subject of numerous discussions and studies. A general mechanism of bifunctional activation with the formation of metal methyl species and CO<sub>2</sub> protonation is favoured and depicted in the [Scheme 42](#).<sup>329,339,340</sup>





**Scheme 42.** Possible scheme for direct conversion of CH<sub>4</sub> and CO<sub>2</sub> over metal-modulated zeolite.

Modelling studies have been most useful for a deeper understanding of the catalysis of metal-modulated zeolites for the direct conversion of CH<sub>4</sub> and CO<sub>2</sub>. A recent theoretical study over Cu-modulated BEA, MFI, MOR and TON zeolites was performed by means of DFT calculations. The results showed that the catalytic activity of Cu-modulated zeolites is closely related to the structure of both active copper species and zeolite pore channels. The isomorphic substitution of Si atom with Al atom in the zeolite framework induces a negative charge that is compensated by mononuclear [Cu]<sup>2+</sup>, binuclear [CuOCu]<sup>2+</sup>, or trinuclear [Cu<sub>3</sub>(μ-O)<sub>3</sub>]<sup>2+</sup> clusters.<sup>341</sup> The study showed that under specific catalyst activation conditions, different Cu-cationic species can be preferentially stabilized in the corresponding optimized structures. The authors showed that [CuOCu]<sup>2+</sup> is preferentially stabilized in the three-dimensional BEA and MFI zeolites while [Cu<sub>3</sub>(μ-O)<sub>3</sub>]<sup>2+</sup> is preferentially stabilized in the one-dimensional MOR and TON zeolites. Experimental data reported in the bibliography also indicated that binuclear [CuOCu]<sup>2+</sup> in the MFI zeolite<sup>342</sup> exhibited high activity, while trinuclear [Cu<sub>3</sub>(μ-O)<sub>3</sub>]<sup>2+</sup> was the dominant active sites in the MOR zeolite.<sup>343</sup> Zeolites incorporating [CuOCu]<sup>2+</sup> and [Cu<sub>3</sub>(μ-O)<sub>3</sub>]<sup>2+</sup> species showed to be active for the direct conversion of CH<sub>4</sub> and CO<sub>2</sub>, in comparison with the mononuclear copper ([Cu]<sup>2+</sup>) species. Specifically, the authors claimed that [CuOCu]<sup>2+</sup> in the MFI and BEA zeolites are suitable to stabilize the transition state of the rate-determining C-C coupling by electrostatic forces and reduce the free energy and enthalpy barrier. On the other hand, the authors claimed the ability of [Cu<sub>3</sub>(μ-O)<sub>3</sub>]<sup>2+</sup> present in the MOR zeolite to stabilize the transition state of the C-C coupling (Figure 13). The differences in stabilization ability, resulted in a higher catalytic activity with a low apparent activation energy (57 kJ mol<sup>-1</sup>) in the MOR zeolite with [Cu<sub>3</sub>(μ-O)<sub>3</sub>]<sup>2+</sup> clusters.



**Figure 13.** Direct conversion of carbon dioxide and methane to acetic acid over Cu-modulated zeolites. Reprinted with permission from ref.<sup>337</sup>. Copyright 2019, Royal Society of Chemistry.

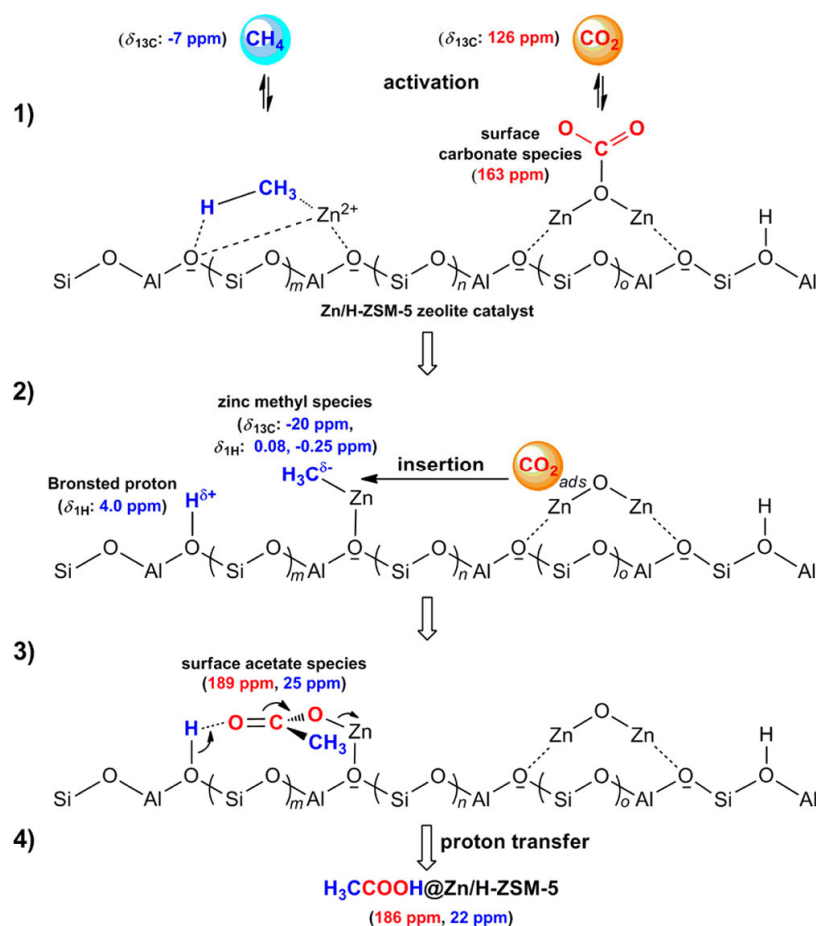
In an experimental study in continuous fixed-bed reactor using Cu-exchanged M-ZSM-5 (M = Li<sup>+</sup>, Na<sup>+</sup>, K<sup>+</sup> and Ca<sup>2+</sup>), it was claimed a synergetic effect between metallic Cu species and the basic cations to allow the simultaneous activation of CH<sub>4</sub> and CO<sub>2</sub> molecules to form acetic acid.<sup>329</sup> The nature of the metallic Cu species was not discussed, and previous reduction of the catalyst was carried out before its use to prevent the formation of CuOx. The results showed that the CO<sub>2</sub> activation depended on the alkali cations, favouring the CO<sub>2</sub> insertion into C-H activated bond of CH<sub>4</sub>. The cation properties as size (Li < Na < K) and cation charge control both charge density and number of cations. Cu-Ca-ZSM5 exhibited the lowest activity. Adsorption studies revealed the higher CO<sub>2</sub> adsorption capacity of Cu-K-ZSM5, attributed to the acid-base interaction between the ZSM-5 framework and CO<sub>2</sub> molecules. Cu-Na-ZSM-5 catalyst gave the highest rate of acetic acid formation at the initial period but showed a higher deactivation after 1h than Cu-K-ZSM-5. At 9 min of TOS, 18% of CH<sub>4</sub> conversion and acetic acid yield can be achieved, at 500°C in the presence of Cu-Na-ZSM-5 catalyst. However, after 1h, 0.6 and 0.15 % of CH<sub>4</sub> conversion and acetic acid yield, respectively, were obtained. The best acetic acid production (0.395 mmol<sub>cat</sub><sup>-1</sup>h<sup>-1</sup>) was registered on Cu-K-ZSM-5 catalyst, at 500°C, for 10h. The recyclability of the catalyst was shown and the regenerated catalysts exhibited similar activities to the fresh catalysts (close to 70% acetic acid). The deactivation was mainly due to Cu<sup>0</sup> aggregation that could be re-dispersed by a calcination process.

Another theoretical study explored the effect of the metal cations within the zeolite for the direct conversion of CO<sub>2</sub> and CH<sub>4</sub> to acetic acid. The analysis and comparison of the catalytic properties of MFI zeolites exchanged with Be, Co, Cu, Mg, Mn and Zn cations to compensate the charge induced by the substitution of two Al atoms, was addressed.<sup>344</sup> The location of exchanged metal was within the six-member ring located at the surface of the straight channel. The calculation results showed CH<sub>4</sub> dissociation is the rate-determining step, and CH<sub>4</sub> dissociation and the free energy barriers of CH<sub>4</sub> dissociation and C-C bond coupling were related to the electronegativity of the metal cation. Therefore, the lowest apparent activation energy of 11.5 kcal mol<sup>-1</sup> was obtained over the Cu-MFI. Additionally, the authors showed that the co-adsorption of H<sub>2</sub>O allowed to reduce the acetic acid desorption energy which can be reduced from 42.0 to 20.5 kcal mol<sup>-1</sup>.

#### b) Zeolite based catalysts containing Zn for acetic acid synthesis

Numerous investigations on the activation of C-H bond, for methanol or acetic acid production have reported the effect of the local structure of the active sites. Following this, the activity of Zn modified H-ZSM-5 containing isolated Zn<sup>2+</sup> cations or small ZnO clusters was studied by means of DFT.<sup>340</sup> The conversion of CH<sub>4</sub> and CO<sub>2</sub> revealed to be strongly dependent on the local

structure of the active sites. Thus,  $\text{Zn}^{2+}$  cations located in the 5-membered rings of the sinusoidal and straight channels exhibited the best catalytic activity, higher than other  $\text{Zn}^{2+}$  cations or small ZnO clusters owing to suitable adsorption properties of  $\text{CH}_4$  and  $\text{CO}_2$  and favourable activation energies. Previously, a work based on solid-state nuclear magnetic resonance (NMR) spectroscopy, reported the direct conversion of  $\text{CH}_4$  and  $\text{CO}_2$  into acetic acid on zinc-modified H-ZSM-5 (Zn/H-ZSM-5), at low temperature (250-500°C), and described the reaction mechanism.<sup>345</sup> The nature of Zn species was not discussed but the efficient activity and selectivity of the bifunctional zeolite was shown. As it was proposed,<sup>346,347</sup> the selective formation of methyl-metal species from methane was confirmed (zinc methyl species ( $-\text{Zn}-\text{CH}_3$ )) with the simultaneous formation of protons. This mechanism can be well accepted in analogy to the activity of organozinc compounds.<sup>348</sup> The adsorption of  $\text{CO}_2$  on the surface provide a reservoir for  $\text{CO}_2$  to be inserted into the Zn-C bond. Finally, the zeolite framework offers excellent ability to stabilize and transfer Brønsted protons and as well to protonate the surface acetate species (Figure 14).



**Figure 14.** Mechanism to the activation of  $\text{CH}_4$  and the formation of zinc methyl species and Brønsted proton, while  $\text{CO}_2$  activation led to the formation of carbonate species (Steps 1 and 2). The insertion of  $\text{CO}_2$  into zinc methyl species provided surface acetate species that produced acetic acid upon protonation with the restoration of Zn/H-ZSM-5 catalyst (Steps 1 and 2). Reprinted with permission from ref.<sup>345</sup>. Copyright 2013, American Chemical Society.

Currently, it is well accepted that the catalytic activity is determined by the structure and nature of the active sites. The results of adsorption energies for zinc-modified H-ZSM-5 catalysts showed that adsorption strength of CH<sub>4</sub> was dependent on Zn<sup>2+</sup> cation location and decreased in the following order for the four-, five-, and six-membered rings in straight and sinusoidal channels, Z4>Z5>Z6 and M5>M6, respectively, accordingly to the charge distribution of Zn/H-ZSM-5 based on the Mulliken charge analysis. Consequently, Zn<sup>2+</sup> cations located in the 5-membered rings of the channels (straight and sinusoidal) exhibited better catalytic activity than other isolated Zn<sup>2+</sup> sites and small ZnO clusters due to the favourable adsorption properties of reactants and activation energies.<sup>340</sup>

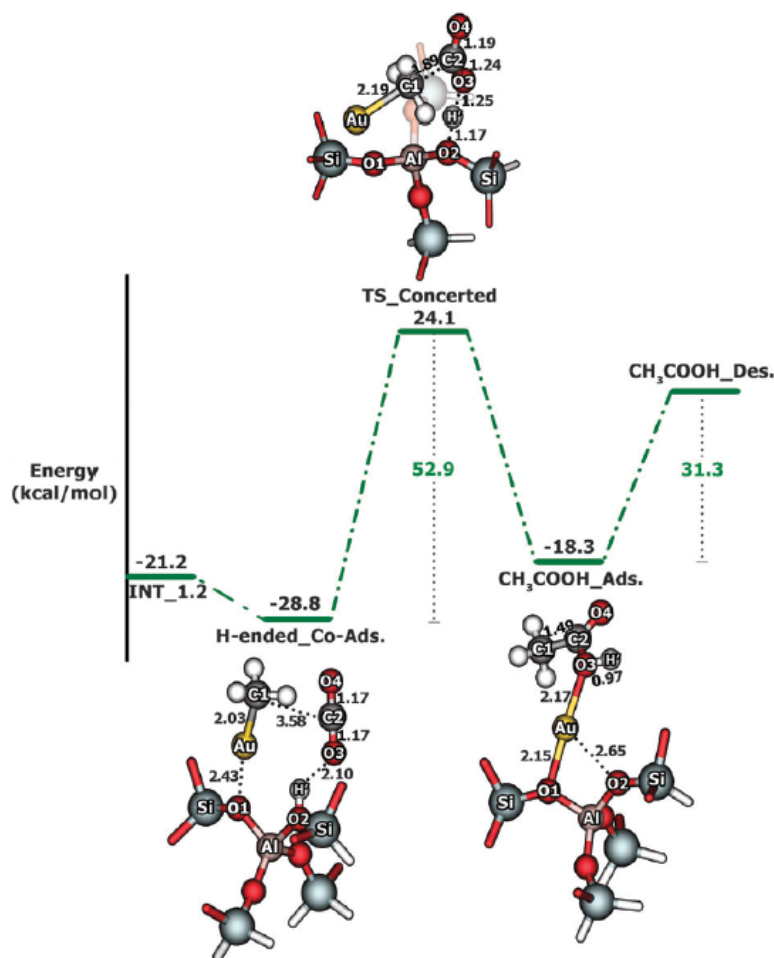
c) Zeolite-based catalysts containing Au for acetic acid synthesis

The possible reaction mechanism for the direct formation of acetic acid from CH<sub>4</sub> and CO<sub>2</sub> over the Au-exchanged ZSM-5A has been explored by DFT study, involving Brønsted acid site to the CO<sub>2</sub> protonation and Au(I) active center to the formation methyl-gold species.<sup>339</sup> The formation of methyl-gold species go through the CH<sub>4</sub> molecule activation over Au(I) active center in which the C-H dissociation proceed via the homolytic  $\sigma$ -bond activation, being the calculated energy barrier for methane dissociation on Au-ZSM-5 of only 10.5 kcalmol<sup>-1</sup>. The methyl-gold species are very stable and the CO<sub>2</sub> insertion difficult being 52.9 kcalmol<sup>-1</sup> the activation energy of the concerted mechanism (Figure 15). The understanding of acetic acid formation over exchanged zeolites is a valuable contribution in the path to the design of more efficient catalysts.

4.2.3. *Conclusion*

The reported works provide relevant and crucial insights about the mechanism of the direct conversion of CO<sub>2</sub> and CH<sub>4</sub> into acetic acid within the pores of microporous materials, the limiting step and barrier energies that catalytic systems have to overcome. The structure and composition of the zeolite framework stabilize extraframework metal species that are able to activate methane and form methyl-metal species. Up to now, among the few reported experimental data, the best results were achieved in the presence of Cu-K-ZSM-5 catalyst with 0.395 mmol<sub>cat</sub><sup>-1</sup>h<sup>-1</sup> acetic acid production, at 500°C, for 10h.<sup>329</sup> The synthesis of an efficient catalyst with active sites for the simultaneous activation of CH<sub>4</sub> activation and CO<sub>2</sub> insertion remains crucial and challenging. Thus, the catalyst based on zeolite or OMS should have metal active sites for CH<sub>4</sub> activation, adequate CO<sub>2</sub> adsorption capacity and CO<sub>2</sub> insertion activity that will be achieved by the incorporation of Lewis acid sites, basic sites and oxygen vacancies. So far, important insights have been made using both experimental and theoretical approaches. However, systemic study and understanding of reaction mechanisms, determination of reaction intermediates and catalyst active species by computational studies and in situ characterization

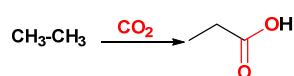
are imperative. Further, a performing reaction system should be designed to overcome the limitations of thermodynamic equilibrium and improve the production of acetic acid. In addition, a reaction system using plasma could offer new opportunities.



**Figure 15.** Energy profile for the acetic acid formation via the concerted bi-functional mechanism. Bond distances are in Å and energies are in kcal mol<sup>-1</sup>. Reprinted with permission from ref.<sup>339</sup>. Copyright 2012, Royal Society of chemistry.

#### 4.3. Synthesis of propanoic acid

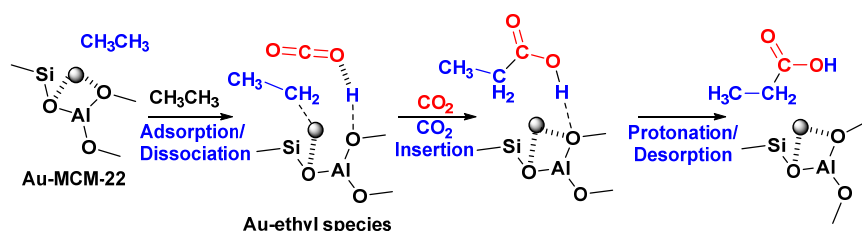
Propanoic acid finds wide application as intermediate in the synthesis of commodity chemicals and polymers, and used as a preservative in food. Propanoic acid is mainly produced by hydrocarboxylation of ethylene in the presence of Pd(AcO)<sub>2</sub><sup>349</sup> and could be ideally prepared from the insertion of CO<sub>2</sub> into ethane (Scheme 43). To overcome thermodynamic limitations the design and preparation of new catalysts is a great challenge. Very few references are reported in the bibliography concerning the preparation of propanoic acid from CO<sub>2</sub>.



**Scheme 43.** Direct synthesis of propanoic acid from CO<sub>2</sub> and ethane

By analogy with the synthesis of acetic acid, metal modulated zeolite can be good candidates to activate CO<sub>2</sub> and C-H bond to allow the insertion of CO<sub>2</sub> into ethane. In this sense, the activation

of short chain alkanes and specially ethane over zeolites has been reported.<sup>350,351</sup> Accordingly, a theoretical study using density functional theory (DFT) has recently investigated possible reaction pathways for the conversion of CO<sub>2</sub> and C<sub>2</sub>H<sub>6</sub> to propanoic acid over Au-exchanged MCM-22 zeolite catalyst.<sup>352</sup> The insertion of CO<sub>2</sub> was envisioned following two different routes. The first one involves only the metal center, the CO<sub>2</sub> insertion into the Au-H bond followed by the C-C coupling and the formation of propanoic acid with an activation energy for the rate-determining step of 48.2 kcal mol<sup>-1</sup>. The second route involves the metal center and framework Brønsted acid sites with the formation of gold ethyl hydride species with the corresponding transfer of hydrogen to the oxygen framework providing the Brønsted-acid site, followed by the protonation of CO<sub>2</sub> and the simultaneous C-C coupling. In this second case, the activation energy is 44.2 kcalmol<sup>-1</sup> and it is the favoured route, at low temperatures (Scheme 44). The authors estimated that an increase of temperature could be enough to overcome the barrier energy to perform the direct insertion of CO<sub>2</sub> into ethane in the presence of Au-exchanged MCM-22.



**Scheme 44.** Proposed mechanism for the direct synthesis of propanoic acid from CO<sub>2</sub> and ethane over Au/MCM-22 catalyst.

#### 4.4. Conclusions

Carboxylic acids would ideally be produced from the direct reaction of carbon dioxide with alkanes and some studies provide essential data to rationalize the activity and selectivity for the conversion of CO<sub>2</sub> and alkanes to carboxylic acids. However, the use of CO<sub>2</sub> as a renewable building block for the synthesis of carboxylic acids via green processes is still at an early stage and, despite great scientific interest and advantages, remains a big challenge. Different synthetic routes involving the use of activated substrates, stoichiometric organometallic reagents, reducing agents, salts, with the co-production of large amounts of residues present some achievements but significant drawbacks. Undoubtedly, the development of efficient and multifunctional heterogeneous catalysts is crucial. In-depth knowledge through computational chemistry and in situ spectroscopy should be important tools to determine the active species and reaction intermediates that will enable the design of new catalysts and processes to achieve environmental and economic goals. For sure, zeolite and OMS will play a crucial role due to their unique tunable properties and their chemical and thermal stability. So far, CO<sub>2</sub> fixation in carboxylic acids remains unattainable from an industrial point of view.

## 5 Hydrogenation of CO<sub>2</sub>

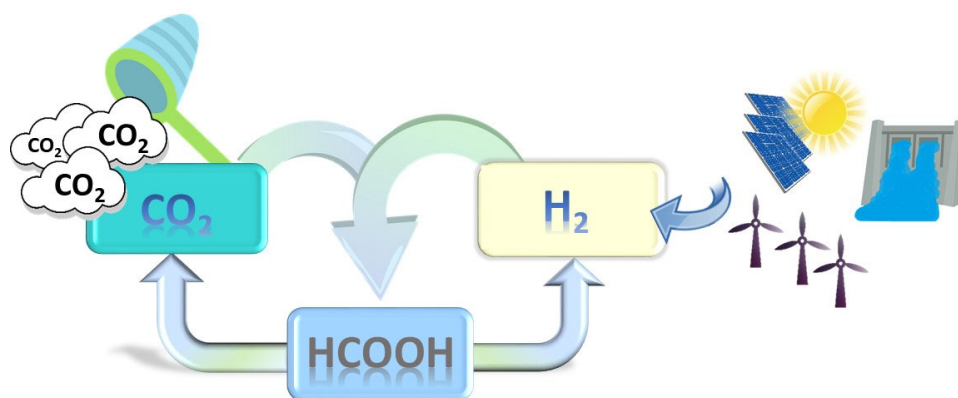
Hydrogen is a promising fuel but it lacks the energy density for practical use. Conversion of CO<sub>2</sub> and hydrogen into liquid fuels such as methane or methanol, via Power-to-Liquid (PtL) processes, is more desirable from an energy density perspective. Moreover, considering the intermittence of renewable sources to produce H<sub>2</sub>,<sup>353</sup> CO<sub>2</sub> hydrogenation to methanol, methane or dimethylether can provide an important approach to store energy. However, significant improvement in catalyst technology for CO<sub>2</sub> conversion is required for carbon capture and utilization to become an economically viable alternative. Hydrogen can be produced from fossil sources such as natural gas and coal, and from water electrolysis using electricity from nuclear plants or from renewable sources, such as wind, solar, geothermal, and hydroelectric power. Therefore, to fulfill concepts of sustainability and green chemistry and make CO<sub>2</sub> hydrogenation a valuable strategy, hydrogen has to be green and produced from non-fossil sources. Currently, different approaches to green H<sub>2</sub> production, such as water electrolysis using fuel cells, biomass thermo-chemical process, anaerobic fermentation or water splitting through photo-electrolysis are being considered.

### 5.1. Hydrogenation/Reduction of CO<sub>2</sub> to formic acid

For several CO<sub>2</sub> conversions, the enthalpy changes revealed that the transformations are exothermic despite the high stability of CO<sub>2</sub>. Nevertheless, in almost all cases the Gibbs free energy changes is positive and thermodynamically unfavoured.<sup>354–357</sup> Negative Gibbs free energy changes often correspond to hydrogenation reaction where very stable compounds such as water is produced, or to CO<sub>2</sub> transformation where C-O bonds are not broken.<sup>358</sup> Besides CO<sub>2</sub> transformations are not thermodynamically favourable, in practice, by working in adequated conditions such as pressure, temperature and ratio of reactants, processes involving CO<sub>2</sub> activation and reaction must be possible and of clear interest. Hydrogenation/reduction process are attractive and valuable processes even if it is still challenging to convert CO<sub>2</sub> into platform molecules with high activity and selectivity. If this is achieved and industrially applied, it will impact over our daily life, economy, CO<sub>2</sub> mitigation, environment and climatic changes.

#### 5.1.1. Introduction

Formic acid is the simplest organic acid. It is eco-friendly, noncorrosive and easily biodegradable, being a valuable chemical used as dyeing in the textile and leather industries, as an intermediate in the chemical and pharmaceutical industry<sup>359</sup>, green solvent and moreover a promising hydrogen storage component. Reversible processes of hydrogenation/ dehydrogenation make possible the hydrogen storage through the formation of formic acid from CO<sub>2</sub> hydrogenation, and the decomposition into CO<sub>2</sub> and H<sub>2</sub> is thermodynamically downhill (Scheme 45).<sup>360,361</sup>



**Scheme 45.** Reversible hydrogen storage.

The current industrial methods for formic acid production include hydrolysis of methyl formate or formamide, oxidation of biomass<sup>359</sup> and the reaction of CO with water.<sup>362</sup> All these methods imply the production of hazardous waste formations and high energetic costs. According to the report of Coval Energy, the global annual demand for formic acid was around 870 ktons in 2021 with a forecasted compound annual growth rate (CAGR) of 3.87% during the period 2022-2027.<sup>363</sup>

The direct hydrogenation of CO<sub>2</sub> into formic acid constitutes a green and 100 % atom economy reaction allowing to mitigate CO<sub>2</sub> emissions and to store H<sub>2</sub> in a liquid form. CO<sub>2</sub> hydrogenation is an important approach to use CO<sub>2</sub> to produce C1 chemicals but it is still challenging due to CO<sub>2</sub> inertness and stability. Moreover, this conversion is entropically disfavoured since involves a phase change from gaseous reagents into a liquid product (Scheme 46).



**Scheme 46.** Hydrogenation of CO<sub>2</sub> into formic acid.

Important progress in the development of highly efficient and robust homogeneous catalytic systems, especially Ru<sup>362,364</sup> and Ir-based metallic complex requiring the use of a co-catalyst such as phosphines, amines or carbonates salts has been achieved.<sup>365-368</sup> Nevertheless, in spite of their excellent catalytic performance in terms of activity and selectivity<sup>369</sup> with TON and TOF up to 110000h<sup>-1</sup>,<sup>370</sup> several drawbacks such as toxicity, difficult separation of formic acid or formic acid derivatives and the no recyclability of the homogeneous catalysts make it necessary to develop efficient, robust and recyclable catalytic systems makes necessary to develop efficient, robust and recyclable catalytic systems.<sup>371,372</sup>

### 5.1.2. Zeolite-based catalysts for formic acid synthesis

Heterogeneous catalysts have been widely explored for formic acid production from CO<sub>2</sub> in the presence of nanoparticulate noble and non-noble metals supported on carbon, metal oxides and silica.<sup>373</sup> See for instance, raney nickel in the presence of amines,<sup>374</sup> synthesized nanoporous



nickel,<sup>375</sup> Pd/C,<sup>376</sup> Au/TiO<sub>2</sub>.<sup>377</sup> However, only few works studied the potential catalytic properties of zeolite based catalysts for this reaction.

Virtual screening constitute an important tool to avoid or support tedious studies based on experimental trial and error studies. Computational screening is a method that broadly combines computational algorithms for selecting promising candidates from a large library of materials. The combination of modular building-block approach and the potential for computational screening has allowed the introduction of the Materials Genome Initiative (MGI) to “discover, develop, and deploy new materials twice as fast”.<sup>378</sup> MGI attempts to combine theory, computation, synthesis, and characterization to boost the discovery and synthesis of new materials.<sup>379</sup> In agreement, a computational screening of well-known zeolites as great catalysts combining molecular simulation and machine-learning techniques it is being of much use for advancing synthesis and reactivity<sup>380–383</sup> and also for conversion of CO<sub>2</sub> into useful products.<sup>384</sup> In this study, the combination of adsorption simulations, dual-adsorption models, energy-entropy calculations, statistical and machine learning modelling techniques allowed to establish structure-property relationships based on structural characteristics (pore size, surface area, voids) and zeolite performance for the production of methane, methanol, formic acid and formaldehyde. Therefore, promising zeolite candidates were determined to have cavity size of around 6 Å to maximize the strength of dual-adsorption of hydrogen and CO<sub>2</sub>. Then, the possible mechanism of CO<sub>2</sub> hydrogenation to formic acid on Lewis acid zeolites has been investigated by using density functional theory (DFT).<sup>385</sup> The CO<sub>2</sub> hydrogenation and formate ion formation was considered to be the rate-determining step for Sn-ZSM-5 zeolites. The activation barrier was calculated for both perfect (38.2 kcalmol<sup>-1</sup>) and defect Lewis center (33.0 kcalmol<sup>-1</sup>). A Sn-ZSM-5 active site allows minimizing the activation energy in comparison to Sn-BEA or Sn-FAU. While the order of activation energy for the metal center was determined as following: Hf > Zr > Sn > Ge, which is dependent on the charge transfer from the catalytic active site to the reacted molecule. This result showed the importance of charge transfer from the metal to CO<sub>2</sub> for the activation of the C=O bond and also the H–H bond breaking via oxygen abstraction on the Sn-OH site of defect zeolites.

Recent studies showed the good catalytic properties of molecular-sized Ir<sub>4</sub> clusters stabilized in FAU and MWW zeolites for hydrogenation dehydrogenation reactions.<sup>51,386,387</sup> Accordingly, a theoretical work reporting the CO<sub>2</sub> mechanism to produce formic acid catalyzed by faujasite-supported Ir<sub>4</sub> clusters was reported.<sup>388</sup> Both hydrogenation of CO<sub>2</sub> into CO, thermodynamically favoured, and hydrogenation of CO<sub>2</sub> into formic acid, kinetically preferred under water free-conditions, can take place. The important effect of confined water cooperation for both hydrogenation process was shown. The co-adsorbed water molecule facilitates the H<sup>+</sup> transfer

step by a water molecule between the zeolite Brønsted acid sites and Ir<sub>4</sub> cluster. However, if the formation of Ir–COOH carboxyl moiety is facilitated by the presence of water this latter also promotes the selective decarbonylation of COOH species and the production of CO. The authors so concluded that was impossible to obtain formic acid in the presence of water using Ir<sub>4</sub>/FAU as catalyst, and that only an effective water-removal and optimize process could ensure the selective formation of formic acid.

#### 5.1.1. OMS-based catalysts for formic acid synthesis

The immobilization of homogeneous catalysts via covalent bonding is an alternative to overcome problems of separation and to improve the environmental impact and costs, by combining the advantages of both homogeneous and heterogeneous catalysis. This strategy has received a lot of interest for the preparation of formic acid.<sup>372,389–391</sup>

Following the above direction, MCM-41 functionalized with  $\gamma$ -NH<sub>2</sub>, CN and SH -propyl trimethoxysilane incorporating RuCl<sub>3</sub> were prepared and tested in the hydrogenation of CO<sub>2</sub> into formic acid, at 80°C, 5.4 MPa H<sub>2</sub> and 9.3 MPa CO<sub>2</sub> (SC) partial pressures, 1h and in the presence of ethanol as solvent.<sup>392</sup> The importance of the nature and use of a solvent as well as of the ligands showed the influence on the activity of the MCM-41 immobilized ruthenium complex. The three types of MCM-41 immobilized ruthenium complex exhibited TON up to 1022. Nevertheless, the stability of the catalyst was limited. The structured mesoporous material with SH groups showed the best stability but the lowest activity while the material with NH<sub>2</sub> groups exhibited lower stability but better activity. The differences in activity and stability were attributed to the complexation ability of the different groups (NH<sub>2</sub>, CN and SH). More recently, the preparation and catalytic performance of SiO<sub>2</sub> and MCM-41 supported Ruthenium materials for the selective hydrogenation of CO<sub>2</sub> to formic acid, at 80°C, 40 bar (P<sub>H<sub>2</sub></sub>:P<sub>CO<sub>2</sub></sub>=1:2) were reported.<sup>393</sup> In terms of TON/TOF values, Ru/MCM-41 exhibited higher catalytic performance than Ru/SiO<sub>2</sub> due to its textural properties and large surface area that allow high metal dispersion. Additionally, the catalytic performance of Ru/MCM-41 was improved with the use of sulfated and fluorinated ionic liquid [DAMI][CF<sub>3</sub>CF<sub>2</sub>CF<sub>2</sub>CF<sub>2</sub>SO<sub>3</sub>] (DAMI= 1,3-di(*N,N*-dimethylaminoethyl)-2-methylimidazolium). In this way, the production of formic acid with TON value up to 1780 with Ru/MCM-41 in [DAMI][CF<sub>3</sub>CF<sub>2</sub>CF<sub>2</sub>CF<sub>2</sub>SO<sub>3</sub>] ionic liquid medium and the stability of catalytic properties in the presence of water were established. The recyclability of the catalyst was shown and Ru/MCM-41 in [DAMI][CF<sub>3</sub>CF<sub>2</sub>CF<sub>2</sub>CF<sub>2</sub>SO<sub>3</sub>] was recycled for eight times with practically not loss of activity. This catalytic reaction system offer a green attempt to the production of formic acid and can be used as a leading direction for further developpements.

### 5.1.2. Conclusion

This short review of the state of the art related with the use of ordered microporous and mesoporous based catalysts for the CO<sub>2</sub> hydrogenation into formic acid clearly revealed that the potential of these types of material has been underconsidered despite the requirement of novel catalytic system for the challenging formic acid production to close the hydrogen cycle.

Indeed, the direct hydrogenation of CO<sub>2</sub> to formic acid is an ideal reaction with 100% atom economy. Nevertheless, at the same time very challenging since activate both H<sub>2</sub> and CO<sub>2</sub> molecules is a hard task, and CO<sub>2</sub> hydrogenation to formic acid is thermodynamically unfavored. Moreover, to achieve higher yield and turnover number, stoichiometric amounts of organic or inorganic bases (DBU, NaOH, KOH, K<sub>2</sub>CO<sub>3</sub>, TEA) are widely used to shift the thermodynamic equilibrium to formate. Notice that the present reaction procedure requires further neutralization steps with stoichiometric amount of acid that produce high amount of salts and waste, and tedious recovery of formic acid. To achieve environmental and economic goals, a greener and more efficient process is imperative, and heterogeneous catalysts are very valuable, attractive, and prime candidates. Thus, an efficient catalyst will have active centers to adsorb and activate hydrogen (metal species) based on noble metals (Ru, Rh, Pd, Au) and other metals such as Co, Ni, Cu and Fe, high CO<sub>2</sub> adsorption capacity and CO<sub>2</sub> activation, which will be achieved by the incorporation of acidic and basic Lewis sites and oxygen vacancies. Undoubtedly, the support will play a key role in adsorbing CO<sub>2</sub>, dispersing and stabilizing the different active species. Zeolite and OMS will be major players due to their unique and tunable properties (high surface area, Lewis and Brønsted acid/base properties, chemical and thermal stability). In addition, a thorough understanding of the reaction mechanism, kinetics and determination of the active species and reaction intermediates will only be possible through computational chemistry and in situ spectroscopy studies, fundamental tools for the design of new catalysts and processes.

## 5.2. Hydrogenation of CO<sub>2</sub> to methanol

### 5.2.1. Introduction

In the context of H<sub>2</sub> and CO<sub>2</sub> conversion into liquid fuels via Power-to-Liquid processes, the methanol production from CO<sub>2</sub> is of much interest. Methanol is a large scale product with industrial production capacity of about approximately 140 million metric tons in 2018 that is expected to double to reach 280 million metric tons by 2030.<sup>394</sup> Industrial production of methanol is from synthesis gas mixtures (H<sub>2</sub>/CO<sub>2</sub>/CO) at high pressures (50-100 bar) and temperatures (200-300°C) over Cu/ZnO/Al<sub>2</sub>O<sub>3</sub> catalysts.<sup>395</sup> Methanol constitutes an important chemical feedstock and a platform molecule to produce a large variety of bulk commodities<sup>396</sup>

and fuels<sup>397</sup> for engines and fuel cells. Numerous methanol commodity derivatives are produced for their use in our daily life such as paints, polymers, plastics, resins, adhesives, and antifreezes. Taking into account the potential of methanol, George A. Olah and co-workers<sup>395</sup> published in 2006 a report of current fossil fuels as energy sources and future alternative sources. There, they discuss the important and future role of methanol and advocated the “methanol economy” whose concept purveys the idea that methanol can be used as an alternative way for storing, transporting and using energy.<sup>398</sup>

Figure 16 illustrates the importance of methanol as carbon feedstock issued from green hydrogenation of CO<sub>2</sub> to reach carbon neutrality, and a crucial pathway to reach circularity. One of the most promising route to produce methanol is the direct CO<sub>2</sub> hydrogenation. The development of active catalysts and specially zeolite-based catalysts for the conversion of methanol to olefins (MTO),<sup>399–402</sup> aromatics, propylene (MTP), dimethyl ether<sup>404,405</sup> and fuels,<sup>406</sup> will play a key role due to the flexibility in their catalytic properties such as the versatility in their composition and the nature of the active sites, robustness, stability and readily availability of zeolite and OMS, and should mark a new breakthrough in the field of molecular sieves.

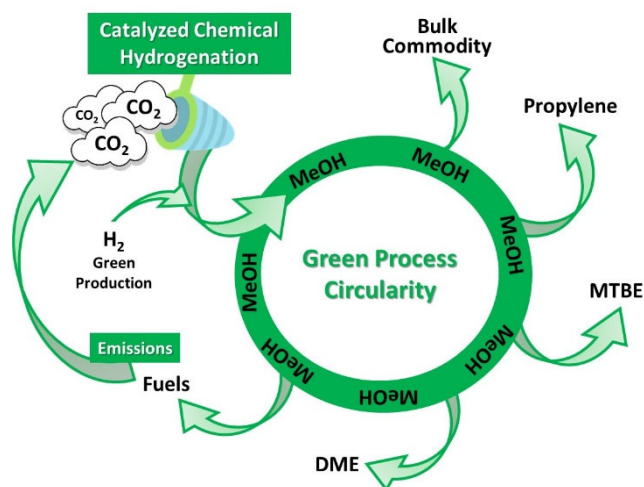
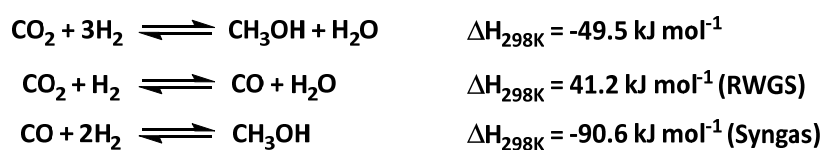


Figure 16. Importance of methanol as carbon feedstock issued from green hydrogenation of CO<sub>2</sub> to reach carbon neutrality.

### 5.2.2. Thermodynamics for CO<sub>2</sub> hydrogenation to methanol

Methanol is typically synthesized from syngas (H<sub>2</sub>+CO) issued from fossil fuels.<sup>371,407</sup> This process is highly exothermic and the major challenge is to control and remove heat excess to shift the equilibrium towards methanol production minimizing side reactions and catalyst sintering. The commercial catalyst generally contains Cu and a mixture of oxides such as ZnO/Al<sub>2</sub>O<sub>3</sub> and operates under relative “soft” conditions, 210-270°C and 50-100 bar.<sup>408</sup> The main side products are higher alcohols, methane, methyl formate and dimethyl ether. The formation of methanol by direct hydrogenation of CO<sub>2</sub> constitutes an alternative and a challenging route. Direct

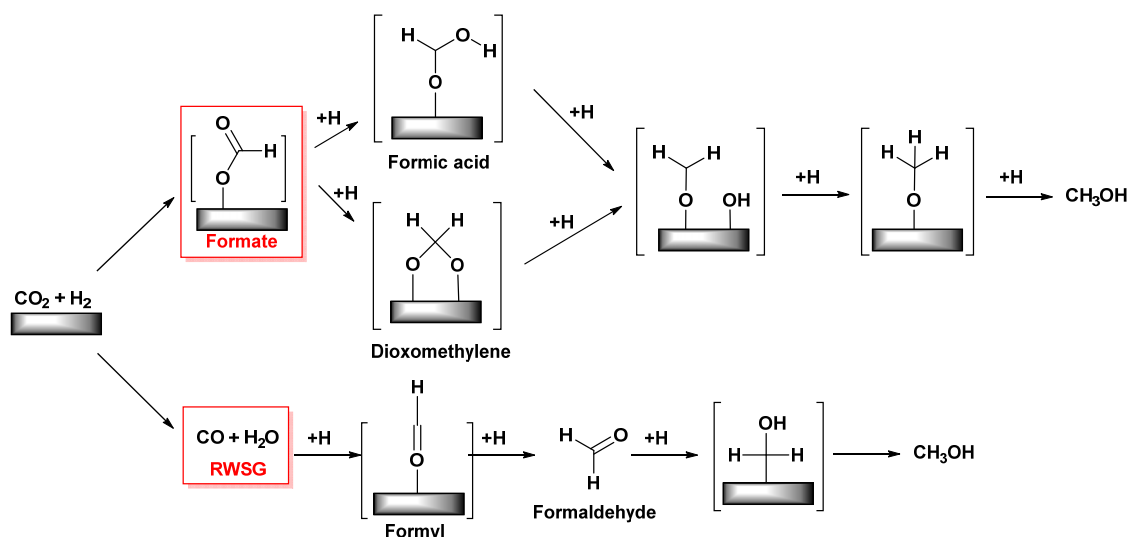
hydrogenation of CO<sub>2</sub> competes directly with reverse water-gas shift (RWGS) and the large production of water has a severe negative effect over the catalyst life and the performance of ternary catalyst Cu-ZnO-Al<sub>2</sub>O<sub>3</sub>. Moreover, the hydrophilic properties of alumina favour sintering and aggregation of metal. CO issued from RWGS can undergo hydrogenation into methanol (Scheme 47). From thermodynamics standpoint, the enthalpies variation show that CO and CO<sub>2</sub> hydrogenation are exothermic and involve a decrease of volume that means that the use of lower reaction temperatures and higher pressures are thermodynamically favourable, while the reverse water-gas-shift reaction is strongly endothermic (Scheme 47). However, a higher temperature favours CO<sub>2</sub> activation, while an increase in temperature also promotes the undesirable formation of CO and H<sub>2</sub>O, limiting CO<sub>2</sub> conversion.



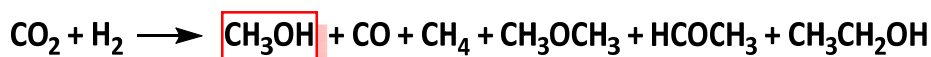
**Scheme 47.** Formation of methanol by direct hydrogenation of CO<sub>2</sub> and CO issued from RWGS.

### 5.2.3. Mechanism insights for CO<sub>2</sub> hydrogenation to methanol

A thorough understanding of the reaction mechanism and how the catalyst participates should help to realise a molecular design of a catalyst able to work at low temperature (< 200°C). Two main kinetic expressions have been reported for the formation of methanol considering commercial Cu/ZnO/Al<sub>2</sub>O<sub>3</sub> catalyst.<sup>409,410</sup> The first kinetic model considers the formation of methanol from both CO and CO<sub>2</sub> whereas the second model only considers CO<sub>2</sub> as source of methanol. Despite the large number of mechanistic studies based on theoretical and experimental data, the mechanism of methanol synthesis from CO<sub>2</sub> remains controversial as evidences for the formation of both, formate,<sup>411–413</sup> being the hydrogenation of HCOO to H<sub>3</sub>CO the rate-limiting step,<sup>414</sup> and CO, as intermediates<sup>415–417</sup> (Scheme 48). Indeed, some reports postulate that the first step of the direct hydrogenation of CO<sub>2</sub> is the formate intermediate formation, while other propose that RWGS takes place followed by CO hydrogenation into methanol.<sup>416</sup> Scheme 49 illustrates the possible oxygenated products issued from CO<sub>2</sub> hydrogenation.



**Scheme 48.** Proposed reaction mechanism for CO<sub>2</sub> hydrogenation to methanol according to different studies.



**Scheme 49.** Possible oxygenated products issued from CO<sub>2</sub> hydrogenation.

#### 5.2.4. Catalysts for CO<sub>2</sub> hydrogenation to methanol

There are more than 200 papers published in the last decade dealing with the hydrogenation of CO<sub>2</sub> into methanol. Nevertheless, few studies reported the direct hydrogenation of CO<sub>2</sub> into MeOH using zeolite based catalysts. However, the textural properties of ordered mesoporous silica have been used to disperse metal-oxides active phase and to take advantage of the confinement. Due to the enhanced catalytic performance of the ternary catalyst Cu/ZnO/Al<sub>2</sub>O<sub>3</sub>, and the similarity between syngas-to-methanol conversion, Cu-based and Cu/ZnO based materials have been extensively investigated. Up to now, Cu is regarded as the main active component for CO<sub>2</sub> hydrogenation and ZnO is regarded to promote hydrogen spillover and the dispersion of Cu nanoparticles. Numerous papers described the catalytic performance of catalysts based on Cu and/or Pd.<sup>371,418</sup> Actually, bifunctional metal-zeolite based materials are preferentially used for the synthesis of dimethylether, olefins or aromatics since it is possible to take advantage of the acid properties of these materials and shift the process selectivity avoiding competitive side reactions. Indeed, the presence of multinuclear metal centers and active sites in a single solid catalyst presents several advantages over mononuclear catalysts due to cooperativity effect between the different centers such as synergetic activation of substrates and electronic interactions between the metal centers, which is potentially beneficial to catalytic activity. Hence, investigations have focussed on the preparation of metal oxide with excellent activity and stability for the hydrogenation of CO<sub>2</sub> and efficient catalysts should exhibit high

specific surface area, high number of active sites, high dispersion, optimum acid/base sites distribution, and small particle size in order to increase the activity and selectivity to methanol.

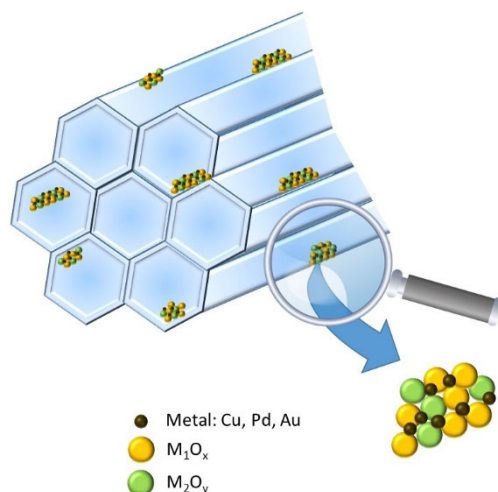
a) OMS-based catalysts for CO<sub>2</sub> conversion to methanol

i) *Cu/OMS-based catalysts for CO<sub>2</sub> conversion to methanol*

Cu is a good monometallic catalyst for the methanol synthesis<sup>419</sup> but, if used alone, results in low catalytic rates and selectivity towards methanol. However, Cu catalytic performance can be enhanced by forming a Cu/ZnO active phase. Indeed, pure Cu surface is shown to convert CO<sub>2</sub> to CO, while combination of Cu and ZnO greatly boosts the methanol formation,<sup>420</sup> since the use of metal oxide allows high dispersion and stabilization of Cu due to special interaction metal/metal, basicity, reducibility properties and oxygen lattice, that favour the coordination and activation of CO<sub>2</sub>, maximizing the catalyst activity for methanol synthesis.<sup>421,422</sup> So far, Cu/ZnO catalysts for industrial applications or theoretical research are still in the forefront of the investigation due to their prominent catalytic properties.<sup>422,423</sup> The studies to improve Cu-based catalysts properties for CO<sub>2</sub> hydrogenation into MeOH focus on improving Cu nanoparticles dispersion by varying the preparation method and/or metal precursor and by incorporating promoters.<sup>424,425</sup>

To optimize the catalytic features, the understanding and definition of the nature of active sites in Cu/ZnO is fundamental. The metal oxide interface is crucial to enhance and create catalytic ability and the synergy of Cu and ZnO<sub>x</sub> at the interface was shown to promote the methanol synthesis.<sup>426,427</sup> Nevertheless, destructive effects of hydrothermal reaction conditions, induce a rupture at Cu-ZnO<sub>x</sub> interface, sintering of Cu particles that modify the catalytic properties and decrease methanol selectivity.<sup>428,429</sup>

The interaction between Cu and oxide components enables the formation of Cu-MO<sub>x</sub> (M=Zn and/or Zr) active species at the Cu-MO<sub>x</sub> interface and the catalytic activity depends on the interaction between Cu and metal oxide components.<sup>430</sup> Therefore, the confinement or encapsulation<sup>431</sup> of Cu-MO<sub>x</sub> on the wall of porous materials was considered as a promising route to improve the metal dispersion and the sintering resistance, and thus enhance the stability and selectivity of the catalytic system to methanol production. Accordingly, due to their textural properties (high surface areas, thermal and chemical stability and pore-size) ordered mesoporous materials offer opportunities to well-disperse and stabilize Cu-MO<sub>x</sub> or other active metal-oxides compounds ([Figure 17](#)).



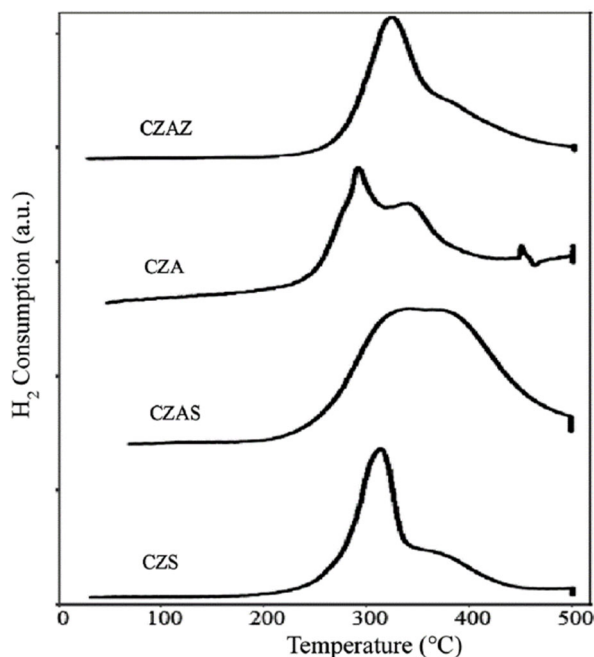
**Figure 17.** High dispersion and stabilization of Metal-MO<sub>x</sub> (active metal-oxides phase) on OMS.

*ii) Binary OMS-based catalysts for CO<sub>2</sub> hydrogenation to methanol*

As we mentioned above, the application of Cu alone-catalysts are limited due to the low stability and selectivity to MeOH. Therefore, modified catalysts with MO<sub>x</sub> (Ce, Mn, Ga, Zr, Ti) have been the purpose of many investigations due to the interfacial effects between the different metal phases that contribute to boost the catalytic performance of the final catalysts.<sup>432–434</sup> Specially, the basic properties of some oxides is expected to enhance the adsorption/activation of CO<sub>2</sub>. For example, in Cu/ZrO<sub>2</sub> catalysts, La doping promoted formate hydrogenation into MeOH and inhibited formate dissociation into CO.<sup>435</sup> Following these leads, Cu-LaO<sub>x</sub> catalysts supported on SBA-15 were prepared wherein a Cu-LaO<sub>x</sub> interface was generated through the interaction of highly dispersed Cu nanoparticles with LaO<sub>x</sub> in the SBA-15 wall.<sup>436</sup> The presence of LaO<sub>x</sub> species was beneficial to prevent the sintering of Cu and to enhance CO<sub>2</sub> activation by adsorption of CO<sub>2</sub> molecules on the Cu-LaO<sub>x</sub> interface. The optimized Cu<sub>1</sub>La<sub>0.2</sub>/SBA-15 catalyst displayed the best catalytic performance in terms of methanol selectivity (81.2%) and stability, with 5.7% CO<sub>2</sub> conversion (Table 4, Entry 2). The preparation and characterization of Cu-Ga/SBA-15 catalysts was also reported.<sup>437</sup> The presence of Ga promotes the dispersion and stabilization of the Cu phase but also provides acidic sites with enhanced acidic strength due to the combination with silica. The addition of Ga improved the catalytic performance of the un-doped Cu-catalysts. 3% CO<sub>2</sub> conversion and 71% MeOH+DME were reached with the Cu-Ga/SBA-15 catalyst (Table 4, Entry 3). Attempts to disperse Cu/ZnO on SBA-15 (CZS), Al-SBA-15 (CZAS), Al<sub>2</sub>O<sub>3</sub> (CZA) and Al<sub>2</sub>O<sub>3</sub>-ZrO<sub>2</sub> (CZAZ) using impregnation methods were also investigated.<sup>438</sup> The Cu/ZnO dispersed on SBA-15 support presented the largest Cu surface area and dispersion, smallest particle size and was easily reduced. H<sub>2</sub>-TPR profiles showed two reduction peaks, at 290°C corresponding to reduction of Cu<sup>2+</sup> into Cu<sup>0</sup>, and reduction of Cu<sup>2+</sup> into Cu<sup>+</sup> and into Cu<sup>0</sup> at 337°C. However, for Cu-ZnO/Al-SBA-15 (CZAS), a single and broad reduction peak at 370°C was registered, attributed



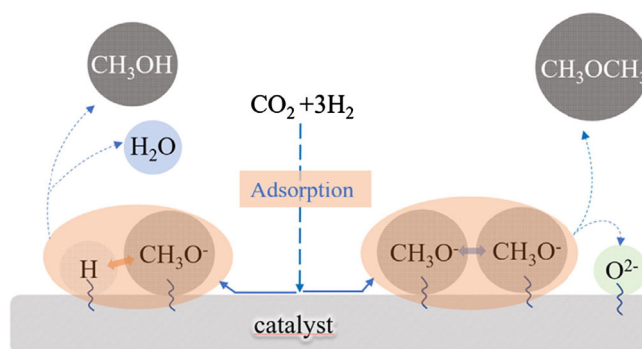
to strong metal-support interactions, in agreement with larger average particle size and lower metallic phase dispersion (Figure 18). Thus, Cu/ZnO-SBA-15 exhibited the highest catalytic activity in comparison to Cu/ZnO-Al-SBA-15, Al<sub>2</sub>O<sub>3</sub> and Al<sub>2</sub>O<sub>3</sub>/ZrO<sub>2</sub>-supported catalysts. The highest 91.32% methanol selectivity was obtained with Cu/ZnO-SBA-15 catalyst with up to 14% CO<sub>2</sub> conversion (Table 4, Entries 4-6). The same group also studied the effect of the Cu/Zn ratio in Cu-Zn-SBA-15 catalysts over the catalytic performance in fixed-bed.<sup>439</sup> A positive effect of the incorporation of Zn was shown over Cu surface areas and dispersion, while high Zn content induced an increase in the particle size and agglomeration of Cu. CO<sub>2</sub> conversion and methanol selectivity increased while the Zn content decreased from 70% to 30%. This trend was attributed to a synergetic effect between Cu and ZnO that promotes H<sub>2</sub> spillover. Then, a maximum 51.4 g<sub>MeOH</sub> h<sup>-1</sup> g<sub>cat</sub><sup>-1</sup> productivity was reached for a metal ratio Cu:Zn=7:3 and a linear relationship between Cu surface area and methanol productivity was shown, with 14.2% CO<sub>2</sub> conversion and 92.1% MeOH selectivity (Table, Entry 7).



**Figure 18.** H<sub>2</sub>-TPR profiles of Cu/ZnO supported catalysts. Reprinted with permission from ref <sup>438</sup>. Copyright 2019, Frontiers.

Recently, the catalytic performance of Cu supported on Zr-doped SBA-15 was explored.<sup>440</sup> The Zr doping allowed promoting the formation of acid sites, and because Cu is prone to occupy the acid sites, higher Cu dispersion was reached. Before Cu nanoparticles confinement inside the pores, the external surface of Zr-SBA-15 was methylated and functionalized with amine groups to promote Cu<sup>2+</sup> coordination. High catalytic activity of Cu/Zr-SBA-15 was reached, achieving 15% CO<sub>2</sub> conversion but with low selectivity to MeOH, close to 27% (Table 4, Entry 8). In a following work, the Cu/Zr-SBA-15 catalytic performance was reported under optimized reaction

conditions and exhibited 25% CO<sub>2</sub> conversion after 14 days with considerably improved methanol selectivity close to 80% (Table 4, Entry 9).<sup>441</sup> More recently, the same group reported, the preparation Cu/Zr-SBA-15 following different synthetic routes. Zr-SBA-15 was synthesized using different silica sources (TEOS and SMS) while Cu was loaded following two methods, infiltration (Inf) or evaporation induced wetness impregnation (EIWI).<sup>442</sup> Zr-SBA-15 presented different morphological properties influenced by silica source and synthesis conditions, while the Cu loading method has an influence on strength and density of acid sites. Differences in catalytic selectivity were attributed to the Zr content that contributes to the electron/oxygen mobility of Cu and controlled the amount of weak and medium acid sites. The DME selectivity increases when increasing the strength of acid sites with medium acid strength. Then, Cu/Zr-SBA-15\_EIWI with high total concentration of acid sites exhibited a high methanol selectivity (92%) at 6.5% CO<sub>2</sub> conversion (Table 4, Entry 10). DRIFTS studies revealed that DME formation came from two surface methoxy groups in the CO<sub>2</sub> hydrogenation reaction, when its concentration is high enough to form DME, while methanol formation is favoured since only requires one molecule (Figure 17).



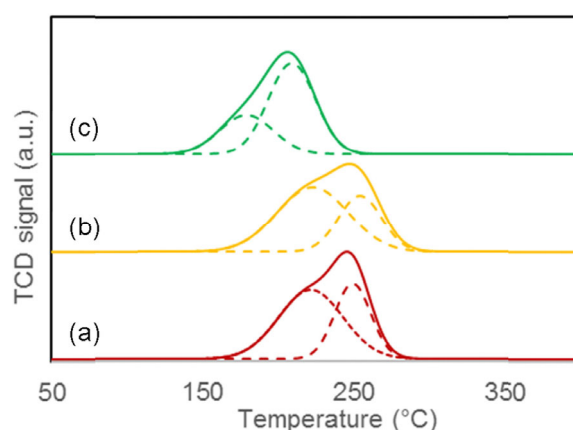
**Figure 19.** Methanol and DME formation from methoxy groups on the catalyst surface. Reprinted with permission from ref<sup>442</sup>. Copyright 2019 Elsevier Inc. All rights reserved.

### iii) Tertiary OMS-based catalysts for CO<sub>2</sub> hydrogenation to methanol

Numerous investigations have focused on the confinement of the Cu-ZnO-ZrO<sub>2</sub> active phase in OMS<sup>443</sup> due to the activity Cu-Zn-Zr catalysts<sup>444,445</sup> for methanol synthesis. Accordingly, the ordered mesoporous channels of SBA-15 were exploited to control the particle size, dispersion, and morphology of Cu-oxides nanoparticles, and to promote the interaction between multi-active sites for the double activation of H<sub>2</sub> and CO<sub>2</sub>. CO<sub>2</sub> is adsorbed on the active support while H<sub>2</sub> is adsorbed on the Cu phase to provide atomic hydrogen. The presence of zirconia was shown to enhance both the yield and selectivity to methanol. A maximum activity for the catalyst CZZS\_20\_1 (Cu-ZnO-ZrO<sub>2</sub>/SBA-15) with a space-time-yield (STY) of methanol of 376 mg<sub>CH<sub>3</sub>OH</sub> h<sup>-1</sup> g<sub>cat</sub><sup>-1</sup>, 37-times higher than the unsupported homologue was reached. The enhanced catalytic performance of the SBA-15 supported catalyst was attributed to the exposure of the active

phase to the CO<sub>2</sub> and H<sub>2</sub>. An experiment of 50 h of TOS supported showed the high performance, stability and the industrial potential of the CZSS\_20\_1 catalyst (Table 4, Entry 11).

The confinement of Cu-ZnO-MnO (CZM) active phase was also achieved in morphologically distinct siliceous porous carriers such as SBA-15, MCF and KIT-6.<sup>446</sup> SBA-15 is a 2D mesoporous silica with pore channels in hexagonal arrangement, MCF (mesostructured cellular foam) is a 3D mesoporous silica with large uniform spherical cells and KIT-6 is an ordered 3-D mesoporous silica with gyroid cubic structure. The effect of different textural properties was expected to greatly influence the catalytic behavior of the prepared catalyst. Indeed, a large surface area carrier was expected to promote the formation of small metal nanoparticles with high dispersion, enabling the exposure of large metal surface area to the reactants. CZM- SBA-15 and KIT-6 resulted to be the most efficient catalysts with 99% methanol selectivity and particularly, CZM KIT-6 exhibited the higher CO<sub>2</sub> conversion (8.2%) and STY (Table 4, Entries 12-13). Cu<sup>0</sup> particle size after reduction followed the order CZM/KIT-6 < CZM/SBA-15 < CZM/MCF, inversely to Cu<sup>0</sup> surface area that followed the order CZM/KIT-6 > CZM/SBA-15 > CZM/MCF. Thus, together with higher copper surface area, the particular morphological features of KIT-6 enabled higher CO<sub>2</sub> effective diffusivity. Therefore, the CO<sub>2</sub> conversion was correlated with the order of copper surface area, since dissociative adsorption of H<sub>2</sub> occurs on the copper sites, and as could be expected, the production of atomic hydrogen increases when increasing the copper surface area. The H<sub>2</sub>-TPR reduction peak was deconvoluted into two peaks assigned to the low-temperature reduction of well-dispersed CuO, and to the high-temperature reduction of bulk CuO (Figure 20).<sup>435</sup> For CZM/KIT-6, lower temperature for both reduction peaks were recorded, indicating higher dispersion of CuO and lower interaction metallic phase/support for this sample.



**Figure 20.** H<sub>2</sub>-TPR profiles of (a) CZM/SBA-15, (b) CZM/MCF and (c) CZM/KIT-6. Reprinted with permission from ref<sup>446</sup>. Copyright 2018, Hydrogen Energy Publications LLC. Published by Elsevier Ltd. All rights reserved.

A study of Ce content Cu-ZnO-CeO<sub>x</sub> dispersed in SBA-15 showed that methanol and CO synthesis can be controlled on the interface of Cu/ZnO/CeO<sub>x</sub> due to the synergistic effects between the three active components and the basic character of CeO<sub>x</sub>.<sup>227</sup> Suitable morphological features of SBA-15 promoted the mass and heat transfer as well as a high dispersion and exposure of the active phases, enabling the production of methanol and CO. Cu is regarded as the active site for activating hydrogen while ZnO and CeO<sub>x</sub> are the promoters, which exhibit excellent adsorption and activation capacities for CO<sub>2</sub>. CeO<sub>2</sub> is more efficient than ZnO in promoting the dispersion of Cu nanoparticles and methanol generation, while ZnO promoted the dispersion of CeO<sub>x</sub> and the production of CO. Both ZnO and CeO<sub>x</sub> were beneficial for hydrogen spillover but mainly took part in CO<sub>2</sub> conversion and influence products selectivity. XPS and Cu LMM XAES spectra of reduced sample showed no satellite peaks of Cu 2p<sub>3/2</sub> and Cu 2p<sub>1/2</sub> in the XPS spectrum, indicating that Cu<sup>2+</sup> was completely reduced, while two peaks at 932.7 and 952.7 eV were assigned to Cu 2p<sub>3/2</sub> and Cu 2p<sub>1/2</sub> of Cu<sup>+</sup> or Cu<sup>0</sup>, respectively. Moreover, a broad Auger kinetic energy peak registered on Cu LMM XAES spectrum was fitted into two peaks centered at 916.9 and 913.8 eV, corresponding to Cu<sup>0</sup> and Cu<sup>+</sup> species, respectively. The shift towards lower values indicates strong interaction between metallic species, Cu, ZnO and CeO<sub>x</sub> due to the Lewis acidity of ZnO and CeO<sub>x</sub> which promotes the presence of Cu<sup>+</sup> beneficial for hydrogenation process. H<sub>2</sub>-TPR profiles of the calcined samples revealed only a symmetrical peak for Zn/Ce≤1 indicating the presence of only one oxidation state of CuO<sub>x</sub> with uniform particle size. High dispersion of metal oxides generally involves strong interactions metal/support leading to a shift to higher temperature of reduction peak. However, the incorporation of Ce also promotes high dispersion of CuO<sub>x</sub> induces a reduction peak shift to lower temperature attributing to easier reduction of the catalyst via hydrogen spillover, on the interface between Cu/CeO<sub>x</sub>.<sup>447</sup> The catalytic performance over 10Cu8Zn2Ce/SBA-15 was maintained for 100 h (Table 4, Entry 14). This study revealed new aspect to design highly dispersed active species with controlled selectivity to methanol synthesis.

*iv) Pd and other metallic catalysts for CO<sub>2</sub> hydrogenation to methanol*

Pd exhibits suitable catalytic properties for CO<sub>2</sub> hydrogenation and the presence of specific metal oxide such as Ga<sub>2</sub>O<sub>3</sub> or CaO were shown to enhance the formation of methanol.<sup>448–450</sup> The catalytic features of Pd catalysts based on morphologically distinct siliceous porous supports (MCM-41, SBA-15, MCM-48, MSU-F and amorphous SiO<sub>2</sub>) for CH<sub>3</sub>OH synthesis integrating alkali/alkaline earth metal additives were investigated.<sup>451</sup> The rate of CH<sub>3</sub>OH formation in the presence of supported Ca/Pd catalysts was a function of average pore diameter, and decreased in the following order: MCM-41 > SBA-15 > MCM-48 > MSU-F ~ amorphous SiO<sub>2</sub>. The study

revealed that the smaller mesopores of MCM-41 and SBA-15 enabled the formation of small Pd nanoparticles increasing the catalytic performance in comparison to amorphous supported catalyst. Moreover, the addition of promoter improved the catalytic activity of the catalysts, Ca promoting the rate of CH<sub>3</sub>OH formation rather than the formation of CO. Pd(6)/Ca(0.4)/SBA-15 was active and stable for 40 h on stream to CH<sub>3</sub>OH and CO production. Nevertheless, the CH<sub>3</sub>OH selectivity (31%) remained low and required to be improved in comparison to CO selectivity (Table 4, Entry 15). A few years later, the same group reported the catalytic performance of bimetallic Cu-Pd catalysts.<sup>452</sup> Characterization results confirmed the formation of Pd-Cu alloys for hydrogen adsorption capacity for facilitating methanol production. In the precedent paper, the rate of methanol formation varied with pore diameter of the supports, while Pd(0.25)-Cu/SiO<sub>2</sub> was the most active catalyst being the methanol formation rate improved by 27%. Two reaction pathways were considered to take place on Pd-Cu alloy surfaces: formate hydrogenation and RWGS + CO hydrogenation. Nevertheless, the methanol STY remained low and cannot be considered for industrial application (Table 4, Entry 16).

In<sub>2</sub>O<sub>3</sub>-based catalysts have been reported to possess oxygen vacancies able to activate CO<sub>2</sub> and to exhibit higher methanol selectivity. Then, very recently, Pd, as a promoter of H<sub>2</sub> dissociation, was introduced into In<sub>2</sub>O<sub>3</sub>/SBA-15.<sup>453</sup> Based on DFT calculations the synergetic effect of Pd with In<sub>2</sub>O<sub>3</sub> was explained on the bases of Pd sites exhibited high ability to dissociate H<sub>2</sub> and thus to promote the formation of more active oxygen vacancies on In<sub>2</sub>O<sub>3</sub> surface suitable to activate CO<sub>2</sub>. Under the best reaction conditions, 84% methanol selectivity, 12.6% CO<sub>2</sub> conversion were achieved, giving STY of 352 mg<sub>CH<sub>3</sub>OH</sub>·h<sup>-1</sup>·g<sub>cat</sub><sup>-1</sup>, at 260°C and 5 MPa. No noticeable catalyst deactivation was observed for 120h on stream. Taking into account the methanol selectivity, the space time yield, and the catalyst stability, these results illustrate the relevance of Pd-In<sub>2</sub>O<sub>3</sub>/SBA-15 for industrial application to methanol production from direct CO<sub>2</sub> hydrogenation (Table 4, Entry 18). In earlier attempts, a ternary Au/ZnO/TiO<sub>2</sub> catalyst with small Au particles was studied for methanol synthesis from CO<sub>2</sub> hydrogenation.<sup>454</sup> Accordingly, Au-CuO/SBA-15 catalysts were prepared and their catalytic behavior studied for the CO<sub>2</sub> hydrogenation. A maximum 13.5% selectivity to methanol was obtained at 24.2% CO<sub>2</sub> conversion in the presence of Au-CuO/SBA-15 catalyst with 2 wt% Au content.<sup>455</sup> The interaction between Au and CuO enables to improve the thermal stability and the hydrogen adsorption/dissociation at the Au/CuO interface. Nevertheless, the stability and catalytic performance of Au-CuO/SBA-15 were limited and unsatisfactory (Table 4, Entry 19).

**Table 4.** Comparison of the catalytic data of the different M-oxides supported on OMS for CO<sub>2</sub> hydrogenation to methanol.

Entry	Catalyst**	T°C, Pressure (MPa)	CO <sub>2</sub> Conv.%	CH <sub>3</sub> OH Sel.%	CH <sub>3</sub> OH, STY mg <sub>CH<sub>3</sub>OH</sub> g <sub>cat</sub> <sup>-1</sup> h <sup>-1</sup>	GHSVmlg <sub>cat</sub> <sup>-1</sup> h <sup>-1</sup>	Year	Ref
1	Cu/ZnO	240°C, 3 MPa	16.5	78.2	550		2015	456
<b><i>Cu-based-binary catalysts</i></b>								
2	10Cu-2La/SBA-15	240°C, 3 MPa	5.7	81.2	190.8	GHSV=1.2 Lg <sub>cat</sub> <sup>-1</sup> h <sup>-1</sup> , H <sub>2</sub> :CO <sub>2</sub> :N <sub>2</sub> =72:24:4	2019	436
3	10Cu-5Ga/SBA-15	250°C, 2.5 MPa	3	71	N/A	CO <sub>2</sub> :Ar:H <sub>2</sub> =5:5:15, GHSV=30000 h <sup>-1</sup>	2018	437
4	4.5Cu-10.5Zn/Al-SBA-15	210°C, 2.25 MPa	14	91.3	N/A	H <sub>2</sub> :CO <sub>2</sub> =3:1, no data for GHSV	2017	438
5	4.5Cu-10.5Zn/SBA-15	210°C, 2.25 MPa	12	80	N/A		2017	438
6	4.5Cu-10.5Zn/Al <sub>2</sub> O <sub>3</sub>	210°C, 2.25 MPa	11	77	N/A		2017	438
7	10Cu-5Zn/SBA-15	250°C, 2.25 MPa	14.2	92.1	51.4	GHSV=46706h <sup>-1</sup> , H <sub>2</sub> :CO <sub>2</sub> =3:1	2016	439
8	15Cu/Zr-SBA-15	250°C, 3.3 MPa	15	27	N/A	CO <sub>2</sub> :H <sub>2</sub> =1:3*	2017	440
9	15Cu/Zr-SBA-15	250°C, 3.3 MPa	25	80	N/A	CO <sub>2</sub> :H <sub>2</sub> =1:3*	2018	441
10	15Cu/Zr-SBA-15_EIWI	250°C, 3.3 MPa	6.5	92	N/A	CO <sub>2</sub> :H <sub>2</sub> =1:3*	2019	442
<b><i>Cu-based-ternary catalysts</i></b>								
11	6.6Cu-6.2Zn-7.5Zr/SBA-15	250°C, 3 MPa	19.2	30.6	376	CO <sub>2</sub> :H <sub>2</sub> :N <sub>2</sub> =22.5:67.5:10, F <sub>T</sub> =333 mLmin <sup>-1</sup> , GHSV=740 mLg <sub>cat</sub> <sup>-1</sup> h <sup>-1</sup>	2019	443
12	39Cu-10Zn-2.6Mn/SBA-15	180°C, 4 MPa	5.7	99	2236	GHSV=120 Lg <sub>cat</sub> <sup>-1</sup> h <sup>-1</sup> , CO <sub>2</sub> :H <sub>2</sub> =1:3	2018	446
13	39Cu-10Zn-2.6Mn/KIT-6	180°C, 4 MPa	8.2	99	3373		2018	446
14	10Cu-8Zn-2Ce/SBA-15	240°C, 4 MPa	13.9	57.5	33.6	GHSV=1200 h <sup>-1</sup> , CO <sub>2</sub> :H <sub>2</sub> =1:3	2019	227
<b><i>Other metal-based catalysts</i></b>								
15	6Pd-0.4Ca/SBA-15	250°C, 4.1 MPa	4	31	N/A	GHSV=3600 mLg <sub>cat</sub> <sup>-1</sup> h <sup>-1</sup>	2012	451
16	5.7Pd-10Cu/SiO <sub>2</sub>	250°C, 4.1 MPa	6.6	34	N/A	GHSV=3600 mLg <sub>cat</sub> <sup>-1</sup> h <sup>-1</sup>	2015	452
17	5.7Pd-10Cu/SBA-15	250°C, 4.1 MPa	6.5	23	N/A		2015	452
18	10Pd-In <sub>2</sub> O <sub>3</sub> /SBA-15	260°C, 5 MPa	12.6	83.9	352.4	GHSV=15 Lg <sub>cat</sub> <sup>-1</sup> h <sup>-1</sup> , CO <sub>2</sub> :H <sub>2</sub> =1:4	2020	453
19	2Au-24CuO/SBA-15	250°C, 3 MPa	24.2	13.5	N/A	GHSV=3600 h <sup>-1</sup> , CO <sub>2</sub> :H <sub>2</sub> =1:3	2017	455

Ratio H<sub>2</sub>:CO<sub>2</sub>=3:1, fixed bed.\* 3 mL HPHT cell (Harrick Scientific).\*\* Metal content is given in wt%.

#### b) Zeolite-based catalysts for CO<sub>2</sub> hydrogenation to methanol

Ab initio molecular orbital and density functional theory calculations have been used to investigate the zeolite-catalyzed hydrogenation of CO<sub>2</sub> into methanol in a concerted pathway.<sup>457</sup> The authors showed that properly designed zeolite could exhibit excellent catalytic activity and allow to reduce the reaction barrier by more than 200 kJ mol<sup>-1</sup>. Thus, an ideal zeolite will be a basic one obtained by exchanging acid protons with alkali metal cations to activate CO<sub>2</sub>. Then the authors proposed for the catalytic hydrogenation of CO<sub>2</sub>, a zeolite incorporating Ge, N, and Na<sup>+</sup> into the framework. Previously, theoretical calculations revealed that a controlled substitution of specific atoms into zeolite framework could improve the catalytic properties to complete hydrogenation of CO<sub>2</sub>.<sup>458</sup> Previous studies reported the activity Ru-zeolite based catalyst to CO<sub>2</sub> hydrogenation with low methanol selectivity. Ru-NaY zeolite and mesoporous FSM-16 catalysts were prepared by ion-exchange and chemical vapor deposition (CVD) methods. High activity for CO<sub>2</sub> hydrogenation but low selectivity to methanol were registered due to high methane selectivity. Co incorporation promoted MeOH selectivity up to 7% over Co-RuY for 16h.<sup>459,460</sup> In previous work, Rh-ion-exchanged zeolite catalysts (RhY) showed high activity to CO<sub>2</sub> conversion with low selectivity (up to 2.7%) to methanol.<sup>461,462</sup>

To overcome the thermodynamic equilibrium limitation for CO<sub>2</sub> hydrogenation and improve MeOH yield and selectivity, the continuous MeOH and water removal via selective membrane separation has received attention. Indeed, higher conversion under milder reaction conditions (lower temperature) can be reached using separation membranes. Zeolite membranes present robustness, different topology and morphology and versatility in their composition, with the corresponding textural and catalytic properties.

So, the use of a zeolite membrane reactor conformed with zeolite A<sup>463,464</sup> revealed the possibility to selectively separate water and methanol with the corresponding increase in conversion, as was predicted with a mathematical model<sup>465</sup> when compared with the operation in a traditional reactor.<sup>466,467</sup> Nevertheless, the zeolite membrane showed limited stability for direct CO<sub>2</sub> hydrogenation into methanol under current process conditions.

#### 5.2.5. *Conclusion*

The direct hydrogenation of CO<sub>2</sub> to form methanol requires further development and improvement of catalyst activity, selectivity and stability for industrial application. The hydrophobic properties of the catalyst surface have to be considered, and further studies on the nature of the catalyst active species and reaction intermediates are required for a successful design of an efficient and selective catalyst. The reported catalysts are multifunctional and multidimensional, characterized by different active sites with different chemical and oxidation

states, with different electronic and geometrical environments with specific activities for each stage of the CO<sub>2</sub> to methanol transformation process. It is therefore crucial to determine and control the active species, reaction intermediates and kinetics for the rational design of more efficient catalysts. Thus a better understanding and knowledge of what happens at the molecular level should help to find consensus on the mechanisms involved in the hydrogenation reaction of CO<sub>2</sub> to methanol of which adsorption phenomena are key. Therefore, the successful design of a new efficient catalyst requires the combination of computational chemistry studies with in situ spectroscopy to elucidate the fundamental steps for the adsorption and activation of CO<sub>2</sub> and H<sub>2</sub>, for the hydrogenation reaction and the desorption of the product.

In addition, special attention should be paid to the morphology of the support to improve the physical isolation and shielding of metal species. In this regard, the use of OMS materials, hierarchical zeolites, two-dimensional zeolite nanosheets and core-shell materials can promote the amount, dispersion and stabilization of the active centers.

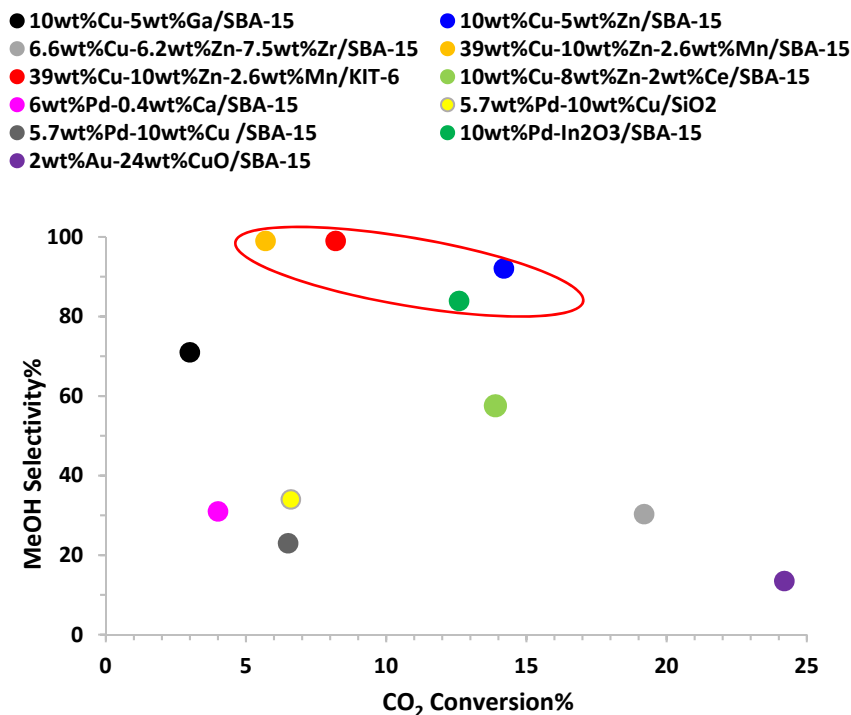
Considering thermodynamics, the development of catalysts able to work at low temperature and high pressure is a clear objective. Morphology, topology, thermal stability, hydrophobic/hydrophilic, acid/base and redox properties of zeolite and OMS materials, are properties that can be tailored when designing new catalysts and they should play a key role.

Considering thermodynamics, the development of catalysts able to work at low temperature and high pressure is a clear objective. Morphology, topology, thermal stability, hydrophobic/hydrophilic, acid/base and redox properties of zeolite and OMS materials, are properties that can be tailored when designing new catalysts and they should play a key role.

Patent literature <sup>468-470</sup> indicates some distinguishable pilote plant processes by Air Liquide Forschung und Entwicklung GmbH (ALFE) and Lurgi GmbH or Mitsui process<sup>471</sup> using a Cu/ZnO/ZrO<sub>2</sub>/Al<sub>2</sub>O<sub>3</sub>/SiO<sub>2</sub> catalysts, while zeolite and OMS based catalysts are far from reaching industrial targets. Air Liquide Forschung und Entwicklung GmbH (ALFE) and Lurgi GmbH use a Cu/ZnO/Al<sub>2</sub>O<sub>3</sub> catalyst developed by Süd-Chemie (Clariant),<sup>468,470</sup> working in Pilot Plant, with a gas composition of 24/2/74=CO<sub>2</sub>:N<sub>2</sub>:H<sub>2</sub> and GHSV of 10 500 h<sup>-1</sup>, at 8 MPa and 250°C give 35-45% CO<sub>2</sub> conversion and MeOH STY of about 0.6 kg/L<sub>cat</sub>.h. The catalyst suffered slight deactivation and was stable over 600h. The water content of MeOH is 30-40wt%, which is superior to the water content in MeOH produced from syngas (10-12wt%). The Mitsui process uses a Cu/ZnO/ZrO<sub>2</sub>/Al<sub>2</sub>O<sub>3</sub>/SiO<sub>2</sub> catalyst<sup>471</sup> at 250°C, 5 MPa, and GHSV=10000h<sup>-1</sup>, and produces high MeOH purity (0.26kg/h), with high water content (0.26kg/h), at CO<sub>2</sub> conversion of up to 86%. No data were provided for methanol selectivity, nor for the H<sub>2</sub>/CO<sub>2</sub> ratio used, so methanol selectivity could not be determined. We present here the results reported on CO<sub>2</sub> conversion

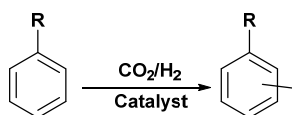


and MeOH selectivity using structured mesoporous materials as supports, and promising results are outlined (Figure 21).



**Figure 21.** MeOH selectivity was plotted versus GSH for different metal-OMS catalysts. The ovoid highlights the best catalytic performance: high MeOH selectivity versus high CO<sub>2</sub> conversion.

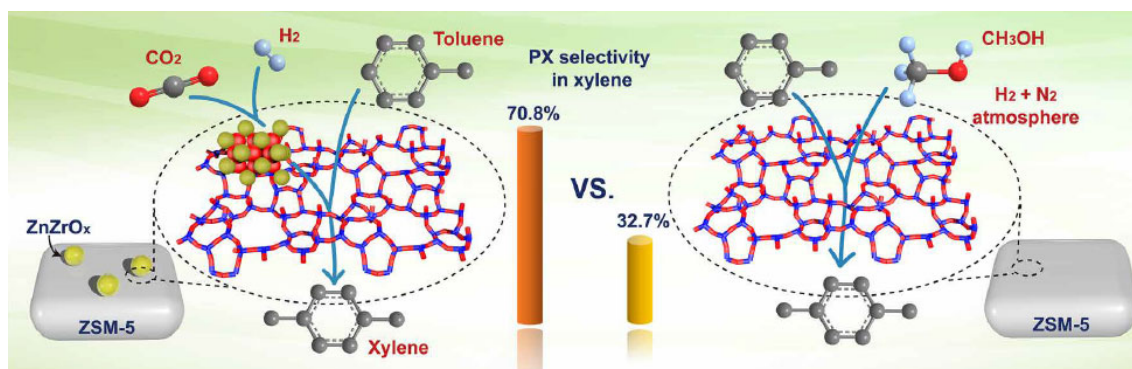
### 5.3. Catalytic methylation of aromatics with CO<sub>2</sub>/H<sub>2</sub>



**Scheme 50.** Catalytic methylation of aromatics with CO<sub>2</sub>/H<sub>2</sub>.

Aromatic are important intermediates for petrochemical and chemical industry. Among them, xylenes found numerous application in polymers (polyester), resins and plasticizers synthesis. Thus, C-methylation is a key transformation for the preparation of xylenes which is usually performed with MeOH and zeolites.<sup>472-474</sup> Methylation of toluene with methanol over zeolite catalyst (ZSM-5) affords water and xylenes with 23.5% p-xylene, 52.4% m-xylene, and 24% o-xylene, which corresponds to the thermodynamic equilibrium composition at 400°C.<sup>475</sup> The modifications of the catalytic properties of zeolites by controlling the acidity on the external surface of the zeolite, the pore sizes and products diffusion inside the pore system allowed to maximize p-xylene selectivity.<sup>474,476-479</sup> Therefore, p-xylene selectivity up to 100% over Mg modified ZSM-5 catalyst at low space time have been reported at 440-450°C with high steam content in feed.<sup>480,481</sup> Taking the above into account, it is clear that the use of CO<sub>2</sub>/H<sub>2</sub> for the catalytic methylation of aromatics constitutes a green alternative and could help to reduce atmospheric CO<sub>2</sub> concentrations (Scheme 50). Since methanol synthesis from CO<sub>2</sub>

hydrogenation<sup>89,371,482,483</sup> has been widely studied, the combination of catalytic properties or directly of catalysts suitable to perform methanol synthesis and C-methylation should enable the methylation of aromatics starting from CO<sub>2</sub>/H<sub>2</sub>. It seems that for this cascade process it may be worthwhile to study micro- and mesoporous catalysts. Very recently, the catalytic methylation of aromatic using CO<sub>2</sub>/H<sub>2</sub> using a physical mixture of Re/TiO<sub>2</sub> and H-MOR, both catalysts suitable for the methanol production and subsequent C-methylation at low temperature, was reported<sup>484</sup> with good catalytic performance at 1 MPa P<sub>CO<sub>2</sub></sub>, 5 MPa; P<sub>H<sub>2</sub></sub>, 250°C and 20h in batch reactor. Under such conditions, 52% and 42% yield of methylated benzenes were obtained on the base of benzene-based yield and CO<sub>2</sub>-based yield, respectively. The catalysts screening showed that the best support for Re was TiO<sub>2</sub> and that Re was the best metal for CO<sub>2</sub> hydrogenation, while H-MOR was the best zeolite for C-methylation among ZSM-5, BEA, FAU and CHA structures, with optimum Si/Al<sub>2</sub>O<sub>3</sub> of 90. The process was also performed over the optimized catalytic system using MeOH, CO/H<sub>2</sub> and HCOOH/H<sub>2</sub>. Best results were obtained with MeOH indicating that MeOH could be the intermediate, with MeOH formation occurring over Re/TiO<sub>2</sub> and methylation over HMOR(90). These results are promising although the selectivity to xylenes and p-xylene are still low and no data for a continuous process have been reported. Most recently, methylation of toluene using CO<sub>2</sub>/H<sub>2</sub> over ZnZrOx–ZSM-5 (ZZO-Z5) dual functional catalysts was also studied.<sup>485</sup> In situ DRIFT study showed, comparing methanol and CO<sub>2</sub>/H<sub>2</sub> methylation routes, that reactive methylation species H<sub>3</sub>CO\* were more easily obtained from CO<sub>2</sub> hydrogenation over ZZO-Z5 catalysts. The results suggested that after CO<sub>2</sub> hydrogenation following the formate route, the reactive methylation species formed over ZZO migrated into zeolite pores where toluene methylation took place. Under optimized reaction conditions in a fixed-bed reactor, the ZSM-5 (Si/Al=85) modified in order to decrease the pore size, with 10wt% of ZZO (ZZO-4SZ5), at 360°C, 3.0 MPa, GHSV=12.000 mLg<sup>-1</sup>hour<sup>-1</sup> and WHSV<sub>Toluene</sub>=1 h, allowed reaching 92.4% xylene selectivity with 70.8% p-xylene selectivity and 13% toluene conversion (Figure 22). These results clearly showed the potential and feasibility of C-methylation of toluene using CO<sub>2</sub>/H<sub>2</sub>.



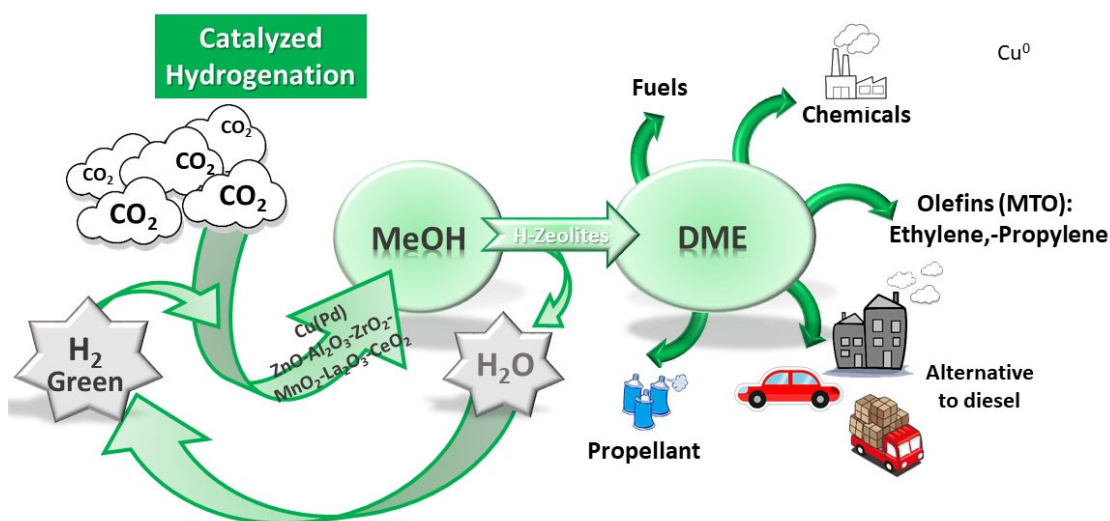
**Figure 22.** Toluene methylation using CO<sub>2</sub>/H<sub>2</sub> over ZZO-Z5 catalyst versus toluene methylation using methanol over optimized Z5. Reprinted with permission from ref <sup>485</sup>. Copyright 2020, The American Association for the Advancement of Science.

We see how these works constitute the seed for the exploration of the C-methylation of aromatics with CO<sub>2</sub>/H<sub>2</sub> and xylene products, showing the great potential of this new reaction and of the multifunctional catalytic system integrating zeolites.

#### 5.4. Direct conversion of CO<sub>2</sub> to dimethylether (DME)

##### 5.4.1. Introduction

Worldwide DME production stands at approximately 5 million tons per year, being mainly obtained by methanol dehydration, and the majority of DME production is currently in China.<sup>486</sup> Dimethyl ether (DME) is the simplest ether, is non-toxic, non-carcinogenic, non-teratogenic, non-mutagenic and environmentally benign<sup>487</sup> with a boiling point of 25°C. Under normal atmospheric conditions, DME is a colorless gas and can be easily stored as liquid at room temperature and low pressure (~0.5 MPa). DME is considered a potential clean transport fuel and an alternative to diesel,<sup>488</sup> especially in compression ignition diesel engines due to high cetane number (55-60)<sup>489</sup> and low auto-ignition temperature (235°C).<sup>490</sup> DME is a clean energy source and does not produce sulfur oxide or soot during combustion, and its environmental impact is low specially if it is produced from renewable resources.<sup>491</sup> DME is used extensively in the chemical industry, progressively replacing petroleum derivatives for the synthesis of a large number of chemicals such as methyl acetate, dimethyl sulphate, olefins, isoparaffin-rich gasoline,<sup>492</sup> methylating agent, solvent and aerosol propellant (Figure 23). A life cycle analysis revealed the interest of methanol and DME as clean transport fuels and showed that methanol and DME can be economically competitive with respect to oil derived fuels.<sup>487,493–495</sup>



**Figure 23.** Illustration of DME synthesis and uses.

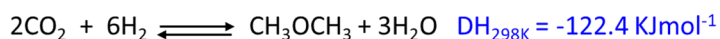
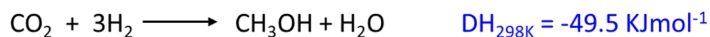
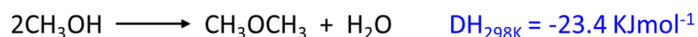
DME synthesis can be performed in either a two-steps or a single-step process, commonly referred as direct or indirect synthesis, respectively. DME is usually produced directly from syngas (CO/H<sub>2</sub>)<sup>405,496–498</sup> eventually with low amount of CO<sub>2</sub> (<3%) or by dehydration of methanol,<sup>404,499–501</sup> which in turn is produced from syngas.

The conventional indirect synthesis undergoes firstly methanol production in the presence of a metallic-based catalyst from syngas or CO<sub>2</sub> hydrogenation, followed in a second step by methanol dehydration over a solid acid catalysts such as  $\gamma$ -alumina or zeolite.<sup>495,502–505</sup> Since methanol synthesis from CO<sub>2</sub> hydrogenation was above reviewed, only the direct DME synthesis in a single-step (with economic advantage over a two-step process), requiring the use of efficient bifunctional catalysts, has been covered here.

The direct DME synthesis from CO<sub>2</sub> hydrogenation is very attractive<sup>506</sup> since is environmentally-friendly and can be an economical route. The catalytic hydrogenation of CO<sub>2</sub> for direct synthesis of DME enables to increase considerably the CO<sub>2</sub> conversion because methanol dehydration breaks the thermodynamic balance of methanol synthesis. However, direct DME synthesis produces larger amount of water than methanol synthesis alone, that damages the activity and stability of the catalysts. It is generally assumed that direct transformation of CO<sub>2</sub> to DME involves methanol synthesis and methanol dehydration and requires bifunctional catalysts. These active sites can be integrated in a hybrid catalyst<sup>507–510</sup> or can be present in two different catalysts physically mixed.<sup>511–513</sup> In the last case, the combination of both types of active sites, metal-oxide and acid sites presents some limitations such as no uniform distribution of active sites, mass transfer constraints and limited reproducibility. Therefore the presence of metal oxide and acid sites in a single system<sup>500,514,515</sup> could improve mass transfer, CO<sub>2</sub> conversion and rates of hydrogenation/dehydration, due to the proximity of active sites.

#### 5.4.2. Thermodynamics of direct DME synthesis

The DME synthesis involves three main reactions, the RWGS, the methanol synthesis and dehydration (Scheme 51). With the exception of RWGS, all the reactions are exothermic and so thermodynamically disfavoured with high temperature. The dehydration reaction of methanol occurs without variation in the number of moles and is slightly exothermic over solid acid catalysts.<sup>516,517</sup> Accordingly, the process pressure does not affect the extent of the dehydration reaction while lower temperatures are thermodynamically beneficial. Besides, the dehydration reaction of methanol allows to shift the thermodynamic equilibrium for CO<sub>2</sub> hydrogenation and to work at lower pressure and higher temperatures (> 240°C) that have been shown to promote CO<sub>2</sub> activation rate and the formation of methanol or carbon monoxide.<sup>518</sup>

**Direct CO<sub>2</sub> hydrogenation into DME:****CO<sub>2</sub> hydrogenation into methanol:****Methanol dehydration:****RWGS and methanol from syngas:**

**Scheme 51.** Equations of different reactions involved in direct DME synthesis from CO<sub>2</sub> hydrogenation.

As it occurs for methanol synthesis where the active catalyst for methanol from syngas showed to be active for CO<sub>2</sub> hydrogenation, the active catalysts for DME synthesis from syngas, exhibit activity to DME synthesis from CO<sub>2</sub>. For methanol synthesis, the suitable properties of Cu<sup>0</sup> for H<sub>2</sub> dissociation, and the dispersion effect of carrier oxides<sup>519–522</sup> such as ZnO, Al<sub>2</sub>O<sub>3</sub>, and ZrO<sub>2</sub> providing an active metaloxide interface to the CO<sub>2</sub> adsorption and activation have been largely described and studied. Accordingly, the direct CO<sub>2</sub> hydrogenation into DME is generally performed in presence of Cu-based methanol synthesis catalyst (CuO-ZnO-Al<sub>2</sub>O<sub>3</sub> or CuO-ZnO-ZrO<sub>2</sub>)<sup>511,523</sup> and an acid catalyst, such as γ-Al<sub>2</sub>O<sub>3</sub>, silica–alumina or zeolites for methanol dehydration. Due to its acid properties γ-alumina could be a good candidate for methanol dehydration reaction but as we discussed for methanol synthesis, alumina presents some limitations. The hydrophilicity of γ-alumina and ZnO have negative effect over the metal particles stability and favours sintering and agglomeration. Moreover, water has strong competitive adsorption with methanol and so inhibits methanol dehydration step. Zeolites offer great potential due to suitable and controllable Brønsted and Lewis acid properties, water resistance and shape-selectivity. Among zeolites, HZSM-5 zeolite based catalysts have been widely used for methanol dehydration due to their suitable acid properties that have to be tuned to avoid the formation of hydrocarbons. Following these leads, numerous catalytic systems based on Cu and HZSM-5 have been studied for the direct hydrogenation of CO<sub>2</sub>. The metal particles size, usually Cu, plays a great role in methanol synthesis activity, and consequently in DME formation. Nevertheless, the stability of Cu particles, under reaction conditions, is limited due to sintering and agglomeration, as it was discussed for methanol synthesis. Hence, different strategies, such as the addition of a dispersive phase or promoters (ZnO, ZrO<sub>2</sub>, La<sub>2</sub>O<sub>3</sub>, CeO<sub>2</sub>, MnO<sub>2</sub>) or the addition of a second hydrogenation metal with suitable properties to dissociate H<sub>2</sub> such as Pd, are followed to improve the bifunctional catalytic system. Then, different

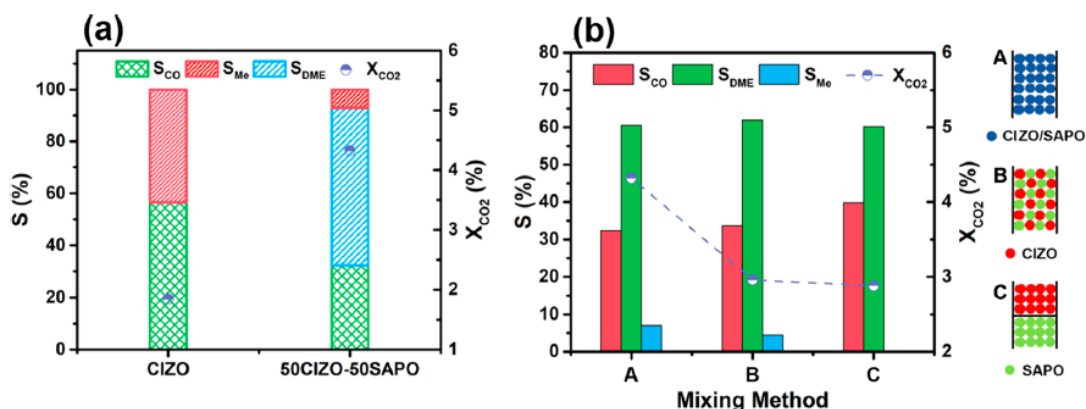
preparation methods have been developed, including co-precipitation, sol-gel, citrate or impregnation routes, in order to increase the catalyst activity and stability. The main challenge is to reach high DME selectivity (>70%) at high CO<sub>2</sub> conversion level, minimizing CO production and avoiding catalyst deactivation.

#### 5.4.3. Cu-based catalysts for direct DME synthesis

Cu-based zeolite catalysts are the main zeolitic catalysts reported up to now for the transformation of CO<sub>2</sub> into DME. Catalytic systems to direct transformation of CO<sub>2</sub> to DME have to contain active sites for methanol synthesis and for methanol dehydration that could be integrated in a hybrid catalyst or which are present in two different catalysts physically mixed. For the first time a hybrid catalyst incorporating both functionalities for methanol synthesis and methanol dehydration was prepared by impregnation in 2001.<sup>524</sup> Cu-Mo supported HZSM-5 catalyst showed to be highly active for DME synthesis. The addition of a small amount of Mo enhanced the catalytic activity of the hybrid catalyst that showed to be stable for 10 h of time of stream. DME was produced with high selectivity up to 77% and low 12.3% CO<sub>2</sub> conversion, at 240°C and 2 MPa (Table 5, Entry 1).

##### a) SAPO-based catalysts for direct DME synthesis

Recently the catalytic performance of Cu-In-Zr-O (CIZO) mixed oxide nanomaterial and commercial SAPO-34 zeolite physically mixed has been reported.<sup>525</sup> The best CIZO/ SAPO ratio was 50/50 by weight, and a maximum of 4.3% CO<sub>2</sub> conversion and 65.1% DME selectivity was reached at 250°C and 3 MPa (Table 5, Entry 2; Figure 24). These catalytic data are low in comparison to the catalytic performance of other multi-functional catalytic system yet reported.



**Figure 24.** (a) Conversion and product distribution over CIZO and 50CIZO-50SAPO mixture. (b) Influence of proximity of active sites on the performance of the CIZO-SAPO catalytic system: (A) powder mixing, (B) pellet mixing, and (C) dual bed. Reprinted with permission from ref<sup>525</sup>. Copyright 2020, American Chemical Society.

##### b) Cu-ZnO-Al<sub>2</sub>O<sub>3</sub>-based zeolite catalysts for direct DME synthesis

A large variety of catalysts for direct CO<sub>2</sub> hydrogenation into DME have been studied such as Cu-ZnO, Pd and bimetallic catalysts. Among them, the Cu-ZnO based catalysts are undoubtedly the

most commonly explored and used. Among Cu based catalysts, the mostly studied and employed catalytic system for direct DME synthesis from CO<sub>2</sub> are conventionally Cu-ZnO-Al<sub>2</sub>O<sub>3</sub> and Cu-ZnO-ZrO<sub>2</sub> based catalysts. Cu-ZnO-Al<sub>2</sub>O<sub>3</sub> based catalysts are traditionally used for direct hydrogenation of CO<sub>2</sub> into methanol and have been widely used and studied for direct hydrogenation of CO<sub>2</sub> into DME. Catalytic system should consist of physical mixture or hybrid catalysts with active sites for both methanol synthesis and dehydration that will involve a zeolite function.

*i) Physical mixture of Cu-ZnO-Al<sub>2</sub>O<sub>3</sub> and zeolite catalysts for direct DME synthesis*

The catalytic performance of CuO-ZnO-Al<sub>2</sub>O<sub>3</sub> prepared by a simple and fast urea-nitrate combustion method that was physically mixed with HZSM-5 by grinding showed to be dependent on the amount of urea used as fuel, affecting the grain size and copper surface areas and so the catalytic properties.<sup>523</sup> The catalyst prepared with 40% of the stoichiometric amount of urea allowed the best catalytic properties due to its higher Cu surface area and the smaller Cu particle size. At 270°C and 3 MPa, maximum 30.6% CO<sub>2</sub> conversion, 15.1% and 49.2% DME yield and selectivity were achieved, respectively (Table 5, Entry 3). A catalytic system based on pretreated carbon nanotubes with graphitized tube-wall (multi-walled carbon nanotube system (MWCNTs)), was used as carrier for the preparation of ultrasound-assisted co-precipitation CuO-ZnO-Al<sub>2</sub>O<sub>3</sub>/HZSM-5 catalysts.<sup>526</sup> CuO-ZnO-Al<sub>2</sub>O<sub>3</sub> nanoparticles were densely deposited outside and inside the wall of carbon nanotubes and bifunctional catalysts were obtained by mechanical mixing of MWCNTs and HZSM-5. At 262°C and 3.0 MPa, 46.2% CO<sub>2</sub> conversion, 20.9% and 45.2% DME yield and selectivity, respectively, were obtained (Table 5, Entry 4). Recently, CuO-ZnO-Al<sub>2</sub>O<sub>3</sub> catalysts with a high BET surface area and Cu surface area were prepared by a co-precipitation method and used after physically mixing with HZSM-5 for DME synthesis.<sup>527</sup> The bifunctional mixture showed a high activity and DME selectivity due to the microstructure of the catalysts that was controlled by the preparation method used. Maximum 21.9% DME yield, 30.5% CO<sub>2</sub> conversion and good 72% DME selectivity were achieved at 260 °C and 4.2 MPa (Table 5, Entry 5). A stability test of the catalyst mixture showed a notable decrease in activity within the first 20h. Nevertheless, high catalytic performance was maintained for 100h, with 21.4% CO<sub>2</sub> conversion and 55.5% DME selectivity. The changes in the catalytic activity during the time on stream were attributed to Cu sintering and alterations in the surface area.

*ii) Hybrid catalyst based on Cu-ZnO-Al<sub>2</sub>O<sub>3</sub> and zeolite for direct DME synthesis*

Cu-ZnO-Al<sub>2</sub>O<sub>3</sub>/FER catalysts have been prepared by co-precipitation<sup>528</sup> giving a maximum production rate of DME for an optimal zeolite Si/Al molar ratio of 12 owing to larger metallic surface area of Cu nanoparticles and relatively higher hydrophobic surface. The authors

reported that smaller Cu particle size decorated with ZnO moiety in the larger Cu-ZnO-Al<sub>2</sub>O<sub>3</sub> matrices increased the hydrophobic surfaces of the catalytic system, preventing the poisoning of acid sites of the zeolite and Cu aggregation. CO<sub>2</sub> conversion of 29.7% with 55.2% DME selectivity at 250°C and 5 MPa were reached (Table 5, Entry 6).

*iii) Morphology and structuration of the catalysts for direct DME synthesis*

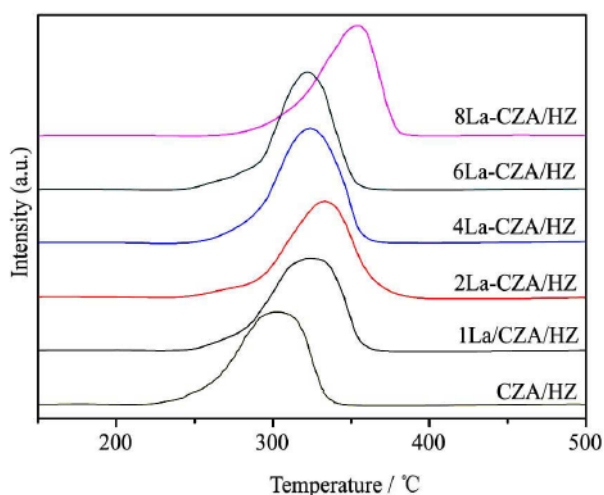
Different strategies to design and prepare new structured zeolitic catalysts with high dispersion and stabilized metallic active sites have been investigated. For methanol synthesis, it was demonstrated that the yield and selectivity were highly dependent on Cu dispersion and surface area. However, Cu in Cu-ZnO based catalyst is thermally unstable and the particle size increases with temperature over 250°C inducing the loss of surface area and sintering. Moreover, the production of water cause poisoning of acid active sites and Cu sintering. The addition of small amounts of rare earth metal oxides usually acts as promoters to improve the dispersion of active phase and the thermal stability of the catalysts. Following these leads, and to improve the catalytic properties of CuO-ZnO-Al<sub>2</sub>O<sub>3</sub>/HZSM-5, a new design of catalyst structure was developed. An encapsulated catalyst constituted by CuO-ZnO-Al<sub>2</sub>O<sub>3</sub> composite nanoparticles as the core and HZSM-5 as the shell was prepared, being the HZSM-5 shell synthesized hydrothermally onto CuO-ZnO-Al<sub>2</sub>O<sub>3</sub> nanoparticles.<sup>529</sup> At 270°C and 3.0 MPa, 48.3% CO<sub>2</sub> conversion and 23.4 and 48.5% of DME yield and selectivity were reached (Table 5, Entry 7). No deactivation of the catalyst was observed for the first 24h. Then, the catalyst stability was attributed to core-shell structure that allowed to control the consecutive order of reaction, methanol synthesis and methanol dehydration. In 2012, an hydrothermal route for the preparation of new hybrid materials composed of CuO-ZnO as core layer and HZSM-5 as shell layer was described.<sup>530</sup> The comparison of hydrothermal, impregnation and mixing preparation methods showed that one-step crystallization method provided a catalyst with higher catalytic performance. CO<sub>2</sub> conversion of 21.3% with 50.8% DME selectivity and MeOH+DME yield up to 12.4%, at 245°C and 3 MPa were achieved by that catalyst preparation method (Table 5, Entry 8).

*iv) Promoters incorporation to the Cu-ZnO-Al<sub>2</sub>O<sub>3</sub> based-zeolite catalysts for direct DME synthesis*

As it was mentioned for methanol synthesis, the incorporation of metal oxides to Cu-based catalysts promotes the Cu dispersion, stabilization and the formation of new metallic active phase for the methanol synthesis by CO and CO<sub>2</sub> hydrogenation. GaO, ZrO<sub>2</sub>, Cr<sub>2</sub>O<sub>3</sub>, MnO<sub>2</sub>, or CeO<sub>2</sub> have been used as promoters and from these, ZrO<sub>2</sub> was particularly prominent. Following these leads, a series of CuO-ZnO-Al<sub>2</sub>O<sub>3</sub>-La<sub>2</sub>O<sub>3</sub>/HZSM-5 (CZA/HZ) bifunctional catalysts with various La loadings were prepared by co-precipitation.<sup>531</sup> The controlled addition of La<sub>2</sub>O<sub>3</sub>



improved the reducibility and dispersion of bifunctional catalysts, and a decrease in the CuO particle size was observed. H<sub>2</sub>-TPR profiles showed that La incorporation induced an increase of peak area of reduction of CuO indicating that CuO species dispersion was improved by incorporating La. Moreover, a shift of the reduction peak positions to higher temperatures was observed with La incorporation up to 2%, as well as a shift to lower temperature. These results indicate that La<sub>2</sub>O<sub>3</sub> also makes difficult the reduction of CuO because of the strong interactions between metallic phases ZnO-CuO-La<sub>2</sub>O<sub>3</sub>. It was concluded that La doping allows enhancing the dispersion of the CuO copper oxide and reduction of CuO while the strong interactions between CuO-ZnO-La<sub>2</sub>O<sub>3</sub> hinder the reduction of CuO, implying that a balance between the benefits and detriments of La<sub>2</sub>O<sub>3</sub> addition have to be found (Figure 25). On the other hand, the addition of La into CuO-ZnO-Al<sub>2</sub>O<sub>3</sub>-La<sub>2</sub>O<sub>3</sub>/HZSM-5 catalyst modified the strength of the strong acid sites, and an optimum catalytic performance was obtained with 2 wt% La content. Indeed, NH<sub>3</sub>-TPD profiles showed that the amount of the strong acid increased to a maximum with La content, up to 2wt%, and then decreased. This behavior was attributed to the acidic properties of the lanthanum ions, and to the polarization of the hydroxyl group of the silicon and aluminum framework, leading to stronger acidity.<sup>532</sup> At higher La contents, the formation of La<sub>2</sub>O<sub>3</sub> with basic properties involves the formation of new basic sites on the catalytic surface.<sup>533</sup> At 250°C and 2 MPa, high 43.8% CO<sub>2</sub> conversion and 71.2% selectivity to DME were reached (Table 5, Entry 9). In the same way, ZrO<sub>2</sub> was added to CuO-ZnO-Al<sub>2</sub>O<sub>3</sub> active phase. A series of composite catalysts were prepared by wet mixing method of CuO-ZnO-Al<sub>2</sub>O<sub>3</sub>-ZrO<sub>2</sub> component to HZSM-5 zeolite with molar ratio 2:1.<sup>521</sup> H<sub>2</sub>-TPR profiles showed that for Zr content <5 wt%, a main reduction peak with a shoulder at higher temperature was registered, implying the presence of different Cu species, being the main peak assigned to high dispersed copper oxide species and the shoulder to CuO bulk. For Zr content >5%, only one reduction peak was recorded, lightly shifted at higher temperature, indicating lower reducibility of CuO due to strong interactions CuO-ZrO<sub>2</sub>-ZnO-Al<sub>2</sub>O<sub>3</sub>. In comparison to other promoted catalysts, 24.1% CO<sub>2</sub> conversion and lower 26.6% and 6.4% of DME selectivity and yield, respectively, were reached at 260°C and 3 MPa, (Table 5, Entry 10).



**Figure 25.** H<sub>2</sub>-TPR profiles for different La content of CZA-HZ catalysts. Reprinted with permission from ref<sup>531</sup>. Copyright 2013, The Chinese Society of Rare Earths. Published by Elsevier B.V. All rights reserved.

c) Cu-ZnO-ZrO<sub>2</sub>-based catalysts for the direct DME synthesis from CO<sub>2</sub> hydrogenation

Hybrid catalysts composed by Cu-ZnO-ZrO<sub>2</sub> and zeolites for methanol dehydration such as ferrierite or ZSM-5 for DME synthesis have been largely explored and showed to be usually more efficient catalysts than conventionally Cu-ZnO-Al<sub>2</sub>O<sub>3</sub>-based catalysts. Indeed, the interactions of Cu metal particles with ZnO and ZrO<sub>2</sub> lead to the stabilization of different Cu species, Cu<sup>1+</sup> and Cu<sup>0</sup>.<sup>418</sup>

i) *Effect of proximity between acid and metallic active sites*

The catalytic behavior of the adequate combination of Cu-ZnO-ZrO<sub>2</sub> materials and commercial H-ZSM5 to the direct CO<sub>2</sub> hydrogenation reaction to DME was studied in different reactor bed configurations (physical mixing (ZZ-M), dual-bed (ZZ-D) and mono-bed prepared by grinding and pelletization (ZZ-G)).<sup>518,534</sup> At 3.0 MPa, CO<sub>2</sub> conversion varied from 1.6 to 16.1%, at 180 and 240°C, respectively. Meanwhile the DME selectivity decreased drastically from 70.9 to 33.9% and methanol selectivity decreased from 21.7 to 11.8% due to a notable CO selectivity increase from 7.4 to 54.3%. The ZZ-M system exhibited the best performance with STY values raising from 130 to 430 g<sub>total MeOH</sub> kg<sub>cat</sub><sup>-1</sup> h<sup>-1</sup>, at 180 and 240°C, respectively, while the ZZ-G system reached the lowest productivity (Table 5, Entry 11). The best results reached over the mixed catalyst in comparison to the dual bed system configuration were attributed to the enhanced methanol mass transfer from the methanol catalyst sites to the zeolite acid sites owing to the proximity of the active centres. Grinding was negative because of deterioration of the interaction between the methanol catalyst and zeolite due to a strong mechanical stress. The methanol catalyst (ZCZ) structure was damaged favouring the redistribution of Cu over zeolite. In this respect, different strategies have been developed to improve the proximity of the different functionalities. One approach is the co-precipitation of metal oxides in the presence of acid carriers in order to

provide hybrid materials with both metal-oxides and acid sites in a single catalyst grain. Accordingly Frusteri and co-workers reported different investigations where the effect of carriers, precipitating agent and the ratio metal oxides:carrier were studied. They compared the DME productivity achieved in the presence of a physical mixture of CuZnZr methanol catalyst and a zeolite, and in the presence of a multifunctional system, in which the different active sites were integrated during gel-oxalate precipitation of the Cu-Zn-Zr precursors in a solution containing dispersed MFI-zeolite.<sup>535</sup> In principle, the synthesis of a hybrid system by co-precipitation should maintained the adequate properties of the active sites and enable higher yield of DME due to the regular and homogeneous distribution, and proximity of the active sites. In the presence of the co-precipitated catalyst, the DME selectivity was higher while the CO<sub>2</sub> conversion was practically the same, 15.9% versus 15.4%. The CO<sub>2</sub> conversion was not improved by the proximity of the acid sites that were supposed to shift positively the equilibrium and reached higher value than for CO<sub>2</sub> hydrogenation into MeOH (18%). Under optimized reaction conditions, 240°C and 5.0 MPa, maximum CO<sub>2</sub> conversion up to 23.6% with lower 24.5% CO selectivity, and therefore higher selectivity to MeOH and DME, 25.5 and 49.3%, were reached, respectively (Table 5, Entry 12). The authors adopted co-precipitation as a simple method to prepare Cu-based hybrid catalysts, and ensure the presence of the multifunctionality grain-to-grain.

*ii) Effect of catalyst preparation over the catalytic activity*

It was shown before that co-precipitation resulted in a simple method to prepare Cu-based hybrid catalysts, and ensure the presence of the multifunctionality grain-to-grain. Therefore, a study of the impact of different parameters of co-precipitation to the preparation of Cu-ZnO-ZrO<sub>2</sub>/H-ZSM5 multifunctional catalysts over their catalytic features was performed.<sup>536</sup> Likewise, different precipitating agents (sodium bicarbonate, ammonium carbonate, oxalic acid and urea) were used under ultrasound to match morphological homogeneity. The multifunctional catalyst prepared via ammonium carbonate precipitation exhibited the best catalytic performance, high DME selectivity, with a maximum DME productivity, 0.225 kg<sub>DME</sub>kg<sub>cat</sub><sup>-1</sup>h<sup>-1</sup> (Table 5, Entry 13). The characterization study revealed that a balanced distribution of different sites on the catalyst surface became determinant: the strength of basic sites, the ratio between acid and basic sites and the Cu particle sizes were crucial to maximize catalytic performance and minimize CO selectivity. CuO-ZnO-ZrO<sub>2</sub>/HZSM-5 system revealed to be a promising catalyst for direct conversion of CO<sub>2</sub> into DME.<sup>534-536</sup> CuO-ZnO-ZrO<sub>2</sub>/HZSM-5 bifunctional catalysts were generally prepared by physical or mechanical mixing methods. However to improve the yield of the consecutive methanol synthesis and dehydration, high and homogeneous dispersion of both

functionalities are crucial to favour efficient mass transfer rate from the metal-oxide sites for methanol synthesis to the acid sites for methanol dehydration.<sup>536</sup> Therefore, co-precipitation methods were developed to prepare the CuO-ZnO-ZrO<sub>2</sub>/HZSM-5 catalysts. Nevertheless, these methods present some drawbacks such as the use of metal salts associated to proton zeolite exchange with both Na and Cu cations. Consequently, acid properties of HZSM-5 is reduced, affecting the methanol dehydration step. A few years ago, the preparation of CuO-ZnO-ZrO<sub>2</sub>/HZSM-5 by solid-state route was reported.<sup>537</sup> A study of calcination temperature showed that catalytic performance of CuO-ZnO-ZrO<sub>2</sub>/HZSM-5 catalysts for DME synthesis decreased gradually with the increase temperature from 300 to 600°C whereas CO yield increased. Characterization study revealed that reduction of metallic copper surface area, adsorption capacity of CO<sub>2</sub>, surface area, and reducibility of CuO were strongly affected by the calcination temperature and suitable temperature was 300°C. Highest 22.2% CO<sub>2</sub> conversion, 67.6 and 15% DME selectivity and yield were reached with DME productivity of 0.507 g<sub>DME</sub>g<sub>cat</sub><sup>-1</sup>h<sup>-1</sup> (Table 5, Entry 14). Recently, the catalytic properties of Cu-ZnO-ZrO<sub>2</sub>-FER catalysts prepared by co-precipitation method allowed to provide materials with smaller CuO and Cu particle sizes resulting in better dispersion of the active phases, higher surface area, and lower reduction temperature.<sup>538</sup> Nevertheless, in comparison to other studies, these data remained low. Highest 17.5% CO<sub>2</sub> conversion, 28.4 and 5% DME selectivity and yield were reached, at 250°C and 2 MPa (Table 5, Entry 15).

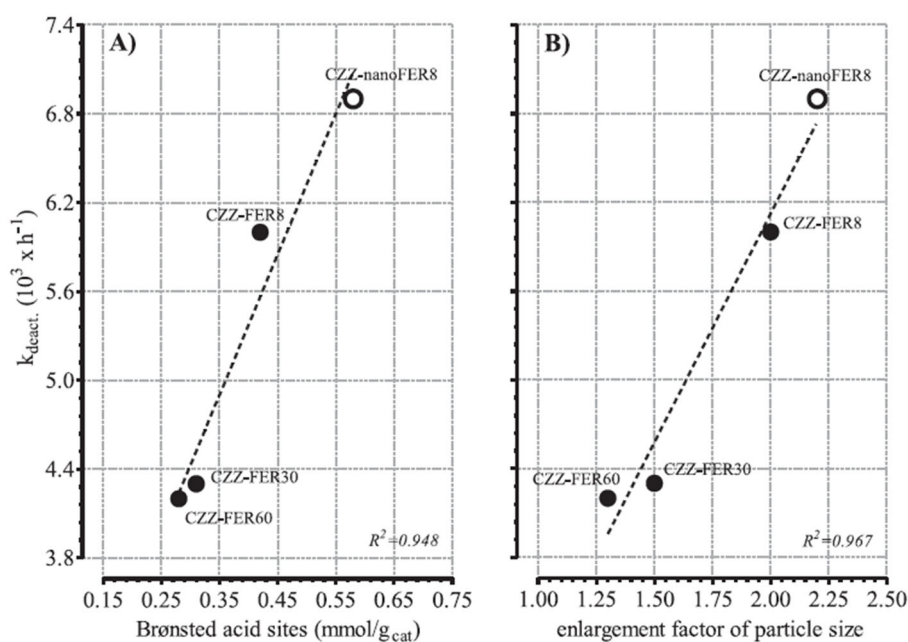
### iii) *Effect of zeolite topology over the catalytic activity*

The effect of zeolite framework topology is well-known to influence the distribution of the reaction products<sup>58</sup> and to control the diffusion and adsorption/deposition of metallic species into the channels. The differences in the voids and microenvironments defined by the topologies of zeolites strongly influenced the stabilization and dispersion of metallic active sites.<sup>50,86,539,540</sup> Accordingly, zeolites with different topologies were used as support of CuZnZr metallic active phase. Recently, the superiority of ferrierite based catalyst respect to other zeolite typically used such as ZSM-5 was shown. Different zeolite structures, FER and MOR,<sup>509</sup> were used as carrier to study the topology impacts on acidity, surface area, microporosity and metal-oxide loading, and in turn on the catalytic performance of the catalysts. The CuZnZr/FER catalyst exhibited a very good activity and selectivity to DME formation, at 5.0 MPa and 280°C, with very interesting results on DME productivity up to 0.752 Kg<sub>DME</sub>Kg<sub>cat</sub><sup>-1</sup>h<sup>-1</sup>, and no coke formation (GHSV=8800 NLKg<sub>cat</sub><sup>-1</sup>h<sup>-1</sup>) (Table 5, Entry 16). The presence of well dispersed metal-oxide clusters of CuZnZr mixed oxides, with size between 30 and 150 nm, on the external surface of FER zeolite revealed to be a key factor to enhance mass transfer of MeOH from CuZnZr sites to acid sites and favoured

the formation of DME. A CuZnZr:FER weight ratio greater than 1 enabled higher catalytic performance, with CO<sub>2</sub> conversion up to 23.6% at 260°C and MeOH/DME yield up to 15% (Table 5, Entry 18).<sup>541</sup> The comparison of the catalytic behavior of Cu-Zn-Zr on MOR, FER, MFI revealed that the metallic and acidic functionalities dispersion and activity were strongly affected by the zeolite structure. The FER zeolite enabled a better dispersion of cluster oxides and the formation of Lewis basic sites for CO<sub>2</sub> activation and provided a high number of suitable Brønsted acid sites for the MeOH dehydration step. The optimum and homogeneous dispersion of active sites was attributed to the ferrierite lamellar structure with interconnection of bi-dimensional channels. A maximum DME productivity of 0.6 kg<sub>DME</sub>kg<sub>cat</sub><sup>-1</sup>h<sup>-1</sup> in the presence of Cu-Zn-Zr/FER catalyst, at 260°C and 5 MPa (Table 5, Entry 18), was achieved owing to enhanced methanol mass transfer owing to the proximity of the active sites. Nevertheless, a progressive deactivation due to water formation was observed. Currently, the same group reported the catalytic performance of CuZnZr hybrid catalyst using different zeolites (Sil-1, MFI, Y, FER, BEA, MOR) and gel-oxalate co-precipitation method.<sup>542,543</sup> Different textural, structural and morphological properties according to carrier structure were observed. Mordenite revealed to be the most efficient carrier for the generation and dispersion of functionalities with high DME productivity of 0.55 Kg<sub>DME</sub><sup>-1</sup> Kg<sub>cat</sub> h<sup>-1</sup> at 280°C and 3.0 MPa (Table 5, Entries 19-23). The deactivation was again attributed to the water formation and inhibition of active sites.

*iv) Effect of Si/Al ratio over the catalytic activity*

Since Si/Al ratio allows controlling acid and adsorption properties of zeolites, the preparation of Si/Al ratio directly influenced their catalytic performance. Accordingly, different Cu-ZnO-ZrO<sub>2</sub>/FER (CZZ/FER) hybrid catalysts using ferrierite samples with different acidity and particle size were prepared.<sup>508</sup> The catalytic results revealed that samples with larger acidity exhibited higher deactivation whereas the use of TEM allowed to attribute the deactivation to metal sintering, which was proportional to the Si/Al ratio (Figure 26; Table 5, Entry 24). An exhaustive FT-IR spectroscopy study allowed to conclude that both Cu particle sintering negatively influenced CO<sub>2</sub> activation and acidity loss due to H<sup>+</sup> exchange with Cu<sup>2+</sup> cations were responsible for the rapid deactivation of Cu-ZnO-ZrO<sub>2</sub>/FER hybrid catalysts.<sup>544</sup>

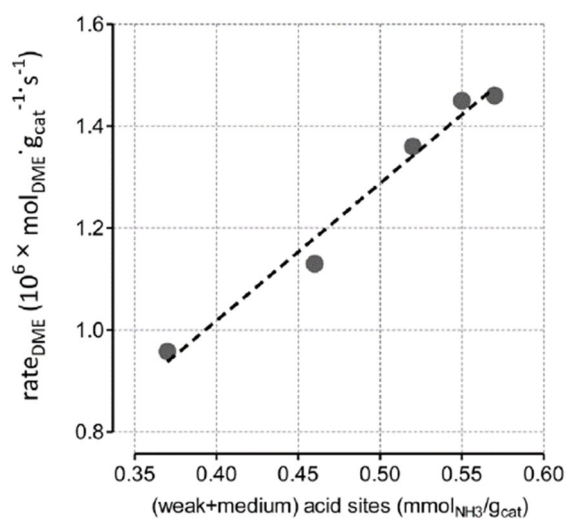


**Figure 26.** Influence of Brønsted acid sites (A) and metal particle sintering (B) on the deactivation kinetics of the hybrid catalysts. Reprinted with permission from ref.<sup>508</sup> Copyright 2018, Elsevier Ltd. All rights reserved.

v) *Effect of promoter incorporation over the catalytic activity*

Many efforts have been done to improve the catalytic properties of bifunctional catalysts modifying synthesis method by sol-gel, co-precipitation and by designing new core-shell structure. Another strategy to improve active metallic phase dispersion and stability is the incorporation of promoters (Ga, Mn, La, Ce, Y, Si and Ti) allowing the formation of new active species for CO<sub>2</sub> activation and establishing strong metal/metal and metal/support interaction.<sup>519–522</sup> In comparison to single oxide, mixed oxides present higher surface area, thermal stability and enhanced acidity, improving their catalytic performance.<sup>545–548</sup> Accordingly, CuO-TiO<sub>2</sub>-ZrO<sub>2</sub>/HZSM-5 catalyst with a Ti/Zr ratio of 1 prepared by co-precipitation revealed to exhibit higher catalytic performance than CuO-TiO<sub>2</sub>/HZSM-5 and CuO-ZrO<sub>2</sub>/HZSM-5 catalysts (Table 5, Entry 25).<sup>512</sup> Maximum 15.6% CO<sub>2</sub> conversion and 47.5 and 7.41% DME selectivity and yield were obtained at 250°C and 3MPa. With suitable 0.5wt%V loading, the catalytic performance of CuO-ZnO-ZrO<sub>2</sub>/HZSM-5 catalyst was improved and a substantial increase of CO<sub>2</sub> conversion from 28.9 to 32.5%, of DME selectivity from 55.1 to 58.8% and DME yield from 15.9 to 19.1% were observed, at 270°C and 3.0 MPa (Table 5, Entry 26).<sup>549</sup> In comparison to 14% DME yield over Pd modified CuO-ZnO-Al<sub>2</sub>O<sub>3</sub>-ZrO<sub>2</sub>/HZSM-5<sup>550</sup> catalyst, this result could be interesting, but the selectivity remained low, 58.8% versus 73.5% (Table 5, Entry 27). Following these leads, CuO-ZnO-CeO<sub>2</sub>-ZrO<sub>2</sub>/HZSM-5 catalysts were prepared.<sup>226</sup> The incorporation of CeO<sub>2</sub> improved the catalytic performance of the bifunctional catalysts, and the CO<sub>2</sub> conversion and DME selectivity were increased from 12.9 to 15.6% and from 17.3% to 46.6%, respectively, over CuO-

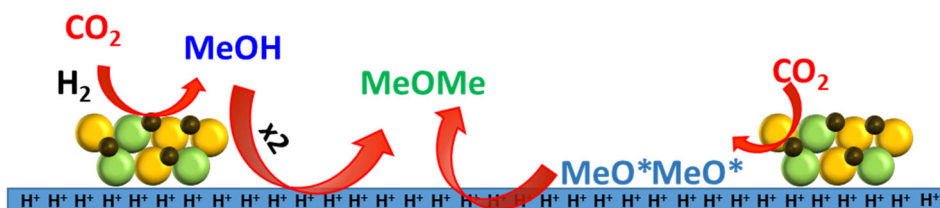
ZnO-CeO<sub>2</sub>-ZrO<sub>2</sub>/HZSM-5 catalyst with Ce/Zr molar ratio of 1/1, at 250°C and 3.0 MPa (Table 5, Entry 28). La doped Cu-ZrO<sub>2</sub> catalysts were also prepared and revealed an increase of the amount of basic sites with La loading as well as a decrease in the crystallite size of CuO improving the Cu dispersion.<sup>435,551</sup> Accordingly, La<sub>2</sub>O<sub>3</sub>-modified CuO-ZnO-ZrO<sub>2</sub>/HZSM-5 catalysts were prepared by an oxalate co-precipitation method for DME direct synthesis (Table 5, Entry 29).<sup>552</sup> Suitable amount of La<sub>2</sub>O<sub>3</sub> enabled to improve catalytic performance of CuO-ZnO-ZrO<sub>2</sub>/HZSM-5, and maximum 34.3% CO<sub>2</sub> conversion and 57.3 and 19.6% DME selectivity and yield were obtained over the catalyst with 1% La<sub>2</sub>O<sub>3</sub> at 270°C and 3MPa. The addition of La<sub>2</sub>O<sub>3</sub> modified the population and strength of acid sites as well as the dispersion of Cu and reducibility of CuO with a larger Cu<sup>+</sup>/Cu ratio. The addition of different oxides promoters (ZrO<sub>2</sub>, CeO<sub>2</sub>, La<sub>2</sub>O<sub>3</sub>, Al<sub>2</sub>O<sub>3</sub>, Ga<sub>2</sub>O<sub>3</sub>) could play an important role over the catalytic performance of Cu-ZnO/FER hybrid catalysts. Accordingly, the incorporation of different promoters in the Cu-ZnO/FER system significantly affected the textural properties of the customized catalysts (surface area, pore volume, copper surface area and dispersion, metal-oxide distribution and acid/base capacity).<sup>553</sup> The reaction rate appeared to be strongly dependent on the number of medium-strong basic sites, being number and strength of the basic sites crucial for the CO<sub>2</sub> activation, whereas the rate of DME formation depended on the concentration of weak-medium acid sites (Figure 27). Consequently, different catalytic behavior were observed and Zr, Al or Ga doped Cu-ZnO/FER catalysts exhibited similar pattern for the DME production, while the incorporation of Ce and La damaged the catalytic properties. CO<sub>2</sub> hydrogenation into DME was performed at 260°C and 3 MPa in the presence of ZrO<sub>2</sub> doped Cu-ZnO/FER hybrid catalyst with MeOH, DME and CO selectivity of 14.4, 36.5 and 49.1% with 21.3% CO<sub>2</sub> conversion (Table 5, Entry 30). Although Cu-ZnO-ZrO<sub>2</sub>/FER hybrid catalyst exhibited high catalytic performance, rapid catalyst deactivation was observed.



**Figure 27.** Influence of acidity on the rate of DME (220°C, 3 MPa; GHSV=8.800 NL kg<sub>cat</sub><sup>-1</sup> h<sup>-1</sup>; CO<sub>2</sub>/H<sub>2</sub>/N<sub>2</sub>: 3/9/1). Reprinted with permission from ref.<sup>553</sup> Copyright 2017, Elsevier B.V. All rights reserved.

d) Mechanistic studies for the direct DME synthesis

Mechanistic insights for the direct DME synthesis from CO<sub>2</sub> hydrogenation with a bifunctional catalyst system formed by physical mixture of Cu-In-Zr-O (CIZO) mixed oxide nanomaterial and commercial SAPO-34 zeolite catalyst were achieved by an in-situ DRIFT study. It was found that changing the distance between CIZO and SAPO could modify the reaction pathways. Likewise, a closely CIZO SAPO location induced a shortcut methoxy-DME pathway instead of a typical methoxy-methanol-DME route, resulting in more efficient DME formation (Scheme 52).<sup>525</sup>

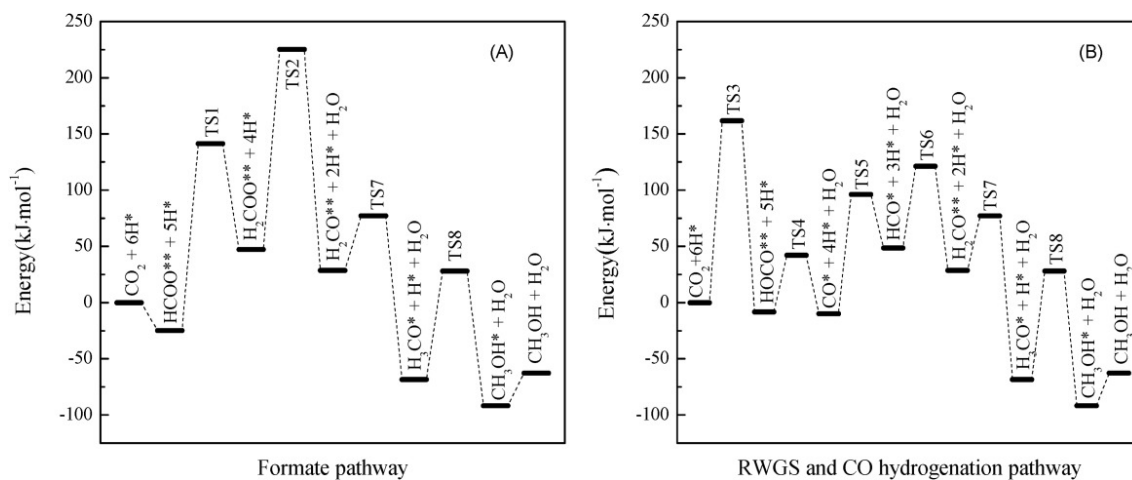


**Scheme 52.** DME synthesis by CO<sub>2</sub> hydrogenation can involve two pathways: methoxy-methanol-DME and methoxy-DME.

Very recently, an intrinsic kinetics model for direct CO<sub>2</sub> hydrogenation to DME over Cu-Fe-Zr/HZSM-5 catalyst has been established.<sup>554</sup> The addition of a small amount of ZrO<sub>2</sub> in a Cu-based catalyst is known to improve Cu dispersion and stability. Therefore, the incorporation of ZrO<sub>2</sub> (1.0 wt %) in Cu-Fe/HZSM-5 catalyst enabled to strengthen the adsorption interactions of the Cu-Fe catalyst and to increase the number of active sites on the catalyst surface. Different DFT studies have revealed that Cu-based catalysts doped with transition metal oxides adsorb H<sub>2</sub> by dissociative adsorption onto Cu, while CO<sub>2</sub> is adsorbed and activated over the transition metal oxides. To continue, CO<sub>2</sub> is desorbed from the transition metal oxide surface and to adsorb on metallic Cu and react with dissociated H on Cu.<sup>555,556</sup> From a thermodynamic point of view, the comparison of formic acid pathway and CO pathway showed that energy barrier for CO generation is lower than for formic acid production (50.46 kJ mol<sup>-1</sup> < 166.31 kJmol<sup>-1</sup>). Moreover, CO formation is an exothermic process while formic acid formation is endothermic (Figure 28). These data allowed to conclude that CO production is more favoured than formate generation. Nevertheless, HCO cannot exist because is unstable and prone to decomposition back into CO and lead to the production and accumulation of CO which becomes the main CO<sub>2</sub> hydrogenation product, implying a very limited contribution of RWGS to CH<sub>3</sub>OH formation. Recently, a reaction mechanism study over of Cu-ZnO-ZrO<sub>2</sub>-FER by DRIFTS revealed that methanol and DME were formed by CO<sub>2</sub> direct hydrogenation rather than through a CO route.<sup>538</sup> Carbonate, formate, and methoxy surface species were the main detected products of CO<sub>2</sub> hydrogenation and no bands for adsorbed formyl or formaldehyde species were observed. A mechanism of methanol formation via the bidentate-formate species that underwent hydrogenation and DME formation

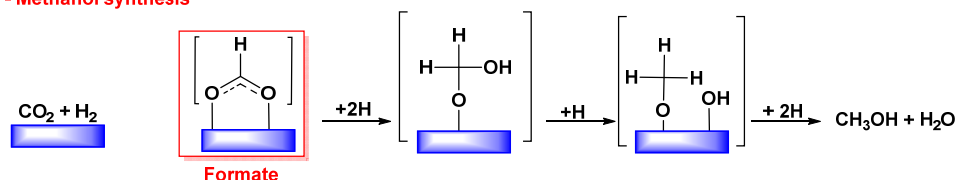


via methanol dehydration and reaction of two surface methoxy groups was proposed (Scheme 53).

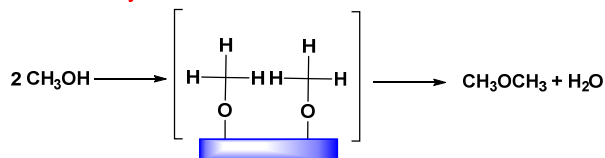


**Figure 28.** Potential energy diagrams for the methanol synthesis reaction via the formate (A) and CO (B) hydrogenation pathways. Reprinted with permission from ref.<sup>554</sup> Copyright 2015, American Institute of Chemical Engineers.

- Methanol synthesis



- Methanol dehydration



**Scheme 53.** Proposed mechanism for DME synthesis via methanol formation and dehydration.

#### 5.4.4. Pd and bimetallic catalytic system for direct DME synthesis

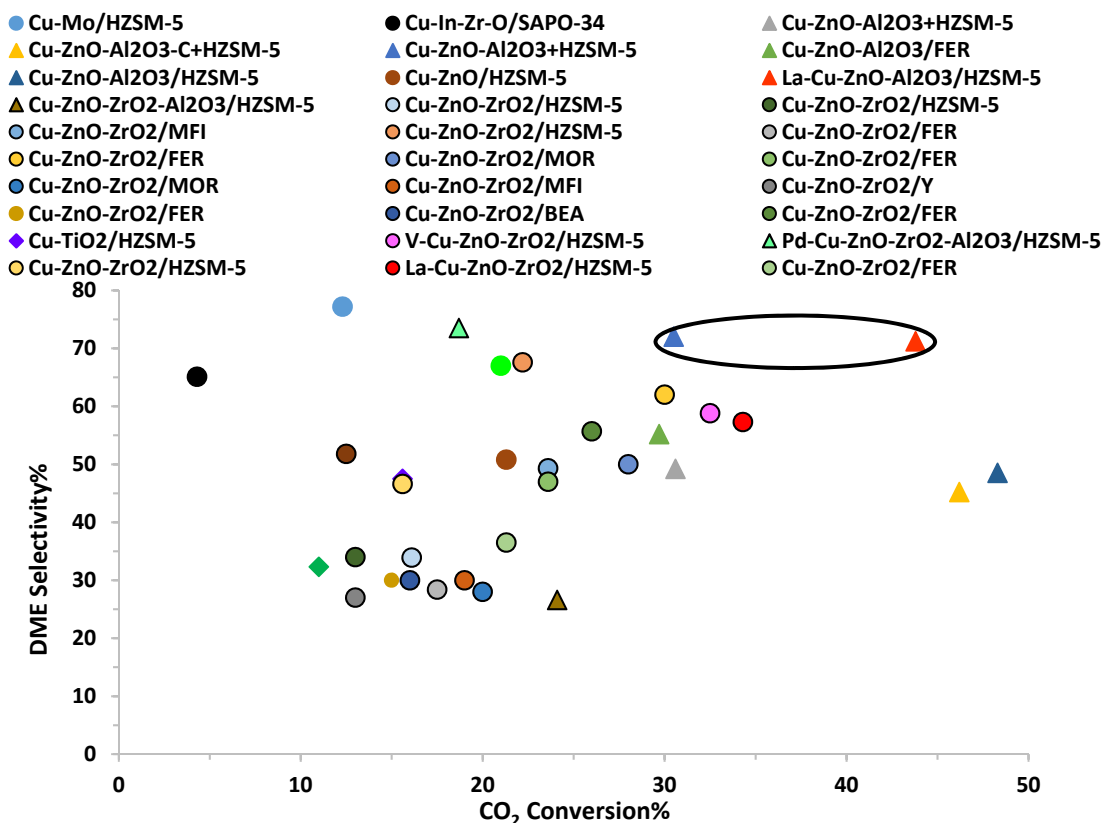
Palladium catalysts have been commonly and widely used as hydrogenation catalysts and used for the direct CO<sub>2</sub> hydrogenation into methanol due to numerous metal active sites for H<sub>2</sub> dissociative adsorption and interfacial sites for CO<sub>2</sub> adsorption and hydrogenation. In 2004, the preparation of bimetallic Pd-Cu catalysts allowed to improve the DME yields and retarded the CO formation.<sup>550</sup> The study of Pd-modified CuO-ZnO-Al<sub>2</sub>O<sub>3</sub>-ZrO<sub>2</sub>/HZSM-5 catalysts performance revealed the enhancement of the catalytic activity was due to hydrogen spillover from metallic Pd to the closer metallic Cu (active component for methanol hydrogenation). Pd doping also improved Cu stabilization against oxidation by CO<sub>2</sub>. CO<sub>2</sub> conversion and DME selectivity of 18.7 and 73.6% were reached at 200°C and 3 MPa (Table 5, Entry 27).

Following these leads, the catalytic activity of PdZn alloy nanoparticles on TiO<sub>2</sub> for the hydrogenation of CO<sub>2</sub> to methanol was also explored.<sup>557,558</sup> The catalytic performance of PdZn

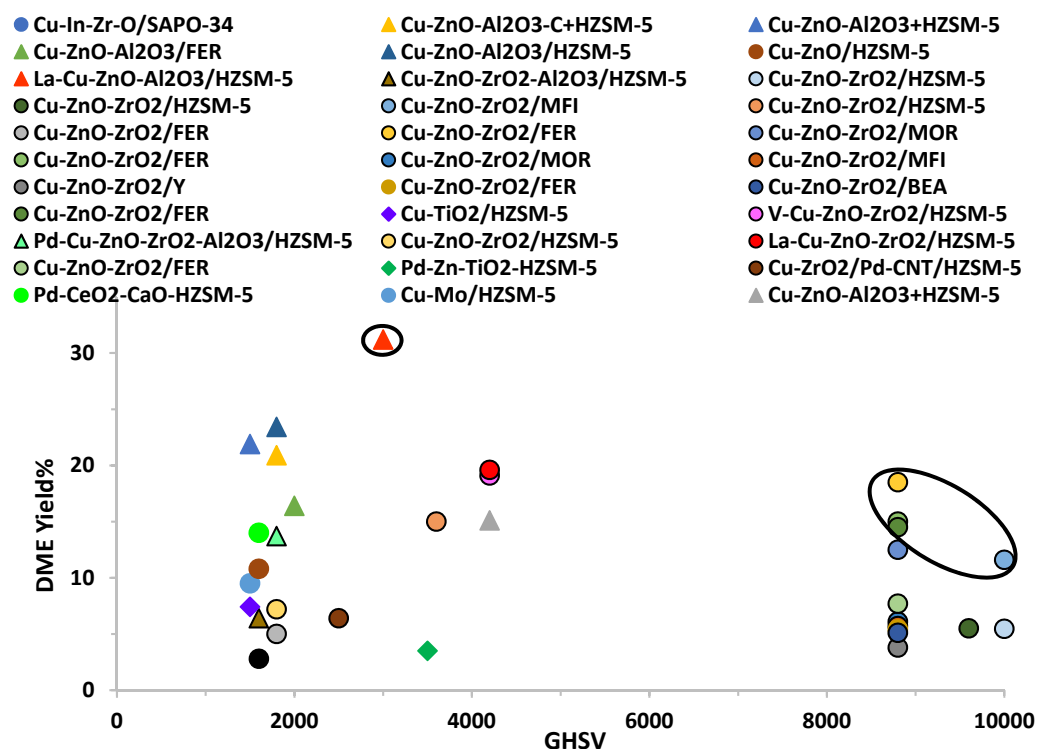
alloy nanoparticles onto the solid acid ZSM-5 via chemical vapor impregnation, and of the mixture of 5% PdZn/TiO<sub>2</sub>+ZSM-5 for the DME production were compared.<sup>559</sup> The catalytic performance of the physical mixture PdZn/TiO<sub>2</sub>-ZSM-5 showed to be superior and this result was attributed to blocking of Brønsted acid sites when PdZn was directly deposited on the zeolite surface. Therefore, 5% PdZn/TiO<sub>2</sub>+ZSM-5 allowed reaching CO<sub>2</sub> conversion of 11% and DME selectivity of 32% at 270°C and 2 MPa with DME production of 0.030 Kg<sub>DME</sub> Kg<sub>cat</sub><sup>-1</sup>h<sup>-1</sup> (Table 5, Entry 31). Previously, hybrid catalyst consisting of deposited Cu-ZrO<sub>2</sub> on Pd-decorated multi-walled carbon nanotubes (CNT) material and mixed with HZSM-5 zeolite following different routes were also used for the synthesis of DME.<sup>510</sup> The study revealed that the mixing method affected the final catalytic performance of the hybrid catalyst and the stepwise precipitation/slurry mixing showed to provide the optimum catalysts. The addition of Pd-decorated CNTs into the Cu-ZrO<sub>2</sub>/HZSM-5 catalyst modified slightly the apparent activation energy for CO<sub>2</sub> hydrogenation, but enabled to increase the metal Cu exposed area, improving H<sub>2</sub> and CO<sub>2</sub> adsorption performance of the catalyst. Over the bi-functional Cu-ZrO<sub>2</sub>-PdCNT/HZSM-5 hybrid catalyst at 250°C and 5.0 MPa, maximum 12.5% CO<sub>2</sub> conversion, 51.8% DME selectivity and STY<sub>DME</sub> 0.579g<sub>DME</sub>h<sup>-1</sup>g<sub>hydr. catal</sub><sup>-1</sup> were reached (Table 5, Entry 32). Under these reaction conditions, the catalyst showed stabilized catalytic performance after 20h of TOS, remaining stable for 200h with CO<sub>2</sub> conversion and DME selectivity around 7.5 and 75%, respectively. Since CO<sub>2</sub> issued from combustion of sulfur-containing substances enclosed numerous sulfur compounds, catalysts for DME synthesis strongly adsorb sulfur compounds and suffer strong poisoning. The Pd-catalysts can maintain good catalytic performance in the presence of sulfur species due to the formation of a Pd-electron-deficient state by transferring an outer electron, resulting in poor interactions between Pd and the electron-acceptor sulfur. Different factors can favour the Pd-electron-deficient state such as the acidity of carrier surface,<sup>560</sup> very small particle size of Pd and the presence of electron-withdrawing additives.<sup>561</sup> Then, Pd/HZSM-5 bifunctional catalysts incorporating CeO<sub>2</sub> and CaO were prepared by impregnation.<sup>562</sup> The study showed that CaO incorporation enabled to reduce the strong acidity and weakened the CO<sub>2</sub> adsorption while the presence of CeO<sub>2</sub> induced an increase in the moderate acidity and favoured weak adsorption of CO<sub>2</sub>. Therefore, CeO<sub>2</sub>-CaO-Pd/HZSM-5 exhibited very good catalytic activity, and stability versus sulfur poisoning and coke deposition. The best catalytic performance was obtained over 3wt%CeO<sub>2</sub>-1wt%CaO-Pd/HZSM-5 catalyst, with CO<sub>2</sub> conversion and DME selectivity of 21% and 67% after 20h reaction (Table 5, Entry 33).

#### 5.4.5. Conclusion

The direct hydrogenation of CO<sub>2</sub> into DME is an attractive route giving the issues at stake from environment and economical standpoints. Efforts are being made to improve the hydrophobic and acid properties of the catalytic surface, and the Cu nanoparticle size and dispersion in order to optimize both methanol dehydration, and CO<sub>2</sub> and H<sub>2</sub> adsorption and activation, by controlling the zeolite structure and/or Si/Al ratio, and/or by incorporating a transition metal. The results showed the importance to balance adequately the acidity of the surface to promote methanol dehydration over strong acid sites. Similarly, the importance of the distance between the two types of active sites, the metal sites for methanol synthesis and the acid sites for methanol dehydration, has been studied. The proximity between the two sites was shown to be crucial to minimize mass transfer restrictions and to improve the DME selectivity, being more convenient to integrate the two types of active sites in a single moiety. Nevertheless, the developed catalysts exhibit limited catalytic performance since low DME selectivity are usually achieved because of high CO production. Moreover, the catalysts suffer drastic deactivation due to the large amount of water produced during the reaction. The [Figures 29 and 30](#) illustrate the catalytic performance of the different zeolite-based catalysts reported and highlight the catalytic performance of La-Cu-ZnO-Al<sub>2</sub>O<sub>3</sub>/HZSM-5 and Cu-ZnO-Al<sub>2</sub>O<sub>3</sub>/HZSM-5 due to the good DME selectivity and productivity. However, the direct transformation of CO<sub>2</sub> into DME needs further development to reach industrial application. Exhaustive studies taking into account catalyst stability and regeneration step are required.



**Figure 29.** CO<sub>2</sub> conversion was plotted versus DME selectivity for all reported zeolite-based catalysts. The ovoid highlights the best catalytic performance: high selectivity versus high conversion level.



**Figure 30.** CO<sub>2</sub> conversion was plotted versus DME selectivity for all reported zeolite-based catalysts. The ovoid highlights the best catalytic performance: high yield versus high GHSV.

**Table 5.** Summary of the catalytic data of the different bifunctional catalysts for the direct DME synthesis discussed in this review.

Entry	Catalysts*	CO <sub>2</sub> Conv.%	Sel. <sub>DME</sub> %	Yield <sub>DME</sub> %	STY <sub>DME</sub> ( $\frac{\text{g}_{\text{DME}}}{\text{g}_{\text{cat}} \cdot \text{h}}$ )	Sel. <sub>CO</sub> %	Sel. <sub>MeOH</sub> %	Conditions	Year	Ref.
1	Cu-Mo/HZSM-5	12.3	77.2	9.5		15.9	6	240°C-2MPa, GHSV=1500 h <sup>-1</sup>	2001	524
<b><i>SAPO-based catalysts</i></b>										
2	Cu-In-Zr-O/SAPO-34	4.3	65.1		0.080	29.7	8	250°C-3MPa, GHSV=1600 h <sup>-1</sup>	2020	525
<b><i>Cu-ZnO-Al<sub>2</sub>O<sub>3</sub>-based zeolite catalysts</i></b>										
<b>• Physical mixture</b>										
3	Cu-ZnO-Al <sub>2</sub> O <sub>3</sub> +HZSM-5	30.6	49.2	15.1			10.4	270°C-3MPa, GHSV=4200 h <sup>-1</sup>	2014	523
4	Cu-ZnO-Al <sub>2</sub> O <sub>3</sub> -Carbon nanotubes+HZSM-5	46.2	45.2	20.9		19.2	35.6	262°C-3MPa, GHSV= 1800 mL g <sup>-1</sup> h <sup>-1</sup>	2013	526
5	Cu-ZnO-Al <sub>2</sub> O <sub>3</sub> +HZSM-5	30.5	72	21.9		20	9	260°C-4.2MPa, WHSV=1500 h <sup>-1</sup>	2019	527
<b>• Hybrid catalyst</b>										
6	Cu-ZnO-Al <sub>2</sub> O <sub>3</sub> /FER	29.7	55.2	16.4	0.566	21.9	22.8	250°C-5MPa, GHSV=2000 L Kg <sup>-1</sup> h <sup>-1</sup>	2021	528
<b>• Morphology and structuration</b>										
7	Cu-ZnO-Al <sub>2</sub> O <sub>3</sub> /HZSM-5	48.3	48.5	23.42		20	32	270°C-3MPa, GHSV=1800 mL g <sup>-1</sup> h <sup>-1</sup>	2015	529
8	Cu-ZnO/HZSM-5	21.3	50.8	10.8		41.62	7.6	245°C-3MPa, GHSV=1600 h <sup>-1</sup>	2012	530
<b>• Promoter incorporation</b>										
9	La-Cu-ZnO-Al <sub>2</sub> O <sub>3</sub> /HZSM-5	43.8	71.2	31.2		24.6	4.3	250°C-2MPa, GHSV=3000 h <sup>-1</sup>	2013	531
10	Cu-ZnO-ZrO <sub>2</sub> -Al <sub>2</sub> O <sub>3</sub> /HZSM-5	24.1	26.6	6.4		29.2	44.2	260°C-3MPa, GHSV=1600 h <sup>-1</sup>	2007	521
<b><i>Cu-ZnO-Al<sub>2</sub>O<sub>3</sub>-based zeolite catalysts</i></b>										
<b>• Proximity between acid and metallic sites</b>										
11	Cu-ZnO-ZrO <sub>2</sub> /HZSM-5	16.1	33.9			54.3	11.8	240°C-3MPa, GHSV=10000 NLKg <sup>-1</sup> h <sup>-1</sup>	2014	518,534
<b>• Catalyst preparation</b>										
12	Cu-ZnO-ZrO <sub>2</sub> /HZSM-5	13	34	5.5	0.225	56	13	240°C-5MPa, GHSV=9600 mLg <sup>-1</sup> h <sup>-1</sup>	2015	536
13	Cu-ZnO-ZrO <sub>2</sub> /MFI	23.6	49.3	11.6		24.5	25.5	240°C-5MPa, GHSV=10000 h <sup>-1</sup>	2015	535
14	Cu-ZnO-ZrO <sub>2</sub> /HZSM-5	22.2	67.6	15	0.507	23.8	8.6	250°C-3MPa, GHSV=3600 mLg <sup>-1</sup> h <sup>-1</sup>	2016	537
15	Cu-ZnO-ZrO <sub>2</sub> /FER	17.5	28.4	5		58.3	13.3	250°C-2MPa, GHSV=1800 mLg <sup>-1</sup> h <sup>-1</sup>	2020	538
<b>• Zeolite topology</b>										
16	Cu-ZnO-ZrO <sub>2</sub> /FER	30	62	18.5	0.752	24	14	280°C-5MPa, GHSV=8800 Lkg <sup>-1</sup> h <sup>-1</sup>	2016	509
17	Cu-ZnO-ZrO <sub>2</sub> /MOR	28	50	12.5	0.680	38	12	280°C-5MPa, GHSV=8800 Lkg <sup>-1</sup> h <sup>-1</sup>	2016	509
18	Cu-ZnO-ZrO <sub>2</sub> /FER	23.6	47	15	0.6	38	15	260°C-5MPa, GHSV=8800 LKg <sup>-1</sup> h <sup>-1</sup>	2017	541
19	Cu-ZnO-ZrO <sub>2</sub> /MOR	20-22	28	~6.1	0.5	58	15	260°C-3MPa, GHSV=8800 LKg <sup>-1</sup> h <sup>-1</sup>	2020	542,543

20	Cu-ZnO-ZrO <sub>2</sub> /MFI	16-19	30	~5.7		57	13	260°C-3MPa, GHSV=8800 LKg <sup>-1</sup> h <sup>-1</sup>	2020	542,543
21	Cu-ZnO-ZrO <sub>2</sub> /Y	13-14	27	~3.8		54	19	260°C-3MPa, GHSV=8800 LKg <sup>-1</sup> h <sup>-1</sup>	2020	542,543
22	Cu-ZnO-ZrO <sub>2</sub> /FER	15-18	30	~5.4		57	13	260°C-3MPa, GHSV=8800 LKg <sup>-1</sup> h <sup>-1</sup>	2020	542,543
23	Cu-ZnO-ZrO <sub>2</sub> /BEA	16-17	30	~5.1		58	12	260°C-3MPa, GHSV=8800 LKg <sup>-1</sup> h <sup>-1</sup>	2020	542,543
<b>● Si/Al ratio</b>										
24	Cu-ZnO-ZrO <sub>2</sub> /FER	26	55.7	14.5	14.5	31.5	12.8	260°C-5MPa, GHSV=8800 LKg <sup>-1</sup> h <sup>-1</sup>	2018	508
<b>● Promoter incorporation</b>										
25	Cu-TiO <sub>2</sub> /HZSM-5	15.6	47.5	7.41		39.2	13	250°C-3MPa, WHSV =1500 h <sup>-1</sup>	2009	512
26	V-Cu-ZnO-ZrO <sub>2</sub> /HZSM-5	32.5	58.8	19.1		28	13.2	270°C-3MPa, GHSV=4200 h <sup>-1</sup>	2014	549
27	Pd-Cu-ZnO-ZrO <sub>2</sub> - Al <sub>2</sub> O <sub>3</sub> /HZSM-5	18.7	73.5	13.7		13	13.3	200°C-3MPa, GHSV=1800 h <sup>-1</sup>	2004	550
28	Cu-ZnO-ZrO <sub>2</sub> /HZSM-5	15.6	46.6	7.2		39	14.1	250°C-3MPa, GHSV=1800 h <sup>-1</sup>	2012	226
29	La-Cu-ZnO-ZrO <sub>2</sub> /HZSM-5	34.3	57.3	19.6	0.212	29.4	13.3	270°C-3MPa, GHSV=4200 h <sup>-1</sup>	2017	552
30	Cu-ZnO-ZrO <sub>2</sub> /FER	21.3	36.5	7.7		49.1	14.4	260°C-3MPa, GH SV=8800 LKg <sup>-1</sup> h <sup>-1</sup>	2017	553
<b><u>Pd and bimetallic catalysts</u></b>										
31	Pd-Zn-TiO <sub>2</sub> -HZSM-5	11	32.3	3.5	0.030	61.7	5.9	270°C-2MPa, GHSV=3500 h <sup>-1</sup>	2018	559
32	Cu-ZrO <sub>2</sub> /Pd-CNT/HZSM-5	12.5	51.8	6.4	0.812	34	65.9	250°C-5MPa, GHSV=2500 mLKg <sup>-1</sup> h <sup>-1</sup>	2013	510
33	Pd-CeO <sub>2</sub> -CaO-HZSM-5	21	67	14	0.579	23.3	9.4	250°C-3MPa, GHSV=1600 h <sup>-1</sup>	2017	562

\* Metal content is given in wt%.

## 5.5. CO<sub>2</sub> methanation

### 5.5.1. Introduction

Nowadays natural gas constitutes 24% of global primary energy consumption of fuel and it is the third fuel used for power generation, and the main one for heat generation in industry and households.<sup>563</sup> Currently, methane can be obtained from natural wells with fossil origin, from purifying biogas obtained by fermentation of organic matter and from synthetic gas route. In 2022, natural gas reserves account for ~50 years of current production. In 1872, CO<sub>2</sub> hydrogenation into methane was firstly discovered applying an electric discharge to a CO/CO<sub>2</sub>/H<sub>2</sub> mixture.<sup>564</sup> At the beginning of the twentieth century, Sabatier developed a process to produce methane and water starting from CO<sub>2</sub> and H<sub>2</sub> in the presence of a heterogeneous nickel catalyst.<sup>565</sup> Since then, CO<sub>2</sub> hydrogenation or CO<sub>2</sub> methanation, also called the “Sabatier reaction”, has been studied for more than 100 years. Nowadays, because of the increasing demand for natural gas and the reduction of greenhouse gases, the production of synthetic natural gas (SNG) constitutes an important future energy carrier due to its environmentally-friendly nature and high calorific value (Figure 31). Moreover, SNG can be stored and distributed easily thanks to its worldwide existing infrastructure consisting of storage facilities, filling stations, and pipeline networks.<sup>566–569</sup> More importantly, CO<sub>2</sub> methanation is one of the most promising strategies within the concept of power-to-gas. Indeed, the main problem found with renewable energy is to adapt the production and demand, as there are situations where the amount of energy produced is greater than demand when there is for examples excess wind, sun or rain. Then the storage results expensive and finally ends up wasting it. Accordingly, Power-to-Gas (P2G) process constitutes an alternative to adjust this demand since it allows the transfer of excess electricity from renewables from the electricity grid to the natural gas grid. P2G consists in the conversion of electricity into thermal energy in the form of methane, and is still an incipient technology. An overview of the production costs of synthetic methane in a P2G process has been recently reported.<sup>570</sup> The production costs depend on three determining economic factors such as the price and market of electricity, the price and market of SNG and the market price of CO<sub>2</sub> and the availability. It was so envisioned that with the future expected development of capital and operational expenditure, electricity prices and gas costs, a viable and economic production of synthetic natural gas for the years 2030, especially for 2050, is feasible. CO<sub>2</sub> methanation process requires H<sub>2</sub> and for sustainability and environment considerations, H<sub>2</sub> has to be green. Therefore, H<sub>2</sub> is issued from water splitting that requires electric energy issued from green and sustainable sources. Current electrolysis technologies at industrial scale are alkaline electrolysis<sup>571</sup> and proton exchange membrane electrolysis.<sup>572</sup>

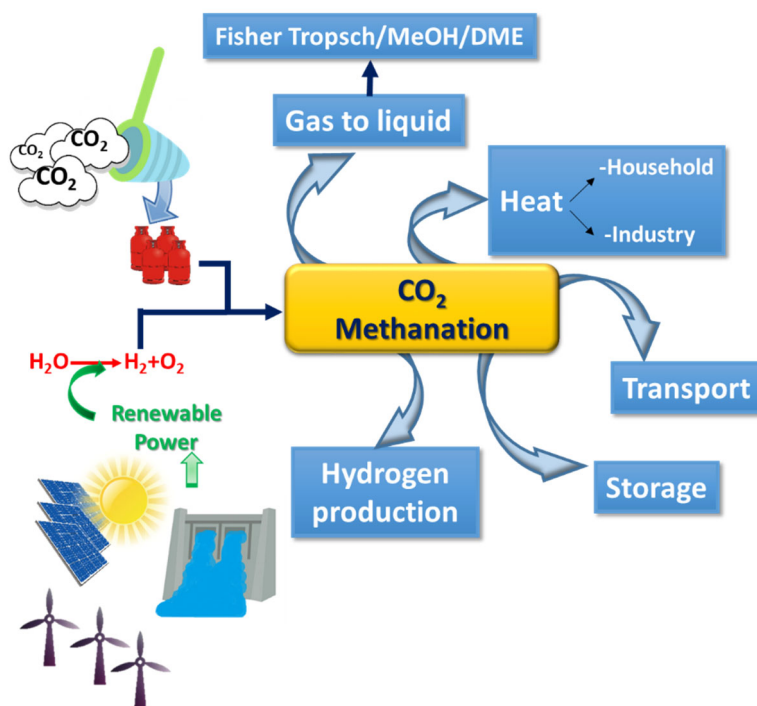
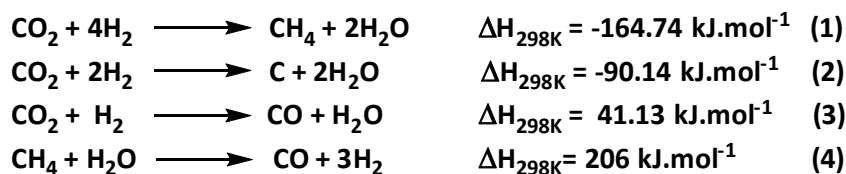


Figure 31. Scheme of methane production and uses.

### 5.5.2. Thermodynamics of CO<sub>2</sub> methanation

Methanation for the production of SNG is a very complicated process and the thermodynamic of the process has to be considered for the evaluation of any proposed technology. Then, numerous studies of thermodynamic equilibrium calculations of complex chemical systems based on the Gibbs free energy minimization have been reported, providing informations such as the type of thermodynamically stable reaction products together with their selectivity and yield, heat transfer requirements (endothermic or exothermic process) and the impact of reaction parameters (temperature, pressure, or reactant ratios).<sup>573–575</sup> CO<sub>2</sub> methanation is known to be a highly exothermic reaction. However, it is difficult to achieve because of the high kinetic barriers of the eight-electron reduction process. The hydrogenation process starting from CO<sub>2</sub> and H<sub>2</sub> involves six possible products, CO<sub>2</sub>, CO, H<sub>2</sub>, CH<sub>4</sub>, H<sub>2</sub>O and C deposit through three independent reactions (Scheme 54). Moreover, CO<sub>2</sub> methanation is a reversible reaction and the reverse process is the steam reforming of methane (Eq. 4).



Scheme 54. Different CO<sub>2</sub> hydrogenation processes.



Based on these reactions, different studies<sup>513,576,577</sup> concluded that reaction temperature superior to 600°C, favours CO formation from the reverse water gas shift reaction (RWGS) (Eq. 3) while CH<sub>4</sub> formation is disfavoured and the C-deposits can be avoided to a great extent. Moreover, a H<sub>2</sub>/CO<sub>2</sub> ratio increase revealed to have a positive effect on the production of CH<sub>4</sub> and it has to be pointed out that carbon formation is not expected at a H<sub>2</sub>/CO<sub>2</sub> ratio  $\geq 4$ .<sup>573</sup> At lower ratios significant carbon formation was observed even at 3 MPa. Then, a control of H<sub>2</sub>/CO<sub>2</sub> ratio and temperature is mandatory for the methanation process. From thermodynamic consideration, CO<sub>2</sub> methanation should be performed at low temperatures (< 300–350°C), elevated pressure, and with a stoichiometric ratio of H<sub>2</sub>/CO<sub>2</sub> = 4.<sup>578</sup>

Although catalytic CO<sub>2</sub> methanation is thermodynamically favourable at low temperatures, because of kinetic limitation and high stability of CO<sub>2</sub> molecules, high temperatures (200–750°C) are normally required to enable the CO<sub>2</sub> methanation. To maximize CH<sub>4</sub> yield, the reaction system has to be maintained away from the region of thermodynamic equilibrium and reactions of equations 2 and 3 have to be avoided. In addition, due to the high exothermicity, the development of local hotspots along the catalytic packed bed is responsible of catalyst sintering and deactivation.<sup>579</sup> Therefore, the design and development of efficient and selective catalysts to methane formation coupled with adequate reactor system is key and very challenging.

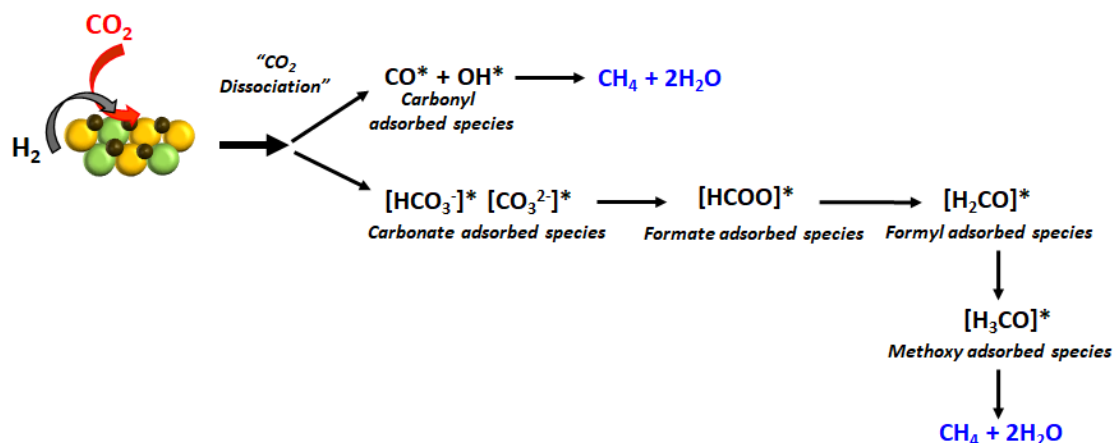
### 5.5.3. Catalysts for CO<sub>2</sub> methanation

Since the discovery of Ni activity for CO<sub>2</sub> methanation numerous group VIII B metals (Fe, Ru, Co, Rh, Ir, Ni, Pt)<sup>574,580–586</sup> have been carefully investigated and Ni, Ru and Rh based catalysts revealed to be the most active for this process. Various strategies have been attempted to enhance the stability and activity of the catalyst. The oxygen mobility and basic properties of the support constitute key parameters. The effect of the support, metal loading and the incorporation of additives such as metal, metal oxides or alkali metals have been shown to enhance the stability and catalytic performance and modify the state of the active phase.<sup>577,587</sup> The addition of a second metal can change the electronic and geometric structures of single-crystal metal,<sup>588</sup> inducing different physical and chemical properties to the metal-active phase.

The specific activity and selectivity of different metals over alumina have been studied by different groups.<sup>589–591</sup> In 1976,<sup>589</sup> the order of activity of supported metals was as following: Ru >> Fe > Ni > Co > Rh > Pd > Pt > Ir, and selectivity order Pd > Pt > Ir > Ni > Rh > Co > Fe > Ru. Previously, a simplified classification was reported considering the most important metal methanation catalysts, Ru, Ni, Co, Fe and Mo. Therefore, ordered activity was reported Ru > Fe > Ni > Co > Mo and ordered selectivity as following Ni > Co > Fe > Ru. Within the CO<sub>2</sub> methanation catalysts, the Ni based remain the most extensively studied catalysts<sup>587,592–598</sup> due to their good

activity for CO<sub>2</sub> hydrogenation, high selectivity to methane, low cost and availability. However, Ni catalysts deactivate easily, even at low temperature, due to the sintering of Ni particles, formation of mobile nickel sub-carbonyls and carbon deposition<sup>599</sup> that results in a fast deactivation of the catalyst, and constituting one of the most important problems in industry. After Ni, Rh has been the most investigated metal for CO<sub>2</sub> methanation. The oxidation state of Rh<sup>574</sup> and particle size, as well as the presence of promoters greatly influence its catalytic performance.<sup>600</sup> Likewise, a study of Rh content over TiO<sub>2</sub> modified metal particle sizes revealed that, at low temperatures (130-150°C), the rate of CH<sub>4</sub> production per surface Rh atoms increased when metal particle size increase up to 7 nm.<sup>582</sup> Ruthenium has been largely used and studied for CO<sub>2</sub> methanation and can be even more active<sup>591,601-605</sup> than Ni but it is considerably more expensive.<sup>606-608</sup>

a) Mechanism of CO<sub>2</sub> methanation



**Figure 32.** Different mechanisms have been investigated based on CO intermediate, or formate (bicarbonate) intermediates.

Several studies have proposed different mechanisms for CO<sub>2</sub> methanation over different catalysts,<sup>577,609-612</sup> and two main routes with CO or bicarbonate/formate as main intermediates have been considered (Figure 32). The nature and composition of the catalyst active sites, more specifically the presence of acid/basic sites (density and strength), control and determine the formation and nature of the reaction intermediates. Respect to the CO<sub>2</sub> dissociation mechanism, it is envisioned that CO<sub>2</sub> adsorption occurs preferably at the metal-support interface while CO<sub>2</sub> dissociation takes place on the active metal surface.<sup>613</sup> Then, CO hydrogenation takes place in the same way than for CO methanation. The other mechanism involves the formation of oxygenated species, carbonates and further, formates, preferably in the presence of basic sites that enable the adsorption and activation of CO<sub>2</sub>.

#### b) Zeolite-based catalysts for CO<sub>2</sub> methanation

Numerous studies and catalytic systems have been developed to perform CO<sub>2</sub> methanation and the design and development of an efficient and selective catalyst, able to perform methanation at relatively low temperature to reduce the costs of the process remain as the main challenges. The development of a successful zeolite based catalyst for the CO<sub>2</sub> methanation could be a new breakthrough in the zeolite field owing to zeolite robustness to work continuously for days under severe conditions (temperature, pressure and moisture).<sup>614,615</sup> Indeed zeolites are well-known to present great stability under severe reaction conditions as evidenced by their use in the FCC industrial process.

Despite the existence of different hydrogenation metals reported for CO<sub>2</sub> methanation, Ni remains the best choice when considering activity, selectivity and price. Interestingly, Ni constitutes practically the sole reported metal supported on zeolites for this application. In the literature, we could find one example of Fe catalyst where Fe/13X was studied as candidate to substitute Ni catalysts at elevated pressure. A very high dispersion of Fe in octahedral sites within the zeolite is necessary for selectively performing CO<sub>2</sub> methanation process and to suppress the Fischer-Tropsch activity towards C-C coupling at elevated pressure. A low Fe loading (1 wt%) and high Fe dispersion were needed to reach high reaction rates with 76% CH<sub>4</sub> selectivity and 82% CO<sub>2</sub> conversion, at 300 °C and 10 bar (Table 6, Entry 1).<sup>616</sup>

Nickel-based zeolite catalysts exhibit maximum CH<sub>4</sub> selectivity but suffer drastic deactivation due to water adsorption on active sites. Therefore, to comply with "Le Chatelier's principle" in situ removal of water from the reaction sites is required and the use of molecular sieves due to their adsorption properties should be beneficial. Accordingly, a recent study showed the importance of regeneration of the active sites of the catalyst (Table 6, Entry 2).<sup>617</sup> The catalytic performance of 5Ni/13X and 5Ni/5A samples were compared for alternated cyclic CO<sub>2</sub> methanation and drying at 300°C. The better catalytic performance of 5Ni/13X was demonstrated and attributed to its higher water adsorption capacity being the optimal catalysts regeneration by a simple drying step under oxidizing (air) atmosphere which allowed the redispersion of the Ni nanoparticles<sup>618</sup> and improved catalyst stability.

Therefore, the development of a robust and successful zeolite-based catalyst is related to three key parameters which are: hydrophobicity, nickel nanoparticles size and dispersion, and CO<sub>2</sub> adsorption and activation.

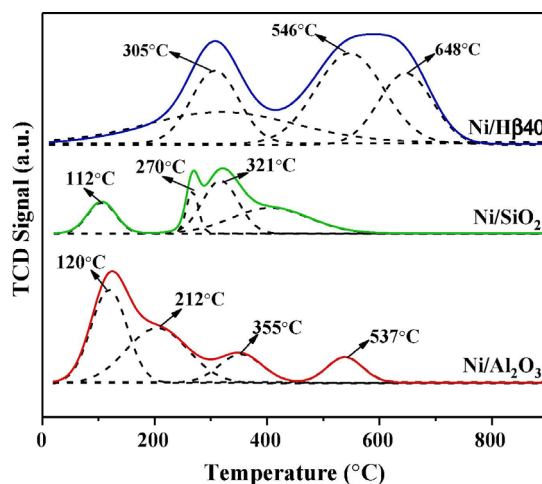
In the literature, numerous works have reported the effect of compensating cation exchange over the basic properties of the zeolite-based catalysts affecting the adsorption and activation of CO<sub>2</sub>, but also on the stabilization and dispersion of Ni nanoparticles that can be additionally modified by adding promoters, the effect of Si/Al ratio on the acid/base properties and the

hydrophobicity, and the effect of the structure on the Ni stability and dispersion but also on the hydrophobicity inherent to each zeolite structure.

*i) Effect of Si/Al ratio of zeolite-based catalysts for CO<sub>2</sub> methanation*

The Al framework content in zeolites allowed to control Brønsted acidity and hydrophobicity and hydrophilicity of the surface.<sup>58,619–621</sup> Zeolites with enhanced hydrophobicity are obtained by increasing framework Si/Al ratio and the number of silanols. For CO<sub>2</sub> methanation, the hydrophobicity of the surface was shown to be of paramount importance due the inhibitory effect for water adsorption.<sup>622,623</sup> Recently, the catalytic performance of Ni-ITQ-2 and ZSM-5 zeolites catalysts with different aluminum content<sup>624</sup> revealed that the Al content is a more determinant factor than the structure of the zeolite. This is because of the lower water adsorption on the high Si/Al ratio zeolites that lowers deactivation of the Ni components by water that reduces the CO<sub>2</sub> surface coverage. Moreover, high Si/Al ratio also improved the dispersion and stability of Ni nanoparticles as it was yet reported.<sup>625</sup> Comparison of the catalytic behavior of both zeolite structures showed higher activity for the pure silica ITQ-2 zeolite indicating the crucial effect of the aluminum content and its impact over hydrophobicity and hydrophilicity of the catalytic surface and nickel particle size and dispersion. 68% CO<sub>2</sub> conversion and 99% CH<sub>4</sub> selectivity were obtained at 350°C (Table 6, Entries 3-4). The results obtained with 5Ni/ITQ-2(Si/Al~∞) are comparable to those reported in the presence of Ni-zeolite with promoters such as La<sub>2</sub>O<sub>3</sub><sup>626</sup> or Ce<sup>627,628</sup>. Previously, the beneficial effect of increasing the Si/Al ratio in Y zeolite over the catalytic behavior of 15%Ni-Y zeolite samples for CO<sub>2</sub> methanation was shown (Table 6, Entry 5).<sup>621</sup> In the case of Y zeolite, a lower Al content obtained by dealumination was associated to the lower affinity of the zeolites to water and the presence of mesopores enabling higher dispersion of the Ni particles regardless of the compensating cation present in the zeolite and their lower basicity. Therefore, the hydrophobicity of the zeolites resulted a more determinant factor than the basicity, that was previously reported as a parameter of importance for CO<sub>2</sub> methanation.<sup>629</sup> Indeed, the influence of the distribution of acidic/basic sites and Ni dispersion on the catalytic behaviors for CO<sub>2</sub> methanation catalysts have been described as key factor for the CO<sub>2</sub> adsorption and activation. Following this direction, a study of physicochemical properties of the Ni/Al<sub>2</sub>O<sub>3</sub>, Ni/SiO<sub>2</sub> and Ni/Beta zeolite (Ni/Hβ40), revealed that even if the mesoporous Al<sub>2</sub>O<sub>3</sub> enabled a higher dispersion of nickel species this sample exhibited a lower catalytic activity than the beta zeolite based catalyst. The distribution of basic sites was determined with CO<sub>2</sub>-TPD profiles showing different desorption peaks assigned to weak, medium and strong basic sites in the temperature range, 100-200°C, 200-400°C and 500-600°C, respectively. Therefore, Ni/Al<sub>2</sub>O<sub>3</sub> sample mainly exhibited weak basic sites, Ni/SiO<sub>2</sub> sample

exhibited mainly medium basic sites while Ni/H $\beta$ 40 sample mainly presented medium-strong basic sites, leading to the basicity order Ni/H $\beta$ 40 > Ni/SiO<sub>2</sub> > Ni/Al<sub>2</sub>O<sub>3</sub>, being the presence of basic sites crucial for CO<sub>2</sub> adsorption and activation (Figure 33). DRIFT study showed different reaction network over the different samples that exhibit the same Ni content but different physicochemical properties such as higher density of Lewis acid sites in Ni/Al<sub>2</sub>O<sub>3</sub> catalyst and higher density of medium-strong strength basic sites in Ni/H $\beta$ 40 catalyst. Therefore, Ni/H $\beta$ 40 catalyst characterized by optimum density of the medium to strong basic sites exhibited superior activity than Ni/SiO<sub>2</sub> while Ni/Al<sub>2</sub>O<sub>3</sub> did not show adequate catalytic properties for CO<sub>2</sub> methanation. Practically 100% CH<sub>4</sub> selectivity and 80% CO<sub>2</sub> conversion were achieved at 300°C in the presence of Ni/H $\beta$ 40 (Table 6, Entry 6).<sup>612</sup> These results showed the importance of suitable hydrophobic and basic properties for CO<sub>2</sub> methanation for both water elimination of the catalytic surface and CO<sub>2</sub> adsorption and activation, respectively, which could be achieved in zeolite by adjusting Si/Al ratio and cation exchange.

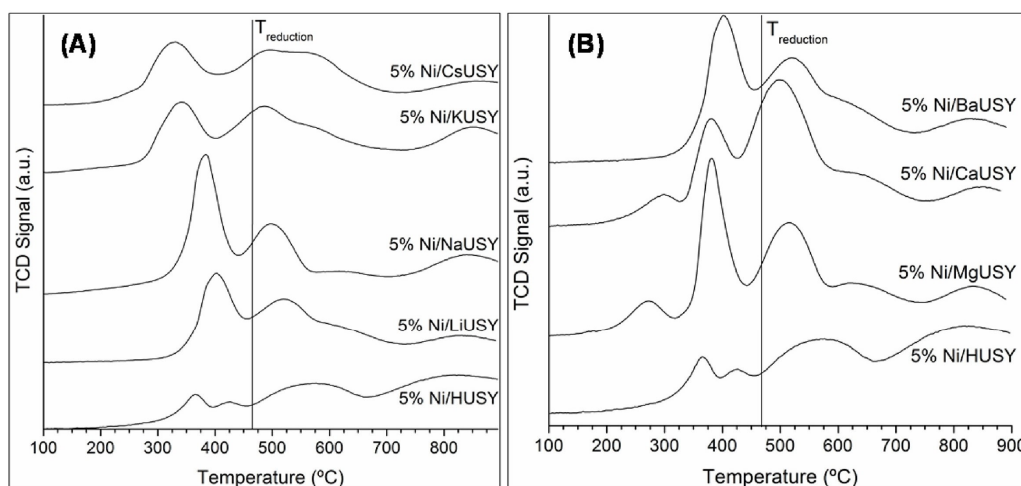


**Figure 33.** CO<sub>2</sub>-TPD profiles of the reduced Ni/Al<sub>2</sub>O<sub>3</sub>, Ni/SiO<sub>2</sub> and Ni/H $\beta$ 40 catalysts. Reprinted with permission from ref.<sup>612</sup> Copyright 2019, Elsevier Ltd. All rights reserved.

ii) *Effect of the cations in exchanged zeolites for CO<sub>2</sub> methanation*

The substitution of SiO<sub>4</sub> with AlO<sub>4</sub><sup>-</sup> tetrahedra in zeolite induces a negative charge that has to be compensated by exchangeable cations (H<sup>+</sup>, Na<sup>+</sup>, K<sup>+</sup>, Cs<sup>2+</sup>, Ca<sup>2+</sup>). The amount, characteristic and properties of each cation determine the properties of the zeolites, such as acid/base properties<sup>612</sup> and consequently affect the CO<sub>2</sub> adsorption capacity.<sup>42,630–632</sup> In addition, the nature of the compensating cation can influence the Ni metallic particles size and stability as well as the reducibility properties owing to electron donation from the alkali metal to Nickel which is greater when the larger the ionic radius is.<sup>633</sup> In this direction, a study of the effect of the environment of Ni particles demonstrated the influence of the size of the alkali metal cations since larger cations are able to inhibit the migration path of the nickel species and so to limit the metal sintering most efficiently than compensation cations with lower size.<sup>634</sup> The effect of the

nature of the compensating cation is greater when the lower the Ni content is, i.e when Ni sintering is lower. Following this direction, a few years ago, a study for CO<sub>2</sub> methanation using USY zeolite exchanged with monovalent (Cs<sup>+</sup>, K<sup>+</sup>, Na<sup>+</sup>, Li<sup>+</sup>) and divalent (Ba<sup>2+</sup>, Ca<sup>2+</sup>, Mg<sup>2+</sup>) cations and impregnated with 15% and 5% of Ni was carried out.<sup>621</sup> H<sub>2</sub>-TPR study demonstrated that the reducibility of Ni species was higher when bigger cations are present and the effect is greater for lower Ni content. This is so even if similar amount of reduced Ni species was obtained (for a same Ni content) (Figure 34), while similar Ni particles sizes were observed for monovalent cation and much bigger for K<sup>+</sup> sample. Therefore, the improvement of the catalytic performance with exchanged samples with monovalent alkaline cations were associated to the enhanced CO<sub>2</sub> adsorption capacity and framework basicity of the exchanged zeolites. Respect to divalent alkaline earth cations, Mg<sup>2+</sup> improved both CO<sub>2</sub> activation and Ni dispersion. When similar study was performed with USY zeolite exchanged with alkali metal and impregnated with 5% of Ni, the authors reported enhancements up to 200% in CO<sub>2</sub> conversion and 300% in CH<sub>4</sub> selectivity in the presence of 5wt%Ni/Cs-USY catalyst, at 450°C (Table 6, Entry 7).<sup>629</sup>



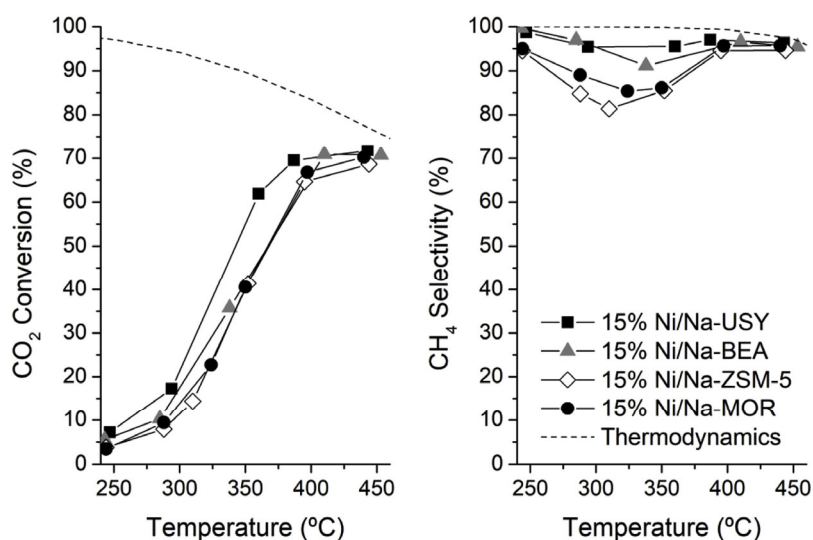
**Figure 34.** H<sub>2</sub>-TPR profiles obtained for mono- and divalent samples containing 5%Ni. Reprinted with permission from ref. <sup>629</sup> Copyright 2017, Elsevier Ltd. All rights reserved.

Soon after, a study comparing the catalytic performance of 10wt%Ni-supported Y and BETA zeolites reported the same benefits of Na<sup>+</sup> cation exchange, that improved the CO<sub>2</sub> conversion due to the reducibility enhancement of NiO (electron donation from Na<sup>+</sup> to Ni) together with the improved CO<sub>2</sub> adsorption owing to the generation of weak basic sites in Na-based catalysts. Various and distinct Ni species were formed in both Ni/Na-BETA and Ni/Na-Y due to differences in their structure involving different Nickel locations with different reducibility. Besides, similar CO<sub>2</sub> methanation activity was obtained for both Ni/Na-Y and Ni/Na-Beta catalysts attributed to similar available surface of active phase during CO<sub>2</sub> methanation. In the presence of Ni/Na-BETA catalyst 73% CO<sub>2</sub> conversion and 71% CH<sub>4</sub> yield were reached at 350°C (Table 6, Entry 8).<sup>27</sup>

iii) *Effect of topology and morphology structure of zeolite-based catalysts for CO<sub>2</sub> methanation*

The zeolite topology not only influences the reaction pathway and products distribution, but it is also crucial to the diffusion and adsorption/deposition of metallic precursors into the channels leading to different nickel location (NiO on external surface, Ni<sup>2+</sup> pseudo-tetrahedrally, tetrahedrally and octahedrally coordinated). Indeed the different voids and microenvironments defined by the zeolites topologies are responsible for stabilization and dispersion of metallic active sites.<sup>48,51,86,539,635</sup> A recent work reported the effect of the zeolite framework type on the catalytic performances of Ni-based catalysts (15wt%) using commercial USY, BEA, ZSM-5 and MOR zeolites with Si/Al closed to 40 and ion-exchanged with Na<sup>+</sup> or Cs<sup>+</sup>.<sup>636</sup> The zeolites exhibit different particle sizes, and the BEA sample had the smallest particle size, and the intercrystalline space of the BEA sample was responsible for the formation of mesoporosity. TEM analysis revealed that USY, ZSM-5 and MOR samples exhibit similar Ni<sup>0</sup> particles sizes, while the BEA exhibited higher dispersion and smallest Ni<sup>0</sup> particles. Even if the zeolites presented similar Si/Al ratio, their H<sup>+</sup> exchange capacities were different, leading to distinct alkali and alkali earth compensating cations contents and so diverse CO<sub>2</sub> adsorption capacities as follows: USY<BEA<ZSM-5<MOR. The H<sub>2</sub>-TPR study demonstrated similar reducibility for USY and BEA with greater amount of NiO reduced at T>500°C, probably due to NiO located in mesopores, and similar reducibility for MOR and ZSM-5 with NiO particles mainly located on external surface. Since the hydrophobicity was established as paramount importance to shift the equilibrium and to avoid the deactivation of active site, the hydrophobicity index was calculated for the different zeolites and followed the order: USY>MOR>BEA≈ZSM-5. Besides these characterization data the catalytic performances followed the order: 15%Ni/Na-USY>15%Ni/Na-BEA>15%Ni/Na-ZSM-5≈15%Ni/Na-MOR. Thus, taking into account that Ni<sup>0</sup> particles size, CO<sub>2</sub> adsorption capacity and hydrophobicity are considered key parameters for the design of an efficient zeolite-based catalyst and the catalytic activity order, the authors concluded that the mandatory parameter was the hydrophobicity. When zeolite sample were Cs<sup>+</sup> exchange, a increase of hydrophobicity index for BEA, ZSM-5 and MOR samples was observed as reported in the literature,<sup>637</sup> while similar for USY sample. Regarding H<sub>2</sub>-TPR profiles there were not considerably changes when comparing Cs<sup>+</sup> and Na<sup>+</sup> exchanged samples. However, Cs<sup>+</sup> exchange favoured the Ni<sup>0</sup> dispersion owing to its ability to inhibit the migration path of the nickel species and to suppress the metal agglomeration as above commented. Thus, the dispersion of Ni<sup>0</sup> particles followed the order BEA>MOR>USY>ZSM-5, while the catalytic activity of the exchanged sample followed the order 15Ni/Cs-USY>15%Ni/Cs-BEA≈15%Ni/Cs-MOR>15%Ni/Cs-ZSM-5. Since the characterization data did not allowed supported the activity order, the authors

attributed the best catalytic performance of USY sample to more favourable interaction metal/support inherent to zeolite structure. Additionally, a characterization study of textural properties and the catalytic performance of a BEA sample with Si/Al=243 was determined. The results showed an improvement of the catalytic activity attributed to its higher hydrophobicity although presented larger Ni<sup>0</sup> particles size and nearly reaching the results obtained in the presence of the USY catalyst.<sup>636</sup> Thus, in the presence of Ni/NaUSY and Ni/NaBEA catalysts, 70-71% CO<sub>2</sub> conversion and 95-96% CH<sub>4</sub> selectivity, at 375-400 °C, were achieved (Figure 35; Table 6, Entries 9-10). These results revealed the importance of the interaction metal/support inherent to zeolites morphology over their catalytic performance.



**Figure 35.** Catalytic performances of the Na-BEA samples with Si/Al= 40 (1) and 243 (2) and of Ni/Na-USY catalyst. Reprinted with permission from ref.<sup>636</sup> Copyright 2018, Elsevier Inc. All rights reserved.

A previous study compared the use of different micro- and mesoporous supports (ZSM-5, SBA-15, MCM-41, Al<sub>2</sub>O<sub>3</sub> and SiO<sub>2</sub>) to prepare Ni-based catalysts. The CO<sub>2</sub> adsorption study evidenced that the incorporation of Ni onto different supports induced the formation of new basic sites. Ni/ZSM-5 presented an optimum amount of weak and medium basic sites able to absorb and activate CO<sub>2</sub> molecules while stronger basic sites present in Ni/SBA-15 and Ni/SiO<sub>2</sub> are not suitable to activate CO<sub>2</sub> molecules and enable methanation.<sup>638</sup> Among the prepared catalysts, Ni/ZSM-5 catalyst displayed the higher catalytic activity and no deactivation was observed up to 100h, attributed to the basic property and higher nickel dispersion (Table 6, Entries 11-13).<sup>597</sup>

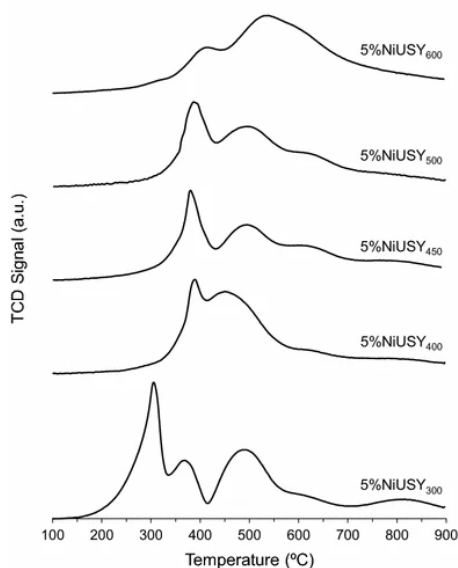
#### iv) Preparation strategies of zeolite-based catalysts for CO<sub>2</sub> methanation

Different strategies for the preparation and reduction of the CO<sub>2</sub> methanation catalysts have been studied in order to optimize the dispersion and stabilization of Ni particles. Ni-based USY zeolites have been largely studied and used as CO<sub>2</sub> methanation catalysts. USY zeolite, due to ultra-stabilization treatments, is characterized by a good stability under CO<sub>2</sub> methanation conditions, i.e. temperature and presence of water, and offer opportunities as support. Then,



the effect of the preparation method and the Ni content on the catalytic performance of Ni-based USY catalysts has been studied. Generally, higher metal loadings led to better catalytic performance, due to a higher availability and amount of Ni active sites.<sup>639</sup> The comparison of catalytic behaviors revealed that Ni and Ce supported NaUSY zeolite prepared by impregnation exhibited higher catalytic performance than samples prepared by ion-exchanged Ni species due to easier reducibility of the NiO species.<sup>639</sup> Besides the effects of the drying method after impregnation, the calcination and the reduction temperature on the catalytic performance of Ni-based USY catalysts, showed that CO<sub>2</sub> conversion and CH<sub>4</sub> selectivity could be maximized by optimizing preparation and pre-reduction conditions.<sup>640</sup> Likewise, the calcination temperature influenced the reducibility and location of the Ni species and particles size after reduction. Therefore, at higher calcination temperatures, NiO located on the external surface was the main Ni species, while at 300°C Ni<sup>2+</sup> species octahedrally coordinated were the main Ni species. Moreover, an increase in the calcination temperature induced a decrease in the amount of Ni reducible species, an increase in reduction temperatures of Ni species, as well as the formation of larger Ni particles (Figure 36).

The pre-reduction temperature also affected the catalytic activity and was dependent on the Ni content, since at lower Ni content (5wt%), the higher reduction temperature required (>550°C) induced sintering, while for higher Ni content (14wt%) no effect of the reduction temperature was observed. Therefore, in the presence of 14wt%Ni/USY calcined at 500°C and reduced at 600°C, maximum 95% CO<sub>2</sub> conversion and 70% CH<sub>4</sub> selectivity were achieved at 400°C (Table 6, Entry 14).



**Figure 36.** H<sub>2</sub>-TPR profiles obtained for the 5%NiUSY samples reduced at different temperatures. Reprinted with permission from ref.<sup>640</sup> Copyright 2015, Springer Science Business Media New York.

The influence of the Ni precursors for the preparation Ni-Zeolite 13X and 5A catalysts was studied and the results showed that the use of nickel citrate and acetate resulted in smaller NiO particle size compared to nitrate. STEM-EDX results indicate that all the Ni-precursor complexes diffuse more efficiently in the 13X than in 5A zeolite structure because of steric hindrance induced by the smaller pore size of the zeolite 5A. Best catalytic performance was achieved using 5%Ni-13X catalysts synthesized with nickel citrate. 79% CO<sub>2</sub> conversion at 320°C and 100% CH<sub>4</sub> selectivity for 200 h were achieved (Table 6, Entries 15-16).<sup>641</sup> A X zeolite synthesized from waste fly ashes coming from the energy sector was also used as support to prepare Ni-based methanation catalysts (Ni/X zeolite<sub>ashes</sub>), and exhibited relatively lower catalytic performance in comparison to other published Ni-catalysts prepared with commercial zeolites (USY and Beta), because of the formation of unreduced Ni species due to remaining fly ash components such as MgO and Al<sub>2</sub>O<sub>3</sub>. At 450°C, 49% CO<sub>2</sub> conversion and 96% CH<sub>4</sub> selectivity were achieved in the presence of 10wt%Ni/X zeolite (Table 6, Entry 17).<sup>642</sup>

A hydrothermal synthesis method was also followed for the preparation of an active and stable 10wt%Ni@HZSM-5 catalyst starting from Ni/SiO<sub>2</sub> catalyst as silicone source.<sup>643</sup> Additionally to superior catalytic performance than 10wt%Ni/ZSM-5 sample prepared by impregnation, 10wt%Ni@HZSM-5 catalyst preserved similar nickel content and structure after use due to its special embedded structure. Good and stable 66.2% CO<sub>2</sub> conversion and 99.8% CH<sub>4</sub> selectivity at 400°C, 0.1 MPa, for 40h, were achieved (Table 6, Entries 18-19). A desilication method was also reported to prepare a Ni-desilicated silicalite zeolite (5wt%/d-S1) with intra-particle voids and mesopores enabling higher Ni dispersion inside the channels and smaller Ni particles by impregnation method. The 5wt%Ni/d-S1 material exhibited higher catalytic performance than the pristine sample and a relevant increase of CH<sub>4</sub> selectivity and stability. At 450°C, 61-64% CO<sub>2</sub> conversion and 95-97% CH<sub>4</sub> selectivity were maintained for 50h (Table 6, Entry 20). In the presence of 5wt%Ni/S1 catalyst, 42% CO<sub>2</sub> conversion and 40% CH<sub>4</sub> selectivity were initially reached, though a drastic decrease in CH<sub>4</sub> selectivity was observed after 10h of TOS.<sup>644</sup>

To overcome mass transfer and diffusion limitations of zeolites for bulky molecules, hierarchical zeolites containing a secondary pore system or nanocrystalline zeolites have been prepared. More recently, the synthesis of a mesoporous material with uniform mesopore diameters and crystalline MFI zeolite walls has been described as a new alternative. Therefore, an amine functionalized mesoporous MFI nanosponge zeolite (AF-NSZ) were used as support for the regioselective precipitation of the Ni species in the mesoporous channels resulting in highly dispersed and stabilized Ni nanoparticles.<sup>626</sup> Good catalytic were obtained with a 15wt%Ni/AF-NSZ mesoporous MFI nanosponge, with 78% CO<sub>2</sub> conversion and 99% CH<sub>4</sub> selectivity at 400°C, 0.1 MPa, for 50h (Table 6, Entry 21). Despite the efforts spent to improve the dispersion and

stabilization of Ni nanoparticles by modifying Ni deposition and by using zeolite-based materials with mesoporosity, the catalytic performance exhibited by these advanced catalysts does not outperform the results achieved in the presence of more conventional Ni/USY zeolite catalysts (Table 6, Entry 5).

v) *Addition of promoter to the zeolite-based catalysts for CO<sub>2</sub> methanation*

For CO<sub>2</sub> methanation, the CO<sub>2</sub> activation is considered the rate-determining step<sup>645–648</sup> and the development of low temperature CO<sub>2</sub> methanation process requires suitable and efficient CO<sub>2</sub> adsorption and activation. The presence of additives such as metal, metal oxides, alkali metals and rare earth oxides have been shown not only to enhance CO<sub>2</sub> activation at lower temperature but also to improve the stability and catalytic performance, and modify the state of the active phase.<sup>577,587,649–651</sup> Among CO<sub>2</sub> methanation catalysts, cerium oxides and mixed oxides based catalysts have exhibited the best catalytic performance<sup>575,587,652–654</sup> due to CeO<sub>2</sub> suitable physicochemical properties for CO<sub>2</sub> adsorption and activation, and oxygen mobility.<sup>655</sup> The remarkable CeO<sub>2</sub> ability is due to the presence of oxygen vacancies that allow the storage and release of oxygen,<sup>225,656</sup> but also promote the high dispersion and activity of supported noble-metal due to strong metal-support bonding.<sup>657</sup> Comparison of the catalytic behavior revealed that Ni and Ce supported NaUSY zeolite prepared by impregnation exhibited higher catalytic performance than samples prepared by ion-exchanged Ni species due to the easier reducibility of the NiO species in the samples prepared by impregnation.<sup>639</sup> Meantime, the Ce incorporation into the Ni-USY zeolite enhanced the catalysts activity and selectivity. At 400°C, in the presence of 14%NiUSY and 5%Ni15%CeUSY catalysts, 65.5 and 68.3% CH<sub>4</sub> selectivity, and 94.2 and 95.1% CO<sub>2</sub> conversion, respectively, were achieved (Table 6, Entries 24-25). The study of the effect of the order of Ce and Ni incorporation in USY zeolite indicated that stronger interactions between Ni and Ce species existed when Ni was incorporated after or simultaneously, with an enhanced reducibility of the Ni species and a decrease in the Ni<sup>0</sup> particle size. On the contrary, CO<sub>2</sub> adsorption capacity decreased when Ce was incorporated before Ni. Therefore, co-impregnation was determined as the best preparation method (Table 6, Entry 26).<sup>628</sup> The incorporation of La<sub>2</sub>O<sub>3</sub> and MgO in nickel mesoporous MFI nanosponge zeolite allowed to modify the surface basicity and promote CO<sub>2</sub> adsorption and the methanation process. The amine functionalization of mesoporous MFI nanosponge zeolite (AF-NSZ) enabled the regioselective precipitation of the Ni precursor in the mesoporous channels resulting in highly dispersed and stabilized Ni nanoparticles method (Table 6, Entries 27-29).<sup>626</sup> Therefore, La<sub>2</sub>O<sub>3</sub> and MgO promoted Ni/AF-NSZ samples (15Ni-5La/AF-NSZ and 15Ni-5Mg/AF-NSZ) exhibited higher catalytic activity than the pristine 15Ni/AF-NSZ catalyst, at lower temperature (280°C),

due to higher CO<sub>2</sub> adsorption and activation. Following the same leads, the addition of La<sub>2</sub>O<sub>3</sub> to 10Ni/Na-BETA enabled to increase and optimize the amount of CO<sub>2</sub> adsorption sites and hydrogenation active sites resulting in an increase of methanation process. In the presence of 10Ni-10La<sub>2</sub>O<sub>3</sub>/Na-BETA at 400°C, maximum 82% CO<sub>2</sub> conversion and 97% CH<sub>4</sub> selectivity were achieved. At 350°C, 65% CO<sub>2</sub> conversion at 350°C, with 99% CH<sub>4</sub> selectivity were maintained for 24 h (Table 6, Entries 30-32).<sup>27</sup>

Owing to the high activity of Ru for CO<sub>2</sub> methanation, especially at lower temperature, the addition of Ru to Ni catalysts may be beneficial to enhance CO<sub>2</sub> methanation.<sup>611</sup> Accordingly, the effect of addition of Ru over the catalytic performance of Ni/13X and Ni/5A catalysts was explored. The catalytic performance of mono and bimetallic Ru and Ni 13X and 5A and the physicochemical characterization results showed that both zeolite structures remained unchanged after Ni, Ru addition. Nevertheless, only good metal dispersion was obtained for Ni into the pores of 13X owing to improved diffusion of Ni precursor while metal dispersion was worse for the bimetallic catalysts. The best results were obtained for the catalysts exhibiting the lower amount of weak acid sites. Thus, in the presence of monometallic 2.5%Ru13X and 5%Ni13X catalysts, good catalytic activity and stability were maintained at 360°C, for 200h with 97% CH<sub>4</sub> selectivity (Table 6, Entries 33-34).<sup>658</sup> It was then concluded that the incorporation of Ru did not allow improving the catalytic performance of Ni catalysts.

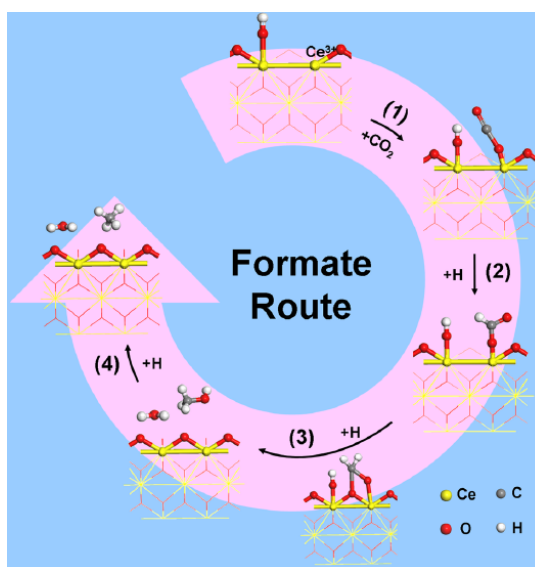
vi) *Mechanistic studies for CO<sub>2</sub> methanation over zeolite-based catalysts*

CO<sub>2</sub> methanation mechanism has been the target of numerous studies and two main pathways can be considered being CO or formate the main intermediates (Figure 39).<sup>577,609–612,647</sup> The physicochemical properties of the catalysts are decisive since the nature and strength of acid and basic sites, and the presence of oxygen vacancies play a determinant role in the CO<sub>2</sub> adsorption and activation, and influence the reaction pathway. CO<sub>2</sub> methanation process involves CO<sub>2</sub> adsorption and activation over active sites (Figures 37-38), preferably, basic sites. Over mixed oxide, the presence of oxygen vacancy on the surface constitutes decisive reactive site for CO<sub>2</sub> activation and formate formation as it was reported on Ru/CeO<sub>2</sub> (Figure 37).<sup>659</sup> As mentioned above, CO<sub>2</sub> hydrogenation involves adsorbed oxygenated species such as monodentate carbonates and formates while H<sub>2</sub> activation and dissociation takes place over Ni<sup>0</sup> nanoparticles.<sup>613</sup> The oxygenated species are so converted into formyl and methoxy species finally hydrogenated into CH<sub>4</sub>. Over Ni/USY<sup>660,661</sup> or Ru/Al<sub>2</sub>O<sub>3</sub><sup>647</sup>, and due to the lack of basic sites and/or oxygen vacancies, CO<sub>2</sub> methanation goes through the monodentate formate dissociation onto Ni particles and the formation of adsorbed CO afterwards converted into CH<sub>4</sub>.<sup>660,662</sup> Therefore, under methanation conditions, dissociated hydrogen reacts with

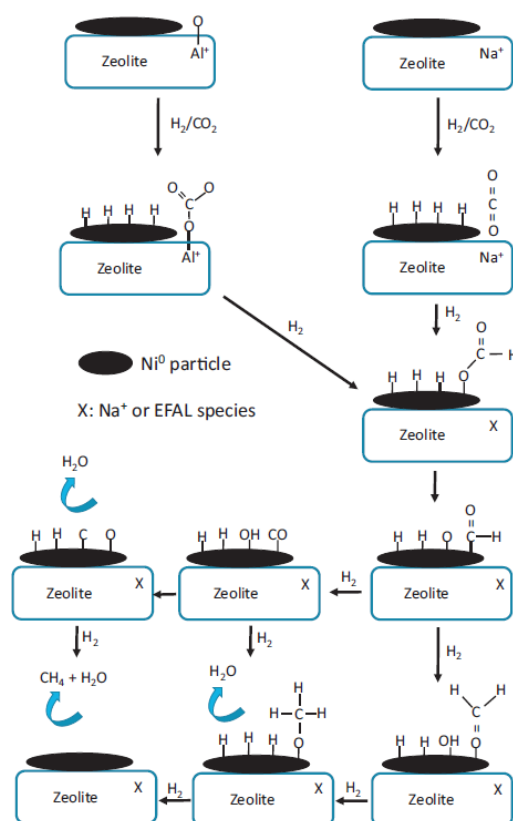
carbonates and/or physisorbed  $\text{CO}_2$ , leading to monodentate formates, then carbonyls adsorbed onto  $\text{Ni}^0$  particles, and finally to methane (Figure 38).

Studies in absence of  $\text{H}_2$  revealed that  $\text{CO}_2$  was not adsorbed over acidic zeolite while in presence of  $\text{H}_2$ , formates and carbonyls species were identified.<sup>660</sup> The results led to conclude that  $\text{CO}_2$  hydrogenation mechanism did not undergo carbonate formation as intermediate, but rather passed through the formate dissociation leading, at low temperatures, to the formation of adsorbed  $\text{CO}$  and in a minor extension to methane. Therefore, in the absence of basic sites,  $\text{CO}$  seems to be the “true” intermediate in the  $\text{CO}_2$  methanation reaction. Moreover,  $\text{CO}$  dissociation/hydrogenation was confirmed to be the rate-determining step.<sup>660</sup> In the same way, a proposed four-step reaction mechanism involving carbonyl pathway and the cleavage of  $\text{C}=\text{O}$  bond from  $\text{CO}_2$  as the rate-determining step was reported over  $\text{Ni}(19\text{wt\%})/\text{MCM-41}$ .<sup>663</sup> The addition of promoters, and especially  $\text{CeO}_2$ , allowed improving the activity and selectivity of Ni-based USY catalysts. A mechanistic study by in situ IR spectroscopy over Ce-Ni/USY catalyst revealed that hydrogen dissociated on  $\text{Ni}^0$  particles reacted with hydrogen and bidentate carbonates, leading to the formation of monodentate formates, and then to  $\text{CH}_4$ .<sup>664</sup> The different mechanisms involved in  $\text{CO}_2$  methanation over the different Ni/USY catalysts are depicted in the Figure 39.

Recently, the catalytic activity of bimetallic Ni-Mo/ $\text{SiO}_2$  catalysts for  $\text{CO}_2$  methanation was

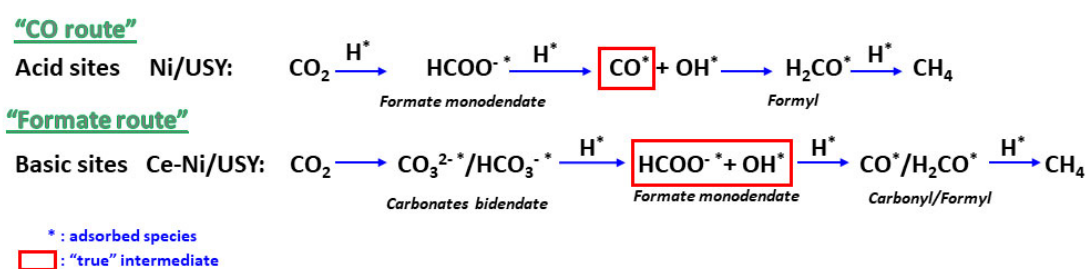


**Figure 37.** Mechanism of  $\text{CO}_2$  methanation on  $\text{Ru}/\text{CeO}_2$ . Reprinted with permission from ref. <sup>659</sup>. Copyright 2016, American Chemical Society.



**Figure 38.** Proposed mechanism for  $\text{CO}_2$  methanation on Ni/USY zeolites. Reprinted with permission from ref. <sup>660</sup>. Copyright 2015, Elsevier B.V. All rights reserved.

investigated. Characterization data revealed that the incorporation of Mo improves the dispersion of Ni through strong interaction metal/metal and was optimum for Ni/Mo=1, preventing CO adsorption at room temperature. Then, the catalytic study through the products composition indicated that CO<sub>2</sub> methanation undergoes RWGS and CO methanation. The Mo content plays a key role over the catalytic pathway since high Mo content favours CO desorption and limits CO hydrogenation because of the presence of smaller Ni ensembles and reduced accessibility to Ni<sup>0</sup> active sites as results of MoO<sub>x</sub> coverage. Therefore, for Ni/Mo ratio closed to 1, RWGS is the main process while low Mo content (Ni/Mo=0.1) favours CO<sub>2</sub> and CO activation promoting CO methanation. Therefore, at 400°C, 25-30% CO<sub>2</sub> conversion controlled by thermodynamic equilibrium of RWGS reaction with 100% CH<sub>4</sub> selectivity were reached.<sup>665</sup>



**Figure 39:** Different mechanisms involved in CO<sub>2</sub> methanation over Ni/USY and Ce-Ni/USY catalysts.

vii) *Plasma assisted CO<sub>2</sub> methanation*

Plasma is superheated matter wherein electrons are ripped away from the atoms to form an ionized gas. Heating a gas, this will form a plasma, generally named the fourth state of the materia together with solid, liquid and gas, occurring naturally in nebulas, stars, auroras, sun and through artificial lights (neons). The properties of plasma have been explored and used by the scientists community for application in different fields such as alternative to thermocatalytic process and especially for reactions that require high energy consumption due to thermodynamic limitations. Indeed, non-thermal plasma (NTP) and thermal assisted plasma systems offer attractive opportunities and have been tested for various processes. In NTP, electrons are highly energetic with very high electron temperature of 10000-100000°C (1-10 eV),<sup>666</sup> while the gas temperature is close to room temperature. Therefore, the impact of high energy electrons is enough to breakdown bonds and produce free radicals, excited atoms, ions and molecules.<sup>667</sup> The non-equilibrium character of plasma system enables to overcome barrier energy and thermodynamic limitations at low temperature in chemical processes such as CO<sub>2</sub> conversions.<sup>668-670</sup> There exist different types of NTP such as dielectric barrier discharges (DBD), corona discharges, glow discharge or gliding arcs. Among them, DBD constitutes a versatile method with some advantages such as uniform distribution of micro-discharges, high-energy electrons and operability at ambient conditions. When an alternative current (AC voltage) is

applied to one or both electrodes formed by two metal plates and covered by an insulator, a discharge is produced (Dielectric barrier discharge plasma (DBD)). When an excessive and rapid discharge is suppressed by the insulator, this discharge does not produce an arc but a bright purple plasma (Figure 40). Dielectric barrier discharge plasma is one of the most popular methods to generate non thermal plasma (NTP) constituted by a host of high-energy electrons, free radicals, chemically active ions and excited species, promoting chemical reactions. The big potential of NTPs to promote reaction in mild conditions is of great interest,<sup>666</sup> and few examples of CO<sub>2</sub> methanation under NTP at temperature <200°C have been reported.

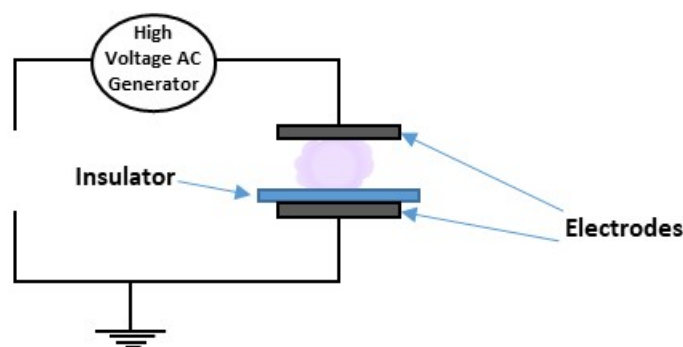
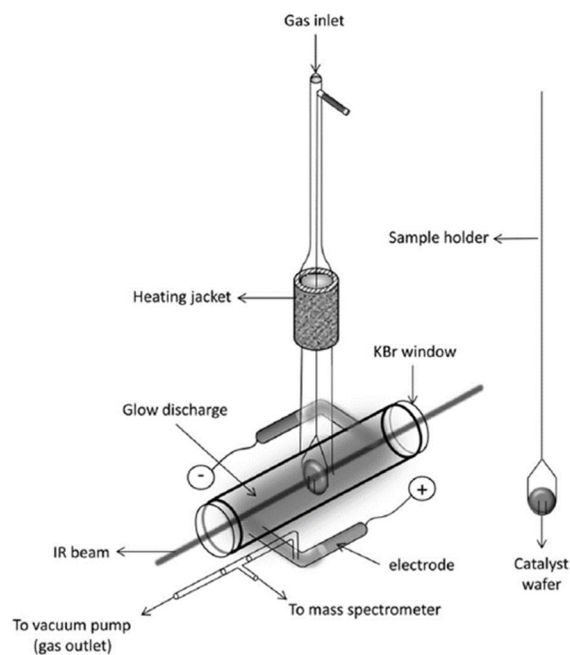


Figure 40. Scheme of planar DBD electrode devices.

The activity of Ni-based zeolite catalysts has been also studied under non-thermal plasma-assisted conditions, and a mechanism of plasma-assisted CO<sub>2</sub> hydrogenation was studied by operando time-resolved FTIR spectroscopy over Ni-HUSY (Figure 41).<sup>662</sup> CO was detected as the main product of the reaction, issued from CO<sub>2</sub> dissociation in the gas phase, and CH<sub>4</sub> was observed as a secondary product. The same authors performed CO<sub>2</sub> hydrogenation using a packed-bed catalytic reactor under two different configurations, in-plasma catalysis (IPC) and post-plasma catalysis and showed that, CH<sub>4</sub> production took place only when CO<sub>2</sub> hydrogenation was performed in IPC mode, only when the catalyst could directly interact with plasma discharges.<sup>671</sup> Thereafter, the effect of Si/Al ratio and Ce addition in the performances of Ni supported Cs-USY samples under DBD plasma-assisted catalysis showed that the hydrophobicity of the surface improved the CO<sub>2</sub> conversion while the addition of Ce favoured the formation of additional sites for CO<sub>2</sub> adsorption and activation. Therefore, in the presence of NiCe/Cs-USY, with a power supply of 25W, 75% CH<sub>4</sub> yield was reached (Table 6, Entries 35-36).<sup>627</sup> NTP assisted catalytic CO<sub>2</sub> methanation over Ni catalysts (15 wt%) supported on BETA zeolite doped with La as the promoter exhibited great catalytic performance for CO<sub>2</sub> methanation.<sup>579</sup> The Na<sup>+</sup> exchange in the H-BETA zeolite enabled to improve the CO<sub>2</sub> conversion by two-fold increase (65%) and fourfold TOF values at 6.0kV, while addition of La allowed to reach maximum 85% CO<sub>2</sub> conversion and 97% CH<sub>4</sub> with excellent stability for 15h (Table 6, Entries 33-34).



**Figure 41.** Operando time-resolved IR reactor. Reprinted with permission from ref.<sup>662</sup>. Copyright 2017, Springer Science Business Media, LLC.

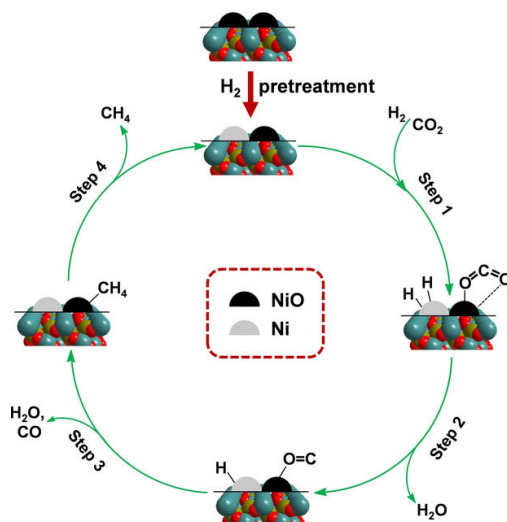
### c) OMS-based catalysts for CO<sub>2</sub> methanation

Metal supported on mesoporous molecular sieves as MCM-41 have been receiving more and more attention as a new type of nanostructured (OMS) materials.<sup>598,672,673</sup> Different parameters have been studied to improve the catalytic properties, robustness and stability of Ni zeolite-based catalysts for CO<sub>2</sub> methanation such as the variation of the Si/Al ratio to optimize adsorption properties (hydrophobicity), the zeolite structure to control the diffusion and adsorption/deposition of metal precursors, the Nickel dispersion and location, the addition of noble metal and/or transition metal to enhance the reducibility and dispersion of Ni by changing the electronic and geometric structure of single crystal-metal, or cation exchange with alkali and alkaline earth metals to create basic sites and enhance the adsorption and activation of CO<sub>2</sub>. Thus, OMS based catalysts owing to high surface area and controllable pores size should allow the diffusion of metal precursor inside the pores and the establishment of favourable interaction metal/support for controlling the nanoparticle size, dispersion and stability to prevent Ni particle sintering. However, despite the opportunities that OMS-based catalysts may offer, few studies using OMS based catalysts for CO<sub>2</sub> methanation have been published.

Ni/MCM-41 catalyst were prepared using different Ni precipitation agents and used as catalysts for CO<sub>2</sub> methanation. AP-XPS and in situ DRIFTS studies revealed the presence of carbonyl intermediates and, the co-existence of NiO and Ni<sup>0</sup> species with a cooperative effect for the adsorption/activation and dissociation of CO<sub>2</sub> and H<sub>2</sub> molecules, respectively (Figure 42). A proposed four-step reaction mechanism involving carbonyl pathway and the cleavage of C=O bond from CO<sub>2</sub> as the rate-determining step was reported. In the presence of Ni(19wt%)/MCM-

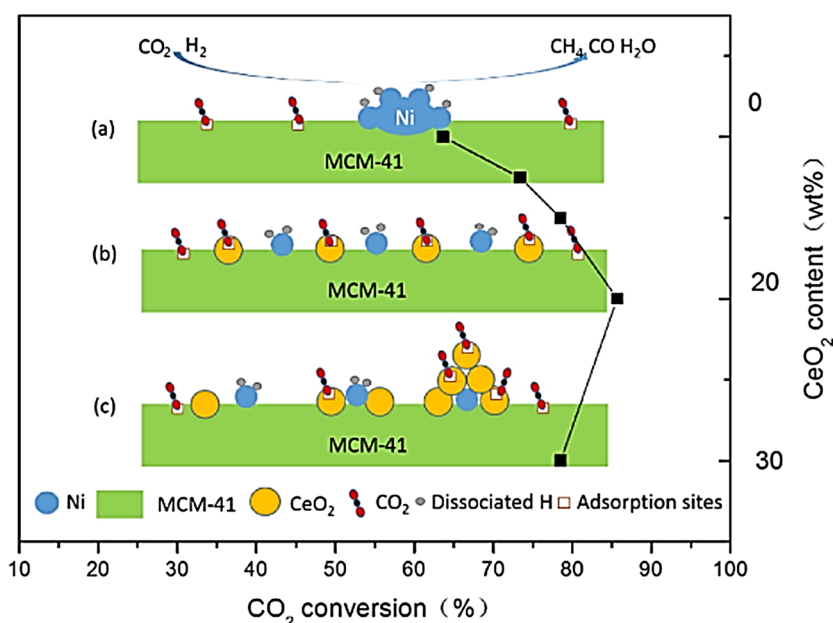


41, 73.2% CO<sub>2</sub> conversion of and 91.6% CH<sub>4</sub> selectivity, at 400°C were obtained and remained stable for 150h (Table 6, Entry 37).<sup>663</sup>



**Figure 42.** Proposed reaction pathway for CO<sub>2</sub> methanation reaction over Ni/MCM-41 catalyst. Reprinted with permission from ref.<sup>663</sup>. Copyright 2019, Wiley-VCH Verlag GmbH & Co. KGaA, Weinheim.

CeO<sub>2</sub> has been shown to effectively promote the adsorption and the activation of CO<sub>2</sub> molecules on the catalysts<sup>674,675</sup>. Moreover, CeO<sub>2</sub> has a great oxygen exchange capacity that allows reversible release and restore of oxygen atoms. Thus, within a certain loading range, it was shown that the addition of CeO<sub>2</sub> improved the catalytic performance of Ni/MCM-41. Indeed, the incorporation of CeO<sub>2</sub> allowed the stabilization of Ni species, with higher dispersion and reduction of Ni species, whereas excess of CeO<sub>2</sub> induced Ni coverage and a decrease in the catalytic performance (Figure 43). Thus, Ni-20CeO<sub>2</sub>/MCM-41 showed the best catalytic performance, with 85.6% CO<sub>2</sub> conversion and 99.8% CH<sub>4</sub> selectivity at 380°C, which remained constant for 30h (Table 6, Entries 38-39).<sup>676</sup>



**Figure 43.** Benefits of the addition of  $\text{CeO}_2$  over the dispersion and stabilization of Ni particle and over the catalytic performance. Reprinted with permission from ref.<sup>676</sup>. Copyright 2017, Elsevier B.V. All rights reserved.

The catalytic performance of Ni-mesoporous SBA-15 and MCM-41 with and without  $\text{CeO}_2$  as promoter were also compared.  $\text{H}_2$ -TPR study showed two main peaks at  $T < 500^\circ\text{C}$  and  $T > 500^\circ\text{C}$  mainly attributed to  $\text{NiO}$  species weakly interacting with the support, mainly located on the external surface, and strongly interacting with the support, respectively. The higher reduction temperature was also attributed to the smaller  $\text{Ni}^0$  particles size and support-dependent, since the larger pores allow for enhanced diffusion of the metal precursor and accommodate metal species with better metal dispersions.<sup>677</sup> On the other hand, the incorporation order, Ce after Ni, affected the reducibility of  $\text{NiO}$  because of reduced accessibility. Despite bigger Ni particles and mainly located on the external surface, ascribed to smaller pores compared to Ni/SBA-15, Ni/MCM-41 exhibited highest conversion and TOF values, attributed to lower amount of non-reactive carbonyl species poisoning  $\text{Ni}^0$  and to the support-dependent electronic properties of Ni (stronger metal/support interactions). However, at high temperature ( $400^\circ\text{C}$ ) the both Ni supported catalysts exhibited similar catalytic performance (Table 6, Entries 40-43).<sup>678</sup>

#### 5.5.4. Conclusion

Among  $\text{CO}_2$  hydrogenation reactions, the  $\text{CO}_2$  methanation is the most favoured reaction from a thermodynamic point of view.<sup>679</sup> However, the development of new catalysts able to perform  $\text{CO}_2$  methanation reaction at lower temperature is still required. The activation of  $\text{CO}_2$  is of paramount importance to reach high methanation activity at lower reaction temperature, and the oxygen mobility and basic properties (strength, number) of the support are key parameters to enhance the adsorption and activation of  $\text{CO}_2$ . Therefore, the improvement of metal

dispersion and reducibility by the addition of promoters, the control of basic properties by cation exchange, the preparation method and the reduction conditions allow to optimize the catalytic performance of CO<sub>2</sub> methanation catalysts. Moreover, the hydrophobicity of the catalyst surface is of paramount importance to limit the water adsorption and avoid the water inhibitory effect on CO<sub>2</sub> adsorption (Figure 44). Then, the zeolite framework composition showed to affect strongly the zeolite-based catalyst activity due to important changes in the catalyst-CO<sub>2</sub> and catalyst-H<sub>2</sub>O interactions. Among the different based-zeolite and OMS catalysts reported, USY based catalysts could present great potential due to improved stability provided by post synthesis treatments and strong interaction metal/support. For future strategies, it should be particularly important to focus on the morphology of the carrier to improve dispersion, physical isolation and protection of metal species, mass transfer and also to avoid pore blockage due to coke formation. Therefore, new strategies will consider the use of OMS materials, hierarchical zeolites, two-dimensional zeolite nanosheets and core-shell materials to promote the amount, dispersion and stabilization of active centers and mass transfer. Moreover, for a better understanding of the active species, mechanism of the activation and cleavage of C-O (CO<sub>2</sub>), and of the H<sub>2</sub> activation, and the determination of reaction intermediates, computational modeling and in situ spectroscopy studies should be fundamental tools for the rational design of efficient and stable catalysts for the methanation. From commercial point of view and industrial applicability, several catalytic processes and reactors technology are available and should be translated to CO<sub>2</sub> methanation since at laboratory scale high conversion and CH<sub>4</sub> selectivity closed to 100% are reached. However, the viability for large scale CO<sub>2</sub> fixation also depends on readily availability and price of CO<sub>2</sub> and H<sub>2</sub> issued from wasted and/or renewables sources in order to develop sustainable process, based on heat produced from renewable (sun, wind) or by nuclear energy to move towards zero carbon footprint.

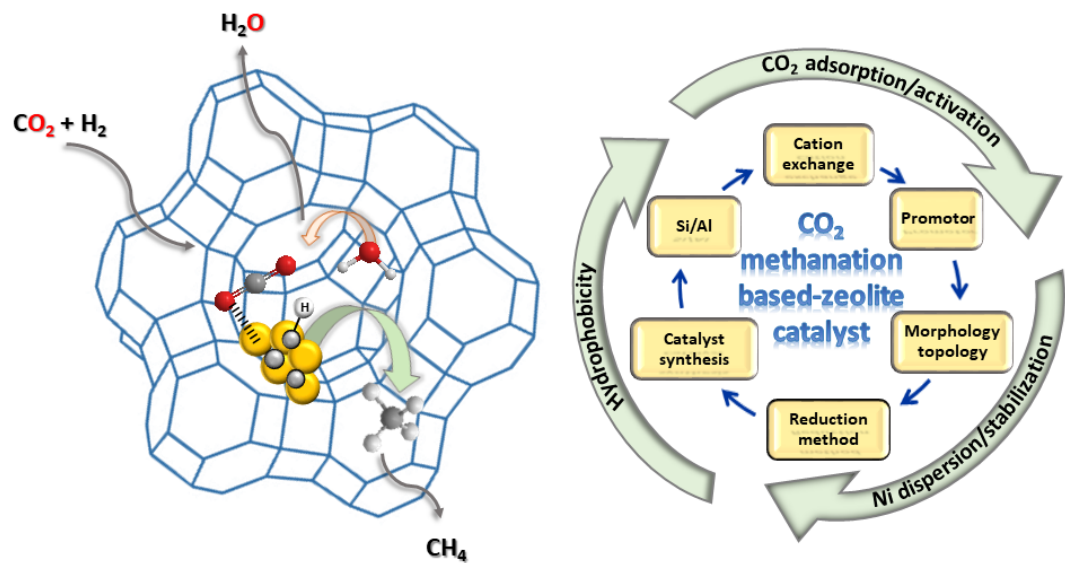


Figure 44. Scheme of key parameters to control catalytic properties of CO<sub>2</sub> methanation catalysts.

**Table 6.** Summary of the catalytic performance of the different reviewed CO<sub>2</sub> methanation zeolite- and OMS-based catalysts.

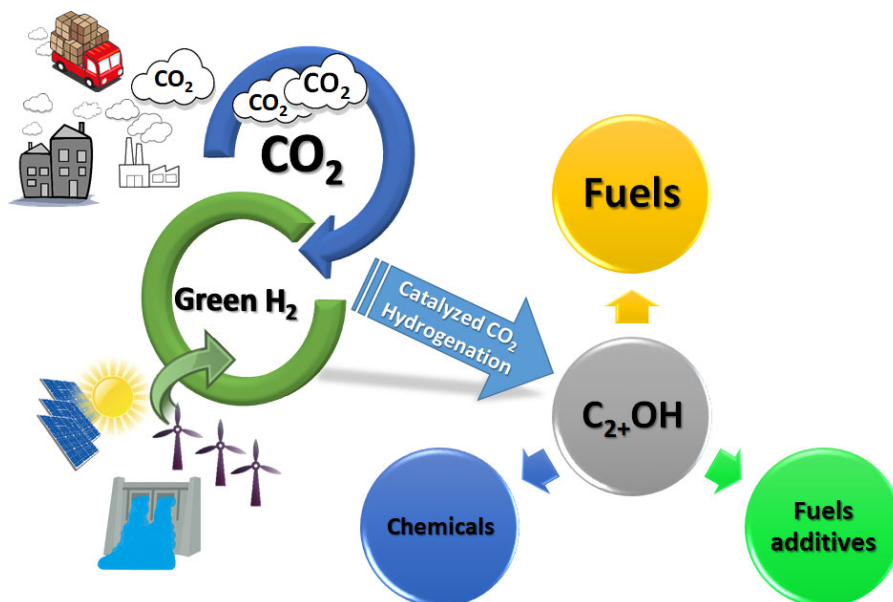
Entry	Catalysts	CH <sub>4</sub> Sel. %	CO <sub>2</sub> Conv. %	Conditions	Preparation	Year	Ref.
<b><i>Zeolite-based catalysts</i></b>							
1	1Fe/13X	76	83	350°C, GSHV=4186h <sup>-1</sup> , 10 bar, CO <sub>2</sub> :H <sub>2</sub> =4:1	Wet impregnation	2020	616
2	5Ni/13X	<b>100</b>	<b>80-83</b>	300°C, CO <sub>2</sub> :H <sub>2</sub> =1:4, GSHV=92h <sup>-1</sup> , 520mL/min	Impregnation	2016	617
<b><i>Effect Si/Al</i></b>							
3	5Ni/ITQ-2	<b>99</b>	<b>82</b>	400°C, GSHV=3500h <sup>-1</sup> , 9000mL/g <sub>cat</sub> h, 0.75g	Incipient wetness	2020	624
4	5Ni/ITQ-2	<b>97</b>	<b>68</b>	350°C CO <sub>2</sub> :H <sub>2</sub> :N <sub>2</sub> =9:36:5	impregnation		
5	15Ni/USY	<b>96</b>	<b>70</b>	400°C, GSHV=43000h <sup>-1</sup> , CO <sub>2</sub> :H <sub>2</sub> :N <sub>2</sub> =9:36:10	Impregnation	2018	621
6	Ni-HB40	<b>#100</b>	<b>80</b>	GSHV=1600h <sup>-1</sup> , CO <sub>2</sub> :H <sub>2</sub> =1:4, 300°C	Impregnation	2020	612
<b><i>Cation exchanged zeolite</i></b>							
7	15Ni/Cs-USY	<b>97</b>	<b>72</b>	400°C, GSHV=43000h <sup>-1</sup> , CO <sub>2</sub> :H <sub>2</sub> :N <sub>2</sub> =9:36:10	Impregnation	2018	621
8	10Ni/NaBeta	<b>97</b>	<b>73</b>	350°C, CO <sub>2</sub> :H <sub>2</sub> :He=1:4:1.25, GSHV=10000h <sup>-1</sup> , 0.5g <sub>cat</sub>	Impregnation	2018	27
<b><i>Topology and morphology structure</i></b>							
9	15Ni/NaUSY	<b>96</b>	<b>70</b>	375°C, GSHV=4300h <sup>-1</sup> , CO <sub>2</sub> :H <sub>2</sub> :He=1:4:1.25,	Impregnation	2019	636
10	15Ni/NaBEA	<b>85</b>	<b>71</b>	400°C, 0.5g <sub>cat</sub> , 250mL/min, GSHV=10000h <sup>-1</sup>		2019	636
11	10Ni-ZSM-5	<b>75</b>	<b>77</b>	400°C, 100h, CO <sub>2</sub> :H <sub>2</sub> =1:4, GSHV=2400h <sup>-1</sup>	Impregnation	2018	597
12	10Ni/SBA-15	<b>66</b>	<b>70</b>			2018	597
13	10Ni/MCM-41	<b>66</b>	<b>68</b>			2018	597
<b><i>Catalyst preparation strategies</i></b>							
14	14Ni/USY	<b>95</b>	<b>70</b>	400°C, H <sub>2</sub> :CO <sub>2</sub> :N <sub>2</sub> =36:9:10, GSHV=43000h <sup>-1</sup>	Impregnation	2016	640
15	5Ni13X-cit	<b>94.5</b>	<b>51.1</b>	280°, 13333mL/g <sub>cat</sub> h,	Evaporation	2021	641
16		<b>100</b>	<b>79</b>	320°C, 200h	impregnation		
17	10Ni/X zeolite	<b>96</b>	<b>49</b>	CO <sub>2</sub> :H <sub>2</sub> :Ar=15:60:25, 450°C, GSHV=12000h <sup>-1</sup> ,	Impregnation, (X synthesis from fly ashes)	2020	642
18	10Ni@HZSM-5	<b>&gt;99</b>	<b>66</b>	CO <sub>2</sub> :H <sub>2</sub> :N <sub>2</sub> =23:72:5, 400°C, GSHV=3600h <sup>-1</sup>	Hydrothermal	2020	643
19	10Ni/HZSM-5	<b>95</b>	<b>68</b>				
20	5Ni/d-S1	<b>95-97</b>	<b>61-64</b>	CO <sub>2</sub> :H <sub>2</sub> =1:4, 60000mL/g <sub>cat</sub> h, 450°C, 50h	Impregnation	2018	644

21	15Ni/AF-NZS	99	~78	12000mL/g <sub>cat</sub> h, CO <sub>2</sub> :H <sub>2</sub> =1:4, 400°C, 50h	Incipient impregnation	wetness	2020	626
<b>Promoter addition</b>								
24	14Ni/USY	94.2	65.5	400°C, 100h, CO <sub>2</sub> :H <sub>2</sub> =1:4, GSHV=4300h <sup>-1</sup>	Impregnation		2014	639
25	14Ni-7Ce/USY	95.1	68.5					
26	15Ni-20Ce/CsUSY(38)	97-98	65-67	CO <sub>2</sub> :H <sub>2</sub> :N <sub>2</sub> =9:36:10, 250mL/min	Impregnation		2018	628
27	15Ni/AF-NZS	99	65	280°C,	Impregnation		2020	626
28	15Ni-5La/AF-NZS	99	79	6000mL/g <sub>cat</sub> h, CO <sub>2</sub> :H <sub>2</sub> =1:4			2020	626
29	15Ni-5Mg/AF-NZS	99	67				2020	626
30	10Ni-10La <sub>2</sub> O <sub>3</sub> /NaBeta	97	82	400°C, CO <sub>2</sub> :H <sub>2</sub> :N <sub>2</sub> =1:4:15,	Impregnation		2018	27
31	10Ni/NaBeta	55	60	350°C-24h			2018	27
32	10Ni-10La <sub>2</sub> O <sub>3</sub> /NaBeta	99	65	350°C-24h			2018	27
33	5Ni-13X	97	70	13.33L/g <sub>cat</sub> h, CO <sub>2</sub> :H <sub>2</sub> :N <sub>2</sub> =1:4:15, 300°C, 200h	Evaporation		2020	658
34	2.5Ru-13X	97	65		impregnation			
<b>Plasma</b>								
35	15Ni20La/NaBeta	97	85	6kV, 23077mL/g <sub>cat</sub> h, CO <sub>2</sub> :H <sub>2</sub> =1:4	Impregnation		2019	579
36	15Ni/NaBeta	72	66				2019	579
37	15Ni-20Ce/CsUSY	97	77	DBD Plasma (25W), CO <sub>2</sub> :H <sub>2</sub> :N <sub>2</sub> =9:36:10,	Impregnation		2018	627
38	15Ni/CsUSY	81	17	0.2g <sub>cat</sub> , 250mL/min, 32000mL/g <sub>cat</sub> h				
<b>OMS-based catalysts</b>								
37	19Ni/MCM-41	91.7	73.2	400°C, 150h, CO <sub>2</sub> :H <sub>2</sub> =1:4, 9000mL/g <sub>cat</sub> h, 0.05g <sub>cat</sub>			2019	663
38	20Ni/MCM-41	93	65	360°C, 21000mL/g <sub>cat</sub> h, CO <sub>2</sub> :H <sub>2</sub> =1:4			2018	676
39	20Ni-20CeO <sub>2</sub> /MCM-41	98	86				2018	676
40	15Ni/MCM-41	98	65	400°C, H <sub>2</sub> :CO <sub>2</sub> :N <sub>2</sub> =36:9:10, 250 mLmin <sup>-1</sup>			2018	678
41	15Ce-15Ni/MCM-41	98	66	400°C, H <sub>2</sub> :CO <sub>2</sub> :N <sub>2</sub> =36:9:10, 250 mLmin <sup>-1</sup>			2018	678
42	15Ni/SBA-15	96	62				2018	678
43	15Ce-15Ni/SBA-15	97	66				2018	678

\* Metal content is given in wt%.

## 5.6. Hydrogenation of CO<sub>2</sub> into higher alcohols (C<sub>2+</sub>OH)

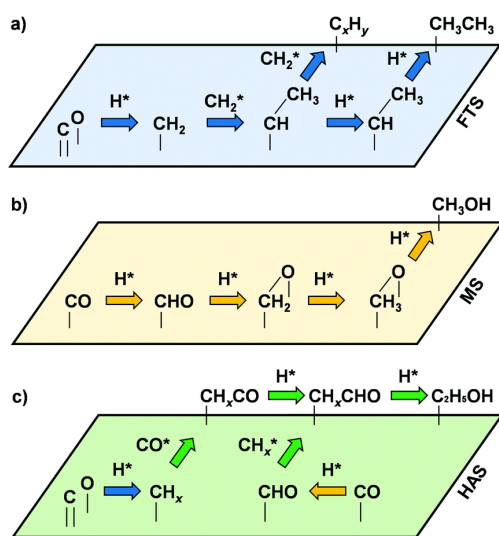
### 5.6.1. Introduction



**Figure 45.** Hydrogenation of CO<sub>2</sub> to C<sub>2+</sub>OH and uses.

Higher alcohols (C<sub>2-4</sub>) present higher energy density, lower vapor pressure, and lower affinity for water than methanol and so constitute an alternative for fuel and fuel additives.<sup>680–682</sup> Additionally, C<sub>2+</sub>OH find applications as solvents and as platform molecules for the synthesis of intermediates for the production of chemicals and fine chemicals (Figure 45).<sup>683,684</sup> Currently, ethanol and isobutanol are mainly produced by fermentation that which is expensive due to difficult distillation and low throughput.<sup>685–688</sup> Other alcohols are traditionally obtained by hydration of the corresponding petroleum-derived olefins.<sup>689,690</sup> Thus, new sustainable routes of synthesis of C<sub>2+</sub>OH using renewable source and green energy are of great interest and the CO<sub>2</sub> hydrogenation, although is very challengeable, offers great opportunities, as well as for mitigating CO<sub>2</sub> emissions. Since the beginning of the 19th century, the synthesis of higher alcohols (HAS) from syngas has been studied in the presence of Rh- and Mo- based catalysts, and modified Fischer-Tropsch synthesis or methanol synthesis catalysts. From mechanistic standpoints, the HAS can be considered as combination of Fischer–Tropsch synthesis (FTS) and methanol synthesis (MS) pathways. FTS has been defined as a surface polymerization, following a carbide-based reaction pathway where the CO dissociative adsorption produces C species subsequently hydrogenated into alkylmonomers which undergo coupling forming hydrocarbons (HC) (Figure 46a).<sup>689,691,692</sup> However, this reaction pathway makes this surface polymerization process different as the adding group may be a fragment, rather than a complete molecule, and the growing chain may also have to undergo further reactions before the addition of the next fragment is possible. During MS, CO is adsorbed and hydrogenated to methanol (Figure 46b).

HAS is considered to require that both FTS and MS processes occur closely to provide new alcohols: the alkyl species ( $\text{CH}_y^*$ ) formed by FTS should couple with adsorbed  $\text{CO}^*$  to give rise to  $\text{CH}_y\text{CO}^*$  ( $\text{C}_x\text{H}_z\text{CO}^*$ ), which, after subsequent hydrogenation, yields alcohol (Figure 46c).



**Figure 46.** Simplified surface reactions occurring upon (a) FTS, (b) MS and (c) HAS results as a combination of the both FTS and MS, involving a CO or CHO insertion step. Reprinted with permission from ref.<sup>689</sup>. Copyright 2017, Royal Society of Chemistry.

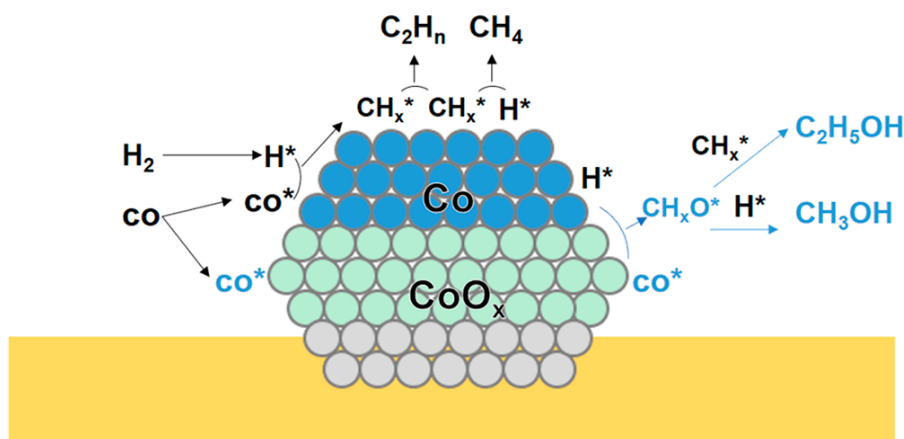
Studies on HAS starting from  $\text{CO}_2$  began in the 1980s, focusing the study on the nature of active species and elucidation of the reaction mechanism for the development of efficient catalyst. Rh-, Cu-, Mo-, and Co-based catalysts have been mainly developed for  $\text{CO}_2$  hydrogenation to  $\text{C}_{2+}\text{OH}$  even if some works reported the activity of Pt, Ru and Pd-based catalysts.<sup>681</sup> Modified catalysts used for FTS and MS have also been used but exhibited still low activity and selectivity under harsh reaction conditions.

Hydrogenation of  $\text{CO}_2$  to  $\text{C}_{2+}\text{OH}$  is an exothermic reaction as methanol synthesis although it is more complex process because it involves C-C coupling, carbon chain growth and termination (Scheme 55). Different mechanistic pathways have been reported in the bibliography, involving firstly the activation and  $\text{CO}_2$  hydrogenation to  $\text{C}_1$  intermediates as  $\text{CH}_x\text{O}$ ,  $\text{CO}$ , and  $\text{CH}_x$ .<sup>693,694</sup> The posterior coupling  $\text{C}_1\text{-CH}_x$  leads to  $\text{C}_{2+}$  intermediates further hydrogenated to produce  $\text{C}_2$  hydrocarbons and oxygenates in which the nature of the catalysts active species play a determinant role. For example, the  $\text{CO}_2$  hydrogenation to ethanol over Cu nanoparticles active centers shaped and confined into Na-Beta zeolite framework<sup>681</sup> described the  $\text{CO}_2$  hydrogenation to  $\text{CH}_3^*$  via  $\text{CH}_3\text{OH}^*$  at the Cu surface with subsequent coupling  $\text{CO}_2^*\text{-CH}_3^*$  to provide  $\text{CH}_3\text{COO}^*$  easily hydrogenated on the catalyst surface to ethanol. On the other hand, the synthesis of  $\text{C}_{2+}\text{OH}$  has also been reported as combination of RWGS with the  $\text{CO}_2$  dissociation into  $\text{CO}^*$  and  $\text{O}^*$ , and the  $\text{CO}^*$  coupling with  $\text{CH}_y^*$  and/or hydrogenation (Figure 47).<sup>682,695</sup> The reaction mechanism requires a precise match (Figure 47) between dissociative C=O bond

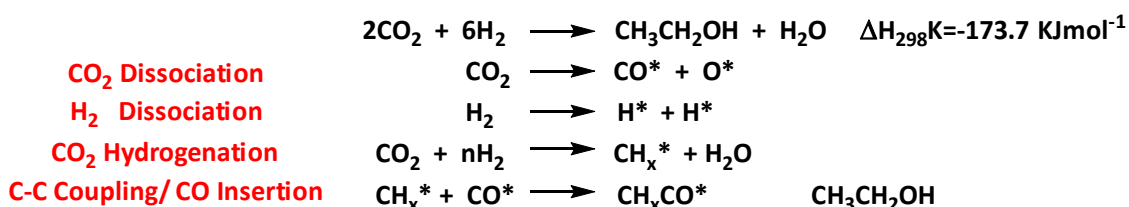


activation, to generate CO and CH<sub>y</sub><sup>\*</sup>, and non-dissociative C–O bond to promote chain growth and the alcohol production (Scheme 55) and not alkanes. These results showed that reported mechanism were highly dependent on the catalysts.

An efficient catalyst should exhibit multiple active sites controlling every reaction step over catalyst surface for CO dissociative adsorption, CO non-dissociative adsorption, C–C bond formation and chain growth for CO<sub>2</sub> hydrogenation to C<sub>2+</sub>OH. Further computational and mechanistic studies are still needed to clarify operando the nature of the intermediates and catalytic active species to design new efficient and selective catalysts.



**Figure 47.** CO<sub>2</sub> hydrogenation into alcohols via CO<sub>2</sub> dissociation into CO\* followed by CO\* insertion into CH<sub>y</sub><sup>\*</sup> or <sup>\*</sup>C<sub>x</sub>H<sub>y</sub> over Co/CeO<sub>2</sub> catalysts. Reprinted with permission from ref.<sup>696</sup>. Copyright 2018, American Chemical Society



**Scheme 55.** CO<sub>2</sub> hydrogenation to higher alcohols involves different elementary reaction steps.

### 5.6.2. Zeolite based catalysts for hydrogenation of CO<sub>2</sub> to C<sub>2+</sub>OH

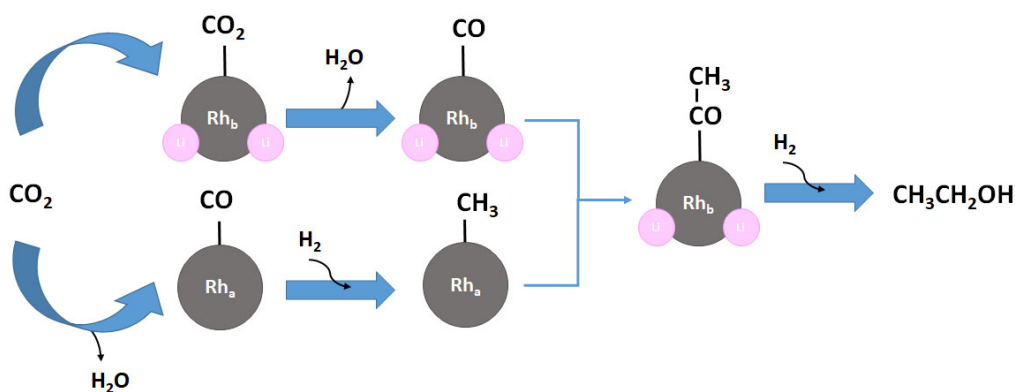
#### a) Rh-based catalysts for CO<sub>2</sub> hydrogenation to C<sub>2+</sub>OH

Rh-based catalysts with promoters have been widely studied for the C<sub>2+</sub>OH synthesis from syngas, since in the presence of Rh catalysts without modification the main products are CH<sub>4</sub> or CO. Moreover, Rh is one of the main metals used for the development of CO<sub>2</sub> hydrogenation catalysts to higher alcohols. The ability of Rh for catalyzing both CO dissociation and CO insertion, lies in the presence of adjacent Rh<sup>0</sup>-Rh<sup>n+</sup> species related to the metal surface modification by the support and/or the presence of promoters (Li, Fe, Co), which allows the formation of C<sub>2</sub> oxygenates (ethanol, acetaldehyde, and acetic acid).<sup>697–702</sup> The promoters addition due to electronic effect induces electronic state modification of Rh, changes the bonding mode and leads to bridge-bonded CO species favouring its breaking. Rh-supported on

metal oxides modified with alkaline and alkaline earth metals or transition metals led to maximum 4.91% of  $C_{2+}OH$  yield in the presence of RhFeLi/TiO<sub>2</sub> catalyst, at 250°C, 3 MPa, GHSV=6000 mLg<sup>-1</sup>h<sup>-1</sup> and CO<sub>2</sub>/H<sub>2</sub> ratio of 1/3.<sup>693</sup> This data indicates that hydrogenation of CO<sub>2</sub> to  $C_{2+}OH$  is still very challenging.

*i) Alkali cation effect in zeolite based catalysts for CO<sub>2</sub> hydrogenation to C<sub>2+</sub>OH*

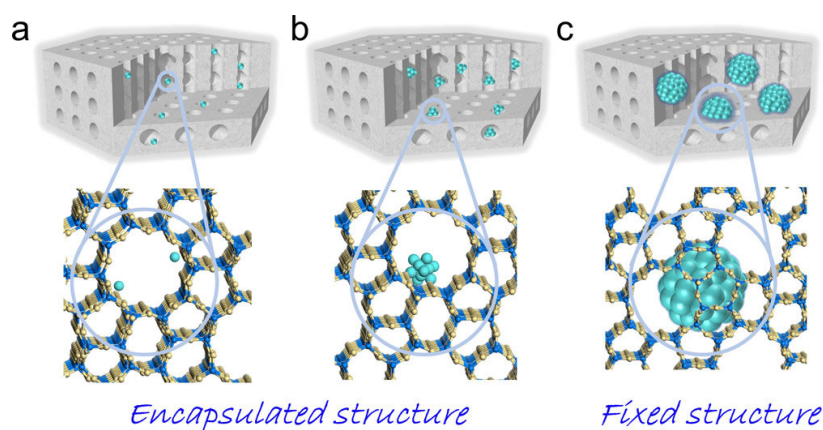
Alkaline metals are electron-donator due to their relatively low electronegativity, and easily release electrons to more electronegative atoms. The presence of alkaline metals leads to higher electron density on Rh, promoting an electron back-donation CO intermediates-Rh, contributing to stronger Rh-CO bond, leading to higher activation and/or stabilization of CO. Moreover, the addition of alkali metals can block active sites and modify hydrogenation activity, decreasing alkanes yield. Additionally, the presence of alkali metal can allow the formation of new active species promoting the  $C_{2+}OH$  synthesis. The adsorption mode of CO can be also modified, and the adsorption of linear versus bridged (tilted) CO has been described, favouring C-O breaking, and lowering H<sub>2</sub> adsorption due to higher coverage surface by CO. Accordingly, the presence of Li in supported Rh catalysts was reported for CO hydrogenation to promote acetic acid<sup>703</sup> formation, and for CO<sub>2</sub> hydrogenation to promote ethanol formation.<sup>704</sup> In fact, the effect of Li addition to RhY zeolite catalysts (RhY), prepared by an ion-exchange method, for CO<sub>2</sub> hydrogenation has been explored.<sup>461</sup> The study of Li/Rh ratio effect revealed that as ratio increased, the methane selectivity decreased, while the CO selectivity, in contrast, increased with simultaneous promoted production of methanol and ethanol. Then, for Li/Rh ratio of 10, maximum 87% CO selectivity, promoted ~1.5% ethanol selectivity, and minimum 8.4% methane selectivity were obtained, while total CO<sub>2</sub> conversion decreased from ~92% to ~52%, at 250°C, 3 MPa, with CO<sub>2</sub>/H<sub>2</sub> ratio of 1/3, and GHSV= 6000 mLg<sup>-1</sup>h<sup>-1</sup>. When 1.8% of CO was added with the CO<sub>2</sub>+H<sub>2</sub>, the ethanol selectivity increased up to 13%. The authors concluded that two Rh active sites existed, no-modified metal centers with reactive adsorbed CO species and Li-modified Rh active sites (Rh<sub>b</sub>) that promoted CO<sub>2</sub> adsorption and conversion into stable adsorbed CO species. Thus, added gas-phase CO was expected to act as a source of CH<sub>3</sub><sup>\*</sup>, preferentially adsorbed and hydrogenated on the unmodified Rh centers (Rh<sub>a</sub>). Thus, stable adsorbed CO<sup>\*</sup> and CH<sub>3</sub><sup>\*</sup> formed acyl groups which were subsequently hydrogenated to ethanol (Figure 48).



**Figure 48.** Proposed mechanism for CO<sub>2</sub> hydrogenation to ethanol via CO\* and CH<sub>3</sub>\* followed by CO\*-CH<sub>3</sub>\* coupling over differentiated Rh active centers confined in Li-Rh/Y zeolite.<sup>461</sup>

*ii) Metal confinement effect in zeolite-based catalysts for CO<sub>2</sub> hydrogenation to C<sub>2+</sub>OH*

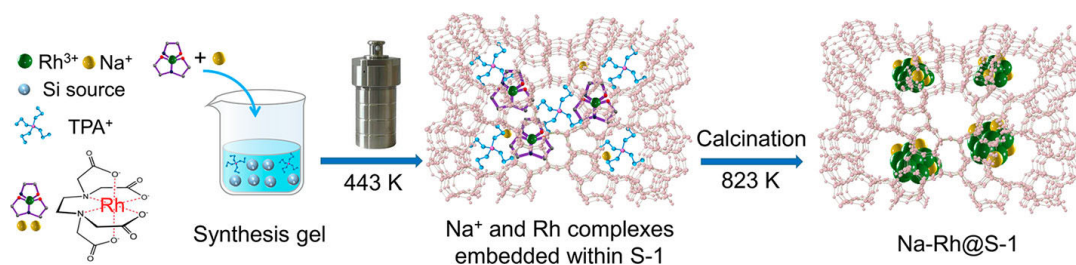
In order to improve the metal sintering resistance, in the last decades, new synthesis methods have been developed to prepare metal species embedded in zeolite crystals to obtain new materials with unique catalytic properties denoted as metal@zeolite (Figure 49).<sup>540,705–707</sup> The interaction between the metal species and the zeolite framework can modify the geometric and electronic structures of the subnanometric metal species and confer new catalytic features. Additionally, these advanced materials owing to the confinement effect can exhibit shape-selective catalysis for reactants and products diffusion, reaction and stabilization, in contrast to traditionally supported metal nanoparticles.



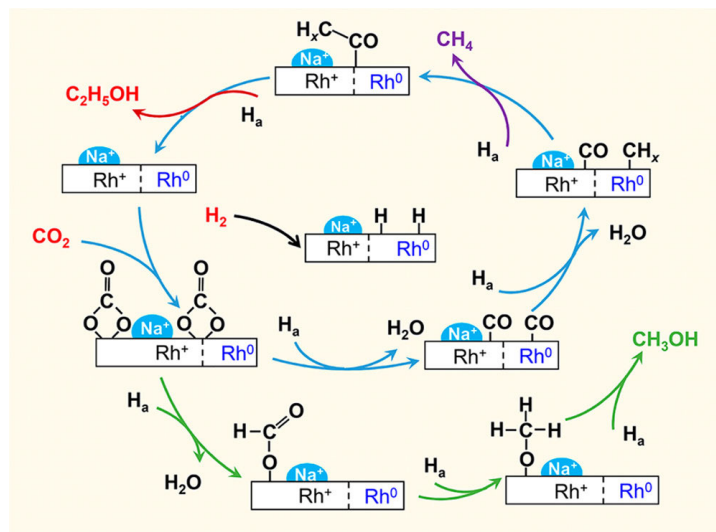
**Figure 49.** Representation of Metal@zeolite, (a) Isolated metal sites and (b) metal nanoclusters encapsulated in the micropores. (c) Metal nanoparticles fixed in the zeolite crystals. Reprinted with permission from ref.<sup>705</sup>. Copyright 2020, American Chemical Society.

Accordingly, the catalytic performance for CO<sub>2</sub> hydrogenation of Rh nanoparticles embedded in Na-zeolite S-1 (Na-Rh@S-1) by a ligand-protected crystallization method, with ~0.75 wt% Rh content and variable Na content in a range of 0.13–0.26 wt% has been reported (Figure 50).<sup>695</sup> The study of Na content revealed that existed an optimum close to 0.19 wt%, and that Na favours the coexistence of Rh<sup>0</sup> and Rh<sup>+</sup> pair species. Moreover, a DRIFT study supported the

hypothesis that  $\text{Rh}^0$  and  $\text{Rh}^+$  pair is crucial for the formation of ethanol, since it participates in the insertion or coupling of adsorbed  $\text{CO}$  and  $\text{CH}_x$  species (Figure 51). The non-dissociative C-O character of  $\text{Rh}^+$  allowed converting  $\text{CO}_2$  into  $\text{CO}^*$  and  $\text{HCOO}^*$  subsequently hydrogenated to methanol, while  $\text{Rh}^0$  sites allowed dissociating  $\text{CO}^*$  and its further hydrogenation into  $\text{CH}_x^*$ . Finally, the  $\text{CO}^*\text{-CH}_x^*$  coupling promoted by the  $\text{Rh}^0$  and  $\text{Rh}^+$  pair leads to ethanol. Therefore, in the presence of 0.19Na-Rh@S-1 catalyst, 10%  $\text{CO}_2$  conversion and 24%  $\text{C}_2\text{H}_5\text{OH}$  selectivity were reached, with space-time yield ( $\text{STY}_{\text{C}_2\text{H}_5\text{OH}}$ ) around  $72 \text{ mmol g}_{\text{Rh}}^{-1}\text{h}^{-1}$ , at  $250^\circ\text{C}$ , with  $\text{H}_2/\text{CO}_2$  ratio of 3, 5 MPa and  $\text{GHSV} = 6000 \text{ mLg}^{-1}\text{h}^{-1}$ . Over Rh@S-1 catalyst, 2.9%  $\text{CO}_2$  conversion was achieved while the main product was  $\text{CH}_4$  with a small amount of  $\text{CH}_3\text{OH}$ . The authors concluded that both the  $\text{Na}^+$  modification of Rh sites ( $\text{Rh}^0$  and  $\text{Rh}^+$  pair species) and the confinement effect allowed shifting the nature of reaction products from methane to  $\text{C}_2+\text{OH}$ .



**Figure 50** Hydrothermal synthesis of Na-Rh@S-1 by a ligand-protected crystallization method. Reprinted with permission from ref.<sup>695</sup>. Copyright 2021, American Chemical Society.



**Figure 51.**  $\text{CO}_2$  hydrogenation into alcohols via  $\text{CO}^*$  and  $\text{CH}_y^*$  coupling over  $\text{Rh}^0$  and  $\text{Rh}^+$  pair species. Reprinted with permission from ref.<sup>695</sup>. Copyright 2021, American Chemical Society.

#### b) Cu-based catalysts for $\text{CO}_2$ hydrogenation to $\text{C}_2+\text{OH}$

Cu-based catalytic performance have been largely explored and demonstrated for methanol synthesis and RWGS, and Cu is one of the main metals studied for the development of  $\text{CO}_2$  hydrogenation catalysts to higher alcohols. In the presence of CuZnFeK catalyst, highest 13.5% higher alcohols yield has been achieved, at  $300^\circ\text{C}$ , with  $\text{H}_2/\text{CO}_2$  ratio of 3, 6 MPa and  $\text{GHSV} =$

5000 mLg<sup>-1</sup>h<sup>-1</sup>.<sup>708</sup> Accordingly, the high-performance of Cu@Na-Beta for CO<sub>2</sub> hydrogenation to ethanol with 100% selectivity on the organic product basis in fixed bed has been recently reported. A two-step preparation method using dry gel conversion and crystallization procedure allowed preparing Cu@Na-Beta consisting of CuO nanoparticles (2-5 nm) embedded in crystalline particles Na-Beta zeolite, with EtOH space-time yield of 398 mg<sup>-1</sup>gcat<sup>-1</sup>h<sup>-1</sup>, at 300°C, 1.3 MPa, with GHSV= 12 Lg<sub>cat</sub><sup>-1</sup>h<sup>-1</sup> and a ratio CO<sub>2</sub>/H<sub>2</sub> of 1/3.<sup>709</sup> Characterization and theoretical studies allowed showing that specific interaction between Beta zeolite structure with enclosed copper was responsible of the superior catalytic performance of Cu@Na-Beta for CO<sub>2</sub> hydrogenation to ethanol.

A comparison study of characterization data and catalytic activity of Cu-impregnated Na-Beta zeolite (Cu/Na-Beta), Cu-impregnated silica (Cu/SiO<sub>2</sub>), and Cu-embedded Na-ZSM-5 following the same procedure (Cu@Na-ZSM-5) was performed to clarify the catalytic mechanism and explain the superior catalytic performance of Cu@Na-Beta. XAFS study revealed similar Cu crystal structure for all the samples that could not explain the significant differences in the catalytic activity for CO<sub>2</sub> hydrogenation, while XPS study showed the presence of a small amount of electropositive Cu species only for Cu@Na-Beta sample, probably due to specific interaction metal/support. For mechanistic insights, GC-MS monitoring for transient experiment with H<sub>2</sub>/<sup>12</sup>CO<sub>2</sub> switch by H<sub>2</sub>/<sup>13</sup>CO<sub>2</sub> was performed over Cu@Na-Beta and revealed a synchronous change in <sup>12</sup>CH<sub>3</sub><sup>13</sup>CH<sub>2</sub>OH signal, indicating the readily coupling of <sup>13</sup>CO<sub>2</sub> with adsorbed methyl species (<sup>12</sup>CH<sub>3</sub>\*). Additionally, density functional and slab model calculations allowed determining that (221) facet of copper was the most effective for CO<sub>2</sub> hydrogenation into ethanol and selected to mimic the catalyst with three models (perfect, Cu vacancy, and O-doped surfaces on the edges). The barrier/reaction heat calculated for a kinetically favourable route of methyl formation (CH<sub>3</sub>\*) indicated that CH<sub>3</sub>\* formation by C-O breaking from CH<sub>3</sub>OH was easier than by CH<sub>3</sub>O\* decomposition into CH<sub>3</sub>\*+O\*. Moreover, the calculation of energy reaction for the coupling CO<sub>2</sub>\* + CH<sub>3</sub>\* into CH<sub>3</sub>COO\* revealed that this step was slightly endothermic while methyl formation from methanol, and CH<sub>3</sub>COO\* reduction to CH<sub>3</sub>CH<sub>2</sub>OH were exothermic reactions. These findings are consistent with the non-detection of methanol, acetic acid and formic acid as reaction products. Therefore, the authors concluded that CO<sub>2</sub> was firstly hydrogenated to CH<sub>3</sub>\* at the Cu-surface that subsequently reacted with adsorbed CO<sub>2</sub>\* to form CH<sub>3</sub>COO\* that cannot desorb due to the high-energy barrier but further easily hydrogenated into ethanol. Two roles were attributed to the zeolitic Na-Beta framework that allowed, on the one hand, the confinement of Cu nanoparticles with unique shapes and surface active sites for CO<sub>2</sub> hydrogenation, and on the other hand, to impose shape constraints to the reactants in the near-surface layer of the nanoparticles to avoid the formation of by-products.

### 5.6.3. OMS-based catalysts for CO<sub>2</sub> hydrogenation to C<sub>2+</sub>OH

As mentioned above, the development of Rh-based catalysts for CO<sub>2</sub> hydrogenation is promising due to the ability of the Rh active sites to dissociate CO together with the fact that CH<sub>4</sub> or CO are the main products over the pure Rh catalyst. These abilities open up the possibility of combining both dissociative/non-dissociative capabilities by incorporating promoters, thus balancing the number of dissociative and non-dissociative metal centers to promote CH<sub>x</sub>\*-CO\* coupling. Accordingly, different Rh-MO<sub>x</sub>/MCM-41 catalysts where MO<sub>x</sub> was WO<sub>x</sub>, FeO<sub>x</sub>, MnO<sub>x</sub>, CeO<sub>x</sub> and NbO<sub>x</sub>, were prepared by co-impregnation method and used for CO<sub>2</sub> hydrogenation, in fixed bed at 250°C, 3.0 MPa, GHSV= 6000 h<sup>-1</sup> and H<sub>2</sub>/CO<sub>2</sub>/N<sub>2</sub> ratio of 3:1:1.<sup>710</sup> Since the VO<sub>x</sub> promoted catalyst exhibited the highest ethanol selectivity and yield, the characterization VO<sub>x</sub> and effect VO<sub>x</sub> loading were studied. When VO<sub>x</sub> loading increased, the CO<sub>2</sub> conversion and ethanol selectivity increased and reached a maximum up to 12 and 24%, respectively, for 0.3 wt% VO<sub>x</sub>. While further increase in VO<sub>x</sub> loading, induced CO<sub>2</sub> conversion decrease, attributed to the passive effect caused by the excessive encapsulation of Rh species by VO<sub>x</sub> species. The authors concluded that the incorporation of VO<sub>x</sub> owing to electronic effect induced the formation of Rh<sup>+</sup> (VO<sub>x</sub>-Rh interfacial active sites) that modified the dissociation capacity of the catalyst due to the presence of tilted CO species leading to the easy cleavage of C-O and its subsequent hydrogenation to form CH<sub>3</sub>\*. The higher ethanol yield was the result of the promoted CO<sub>2</sub> activation and CO dissociation for an adequate VO<sub>x</sub> loading. Thus, at 0.3 wt% VO<sub>x</sub>, the amount of dissociative adsorbed CO is similar to that of non-dissociative adsorbed CO, leading to the highest selectivity and ethanol yield.

### 5.6.4. Conclusion

CO<sub>2</sub> hydrogenation to C<sub>2+</sub>OH is an attractive process to obtain new building blocks molecules (olefins from alcohols dehydration) and energy carrier since C<sub>2+</sub>OH have higher energy densities, lower toxicity and corrosiveness than methanol. But, if CO<sub>2</sub> hydrogenation to C<sub>2+</sub>OH has been widely studied in the last decades, very few studies focusing on the development of hydrogenation catalysts based on zeolites or OMS have been reported besides the benefits of confinement effect, nanoparticle stabilization by electronic features and shape-selectivity (reactant, product, transition state). Accordingly, if the best yield for heterogeneous catalysts has been achieved over RhFeLi/TiO<sub>2</sub> catalyst with 4.91% C<sub>2+</sub>OH yield, maximum 100% ethanol selectivity on the organic product basis has been reached over Cu@Na-Beta catalyst.

However, high yield and selectivity of C<sub>2+</sub>OH remain a major challenge and could be achieved by ab initio design of the catalysts, introducing the necessary active sites, which can be rationalized and simulated by computational chemistry. Therefore, additional thorough mechanistic studies,

based on operando analysis and characterization of the catalysts, reactants, products and intermediates are required to understand the reaction pathways and the nature of active sites to generate fundamental knowledge. Thus, the selectivity could be improved towards selected alcohol ( $C_{2-4}$ ), controlling the nature and number of active sites with dissociative, non-dissociative and propagation chain abilities. Actually, up to now, different mechanisms based on products, by-products and intermediates formations detected by DRIFT studies have been proposed and highly depended on the catalyst. Moreover, the cost and stability of the catalyst has to be optimized, and the metal choice is of paramount importance. In the case of the few reported works for OMS and zeolite based catalysts, both Cu and Rh exhibited high abilities for  $CO_2$  hydrogenation to  $C_{2+}OH$ , nevertheless, considering catalyst costs, Cu seems more indicated for industrial application. It is clear that zeolites and OMS based catalysts are good candidate for the development of selective and stable catalysts for  $CO_2$  hydrogenation to  $C_{2+}OH$ , and which have so far been under-considered.

## 5.7. Hydrogenation of $CO_2$ to $C_{2+}$

### 5.7.1. Introduction

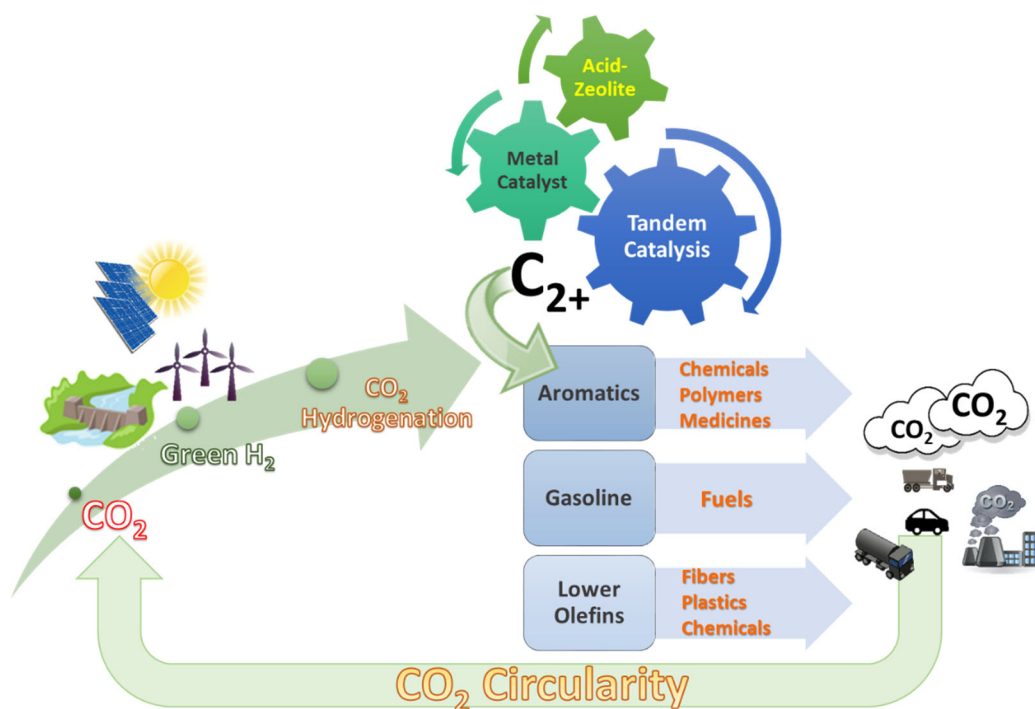


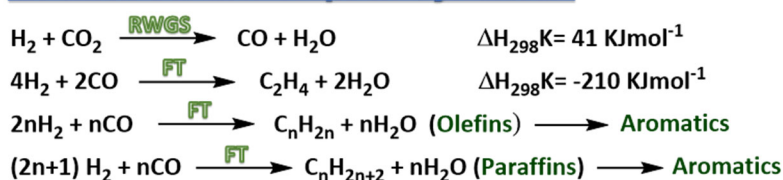
Figure 52. Hydrogenation of  $CO_2$  to  $C_{2+}$  and uses.

The production of hydrocarbons, aromatics, and olefins via catalytic hydrogenation of  $CO_2$  is an attractive route to produce fuels ( $C_{2+}$ ) and pave a way to the  $CO_2$  circularity. In comparison to  $C_1$  products,  $C_{2+}$  products possess higher energy densities. Light olefins such as ethylene, propylene, and butylene are the top-produced petrochemicals worldwide and constitute important raw materials for chemical industry and the production of plastics, fibers, and

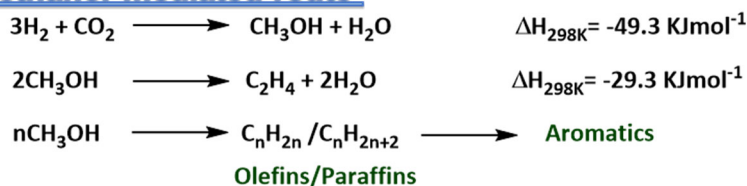
chemicals. They are generally produced through the hydrocracking of hydrocarbons of fossil sources under high temperature. Aromatics also constitute important platform chemicals, for the synthesis of petrochemicals, polymers, and medicines. They are usually produced by oil thermal cracking and naphtha reforming. The alternative strategy to produce gasoline, olefins and aromatics from CO<sub>2</sub> is an important way to mitigate greenhouse gas emissions, develop new sustainable routes for the production of value-added chemicals and reduce dependence on fossil sources (Figure 52).

The production of C<sub>2+</sub> from CO<sub>2</sub> hydrogenation involves a cascade process consisting of a first step of production of CO intermediate by RWGS or MeOH (DME), followed by Fisher Tropsch synthesis (FTS) or methanol to hydrocarbons route (MTH), respectively, comprising oligomerization, cracking and aromatization reactions (Scheme 56).

### Modified Fischer-Tropsch Synthesis



### Methanol mediated route



**Scheme 56.** CO<sub>2</sub> hydrogenation to liquid fuels, olefins and aromatics by modified FTS or methanol mediated route.

The main drawback for C<sub>2+</sub> hydrocarbon production is the kinetic barriers for C-C coupling. Therefore, the great advantage of combining RWGS with FTS or methanol synthesis and conversion to hydrocarbons is the thermodynamics of the overall process.<sup>87,711</sup>

RWGS is an endothermic process, whereas the FTS reaction is exothermic, which makes the RWGS-FTS tandem thermodynamically favorable (Scheme 56). Thus, the equilibrium of the RWGS reaction can be shifted due to the consumption of CO by the FTS for hydrocarbon production. Similarly, for the methanol-mediated route, the hydrogenation of CO<sub>2</sub> to methanol is exothermic and thermodynamically limited at high temperature, and kinetically limited at low temperature. However, the combination of methanol synthesis with conversion to hydrocarbons allows shifting the equilibrium due to methanol consumption.

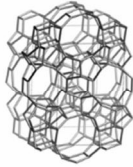
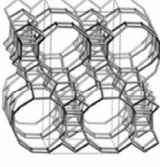
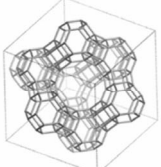
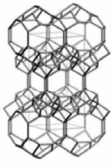
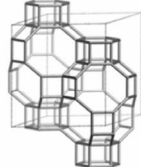
Different catalysts (metals, metal oxides, metal carbides, MOFs, zeolite) that have been applied for the synthesis of hydrocarbons from synthesis gas or methanol to olefins or aromatics (MTO/MTA), have also been tested for the hydrogenation of CO<sub>2</sub> to hydrocarbons via the



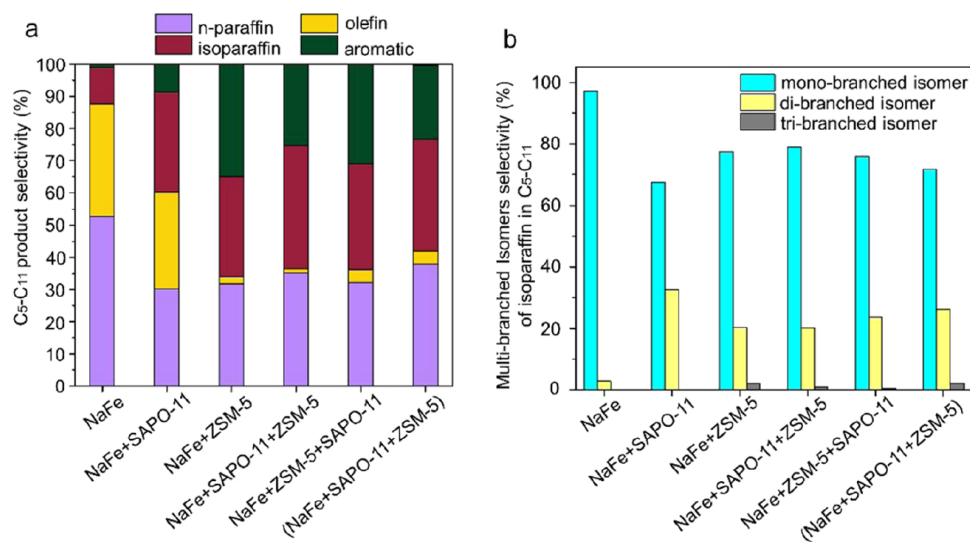
tandem process. Different strategies have been followed to optimize catalytic properties and reaction conditions to enhance CO<sub>2</sub> activation, decrease the energy barrier for C-C coupling and minimize CO and methane yields. Therefore, the effects of the addition of alkali promoters, addition of iron to enhance CO<sub>2</sub> adsorption and increase surface CO/H<sub>2</sub> ratio, addition of a second metal to improve strong interactions between the support and active phase and modify the electronic environment of active species, the modification of acid-base properties, for example to weak the secondary hydrogenation ability of olefins or to avoid undesirable alkylation and isomerization have been explored.

Usually, hydrogenation of CO<sub>2</sub> over Fe and Co based catalysts produces CO as intermediates while over Cu/Zn catalysts methanol is the main intermediate. Only Fe, Co, Ni, and Ru of the group VIII, exhibit sufficiently high activities for the hydrogenation of CO to warrant their use as effective FT catalysts and among them, only Co- and Fe- based catalysts may be considered as practical FT catalysts, while Fe-based catalysts remain the preferred for commercial FT synthesis.<sup>712</sup>

The synthesis of C<sub>2+</sub> products through CO<sub>2</sub> hydrogenation process is a combination of MeOH or CO production in a first step, in the presence of a multi-centers metal-based catalyst, and of a second step involving oligomerization, cracking and aromatization processes in which the zeolite-based catalysts have played a key role. In the literature, recent reviews described the catalytic performance of metal-based solid catalysts, and zeolite owing to their unique and tunable properties have been widely applied for both their carrier and chemical properties.<sup>81,82,84-86</sup> The combination of zeolites and metal sites through the presence of metals nanoparticles or metallic oxides offers great opportunities for the conversion of CO<sub>2</sub> into liquid fuels, olefins and aromatics. The presence of targeted metal active species allows the activation and conversion of CO<sub>2</sub> to intermediate CO or methanol (DME), while zeolites, due to their tunable acidity and pore structure, allow to control and direct the nature and distribution of the products, as illustrated in the [Figure 53](#). Accordingly the combination of NaFe<sub>2</sub>O<sub>3</sub>, ZSM-5 and SAPO-11 with defined pores and acidic sites are responsible for enhancing the isomerization activity and improving the composition of isoparaffins for direct CO<sub>2</sub> hydrogenation ([Figure 54](#)).<sup>713</sup>

Zeolite type	ZSM-5	Beta	Y	RUB-13	SAPO-34, SSZ-13
Framework type code	MFI	BEA*	FAU	RTH	CHA
Framework structure					
Dimensionality of pore system	3D	3D	3D	2D	3D
Pore size (Å)	5.1 x 5.5 5.3 x 5.6	6.6 x 6.7 5.6 x 5.6	7.4 x 7.4	3.8 x 4.1 2.5 x 5.6	3.8 x 3.8
Product preference	Aromatics		Iso-alkanes / gasoline-range hydrocarbon		Olefins

**Figure 53.** Effect of zeolite pore size and structure over the nature and distribution of the direct CO<sub>2</sub> hydrogenation products. Reprinted with permission from ref.<sup>82</sup>. Copyright 2022, Elsevier Ltd. All rights reserved.



**Figure 54.** Effect of combination of NaFe<sub>2</sub>O<sub>3</sub>, ZSM-5 and SAPO-11 for enhancing the isomerization and aromatization activity and improving the composition of isoparaffins and aromatics for direct CO<sub>2</sub> hydrogenation. Reprinted with permission from ref.<sup>713</sup>. Copyright 2020, American Chemical Society.

Since excellent and comprehensive reviews<sup>80–83</sup> reported the recent advances in the direct CO<sub>2</sub> hydrogenation to liquid fuels, olefins and aromatics this section describes the major achievements and proposes some future research approaches.

### 5.7.2. Direct hydrogenation of CO<sub>2</sub> to fuels over bifunctional catalytic system incorporating zeolites.

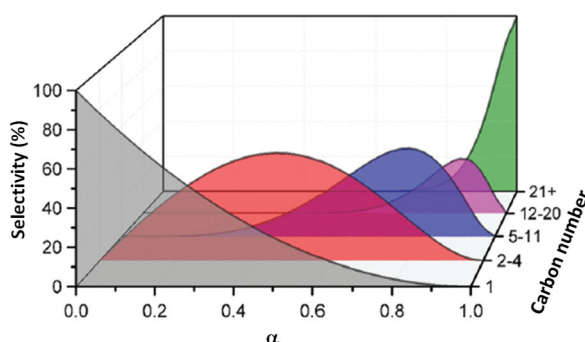
#### a) Direct hydrogenation of CO<sub>2</sub> via modified FTS

The direct hydrogenation of CO<sub>2</sub> via modified FTS produces a mixture of hydrocarbons with broad distributions that can be adjusted by optimizing the morphology and structure of FT catalysts by controlling the metal active species (nanoparticle size, crystalline phase and exposed

facets) and the properties of the zeolite (acidity, pore size and structure) and the addition of promoters. Accordingly, zeolites have shown to exhibit high activity for hydrocracking and isomerization of hydrocarbons and have been widely used.<sup>714,715</sup>

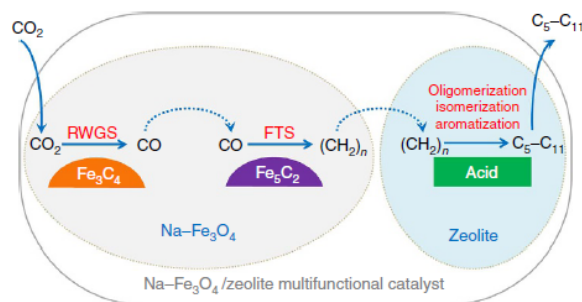
The direct hydrogenation of CO<sub>2</sub> via modified FTS involves the hydrogenation of CO<sub>2</sub> to CO via RWGS reaction, followed by hydrogenation of CO to hydrocarbons by FT synthesis. The most active catalysts reported for RWGS are Fe-based being Fe<sub>3</sub>O<sub>4</sub> the active phase, while iron carbide (Fe<sub>5</sub>C<sub>2</sub>) have been reported as the most active catalysts for FT synthesis.<sup>716–718</sup>

Therefore, the main challenge is controlling the chain growth via C–C coupling on metal surfaces. The FTS products has been ascribed to polymerization reaction and thus products distribution determined by the Anderson–Schulz–Flory (ASF) distribution. According to the ASF model, the molar fraction (M<sub>n</sub>) of a hydrocarbon product with a carbon number of n depends on the chain growth probability (α) is given by the following equation:  $M_n = (1-\alpha)\alpha^{n-1}$  where α is determined by the rates of chain growth (r<sub>p</sub>) and chain termination (r<sub>t</sub>),  $\alpha = r_p / (r_p + r_t)$ .<sup>81,712</sup> The modification of catalysts composition and structure play a key role on the chain growth value and in turn on the hydrocarbon products distribution (Figure 55). However, the selectivity for specific hydrocarbons C<sub>2+</sub> range is limited, and maximum 58%, 48%, 41% and 40% selectivities for C<sub>2</sub>-C<sub>4</sub>, C<sub>5</sub>-C<sub>11</sub>, C<sub>12</sub>-C<sub>20</sub> and C<sub>21+</sub> were predicted, respectively.



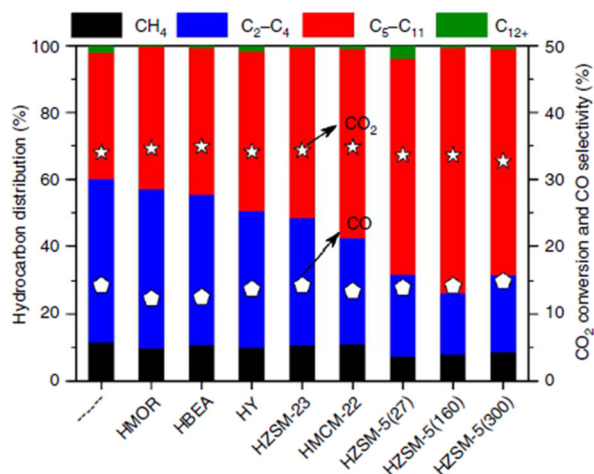
**Figure 55.** Hydrocarbon products distribution versus chain growth probability (α). Reprinted with permission from ref.<sup>81</sup>. Copyright 2019, Royal Society of Chemistry.

A recent study revealed the high catalytic performance of the multifunctional Na-Fe<sub>3</sub>O<sub>4</sub>/H-ZSM-5 catalyst for the CO<sub>2</sub> reduction to C<sub>5</sub>-C<sub>11</sub> (gasoline) with total hydrocarbons selectivity up to 78%, low 4% methane selectivity at 22% CO<sub>2</sub> conversion, with H<sub>2</sub>/CO<sub>2</sub>=3, at 320°C, 3 MPa and WHSV=4 Lh<sup>-1</sup>g<sub>cat</sub><sup>-1</sup> (Table 7, Entry 1).<sup>719</sup> The cooperation of the three types of active sites properly spaced, Fe<sub>3</sub>O<sub>4</sub> (to catalyze RWGS), Fe<sub>5</sub>C<sub>2</sub> (to catalyze FTS) and acid sites (to catalyze oligomerization, isomerization and aromatization), allowed catalytic conversion of CO<sub>2</sub> to gasoline through cascade reactions (Figure 56). Moreover, the multifunctional catalyst exhibited stable activity along 1000 h on TOS. These results showed the potential of catalytic system based on zeolite for industrial application for the CO<sub>2</sub> conversion to liquid fuels.



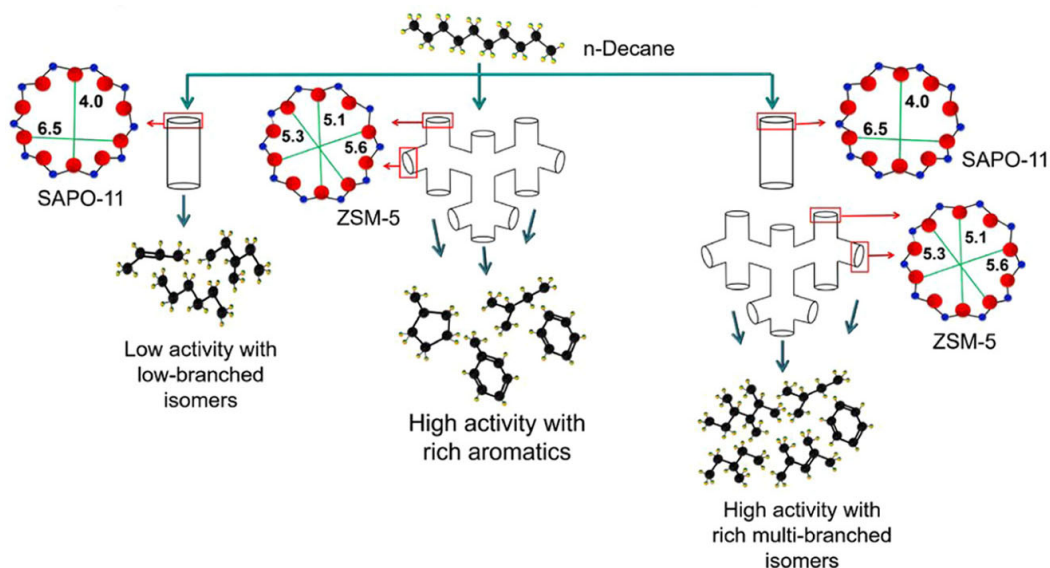
**Figure 56.** CO<sub>2</sub> hydrogenation reaction over Na-Fe<sub>3</sub>O<sub>4</sub>/Zeolite multifunctional catalyst. Reprinted with permission from ref.<sup>719</sup>. Copyright 2017, Jian Wei et al.

Another study showed the effect of the pore size and structure over the isoparaffin/aromatic ratio in the gasoline-range hydrocarbons (Figure 57). The catalytic performance of catalytic system based on MFI structure, with different Si/Al ratio, in the presence of Na-Fe<sub>3</sub>O<sub>4</sub>/HZSM-5(27), Na-Fe<sub>3</sub>O<sub>4</sub>/HZSM-5(160) and Na-Fe<sub>3</sub>O<sub>4</sub>/HZSM-5(300) produced higher amount of aromatics (up to 61% of aromatics), while when the process was carried out over Na-Fe<sub>3</sub>O<sub>4</sub>/HMCM-22 (MWW structure) isoparaffins were the main hydrocarbon products (46% of isoparaffins). This last result was attributed to 10 MR pore openings with lamellar structure consisting of two independent pore systems of the MWW structure with demonstrated catalytic properties for isomerization, alkylation and disproportionation.<sup>720</sup> Additionally, a study of the adequate distance of the different active sites showed the effects over the selectivity of hydrocarbon products. When Na-Fe<sub>3</sub>O<sub>4</sub> and HZSM-5 powders were mixed, the closest proximity of iron-based sites and acid sites led to the acid sites poisoning by Na. However, when Na-Fe<sub>3</sub>O<sub>4</sub> and HZSM-5 were combined by granule mixing, the adequate distance between iron-based and zeolite acid sites allowed the formation of the olefin intermediates on iron-based sites and its diffusion through the pores of the zeolite towards the acid sites, where underwent oligomerization, isomerization and aromatization reactions. Therefore, maximum 73% C<sub>5</sub>-C<sub>11</sub> selectivity at 34% CO<sub>2</sub> conversion was reached. Nevertheless, when hydrogenation process was carried out in the dual-bed configuration with HZSM-5 packed below Na-Fe<sub>3</sub>O<sub>4</sub> and separated by a thin layer of inert quartz sand, lower 67% C<sub>5</sub>-C<sub>11</sub>selectivity (67%) at 34% CO<sub>2</sub> conversion was reached and attributed to the larger distance of active sites.



**Figure 57.** CO<sub>2</sub> hydrogenation reaction over Na-Fe<sub>3</sub>O<sub>4</sub>/Zeolite multifunctional catalysts, with H<sub>2</sub>/CO<sub>2</sub>=3, at 320°C, 3 MPa and WHSV=4 Lh<sup>-1</sup>g<sub>cat</sub><sup>-1</sup>. Reprinted with permission from ref.<sup>719</sup>. Copyright 2017, Jian Wei et al.

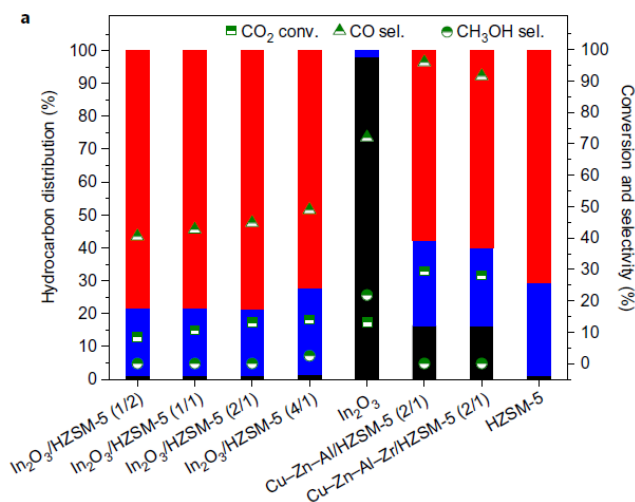
A recent work demonstrated the critical role of the structure and pore size of the zeolite over the isoparaffin selectivity.<sup>713</sup> Indeed, the combination of SAPO-11 and ZSM-5 with Na/Fe<sub>3</sub>O<sub>4</sub> catalysts allowed enhancing the long-chain-hydrocarbon selectivity by performing oligomerization on the shorter chains, while the isomerization ability favored long-chain hydrocracking along with aromatization (Figure 58). Further study of configuration of the different catalysts showed that the triple-bed system with first the Na/Fe<sub>3</sub>O<sub>4</sub> catalyst followed sequentially with SAPO-11 and ZSM-5 allowed maximizing isoparaffins selectivity. Likewise, The 71.7% gasoline selectivity was reached with 38.2% isoparaffins selectivity, at 31.2% CO<sub>2</sub> conversion of 31.2% (Figure 58; Table 7, Entry 2).



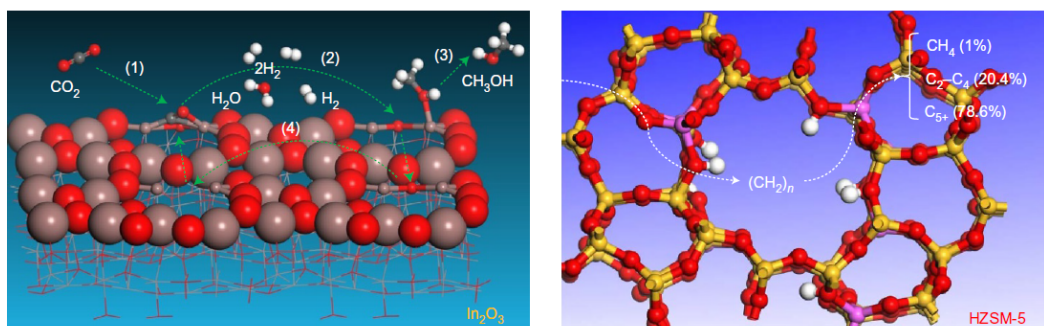
**Figure 58.** Effect of the combination of ZSM-5 and SAPO-11 over the isomerization and hydrocracking abilities over the formation of paraffins and aromatics. Reprinted with permission from ref.<sup>713</sup>. Copyright 2020, American Chemical Society.

b) Direct hydrogenation of CO<sub>2</sub> via methanol mediated route

Direct hydrogenation of CO<sub>2</sub> via methanol mediated route was performed over a bifunctional catalyst constituted by reducible In<sub>2</sub>O<sub>3</sub> and H-ZSM-5, reaching high 78.6% gasoline-range (C<sub>5+</sub>) and low 1% methane selectivity, at 13.1% CO<sub>2</sub> conversion.<sup>721</sup> Since direct hydrogenation of CO<sub>2</sub> via methanol mediated route usually occurs over Cu/Zn catalysts,<sup>434,527</sup> the catalytic performance of In<sub>2</sub>O<sub>3</sub>/H-ZSM-5 was compared to Cu-Zn-Al/H-ZSM-5 and Cu-Zn-Al-Zr/H-ZSM-5 bifunctional catalysts. When the typical Cu-Zn-Al/H-ZSM-5 and Cu-Zn-Al-Zr/H-ZSM-5 catalysts were used, the main product was CO with higher CH<sub>4</sub> selectivity in the hydrocarbons distribution, similarly to other reported studies combining Cu-Zn, Cu-Zn-Zr and Cu-Zn-Cr oxides with zeolite (HY, H-Beta, SAPO-5, SAPO-44).<sup>722,723</sup> The high activity of In<sub>2</sub>O<sub>3</sub> for the direct hydrogenation of CO<sub>2</sub> to methanol was previously reported,<sup>724</sup> and the combination of In<sub>2</sub>O<sub>3</sub> with H-ZSM-5 allowed reaching high C<sub>5+</sub> hydrocarbons yield and selectivity (Figure 59), at 340°C, with H<sub>2</sub>/CO<sub>2</sub>=3 and 3.0 MPa, with good catalytic stability along 150 h of TOS. These results were attributed to the higher stability of intermediates involved in CH<sub>3</sub>OH synthesis on the defective In<sub>2</sub>O<sub>3</sub> surface with surface oxygen vacancies than on the Cu surface which strongly suppressed the formation of CO.<sup>723</sup> On the other hand, the catalytic performance of In<sub>2</sub>O<sub>3</sub>/H-ZSM-5 bifunctional catalyst was higher than one of other reducible metal oxides combined with H-ZSM-5 such as Ga<sub>2</sub>O<sub>3</sub>, Fe<sub>2</sub>O<sub>3</sub>, ZnO-Cr<sub>2</sub>O<sub>3</sub> and ZnO-ZrO<sub>2</sub> combined with a higher activity and C<sub>5+</sub> selectivity (Table 7, Entries 3-7). A hydrocarbon-pool mechanism was proposed for methanol conversion into hydrocarbons inside HZSM-5. Firstly, CO<sub>2</sub> is hydrogenated into methanol at the oxygen vacancy on the In<sub>2</sub>O<sub>3</sub> surface. Methanol further diffused inside the pore of the zeolite at the acidic site inside where it is transformed to hydrocarbons after oligomerization, isomerization and aromatization reactions (Figure 60). A study of integration manner of the active components revealed, as was observed in other works, that the hydrocarbon selectivity and distribution depended on the different active sites distance. When the hydrogenation process was performed in a dual-bed configuration, with HZSM-5 packed above the In<sub>2</sub>O<sub>3</sub> below, high 66.3% methane selectivity was achieved. However, when In<sub>2</sub>O<sub>3</sub> was packed above and HZSM-5, methanol was completely converted into hydrocarbons with 70.4% C<sub>5+</sub> selectivity and 4.5% methane selectivity. Finally, a closer disposition of the active sites allowed to suppress undesired RWGS and maximized C<sub>5+</sub> (78.6%). Finally, experiments using the pellet catalyst were performed to show that tail-gas recycling, commonly used in industry for a more efficient utilization of the feed, allowed further improving the catalytic performance, with increase of both CO<sub>2</sub> conversion, from 8.7 to 18.2% and C<sub>5+</sub> selectivity, from 78.6 to 84.1%, while CO selectivity decreased from 44.5 to 30%. These results showed the great potential of bifunctional catalysts based on zeolite for industrial applications.



**Figure 59.** CO<sub>2</sub> hydrogenation over bifunctional Cu- and In<sub>2</sub>O<sub>3</sub>-based HZSM-5 catalysts with different mass ratios, at 340°C, 3.0 MPa, 9 Lh<sup>-1</sup>g<sub>cat</sub><sup>-1</sup>, H<sub>2</sub>/CO<sub>2</sub>/N<sub>2</sub>=73/24/3, and MeOH conversion over HZSM-5 (■ C<sub>5+</sub>, ■ C<sub>2-4</sub>, ■ CH<sub>4</sub>). Reprinted with permission from ref.<sup>721</sup>. 2017, Nature Publishing Group.



**Figure 60.** Proposed mechanism for the formation of CH<sub>3</sub>OH at the oxygen vacancy on In<sub>2</sub>O<sub>3</sub> surface and further transformation to hydrocarbons at the acidic site inside the pores of HZSM-5. Reprinted with permission from ref.<sup>721</sup>. 2017, Nature Publishing Group.

**Table 7.** Catalytic results of zeolite-based catalyst for CO<sub>2</sub> hydrogenation to hydrocarbons through several routes

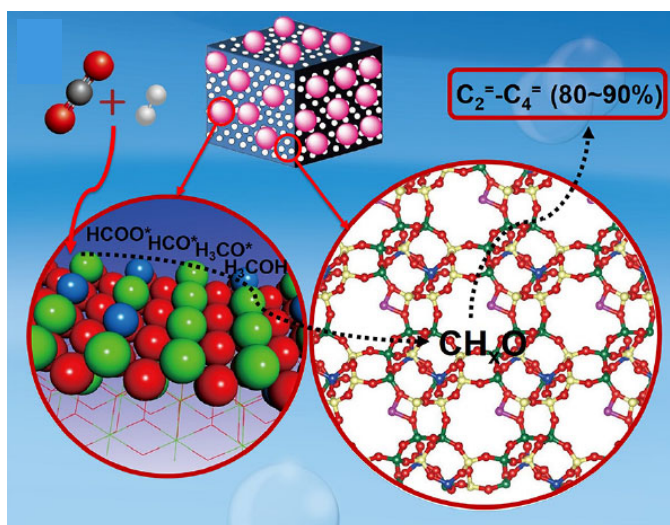
Entry	Catalysts	$\chi_{\text{CO}_2}$ %	Selectivity %		HC* distribution			Reaction conditions	Year	Ref
			CO	HC*	CH <sub>4</sub>	C <sub>2</sub> -C <sub>4</sub>	C <sub>5</sub> +			
<b><i>Modified FTS route</i></b>										
1	Na-Fe <sub>3</sub> O <sub>4</sub> /H-ZSM-5	34.5	18.8	71.2	11	17	70.5	320°C, H <sub>2</sub> /CO <sub>2</sub> =3, 3 MPa, WHSV=4 Lh <sup>-1</sup> g <sub>cat</sub> <sup>-1</sup>	2017	719
2	Na-Fe <sub>3</sub> O <sub>4</sub> /ZSM-5/SAPO-11	31.2	15	85	4	12	33	320°C, H <sub>2</sub> /CO <sub>2</sub> =3, 3 MPa, W <sub>NaFe</sub> /F=6 g <sub>mol</sub> <sup>-1</sup>	2020	713
<b><i>Methanol mediated route</i></b>										
3	In <sub>2</sub> O <sub>3</sub> /HZSM-5	13.1	44.8	55.2	1	20.4	78.6	340°C, 3.0 MPa, WHSV=9	2017	721
4	Ga <sub>2</sub> O <sub>3</sub> /HZSM-5	8.7	85.9	14.1	4.5	34.9	60.7	Lh <sup>-1</sup> g <sub>cat</sub> <sup>-1</sup> ,	2017	721
5	Fe <sub>2</sub> O <sub>3</sub> /HZSM-5	7.1	73.5	26.5	2	27.5	70.5	H <sub>2</sub> /CO <sub>2</sub> /N <sub>2</sub> =73/24/3	2017	721
6	Zn-Cr/HZSM-5	8.1	60.6	39.4	1.5	34.5	61.2		2017	721
7	Zn-Zr/HZSM-5	4.3	44.1	55.9	2.3	44	53.7		2017	721

\*HC:hydrocarbons



### 5.7.3. Direct hydrogenation of CO<sub>2</sub> to olefins over bifunctional catalytic system incorporating zeolites via methanol mediated route

The catalytic performance of bifunctional catalysts with high selectivity for the syngas conversion to lower olefins have been explored for the hydrogenation of CO<sub>2</sub> as ZnO-ZrO<sub>2</sub>/SAPO-34 catalyst (Table 8, Entry 1).<sup>723</sup> 80% C<sub>2</sub>-C<sub>4</sub> olefins selectivity was reached with a low 3% methane selectivity at 12.6% CO<sub>2</sub> conversion, at 380°C, 2 MPa and H<sub>2</sub>/CO<sub>2</sub>=3. Compared catalytic performance for CO<sub>2</sub> hydrogenation over ZnO-ZrO<sub>2</sub> and ZnO-ZrO<sub>2</sub>/SAPO-34 allowed concluding that hydrogenation over tandem catalyst was not a simple sum of the two individual reactions but rather, a coupling reaction.<sup>725</sup> Thus, if thermodynamics of CO<sub>2</sub> hydrogenation of is unfavorable, the conversion of methanol to lower olefins is thermodynamically favorable as well as the global process due to the coupling of both reactions. CO<sub>2</sub> and H<sub>2</sub> molecules were activated on ZnZrO, while the C-C coupling occurred on SAPO. Tandem catalysis improved thermodynamics and kinetics coupling through the transferring and migrating of CH<sub>x</sub>O intermediate species, not methanol, which promoted the efficient conversion of CO<sub>2</sub> to lower olefins (Figure 61).

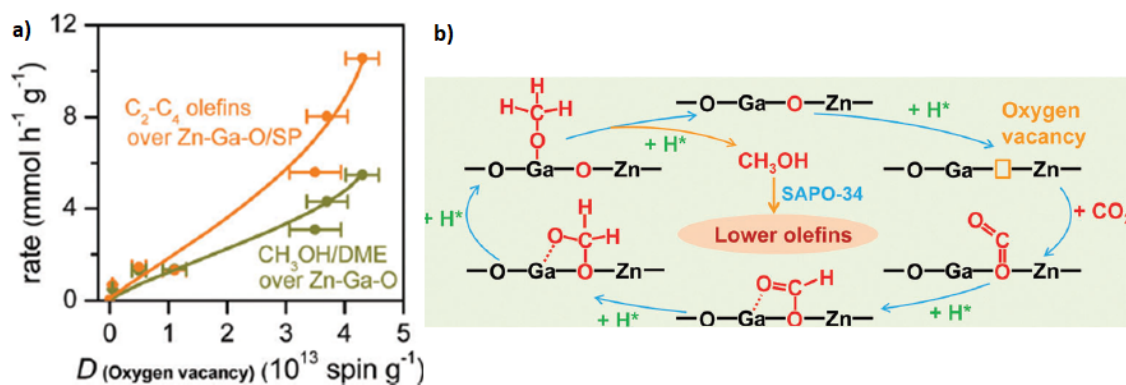


**Figure 61.** Proposed reaction mechanism of CO<sub>2</sub> hydrogenation on the tandem ZnZrO<sub>2</sub>/SAPO-34 catalyst. Reprinted with permission from ref.<sup>725</sup>. Copyright 2017, American Chemical Society.

Newly the effect of the proximity of the different active sites of the tandem catalyst was demonstrated from the catalytic performance registered when the CO<sub>2</sub> hydrogenation was carried out with both catalysts integrated in different configurations: in dual-fixed bed or physical mixtures of metal oxides and SAPO-34 powders or granules and with or without quartz sand as separator. Optimum catalytic results was obtained for physical mixtures of metal oxides and SAPO-34 powders offering the proper distance between the different active sites to perform the tandem catalysis.

Similarly, the catalytic performance of the bifunctional catalyst  $\text{In}_2\text{O}_3\text{-ZrO}_2/\text{SAPO-34}$  was explored due to the high catalytic activity of  $\text{In}_2\text{O}_3$ <sup>724</sup> for the hydrogenation of  $\text{CO}_2$  to methanol.<sup>726</sup> A 80% lower olefins selectivity with only 4% methane selectivity was reached with hydrocarbon product distribution different from classical ASF distribution (Table 9, Entry 2). The bifunctional catalyst exhibited good stability over 150 h of TOS, opening up opportunities for industrial applications.

A bifunctional  $\text{ZnGa}_2\text{O}_4/\text{SAPO-34}$  catalyst,  $\text{ZnGa}_2\text{O}_4$  with a spinel structure, was also explored for the hydrogenation of  $\text{CO}_2$  to lower olefins.<sup>727</sup> A 86% lower olefins selectivity, at 13%  $\text{CO}_2$  conversion with 1% methane selectivity was reached (Table 8, Entry 3). A study of correlation of the rates of formation of  $\text{CH}_3\text{OH}/\text{DME}$  ( $\text{Zn-Ga-O}$ ) and lower olefins ( $\text{C}_2^--\text{C}_4^--$ ) ( $\text{Zn-Ga-O}/\text{SAPO-34}$ ) with the density of oxygen vacancies demonstrated their fundamental role in the activation and selective conversion of  $\text{CO}_2$  to methanol/DME on the  $\text{Zn-Ga-O}$  surfaces and their subsequent transformation at the acid sites of SAPO to lower olefins (Figure 62). On the other hand, in situ IR study allowed to propose a mechanism for the activation of  $\text{H}_2$  on the  $-\text{Ga-O}-$  and  $-\text{Zn-O}-$  pairs and formation of H species ( $\text{H}^*$ ) for the conversion of  $\text{CO}_2$  to  $\text{CH}_3\text{O}^*$  species further converted to methanol and DME which after diffusion through the SAPO-34 pores towards the acid sites selectively form lower olefins.



**Figure 62.** a) Correlation of the rates of formation of  $\text{CH}_3\text{OH}/\text{DME}$  ( $\text{Zn-Ga-O}$ ) and lower olefins ( $\text{C}_2^--\text{C}_4^--$ ) ( $\text{Zn-Ga-O}/\text{SAPO-34}$ ) with the density of oxygen vacancies b) Proposed reaction mechanism of  $\text{CO}_2$  hydrogenation on the tandem  $\text{ZnGa}_2\text{O}_4/\text{SAPO-34}$  catalyst. Reprinted with permission from ref.<sup>727</sup>. Copyright 2018, Royal Society of Chemistry.

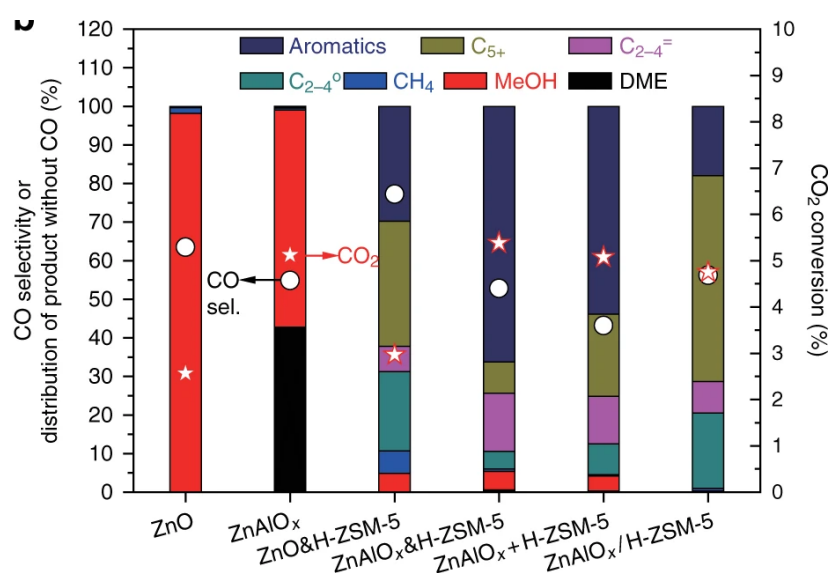
#### 5.7.4. Direct hydrogenation of $\text{CO}_2$ to aromatics over bifunctional catalytic system incorporating zeolites

##### a) Direct hydrogenation of $\text{CO}_2$ to aromatics via methanol mediated route

The selective hydrogenation of  $\text{CO}_2$  to gasoline and olefins have been successfully explored and achieved. Nevertheless, the selective hydrogenation of  $\text{CO}_2$  to aromatics remains challenging due to the high unsaturation degree and complex structures of aromatics.

Recently, an attempt of conversion of  $\text{CO}_2$  to aromatics in the presence of a bifunctional catalyst composed by nano-scaled spinel structural  $\text{ZnAlO}_x$  and H-ZSM-5 was reported.<sup>728</sup> A

characterization study was performed to determine the active sites and the combination mode of both catalysts. The TPR results showed that both of ZnAlO<sub>x</sub> and ZnO can be hardly reduced by H<sub>2</sub> below 430°C and 7% less zinc oxides could be reduced above 730 °C. Therefore, it was concluded that Zn<sup>2+</sup> are responsible for the activation of CO<sub>2</sub> hydrogenation. The IR study of absorption of DTBPY (2,6-di-tert-butyl-pyridine absorption) to investigate the external surface Brønsted acid sites that are able to catalyze the hydrogenation of CO<sub>2</sub> to paraffins and not to aromatics, revealed that the characteristic bands at 3365, 1614 and 1531 cm<sup>-1</sup> disappeared after mixing, grinding and pressing under high pressure with ZnAlO<sub>x</sub>. These results indicated that external Brønsted acid of H-ZSM-5 are shielded by ZnAlO<sub>x</sub> after mixing that is beneficial for the aromatization process what was demonstrated by the catalytic performance registered over different combination of both catalysts ZnAlO<sub>x</sub> and H-ZMS-5: ZnAlO<sub>x</sub>&H-ZSM-5 prepared by grinding, ZnAlO<sub>x</sub>+H-ZSM-5 prepared by granules mixing, ZnAlO<sub>x</sub>/HZSM-5 denoted as dual-bed catalysts (Figure 63). The aromatics or C<sub>2-4</sub> olefins selectivity follows the order ZnAlO<sub>x</sub>&H-ZSM-5 > ZnAlO<sub>x</sub>+H-ZSM-5 > ZnAlO<sub>x</sub>/H-ZSM-5, in contrast to C<sub>2-4</sub> paraffins selectivity follows opposite order. Therefore, when the CO<sub>2</sub> hydrogenation was performed over ZnAlO<sub>x</sub>&H-ZSM-5 high 73.9% aromatics selectivity with low 0.4% methane selectivity was reached. Among aromatics, 58.1% selectivity p-xylene in xylenes is achieved, while CO selectivity was 57.4% (Table 9, Entry 1). A proposed mechanism involves the formation of methanol and dimethyl ether by hydrogenation of formate species formed on ZnAlO<sub>x</sub> surface, which diffuse to H-ZSM-5 at acid sites where they are successively converted to olefins and aromatics.

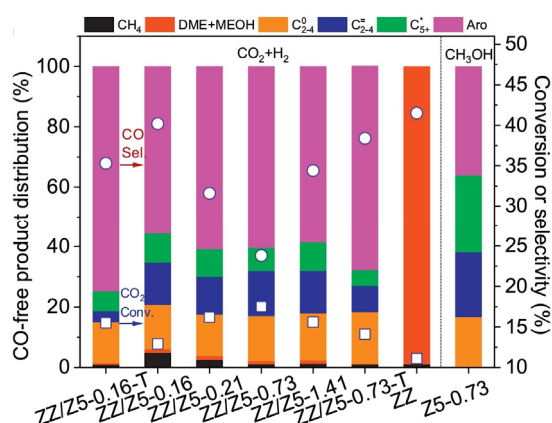


**Figure 63.** Comparisons of the CO<sub>2</sub> conversion and product selectivity over various combination of ZnAlO<sub>x</sub> and H-ZMS-5 catalysts, at 320°C, 3 MPa, WHSV = 6 Lh<sub>·</sub>g<sub>cat</sub><sup>-1</sup>, H<sub>2</sub>/CO<sub>2</sub>/Ar=3/1/0.2. Reprinted with permission from ref.<sup>728</sup>. Copyright 2018, Youming Ni et al.

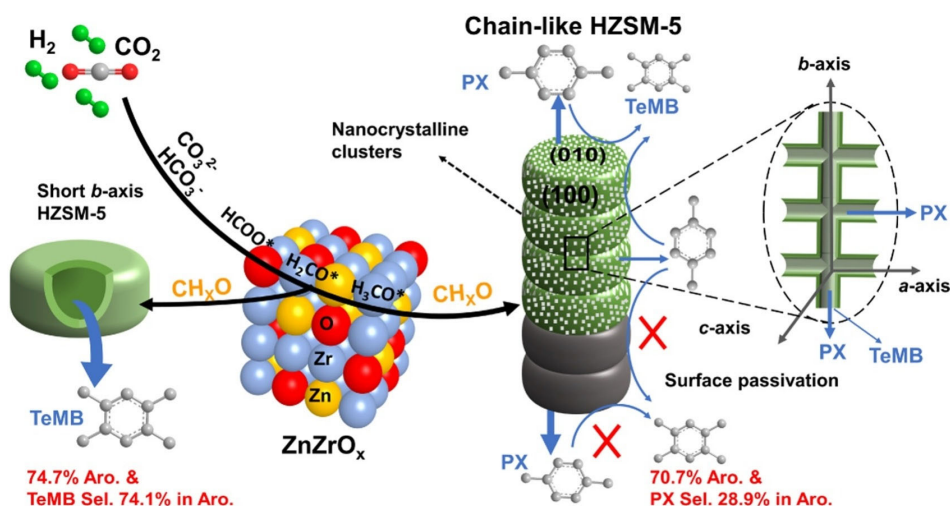
Although good catalytic performance has been reported for the hydrogenation of CO<sub>2</sub> to hydrocarbons, especially, the methanol-mediated route allows to achieve high aromatic

selectivity within the hydrocarbon products in the presence of bifunctional catalysts composed of metal oxides and acid zeolites, the CO selectivity is still too high.

ZnO-ZrO<sub>2</sub>/H-ZSM-5 bifunctional catalysts that have exhibited high catalytic performance to convert selectively syngas to aromatics<sup>80,729</sup> have also been explored for the direct hydrogenation of CO<sub>2</sub> to aromatics. Accordingly, recently, the catalytic performance of a composite consisting of ZnZrO<sub>x</sub> and chain-like nanocrystal HZSM-5 was explored.<sup>730</sup> A series of novel HZSM-5 nanocrystal clusters with chain-like morphology and chain length ranging from 0.16 to 1.41 μm were prepared through the incorporation of different amounts of n-octyltrimethoxysilane. The samples were denoted according to their chainlike morphology length Z5-0.16, Z5-0.21, Z5-0.73, and Z5-1.41. When the CO<sub>2</sub> hydrogenation was carried out over the ZnZrO<sub>x</sub> the main products were methanol (53.8 %) and CO (41.5 %). The use of physical mixtures of ZnZrO<sub>x</sub>/HZSM-5 zeolites allowed the formation of aromatics with selectivity up to 75% (Figure 64). Moreover, the passivation of external surface acid sites of HZSM-5 (with TPAOH) together with the b-axis length allowed enhancing the p-xylene selectivity up to 28.9 %, while shortening the length of b-axis favored tetramethylbenzene (TeMB) production with 74.1% selectivity (Table 9, Entry 2). Characterization study showed that CO<sub>2</sub> activation at the surface oxygen vacancies of ZnZrO<sub>x</sub> enable the hydrogenation to CH<sub>x</sub>O species (formate, formaldehyde, methoxy, methanol), which are further transformed into aromatics at the acid site of HZSM-5. High 76% aromatic selectivity at 17.5% CO<sub>2</sub> conversion, with lower 23.8% CO selectivity over the ZnZrO<sub>x</sub>/HZSM-5 owing to a directional component distribution in the bifunctional catalyst (Figure 65). These results showed that the control of the morphology and the location of the active sites allowed to direct the selectivity of the reaction towards the desired products.



**Figure 64.** Comparisons of the CO<sub>2</sub> conversion and product selectivity over various combination of ZnZrO<sub>x</sub> and H-ZMS-5 catalysts, at 315°C, 3 MPa, H<sub>2</sub>/CO<sub>2</sub>/N<sub>2</sub>=72/24/4, F = 17 mLmin<sup>-1</sup>. Reprinted with permission from ref.<sup>730</sup>. Copyright 2021 Elsevier B.V. All rights reserved.



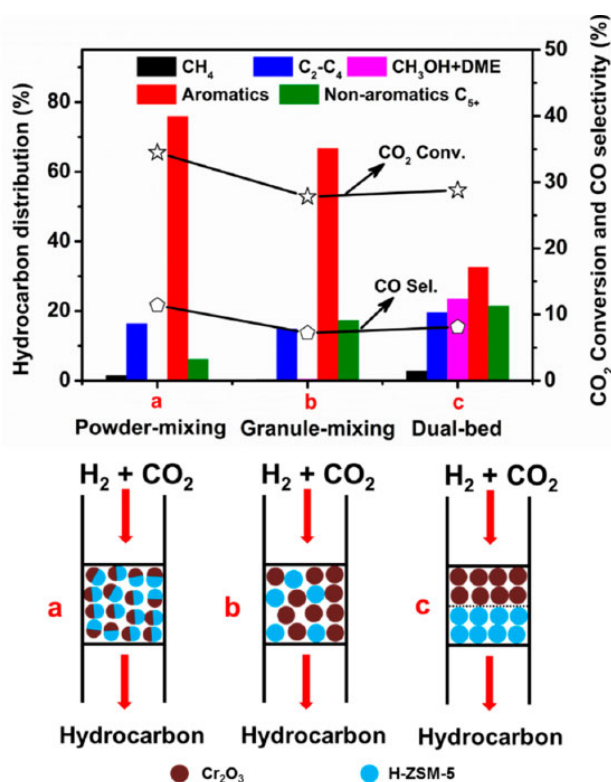
**Figure 65.** Selective hydrogenation of CO<sub>2</sub> to aromatics over ZnZrO<sub>x</sub> and chain-like nanocrystal H-ZSM-5 catalysts. Reprinted with permission from ref.<sup>730</sup>. Copyright 2021, Elsevier B.V. All rights reserved.

Previously, direct CO<sub>2</sub> conversion was carried out over the ZnZrO/ZSM-5 bifunctional catalyst. Tandem catalysis is thermodynamically favorable and enables the selective formation of aromatics through the coupling of CO<sub>2</sub> hydrogenation over ZnZrO to CH<sub>x</sub>O species and aromatics formation over H-ZSM-5. High 70-73% aromatics selectivity at 9-14% CO<sub>2</sub> conversion was reached and the CO selectivity was lowered to 42-44% (Table 9, Entries 3-4).<sup>731,732</sup>

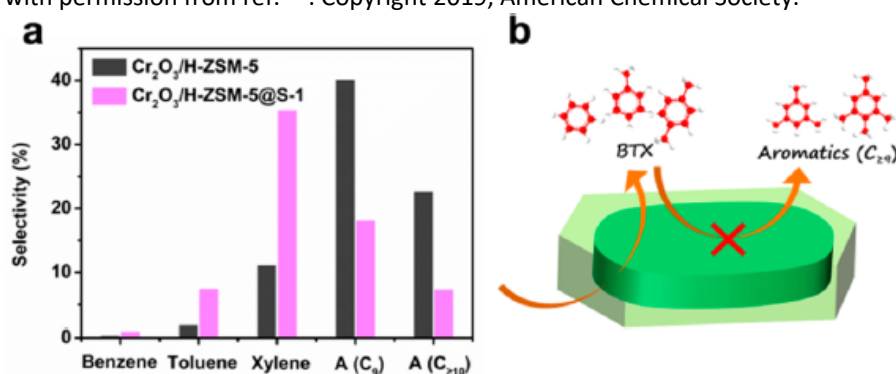
The main drawback of the direct conversion of CO<sub>2</sub> to aromatics is the high CO selectivity (>40%) produced by RWGS reaction. Therefore, an attempt of increasing the oxygen vacancy content has been recently considered in order to promote CO<sub>2</sub> activation and hydrogenation into stable intermediate species and lower RWGS.<sup>733</sup> Indium oxide has been shown to contribute to the formation of vacancy-rich Zn<sub>5</sub>In<sub>2</sub>O<sub>8</sub> oxide<sup>734</sup> that in turn could contribute to the formation of stable methanol intermediate species. Thus, a series of highly efficient bifunctional catalysts consisting of physical mixtures of InZnZrO<sub>x</sub> solid solution and nano-ZSM-5 zeolite were used as bifunctional catalysts to convert CO<sub>2</sub> into aromatics. High 90.6% aromatic selectivity at 13.8% CO<sub>2</sub> conversion was reached with low 19.8% CO selectivity. These results were attributed to the formation of high amount of oxygen vacancies on InZnZrO<sub>x</sub> surfaces, which directly improve CO<sub>2</sub> activation and the formation of CH<sub>x</sub>O intermediates, to the synergistic effect of hydrogenation and acid properties of InZnZrO<sub>x</sub> and H-ZSM-5, respectively, together with the improved mass transfer properties of nanostructured ZSM-5 zeolite for further conversion to aromatics (Table 9, Entry 5).

The conversion of syngas to p-xylene has also been successfully performed over a hybrid catalyst, consisting of ZnCr<sub>2</sub>O<sub>4</sub> spinel and core-shell structured zeolite.<sup>735</sup> Accordingly, the direct conversion of CO<sub>2</sub> to aromatics has been checked over a bifunctional catalyst composed of Cr<sub>2</sub>O<sub>3</sub> and H-ZSM-5 zeolite.<sup>736</sup> High 76% aromatics selectivity with 11.4% CO selectivity was reached at 34.5% CO<sub>2</sub> conversion over the bifunctional Cr<sub>2</sub>O<sub>3</sub>/H-ZSM-5 catalyst that exhibited high over 100

h TOS (Table 9, Entry 6).<sup>736</sup> A study of the effects of the proximity of the different type of active sites revealed that conversion of CO<sub>2</sub> to aromatics was optimum for the closest proximity between Cr<sub>2</sub>O<sub>3</sub> and ZSM-5 (Figure 66, mode a). A prolonged distance between the oxide and zeolite (mode b and c) was prejudicial for the formation of aromatics. A further modification of the zeolite catalyst to passivate the external acid site allowed enhancing the selectivity towards BTX (benzene, toluene, and xylene) avoiding undesirable alkylation and isomerization. For this, a core-shell structured zeolite capsule catalyst was fabricated using H-ZSM-5 as core and neutral silicalite-1 (S-1) as shell. Thus, higher 43.6% BTX selectivity and 25.3%PX selectivity were achieved over Cr<sub>2</sub>O<sub>3</sub>/H-ZSM-5@S-1 catalyst (Figure 67).



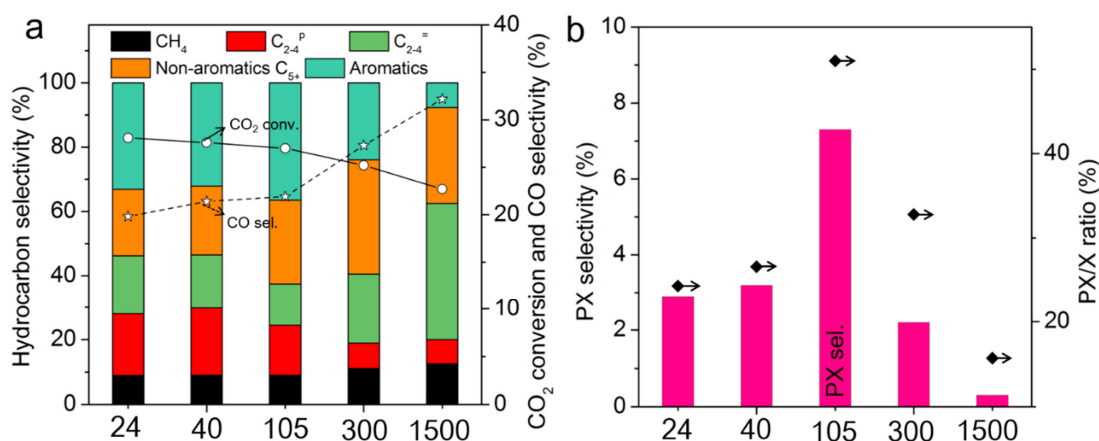
**Figure 66.** Selective hydrogenation of CO<sub>2</sub> to aromatics over Cr<sub>2</sub>O<sub>3</sub>/ZSM-5 catalysts. (a) physical mixing; (b) granule mixing; (c) dual bed. Reaction conditions: 350°C, 3 MPa, H<sub>2</sub>/CO<sub>2</sub>=3, GHSV = 1.2 Lh<sup>-1</sup>.g<sub>cat</sub><sup>-1</sup>. Reprinted with permission from ref.<sup>736</sup>. Copyright 2019, American Chemical Society.



**Figure 67.** Selective hydrogenation of CO<sub>2</sub> to aromatics over Cr<sub>2</sub>O<sub>3</sub>/ZSM-5 and Cr<sub>2</sub>O<sub>3</sub>/H-ZSM-5@S-1 (a) Fractions of products in aromatics, (b) scheme of highly selective production of BTX over Cr<sub>2</sub>O<sub>3</sub>/H-ZSM-5@S-1 catalysts. Reprinted with permission from ref.<sup>736</sup>. Copyright 2019, American Chemical Society.

Similar strategy was followed to prepare a bifunctional catalyst based on core-shell structured Zn-doped HZSM-5 (Zn-ZSM-5@SiO<sub>2</sub>) and a Cr<sub>2</sub>O<sub>3</sub> oxide.<sup>737</sup> A control of the acidity of Zn-ZSM-5@SiO<sub>2</sub> allowed improved the para-xylene selectivity up to 38.7% at 22.1% CO<sub>2</sub> conversion (Table 9, Entries 7-8).

More recently, an efficient solvent-free method was reported for the preparation of capsule-like zeolite catalyst (HZSM-5@Silicalite-1-S) for the selective hydrogenation of CO<sub>2</sub> to para-Xylene. A study of the effects of the configuration modes of Na-FeMn and HZSM-5@S1-S core-shell zeolite over the catalytic performances was performed.<sup>738</sup> The best catalytic performance was achieved for the granule-mixing 2.83Na-FeMn (90/10) and HZSM-5@S1-S zeolite without quartz stand, with 17% aromatics selectivity and 75.4% para-Xylene (among xylenes). This was attributed to the efficient mass transfer of intermediates to the micropores of HZSM-5@S1. After optimization of the Na-FeMn and HZSM-5@S1-S ratio (1/2), maximum 81.1% para-Xylene (among xylenes) was achieved, which was higher than ones achieved over above described core-shell zeolite (HZSM-5@SiO<sub>2</sub> and HZSM-5@S-1-S) (Figure 68, Table 9, Entry 9).



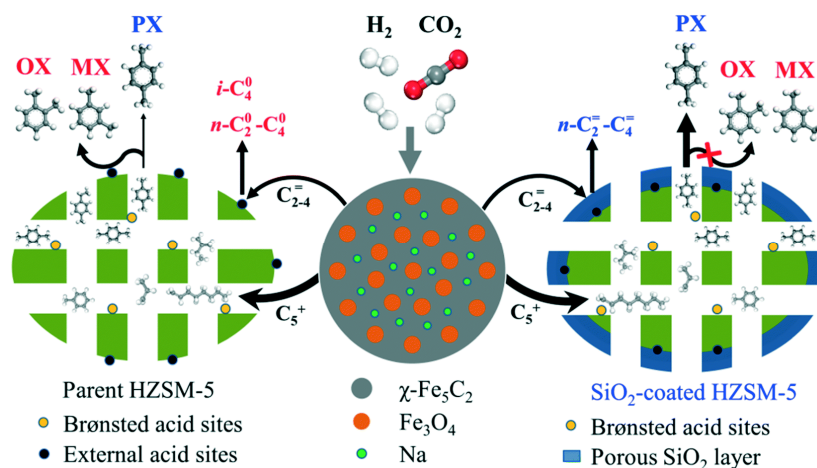
**Figure 68.** Selective hydrogenation of CO<sub>2</sub> to aromatics over Na-FeMn and HZSM-5@S1-S with different iron/zeolite mass ratios (granule-mixing). Reprinted with permission from ref.<sup>738</sup>. Copyright 2021, Elsevier B.V. All rights reserved.

b) Direct hydrogenation of CO<sub>2</sub> to aromatics via modified FTS

Iron-based catalysts have been widely studied for the catalytic conversion of CO<sub>2</sub> via modified FTS due to its properties to catalyze both the RWGS and FTS reactions.<sup>739,740</sup> Under working reaction conditions, iron based catalysts exhibit Fe<sub>3</sub>O<sub>4</sub> active sites for RWGS and Fe<sub>5</sub>C<sub>2</sub> active sites for FTS.<sup>741</sup> Moreover, the addition of alkali metals such as K and Na allowed improving the effectiveness of iron catalysts owing to improved surface carburization and weakened secondary hydrogenation ability of olefins.<sup>742</sup> On the other hand, the addition of Zn allowed promoting FTS, catalyst stability as well as light olefins selectivity owing to the formation of ZnFe<sub>2</sub>O<sub>4</sub> spinel phase and the ZnO phase, that induced an increase of the surface area, improve the Fe-Zn interaction, and modify the redox and adsorption properties.<sup>743</sup> On all of the above, a

series of Fe-Zn catalysts promoted by K were prepared and combined with ZSM-5 zeolites for the direct conversion of CO<sub>2</sub> to olefins and aromatics.<sup>744</sup> Moreover, to improve aromatic selectivity, the morphology of H-ZSM-5 zeolites was modified by treatment with NaOH solution, which could form a hollow structure in the zeolite channel and thus reduce the residence time of aromatic intermediates in the channel, which not only improved the aromatic yield, but also prevented the over-hydrogenation of hydrocarbons. Thus, 45.2% aromatic selectivity was reached at 42.6% CO<sub>2</sub> conversion over K-3Fe/Zn-H-ZSM-5 (Table 9, Entry 10). These results showed that an efficient bifunctional catalyst can be rationally designed and constructed by modifying the component composition and zeolite morphology to directly and selectively convert CO<sub>2</sub> to aromatics.

Similarly, the catalytic performance of tandem catalyst composed by Na/Fe and HZSM-5 catalyst system was explored for the direct and selective production of aromatics from CO<sub>2</sub>.<sup>745</sup> A 94% aromatics selectivity from hydrocarbon products was reached over under industrially relevant conditions, with para-xylene selectivity up to 70% for Na/Fe and SiO<sub>2</sub>-coated HZSM-5 zeolite bifunctional catalyst (Table 9, Entries 11-12). Results of experiments and DFT calculations revealed that the Na-promoted Fe catalyst and HZSM-5 with high Brønsted acidity are key factors for enhancing the CO<sub>2</sub> conversion and aromatics synthesis, while the SiO<sub>2</sub>-coated HZSM-5 zeolite allowed suppress the isomerization of the initially formed p-xylene and p-ethyltoluene in the zeolite channels when they diffuse out of the channels onto the external SiO<sub>2</sub>-coated surface (Figure 69).



**Figure 69.** Reaction routes for CO<sub>2</sub> hydrogenation to aromatics over the composite Na/Fe-HZSM-5 and Na/Fe-SiO<sub>2</sub>-coated HZSM-5 catalysts. Reprinted with permission from ref.<sup>745</sup>. Copyright 2019, Royal Society of Chemistry.

A long 100 h test over the composite catalyst system showed that the Na/Fe catalyst exhibited good stability activity for both the RWGS and FTS reactions with CO<sub>2</sub> conversion and CO selectivity to CO almost stable and around 30% and 27%, respectively. Unfortunately, the content of aromatics amount liquid hydrocarbons decreased from 91.6% (



to 70.3% as well as the selectivity to p-xylene in the xylenes that decreased from 69% to 57%. The decrease in aromatic was attributed to the coke formation over coated-HZSM-5 zeolite with time on stream that implies lower activity for aromatization due to lower amount of acid active sites, which led to the gradual increase of non-aromatic hydrocarbon products.

#### 5.7.5. Conclusion

CO<sub>2</sub> hydrogenation to gasoline, olefins and aromatics offers new opportunities to convert CO<sub>2</sub> into value-added products and pave a path to the CO<sub>2</sub> circularity. In the last decade, significant advances in the development of tandem catalysts based on metal oxides and zeolites have been made for the selective hydrogenation of CO<sub>2</sub> to lower olefins (C<sub>2</sub>-C<sub>4</sub>), gasoline (C<sub>5</sub>-C<sub>11</sub>) and aromatics (C<sub>6</sub>-C<sub>8</sub>) of wide interest for the chemical industry.

The high activity of heterogeneous catalyst is usually attribute to the synergy between the active sites and the support and/or the promoter. Nevertheless, the nature of the active sites responsible of the activation of CO<sub>2</sub> and H<sub>2</sub> and the intermediates species and reaction mechanisms are still elusive. Undoubtedly, the systematic study and understanding of the reaction mechanism, kinetics, thermodynamics, determination of reaction intermediates and active species due to the advantages of computational chemistry, and in situ and operando spectroscopy should allow a great understanding, to help to rationalize experimental results and thus the design of new efficient tandem metal oxide/zeolite catalysts and processes.

Besides the hydrogenation of CO and CO<sub>2</sub> on metal oxide surfaces followed the same mechanism involving formate and methoxide species, the cofeeding of CO<sub>2</sub> and CO offers also interesting strategy to lower CO formation by RWGS and maximize yield and selectivity to hydrocarbon products.

Moreover, the hydrogenation of CO<sub>2</sub> to hydrocarbons requires further development and improvement of catalyst activity, selectivity and stability for industrial application. Long test of catalyst stability should be perform as well as of regeneration. Since CO<sub>2</sub> conversion remains low, study of recycling is necessary. While in the case of gasoline and aromatics, the separation should be easier, for lower olefins would be a challenging issue.

In the same way, improvement of process selectivity are still required and challenging and should avoid expensive separation step. Thus, new studies for the specific modifications of zeolite morphology such as pore-size tuning and the poisoning of external acid sites, should allow controlling the hydrocarbon product selectivity.

As mentioned above, CO<sub>2</sub> large-scale transformation will depend on CO<sub>2</sub> availability and so on the capture technique, and H<sub>2</sub> production that will be green to ensure a CO<sub>2</sub>-neutral process and

a sustainable effective approach to the production of hydrocarbons. Undoubtedly, the future tandem catalyst for direct hydrogenation of CO<sub>2</sub> to C<sub>2+</sub> will be based on zeolite-type material.

**Table 8.** Catalytic results of zeolite-based catalyst for CO<sub>2</sub> hydrogenation to lower olefins through several routes.

Entry	Catalysts	$\chi_{\text{CO}_2}$ %	Selectivity %		HC* distribution				Reaction conditions	Year	Ref
			CO	HC*	CH <sub>4</sub>	C <sub>2</sub> -C <sub>4</sub>	C <sub>2</sub> <sup>-</sup> -C <sub>4</sub> <sup>-</sup>	C <sub>5+</sub>			
1	ZnO-ZrO <sub>2</sub> /SAPO-34	12.6	47	53	3	14	80	3	380°C, 2 MPa, H <sub>2</sub> /CO <sub>2</sub> =3, WHSV=3.6 Lh <sup>-1</sup> g <sub>cat</sub> <sup>-1</sup>	2017	725
2	In <sub>2</sub> O <sub>3</sub> -ZrO <sub>2</sub> /SAPO-34	35.5	85	15	4	12	80	4	400°C, 3 MPa, H <sub>2</sub> /CO <sub>2</sub> /N <sub>2</sub> =73/24/3, WHSV=9 Lh <sup>-1</sup> g <sub>cat</sub> <sup>-1</sup>	2018	726
3	ZnGa <sub>2</sub> O <sub>4</sub> /SAPO-34	13	46	54	1	10	86	3	370°C, 3 MPa, F=45 mL min <sup>-1</sup> , H <sub>2</sub> /CO <sub>2</sub> =3	2018	727

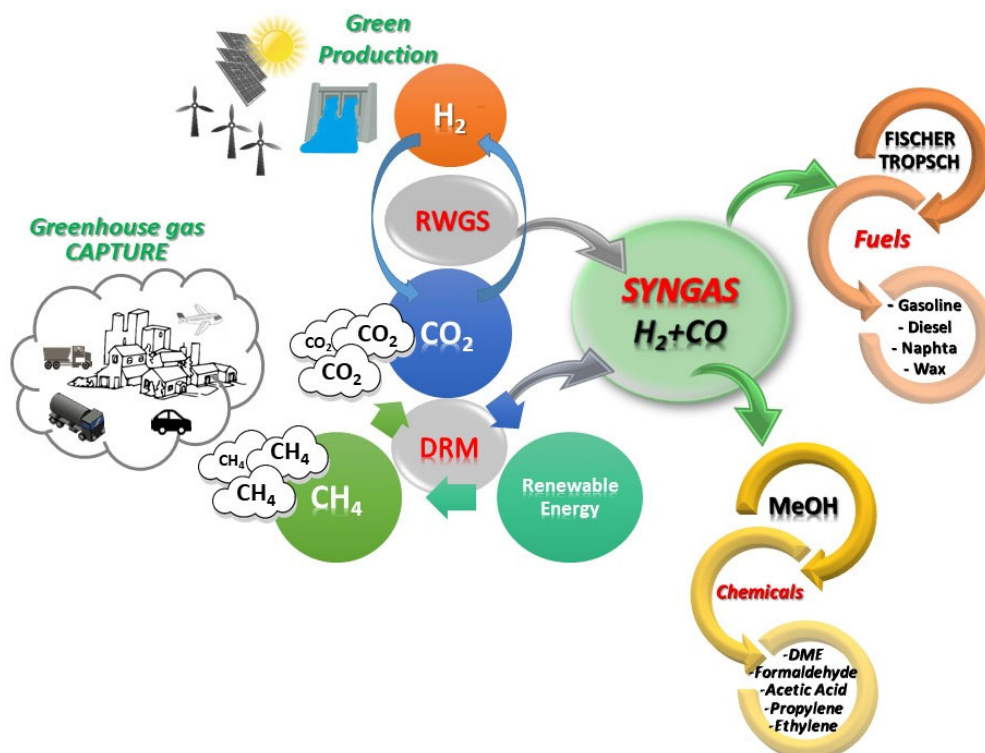
\*HC:hydrocarbons

**Table 9.** Catalytic results of zeolite-based catalyst for CO<sub>2</sub> hydrogenation to lower aromatics through several routes.

Entry	Catalysts	$\chi_{\text{CO}_2}$ %	Selectivity %			HC* distribution			Reaction conditions	Year	Ref
			CO	HC*	CH <sub>4</sub>	C <sub>2</sub> -C <sub>4</sub>	C <sub>2</sub> -C <sub>4</sub>	Ar.*			
<b><i>Methanol mediated route</i></b>											
1	ZnAlO <sub>x</sub> /H-ZMS-5	9.1	57.4	42.6	0.4	9.6	10	73.9	320°C, 3 MPa, WHSV=6 Lh <sup>-1</sup> g <sub>cat</sub> <sup>-1</sup> , H <sub>2</sub> /CO <sub>2</sub> /Ar=3/1/0.2	2018	728
2	ZnZrO <sub>x</sub> /H-ZMS-5	17.5	35	65	0.5	17	2.5	75	315°C, 3 MPa, H <sub>2</sub> /CO <sub>2</sub> =3:1, WHSV=1.02 Lh <sup>-1</sup> g <sub>cat</sub> <sup>-1</sup>	2021	730
3	ZnZrO/ZSM-5	14	44	56	0.3	14.7	5	73	320°C, 4 MPa, WHSV=1.2 Lh <sup>-1</sup> g <sub>cat</sub> <sup>-1</sup> , H <sub>2</sub> /CO <sub>2</sub> =3	2019	731
4	ZnZrO/ZSM-5	9.1	42.5	57.5	0.6	11.4	10	70	340°C, 3 MPa, WHSV=2.7 Lh <sup>-1</sup> g <sub>cat</sub> <sup>-1</sup> , H <sub>2</sub> /CO <sub>2</sub> =3	2019	732
5	InZnZrO <sub>x</sub> /ZMS-5	13.8	19.8	81.2	0.19	6	1.5	90.6	330°C, 3 MPa, WHSV=4 Lh <sup>-1</sup> g <sub>cat</sub> <sup>-1</sup> , H <sub>2</sub> /CO <sub>2</sub> =3	2022	733
6	Cr <sub>2</sub> O <sub>3</sub> /ZSM-5	34.5	11.4	88.6	1.5	15	1.5	76	350°C, 3 MPa, H <sub>2</sub> /CO <sub>2</sub> =3, GHSV=1.2 Lh <sup>-1</sup> g <sub>cat</sub> <sup>-1</sup>	2019	736
7	Cr <sub>2</sub> O <sub>3</sub> /Zn-ZSM-5	16	38.2	61.8	3.9	15.6	9.8	67.9	350°C, 3 MPa, H <sub>2</sub> /CO <sub>2</sub> =3, GHSV=1.2 Lh <sup>-1</sup> g <sub>cat</sub> <sup>-1</sup>	2019	737
8	Cr <sub>2</sub> O <sub>3</sub> /Zn-ZSM-5@SiO <sub>2</sub>	22.1	35.1	64.9	4.5	16.4	6.2	70.1	GHSV=1.2 Lh <sup>-1</sup> g <sub>cat</sub> <sup>-1</sup>	2019	737
9	Na-FeMn/HZSM-5@S1-S	22	24	76	11	17	28	24	320°C, 3.0 MPa, H <sub>2</sub> /CO <sub>2</sub> =3, WHSV=4 Lh <sup>-1</sup> g <sub>cat</sub> <sup>-1</sup>	2022	738
<b><i>Modified FTS route</i></b>											
10	K-3Fe/Zn-H-ZSM-5	42.6	10.1	89.1	12.5	3.2	6.9	45.2	320°C, 3 MPa, W/F=6 ghmol <sup>-1</sup> , H <sub>2</sub> /CO <sub>2</sub> /Ar=71.2:25.1:3.7	2022	744
11	Na/Fe-SiO <sub>2</sub> -coated HZSM-5 (10 h)								340°C, 1.0 MPa, H <sub>2</sub> /CO <sub>2</sub> =3, WHSV=4.8 Lh <sup>-1</sup> g <sub>cat</sub> <sup>-1</sup>	2019	745
12	(100 h)										

\*Ar=aromatics

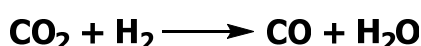
On the path to greenhouse gas mitigation, the CO<sub>2</sub> transformation into syngas constitutes a winning approach towards the sustainable production of chemicals and fuels. Further syngas conversion into MeOH or hydrocarbons allow reducing the CO<sub>2</sub> emission and is a direct route for the production of fuels and chemicals through technologies already explored, developed and implemented (Figure 70).



**Figure 70.** Scheme of renewable SYNGAS production from greenhouse gas capture and conversion into fuels and chemicals.

## 6.1. Catalytic reduction of CO<sub>2</sub> with hydrogen (RWGS)

### 6.1.1. Introduction



**Scheme 57.** RWGS reaction.

The conversion of CO<sub>2</sub> to CO via a reverse water gas shift (RWGS) reaction has been widely explored due the availability of technologies such as Fischer-Tropsch and methanol synthesis to further convert CO into chemicals and fuels (Scheme 57; Figure 71).<sup>98,746,747</sup> Indeed, a sustainable and renewable production of syngas will guarantee the sustainability of Fischer-Tropsch process. On the other hand, RWGS is an important reaction that can occur during several CO<sub>2</sub> conversion process such as methanation, as a possible first step for CO<sub>2</sub> activation.<sup>748</sup> Then, the main issues of RWGS reaction are the competitive CO<sub>2</sub> methanation, and methanol formation limiting CO yield.<sup>749</sup> RWGS is an endothermic process and due to stability and inertness of the CO<sub>2</sub> molecule high reaction temperature (500°C) is required to produce CO and H<sub>2</sub>O.<sup>646</sup> From thermodynamics

standpoint, low pressures allow to limit methanol synthesis<sup>358</sup> and high temperatures favour RWGS reaction and practically inhibit the high exothermic methanation.<sup>573,750</sup> Nevertheless, for economic and environment considerations, lower temperatures are desired and avoiding CO<sub>2</sub> methanation becomes a great challenge since methane is then a common side product.<sup>749</sup> Up to now, the RWGS has not been industrialized due to high energy consumption and industrial costs.<sup>751</sup> Precisely, the thermal design and optimization of the reactor is of paramount importance and heat energy will have to be produced from renewable or nuclear sources to minimize carbon footprint. Actually, only one industrial application in the tandem reaction of methanol synthesis, in the CAMERE process for RWGS process, has been implemented.<sup>752–754</sup>

### 6.1.2. Mechanism

In-situ characterization techniques are key to determine the formation and nature of intermediates and adsorption strength on the catalyst surface. Then, techniques such as transient quantitative temporal analysis of products (TAP), ATR-FT-IR or DRIFT spectroscopy and micro-calorimetry, as well as the use of isotopic kinetic studies to follow the evolution of intermediates have been used. The combination of in-situ characterization techniques together with kinetic computational DFT calculations and modelling are essential for the elucidation of reaction mechanisms, the nature of the active sites involved and the rational design and development of efficient and selective catalysts.<sup>313</sup> For CO<sub>2</sub> adsorption and activation, the catalytic surface properties, and more specifically, the redox and acid/base properties of the support play a fundamental role in the formation of intermediates. Supports with oxygen vacancies such as TiO<sub>2</sub> or CeO<sub>2</sub> in contrast to Al<sub>2</sub>O<sub>3</sub> or SiO<sub>2</sub> allow strong adsorption and activation of CO<sub>2</sub> molecule and when an oxygen vacancy is in proximity to a metal site with adsorbed and dissociated H, it enhances the activity for RWGS process.<sup>750,755,756</sup>

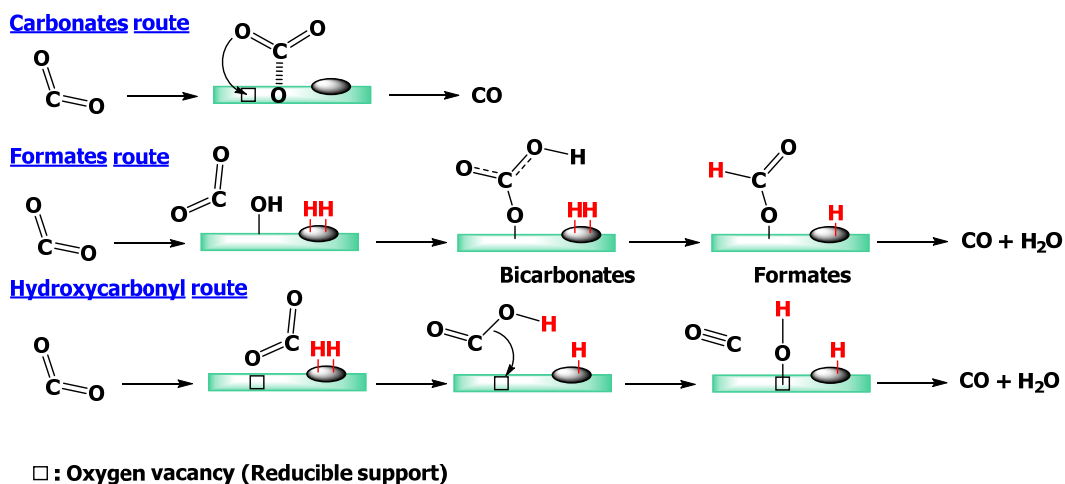
The RWGS mechanism has been studied on several metal supported catalysts, and different possible pathways for CO<sub>2</sub> conversion, as presented below, have been proposed mainly based on the CO<sub>2</sub> adsorption and reaction with dissociated H to form different intermediate species (formate, hydroxycarbonyl, bicarbonates) or to be reduced directly into CO (Scheme 58; Figure 71)<sup>755</sup>:

- The carbonate route via CO<sub>2</sub> adsorption over the surface to form carbonates that react with oxygen vacancies of a reducible support (TiO<sub>2</sub>, CeO<sub>2</sub>)<sup>756</sup>
- The formate route via the adsorption on OH groups present on the surfaces (Al<sub>2</sub>O<sub>3</sub>)
- The hydroxycarbonyl route<sup>757</sup> after hydrogenation of CO<sub>2</sub> at lower temperature

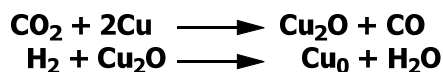
Another mechanism was proposed for catalysts containing reducible oxides and originally for Cu that can be readily reduced and oxidized under reaction conditions. In that case a metal (Cu) is

oxidized by CO<sub>2</sub> and reduced again by H<sub>2</sub>. This redox mechanism or direct CO<sub>2</sub> dissociation over Cu-based catalysts involved the Cu<sup>0</sup> oxidation into Cu<sup>+</sup> by CO<sub>2</sub> reduced into CO, while H<sub>2</sub> reduces Cu<sup>+</sup> to form H<sub>2</sub>O (Scheme 59).<sup>758,759</sup>

However, the formate formation and decomposition to CO production is a widely accepted pathway mechanism in which firstly CO<sub>2</sub> is hydrogenated into formate and afterwards the cleavage of C-O bond takes place, while the carbonyl route by dissociation of CO<sub>2</sub> into CO over the metal was ruled out for metal based catalysts on reducible support such as TiO<sub>2</sub> or CeO<sub>2</sub>.



Scheme 58. Possible proposed routes for the formation of CO over different types of support and active sites.<sup>755,757</sup>



Scheme 59. Redox mechanism or direct CO<sub>2</sub> dissociation over Cu-based catalysts.

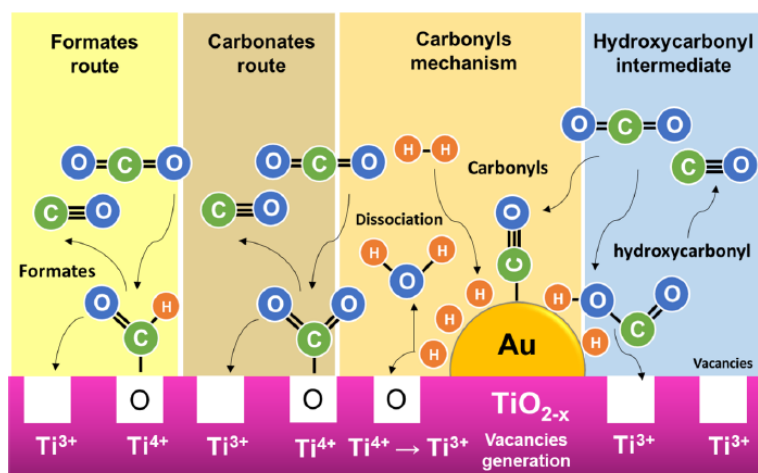


Figure 71. Representation of the different mechanism pathways over Au/TiO<sub>2</sub>. Reprinted with permission from ref. <sup>755</sup>. Copyright 2018, American Chemical Society.

### 6.1.3. Catalysts for RWGS process

The design and development of highly active and selective solid catalysts for RWGS reaction should include the presence of well-defined multiple active sites combined with molecular

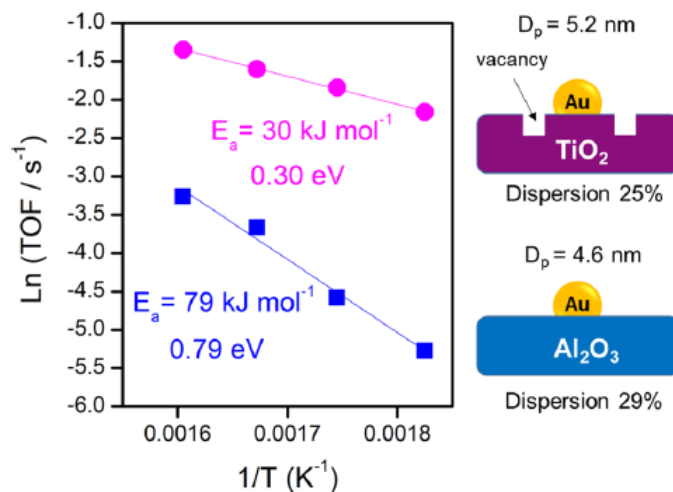
selection through controlled adsorption, interactions and geometrical parameters that will lead to the formation of intermediates and transition-state stabilization. Accordingly, an efficient catalyst for RWGS reaction requires:

- Active sites for the adsorption of CO<sub>2</sub> and cleavage of C–O bond but limited CO adsorption to avoid CO dissociation and subsequent hydrogenation into methane or CO hydrogenation into methanol. Therefore to obtain an active and selective catalyst for CO<sub>2</sub> reduction into CO, optimal catalytic properties should be adjusted to adsorb and activate CO<sub>2</sub>, but not CO, by controlling the physicochemical properties of the support such as the presence of oxygen vacancies and/or of a promoter.

- Active sites (transition metal) for H<sub>2</sub> dissociation and hydrogenation of released O (CO<sub>2</sub>) to produce H<sub>2</sub>O. Maximum metal activity should be achieved with suitable metal dispersion by selecting optimal support and/or the addition of a promoter.

In the literature, the most frequently metals used for the development of catalysts for RWGS process are Cu, Pt, and Rh supported on different type of supports (SiO<sub>2</sub>, Al<sub>2</sub>O<sub>3</sub>, TiO<sub>2</sub>, CeO<sub>2</sub>) whose reducibility and acid-base properties play a key role over the activation of CO<sub>2</sub> molecules and the reaction mechanism.<sup>760</sup> Among them, the most commonly used catalyst for RWGS process is Cu-ZnO/Al<sub>2</sub>O<sub>3</sub> at low temperature (170-250°C) where high Cu dispersion was achieved.<sup>759,761,762</sup> The advantage to prepare Cu-based catalysts is that Cu exhibits high catalytic activity at low temperature for H<sub>2</sub> dissociation with low methane production.<sup>758,763–766</sup> Likewise, no CH<sub>4</sub> production was observed over Au- and Cu- based catalysts.<sup>447,755</sup> For CO<sub>2</sub> adsorption and activation, the physicochemical properties of the support play a fundamental role and influence the formation of intermediates as above mentioned. Then, irreducible supports such as Al<sub>2</sub>O<sub>3</sub> or SiO<sub>2</sub> mainly enable high dispersion of the metal while support with oxygen vacancy such as TiO<sub>2</sub> or CeO<sub>2</sub> allow strong adsorption and activation of CO<sub>2</sub>, while the presence of an oxygen vacancy closely to a metal site with adsorbed and dissociated H, allows enhancing the activity for RWGS process, as it was indicated by the differences in the activation energy for Au/TiO<sub>2</sub> and Au/Al<sub>2</sub>O<sub>3</sub> that imply different rate-determining steps (Figure 72).<sup>755</sup> Numerous catalytic systems have been reported in the literature for RWGS reaction,<sup>755,760,767</sup> and despite their huge potential to envelop or support metal nanoparticles, oxide mixtures, their high thermal stability, robustness and versatility in chemical composition, metal-based zeolites and OMS have been under-exploited to perform RWGS reaction, and few references have been collected.





**Figure 72.** Arrhenius plot for the Au/Al<sub>2</sub>O<sub>3</sub> and Au/TiO<sub>2</sub> catalysts in the RWGS reaction illustrate the differences in the activation energy. Reprinted with permission from ref. <sup>755</sup>. Copyright 2018, American Chemical Society.

a) Oxide-based catalysts for RWGS

i) *Monometallic oxide-based catalyst for RWGS*

Nickel finds numerous applications for CO<sub>2</sub> conversion due to its high activity, and its abundance and low price with respect to other metals. As demonstrated for the synthesis of DME, the use of ordered mesoporous materials has allowed to achieve a high dispersion of active metal centers following the optimized synthesis pathway.<sup>768–770</sup> Accordingly, a novel hydrophobic encapsulation strategy was described for the preparation of monodispersed NiO particles in SBA-15 by direct hydrothermal synthesis method.<sup>770,771</sup> The results showed that NiO content affected CO selectivity at lower temperature though high NiO loading was required to achieve high CO<sub>2</sub> conversion and 100% CO selectivity as it was previously reported (Table 8, Entries 1-3).<sup>770</sup> The high surface area and the mesoporous channels of MCM-41 was also advantageously used for the preparation of new RWGS catalysts. A direct hydrothermal synthesis route allowed preparing well-ordered mesoporous silica incorporating transition metals, Ni, Cu, Zn, Co with a high Si/metal ratio of 5. Ni-MCM-41, Cu-MCM-41 and Co-MCM-41 catalysts showed good catalytic activity for CO<sub>2</sub> conversion into CO while Zn-MCM-41 exhibited very low catalytic performance. The activation energy values obtained for the different samples showed that Ni-MCM-41 catalytic activity for CO<sub>2</sub> hydrogenation was up to seven times higher than Co-MCM-41 and Cu-MCM-41 materials with high selectivity to CO<sub>2</sub> methanation whereas no methanation was observed for Cu-MCM-41. Cu-MCM-41 catalyst exhibited the best catalytic properties for RWGS with maximum CO selectivity at 550°C.<sup>772</sup> Co-MCM-41 and Ni-MCM-41 materials exhibited high catalytic activity although showed lower CO selectivity, 95 and 70%, respectively (Table 7, Entries 4-7). Fe-KIT-6 prepared by direct hydrothermal synthesis with different Fe loadings showed well-ordered cubic structures and its structural integrity was

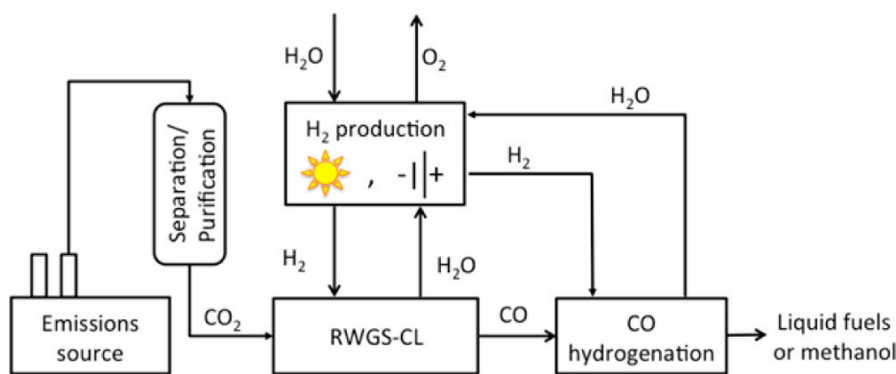
preserved for Si/Fe ratios up to 10.<sup>773</sup> Characterization of the Fe-KIT-6 sample (Si/Fe=30) by EPR and XPS spectroscopy showed that Fe was present as tetrahedrally coordinated iron atoms in the KIT-6 framework, although the presence of extra-framework species/small iron oxide clusters could not be discarded. Fe-KIT-6 sample with a higher Fe content exhibited the best catalytic performance for the RWGS reaction being the rate of hydrogenation a direct function of the amount of iron active sites and the reaction temperature, so high iron content favoured the methanation. Therefore, 97% CO selectivity at low 16% CO<sub>2</sub> conversion were reached at 500°C over Fe-KIT-6 (Si/Fe= 10) (Table 10, Entry 8).

*ii) Bimetallic OMS-based catalysts for RWGS*

As aforementioned for methane, methanol or dimethylether synthesis, the addition of promoters allows modifying the CO<sub>2</sub> adsorption capacity and activation, the reducibility, dispersion and stability of the metal, and the formation of new active species at the interface metal/support.<sup>519,774–776</sup> The promoter can be a reducible transition metal oxide with oxygen vacancies such as TiO<sub>2</sub> or CeO<sub>2</sub> that play a key role for the CO<sub>2</sub> activation, or a second metal such Fe, Co, Ni Cu, Zn etc.<sup>750,763</sup>

Accordingly, the catalytic performance of bimetallic CuO-NiO/SAB-15, NiO-CeO<sub>2</sub>/SBA-15 and CuO-CeO<sub>2</sub>/SAB-15 materials synthesized by direct hydrothermal method in a strongly acidic medium was investigated. TEM-EDX analysis and characterization data revealed that for bimetallic materials, in the case of NiO and CeO<sub>2</sub> both oxides were simply mixed and well dispersed on SBA-15, in the case of CeO<sub>2</sub> and CuO, CeO<sub>2</sub> was covered by CuO while in the case of CuO and NiO, both oxides were separately well-dispersed on SBA-15. Compared with monometallic oxide/SBA-15, the obtained bimetallic oxides/SBA-15 catalysts exhibited excellent efficiency in terms of reducing CO<sub>2</sub> to CO via RWGS reaction and the CO<sub>2</sub> conversion increased with temperature for all mono and bimetallic catalysts. Moreover, CO<sub>2</sub> conversion over bimetallic samples was higher than over monometallic ones. These results were attributed to the strong electronic interaction between metal active sites and the promoter, and/or the promoter and the reactant (CO<sub>2</sub>), that favour RWGS reaction at lower temperature. Thus, CeO<sub>2</sub> doping allowed improving the catalytic properties of CuO and NiO owing to the presence of oxygen vacancies enhancing CO<sub>2</sub> conversion. All the prepared mono and bimetallic catalysts exhibited 100% CO selectivity regardless the temperature, except NiO-CeO<sub>2</sub>/SBA-15 which showed higher catalytic activity than all catalysts, at lower temperature, but lower selectivity, in the temperature range of 400-700°C due to methane production. However, at T°C>700, the best catalytic performance was reached over NiO-CeO<sub>2</sub>/SBA-15, and 100% CO selectivity and maximum 55% CO<sub>2</sub> conversion were achieved at 900°C (Table 10, Entries 9-14).<sup>777</sup>

Solid materials able to store and release oxygen reversibly at moderate temperatures are named oxygen storage materials (OSM) or oxygen carrier. OSM usually composed by transition metal oxides have received attention in the last decades for the combustion of fuels with CO<sub>2</sub> capture (as oxidant)<sup>778</sup> and for RWGS<sup>779</sup> through chemical looping, involving cyclic reduction and oxidation with oxygen storage materials (OSM). Thus, numerous studies have investigated RWGS-chemical looping (REWGS-CL) involving cyclic reduction and oxidation of oxygen storage materials (OSM) in order to maximize the efficiency of renewable H<sub>2</sub>, captured CO<sub>2</sub> and the further CO conversion into fuels and methanol (Figure 73).



**Figure 73.** Overall process of CO<sub>2</sub> capture and conversion on H<sub>2</sub>-reduced oxides in the RWGS for further convert CO into fuels or methanol. Reprinted with permission from ref.<sup>779</sup>. Copyright 2014, American Chemical Society.

The RWGS-CL reaction is divided in two consecutive reduction and oxidation steps and the oxide material has to be able to form oxygen vacancies, adsorb and activate CO<sub>2</sub> to exchange oxygen and produce CO and to be further reduced under H<sub>2</sub> flow with water production (Scheme 60).<sup>779,780</sup>



**Scheme 60.** Cyclic reduction and oxidation of oxygen storage materials (OSM).

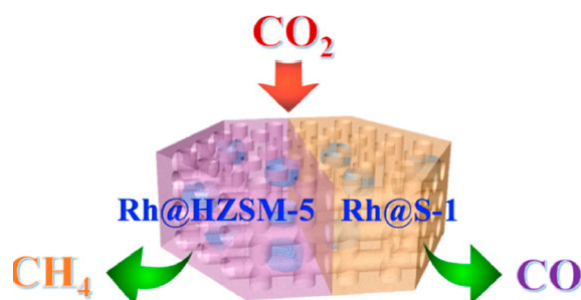
The challenge is the design of an oxide material with high capacity to generate oxygen vacancies and stable over numerous cycles being the main drawback the metal oxide sintering at high temperature. Perovskite-type oxides (ABO<sub>3</sub>) offer numerous synthesis and composition opportunities for matching and optimizing the redox abilities.<sup>779,781–783</sup> Due to their potential, perovskite oxides have been studied as potential catalysts for RWGS-chemical looping and specifically, the La<sub>0.75</sub>Sr<sub>0.25</sub>FeO<sub>3</sub> (LSF) perovskite.<sup>784–786</sup> However there is a limitation derived from the low surface area of the perovskites and different strategies have been followed to disperse perovskite on support or to form composites. Accordingly, perovskite oxide (LSF) was supported on SBA-15 by addition of SBA-15 to the sol-gel perovskite synthesis media. The final material was tested for RWGS-chemical looping, and the CO yield was improved up to 10 times in the

presence of LSF/SBA-15 material in comparison to pure LSF. Nevertheless, the CO yield was low and between 2.5 and 3.6 mmol/g<sub>LSF</sub> at 700°C (Table 10, Entries 15-20). This attempt of supported perovskite oxides can be of interest for further studies.<sup>787</sup>

b) Zeolite-based catalysts for RWGS

i) *Monometallic zeolite-based catalysts for RWGS*

It has been demonstrated that the local environment of an active site influences strongly the activity and selectivity of a given reaction by adsorption and for stabilization of a reaction transition state on solid catalysts.<sup>788</sup> Moreover, Rh is well-known to exhibit high activity for CO<sub>2</sub> hydrogenation. Therefore, a recent study explored the effect of the surroundings of Rh nanoparticles over the CO<sub>2</sub> hydrogenation selectivity towards methane or CO production.<sup>789</sup> In the case of zeolites, the neighbouring of the Rh metal nanoparticles could be varied by changing the framework composition and/or the zeolite structure. Then, a new and efficient strategy for the preparation of supported metal nanoparticles with high resistance to sintering by fixing the nanoparticles within zeolite crystals by seed-directed growth technique was carried out.<sup>790</sup> Therefore, the Rh nanoparticles were enveloped within the crystals with defined and specific environment controlled by zeolite composition (Si/Al ratio) that determines the hydrogenation pathway towards methanation or RWGS. Catalytic data showed that in the presence Rh@S-1 (pure silica, silicalite 1) maximum 79.8% CO selectivity with 51.6% CO<sub>2</sub> conversion were reached, while in the presence of Rh@ZSM-5 (Si/Al=30) 98.2% CH<sub>4</sub> selectivity with 68.2% CO<sub>2</sub> conversion were achieved, under the same reaction conditions (Table 10, Entries 21-22; Figure 74). In operando IR measurements allowed attributing these results to limited hydrogen spillover due to the absence of acid sites and fast CO desorption over Rh@S-1 catalyst. These results offers new opportunities for the rational design of efficient and selective catalyst for a well-defined process.

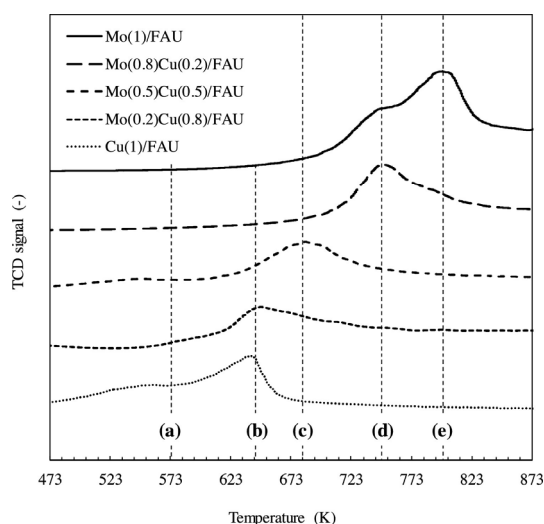


**Figure 74.** Surroundings of Rh nanoparticles controlled by Si/Al ratio of MFI structure determine the CO<sub>2</sub> hydrogenation selectivity towards methane or CO production. Reprinted with permission from ref.<sup>789</sup>. Copyright 2019, American Chemical Society.

ii) *Bimetallic zeolite-based catalysts for RWGS*

The combination of two metal in an oxide matrix provides a material with new physical-chemicals properties and specially affects the redox abilities due to electronic interactions. Cu-

based catalysts exhibit high activity at low temperatures for CO<sub>2</sub> hydrogenation and WGS reaction, but are unstable at higher temperature due to sintering, while Mo-based catalyst are selective catalyst for the conversion of CO<sub>2</sub> into CO. Therefore, the activity of bimetallic Mo-Cu-supported FAU zeolite catalyst was investigated for RWGS and Mo/FAU catalysts doped with different amount of Cu were prepared.<sup>791</sup> H<sub>2</sub>-TPR study revealed a shift in the reduction temperature for MoO<sub>3</sub> indicating that the presence of Cu modify the electronic properties of Mo, leading to an easier reduction for Mo oxide (Figure 75). The catalytic study showed that Mo-FAU catalyst reached 99% CO selectivity and 14.3% CO<sub>2</sub> conversion at 500°C while the doped-Cu catalyst, 7.6wt%Mo-1.25wt%Cu/FAU, exhibited the best catalytic performance, and reached 18.5 and 23.5 % CO yield with 99% CO selectivity, at 500 and 600°C, respectively (Table 10, Entries 23-26). Then, the enhanced activity of 7.6wt%Mo-1.25wt%Cu/FAU catalyst was attributed to the presence of Cu that improved the reducibility of MoO<sub>3</sub> into MoO<sub>2</sub>.

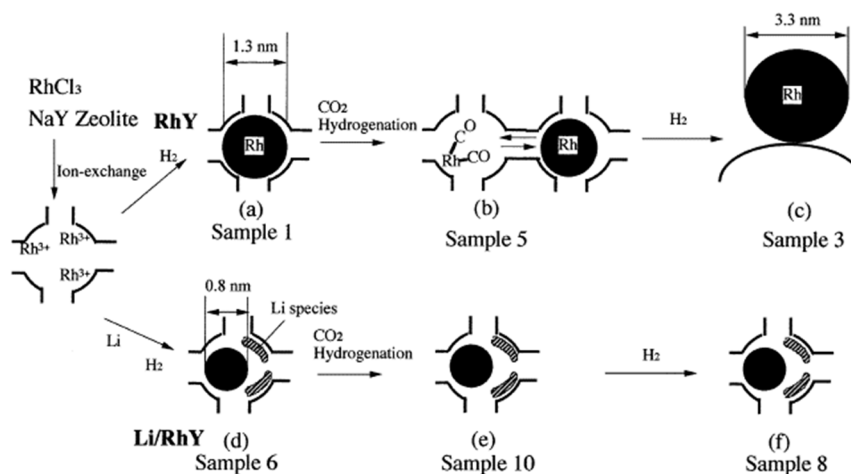


**Figure 75.** H<sub>2</sub>-TPR spectra of Mo(x)Cu(1-x)/FAU samples (x: metal content, mmol/g). Reprinted with permission from ref.<sup>791</sup>. Copyright 2020, Elsevier B.V. All rights reserved.

### iii) Alkali effect over the catalytic activity of zeolite-based catalysts for RWGS

The addition of alkali metals can greatly improve the activity or modify the selectivity of a catalyst for CO<sub>2</sub> conversion due to enhanced adsorption and activation of CO<sub>2</sub> on basic sites.<sup>765,792</sup> Following these leads, a recent study of catalytic activity of Rh supported Y zeolite catalyst (RhY) and Li-doped RhY catalysts (Li/RhY) for CO<sub>2</sub> hydrogenation revealed the great impact of incorporation of alkali on selectivity of the catalyst. CH<sub>4</sub> was the main product over RhY catalyst, while CO was the main product over Li-doped RhY.<sup>793</sup> The geometric and electronic structure of Rh species in Y zeolites were similar before the reaction but different after reaction. Rh particles migration and aggregation out of the pores in RhY, while Rh particles remained stable in Li/RhY owing to the presence of Li (Figure 76). Different reaction mechanisms were proposed, and the difference in selectivity process was attributed to the accumulation of CO on the particle

surface on Li/RhY inhibiting H<sub>2</sub> adsorption, while on RhY, CO adsorbed species react with OH groups and desorbed to enable H<sub>2</sub> adsorption and CH<sub>4</sub> formation. Thus, in the presence of Li/RhY catalyst, at 450°C, 87% CO selectivity at ~15% CO<sub>2</sub> conversion level were reached whereas in the presence of RhY, 100% CH<sub>4</sub> selectivity at ~25% CO<sub>2</sub> conversion level were achieved (Table 10, Entries 27-28).



**Figure 76.** Formation of smaller particle size in Li/RhY than in RhY owing to the deposition of Li atoms on the walls of the cages. Reprinted with permission from ref.<sup>793</sup>. Copyright 2000, Academic Press. All rights reserved.

#### 6.1.4. Conclusion

The production of CO from RWGS is a very attractive process due to its use as building block for the synthesis of chemicals and hydrocarbons from Fischer-Tropsch synthesis, always considering the use of anthropogenic CO<sub>2</sub> and green and renewable hydrogen. The main issue is the co-production of methane. It is crucial to make the RWGS catalysts 100% CO selective for commercialization, as an increase in hydrogen consumption will make the process more expensive, will require a subsequent separation process and will also affect the carbon footprint. For the last decades, numerous studies on RWGS using, specially, supported metals, have been carried out. The CO<sub>2</sub> adsorption and CO desorption appear key factors for enhancing CO<sub>2</sub> conversion and CO selectivity. Nevertheless new efforts are still required to determine the reaction mechanism and to find the working active sites to finally establish structure-activity/selectivity relationship. Therefore, computational modeling and in situ spectroscopy studies will be fundamental tools for the rational design of efficient and highly selective catalysts for RWGS. In the present review, a short compilation of works showed that the potential of ordered micro and mesoporous materials has been scarcely considered and undervalued. The studies described present strategies to maximize CO selectivity and CO<sub>2</sub> conversion, improving metal-support interaction and stability, potentially through the incorporation of a promoter (alkali, second metal), increasing the oxygen mobility generating oxygen vacancies owing to the presence of reducible transition metal oxide or maximizing the dispersion and stability of metal

nanoparticles by enveloping within the zeolite pore channels system. Enhancement of CO<sub>2</sub> adsorption/activation and fast and easy CO desorption are key steps to consider for the design of new RWGS catalysts, as well as catalyst issues. In addition, future studies will focus on catalyst deactivation mechanism in order to improve the stability of catalysts for RWGS. Undoubtedly, the unique properties of zeolite and OMS as a support to confine, disperse and stabilize metal species due to their pore structure and high surface area make them attractive supports for the development of RWGS catalysts. The benefits of support morphology and pore topology to enhance the dispersion and attachment of metal species should be fundamental. Therefore, future studies should focus on hierarchical zeolites, two-dimensional zeolite nanosheets and core-shell materials to promote physical isolation and protection of particles as well as mass transfer.

**Table 10.** Summary of the catalytic performance of the reviewed RWGS zeolite- and OMS-based catalysts.

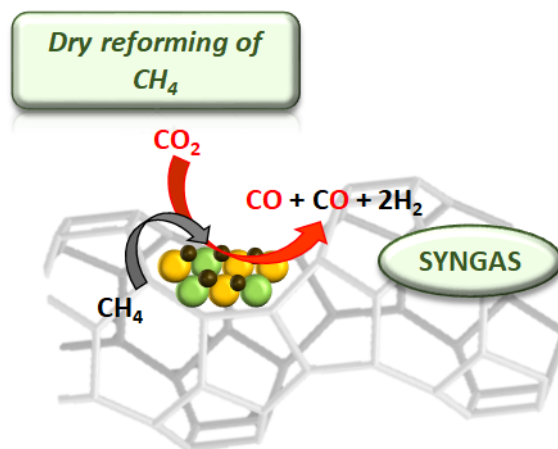
Entry	Catalysts	T°C	%CO <sub>2</sub> Conv.	% CO Sel.	Conditions	Ea (Kcal/mol)	Year	Ref
<b><i>OMS based-catalysts</i></b>								
1	10NiO/SBA-15	400	5	100	CO <sub>2</sub> :H <sub>2</sub> =1,	23.6	2012	770
2		600	42	100	0.1 MPa			
3		900	45	100	H <sub>2</sub> = 60mLmin <sup>-1</sup>			
4	M/MCM-41	550	TOF(s <sup>-1</sup> )		CO <sub>2</sub> :H <sub>2</sub> =1,		2014	772
	Co (Si/Co=5)		3.55	95	0.1 MPa	67.5		
5	Zn (Si/Zn=5)		0.15	99	H <sub>2</sub> = 120mLmin <sup>-1</sup> ,			
6	Cu (Si/Cu=5)		3.75	99	GHSV=7200mLg <sub>cat</sub> <sup>-1</sup> h <sup>-1</sup>	75.3		
7	Ni (Si/ni=5)		3.65	70		10.2		
8	Fe/KIT-6	500	16	97	H <sub>2</sub> :CO <sub>2</sub> =4, 0.1 MPa, H <sub>2</sub> = 40mLmin <sup>-1</sup> ,		2015	773
	Si/Fe=10				GHSV=12000mLg <sub>cat</sub> <sup>-1</sup> h <sup>-1</sup>			
9	5CuO/1NiO-SBA-15	700	47	100	CO <sub>2</sub> :H <sub>2</sub> =1, 0.1 MPa, GHSV=320h <sup>-1</sup>	9.5	2015	777
10		900	54	100				
11	10CuO/1CeO <sub>2</sub> -SBA-15	700	26	100		63.5		
12		900	52	100				
12	1NiO/1CeO <sub>2</sub> -SBA-15	700	17	100		53.6		
14		900	45	100				
15	Perovskite/SBA-15	600	CO mmol/g <sub>LSF</sub>		50 mLmin <sup>-1</sup>	-	2020	787
	50LSF/SBA-15		cycle 1: 2.5		10% CO <sub>2</sub> /He			
16			cycle 2: 2.8		10% H <sub>2</sub> /He,			
17			cycle 3: 3.2		GHSV=40000mLg <sub>cat</sub> <sup>-1</sup> h <sup>-1</sup>			
18			cycle 4: 3.3					
19			cycle 5: 3.6					
20			cycle 6: 3.4					
<b><i>Zeolite based-catalysts</i></b>								
21	0.4Rh@S1	450	~15	87	H <sub>2</sub> :CO <sub>2</sub> =4, 3 MPa,	-	2019	789
22	0.43Rh@ZSM-5		~25	100	GHSV=3600mLg <sub>cat</sub> <sup>-1</sup> h <sup>-1</sup>			
23	9.6Mo/FAU	500	18.5	99	H <sub>2</sub> :CO <sub>2</sub> =1, 0.1 MPa, H <sub>2</sub> = 12.5	-	2020	791
24		600	23.5	99	mLmin <sup>-1</sup> , GHSV=7500mLg <sub>cat</sub> <sup>-1</sup> h <sup>-1</sup>			
25	7.6Mo-1.25Cu/FAU	500	14.5	99				
26		600	19.5	99				
27	5Rh/Y	450	~15	87	H <sub>2</sub> :CO <sub>2</sub> =3, 3 MPa,	-	2000	793
28	Li-5Rh-Y (Si/Rh=10)		~25	100	GHSV=12000mLg <sub>cat</sub> <sup>-1</sup> h <sup>-1</sup>			

\* Metal content is given in wt%.



## 6.2. Dry reforming of methane (DRM)

### 6.2.1. Introduction



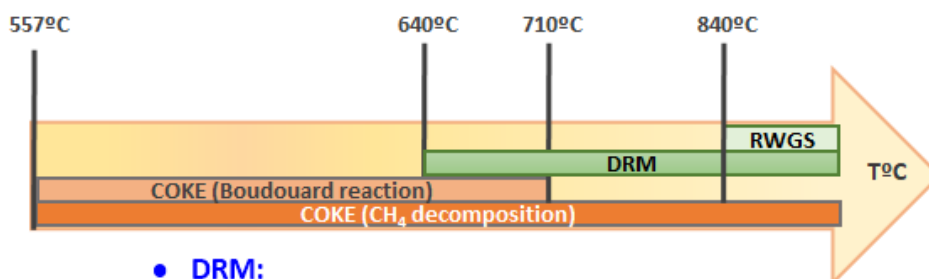
**Figure 77.** Dry reforming of methane to syngas production over metal based catalysts.

The catalytic dry reforming of methane into synthesis gas ( $H_2+CO$ ) is a very attractive  $CO_2$  conversion since it makes possible the simultaneous mitigation of two important greenhouse gases,  $CH_4$  and  $CO_2$  (Figure 77). DRM is a 100% atom efficiency process and provide a highly regarded  $H_2/CO$  ratio of 1 for further industrial conversion such as Fischer-Tropsch and other valuable chemicals (methanol). However, in practice, DRM requires high energy consumption due to the very endothermic character of the reaction. Moreover, the high temperatures required by the process induce a rapid deactivation of the catalyst due to sintering of the metal and severe coke deposition. So far, the rapid deactivation of the catalyst together with the high energy use constitute the biggest obstacle to the development of an environmentally friendly industrial application to date. Therefore, the design of robust and efficient catalyst at “low temperature” is topical and very challenging.

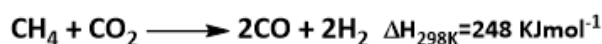
### 6.2.2. Thermodynamics

DRM is highly endothermic and high temperature is required to reach high thermodynamic conversions. Hence, for an industrial implementation, renewable energy sources must be considered in order to achieve an economically and environmentally sustainable process. Simultaneously, RWGS can take place and decrease  $H_2/CO$  ratio to lower value than ideal ratio=1. However, the main drawback remains the strong deactivation of the catalyst because of coke deposition originated mainly from methane decomposition (cracking) and CO disproportionation (Figure 78). A study based on the standard free energy change, determined that DRM occurs above  $640^\circ C$  and RWGS above  $840^\circ C$ , while coke formation by methane cracking takes place from  $557^\circ C$  and coke formation by CO disproportionation (Boudouard reaction) is inhibited above  $710^\circ C$  due to high exothermicity.<sup>794–796</sup> Therefore, at

temperature > 800°C, superficial carbon species are issued from CH<sub>4</sub> cracking, and can be easily oxidized by CO<sub>2</sub>, limiting the formation of coke (route 2, Figure 79). At lower temperature, low reactive carbon species issued from Boudouard reaction are formed and coke deposition is more critical.<sup>797</sup> Coke formation not only induces severe catalyst deactivation because of the encapsulation of the active sites or carbon fibers formation on the catalysts surface but also can cause reactor plugging. Different studies have determined the limit temperature for carbon deposition for different CO<sub>2</sub>/CH<sub>4</sub> ratios in the feed, and showed for the same feed ratio, that the temperature limit for carbon deposition increased as the pressure increased and, that at a given pressure, the temperature limit for carbon deposition increased as the CO<sub>2</sub>/CH<sub>4</sub> feed ratio decreased, indicating that CO<sub>2</sub> excess in the feed has to be used to avoid coke.<sup>794-796</sup> However, it was shown that higher CO<sub>2</sub>/CH<sub>4</sub> favours RWGS and produces lower H<sub>2</sub>/CO ratio,<sup>796,798</sup> while the incorporation of steam into the system can help to prevent the coke formation but decreases CO<sub>2</sub> conversion.<sup>799,800</sup> Moreover, the use of high pressure even if is of interest from industrial standpoints, promotes carbon deposition.<sup>801,802</sup> The equilibrium constant for the endothermic DRM reaction increases significantly when increasing temperature, maximizing CO<sub>2</sub> and CH<sub>4</sub> conversion, while Boudouard reaction and CH<sub>4</sub> cracking are also favoured. Therefore, the design of active, efficient and highly stable catalyst is decisive for a kinetic control of DRM process and to avoid coke formation.

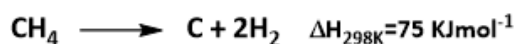


- **DRM:**

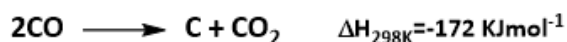


- **Coke formation:**

*Methane decomposition:*



*CO disproportionation (Boudouard reaction):*



- **RWGS**

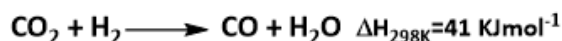
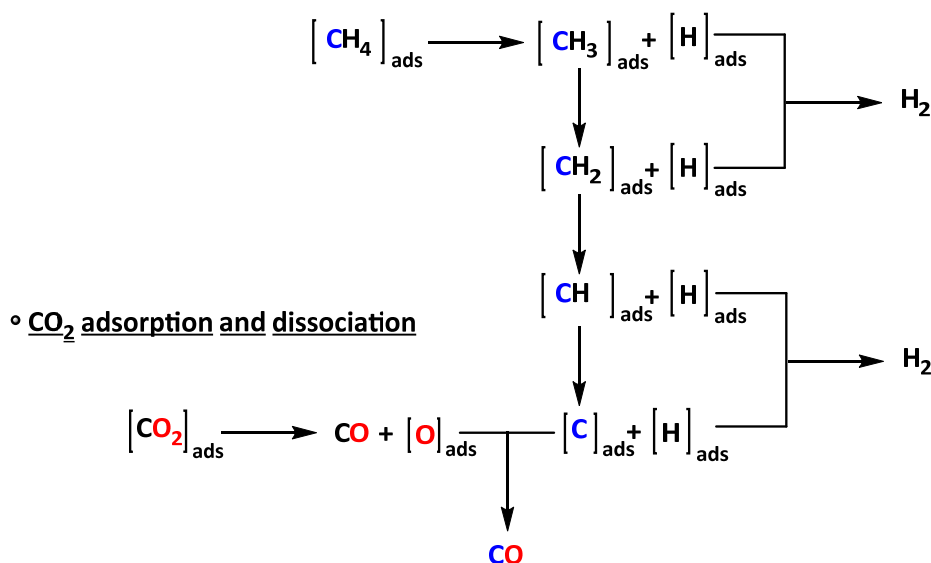


Figure 78. DRM and competitive reactions.

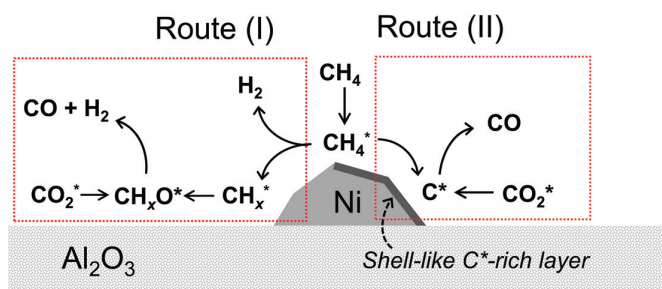
### 6.2.3. Mechanism of dry reforming of methane

The main accepted mechanism for DRM involves the reversible adsorption and dissociation of CH<sub>4</sub> on the catalyst active sites to produce four adsorbed hydrogen active species (that are further converted into H<sub>2</sub>), and adsorbed carbon species oxidized into CO (reduction of the catalyst/lattice oxygen) and on adsorption and dissociation of CO<sub>2</sub> on the support to yield CO and lattice oxygen (oxidation of the catalyst/oxygen vacancy) (Scheme 61; Figure 79).<sup>803,804</sup> A suitable catalyst has to present high reducibility and oxygen storage capacity enabling high oxygen mobility to successfully support redox cycle: CO<sub>2</sub> being reduced into CO.

#### ◦ CH<sub>4</sub> adsorption and dissociation



**Scheme 61.** Main accepted mechanism of adsorption and dissociation of CH<sub>4</sub> and CO<sub>2</sub> for DRM.



**Figure 79.** Mechanism for adsorption and dissociation of CH<sub>4</sub> and CO<sub>2</sub> to produce syngas (Route (I)) and for oxidation of active dehydrogenated carbon species by CO<sub>2</sub> (Route (II)). Reprinted with permission from ref.<sup>805</sup>. Copyright 2018, Zunrong Sheng et al. Licensee IntechOpen.

### 6.2.4. Catalysts for DRM

In spite of the great challenges from environmental and industrial standpoints, DRM is not currently perceived as an industrially viable process, because of carbon formation, quick sintering/deactivation of conventional reforming catalysts and high energy consumption. Over the last 30 years, DRM studies have shown that Ni catalysts are the most suitable candidates for industrial implementation owing to their low cost and availability in comparison to noble metal

(Pt, Ru, Rh) based catalysts. Noble metals exhibit higher activity because of their ability to dissociate CO<sub>2</sub> into CO and O species that favour the CH<sub>4</sub> dissociation into CH<sub>n</sub> and H species. However, unlike noble metal catalysts,<sup>806</sup> Ni suffers from strong coke formation and deactivation.<sup>807,808</sup> To prevent carbon and nickel carbide formation, an optimum range of operation temperature, between 870 and 1040°C, was determined.<sup>794</sup> Hence, numerous strategies were developed to minimize coke deposition on Ni catalysts, consisting mainly in minimizing and stabilizing the Ni particle size since carbon deposition on Ni surface requires Ni ensembles, and thus large Ni particles enable severe coke deposition.<sup>809,810</sup> Several studies defined optimum Ni nanoparticle size of few nanometres (<10), for which the carbon deposition is significantly minimized.<sup>811,812</sup> Nevertheless, small Ni nanoparticles present low thermal stability under DRM reaction conditions.<sup>813,814</sup> Hence different approaches have been followed to minimize Ni particle size and maximize Ni sintering resistance. The choice of a suitable support not only enables high dispersion of metallic nanoparticles but also can provide specific physicochemical properties such as basicity (CaO, La<sub>2</sub>O<sub>3</sub>, MgO), high oxygen mobility (oxygen vacancies/storage capacity) (CeO<sub>2</sub>, ZrO<sub>2</sub>, TiO<sub>2</sub>), modify reducibility, and can enhance the catalytic activity or improve the catalyst stability, avoiding carbon formation. Additionally, the incorporation of one or more metals as promoters can play different roles such as improving the dispersion and stabilization of the active phase, usually by forming homogeneous solution of oxides and strong metal support interactions, and/or enhancing the catalytic activity owing to the introduction of new physicochemical properties (redox, acid/base).<sup>815</sup> Likewise, the incorporation of basic metals such as lanthanides, alkali and rare earth metals showed to enhance the stability of Ni nanoparticles in addition to promote the chemisorption and activation of CO<sub>2</sub>, and accelerate the reaction of CO<sub>2</sub> with carbon species to form CO.<sup>816,817</sup> Accordingly, several studies showed that carbon deposition could be limited or suppressed due to the presence of strong Lewis basic sites.<sup>818-821</sup>

a) DRM zeolite-based catalysts

Among suitable supports, zeolites are of potential interest due to their physicochemical properties to deliver high metal dispersions and stable catalysts under hard reaction conditions. More specifically, MFI and USY zeolites present suitable properties such as microporous structures, high surface area, and high capacity for CO<sub>2</sub> adsorption, and consequently, zeolites based catalysts have been extensively studied for DRM process.

Different comparative studies showed the impacts of the acidity, reducibility and the structure of a zeolite on the catalytic properties for DRM. The catalytic performance of Ni based-zeolites (A, X, Y and ZSM-5) prepared by impregnation investigated the effects of Ni loading and the

zeolite structure.<sup>822</sup> Maximum catalytic activity was achieved with 7wt% Ni content while coke deposition was observed with following order of deactivation: Ni/Y < Ni/X < Ni/ZSM-5 < Ni/A. Maximum 91% CH<sub>4</sub> and 93% CO<sub>2</sub> conversions with H<sub>2</sub>/CO around 1.8 were maintained at 700°C for 5h TOS over 7% Ni/Y that exhibited the highest performance and good potential for DRM (Table 11, Entries 1-4). Previously, a comparison of the catalytic performance of Ni/Al<sub>2</sub>O<sub>3</sub>, Ni/ZSM-5 and Ni/USY showed the impacts of acidity and zeolite structure over the catalytic properties of the catalyst and the metal reducibility due to strong interaction metal support, which determine the following order of reducibility: Ni/ZSM-5 > Ni/USY > Ni/γ-Al<sub>2</sub>O<sub>3</sub>.<sup>823</sup> Ni/USY and Ni/γ-Al<sub>2</sub>O<sub>3</sub> catalysts exhibited superior catalytic performance than Ni/ZSM-5 but also had a superior Ni content, 8.7, 8.1 versus 3.5%, respectively. After 6h TOS, at 650°C, 71% and 54% of CH<sub>4</sub> conversion and 71.2% and 56.3% CO<sub>2</sub> conversion, were obtained over Ni/USY and Ni/ZSM-5, respectively (Table 11, Entries 5-7). Later on, another study of catalytic activity of Ni/γ-Al<sub>2</sub>O<sub>3</sub>, Ni/Y, and Ni/H-ZSM-5 samples prepared by impregnation, with 5wt% Ni content, confirmed the dependence on CH<sub>4</sub> conversion on the support.<sup>824</sup> However, a different stability order of the Ni-based catalysts was established: Ni/H-ZSM-5 > Ni/γ-Al<sub>2</sub>O<sub>3</sub> > Ni/Y. The best catalytic data were obtained over Ni/H-ZSM-5 with H<sub>2</sub>/CO ratio close to 1 owing to the lower carbon deposition registered as well as to the higher stability of the textural properties of the catalyst (BET area). High CH<sub>4</sub> and CO<sub>2</sub> conversions were achieved over all the Ni catalysts, close to 80% with H<sub>2</sub>/CO ratio close to 1 along 9h TOS (Table 11, Entries 8-10). The very stable MOR was compared with FAU, both with 2.5-3wt% Ni content.<sup>825</sup> The MOR based catalysts exhibited the better catalytic performance in terms of conversion and stability (Ni/HMOR > Ni/NaMOR > Ni/HY). At 750°C, for 24h TOS, 92% and 87% CO<sub>2</sub> conversion and 86% and 75% CH<sub>4</sub> conversion were achieved over Ni/H-MOR and Ni/NaMOR, respectively (Table 11, Entries 11-14). Data of CO, H<sub>2</sub> and H<sub>2</sub>/CO were not provided. The mixing Ni/H-MOR and Ni/NaMOR and Ni/HY with Al<sub>2</sub>O<sub>3</sub> allowed improving the stability of the catalyst by reducing coke deposition.

These comparative studies evidenced the potential of zeolites as support for the design of DRM catalysts. Nevertheless, short-term experiments were performed indicating low catalytic stability. Different strategies were reported to improve robustness of the zeolite based catalysts and the preparation method, metal doping, and modification of basicity or morphology have been studied. MFI zeolites were the most support used for the design and development of DRM catalysts while other zeolite structures have been investigated more occasionally being the use of FAU more common.

i) *MFI as support for the preparation of DRM catalysts*

\* *ZSM-5 as support for the preparation of DRM catalysts*

ZSM-5 has been widely used as support for DRM catalysts due to its easy synthesis within a wide range of compositions. Recently, hierarchical ZSM-5 zeolite with micro and mesopores was impregnated with Ni and used for DRM. Data of CO<sub>2</sub>, CH<sub>4</sub> conversion and H<sub>2</sub>/CO ratio revealed that a sample with Si/Al=30 exhibited highest catalytic performance, at 800°C. Maximum 98% CO<sub>2</sub> and 95% CH<sub>4</sub> conversions with H<sub>2</sub>/CO ratio close to 0.9 were maintained for 30h (Table 11, Entry 15).<sup>826</sup> These results were attributed to acid strength and crystallinity of ZSM-5 structure. Samples with lower acidity exhibited lower catalytic activity and showed lower crystallinity and BET area. In addition to high catalytic performance, Ni/ZSM-5(30) micro-mesoporous sample exhibited high stability and resistance to coke deposition, with no-deactivation registered after 30h TOS. For all samples, the same tendency was observed, and due to the endothermicity of DRM, CH<sub>4</sub> and CO<sub>2</sub> conversion and H<sub>2</sub>/CO ratio increased when temperature increased.

- *Effect of preparation method of Ni/ZSM-5-based catalysts for DRM*

The activity and stability of DRM catalysts strongly depend on Ni nanoparticles dispersion, metal-support interactions, that in turn influence metal sintering and coke resistance. Therefore, the preparation method constitutes an important strategy to control the metal location, deposition and dispersion. The benefits of chemical and physical effects of high intensity ultrasound for the synthesis of metal supported nanoparticles catalysts and nanomaterials have shown to minimize metal particle size and to improve the distribution and dispersion of the particles, and to enhance the catalytic features.<sup>827-829</sup> Following this strategy, sonochemical method was applied to the preparation of Ni/ZSM-5 with different Ni contents (3-20wt%).<sup>830</sup> Characterization data showed that ZSM-5 crystallinity decreased slightly upon Ni incorporation. A positive effect of the use of ultrasound was observed for lower 3-8wt% Ni contents with a better dispersion and a decrease in Ni particle size (lower than 100 nm). Nevertheless, an average large Ni particle size about 43 nm was determined that can be considered still too large. Indeed, Ni particle size and stability is a critical parameter to control and minimize coke deposition which is formed on Ni-ensemble and consequently low Ni particles with size <10 nm is desirable.<sup>809,810</sup> 8wt% Ni/ZSM-5 sample exhibited the better catalytic performance with 70% CH<sub>4</sub> conversion and H<sub>2</sub>/CO ratio around 0.8-0.9 for 24h TOS, at 850°C (Table 11, Entry 16), while no data on coke analysis were provided.

- *Bimetallic ZSM-5-based catalysts for DRM*

The addition of a second metal or promoter, especially noble metal and rare earth metals, is well known to enhance the activity, selectivity, dispersion and stabilization of metal nanoparticles and coke resistance. The presence of a second suitable metal allow for strong

metal/metal and metal/support interactions due to electronic interactions leading to increase of the metal surface area, modifications of surface structure and improved lattice oxygen mobility compared to monometallic catalysts.<sup>831–836</sup> Some studies reported that in the case of lanthanide doped catalysts, coke deposition was filamentous and did not affect the catalytic activity but may cause reactor plugging.<sup>837–840</sup>

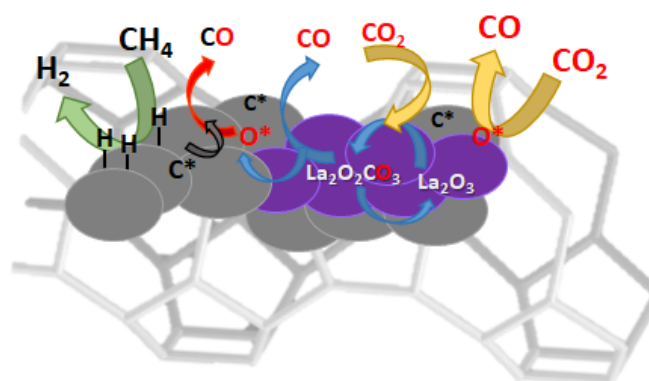
*Effect of transition metal doping of Ni/ZSM-5-based catalysts for DRM*

Recently, the catalytic performance of Ni-Co/ZSM5 monometallic and bimetallic catalysts was studied.<sup>841</sup> Cobalt was shown to reduce carbon deposition due to its ability to oxidize adsorbed carbon into CO and CO<sub>2</sub>.<sup>842</sup> Therefore, the preparation of bimetallic catalysts allowed enhancing the catalytic activity and minimizing coke deposition due to the synergetic effect between Ni and Co.<sup>842–846</sup> Then, the bimetallic 2.3wt%Ni-4.6wt%Co/ZSM5 catalyst exhibited the best catalytic activity and stability with 5wt% coke formation in comparison with 46 wt% coke formed on monometallic samples.<sup>841</sup> At 800°C, 80% CH<sub>4</sub> conversion and 85% CO<sub>2</sub> conversion with 65 and 61% H<sub>2</sub> and CO selectivities, respectively, were achieved (Table 11, Entries 17-20). The results showed that coke deposition was dependent on temperature and catalyst composition. Over 2.3wt%Ni-4.6wt%Co/ZSM5 at 700°C and after short 12h TOS, CH<sub>4</sub> and CO<sub>2</sub> conversion decreased from 66 to 50% and 71% to 61%, respectively, while C balance increased from 73 to 80%. Mn has also been studied as promoter for DRM Ni-based catalysts and enabled to suppress carbon deposition and to improve catalyst life. Following these leads, the effect of the incorporation of different Mn loading on Ni(10wt%)-zeolites (NH<sub>4</sub>-ZSM5, NH<sub>4</sub>-Y, Na-Y) over their catalytic performance was explored.<sup>847</sup> The catalytic results showed that the initial best catalytic activity was achieved in the presence of 10wt%Ni-ZSM-5 catalyst, but the CH<sub>4</sub> conversion and H<sub>2</sub> production dropped within the first 5h TOS. After the first 5 hours, similar activity was reported for all the 10wt%Ni-zeolite catalysts. CH<sub>4</sub> and CO<sub>2</sub> conversions ranged between 22-25% and 34-36%, respectively. The addition of Mn affected the catalytic activity of three types of zeolite supports differently, but their catalytic performance was not improved (Table 11, Entries 21-24). The positive effects of low Mn loading were the reduction of carbon deposition and the decrease in the Ni nanoparticle size and dispersion on the zeolite. However, as Mn loading increased, the crystallinity of the zeolite structure and its micropore surface area generally decreased. The incorporation of different ZrO<sub>2</sub> loading to Ni-ZSM-5 catalyst showed that the presence of ZrO<sub>2</sub> enhanced the Ni nanoparticles dispersion and minimized the Ni particles size due to metal-support strong interaction, and 8wt% Ni and 5wt% ZrO<sub>2</sub> contents were optimum.<sup>848</sup> In the presence of Ni(8%)/ZrO<sub>2</sub>(5%)-ZSM-5, at 850°C, 95% CO and 90% H<sub>2</sub> yields were reached and remained constant for 10h TOS (Table 11, Entry 25). Very high CO and

H<sub>2</sub> yields were reached but the catalytic stability was demonstrated over too short TOS to evaluate its potential as industrial catalyst.

*Effect of rare earth metal doping of Ni/ZSM-5-based catalysts for DRM*

Numerous studies of DRM using Ni-based catalysts showed that the incorporation of second metal or metal oxide such as La, Y, Ce improved considerably the catalytic activity and limited coke deposition due to strong electronic interaction between Ni species and the second metal and/or the support favouring high dispersion of Ni nanoparticles and the formation of new active species.<sup>849–851</sup> Accordingly, the benefits of La doping on the Ni/ZSM-5 catalytic activity for DRM was explored.<sup>852</sup> La<sub>2</sub>NiO<sub>4</sub>/ZSM-5 was prepared by sol-gel technique and RXD pattern confirmed the formation of La<sub>2</sub>NiO<sub>4</sub> species with spinel structure in the fresh sample, uniformly and highly dispersed on ZSM-5. Catalytic study showed that 69% CO<sub>2</sub> and 67% CH<sub>4</sub> conversions and H<sub>2</sub>/CO ratio close to 0.9 were higher over the La<sub>2</sub>NiO<sub>4</sub>/ZSM-5 catalyst than over Ni/ZSM-5 or La<sub>2</sub>NiO<sub>4</sub>/γ-Al<sub>2</sub>O<sub>3</sub> catalysts. Moreover, La<sub>2</sub>NiO<sub>4</sub>/ZSM-5 presented higher stability over 35h TOS. The improved stability of La<sub>2</sub>NiO<sub>4</sub>/ZSM-5 catalyst was attributed to the formation and decomposition of the La<sub>2</sub>O<sub>2</sub>CO<sub>3</sub> species that enable the oxidation of dehydrogenated carbon species accumulated on Ni particles. XRD patterns revealed the disappearance of La<sub>2</sub>O<sub>3</sub> species and the formation of the La<sub>2</sub>O<sub>2</sub>CO<sub>3</sub> species by CO<sub>2</sub> adsorption on La<sub>2</sub>O<sub>3</sub> during DRM process. Afterwards, La<sub>2</sub>O<sub>2</sub>CO<sub>3</sub> species decompose into CO and oxygen species that enable the oxidation of carbon species accumulated on Ni particles into CO (Figure 80), as it was previously described.<sup>851,853</sup> The same group studied the catalytic performance of LaNiO<sub>x</sub>/ZSM-5 in pilot plant, that were shaped as cylinder of LaNiO<sub>x</sub>/ZSM-5 (∅=3 mm\*10-15mm), and prepared by a sol-gel method.<sup>854</sup> 97% CH<sub>4</sub> and 94% CO<sub>2</sub> conversion were achieved and remained constant for 100h, at 850 °C but with low GHSV= 1.3 Lh<sup>-1</sup>g<sub>cat</sub><sup>-1</sup> (Table 11, Entries 26-27).

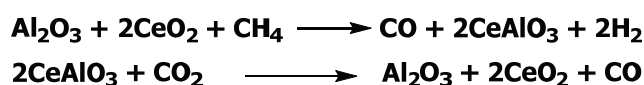


**Figure 80.** Adsorption and dissociation of CH<sub>4</sub> and CO<sub>2</sub> to produce syngas and for oxidation of active dehydrogenated carbon species by oxygen issued from La<sub>2</sub>O<sub>2</sub>CO<sub>3</sub> decomposition.

The benefits of the CeO<sub>2</sub> addition to Ni based-catalysts have been widely reported such as improvement of Ni nanoparticles dispersion, enhancement of redox properties, high oxygen



storage capacity enabling splitting of C-O bond and formation of Lewis basic sites promoting adsorption and activation of CO<sub>2</sub>.<sup>832</sup> Moreover, the enhanced oxygen mobility allowed oxidizing adsorbed carbon species on metallic particles into CO and preventing coke deposition.<sup>855,856</sup> Following these leads, the effect of Ce, Ni loading and temperature calcination over the catalytic performance of Ni-Ce/ZSM-5 catalysts was studied under optimized DRM conditions (temperature, CH<sub>4</sub>/CO<sub>2</sub> ratio and space velocity).<sup>857</sup> Catalytic data revealed that CH<sub>4</sub> and CO<sub>2</sub> conversions increased with Ni loading until stabilization (10 wt%) while an optimum in Ce was determined. Previously, it was reported that Ce content enabled to improve oxygen mobility, Ni dispersion and enhance the DRM rate.<sup>627,858,859</sup> Highest activity was achieved for 2wt% Ce loading with 90% CH<sub>4</sub> and 78% CO<sub>2</sub> conversions, and under optimized parameters of reaction, up to 99% CH<sub>4</sub> and 94% CO<sub>2</sub> conversion. Stability test evidenced good catalytic performance and stability, maintaining 95% CH<sub>4</sub> and 85% CO<sub>2</sub> conversion with syngas ratio close to 1, for 40h TOS without notable deactivation (Table 11, Entry 28). Later on, the effect of the addition of controlled amount of Ce to Ni/ZSM-5 catalysts and the role of Ce in the improvement of the catalytic performance, and the limitations of coke deposition was studied.<sup>860</sup> Optimum catalytic results were achieved over 5wt%Ni-5wt%Ce/ZSM-5, at 800°C, excellent 97% CH<sub>4</sub> and 91% CO<sub>2</sub> conversions with 98% H<sub>2</sub> selectivity and H<sub>2</sub>/CO~1 for short 24h TOS while no longer stability test was performed neither regeneration study (Table 11, Entry 29). Similar conclusions were reached. The addition of Ce enhanced Ni particles dispersion, favoured CH<sub>4</sub> dissociation and H<sub>2</sub> production, and strengthened the gasification of coke owing to enhanced CO<sub>2</sub> adsorption and oxidation of adsorbed carbon. XPS study allowed determining the presence of CeO<sub>2</sub> and CeAlO<sub>3</sub> in the reduced and used catalysts leading to a proposed redox cycle in which CO<sub>2</sub> enabled the oxidation of CeAlO<sub>3</sub> and regeneration of CeO<sub>2</sub> + Al<sub>2</sub>O<sub>3</sub> (Esquema 58). Moreover, calculated apparent activation energies of CH<sub>4</sub> and CO<sub>2</sub> could be reduced by 30% and 40%, respectively.



**Esquema 58.** Proposed redox cycle for CeO<sub>2</sub> + Al<sub>2</sub>O<sub>3</sub> regeneration during DRM over Ni-Ce/ZSM-5 catalysts. The effect of different additives (Cu, Nd, Mo) over acidity, Ni dispersion and turn over during catalytic performance in DRM process was studied using Al<sub>2</sub>O<sub>3</sub>-HZSM-5 zeolite as support <sup>861</sup>. The study of addition of metal oxide revealed that the presence Cu maximized the H<sub>2</sub> yield. While the addition of rare-earth elements influenced the catalytic activity and the Nd incorporation maximized H<sub>2</sub> yield. Finally, the Mo addition maximized H<sub>2</sub> yield up to 70%. The authors concluded that the incorporation of different metal oxides increased the complexity of the catalyst and the acidity, responsible of the improved catalytic activity. Under optimized reaction conditions, at 850°C, 98% CH<sub>4</sub> and 97% CO<sub>2</sub> conversions with H<sub>2</sub>/CO ratio close to 1 were

achieved over NiCuNdMo/Al<sub>2</sub>O<sub>3</sub>HZSM-5 (Table 11, Entry 30). Unfortunately, no stability test was performed.

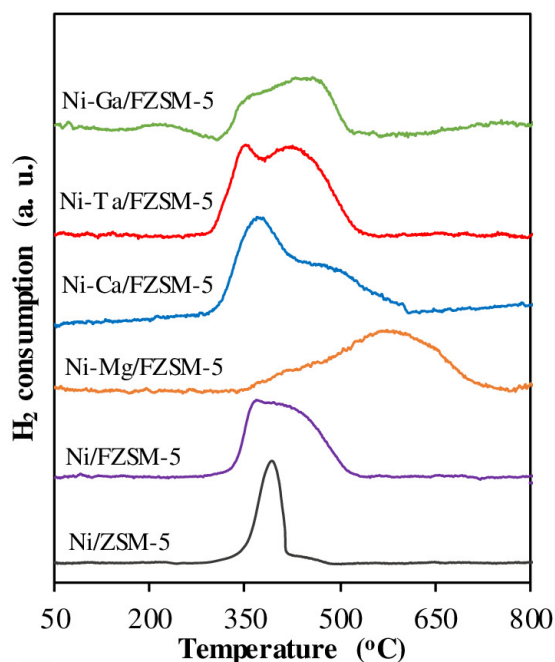
*Effect of noble metal doping of Ni/ZSM-5-based catalysts for DRM*

The benefits of the addition of noble metal to Ni zeolite-based catalysts due to their resistance to coke deposition have also been explored. Then, the preparation of Ni/ZSM-5 catalysts incorporating a small amount of noble metal (Pt) for DRM process was described.<sup>839,862</sup> Catalytic study revealed that the maximum catalytic results corresponded to optimum Ni and Pt metal loadings of 6% and 0.5%, respectively.<sup>862</sup> The characterization data allowed attributing the enhancement of catalytic activity and coke resistance to the higher Ni dispersion and decrease of Ni nanoparticle size and improved NiO reducibility owing to the presence of Pt. TPR study indicated a shift to lower temperature of NiO reduction for higher Ni contents for monometallic samples. This result was attributed to the formation of nickel species with a larger particle size, with small interface with the support, and weak interaction NiO/support that make nickel oxide easy to be reduced. Therefore, the larger the particle size, the lower the reduction temperature. On the other hand, the presence of small amount of Pt in Ni catalysts evidenced and easier reduction of NiO, probably because Pt is reduced firstly and activates hydrogen which favours the reduction of NiO by spillover. Moreover, the improved coke resistance of Pt promoted Ni catalysts was attributed to the formation of Pt-Ni particles covered mainly by Ni, leading to high Ni particles dispersion and the formation of higher amount of active carbon species further oxidized into CO. Thus, at low reaction temperature (600°C), modest 28% CH<sub>4</sub> and 69% CO<sub>2</sub> conversion were achieved (Table 11, Entries 31-32). Previously, the preparation of Ni-Ru bimetallic catalysts already showed the effect of the Ru incorporation over the catalytic activity and stability (Table 11, Entries 33-34).<sup>839</sup> The Ru addition effect was more important for silica than for H-ZSM5 supported catalysts. Improvement in catalytic activity and stability were observed for bimetallic samples, that was related to higher dispersion of Ni nanoparticles due to the Ni-Ru clusters formation. Nevertheless, no data of conversion neither yield were provided.

- *Effect of basic properties of the Ni/ZSM-5-based catalysts for DRM*

The presence of alkali metals may influence the physicochemical properties of Ni catalysts due to electronic interactions alkali metal/Ni modifying the reducibility of Ni and dispersion, surface acidity and surface CO<sub>2</sub> adsorption by forming carbonate species. Indeed, the surface basicity influence strongly the CO<sub>2</sub> adsorption and activation and plays a key role in C-O bond splitting. Moreover, the CO<sub>2</sub> coverage of catalytic surface allows minimizing CH<sub>4</sub> adsorption/dissociation and coke formation. Therefore, to take advantage of basicity, a study of the presence of alkaline promoters such as Ca and K over the catalytic activity of Ni-ZSM-5 catalysts for DRM was carried

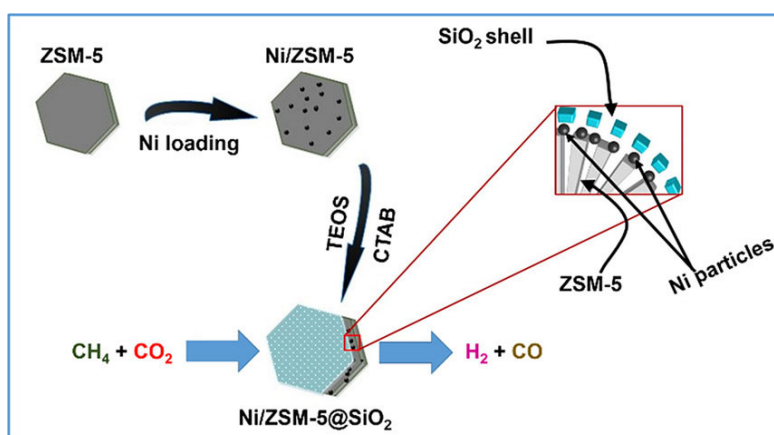
out. The resistance to coke deposition of KNiCa/ZSM-5 was attributed to the CO<sub>2</sub> coverage on the catalytic surface limiting CH<sub>4</sub> decomposition. At 800°C, high 94% CH<sub>4</sub> and 95% CO<sub>2</sub> conversions and 94% H<sub>2</sub> and 95% CO selectivities were registered (Table 11, Entry 35).<sup>863</sup> A previous study showed that the high 95% CO<sub>2</sub> conversion over KNiCa/ZSM-5 with high resistance to coke formation along 140h TOS, at 800°C, was due to the formation of carbonate species on alkaline metals (Ca) located adjacent to Ni sites, as well as to CO<sub>2</sub> dissociation.<sup>863–865</sup> Not long ago, the preparation of doped Ni/Fibrous-ZSM-5 catalysts with Ta, Mg, Ca illustrated the new catalytic properties of fibrous catalysts for DRM reaction.<sup>866</sup> The addition of promoters modified the surface acidity with the following trend Ni-Ga/FZSM-5 > Ni/FZSM-5 > Ni-Mg/FZSM-5 > Ni-Ta/FZSM-5 > Ni-Ca/FZSM-5. The Ta incorporation implies the disappearance of strong acid sites and the formation of medium acid sites enabling the stabilization and redispersion of Ni particles. The incorporation of Mg and Ca involved an increase in the concentration of weak acid sites, while the addition of Ga species increases the concentration of strong acid sites promoting side reactions and coke formation. H<sub>2</sub>-TPR study revealed the synergism between Ta-Ni, promoting the reducibility of NiO as it was observed with the addition of Ca and in contrast to the incorporation of Mg where a shift to higher reduction temperature was formed (Figure 81). The surface basicity order was Ni-Ca/ZSM-5 > Ni-Mg/FZSM-5 > Ni-Ta/FZSM-5 > Ni-Ga/FZSM-5 > Ni/FZSM-5. Catalytic data showed that samples with higher acidity suffered rapid deactivation, while excessive basicity (Ca) promoted RWGS reaction. The catalytic results showed that there is a balance between reducibility and acid-base properties to manage optimum adsorption and activation of CO<sub>2</sub>, preventing CH<sub>4</sub> decomposition and enhancing metal activity through strong metal-support interaction, while preventing coke deposition. High catalytic performance was achieved over Ni-Ta/FZSM-5 with 93% CH<sub>4</sub> and 98% CO<sub>2</sub> conversions and 0.97 H<sub>2</sub>/CO ratio, with high stability over 80h TOS, at 800°C (Table 11, Entries 36-41). Very good performance was reported but reaction temperature was too high. However, since H<sub>2</sub> and CO yields were not given, neither information on catalyst regeneration was supplied, it is difficult to ascertain the potential of this catalyst.



**Figure 81.** H<sub>2</sub>-TPR study of the alkali metal doped Ni-fibrous ZSM-5 catalysts. Reprinted with permission from ref.<sup>866</sup>. Copyright 2020, John Wiley & Sons Ltd.

- Effect of morphology of the ZSM-5-based catalysts for DRM

In the last years, the preparation of microcapsule catalysts with core/shell structure has been widely explored to improve the stability of metal nanoparticles due to confinement effect preventing sintering, and the resultant catalysts have been applied in different processes.<sup>644,867–871</sup> Following these leads, a microcapsule catalyst, Ni/ZSM-5@SiO<sub>2</sub>, was prepared by sol-gel method with Ni/ZSM-5 as core and amorphous SiO<sub>2</sub> as shell.<sup>872</sup> The characterization data showed high Ni nanoparticles dispersion and stability due to strengthened interactions between Ni particles and ZSM-5 core, and the spatial confinement provided by the core-shell structure (Figure 83).



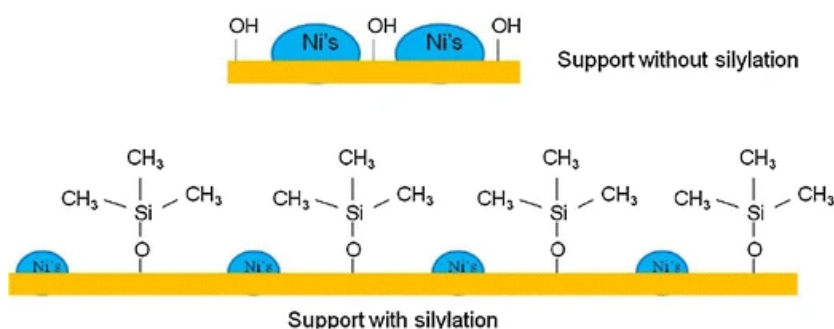
**Figure 83.** Spatial confinement of Ni-metal particles owing to core-shell structure of ZSM-5 and SiO<sub>2</sub>. Reprinted with permission from ref.<sup>872</sup>. Copyright 2019, WILEY-VCH Verlag GmbH & Co. KGaA, Weinheim.

Therefore, CH<sub>4</sub> and CO<sub>2</sub> conversion were higher over coated catalysts than uncoated ones. The superior catalytic performance of 10wt%Ni/ZSM-5@SiO<sub>2</sub> catalyst in comparison to

10wt%Ni/ZSM-5 catalyst was ascribed to coke deposition resistance induced by SiO<sub>2</sub> shell owing to the large surface area and pore volume of 10wt%Ni/ZSM-5@SiO<sub>2</sub> composite, ensuring higher dispersion and immobilization of Ni particles. A test of catalyst activity and stability over 50h for 10wt%Ni/ZSM-5 and 10wt%Ni/ZSM-5@SiO<sub>2</sub> catalysts showed high catalytic performance with activity decay attributed to coke deposition and Ni-sintering. At 800°C, CH<sub>4</sub> and CO<sub>2</sub> conversions between 90 and 83% over 50h of TOS were achieved (Table 11, Entries 42-43). Recently, the preparation of fibrous materials and particularly of fibrous zeolites offers new opportunities for synthesizing catalysts with large pore constituted by porous and dendrimeric silica fibres with great accessibility to active sites. Fibrous materials not only provides materials with large pore system allowing the diffusion of bulky reactants and high surface area, but also spatial confinement effect of Ni particles. Likewise, Ni/Fibrous-ZSM-5 catalysts exhibited superior catalytic properties for DRM reaction than microporous Ni/ZSM-5.<sup>866</sup> At 750°C, 55 and 78% CH<sub>4</sub> conversion and 61 and 79% CO<sub>2</sub> conversion were achieved over Ni/ZSM-5 and Ni/FZSM-5, respectively (Table 11, Entries 36-37).

\* *Silicalite-1-based catalysts for DRM*

The peculiarity of silicalite-1 zeolite is the large number of structural defects (silanol groups), up to 32 per unit cell, whose weak acidity affects both the activity and selectivity of the catalyst for different processes.<sup>873,874</sup> Therefore, the effect of post-synthesis modifications by thermal treatment after ionic exchange and silylation procedure over Ni-Silicalite-1 catalytic performance (CH<sub>4</sub> and CO<sub>2</sub> conversion, H<sub>2</sub>/CO and coke deposition) for DRM process was studied.<sup>875,876</sup> Silylation enabled the formation of smaller and more reducible Ni-oxide species, avoiding the formation of nickel silicates (Figure 84). Therefore, silylated samples reached better CH<sub>4</sub> conversion with low coke formation of whisker-type that is favoured over Ni ensemble of a minimum seven Ni atoms, with particle size larger than 5 nm, being Ni very small particle size, <2nm,<sup>811</sup> a key factor to inhibit tubular whisker carbon formation.<sup>812</sup> At 700°C, 78-72% CH<sub>4</sub> and 88-80% CO<sub>2</sub> conversions with H<sub>2</sub>/CO around 1.05 were maintained over 26h TOS (Table 11, Entry 44-45).

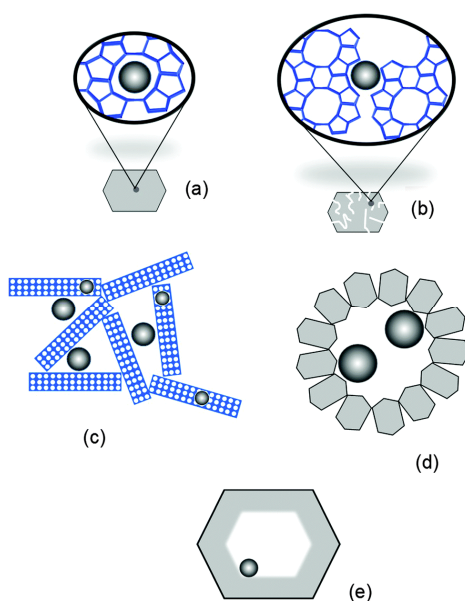


**Figure 84.** Effect of the presence of organo-silanes on the silicalite-1 surface over the formation Ni agglomerates. Reprinted with permission from ref.<sup>876</sup>. Copyright 2011, Springer Science Business Media B.V.

Recently, encapsulated Ni clusters into microporous silicalite-1 catalysts were prepared and used for DRM. Ni/Silicalite catalyst exhibited high stability and no coke deposition under a wide range of conditions.<sup>877</sup> The authors claimed the presence of Ni-O-Si species intercalated into the silicalite-1 framework that enables the stabilization of small metallic Ni-clusters preventing sintering and coke formation (Table 11, Entry 46).

- Effect of the morphology of the silicalite-1-based catalysts for DRM

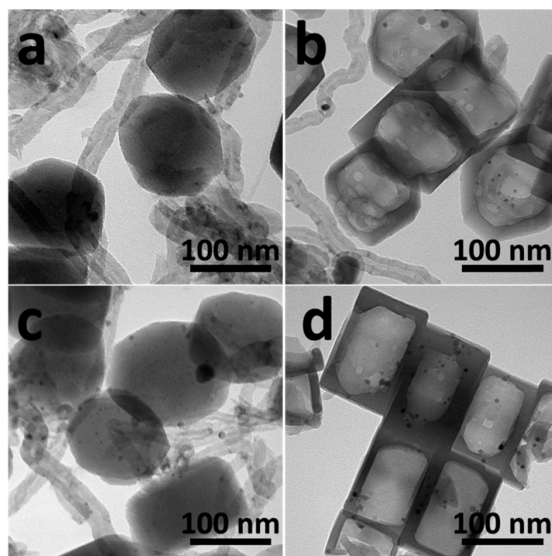
The benefits of fibrous mesostructures, with micro and mesopores system, such as their high surface area, enhanced diffusion for bulky molecules and accessibility to active sites are of great interest for the synthesis and development of efficient catalysts and their use as support, to achieve high dispersion of metallic particles and stabilization by spatial confinement effect.<sup>878</sup> In line, mesostructured fibrous MFI was synthesized by microemulsion zeolite seed crystallization method, and Ni supported by incorporation via different routes. Ni-mesostructured fibrous MFI catalysts owing to fibrous morphology, high Ni dispersion, strong metal-support interaction and moderate acidity, exhibited improved stabilization of Ni particles and catalytic activity over time on stream.<sup>879</sup> Thus, excellent catalytic performance and high stability of the 5wt%Ni/MFI prepared by wet-impregnation was registered, with 70% CH<sub>4</sub> and 73% CO<sub>2</sub> conversions (Table 11, Entry 47). Kinetic studies revealed that activation energy of CH<sub>4</sub> and CO<sub>2</sub> was dependent on surface acidity that boosted CH<sub>4</sub> cracking and other side reactions. The encapsulation of metal particles into zeolite micropores or cavities allows increasing the activity, selectivity and stability of the catalyst reducing metal sintering (Figure 85).<sup>48,51,707,870,880,881</sup>



**Figure 85.** Encapsulation of metal particles into zeolite-based architectures: in framework cavities (a), in intracrystalline mesopores (b), inside or between zeolite nanosheets (c), in polycrystalline shells (d) and

in hollow single crystals (e). Reprinted with permission from ref.<sup>882</sup>. Copyright 2015, Royal Society of Chemistry.

Since encapsulation can present limitations of diffusion and accessibility to nanoparticles of reactants in sub-nanometric micropores, new developments in zeolite synthesis allowed the preparation of new materials with hierarchical structures containing micro and mesopores systems or more advanced architectures such core-shell or hollow structures.<sup>882</sup> Hollow zeolites are very attractive due to their crystalline structure, hydrothermal and chemical stability and shape-selectivity due to their pores system and versatility in their properties and composition.<sup>883</sup> Accordingly, the catalytic performance of encapsulated Ni-Pt bimetals in hollow silicalite-1 was reported for the first time in 2015.<sup>884</sup> The preparation of hollow 1.5wt%Ni-0.5 wt%Pt@HolS-1 enabled high dispersion of Ni-Pt bimetallic nanoparticles encapsulated in hollow silicalite-1. 1.5wt%Ni-0.5wt%Pt@Hol S-1 catalyst exhibited higher catalytic performance for DRM over brief 6h TOS than 1.5wt%Ni-0.5wt%Pt/S-1 that suffered rapid deactivation after 1h, and than 1.5wt%Ni@Hol S-1 due to Pt doping effect and improved stability against sintering and coke deposition, only 1.0% carbon deposition was observed. Although 1.5wt%Ni-0.5wt%Pt/S-1 and 1.5wt%Ni@Hol S-1 had similar coke deposition, they exhibited different catalytic stability (Figure 86).



**Figure 86.** Coke deposition over spent catalysts. TEM images of (a) 1.5Ni/S-1, (b) 1.5Ni@HolS-1, (c) 1.5Ni-0.5Pt/S-1, (d) 1.5Ni-0.5Pt@Hol S-1. Reprinted with permission from ref.<sup>884</sup>. Copyright 2015, Royal Society of Chemistry.

Ensemble of Ni atoms with minimum metal particle diameter was required to form filamentous carbon. In the case of 1.5wt%Ni/S-1, because of large Ni particles, filamentous carbon deposition occurred inducing rapid deactivation. Since 1.5wt%Ni@HolS-1 supported well dispersed and encapsulated Ni nanoparticles in hollow zeolite with small particle size (~3.44 nm) and Ni larger particles on the outer surface (~14.6 nm), filamentous carbon was also formed but catalytic

activity was maintained. Although the Ni-Pt particles exhibit sintering resistance, 1.5Ni–0.5Pt/S-1 deactivated quickly due to coke deposition without the protective shell, while 1.5Ni–0.5Pt@Hol S-1 exhibited the best catalytic performance and stability owing to the high bimetallic nanoparticles dispersion and spatial confinement effect of the shell, lowering coke formation. At 800°C, 0.1 MPa, 72% CH<sub>4</sub> and 80% CO<sub>2</sub> conversions were maintained for 6h TOS over 1.5Ni–0.5Pt@Hol S-1 (Table 11, Entries 48-51). Good catalytic results were reported over short TOS, no data of H<sub>2</sub> and CO yield nor selectivity were reported, which together with low metal content augured low yields and a short operating life.

- Pt/silicalite-1-based catalysts for DRM

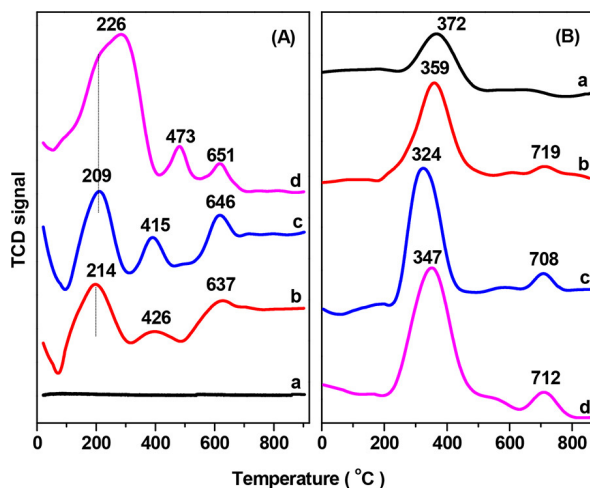
As above mentioned, among the strategies to improve metal supported catalysts and minimize sintering, the encapsulation of metal nanoparticles within zeolite, hollow or core-shell material constitutes an emerging approach. Accordingly, amorphous-silica-coated metal nanoparticles (< 2 nm) were successfully prepared and used in the presence of organic structure-directing agent, under hydrothermal conditions to convert amorphous-silica-coated Pt nanoparticles into the zeolite and provide a Birdcage-type zeolite catalyst encapsulating small metal nanoparticles (Pt@Silicalite-1).<sup>885</sup> Pt@Silicalite-1 with low Pt content, 0.1 wt%, exhibited higher and more stable activity than Pt/Silicalite-1 for DRM, at 670°C, over 12h, moderate 66-56% CO<sub>2</sub> and 54-38% CH<sub>4</sub> conversions with 0.8-0.6 H<sub>2</sub>/CO ratio (Table 11, Entry 52). The superior catalytic performance of Pt@Silicalite-1 was attributed to higher metal dispersion and good sintering resistance. Nevertheless, at 670°C, rapid deactivation was registered due to zeolite structure collapse, implying that the thermal stability of the zeolite could play an important role in the catalytic stability of Birdcage-type catalysts for DRM process.

\* CeO<sub>2</sub>-Ni/MCM-22 catalysts for DRM

The effect of ceria incorporation to metal nanoparticles supported catalysts have been largely reported due to the improvement of metal dispersion and stability, and of NiO reducibility due to the presence of high amount of oxygen vacancies and high oxygen mobility. Accordingly, the catalytic performance for DRM of a series of Ni-MCM-22-based catalysts with different CeO<sub>2</sub> contents, prepared by a sol-gel method, was recently reported.<sup>886</sup> Catalytic data showed an optimum cerium content (8wt%), and the best catalytic performance was obtained over 8wt%CeO<sub>2</sub>-9wt%Ni/MCM-22 catalyst owing to high oxygen storage capacity together with improved NiO reducibility (O<sub>2</sub> and H<sub>2</sub>-TPR, Figure 87). Higher CeO<sub>2</sub> loading is unfavourable because Ni particles are partially covered. Characterization data revealed the stability of the spent catalyst structure at 750 °C, and that the addition of CeO<sub>2</sub> enabled higher Ni nanoparticles dispersion and improved reducibility. Moreover, the presence of CeO<sub>2</sub> in Ni/MCM-22 minimized



coke deposition (3-4wt%) on Ni due to high oxygen storage capacity at the interface Ni/CeO-Si groups leading to easy oxidation of adsorbed carbon species into CO. Thus, at 750°C, very good 83-75% CH<sub>4</sub> and 99-92% CO<sub>2</sub> conversions with H<sub>2</sub> and CO selectivity over 8wt%CeO<sub>2</sub>-9wt%Ni/MCM-22 catalyst with H<sub>2</sub>/CO ratio around 0.84 were maintained during 60h TOS (Table 11, Entries 53-54). These results illustrated great potential of MCM-22 to the development of industrial catalyst although no patent was published.



**Figure 87.** (A) O<sub>2</sub>-TPD and (B) H<sub>2</sub>-TPR profiles of (a) 9Ni/MCM-22, (b) 4CeO<sub>2</sub>-9Ni/MCM-22, (c) 8CeO<sub>2</sub>-9Ni/MCM-22, and (d) 12CeO<sub>2</sub>-9Ni/MCM-22. Reprinted with permission from ref.<sup>886</sup>. Copyright 2017, American Chemical Society.

\* FAU-based catalysts for DRM

- Co/Y-based catalysts for DRM

The use of sonochemical, plasma and microwave for materials synthesis has much interest due to the impacts of these catalyst preparation methods on physicochemical properties such as dispersion and stability of metal nanoparticles, surface area, reduced particle size, higher homogeneity, softened synthesis conditions (time, temperature) and reduced cost.<sup>887-891</sup> Then, the effect of ultrasounds and Co-loading over Y zeolite catalytic performance for DRM was shown to enhance the dispersion of Co nanoparticles and surface area in comparison to impregnation methods,<sup>892</sup> and nanoparticles with an average crystallite size around 30-40nm were formed. The best catalytic results were obtained for 10wt% Co content at 850°C reaction temperature. Maximum 81% CH<sub>4</sub> and 90% CO<sub>2</sub> conversions with H<sub>2</sub>/CO ratio close to 0.76 were achieved, with good selectivity towards H<sub>2</sub> and CO production, being those 75 and 88%, respectively, with catalyst moderate stability over 10h TOS with continuous decrease in CH<sub>4</sub> and CO<sub>2</sub> conversions (Table 11, Entries 55-57).

- Catalytic performance of bimetallic Faujasite-based catalysts for DRM

The addition of a second metal, especially a noble metal and rare earth metal is well known to enhance activity, selectivity and the catalyst coke resistance in comparison to monometallic catalysts. The influence of different preparation methods, wetness impregnation and two solvent routes were compared for the preparation of bimetallic Ni-Rh/Y catalysts for DRM. The catalytic results showed an enhancement of 7.5wt%Ni/NaY catalytic properties prepared following two solvents routes.<sup>893</sup> Moreover, the incorporation of Rh allowed improving the reducibility of NiO particles due to higher Ni dispersion and enhanced stability. With 0.1wt% Rh content, excellent 100% CH<sub>4</sub> and CO<sub>2</sub> conversions were achieved at 584°C, respectively, while only 60% CH<sub>4</sub> and CO<sub>2</sub> conversion were reached at 559°C, over 0.1wt%Rh-7.5wt%Ni/NaY (Table 11, Entries 58-59). Interesting results were achieved at low temperature along short 12h TOS. A study of Mn incorporation effect over the catalytic activity and stability of three Ni-based zeolites catalysts showed different impacts depending on the support, but the catalytic results were not improved (Table 11, Entries 64-67).<sup>847</sup> The positive effects of low Mn loading were the reduction of carbon deposition and the decrease of the Ni nanoparticle size and dispersion on the zeolite support. However, as Mn loading increased, the crystallinity of the zeolite structure and its micropore surface area generally decreased.

- Effect of basic properties of Ni/Y-based catalysts for DRM

As above mentioned, the presence of basic sites enables to minimize carbon deposition owing to higher CO<sub>2</sub> coverage of the catalytic surface and lower methane decomposition. Accordingly, MgO has been considered a suitable additive to DRM catalysts improving activity and stability.<sup>894,895</sup> A study of Mg, Mn, K, and Ca addition onto Ni/HY catalysts revealed the improved resistance of the catalyst to coke deposition.<sup>894</sup> Mg, Mn and Ca doping induces an increase in activity and stability of Ni/HY catalyst while K doping worsens them with a high coke formation and reactor plugging. BET and XRD characterization data indicated that the presence of Mg allowed reducing the Ni nanoparticles size and enhancing Ni dispersion owing to partial coverage of NiO particles by MgO<sub>x</sub>. Moreover, the presence of basic sites favoured the CO<sub>2</sub> coverage of the Ni-Mg/HY catalyst surface minimizing the CH<sub>4</sub> decomposition and coke deposition. Other characterization data were not provided. At 700°C, 93% CH<sub>4</sub> and 89% CO<sub>2</sub> conversions with H<sub>2</sub>/CO ratio close to 0.94 were maintained over 720h (Table 11, Entry 68). High catalytic performance was disclosed but no data of H<sub>2</sub> and CO selectivities were provided and high CH<sub>4</sub>/CO<sub>2</sub> ratio=3 was used.

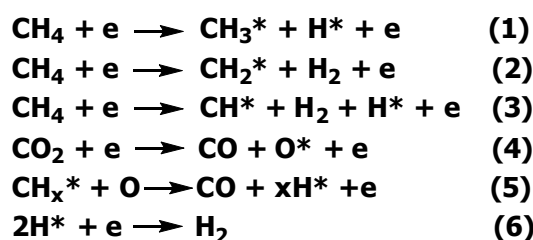
\* *BEA zeolite-based catalysts for DRM*

The beta zeolite was scarcely used as support for the development of DRM catalysts. The catalytic activity of bimetallic based zeolite catalysts has been reported, specially incorporating Ni-Rh over MFI or FAU type zeolites due to the great influence of the support.<sup>896</sup> Accordingly, the benefit of Rh incorporation into Ni/Beta zeolites was recently described.<sup>896</sup> The Rh-Beta sample exhibited the higher catalytic results and stability while the addition of Rh to Ni catalyst allowed to enhance the activity and stability in comparison to monometallic Ni sample. At 700°C, 74% CH<sub>4</sub> and 78% CO<sub>2</sub> conversions and moderate selectivity to CO and H<sub>2</sub> with H<sub>2</sub>/CO~1.17 were achieved over Rh-Ni/Beta catalysts with good resistance to coke formation (2.85wt%) (Table 11, Entries 69-71). Because the presence of basic sites plays an important role over carbon deposition and CH<sub>4</sub> decomposition, MgO has been considered a suitable additive to DRM catalysts improving activity and stability.<sup>894,895</sup> Accordingly, the addition of MgO to Ni/Beta catalysts was shown to enhance the catalytic performance and stability of the DRM catalyst.<sup>897</sup> The Ni/10wt%MgO-beta catalysts exhibited better activity with low carbon deposition (2.0 wt%) after 7.5h TOS. At 800°C, 95% CH<sub>4</sub> conversion and 97% CO<sub>2</sub> conversion with H<sub>2</sub>/CO ratio close to 1.05 were achieved (Table 11, Entry 72). Earlier, a comparison study of Beta and Y zeolites as support for Ni-Pt based catalysts was reported.<sup>898,899</sup> Dealuminated Y and Beta zeolites were used as supports for the preparation of bimetallic Ni and Pt catalysts. The dealumination process created mesopores enabling higher dispersion of the metals nanoparticles and improving catalytic activity. The Y zeolite exhibited higher total acidity in comparison to Beta zeolite. The catalytic performance of bimetallic Ni-Pt/zeolite catalysts revealed lower activity than monometallic Pt samples, 1.70 and 1.90 molg<sub>metal</sub><sup>-1</sup>h<sup>-1</sup> for Ni-Pt/Y and Ni-Pt/β respectively, and 2.0 and 3.20 molg<sub>metal</sub><sup>-1</sup>h<sup>-1</sup> for Pt/Y and Pt/β, respectively, while Ni/Y and Ni/β were practically inactive due to severe carbon deposition (~60wt%) (Table 11, Entries 60-63). The higher activity of bimetallic in comparison to Ni samples was attributed to the adsorption of CO<sub>2</sub> on the adjacent Ni site together with Pt. However, the best catalytic data were achieved in the presence of Pt-Beta catalyst, due to the higher accessibility and stability of the Beta and lower acidity in comparison to Y zeolite that suffered strong carbon deposition. On the other hand, Pt-Beta catalyst exhibited higher activity and stability than Pt/Al<sub>2</sub>O<sub>3</sub> and Pt/C due to superior resistance to coke deposition (16 wt%) attributed to improved Pt nanoparticles dispersion. Nevertheless, low catalytic results were reported, especially CH<sub>4</sub> conversion decreased gradually on 24h from 30 to 20%.

\* *DRM-combined technology*

- DRM-combined plasma technology

As described above, the non-equilibrium character of plasma system enables to overcome barrier energy and thermodynamic limitations at low temperature in chemical processes such as CO<sub>2</sub> conversions.<sup>668-670</sup> There exist various types of non-thermal plasma and among them, DBD constitutes a versatile technique with some advantages such as uniform distribution of micro-discharges, high-energy electrons and operability at ambient conditions.<sup>900</sup> Accordingly, DRM was studied under thermal, plasma and plasma-assisted thermal conditions in the presence of Ni (15%) on Al<sub>2</sub>O<sub>3</sub>, TiO<sub>2</sub> and ZSM-5.<sup>901</sup> The best catalytic performance were achieved over Ni/Al<sub>2</sub>O<sub>3</sub> under plasma conditions due to Ni lower particles size and higher surface area. The best reaction conditions were reached under plasma (DBD) thermal conditions since the reactants can be previously activated in the DBD zone and react in the thermocatalytic reactor (Scheme 62). Moreover, the recombination of different carbon species can lead to the formation of hydrocarbons and alcohols. Good 76% CH<sub>4</sub> and 71% CO<sub>2</sub> conversions were obtained over 15Ni/ZSM-5, at 500°C, under plasma-assisted thermal conditions, while 73% CH<sub>4</sub> and 68% CO<sub>2</sub> conversions were achieved under thermal conditions (Table 11, Entries 73-74). No data of stability were provided.

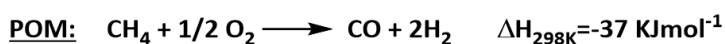
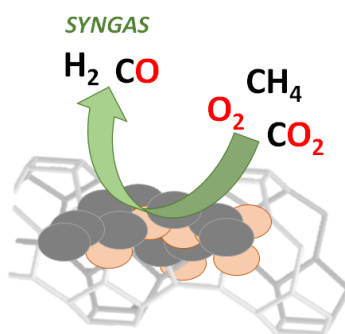


**Scheme 62.** Equations of formation of different reactants species and reaction under plasma activation.

Few years earlier, a study of DRM process under DBD plasma in the presence of 4A zeolite was reported.<sup>902,903</sup> The effects of peak voltage, total gas flow rate and CO<sub>2</sub>/CH<sub>4</sub> ratio over CO<sub>2</sub> and CH<sub>4</sub> conversions and H<sub>2</sub>/CO were studied. At high-applied voltage level (from 6 kV to 12 kV), the high energy electrons generated in the plasma discharge zone may dissociate CO<sub>2</sub> and CH<sub>4</sub> molecules in the gas phase and on the catalyst surface. The results of DBD process showed that CO<sub>2</sub> and CH<sub>4</sub> conversion increased by the increase of peak voltage that greatly affected H<sub>2</sub>/CO ratio that varied from 1.8 to 1.3. For DBD process with catalyst, the H<sub>2</sub>/CO ratio was close to 1 for all applied voltage, indicating a simultaneous production of H<sub>2</sub> and CO due to catalytic reactions. Therefore, the best catalytic results were reached with 12KV, 900 Hz and CO<sub>2</sub>/CH<sub>4</sub> with 50% CO<sub>2</sub> conversion, 46% CH<sub>4</sub> conversion and H<sub>2</sub>/CO~1 in the presence of the zeolite (Table 11, Entries 75-76).

- DRM+POM (Partial Oxidation of Methane) combined processes

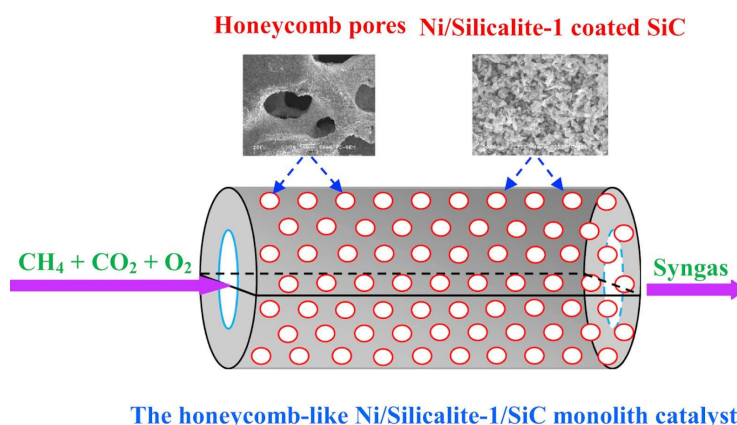
Up to now, the DRM commercialization is not envisioned due to strong limitations such as high energy consumption due to endothermic process, rapid catalysts deactivation because of coke deposition and water formation that reduce the syngas selectivity and H<sub>2</sub>/CO ratio. The possible combination of DRM and POM (Partial Oxidation of Methane) processes constitutes a promising alternative to the DRM commercialization since presents several advantages and allows counteracting the deficiencies of the stand-alone DRM (Scheme 63). The combination of DRM/POM is supposed to improve heat transfer due to the coupling of both exothermic and endothermic reactions leading to more efficient energy process, while the variation in the feed composition allows to tailor H<sub>2</sub>/CO ratio, and the O<sub>2</sub> addition limits the coke formation and improves CH<sub>4</sub> conversion and catalyst stability.<sup>904–906</sup> Ni-based catalysts are suitable for the development of combined POM+DRM owing to the high nickel activity, availability and price. Moreover, in the two last decades, great efforts have been spent to improve the activity, robustness and stability of Ni-based catalysts through the addition of different type and nature of promoters, control of Ni nanoparticles size and dispersion, Ni nanoparticles confinement and Ni improved reducibility, being Ni-based catalysts good candidates for industrial implementation.



**Scheme 63.** Equation of POM+DRM reactions.

Efforts in developing new class of supported catalysts based on silicon carbide (SiC) showed the SiC great mechanical and thermal properties and inertness. SiC can be prepared in commercially viable shapes into monolith or honeycomb. These desirable properties make SiC a valuable support in comparisons to conventional ones (SiO<sub>2</sub>, Al<sub>2</sub>O<sub>3</sub>, ZrO<sub>2</sub>).<sup>907</sup> The honeycomb-shaped SiC as catalyst support can strengthen the heat transfer and mass transfer and due to its hardness and light weight is an attractive catalyst support for fluidized bed reactor. Then, Silicalite-1 zeolite was deposited on the honeycomb-like monolithic SiC foam by hydrothermal synthesis. Ni-Silicalite-1-coated SiC (Ni/S-1/SiC) catalyst was so prepared by impregnation and used for

combined DRM and POM (Figure 88).<sup>908</sup> POM is a mildly exothermic reaction and enables the production of syngas. Nevertheless, due to the presence of a hot spot and explosion danger this reaction can be applied only in combination with endothermic reaction such as DRM. Ni/S-1/SiC monolith catalyst exhibited high catalytic performance and stability for DRM/POM processes over 30h TOS, and higher than Ni/S-1 and Ni/SiC catalysts. At 750°C, 0.1 MPa, 56.1% CH<sub>4</sub> and 52.1% CO<sub>2</sub> conversions with H<sub>2</sub>/CO ratio close to 1.07 were maintained for 30h TOS with CH<sub>4</sub>:CO<sub>2</sub>:O<sub>2</sub>=8:4:2 ratio (Table 11, Entry 77). On the other hand, the H<sub>2</sub>/CO molar ratio obtained over Ni/S-1/SiC catalyst could be optimised varying CH<sub>4</sub>:CO<sub>2</sub>:O<sub>2</sub> ratio. The better catalytic results of Ni/S-1/SiC monolith catalyst were attributed to the strong interactions between SiC support and metal Ni particles improved by the Silicalite-1 coated SiC, inhibiting the aggregation and sintering of Ni particles. TG analysis of used catalyst revealed that Ni/S-1/SiC monolith catalyst showed good resistance to coke deposition being of 4 wt%.

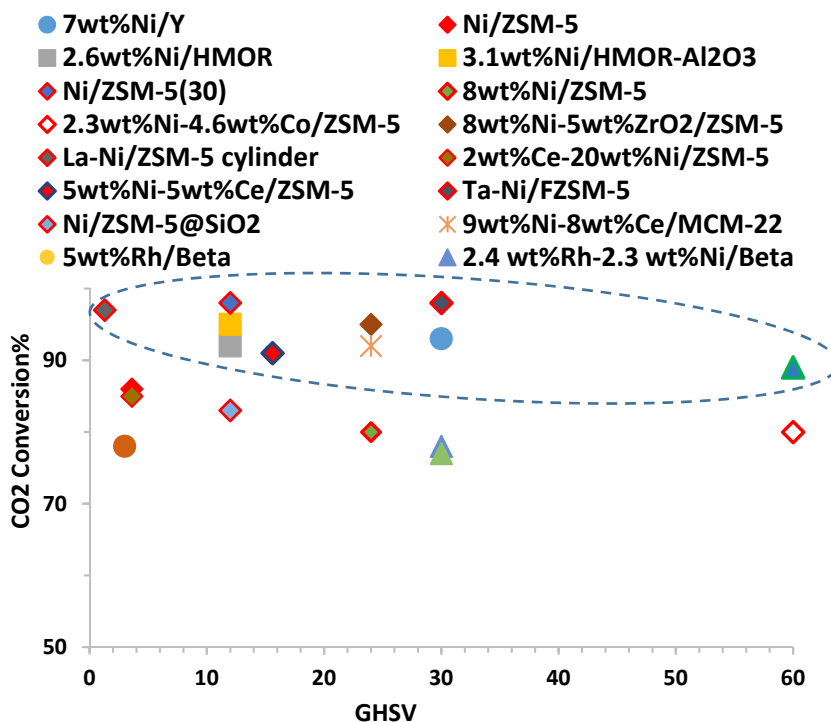


**Figure 88.** Ni-Silicalite-1-coated SiC (Ni/S-1/SiC) catalyst for combined DRM and POM. Reprinted with permission from ref.<sup>908</sup> Copyright 2017, Elsevier B.V. All rights reserved.

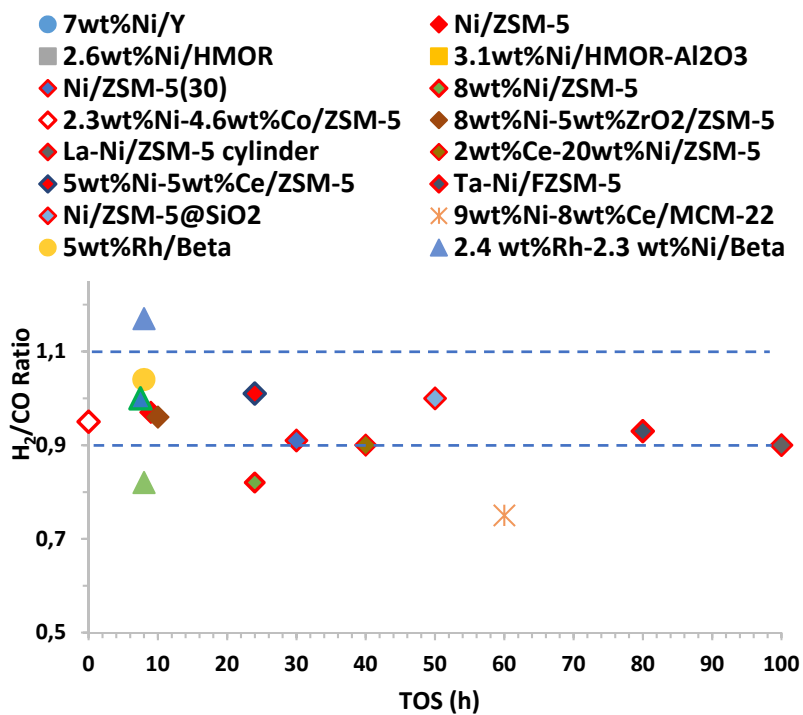
Another strategy to enhance the catalyst stability, is the addition of a second metal improving distribution of Ni over the support due to the formation of strong interactions metal-support and smaller metallic particle size.<sup>909</sup> Accordingly, the mixing of Co and Ni resulted to enhance the catalysts activity and stability for DRM process.<sup>836,910,911</sup> Following these approach, Ni, Co, and Ni-Co supported on ZSM-5 synthesized by the microwave assisted hydrothermal method (ZSM-5<sub>mw</sub>) and on commercial sample (ZSM-5<sub>HT</sub>) were prepared and used as catalysts for POM and DRM processes to syngas production.<sup>912</sup> The Ni and Ni-Co based ZSM-5<sub>mw</sub> and based ZSM-5<sub>HT</sub> catalysts exhibited high catalytic activity for POM and DRM processes with a low 2wt% of metal content with syngas yield up to 97% in the range of temperature 850-950°C (Table 11, Entries 78-80). The simultaneous presence of Ni and Co increased the resistance to coke deposition for DRM reaction and prevent the formation of carbon fibres usually observed on Ni catalysts. The authors did not explained the higher resistance of the bimetallic catalyst to coke deposition and only described the formation of Co<sub>3</sub>O<sub>4</sub> for Ni-Co based ZSM-5 samples.

ii) Conclusion

Catalytic dry reforming of methane is an important strategy to mitigate the emissions of CH<sub>4</sub> and CO<sub>2</sub> greenhouse gases. Ni based-zeolite catalysts owing to the huge properties of zeolites such as high surface area and thermal stability offer opportunities for the preparation of DRM catalysts. Moreover, different strategies have been reported to improve dispersion and stabilization of nickel particles by the addition of suitable second metal (promoter), enabling the establishment of new electronic interactions metal/metal and metal/support that enhance the NiO reducibility and coke resistance owing to oxidation of carbon species deposited on Ni particles surface, or by the control of acidity/basicity through the incorporation of alkali metal promoting CO<sub>2</sub> adsorption and activation (C-O cleavage). Thus, great opportunities for the development of robust catalysts based on zeolites have been reported and the results summarised in the Table 11 illustrate the high activity of zeolite-based catalysts for DRM reaction at high temperature. The high energy consumption remains the main drawback of the technology that will be produced from renewable (wind, water, sun) or nuclear sources. Considering CO<sub>2</sub> conversion and ratio H<sub>2</sub>/CO as function of GHSV and TOS some results can be highlighted as it is displayed in the Figures 89 and 90 where Ni/ZSM-5(30), 5wt%Ni-5wt%Ce/ZSM-5, La-Ni/ZSM-5 cylinder, Ta-Ni/FZSM-5, 5wt%Mg-Ni13wt%/HY and 10wt%Ni-10wt%MgO/BEA (Table 11, Entries 15, 29, 27, 41, 68, 72) exhibited interesting catalytic performance. Nevertheless, only for 5wt%Ni-5wt%Ce/ZSM-5 data of H<sub>2</sub> and/or CO<sub>2</sub> yield and/or selectivity is given and so productivity can only be evaluated in this case.



**Figure 89.** CO<sub>2</sub> conversion was plotted versus GHSV for different DRM zeolite-based catalysts. The ovoid highlights the best catalytic performance: high conversion versus GHSV.



**Figure 90.** H<sub>2</sub>/CO ratio was plotted versus TOS (h) for different DRM zeolite-based catalysts.



**Table 11.** Summary of the catalytic performance of the different reviewed DRM zeolite-based catalysts at 0.1 MPa.

Entry	Catalysts*	Conditions	$\chi_{\text{CH}_4}$ (%)	$\chi_{\text{CO}_2}$ (%)	H <sub>2</sub> /CO	Sel. H <sub>2</sub> /CO	Coke wt%	Year <sup>Ref</sup>
<b>Comparison studies: Ni based zeolites catalysts</b>								
1	7Ni/Y	700°C, GHSV=30 Lg <sub>cat</sub> <sup>-1</sup> h <sup>-1</sup>	91 (91.6)	93 (93)	1.79	~65 (65) (H <sub>2</sub> )	6.83	2008 <sup>822</sup>
2	7Ni/X	<sup>1</sup> ,CH <sub>4</sub> :CO <sub>2</sub> =1, TOS=0.5 h (5h)	89 (78)	90 (80)	1.27	~60 (60) (H <sub>2</sub> )	0.24	
3	7Ni/A		72 (18)	80 (20)	0.31	58 (30) (H <sub>2</sub> )	0.25	
4	7Ni/ZSM-5		92 (57.8)	92 (62)	1.03	~ 62 (50) (H <sub>2</sub> )	2.16	
5	3.5Ni/Y	650°C, GHSV=12 Lg <sub>cat</sub> <sup>-1</sup> h <sup>-1</sup> ,	53 (40)	64 (56)	-	-	-	2005 <sup>823</sup>
6	8.7Ni/ZSM-5	0.1g <sub>cat</sub> , CH <sub>4</sub> :CO <sub>2</sub> =1, TOS=1h (6h)	78 (72)	75 (71)	-	-	-	
7	8.1Ni/Al <sub>2</sub> O <sub>3</sub>		78 (70)	85 (77)	-	-	-	
8	Ni/Al <sub>2</sub> O <sub>3</sub>	700°C, F <sub>T</sub> =36 mLmin <sup>-1</sup> ,	80.1	82.9	0.96	76.2/78.1	8	2013 <sup>824</sup>
9	Ni/Y	GHSV=3.6 L <sub>cat</sub> <sup>-1</sup> h <sup>-1</sup> , 0.6g <sub>cat</sub> ,	70.8	67.4	0.97	66.3/65.8	13.5	
10	Ni/ZSM-5	TOS=9h, CH <sub>4</sub> :CO <sub>2</sub> =1	<b>78.2</b>	<b>86.3</b>	0.97	85.4/76.8	3.3	
11	2.6Ni/HMOR	750°C, GHSV=12 L <sub>cat</sub> <sup>-1</sup> h <sup>-1</sup> ,	<b>86</b>	<b>92</b>	-	-	5.4	2002 <sup>825</sup>
12	3.2Ni/HY	CH <sub>4</sub> :CO <sub>2</sub> :He=20:20:40 mLmin <sup>-1</sup> ,	10	15	-	-	-	
13	2.5Ni/NaMOR	0.2g <sub>cat</sub> , TOS=6h	75	87	-	-	-	
14	3.1Ni/HMOR-Al <sub>2</sub> O <sub>3</sub>		<b>87</b>	<b>95</b>	-	-	3.5	
<b>MFI: Ni/ZSM-5</b>								
15	Ni/ZSM-5(30)	800°C, GHSV=12 Lg <sub>cat</sub> <sup>-1</sup> h <sup>-1</sup> , TOS=30h, CH <sub>4</sub> :CO <sub>2</sub> =1	<b>95</b>	<b>98</b>	0.91	-	-	2016 <sup>826</sup>
● <b>Preparation method</b>								
16	8Ni/ZSM-5	850°C, GHSV=24 Lg <sub>cat</sub> <sup>-1</sup> h <sup>-1</sup> , 0.05g <sub>cat</sub> , CH <sub>4</sub> :CO <sub>2</sub> =1, TOS=24h	<b>82</b>	<b>80</b>	0.82	42/50 (Yield)	-	2013 <sup>830</sup>
● <b>Bimetallic:</b>								
<i>Transition metal</i>								
17	2.3Ni-4.6Co/ZSM-5	750°C	<b>72</b>	<b>80</b>	<b>0.95</b>	64/62.5	5	2015 <sup>841</sup>
18		850°C	80	85	0.97	65/61	-	
19	7Ni/ZSM-5	750°C	55	65	0.9	62.5/62.5	46.4	
20	7Co/ZSM-5	750°C	66	87	0.9	62.5/62.5	3.6	
GHSV=60 Lg <sub>cat</sub> <sup>-1</sup> h <sup>-1</sup> , CH <sub>4</sub> :CO <sub>2</sub> =1 (20 mLmin <sup>-1</sup> )								
21	10Ni/ZSM-5		67 (0.5h)	62 (0.5h)	0.91	69/79	-	2020 <sup>847</sup>
22		700°C, 0.025g <sub>cat</sub> , 60 mLmin <sup>-1</sup> ,	24 (20h)	36 (20h)	0.59	69/94	-	
23	5Mn10Ni/ZSM-5	GHSV=144 Lg <sub>cat</sub> <sup>-1</sup> h <sup>-1</sup> , CH <sub>4</sub> :CO <sub>2</sub> =1,	24 (0.5h)	37 (0.5h)	0.55	65/95	-	
24			13 (20h)	22 (20h)	0.62	78/93	-	

25	8Ni-5ZrO <sub>2</sub> /ZSM-5	850°C, GHSV=24 Lg <sub>cat</sub> <sup>-1</sup> h <sup>-1</sup> , CH <sub>4</sub> :CO <sub>2</sub> =1, TOS=10h	96	95	~0.96	95/90 (Yield)	2014 <sup>848</sup>
<b>Rare earth metal (lanthanides)</b>							
26	La-Ni/ZSM-5	700°C, GHSV=48 Lg <sub>cat</sub> <sup>-1</sup> h <sup>-1</sup>	67	69	~0.9		2005 <sup>852</sup>
27	La-Ni/ZSM-5 cylinder	850°C, GHSV=1300h <sup>-1</sup> , Pilot Plant, TOS=100h	94	97			2009 <sup>854</sup>
28	2Ce-20Ni/ZSM-5	800°C, TOS=40h, GHSV=3.6Lg <sub>cat</sub> <sup>-1</sup> h <sup>-1</sup> , H <sub>2</sub> O/C=0.5	95	85	0.9-1		2020 <sup>857</sup>
29	5Ni-5Ce/ZSM-5	800°C, GHSV=15.6 Lg <sub>cat</sub> <sup>-1</sup> h <sup>-1</sup> , CH <sub>4</sub> :CO <sub>2</sub> =1, TOS=24h	97.1	91.4	1.01	98 (H <sub>2</sub> )	2014 <sup>860</sup>
30	NiCuNdMo/Al <sub>2</sub> O <sub>3</sub> -ZSM-5	850°C, F <sub>T</sub> =100 mLmin <sup>-1</sup> , GHSV=3600h <sup>-1</sup> , CH <sub>4</sub> :CO <sub>2</sub> =2	98	97	1		2016 <sup>861</sup>
<b>Noble metal doping</b>							
31	0.3Pt-6 Ni/ZSM-5	500°C	9.9	23.5	0.68		2007 <sup>862</sup>
32		600°C CH <sub>4</sub> :CO <sub>2</sub> :N <sub>2</sub> =20:20:60, F <sub>T</sub> =100 mLmin <sup>-1</sup> , 0.1g <sub>cat</sub> , GHSV=60Lg <sub>cat</sub> <sup>-1</sup> h <sup>-1</sup>	28	69	0.86		
			Activity mol <sub>CO2</sub> g <sub>metal</sub> <sup>-1</sup> h <sup>-1</sup>				
33	1.97Ni/0.63Ru/ZSM-5	600°C, 100 mLmin <sup>-1</sup> , CH <sub>4</sub> :CO <sub>2</sub> :H <sub>2</sub> =15:15:70		0.41			2002 <sup>45</sup>
34	Ni/ZSM-5			0.12			
<b>• Basic properties</b>							
35	K-5Ni-Ca/ZSM-5	24KPa, 800°C, GHSV=44000h <sup>-1</sup> , CH <sub>4</sub> :CO <sub>2</sub> :N <sub>2</sub> =1:1:2.2	94	95	~1	94 95	1998 <sup>865</sup>
36	Ni/ZSM-5	750°C, 0.2g <sub>cat</sub> , F <sub>T</sub> =100 mLmin <sup>-1</sup> ,	55	61	~0.8		2020 <sup>866</sup>
37	Ni/FZSM-5	CH <sub>4</sub> :CO <sub>2</sub> :N <sub>2</sub> =1:1:3,	78	79	~0.9		
38	Ca-Ni/FZSM-5	GHSV=30Lg <sub>cat</sub> <sup>-1</sup> h <sup>-1</sup>	81	80	~0.85		
39	Mg-Ni/FZSM-5	TOS=1h	85	90	~0.91		
40	Ta-Ni/FZSM-5		90	98	~0.93		
41	Ta-Ni/FZSM-5	TOS=80h	91	98-96			
<b>• Morphology</b>							
42	Ni/ZSM-5@SiO <sub>2</sub>	800°C, 40 mLmin <sup>-1</sup> , CH <sub>4</sub> :CO <sub>2</sub> =1,	90-83	90-83	~1		2019 <sup>872</sup>
43	Ni/ZSM-5	TOS=50h, GHSV=12Lg <sub>cat</sub> <sup>-1</sup> h <sup>-1</sup>	83-72	80-67	1.03- 1.07		

**MFI: Silicalite 1**

44	5Ni/Silicalite	700°C, 1 MPa, 100 mLmin <sup>-1</sup> ,	82-80	70-65	1.15		2011 <sup>875,87</sup>
45	5Ni/Silicalite-S	CH <sub>4</sub> :CO <sub>2</sub> =1, 26h,	85-88	83-80	1.05		6
46	5Ni/Silicalite	650°C, GHSV=1800 Lg <sub>cat</sub> <sup>-1</sup> h <sup>-1</sup> , CH <sub>4</sub> :CO <sub>2</sub> :Ar=40:40:20	TOF: 26 mol <sub>CH4</sub> mol <sub>metal</sub> <sup>-1</sup> s <sup>-1</sup>				2019 <sup>877</sup>
<b>• Morphology</b>							
47	5Ni/MFI	800°C, TOS=30h, CH <sub>4</sub> :CO <sub>2</sub> :N <sub>2</sub> =1:1:3, GHSV=30Lg <sub>cat</sub> <sup>-1</sup> h <sup>-1</sup>	~70	~73	~0.95		2020 <sup>879</sup>
48	15Ni@S1	800°C, GHSV=72Lg <sub>cat</sub> <sup>-1</sup> h <sup>-1</sup> ,	70 (80)	75			2015 <sup>884</sup>
49	15Ni/S1	CH <sub>4</sub> :CO <sub>2</sub> =1, 6h (initial)	0 (74)	0 (73)			
50	15Ni-0.5Pt/S1		0(70)	0 (71)			
51	15Ni-0.5Pt@HoS1		72 (80)	78 (82)			
52	0.1Pt@S1	670°C, W/F=1.1*10 <sup>-3</sup> hg <sub>Pt</sub> g <sub>CH4</sub> <sup>-1</sup> , CH <sub>4</sub> :CO <sub>2</sub> =1, initial (12h)	54 (38)	66 (56)	0.8 (0.62)		2019 <sup>885</sup>
<b>MWW: Ni/MCM-22</b>							
53	9Ni-8Ce/MCM-22	700°C (0-10h)	77-78	97-98	~0.75	90/95	2017 <sup>886</sup>
54		750°C (0-60h) GHSV=24Lg <sub>cat</sub> <sup>-1</sup> h <sup>-1</sup> , CH <sub>4</sub> :CO <sub>2</sub> =1	83-77	97-92		91-83/97	
<b>FAU: Co/FAU catalyst</b>							
55	Co/Y	5wt%Co/Y	26	45		4/13 (Yield)	2015 <sup>892</sup>
56		10wt%Co/Y	81	90		61/80 (Yield)	
57		10wt%Co/Y (10h) 850°C, GHSV=24Lg <sub>cat</sub> <sup>-1</sup> h <sup>-1</sup> , CH <sub>4</sub> :CO <sub>2</sub> =1	<b>88-70</b>	<b>79-57</b>	<b>0.7- 0.58</b>	-	
<b>• Bimetallic</b>							
58	0.1Rh-7.5NiS/NaY	500°C		60		71 <1	2015 <sup>893</sup>
59		550°C GHSV=193.5Lg <sub>cat</sub> <sup>-1</sup> h <sup>-1</sup> , CH <sub>4</sub> :CO <sub>2</sub> =1, TOS=12h,		100		100 ~1	
Activity mol <sub>CO2</sub> g <sub>metal</sub> <sup>-1</sup> h <sup>-1</sup>							
60	0.9Pt/FAU	640°C, 0.1MPa, 0.07g <sub>cat</sub> ,		2			53 2009 <sup>899</sup>
61	0.6Pt-0.6Ni/FAU	100 mLmin <sup>-1</sup>		1.96			48
62	0.6Pt-0.5Ni/Beta	SV=85.7Lg <sub>cat</sub> <sup>-1</sup> h <sup>-1</sup> , CH <sub>4</sub> :CO <sub>2</sub> =1,		1.7			23
63	0.8Pt/Beta			3.2			16
64	10Ni-NH <sub>4</sub> Y	750°C; GHSV=144Lg <sub>cat</sub> <sup>-1</sup> h <sup>-1</sup>	40 (0.5h)	56 (0.5h)	0.57	64/96	2020 <sup>847</sup>

65		CH <sub>4</sub> :CO <sub>2</sub> =1,	22 (20h)	35 (20h)	0.55	67/96		
66	10Mn-10Ni-NH <sub>4</sub> Y		49 (0.5h)	56 (0.5h)	0.73	63/87		
67			23 (20h)	33 (20h)	0.64	72/91		
	<b>• Basic properties</b>							
68	5wt%Mg-Ni13wt%/HY	700°C, GHSV=3000h <sup>-1</sup> , CH <sub>4</sub> +CO <sub>2</sub> =200 mLg <sub>cat</sub> <sup>-1</sup> h <sup>-1</sup> N <sub>2</sub> :CH <sub>4</sub> :CO <sub>2</sub> =5/3/1, TOS=720h	93-79	89-78	0.94			2006 <sup>894</sup>
<b>BEA: Ni/Beta</b>								
	<b>• Rh-doping</b>							
69	5Rh/Beta	700°C, F <sub>T</sub> =100 mLmin <sup>-1</sup> , 0.2g <sub>cat</sub> ,	<b>74.5 (73)</b>	<b>77.2</b>	1.04	61/38	-	2010 <sup>896</sup>
70	2.4Rh-2.3Ni/Beta	CH <sub>4</sub> :CO <sub>2</sub> =1, GHSV=30Lg <sub>cat</sub> <sup>-1</sup> h <sup>-1</sup> ,	<b>74.4 (74)</b>	<b>78</b>	1.17	58/36	2.85	
71	5Ni/Beta	TOS=2h (8h)	67.7 (38.6)	76.9	0.82	53/41	6.83	
	<b>• Basic properties</b>							
72	10Ni-10MgO/BEA	800°C, F <sub>T</sub> =50 mLmin <sup>-1</sup> , 0.05g <sub>cat</sub> , GHSV=60Lg <sub>cat</sub> <sup>-1</sup> h <sup>-1</sup> , CH <sub>4</sub> :CO <sub>2</sub> =1, TOS=7.5h	<b>95-85</b>	<b>97-89</b>	<b>1.12-0.9</b>		2	2017 <sup>897</sup>
<b>Plasma</b>								
73	15wt%Ni/ZSM-5	DBD-24kV+500°C	77	71	1.23	45/58		2019 <sup>901</sup>
74		500°C 30 mLmin <sup>-1</sup> , 500°C, 0.6 Lmin <sup>-1</sup>	68	65	1.22	42/56		
75	Zeolite 4A	CH <sub>4</sub> :CO <sub>2</sub> =1	45	48	1.3	61/53		2015 <sup>902,903</sup>
76	DBD plasma, 10kV, 900 Hz,	CH <sub>4</sub> :CO <sub>2</sub> =4	52	57	1.3	63/54		
<b>DRM+POM</b>								
77	14Ni/S1/SiC	750°C, 0.1 MPa, GHSV=1.5Lg <sub>cat</sub> <sup>-1</sup> h <sup>-1</sup> , CH <sub>4</sub> :CO <sub>2</sub> :O <sub>2</sub> =8:4:2	56.1	52.1	1.07		4	2017 <sup>908</sup>
78	1Ni-1Co/ZSM-5 <sub>MW</sub>	850°C	92	94	0.87			2018 <sup>912</sup>
79		900°C	95	97	0.95			
80		920°C CH <sub>4</sub> :CO <sub>2</sub> =1, 15-16 Lg <sub>cat</sub> <sup>-1</sup> , CH <sub>4</sub> :O <sub>2</sub> =1, 11-12 Lg <sub>cat</sub> <sup>-1</sup>	97	98	1			

\* Metal content is given in wt%.  $\chi$ =conversion.

#### b) Oxide-based catalysts for DRM

Different strategies have been followed to improve the catalytic properties, robustness and stability of Ni based catalyst towards Ni sintering and coke deposition, such as the incorporation of noble metals and transition metal to enhance the reducibility and dispersion of Ni, or of alkali and alkaline earth metals to create basic sites enhancing the adsorption and activation of CO<sub>2</sub> (C-O cleavage), or the confinement of nanoparticles inside hollow, core-shell or mesoporous structures. Accordingly, OMS have been explored as support, especially to control the nanoparticle size, dispersion and stability owing to high surface area, controllable pores size providing beneficial spatial confinement effect to prevent Ni particle sintering. Recently, a study of the role of the pore size and the walls thickness of a series of mesoporous structures including MCM-41, KIT-6 and SBA-15 over the activity of Ni-catalysts prepared by impregnation method for DRM was reported.<sup>913</sup> The results indicated that small pore diameters and thin silica walls of MCM-41 were responsible of lower catalytic performance due to low ability to prevent Ni sintering. Thus, Ni-MCM-41 exhibited the lower activity in comparison to Ni-SBA-15 and Ni-KIT-6 (Table 12, Entries 1-3). Previously, a comparative study of Ni supports over OMS and zeolites showed that CH<sub>4</sub> and CO<sub>2</sub> conversions were dependent on Ni particles average size that was controlled by high specific area of the support, strong interaction metal support and metal reducibility.<sup>914</sup> Thus, larger Ni particles (23-29 nm) were preferentially obtained from more readily reduced Ni owing to weaker interaction with zeolites support. In the contrary, smaller Ni particles (9-11 nm) were formed from slowly reduced Ni due to strong interaction with the SBA-15 and Al-MCM-41 supports through Ni-O-Si or Ni-Al bonds. Moreover, smaller particles exhibited higher sintering resistance and the formation of filamentous coke did not induce catalytic deactivation. Filamentous carbon deposition was observed by SEM and from DTG profiles, with amount increasing in the following order Ni/Al-MCM-41>Ni/SBA-15>Ni/MFI and negligible for Ni/FAU. At 750°C, over Ni/Al-MCM-41 and Ni/MFI, respectively, 94 and 70-60% CH<sub>4</sub> conversion and 93 and 65-55% CO<sub>2</sub> conversion, were achieved, respectively, along 12h TOS (Table 12, Entries 4-7). These results illustrated the higher physicochemical properties exhibited by OMS than zeolites to support and disperse metallic active sites, and design and develop robust and efficient DRM catalysts.

#### i) *Ni/SBA-15-based catalysts for DRM*

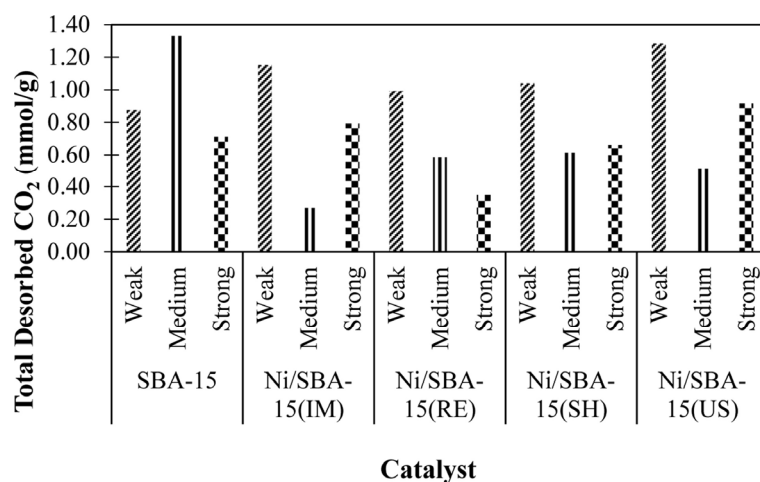
In 2006, the confinement effect of Ni nanoparticles into the stable mesoporous structure of SBA-15 was reported.<sup>915</sup> The catalytic performance of Ni/SBA-15 with different Ni contents prepared by impregnation exhibited excellent and stable 90% CO<sub>2</sub> and CH<sub>4</sub> conversions at 800°C, over 600h of TOS, with 92 and 94% H<sub>2</sub> and CO selectivity, respectively, over 12.5% Ni/SBA-15 (Table

12, Entry 8). After 600h of TOS, CO<sub>2</sub> and CH<sub>4</sub> conversion the catalysts suffer severe deactivation due to coke deposition (14.8wt%). An additional study of catalyst regeneration would have been key. The reported catalyst exhibited excellent catalytic performance over long-term test and its potential to the development of industrial catalyst should be considered.

\* *Effect of preparation method of Ni/SBA-15-based catalysts for DRM*

The preparation method of Ni supported catalysts can strongly affect the metal dispersion, particle size and interaction with the support. Therefore, different methods have been reported with the aim to improve dispersion, stability of metal nanoparticles and favour strong interaction metal-support. Recently, the catalytic behavior of previously prepared Ni nanoparticles with homogeneous ~5 nm size and further supported on ordered mesoporous silica (SBA-15), alumina and commercial silica was described.<sup>916</sup> The characterization and catalytic data revealed that the ordered mesoporous structures were more suitable to stabilize Ni nanoparticles due to beneficial confinement effects preventing nanoparticles aggregation. The presence of Lewis acid sites in the case of alumina support was responsible for higher coke formation at lower temperature. Ni/SBA-15 with 1wt%Ni exhibited the best catalytic properties. A study of reaction temperature revealed that 800°C was optimum temperature to perform DRM avoiding strong aggregation phenomenon of Ni nanoparticles that took place at 850°C. Indeed, at 800 and 850°C, 91.4 and 45.9% CH<sub>4</sub> conversion, 91 and 70% CO<sub>2</sub> conversion were reached with 0.79 and 0.97 H<sub>2</sub>/CO ratio, respectively, over Ni/SBA-15 (Table 12, Entries 9-12). The use of organic solvents as dispersants and stabilizing agents for the preparation of supported metallic nanoparticles have been recently developed. The use of ethylene glycol (EG) to support Ni (11wt%) on SBA-15 as solvent and delivery conveyor of Ni precursor inside the SBA-15 pore systems was firstly described in 2014.<sup>917</sup> The resulting catalyst exhibited improved coke and sintering resistances owing to confinement effect of SBA-15 and smaller Ni nanoparticles. At 750°C, 96% CH<sub>4</sub> and 87% CO<sub>2</sub> conversion with ~1 H<sub>2</sub>/CO ratio, were maintained over Ni/SBA-15-EG along 20 h TOS (Table 12, Entries 13-14). Later, EG was newly used as the solvent and delivery conveyor to study the spatial confinement effect of SBA-15 walls over Ni/SBA-15 physicochemical and catalytic features.<sup>918</sup> High dispersion of Ni nanoparticles (7wt%) with small particles size (~3.1nm) embedded into Al-SBA-15 mesostructure was successfully achieved. The comparison of catalytic behavior of Ni/SBA-15 catalysts revealed that sample prepared with EG exhibited better catalytic activity. Moreover, a study of catalytic stability showed that Al conferred higher hydrothermal stability to Ni/Al-SBA-15-EG catalyst and potential for prolonged use under harsh conditions. The benefit of confinement effect to prevent sintering was demonstrated with average Ni particles sizes of 3.2 and 3.6nm for fresh and spent catalysts. At

700°C, 70 and 72% CH<sub>4</sub> conversions, and 79% CO<sub>2</sub> conversion were achieved over Ni/SBA-15-EG and Ni/Al-SBA-15-EG respectively, with 0.91 and 0.95 H<sub>2</sub>/CO ratio, respectively, along 15h TOS (Table 12, Entries 15-17). The effect of different impregnation techniques (impregnation (IM), rotary evaporator- (RE), shaker (SH) and ultrasounds (US)) for the preparation 3wt%Ni/SBA-15 catalysts from waste POFA (palm oil fuel ash) over their catalytic and physicochemical properties was recently investigated.<sup>919</sup> The characterization and catalytic data revealed that impregnation method influenced Ni particle size and dispersion, and interaction with the support through the formation of Si-O-Ni bonds (FTIR spectra) with the following order of Ni-support interaction for Ni/SBA-15 samples: RE < SH < IM < US. The basicity distribution of the Ni-containing mesoporous catalysts determined by CO<sub>2</sub>-TPD evidenced three peaks with different temperature regions, indicating three types of basic active sites for CO<sub>2</sub> adsorption on the catalyst surface with different strengths (Figure 91). The Ni/SBA-15 sample prepared by impregnation under ultrasound exhibited the higher amount of strong basic sites. Finally, the catalytic study showed that the activity and stability varied with the preparation method in the following order: US > IM > SH > RE. Ultrasounds showed to provide the catalysts with smaller Ni particle size with good dispersion and stronger interaction with the support responsible of the higher catalytic activity and resistance to Ni sintering and and coke deposition of the 3wt%Ni/SBA-15(US) sample. Thus, 80% CO<sub>2</sub> conversion and 95-90% CH<sub>4</sub> conversion with 0.89 H<sub>2</sub>/CO ratio were maintained over 24h TOS at 800°C in the presence of 3wt%Ni/SBA-15(US) catalyst (Table 12, Entries 18-21).



**Figure 91.** Amount of CO<sub>2</sub>-TPD of 3wt%SBA-15, Ni/SBA-15 prepared by IM, RE, SH and US. Reprinted with permission from ref.<sup>919</sup> Copyright 2019, Hydrogen Energy Publications LLC. Published by Elsevier Ltd. All rights reserved.

On the other hand, the impact of homogeneous precipitation (HP) and impregnation (imp) preparation methods over the catalytic performance of Ni/SBA-15 samples were also compared.<sup>920</sup> The characterization results revealed high dispersion and small size (2-5 nm) of Ni nanoparticles and improved NiO reducibility owing to strong metal-support interaction with

improved sintering resistance. Consequently, the catalytic results showed the better catalytic performance of Ni/SBA-15(HP) than Ni/SBA-15(imp). At 800°C and 100h TOS, good and stable 74% and 80% CH<sub>4</sub> and CO<sub>2</sub> conversion with H<sub>2</sub>/CO up to 0.9 were achieved over Ni/SBA-15(HP) and with certain amount of filamentous coke deposition (Table 12, Entries 22-23). Previously, the influence of the three Ni/SBA-15 preparation methods, impregnation (IM), precipitation (PM) and precipitation-reduction with ascorbic acid (RM), over their physicochemical and catalytic properties was investigated.<sup>921</sup> The characterization data revealed that confined and small Ni particles size (~5 nm) were obtained through PM and RM methods, while through IM route, Ni was mainly present on the outer support surface with worst dispersion and higher particle size (~12 nm). Moreover, different Ni-active phases were dispersed and Ni-species met in IM sample are NiO species, in PM sample are only phyllosilicate species, while in RM sample are both phyllosilicate species and NiO-species. During DRM process, IM catalyst suffered rapid deactivation, while PM and RM catalysts exhibited improved stability, and PM catalyst showed slightly higher activity and selectivity than RM sample, resulting in a higher H<sub>2</sub>/CO ratio (0.87). Thus, 8wt%Ni/SBA-15(RM) exhibited higher catalytic performance with stable 65% CH<sub>4</sub> and 90% CO<sub>2</sub> conversions, at 600°C, over 24h TOS (Table 12, Entries 24-26). Moreover lower coke deposition in form of filamentous carbon was formed, closed to 11wt% for RM catalyst while 46wt% was formed over IM catalyst inducing severe deactivation. The effect of the use of different chelating agents such as ethylenediamine (en), acetic (ace) and citric (cit) acids and without (conventional (cm)) to prepare Ni/SBA-15 by impregnation over Ni dispersion and nanoparticles size was recently examined.<sup>922</sup> The benefits of electron-pair donor atoms (O, N) of ligands such as ethylenediamine and citric acid, which possess two and three electron-pair donor atoms respectively, able to form a chelate ring with a single metal with strong steric hindrance, in contrast to citric acid that will always give rise to multimetal ring structure favourable to metal agglomeration, were shown. Moreover, the viscosity of the chelated metal solution is higher than solution of inorganic salts, reducing the evaporation of the solvent that prevents the agglomeration of metal particles. Therefore, assisted chelating agent impregnation method allowed preparing catalysts with highly dispersed and ultrafine Ni nanoparticles (4-6nm) and with improved coke deposition resistance. At 800°C, all the samples initially exhibited high activity while the stability test, over 50h TOS, showed that samples issued from modified impregnation method exhibited higher and stable activity with good CO<sub>2</sub> and CH<sub>4</sub> conversion up to 85% and 80%, respectively (Table 12, Entries 27-31). The characterisation data determined a coke formation of less than 10-20wt% for the catalysts prepared in the presence of the chelating agent, while 40wt% coke was analysed for the sample prepared by the conventional method.



Ni nanoparticles deposition through conventional impregnation method is usually controlled by diffusion and by bulk oxide type formation with weak metal-support interaction. Consequently, the resistance to sintering of Ni nanoparticles is low. As an alternative, a new ammonia evaporation (AE) method was developed where the solvated metal precursor by ammonia is dispersed over the surface of the support which is in suspension in aqueous solution and a subsequent heating evaporates the ammonia leading to the hydrolysis of the metal-ammonia complex. Following this synthetic route, Ni/SBA-15 catalyst was prepared and the catalytic performance checked and compared to the results obtained in the presence of a sample prepared by conventional impregnation method.<sup>923</sup> Therefore, smaller Ni particles size from 3.05 to 5.17 nm, higher dispersion and homogeneously distribution with an average diameter of 4.09 nm inside the mesopores were obtained following the described AE method, leading to strong metal-support interaction. Then, a higher metal/support interaction allows to achieve the metal with smaller particle size. In contrast, broad range of particle size from 2.47 to 17.1 nm were obtained for Ni/SBA-15(IM) sample prepared by impregnation. Therefore, even if both catalysts exhibited high initial activity they showed different stability along 100h TOS. Ni/SBA-15(AE) catalyst displayed high coke deposition and sintering resistance owing to strong metal-support interactions. Thus at 750°C, 75% CH<sub>4</sub> and 80% CO<sub>2</sub> conversions were maintained over Ni/SBA-15(AE) over 100h TOS with H<sub>2</sub>/CO close to 0.85 (Table 12, Entries 32-35). All these results showed the impacts of preparation method on metal dispersion and particle size controlled by metal-support interaction, and its impact on the catalytic activity, stability and the resistance of Ni-particles to sintering and coke deposition.

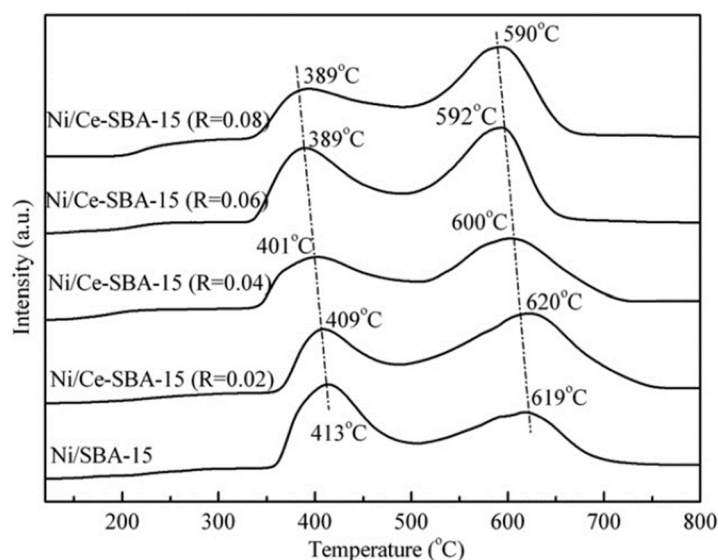
\* *Preparation of bimetallic Ni/SBA-15-based catalysts for DRM*

The impacts of the addition of suitable second metal or promoter are well known to modify the electronic properties of Ni and contribute to enhance the dispersion and stabilization of metal nanoparticles by establishing strong-interaction metal-support and so promoting the catalytic activity, stability and coke resistance.

- Effect of the addition of rare earth metals to Ni/SBA-15-based catalysts for DRM

The benefits of the incorporation of CeO<sub>2</sub> has been well described to enhance the catalytic properties and stability of metal-based catalysts by establishing strong metal-support interaction, providing high oxygen mobility and the formation of active sites at the interface metal/support. Accordingly, the effect of the Ce loading over the catalytic properties of Ni/SBA-15 prepared by sol-gel method were explored for DRM.<sup>924</sup> The results showed that optimum 7wt% Ce content existed corresponding to high catalytic activity and good catalytic stability with

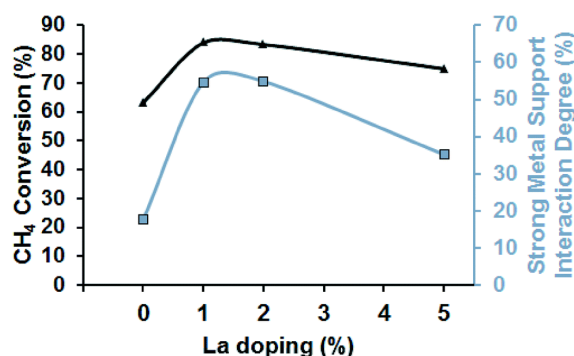
95% CH<sub>4</sub> and CO<sub>2</sub> conversions, and ~1 H<sub>2</sub>/CO ratio, at 700°C for short 6h TOS (Table 12, Entries 40-41). The incorporation of Ce improved Ni dispersion and interaction of metal-support and minimized coke deposition due to its ability to oxidize carbon species formed on Ni particles. Previously, a study of Ce incorporation into Ni-Ce/SBA-15 physicochemical and catalytic features revealed the promoting effect over Ni nanoparticles dispersion and the increased of oxygen mobility and activity owing to Ce incorporation.<sup>925</sup> Ce was incorporated by direct hydrothermal method, favouring high Ce dispersion onto SBA-15 surface that in turn promoted the formation of small and highly dispersed Ni nanoparticles deposited by impregnation method. H<sub>2</sub>-TPR study showed shifts of the high temperature reduction peak to lower temperature indicating change in NiO reducibility attributed to surface oxygen species on Ni/Ce-SBA-15 samples with higher mobility and activity when increasing Ce content due to Ce redox property and the formation of oxygen vacancy (Figure 92).<sup>926,927</sup> Moreover, the presence of oxygen species on the catalytic surface helps to prevent the carbon formation. The best catalytic performance was achieved over 12wt%Ni/Ce-SBA-15 (Si/Ce=0.04) with good ~78% CO<sub>2</sub> and 76% CH<sub>4</sub> conversions over 40h TOS at 700°C (Table 12, Entries 42-44).



**Figure 92.** H<sub>2</sub>-TPR profiles of Ni/Ce-SBA-15 (R= Ce/Si) samples. Reprinted with permission from ref. <sup>925</sup>. Copyright 2011, Hydrogen Energy Publications, LLC. Published by Elsevier Ltd. All rights reserved.

Recently, a study of addition of La and Ce to 10wt%Ni/SBA-15 catalysts by co-impregnation method over physical and chemical properties of the catalysts showed that the incorporation of the promoters enabled to reduce the Ni nanoparticles size and improve the dispersion of metallic particles.<sup>928</sup> TPO analysis enabled evaluating coke deposition amount with the following decreasing order 10wt%Ni/SBA-15 > 3wt%Ce-10wt%Ni/SBA-15 > 3wt%La-10wt%Ni/SBA-15 revealing that the promoter addition improved coke deposition resistance because of their basic properties, favouring CO<sub>2</sub> adsorption and dissociation, and carbon oxidation and posterior

elimination. Thus, the best catalytic activity and stability were achieved over 3wt%La-10%Ni/SBA-15 sample with 93% CH<sub>4</sub> and 95% CO<sub>2</sub> conversion at 750°C for 24h TOS (Table 12, Entries 45-47). The La addition to highly dispersed Ni/SBA-15 catalyst following a new synthetic route using oleic acid as the precursor was previously investigated.<sup>929</sup> The benefits of the La incorporation in promoting the strong metal-support interaction was shown by H<sub>2</sub>-TPR study. An increase in the La amount from 1 to 2 wt% resulted in an increase in the amount of strongly bound NiO species and a simultaneous decrease in the amount of weakly bound NiO species on the support, while further increase produced the opposite effect. Deconvoluted TPR at T>600°C allowed quantified the strong interaction NiO/support and evaluated the strong metal support interaction degree after normalization of metal-support interactions. Therefore, a correlation between strong metal support interactions and CH<sub>4</sub> conversion was established (Figure 93). Moreover, 1% La-Ni/SBA-15 and 2% La-Ni/SBA-15 catalysts had the smallest metal particle size, 2.8 and 3.2 nm, respectively, due to the stronger interaction metal-support. Thus, an optimum in La loading of 1wt% was determined based on the analysis of catalytic performance and characterization data (Ni nanoparticle size, dispersion and stability). At 700°C, over 1wt%La-5wt%Ni/SBA-15, ~84% CH<sub>4</sub> and ~86% CO<sub>2</sub> conversions along brief 12h TOS were achieved (Table 12, Entries 48-49). Additionally, a CO<sub>2</sub> isotopic studies evidenced that CH<sub>4</sub> dissociation took place over highly dispersed Ni active centres while CO<sub>2</sub> was adsorbed and decomposed on La active centres and enabled the oxidation of deposited carbon on the surface, improving the catalytic stability and minimizing carbon deposition.



**Figure 93.** Relationship between La content, strong metal-support interaction degree (%) and CH<sub>4</sub> conversion. Reprinted with permission from ref.<sup>929</sup>. Copyright 2016, Royal Society of Chemistry.

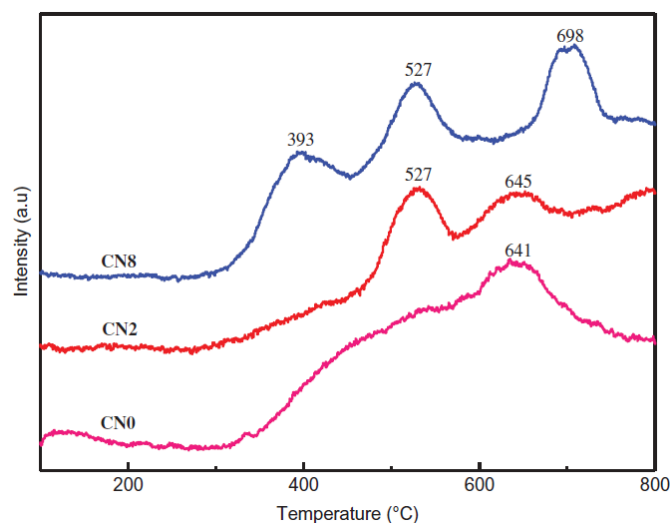
The benefits of Sm doping over the catalytic and physicochemical properties of Ni and Co/SBA-15 prepared in two steps by two-solvents impregnation method was also examined for DRM.<sup>930</sup> Different tendencies for Sm addition to 10wt%Co and 10wt%Ni/SBA-15 were observed. The incorporation of 1wt%Sm enabled to improve the dispersion and reduce the particle size of NiO mainly located inside the mesopores while in the case of Co<sub>3</sub>O<sub>4</sub>, higher agglomeration and lower dispersion was observed with particles located mainly on external surface. H<sub>2</sub>-TPR study

confirmed that stronger interactions metal/support are established after the Sm doping in the case of NiO promoting to lower particle size and higher sintering resistance. Therefore, the catalytic activity study confirmed the positive effect of the Sm addition to Ni/SBA-15 sample due to higher Ni dispersion, strong interaction metal-support, and improved oxygen storage capacity. In contrast a negative effect was observed over the catalytic performance of Co/SBA-15 after the addition of Sm attributed to the favoured Co oxidation and deactivation. Thus, at 700°C medium catalytic results were obtained over 1wt%Sm-10wt%Ni/SBA-15 with 58-56% CH<sub>4</sub> and 66-64% CO<sub>2</sub> conversion over brief 5h TOS while small amount of a filament type carbon deposition was observed (Table 12, Entries 50-51).

- Effect of the addition of transition metal to Ni/SBA-15-based catalysts

Studies of preparation of Ni-Co bimetallic catalysts showed the benefits of the formation of Ni-Co alloy that enhanced the catalytic stability in comparison to monometallic samples mainly due to the accelerated CH<sub>4</sub> decomposition and prevention of Co<sup>0</sup> oxidation.<sup>836,931</sup> Accordingly, the catalytic performance of bimetallic Ni-Co/SBA-15 versus monometallic catalyst for DRM was recently studied and revealed the positive synergetic effect between Ni and Co.<sup>932</sup> The Co incorporation enabled to prevent sintering of Ni nanoparticles due to the formation of Ni-Co alloy that allowed avoiding the reoxidation of Co and reducing coke deposition. At 750°C, up to 79% CH<sub>4</sub> and 89% CO<sub>2</sub> conversions were obtained over 4wt%Ni-1wt%Co/SBA-15 (Table 12, Entry 52). Previously, the catalytic behavior of bimetallic Ni-Co/SBA-15 with 13wt% Ni and different Co contents (N=wt%) were studied for DRM reaction.<sup>933</sup> The CO<sub>2</sub> desorption results showed that Co doping improved the basic properties since three CO<sub>2</sub> desorption peaks were registered for CN8 sample corresponding to weak (393°C), moderate (527°C), and strong (698°C) basic sites (Figure 94). The enhanced basicity will boost CO<sub>2</sub> adsorption and dissociation which would supply oxygen species to effectively improve the ability of CO<sub>2</sub> in oxidizing carbons species formed from CH<sub>4</sub> decomposition, and preventing coke formation. Optimum Co content existed, while Co excess favoured the formation of large number of O species inducing Co<sup>0</sup> oxidation and catalysts deactivation. Moreover, the morphology of carbon deposition varied with the presence of Co, besides on Ni/SBA-15 coke was present as shell-like inducing severe deactivation, on Co-Ni/SBA-15 coke adopted whisker form with minor poisoning effect. Very good catalytic performance was obtained over 2wt%Co-13wt%Ni/SBA-15 catalyst, at 800°C, with 76% CH<sub>4</sub> and 90% CO<sub>2</sub> conversions for the first 300h of TOS and 80% CH<sub>4</sub> and 80% CO<sub>2</sub> conversion values for the the following 500h of TOS (Table 12, Entries 53-54). Similar catalytic behavior were reported for bimetallic Ni-Co/SBA-15 prepared by a β-cyclodextrin modified impregnation method.<sup>934</sup> The confinement of SBA-15 and Ni-Co synergetic effects enabled to improve the activity and stability

of Ni-Co/SBA-15 catalysts. The best catalytic performance was achieved over 4.5wt%Ni-0.5wt%Co/SBA-15 and 3wt%Ni-2wt%Co/SBA-15 with 90 and 88% CH<sub>4</sub> conversion, and 95 % CO<sub>2</sub> conversion, respectively, at 800°C for 30h TOS (Table 12, Entries 55-56).



**Figure 94.** CO<sub>2</sub>-TPD profiles of Ni/Co-SBA-15 (N=Co wt%) samples. Reprinted with permission from ref. <sup>933</sup>. Copyright 2015, Taylor & Francis.

The effects of titanium nitride (TiN) incorporation into Ni-SBA-15 by hydrothermal method and further impregnated with Ni over textural and catalytic features were explored.<sup>935</sup> Titanium nitride (TiN) presents interesting electronic properties, basic properties, high density, great surface area and high thermal and oxidation stability. The test of activity showed that both CH<sub>4</sub> and CO<sub>2</sub> conversion increased with Ni loading while the incorporation of TiN enhanced the catalytic activity of Ni-based catalyst owing to basicity improvement favourable to CO<sub>2</sub> absorption and dissociation, and the creation of strong interaction between TiN, Ni and the support. Stability test showed that the presence of TiN allowed lowering carbon deposition. Moderate catalytic results were obtained with 70-65% CH<sub>4</sub> and ~70% CO<sub>2</sub> conversion at 700°C, over 10wt%Ni/5wt%TiN-SBA-15 for 12h TOS (Table 12, Entries 57-59).

Years ago, a DRM study of catalytic activity of Molybdenum carbide (Mo<sub>2</sub>C) exposed that these catalysts exhibited high resistance to coke deposition similarly to noble metals.<sup>936</sup> Other report showed that the addition of a suitable Ni amount to MoO<sub>3</sub> improved the Mo<sub>2</sub>C catalytic activity and stability for DRM.<sup>937</sup> Based on these results, a Ni/Mo<sub>2</sub>C/SBA-15 catalyst was prepared by impregnation of SBA-15 in order to take advantage of nickel deactivation by coke deposition to enable carbonaceous species migration onto Mo<sub>2</sub>C preventing Mo<sub>2</sub>C oxidation and accelerating carbon elimination.<sup>938</sup> Ni/Mo<sub>2</sub>C/SBA-15 catalyst exhibited very high catalytic performance along 130h, with 98 % CH<sub>4</sub> and 95% CO<sub>2</sub> conversions with H<sub>2</sub>/CO ratio close to 0.8 at 800°C (Table 12, Entries 60-61). Nevertheless, besides these promising results no further study was pursued.

Noble metals exhibit higher resistance against coke formation and sintering than Ni at high temperature. Accordingly, the benefits of the Rh doping over the catalytic performance of Ni-SBA-15 for DRM was explored. The comparison of catalytic data of Ni/SBA-15 and Rh-Ni/SBA-15 samples showed the Rh promoting effect over catalytic activity and stability with small Rh content (0.02wt%) due to electronic interaction between Ni and Rh enabling higher metal dispersion and improving NiO species reducibility. Moreover, the formation of Rh-Ni species promotes the activation and dissociation of CO<sub>2</sub> with active oxygen release for the gasification of deposited carbon.<sup>939</sup> At 650°C, 66-59% CH<sub>4</sub> and 79-78% CO<sub>2</sub> conversions were achieved over 0.02wt%Rh-10wt%Ni/SBA-15 for 30 h TOS (Table 12, Entries 62-63).

\* *Preparation of trimetallic Ni/SBA-15-based catalysts for DRM*

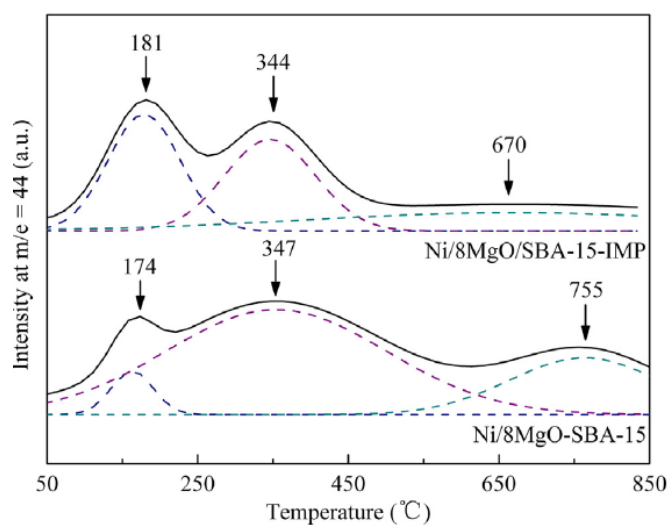
The influence of impregnation method in two or three steps and the Ce-Zr incorporation over the physicochemical and catalytic features Ni/SBA-15 catalysts for DRM was explored. Owing to their redox properties, Zr and Ce generate high amount of oxygen vacancies near the Ni particles that favours carbon removal from the metallic surface. Catalytic study showed that Ce-Zr addition enhanced the Ni/SBA-15 catalysts selectivity and stability owing to the decrease of the Ni particle size and higher reducibility of NiO species.<sup>940</sup> Over 6wt%Ce-4wt%Zr-10wt%Ni/SBA-15 50-40% CH<sub>4</sub> and 66-58% CO<sub>2</sub> conversions were achieved along 30h TOS, with H<sub>2</sub>/CO ratio close to 0.78, at low temperature (600°C). Low 2wt% coke deposition was determined owing to high amount of Ce and Zr oxygen vacancies (Table 12, Entries 64-65). The same group also reported the effect of preparation method of Ce-Zr-Ni/SBA-15 following, one and two-steps impregnation and co-precipitation routes over their physicochemical and catalytic properties.<sup>941</sup> Co-precipitation method allow achieving sample with confined Ni phyllosilicate with stronger interaction metal-support while by impregnation method pore blockage occurred with Ni particles mostly located on outer surface support. It was concluded that catalyst prepared by co-precipitation did not favour methane decomposition, thus coke deposition was minimized and the catalytic stability was slightly improved, with 63-61% CH<sub>4</sub> and 71-68% CO<sub>2</sub> conversions with ~0.85 H<sub>2</sub>/CO ratio maintained along 24h TOS at 600°C (Table 12, Entries 66-68). A study of the benefits of the incorporation of CeO<sub>2</sub> into Ni-Mo/SBA-15 catalyst showed the high catalytic performance of both Ni-Mo/SBA-15 and CeO<sub>2</sub>-Ni-Mo/SBA-15 catalysts. CeO<sub>2</sub>-Ni-Mo/SBA-15 exhibited slightly higher activity and stability over 100h, supporting the benefits of the CeO<sub>2</sub> incorporation.<sup>942</sup> CO<sub>2</sub> desorption revealed three peaks and so three kinds of basic sites for CeO<sub>2</sub>-Ni-Mo/SBA-15 sample, while N<sub>2</sub> adsorption determined higher specific surface area and pore volume for CeO<sub>2</sub>-Ni-Mo/SBA-15 sample. These characterization data indicated that CeO<sub>2</sub>

lowered the acidity of the support preventing carbon formation by methane decomposition while basic sites enhance adsorption and dissociation of CO<sub>2</sub> and oxygen release to carbon gasification. Moreover, CeO<sub>2</sub> improved dispersion of metallic active phase in SBA-15 as well as the reducibility of NiO particles (H<sub>2</sub>-TPR study). Then, 90% CH<sub>4</sub> and 98% CO<sub>2</sub> conversions with 0.9 H<sub>2</sub>/CO ratio were maintained over 100h and no coke deposition was formed, at 800°C over CeO<sub>2</sub>-Ni-Mo/SBA-15 (Table 12, Entries 69-70). Few years ago, a study of catalytic performance of Ni-Mo/SBA-15 doped with La<sub>2</sub>O<sub>3</sub> revealed that small amount of La<sub>2</sub>O<sub>3</sub> allowed improving Ni dispersion and stability owing to spatial confinement effects of SBA-15 mesopores and the creation of strong interaction with the support, while the formation of La<sub>2</sub>O<sub>2</sub>CO<sub>3</sub> favoured the elimination of carbon species from the catalytic surface preventing coke deposition (Figure 81).<sup>943</sup> Very good 92% CH<sub>4</sub> and 96% CO<sub>2</sub> conversions with 0.9 H<sub>2</sub>/CO ratio were maintained over long 200 h TOS in the presence of Ni-Mo/SBA-15-La<sub>2</sub>O<sub>3</sub> catalyst (Table 12, Entries 71-72). Unfortunately, no data of H<sub>2</sub> and CO selectivity were provided. The catalytic performance of Co-Ni/Sc-SBA-15 catalysts with 5wt% Co, 5wt% Ni and different Sc content prepared by successive impregnation was also reported for DRM.<sup>944</sup> Co and Ni were successfully and highly dispersed in SBA-15 while the addition of Sc improved their resistance to sintering. The Sc incorporation allowed increasing the basicity of catalyst and thus the adsorption and activation of CO<sub>2</sub>. Consequently the higher oxygen coverage enabled minimizing carbon formation due to easily oxidation into CO. Finally, Sc incorporation also improved the catalytic performance of Ni-Mo/SBA-15, and high 92-87% CH<sub>4</sub> conversion and 93-92% CO<sub>2</sub> conversion were maintained over 40 h with H<sub>2</sub>/CO ratio close to 1 at 800°C over 5Co-5Ni/5Sc-SBA-15 catalyst (Table 12, Entries 73-75).

\* *Effect of basic properties of Ni/SBA-15-based catalysts for DRM*

As aforementioned, the basic properties influence strongly the CO<sub>2</sub> adsorption and dissociation, while CO<sub>2</sub> coverage of the catalytic surface allows avoiding CH<sub>4</sub> adsorption and decomposition and favours carbon species oxidation. Therefore, the benefits of basic properties of DRM catalysts have been largely investigated. Accordingly, the catalytic features of a serie of MgO/SBA-15 catalysts prepared by one pot synthesis and further impregnated with 10wt% Ni, and MgO-Ni/SBA-15 sample were compared.<sup>945</sup> Through hydrothermal synthesis, MgO was successfully coated on SBA-15 walls while the mesoporous structure was maintained. It was shown that the coating of MgO enabled a decrease in NiO particle size with higher dispersion, which provide more active sites for DRM. Moreover, MgO incorporation improved the surface basicity enhancing catalytic stability and coke resistance. CO<sub>2</sub>-TPD study revealed the appearance of medium and strong basic sites on Ni/8MgO-SBA-15 sample indicating the

formation of superbasicity on mesoporous silica (Figure 95). Thus, the best catalytic performance was obtained over 8wt%MgO-10wt%Ni/SBA-15 prepared by one-pot method, with medium 71-68% CH<sub>4</sub> and 66-62% CO<sub>2</sub> conversion, at 800°C over 40h TOS (Table 12, Entries 76-78). Carbon deposition was responsible of catalyst deactivation in form of filamentous carbon species. At the same time, the preparation and catalytic performance of Mg-modified Ni/SBA-15 with different Mg loading contents were examined.<sup>946</sup> Similar features and results were obtained. The Mg addition improved Ni dispersion and basic properties of the catalyst owing to strong metal-support interaction and consequently, coke resistance and catalyst stability. H<sub>2</sub>-TPR study revealed a shift of reduction temperature of NiO to higher temperatures attributed to strong interaction Ni/support due to the addition of Mg. Before the formation of NiO and MgO solid solution with different compositions, new interactions metallic phase/support and changes in reducibility was reported.<sup>947</sup> The enhanced basicity and high CO<sub>2</sub> adsorption lowered the coke deposition reducing CO disproportionation and accelerating the oxidation of adsorbed carbon species. Thus, over 8wt%Mg-10wt%Ni/SBA-15, 58-66% CH<sub>4</sub> and 62-57% CO<sub>2</sub> conversion and H<sub>2</sub>/CO~1, at 700°C, were reached over 40h TOS (Table 12, Entries 79-80).



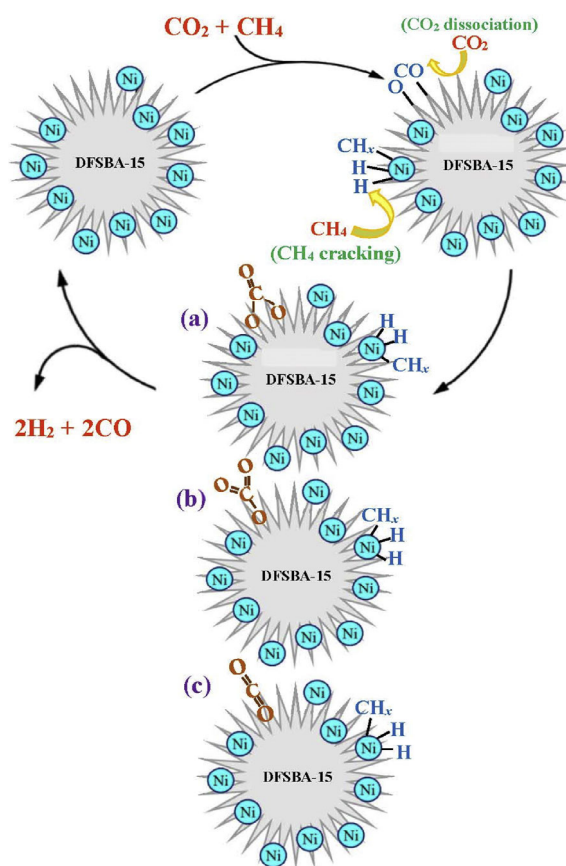
**Figure 95.** CO<sub>2</sub>-TPD profiles of MgO-Ni-SBA-15 samples. Reprinted with permission from ref.<sup>945</sup>. Crown Copyright 2013, Published by Elsevier Ltd. All rights reserved.

\* *Effect of morphology of Ni/SBA-15-based catalysts for DRM*

A new breakthrough was recently done with the synthesis of fibrous nanosilica such as KCC-1 and FZSM-5 that exhibit high area and micro- and mesopores, increasing the accessibility to active sites and improving considerably their catalytic and diffusion properties. Hence, recently the successful preparation of spherical mesoporous Ni/Dendritic Fibrous SBA-15 (Ni/DFSBA-15) catalysts for DRM was reported.<sup>948</sup> The catalytic data revealed that CH<sub>4</sub> and CO<sub>2</sub> conversions increased with Ni loading, with a maximum around 10wt%, and further decreased. Characterization data showed that NiO nanoparticles size increased with Ni loading while BET



area decreased. The best catalytic performance was achieved over 10wt%Ni/DFSBA-15 with 93% CO<sub>2</sub> and 91% CH<sub>4</sub> conversions, 92% H<sub>2</sub> and 96% CO selectivity and 0.95 H<sub>2</sub>/CO for 30 h TOS, at 800°C (Table 8, Entries 81-82). Recently, the same authors reported a study of the influences of operating parameters (reaction temperature, GHSV and CH<sub>4</sub>/CO<sub>2</sub> ratio) over 10Ni/DFSBA-15 using mathematical modelling.<sup>949</sup> The results indicated that temperature had determinant effect over CO<sub>2</sub> conversion while CH<sub>4</sub>/CO<sub>2</sub> ratio mainly influenced the CH<sub>4</sub> conversion and H<sub>2</sub>/CO. The predicted theoretical DRM allowed achieving high catalytic performance and stability over 30h TOS. At 794°C, 93-90% both CH<sub>4</sub> and CO<sub>2</sub> conversions with H<sub>2</sub>/CO ratio were obtained over 10wt%Ni/DFSBA-15 sample that could be regenerated under air (Table 12, Entry 83). In-situ IR study determined that DRM reaction involved the formation of unidentate (a) and bidentate (b) carbonate species as intermediates by CO<sub>2</sub> adsorption and dissociation, while H<sub>2</sub> and CO were issued of the reaction carbonate species with CH<sub>4</sub> (Figure 96).

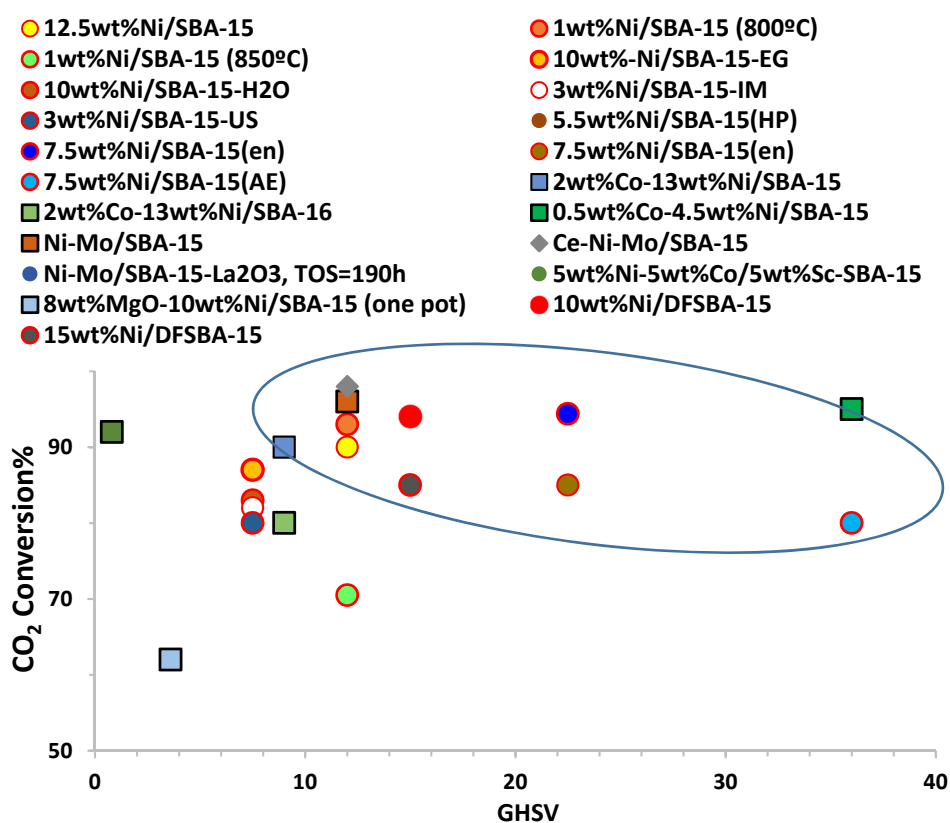


**Figure 96.** Formation of (a) bidentate carbonate, (b) unidentate carbonate, and (c) linear carbonyl over Ni/DFSBA-15 during DRM. Reprinted with permission from ref.<sup>949</sup>. Copyright 2020, Hydrogen Energy Publications LLC. Published by Elsevier Ltd. All rights reserved.

\* *Conclusion*

SBA-15 due to its high surface area and thermal stability is of interest to prepare Ni-based catalysts for DRM process making use of the confinement effect of its mesopore system, and numerous works have been published. Different approaches have been followed to improve

dispersion and stabilization of nickel particles by addition of suitable promoter and establishing new metal/metal and metal/support interactions and synergies, to enhance the NiO reducibility, coke resistance, and control surface basicity to promote CO<sub>2</sub> adsorption and dissociation. The results of Table 12 illustrate the high activity of SBA-15-based catalysts although the yield or syngas cannot usually be assessed due to lack of data on H<sub>2</sub> and/or CO yield and/or selectivity. We have attempted to compare all catalysts considering CO<sub>2</sub> conversion and H<sub>2</sub>/CO ratio as function of GHSV and TOS. Then, some results can be highlighted as it is displayed in Figures 97 and 98. There, catalysts 12.5wt%Ni/SBA-15, 1wt%Ni/SBA-15 (800°C), 7.5wt%Ni/SBA-15(en), 7.5wt%Ni/SBA-15(AE), 2wt%Co-13wt%Ni/SBA-15, 0.5wt%Co-4.5wt%Ni/SBA-15, Ni-Mo/SBA-15, 10 and 15wt%Ni/DFSBA-15 (Table 12, Entries 8, 9, 31, 32, 53, 55, 69, 81, 82) exhibited interesting catalytic performance. Nevertheless, only for 12.5wt%Ni/SBA-15, 10 and 15wt%Ni/DFSBA-15 data of H<sub>2</sub> and/or CO<sub>2</sub> yield and/or selectivity are given and so productivity can only be evaluated, with H<sub>2</sub> and CO selectivities around 92-96%.



**Figure 97.** CO<sub>2</sub> conversion was plotted versus GHSV for different DRM SBA-15-based catalysts. The ovoid highlights the best catalytic performance: high conversion versus GHSV.

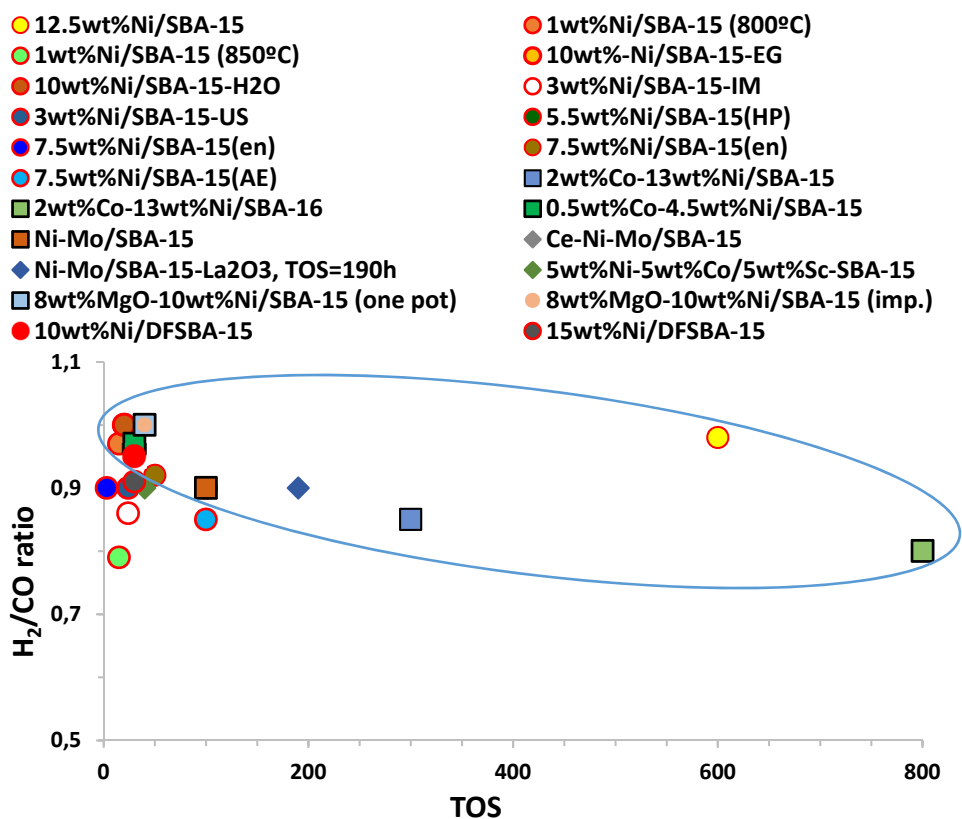


Figure 98. H<sub>2</sub>/CO ratio was plotted versus TOS for different DRM SBA-15-based catalysts. The ovoid highlights the best catalytic performance: H<sub>2</sub>/CO close to 1 versus TOS.

**Table 12.** Summary of the catalytic performance of the different reviewed DRM OMS-based catalysts at 0.1MPa.

Entry	Catalysts*	Conditions	$\chi_{\text{CH}_4}$ (%)	$\chi_{\text{CO}_2}$ (%)	H <sub>2</sub> /CO	Sel. H <sub>2</sub> /CO	Coke wt%	Year	Ref
1	11.8Ni/MCM-41	700°C; GHSV=5.2*10 <sup>4</sup> mLg <sub>cat</sub> <sup>-1</sup> h <sup>-1</sup> ;	49-48	~62				2020	913
2	11.8Ni/SBA-15	CH <sub>4</sub> :CO <sub>2</sub> =1, TOS=44h	85-66	92-74					
3	11.8Ni/KIT-6		79-76	89-87					
4	11Ni/Al-MCM-41	GHSV=150000 mLg <sub>cat</sub> <sup>-1</sup> h <sup>-1</sup> ,	93	94				2017	914
5	11Ni/SBA-15	CH <sub>4</sub> :CO <sub>2</sub> :He=10:10:80, 0.04g <sub>cat</sub> ,	84	90					
6	11Ni/MFI	TOS=12h, 750°C	65-55	70-60					
7	11Ni/FAU		20-3	30-3					
<b>SBA-15</b>									
● <b>Preparation method</b>									
8	12.5Ni/SBA-15	800°C, GHSV=1.2*10 <sup>4</sup> h <sup>-1</sup> , CH <sub>4</sub> :CO <sub>2</sub> =1, TOS=600h	90	90		92/94		2006	915
9	1Ni/SBA-15 (800°C)	0.1 MPa, GHSV=12000 mLg <sub>cat</sub> <sup>-1</sup> h <sup>-1</sup> ,	91	93	0.97			2020	916
10	1Ni/SBA-15 (850°C)	CH <sub>4</sub> :CO <sub>2</sub> :N <sub>2</sub> =1:1:2, TOS=15h	45.9	70.5	0.79				
11	1Ni/Al <sub>2</sub> O <sub>3</sub> (800°C)		79	80					
12	1Ni/SiO <sub>2</sub> (800°C)		45	65					
13	10Ni/SBA-15-EG	GHSV=7.5 Lg <sub>cat</sub> <sup>-1</sup> h <sup>-1</sup> , 0.12g <sub>cat</sub> ,	~96	~87	1.02-0.98		3.8	2014	917
14	10Ni/SBA-15-H <sub>2</sub> O	TOS=20h, CH <sub>4</sub> :CO <sub>2</sub> =1, 15 mLmin <sup>-1</sup>	94-92	85-82	1.02-1		32.3		
15	7Ni/SBA-15-H <sub>2</sub> O	GHSV=18000 mLg <sub>cat</sub> <sup>-1</sup> h <sup>-1</sup> ,	~60	~70	~0.85	92 (H <sub>2</sub> )		2018	918
16	7Ni/SBA-15-EG	CH <sub>4</sub> :CO <sub>2</sub> =1,	~71 (~71)	~79	~0.91	96 (H <sub>2</sub> )			
17	7Ni/Al-SBA-15-EG	30 mLmin <sup>-1</sup> , 0.1g <sub>cat</sub> , TOS=15h 700°C (800°C)	~72 (~90)	~79	~0.95	99 (H <sub>2</sub> )			
18	3Ni/SBA-15-RE	700°C, 25 mLmin <sup>-1</sup> ,	95-40	75-58	~0.6		16.5	2020	919
19	3Ni/SBA-15-SH	CH <sub>4</sub> :CO <sub>2</sub> :N <sub>2</sub> =1:1:1, 0.2g <sub>cat</sub> ,	97-70	82-72	~0.79		13.7		
20	3Ni/SBA-15-IM	TOS=24h	95-88	~82	~0.86		13.4		
21	3Ni/SBA-15-US		95-91	~80	~0.9		12.4		
22	5.5Ni/SBA-15(IM)	700°C, GHSV=36 Lg <sub>cat</sub> <sup>-1</sup> h <sup>-1</sup> ,	60-40	70-52	~0.8			2017	920
23	5.5Ni/SBA-15(HP)	CH <sub>4</sub> :CO <sub>2</sub> =1, 0.05g <sub>cat</sub> , TOS=100h	~74	~80	0.90-0.95				
24	8.7Ni/SBA-15(IM)	600°C, 100 mLmin <sup>-1</sup> , GHSV=20	52-40	87-69	0.80-0.77		46.5	2015	921
25	9.6Ni/SBA-15(PM)	Lg <sub>cat</sub> <sup>-1</sup> h <sup>-1</sup> , CH <sub>4</sub> :CO <sub>2</sub> =1, TOS=24h	~68	~75	~0.87		-		

26	8Ni/SBA-15(RM)		~65	~90	~0.82		10.8			
27	7.5Ni/SBA-15(en)	800°C, 0.08g <sub>cat</sub> , GHSV=22.5 Lg <sub>cat</sub> <sup>-1</sup>	94.2	94.4	0.9	~80/85	9.9	2017	922	
28	7.5Ni/SBA-15(cit)	<sup>1</sup> h <sup>-1</sup> , CH <sub>4</sub> :CO <sub>2</sub> =1, TOS=3h	93.3	94.5	0.9	~75/85	10.6			
29	7.5Ni/SBA-15(ace)		95.3	94.1	1.05	~76/82	19.5			
30	7.5Ni/SBA-15(st)		93	94.6	1.1		40.4			
31	7.5Ni/SBA-15(en)	700, TOS=50h	~80	~85	~0.92					
32	7.5Ni/SBA-15(AE)	750°C	90	90	0.9			2015	923	
33		TOS=100h, 700°C	~75	~80	~0.85					
34	Ni/SBA-15(IM)	750°C	80	81	0.82					
35		TOS=100h, 700°C, CH <sub>4</sub> :CO <sub>2</sub> =1,	75-57	68-45	0.82-0.77					
	Ni/Si ratio=0.06	GHSV=36000 mLg <sub>cat</sub> <sup>-1</sup> h <sup>-1</sup> , 0.05g <sub>cat</sub>								
	<b>• Bimetallic</b>									
	<b><i>Ce-doping</i></b>									
36	7.5Ni/SBA-15	600°C	82	80				2016	950	
37		500°C (12h)	66	-	0.99					
38	7.5Ni-6Ce/SBA-15	600°C	96	84						
39		500°C (12h)	72		0.98					
		GHSV=52.8 Lg <sub>cat</sub> <sup>-1</sup> h <sup>-1</sup> , CH <sub>4</sub> :CO <sub>2</sub> =1:1 <sub>t</sub>								
40	7Ce-5Ni/SBA-15	700°C, ST=20.26 s, CH <sub>4</sub> :CO <sub>2</sub> =1,	98-95	96-95	~1			2017	924	
41	1Ce-5Ni/SBA-15	TOS=6h	~52	62-55	0.75-0.9					
42	12Ni/Ce-SBA-15 (Si/Ce=0.04)	GHSV=36 Lg <sub>cat</sub> <sup>-1</sup> h <sup>-1</sup> , 0.1 g <sub>cat</sub> ,	78-77	77-76			7.6	2010	925	
43	12Ni/SBA-15	CH <sub>4</sub> :CO <sub>2</sub> =1, TOS=40h, 700°C	70-63	70-66			11.2			
44	12Ni/CeO <sub>2</sub>		47-27	30-18						
	<b><i>La-doping</i></b>									
45	3La-10Ni/SBA-15	GHSV=24 Lg <sub>cat</sub> <sup>-1</sup> h <sup>-1</sup> , F <sub>T</sub> =60mlmin <sup>-1</sup> ,	~93	~95				2016	928	
46	3Ce-10Ni/SBA-15	P <sub>CH4</sub> =P <sub>CO2</sub> =20KPa, 750°C, TOS=24h	87-85	92-87						
47	10Ni/SBA-15		86-78	90-86						
48	1La-5Ni/SBA-15	GHSV=7.2 Lg <sub>cat</sub> <sup>-1</sup> h <sup>-1</sup> , TOS=12h,	~84	~86	~0.92			2016	929	
49	5Ni/SBA-15	CH <sub>4</sub> :CO <sub>2</sub> :N <sub>2</sub> =1:1:1, 700°C	65-63	72-73	0.8-0.78					
	<b><i>Sm-doping</i></b>									
50	1Sm-10Ni/SBA-15	700°C, GHSV=1.2 Lg <sub>cat</sub> <sup>-1</sup> h <sup>-1</sup> , 0.2	58-54	66-64				2017	930	
51	10Ni/SBA-15	g <sub>cat</sub> , CH <sub>4</sub> :CO <sub>2</sub> =1, TOS=5h	53	64						
	<b><i>Co-doping</i></b>									

52	4Co-1Ni/SBA-15	TOS= 4h, GHSV=36 Lg <sub>cat</sub> <sup>-1</sup> h <sup>-1</sup> , CH <sub>4</sub> :CO <sub>2</sub> :Ar=1:1:1, 750°C	90	79	0.8	4	2018	932	
53	2Co-13Ni/SBA-15	TOS= 0-300h	~96	~90	~0.85		2015	933	
54		TOS= 300-800h GHSV=9000 mLg <sub>cat</sub> <sup>-1</sup> h <sup>-1</sup> , CH <sub>4</sub> :CO <sub>2</sub> =1, 0.4g <sub>cat</sub> , 800°C	~80	~80	~0.80	1.79			
55	0.5Co-4.5Ni/SBA-15	GHSV=3.6*10 <sup>4</sup> mLg <sub>cat</sub> <sup>-1</sup> h <sup>-1</sup> ,	~90	~95	~0.97		2016	934	
56	2Co-3Ni/SBA-15	CH <sub>4</sub> :CO <sub>2</sub> =1, 800°C, TOS=30h	~88	~95					
<b>TiN-doping</b>									
57	10Ni/SBA-15	20 mLmin <sup>-1</sup> , CH <sub>4</sub> :CO <sub>2</sub> =1, 700°C,	70-40	65-40	0.9-0.6		2018	935	
58	10Ni/5TiN-SBA-15	0.05 g <sub>cat</sub> , TOS=12h	70-65	~70	0.9-0.75				
59	7.5Ni/10TiN-SBA-15		70-60	~68	0.9-0.75				
<b>Mo<sub>2</sub>C-doping</b>									
60	Mo <sub>2</sub> C-Ni/SBA-15	800°C, GHSV=8 Lg <sub>cat</sub> <sup>-1</sup> h <sup>-1</sup> ,	~98	~95	~0.8		2011	937	
61	Mo <sub>2</sub> C	CH <sub>4</sub> :CO <sub>2</sub> =1, 0.3 g <sub>cat</sub> , TOS=130h	~78 (8h)	~20 (8h)					
<b>Rh-doping</b>									
62	10Ni/SBA-15	GHSV=12 Lg <sub>cat</sub> <sup>-1</sup> h <sup>-1</sup> , 0.04 g <sub>cat</sub> ,	65.5-63.5	79-75.5		27.3	2014	939	
63	0.02Rh-10Ni/SBA-15	CH <sub>4</sub> :CO <sub>2</sub> =1:1, 650°C, TOS=30h	66.5-59.5	79-78.5		14.7			
<b>• Trimetallic</b>									
<b>Ce-Zr-doping</b>									
64	10Ni/SBA-15	600°C, GHSV=20 Lg <sub>cat</sub> <sup>-1</sup> h <sup>-1</sup> ,	52-40	87-69	0.8-0.78	3.5	2013	940	
65	6Ce-4Zr-10Ni/SBA-15	CH <sub>4</sub> :CO <sub>2</sub> =1, TOS=30h	50-40	66-58	0.78	2			
66	6Ce-4Zr-10Ni/SBA-15	1 step IM	45-40	51-42	0.8-0.76	39	2015	941	
67	6Ce-4Zr-10Ni/SBA-15	2 steps IM	49-42	56-48	0.77-0.72	52			
68	6Ce-4Zr-10Ni/SBA-15	Co-precipitation 600°C, GHSV=20 Lg <sub>cat</sub> <sup>-1</sup> h <sup>-1</sup> , CH <sub>4</sub> :CO <sub>2</sub> =1, TOS=24h	63-61	71-68	0.85-0.84	3.5			
<b>Ce-Mo-doping</b>									
69	Ni-Mo/SBA-15	GHSV=12000 mLg <sub>cat</sub> <sup>-1</sup> h <sup>-1</sup> ,	87.6-83	~96	0.9		2012	942	
70	Ce-Ni-Mo/SBA-15 5wt%Ni, 25wt% MoO <sub>3</sub> , 2wt%CeO <sub>2</sub>	CH <sub>4</sub> :CO <sub>2</sub> =1, TOS=100h, 800°C	~90	~98	0.9				
<b>La-Mo-doping</b>									
71	Ni-Mo/SBA-15, TOS=120h	GHSV=12000 mLg <sub>cat</sub> <sup>-1</sup> h <sup>-1</sup> ,	90-85	96-97			2011	943	
72	Ni-Mo/SBA-15-La <sub>2</sub> O <sub>3</sub> , TOS=190h	CH <sub>4</sub> :CO <sub>2</sub> =1, 800°C	92-94	96-96	~0.9				

<b>Co-Sc-doping</b>									
73	5Ni-5Co/SBA-15	700°C, GHSV=0.8 Lg <sub>cat</sub> <sup>-1</sup> h <sup>-1</sup> ,	55-48	69-61				2018	944
74	5Ni-5Co/5Sc-SBA-15	CH <sub>4</sub> :CO <sub>2</sub> :N <sub>2</sub> =17:17:6, 6.5h, N <sub>2</sub> =40mLmin <sup>-1</sup>	74-72	78-80					
75	5Ni-5Co/5Sc-SBA-15	40h	92-87	93-92	0.9	43 (H <sub>2</sub> sel.)			
<b>• Basic properties</b>									
76	8MgO-10Ni/SBA-15 (one pot)	GHSV=3600 mLg <sub>cat</sub> <sup>-1</sup> h <sup>-1</sup> , CH <sub>4</sub> :CO <sub>2</sub> =1, TOS=40h, 700°C	~ 95 (800°C)	~ 90 (800°C)	1.05	80 (H <sub>2</sub> )	83.3	2013	945
77			~71-68	~66-62	1.15-0.88	~75-60	74.9		
78	8MgO-10Ni/SBA-15 (imp.)		~70-65	~65-52	1.1-0.88	~65-50	62.5		
79	8Mg-10Ni/SBA-15	GHSV=36 Lg <sub>cat</sub> <sup>-1</sup> h <sup>-1</sup> , 0.1 g <sub>cat</sub> ,	58-66	62-57	~1.05			2013	946
80	10Ni/SBA-15	CH <sub>4</sub> :CO <sub>2</sub> =1, TOS=40h, 700°C	58-51	56-43	~1.05				
<b>• Morphology</b>									
81	10Ni/DFSBA-15	800°C, GHSV=15000 mLg <sub>cat</sub> <sup>-1</sup> h <sup>-1</sup> ,	~91	~94	0.95	92/96		2019	948
82	15Ni/DFSBA-15	CH <sub>4</sub> :CO <sub>2</sub> =1, 0.2g <sub>cat</sub> , TOS=30h	~89-85	~87-85	0.91	85/93			
83	10Ni/DFSBA-15	794°C, GHSV=23815 mLg <sub>cat</sub> <sup>-1</sup> h <sup>-1</sup> , CH <sub>4</sub> :CO <sub>2</sub> =1.2, TOS=30h	~93-90	~93-90	~1			2020	949

\* Metal content is given in wt%.  $\chi$ =conversion

ii) *Ni/MCM-41 based catalysts for DRM*

\* *Effect of the preparation method of Ni/MCM-41-based catalysts for DRM*

Years ago, Ni-MCM-41 in where Ni ions were incorporated into the silica framework were prepared by direct hydrothermal synthesis, in that case with Ni loading of up to 3.9wt%.<sup>673</sup> The comparison of catalytic data of Ni-MCM-41 catalysts issued from hydrothermal synthesis and by standard impregnation showed improved catalytic properties for samples prepared by hydrothermal method. The characterization of Ni/MCM-41 samples indicated a slight increase of the unit cell parameter when increasing nickel content, supporting the framework incorporation of nickel. H<sub>2</sub>-TPR profiles did not depict any reduction peak before 360°C confirming the absence of NiO crystals on the surface. Thus higher Ni dispersion and lower particle size was reached with sample prepared by hydrothermal method. At 750°C, 71-67% CH<sub>4</sub> conversion was achieved with good catalytic stability over 30h, in the presence of 3.9wt%Ni/MCM-41 sample prepared by hydrothermal synthesis (Table 15, Entries 1-2). In a recent work, the effect of spatial confinement of MCM-41 mesoporous structure over Ni nanoparticles sintering resistance varying Ni nanoparticles deposition method and location has been investigated.<sup>951</sup> Thus, samples with Ni nanoparticles in the inner, outer and inner+outer surface were prepared. The characterization results disclosed high dispersion of Ni inner surface, owing to nanoparticles confinement, with small size around 2nm, and the presence of strong metal-support interactions. Moreover, TEM results and XRD patterns of spent catalysts indicated that the confinement effect of Ni particles inside the pores prevent both the sintering and carbon desposition on Ni<sub>in</sub> particles and ensure the catalytic stability over long TOS. Therefore, the best catalytic performance was achieved over 10wt%Ni<sub>in</sub>/MCM-41 catalyst, at 700°C with 72-67% CH<sub>4</sub> and 82-78% CO<sub>2</sub> conversions and H<sub>2</sub>/CO around 0.78, that was maintained for at least 200h (Table 15, Entries 3-5). High resistance to sintering and carbon deposition were observed since the unconfined Ni/MCM-41 samples (10wt%Ni<sub>out</sub>/MCM-41, 10wt%Ni<sub>in+out</sub>/MCM-41) deactivated within 12h.

\* *Preparation of bimetallic Ni/MCM-41-based catalysts for DRM*

Suitable metal doping could be key to improve both the metal particle size and dispersion by establishing metal-metal and metal active phase/support interactions. Consequently, metal sintering and catalyst coke resistances should be enhanced. Moreover, the modification of surface basicity would improve the CO<sub>2</sub> adsorption and dissociation unfavouring the CH<sub>4</sub> adsorption and decomposition, promoting CO<sub>2</sub> dissociation and the release of active oxygen species to boost gasification of adsorbed carbon species.



Numerous papers disclosing different metal doping impacts of DRM catalysts have been published. For instance, a study of the benefits of Ga-doping over catalytic and textural features of a 5wt%Ni/MCM-41 showed an optimum Ga content, close to 2wt% to maximise the catalytic performance and stability.<sup>952</sup> Due to metal doping, H<sub>2</sub>-TPR profiles revealed that the reduction of nickel shifted at higher temperature which was attributed to strong metal-support interaction that improved Ni particles dispersion and low Ni particles size. A decrease in the amount of medium and strong basic sites amount was observed when increasing Ga loading, that was attributed to the formation of extra-framework acid sites. For Ga content <3wt%, the catalytic results of Ga-doped 5wt%Ni/MCM-41 sample were superior to those for the un-doped sample and a maximum was observed for 2wt%Ga-5wt%Ni/MCM-41. High 90-85% CO<sub>2</sub> and 88-83% CH<sub>4</sub> conversion, for H<sub>2</sub>/CO close to 1 and 50% H<sub>2</sub> selectivity were achieved at 800°C along 30h TOS (Table 15, Entry 6). Moreover, the doped catalyst exhibited higher resistance to coke deposition and Ni sintering. The Sc doping effect over 5wt%Ni/MCM-41 physicochemical properties demonstrated that Sc loading induced a decrease in the surface area and catalytic activity of 5%Ni/MCM-41 catalysts.<sup>953</sup> While Sc loading <1wt% enabled an increase in CO<sub>2</sub> conversion up to 38% for 0.1 wt% Sc content. The presence of Sc small amount favoured strong interaction between metal-support leading to higher dispersion of Ni nanoparticles and also increased the surface basicity. Therefore, enhanced CO<sub>2</sub> adsorption and activation led to the presence of high amount of active oxygen species promoting oxidation of carbon species and lowering coke deposition. At 800°C, the best catalytic performance were achieved over 0.1wt%Sc-5wt%Ni/MCM-41 catalyst, achieving stable and high 87% CH<sub>4</sub> and 85% CO<sub>2</sub> conversions with 0.94 H<sub>2</sub>/CO ratio and H<sub>2</sub> yield close to 86%, along short 7h TOS (Table 15, Entries 7-9). Years ago, the impact of different transition metals (Zr, Ti, Mn) incorporation into the silica framework over the catalytic and textural properties of Ni/MCM-41 samples prepared by hydrothermal method was explored.<sup>954</sup> Characterization data disclosed that higher Ni dispersion was achieved for Zr-doping in contrast to Ti- and Mn-doping. XRD patterns evidenced the presence of amorphous silica matrix for Ni-Ti/ and Ni-Mn/ MCM-41 spent catalysts, suggesting that the Ti or Mn incorporations worsen thermal stability of MCM-41 silica support. On the contrary, the presence of Zr cations in the framework stabilizes the MCM-41 structure. The catalytic performance of Zr-doped Ni/MCM-41 catalysts was similar or superior to catalytic activity than Ni/MCM-41 catalyst. On the contrary, the decoration of Ni particles by TiO<sub>x</sub> and MnO<sub>x</sub> for Ti- and Mn-based Ni/MCM-41 catalysts hindered the accessibility to Ni-active centers and lowered their catalytic performance. Accordingly, Zr doped catalysts exhibited higher activity and stability, and were maximum over 1wt%Zr-2wt%Ni/MCM-41, with maintained 92% CH<sub>4</sub> conversion, H<sub>2</sub>/CO ratio close to 0.95, at 750°C over 72h TOS (Table 15, Entries 10-13). However, no data of CO<sub>2</sub>

conversion neither H<sub>2</sub> nor CO selectivity were reported. Gd doping study of 5wt%Ni/MCM-41 prepared by co-impregnation method revealed the improvement of CO<sub>2</sub> adsorption and activation through the Gd<sub>2</sub>O<sub>2</sub>CO<sub>3</sub> species formation similarly to La<sub>2</sub>O<sub>2</sub>CO<sub>3</sub> (Figure 81) preventing coke deposition and also enhancing Ni reducibility.<sup>955</sup> Over 0.1wt% Gd-promoted catalyst, high 88% CH<sub>4</sub> and 92% CO<sub>2</sub> conversions, with H<sub>2</sub>/CO close to 1 were maintained over short 6.5h TOS while carbon deposition was negligible (Table 15, Entries 14-17). The catalytic performance of Ni/MCM-41 catalysts doped with Ru and Mg by impregnation showed that Ru incorporation improved the activity and stability of Ni/MCM-41 catalysts, being maximum H<sub>2</sub> selectivity achieved over 1wt%Ru@Ni/MCM-41, while Mg doping enhanced the 1wt%Ru@Ni-MCM-41 catalytic performance increasing CH<sub>4</sub> conversion and limiting RWGS reaction.<sup>956</sup> However, low 31% CH<sub>4</sub> and 37% CO<sub>2</sub> conversions with H<sub>2</sub>/CO<1 were achieved at 600°C after 4h of TOS (Table 15, Entries 18-23). TGA analysis revealed coke formation with high weight loss for all samples (45-65%) that did not particularly affected the catalytic activity of the catalyst over 4h TOS, but induced blockage of reactor at longer 7h TOS. The same group previously described a similar study of preparation and catalytic performance of Ni/MCM-41 samples doped with Rh.<sup>957</sup> Mono- and bimetallic MCM-41 catalysts were prepared either by Rh impregnation (Rh@Ni-MCM-41) or by one-pot hydrothermal synthesis (Rh-Ni/MCM-41). Optimum 0.19 Ni/Si ratio was determined achieving low 31% CH<sub>4</sub> and 41% CO<sub>2</sub> conversions for 14h at 600°C (Table 15, Entries 24-29). The Rh incorporation was shown to improve the catalytic activity and stability. However, the catalyst prepared by impregnation method suffered higher coke deposition at longer reaction times. Earlier, a comparative study of the catalytic behavior of monometallic 20wt%Ni/MCM-41 and bimetallic Pd-20wt%Ni/MCM-41 samples demonstrated the promoting effect of Pd-doping on the activity and stability of 20wt%Ni/MCM-41 catalysts owing to synergetic effect between Ni and Pd improving Ni nanoparticles dispersion and reducibility.<sup>958</sup> At 650°C, over 0.3wt%Pd-20wt%Ni/MCM-41, the best catalytic results were achieved and maintained for 10h TOS. Low 36% CH<sub>4</sub> and 51 % CO<sub>2</sub> conversion with 19% H<sub>2</sub> and 24% CO selectivity, and H<sub>2</sub>/CO ratio close to 1 (Table 15, Entries 30-32). Despite their high thermal stability against sintering and the formation of coke, the doping of Ni/MCM-41 catalysts with noble metal did not provide much improvement in the catalyst resistance to coke formation and deactivation, and neither in catalytic activity.

\* *Effect of basic properties over the Ni/MCM-41-based catalysts activity for DRM*

Suitable basic properties are well-known to allow CO<sub>2</sub> adsorption and optimum catalytic coverage preventing CH<sub>4</sub> decomposition and severe carbon deposition. Therefore the addition of ceria, zirconia or magnesia positively modified the physicochemical properties of the support

and improved not only CO<sub>2</sub> adsorption but also the Ni interaction with the support enhancing Ni dispersion and stability. Following these leads, Y<sub>2</sub>O<sub>3</sub>-Ni/MgO-MCM-41 catalysts were successfully prepared by the one-pot synthesis that revealed to be a suitable route to manage uniform distribution of MgO, NiO and Y<sub>2</sub>O<sub>3</sub> on MCM-41 surface.<sup>959</sup> The incorporation of MgO allowed improving the basicity while the incorporation of Y<sub>2</sub>O<sub>3</sub> enabled to promote the reducibility and prevent the formation of intermediate phase between Ni (Mg) and the support limiting Ni sintering. Moreover, the incorporation of Y<sub>2</sub>O<sub>3</sub> enhanced the amount of oxygen vacancies favourable to CO<sub>2</sub> adsorption, activation and dissociation lowering carbon deposition. H<sub>2</sub>-TPR study showed a shift to lower temperature of broader NiO reduction peak, after Y<sub>2</sub>O<sub>3</sub> incorporation, indicating that Y<sub>2</sub>O<sub>3</sub> promotes nickel dispersion and strongly modifies the metal reducibility. Then, the best catalytic performance was achieved over 2wt%Y<sub>2</sub>O<sub>3</sub>-Ni/MgO-MCM-41 with 71% CH<sub>4</sub> and 84 % CO<sub>2</sub> conversions, 0.85 H<sub>2</sub>/CO ratio and with good stability over 20h TOS at 750°C (Table 15, Entries 33-34). Coke deposition in form of tip type of nanotube caused almost no deactivation catalyst. Good catalytic results were reported but no data of Ni and MgO contents were provided.

\* *Conclusion*

Similar approaches to SBA-15 were followed to develop improved DRM catalysts using MCM-41 as support. Therefore different attempts to improve dispersion and stabilization of nickel particles by adding suitable metal to control the surface basicity to promote CO<sub>2</sub> adsorption and dissociation favouring carbon gasification were reported. The results of Table 15 summarise the catalytic data reached in the presence of MCM-41-based catalysts for DRM reaction at high temperature. Considering GHSV, reaction temperature and TOS some results can be highlighted as it is displayed in the Figures 99 and 100. High CO<sub>2</sub> conversion and suitable H<sub>2</sub>/CO may be achieved, however data of H<sub>2</sub> and/or CO<sub>2</sub> yield and/or selectivity are required to evaluate H<sub>2</sub>/CO productivity and the potential of the catalysts.

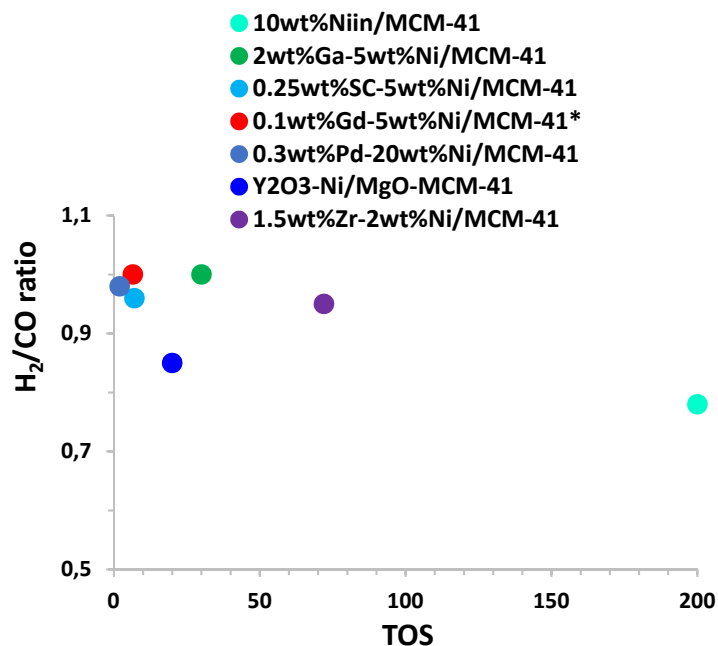


Figure 99. H<sub>2</sub>/CO ratio was plotted versus TOS for different DRM MCM-41-based catalysts.

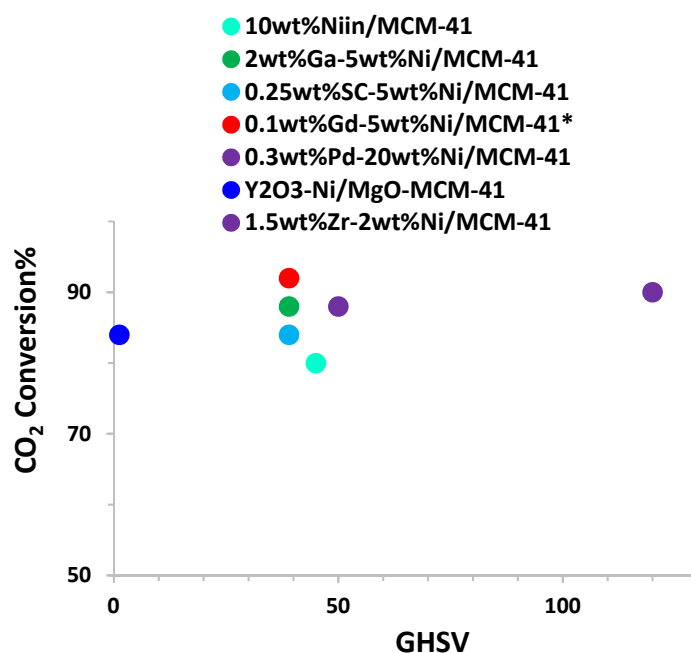


Figure 11. CO<sub>2</sub> conversion was plotted versus GHSV for different DRM MCM-41-based catalysts.

### iii) Conclusion

The main drawback of DRM is the high temperature required due to the endothermicity of the process, which not only results in high energy consumption that is not economically and environmentally sustainable, but is also incompatible with the reduction of CO<sub>2</sub> emissions. Therefore, any industrial application must foresee the exclusive consumption of heat produced from renewable (sun, wind, water) or nuclear sources. In addition to the high energy cost, the rapid deactivation of the catalyst must be overcome. The present review illustrates the high

activity of Ni-based zeolite and OMS catalysts, despite deactivation due to Ni sintering and coke deposition which, in turn, can plug the reactor in long-term tests. Thus, numerous attempts have been followed to improve Ni-catalysts stability minimizing metal particles size, and improving metal dispersion and reducibility. The use of high surface area support and a second or multi metal-doping constitute the main strategies, improving the metal-support interaction and modifying acid-base and redox properties. Thus, zeolites and OMS offer opportunities for the development of robust and efficient DRM catalyst. Unfortunately, most of the here referenced works remained far from an industrial implementation since the studies lack of long-term stability test, catalytic regeneration study, and the process were performed at high temperature (>750°C) with catalytic performance close to thermodynamic equilibrium. The small pore size system of zeolites compared to mesoporous materials may be a weakness to reach a high dispersion of small metal nanoparticles and probably more prone to pore blockage due to metal sintering and/or coke deposition. Hence, the collection of references shows a greater number of studies exploring the potential of SBA-15 as support fully supported by promising results that should make it a good candidate for the development of DRM catalysts. The high surface area, confinement effect of mesoporous structure and thermal stability of SBA-15 should be key to achieve high Ni nanoparticles dispersion and stability using optimum preparation method and suitable metal promoters. The [Figures 101 and 102](#) compared the best catalytic results reached over Ni-OMS and Ni-zeolites based catalysts compiled in the literature. Actually, data of CO and/or H<sub>2</sub> yield and/or selectivity are missing and would be necessary to validate this ranking where Ta-Ni/FZSM-5, 0.5wt%Co-4.5wt%Ni/SBA-15, 2wt%Ga-5wt%Ni/MCM-41, 1.5wt%Zr-2wt%Ni/MCM-41, 10wt%Ni-10wt%MgO/BEA, 10wt%Ni/DFSB-15, 5wt%Ni-5wt%Ce/ZSM-5, 1wt%Ni/SBA-15 and Ni-Mo/SBA-15 exhibited the more relevant catalytic features considering H<sub>2</sub>/CO ratio and CO<sub>2</sub> conversion as function of GHSV and TOS. Furthermore, the design of DRM reactor alternating cycles of reaction and catalysts regeneration should be key.

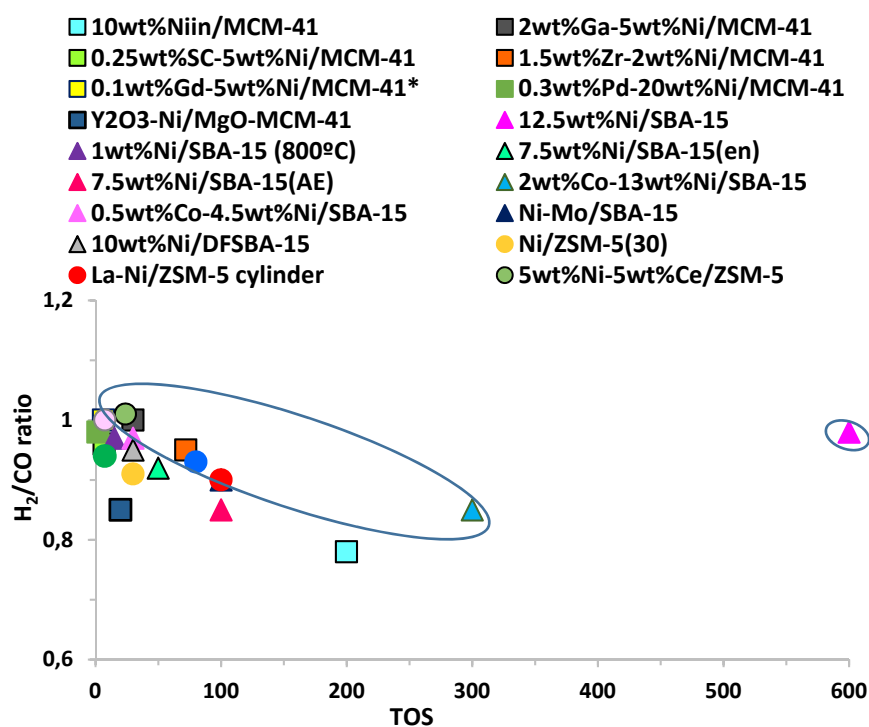
On the other hand, the combination of POM and DRM processes constitutes a great strategy and challenge to overcome the main limitation of energetic cost taking advantage of the POM exothermicity. Up to now, POM+DRM route has been insufficiently explored and even less in the presence of zeolite and OMS based materials.

To conclude, future approaches should focus on the structure and morphology of the DRM catalyst to improve the stability and dispersion of metal active species due to confinement effect and on the elimination or prevention of coke formation. Therefore, to improve catalyst stability, a crucial approach must be to avoid coke formation by modifying the catalyst composition and incorporating active sites for rapid carbon oxidation. Thus, the properties of the DRM catalyst should be improved to tune the redox properties, enhance the dispersion and stabilization of

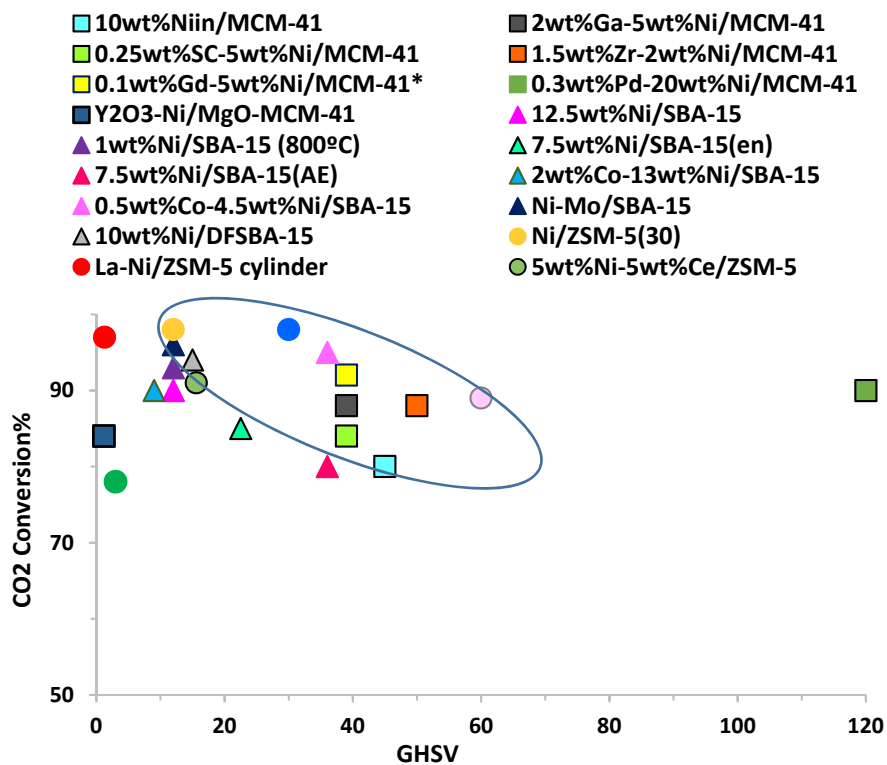
metal active species, and maximize oxygen mobility by incorporating suitable promoters. In addition, greater consideration should be given to the morphology of the support in order to disperse, stabilize and also isolate the metal species.

Following this, a special focus should be given to OMS materials, hierarchical zeolites due to their meso- and macroscale secondary porosity coupled with microporous primary structure, two-dimensional zeolite nanosheets and core-shell materials to promote physical isolation and shielding of the particles could be of interest.

Finally, validation of catalytic activity and stability will be performed under realistic conditions for long TOS.



**Figure 101.**  $H_2/CO$  ratio was plotted versus TOS for different DRM zeolites and OMS-based catalysts. The ovoid highlights the best catalytic performance:  $H_2/CO$  ratio close to 1 versus TOS.



**Figure 102.** CO<sub>2</sub> conversion was plotted versus GHSV for different DRM zeolites and OMS-based catalysts. The ovoid highlights the best catalytic performance: high conversion versus GHSV.

**Table 15.** Summary of the catalytic performance of the different reviewed DRM MCM-41-based catalysts at 0.1 MPa.

Entry	Catalysts	Conditions	$\chi_{\text{CH}_4}$ (%)	$\chi_{\text{CO}_2}$ (%)	H <sub>2</sub> /CO	Sel. H <sub>2</sub> /CO	Coke wt%	Year	Ref
1	3.9Ni/MCM-41	750°C, GHSV=50000 mL <sub>cat</sub> <sup>-1</sup> h <sup>-1</sup>	71-67				29.7	2009	<sup>673</sup>
2	1.2Ni/MCM-41	<sup>1</sup> , CH <sub>4</sub> :CO <sub>2</sub> :He=1:1:2, 0.12g <sub>cat</sub> , TOS=30h	75-70				7.1		
3	10Ni <sub>in</sub> /MCM-41	700°C, GHSV=45 Lg <sub>cat</sub> <sup>-1</sup> h <sup>-1</sup> ,	72-67	82-78	~0.78			2019	<sup>951</sup>
4	10Ni <sub>out</sub> /MCM-41	CH <sub>4</sub> :CO <sub>2</sub> =1, 0.1g <sub>cat</sub> , TOS=200h	68-43	77-53					
5	10Ni <sub>in+out</sub> /MCM-41		70-43	67-33					
<b>• Bimetallic</b>									
<b><i>Ga-doping</i></b>									
6	2Ga-5Ni/MCM-41	800°C, GHSV=39 Lg <sub>cat</sub> <sup>-1</sup> h <sup>-1</sup> , 0.1g <sub>cat</sub> , TOS=30h CH <sub>4</sub> :CO <sub>2</sub> :N <sub>2</sub> =30:30:5,	88-83	90-85	1-0.98	~50 (H <sub>2</sub> Yield)		2018	<sup>952</sup>
<b><i>Sc-doping</i></b>									
7	5Ni/MCM-41	800°C, GHSV=39 Lg <sub>cat</sub> <sup>-1</sup> h <sup>-1</sup> ,	68	61	0.92			2019	<sup>953</sup>
8	0.1Sc-5Ni/MCM-41	CH <sub>4</sub> :CO <sub>2</sub> :N <sub>2</sub> =30:30:5, 0.1g <sub>cat</sub> ,	87	85	0.94	~86 (H <sub>2</sub> Yield)			
9	0.25Sc-5Ni/MCM-41	TOS=7h	90	84	0.96	~86 (H <sub>2</sub> Yield)			
<b><i>Sc-doping</i></b>									
10	2Ni/MCM-41	750°C, GHSV=50 Lg <sub>cat</sub> <sup>-1</sup> h <sup>-1</sup> ,	84-45		~1.1		4	2009	<sup>954</sup>
11	1Zr-2Ni/MCM-41	CH <sub>4</sub> :CO <sub>2</sub> :He=1:1:2, 0.12g <sub>cat</sub> ,	~92		~0.95		6		
12	1.5Zr-2Ni/MCM-41	TOS=72h	~88		~0.95		5		
13	2Zr-2Ni/MCM-41		~88-86		~0.95		8		
<b><i>Gd-doping</i></b>									
14	5Ni/MCM-41	800°C, GHSV=39 Lg <sub>cat</sub> <sup>-1</sup> h <sup>-1</sup> ,	60	68	0.85			2019	<sup>955</sup>
15	0.1Gd-5Ni/MCM-41	CH <sub>4</sub> :CO <sub>2</sub> :N <sub>2</sub> =30:30:5, 0.1g <sub>cat</sub> ,	83	83	0.9				
16	1Gd-5Ni/MCM-41	TOS=6.5h, T <sub>reduction</sub> =600°C	80	80	0.8				
17	0.1Gd-5Ni/MCM-41*	*T <sub>reduction</sub> =800°C	88	92	1				
<b><i>Noble metal doping</i></b>									
18	Ni/MCM-41	600°C, 0.9 sg <sub>cat</sub> mL <sup>-1</sup> ,	0.3 (0h)	0.41 (0h)		1.6/2.5		2011	<sup>956</sup>
19		CH <sub>4</sub> :CO <sub>2</sub> :Ar=1:1:1, Flow=60	0.38 (4h)	0.39 (4h)	0.63	1.5/2.4			
20	1Ru-Ni/MCM-41	mLmin <sup>-1</sup> , TOS=4h, Ni/Si=0.22	0.29 (0h)	0.44 (0h)		1.65/2.5			
21			0.34 (4h)	0.4 (4h)	0.68	2/2.2			
22	1Mg-1Ru-Ni/MCM-41		0.31 (0h)	0.455 (0h)		1.6/2.4			

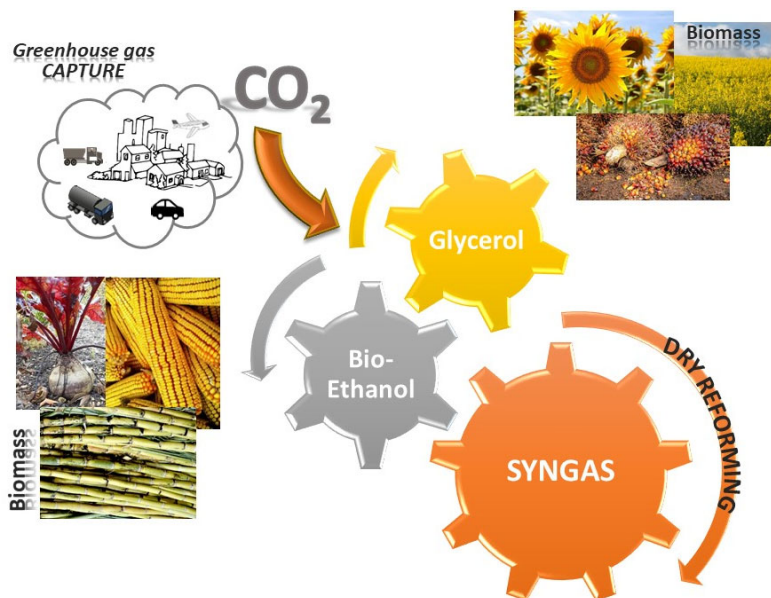


23			0.31 (4h)	0.37 (4h)	0.95	1.9/2.05				
24	Ni/MCM-41	600°C, 0.9 sg <sub>cat</sub> mL <sup>-1</sup> ,	0.31 (0h)	0.31 (0h)		1.6/2.4	1.2	2010	<sup>957</sup>	
25	(Ni/Si=0.2)	CH <sub>4</sub> :CO <sub>2</sub> :Ar=1:1:1, Flow=60	0.41 (4h)	0.41 (4h)		1.6/2.4				
26	Rh@Ni/MCM-41	mLmin <sup>-1</sup> , TOS=4h, Ni/Si=0.22	0.34 (4h)	0.4 (4h)		1.7/2.3				
27		TOS=14h	0.33-0.18	0.46-0.42		0.9/1.5				
28	Rh-Ni-MCM-41		0.34 (4h)	0.4 (4h)		1.3/1.7				
29	(Ni/Si=0.2, Rh/Ni=0.01)	TOS=14h	0.33-0.27	0.4-0.4		1.1/1.7				
30	20Ni/MCM-41	550°C, 0.05g <sub>cat</sub> , GHSV=120	16-10	24-18	0.69	10-7/14-9		2009	<sup>958</sup>	
31	0.3Pd-20Ni/MCM-41	Lg <sub>cat</sub> <sup>-1</sup> h <sup>-1</sup> ,	36	51	0.81	19/24				
32		CH <sub>4</sub> :CO <sub>2</sub> :N <sub>2</sub> =20:20:60,	80	90	0.98	57/58				
		TOS=10h								
		650°C, TOS=2h								
	<b>• Basic properties</b>									
33	2Y <sub>2</sub> O <sub>3</sub> -Ni/MgO-MCM-41	TOS=4h	80	90	0.85	~93 (H <sub>2</sub> )		2020	<sup>959</sup>	
34		TOS=20h	71	84	0.85					
		750°C, 0.2g <sub>cat</sub> , GHSV=1.2 Lg <sub>cat</sub> <sup>-1</sup> h <sup>-1</sup> , CH <sub>4</sub> :CO <sub>2</sub> :Ar=1:1:1								

\* Metal content is given in wt%.  $\chi$ =conversion

### 6.3. Dry reforming of alcohols (DR-alcohols)

Synthesis gas (syngas) is the feedstock for a broad range of processes such as Fischer-Tropsch, MeOH and DME synthesis that in turn outline the worldwide market of fuels and chemicals. An additional source based on renewable feedstock to produce syngas is the dry reforming (DR) or reforming with CO<sub>2</sub> of alcohols providing from bio-resources (Figure 103). In this context, bio-ethanol and glycerol issued from biodiesel constitute ideal feedstock to effectively close carbon cycle providing valuable chemicals and using the main greenhouse gases, helping to mitigate the effect of anthropogenic CO<sub>2</sub>. In this sense, a recent mini review exposed the potential of DR of ethanol (DRE) and glycerol (DRG).<sup>960</sup> Considering DRM to manufacture syngas, the main drawback is that CH<sub>4</sub> is not a renewable feedstock in contrast to ethanol that constitutes an important substrate readily available from biomass (forest and agro-industrial wastes, energy crops). Moreover, from thermodynamics standpoints DRE is favoured at temperature higher than 318 °C whereas DRM at temperature above 600°C. Thus, DRE may allow diversifying and making more flexible and sustainable the production of syngas. The production of glycerol is more limited although the DRG constitutes a great opportunity to value the main byproduct of biodiesel production. Despite the advantages of DRE and DRG, these represent emerging technologies poorly explored and several papers covered the use of zeolites and OMS based catalysts.



**Figure 103.** Production of syngas from DR of renewable alcohols issued from biomass.

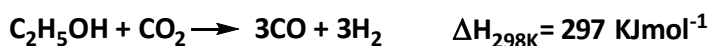
#### 6.3.1. Dry reforming of ethanol (DRE)

##### a) Thermodynamics

A recent paper explored the thermodynamics of ethanol reforming with CO<sub>2</sub>.<sup>961</sup> DRE is an endothermic process that involves numerous competitive and parallel reactions that determine

the syngas yield and are influenced by different parameters such as temperature, pressure and CO<sub>2</sub>/EtOH ratio. Ethanol can undergo dehydrogenation, dehydration and decomposition as well as the side products formed are involved in different secondary reactions. Some reactions of the complex reaction system are displayed in the [Scheme 64](#). In order to evaluate the impacts of some parameters of reaction such as temperature, CO<sub>2</sub>/EtOH, pressure and addition of inert gas over H<sub>2</sub> and CO yields, a thermodynamic analysis via Gibbs free energy minimization method was performed indicating that high H<sub>2</sub> and CO yield up to 95 and 97% may be reached at high temperature (900-1050°C), with CO<sub>2</sub>/EtOH molar ratio around 1 and atmospheric pressure, being the main reaction products CH<sub>4</sub> and C with H<sub>2</sub>, H<sub>2</sub>O, CO and CO<sub>2</sub>, and the carbon formation favoured at low temperature.<sup>961</sup>

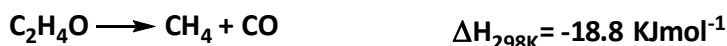
**- DRE**



**- Oxidation into Acetaldehyde**



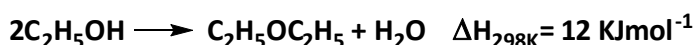
**- Acetaldehyde decomposition**



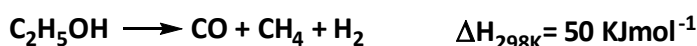
**- DR-Acetaldehyde into SYNGAS**



**- Ethanol dehydration into ethylene or ether**



**- Ethanol decomposition**



**- Methanation**

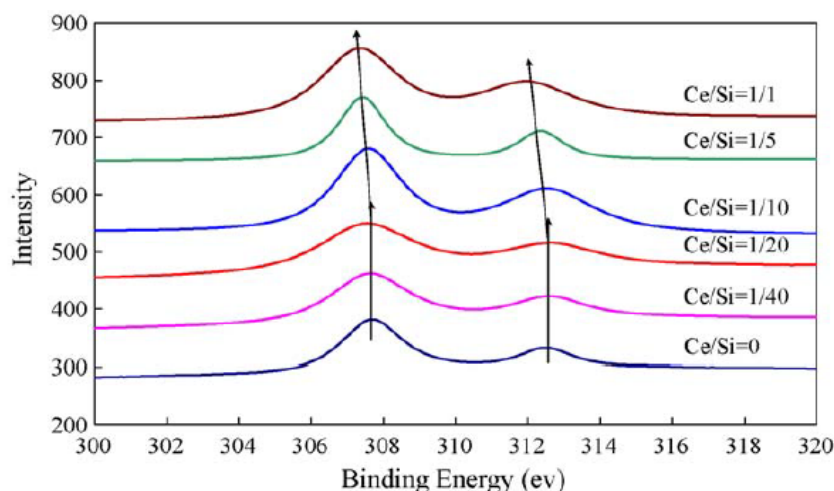


**Scheme 64.** Some parallel reactions involved in the complex DRE reaction system.

b) Catalysts for DRE

To make possible the development of viable DRE technology, the design and development of efficient, selective and robust catalyst is key. Therefore, the addition of suitable promoters, multiple active phases maximizing the metal nanoparticles dispersion and stability through strong interaction metal/support are crucial together with the design of optimized catalyst

regeneration. As it occurs for dry reforming of  $\text{CH}_4$ , Cu, Co, Rh and Ni supported solid catalysts have been largely used for DRE, being Ni the most explored metal because of its high activity, selectivity, availability and price, besides its rapid sintering and deactivation at high temperature.<sup>962-965</sup> Therefore the choice of suitable support with high surface area and/or appropriate redox properties have shown to be crucial to achieve high NiO dispersion with small particle size which give Ni higher resistance to coke deposition and sintering. As discussed in this review, the addition of a suitable promoter (Zr, Ce, La, Mn, Co, Mg) contributes to improve the activity and stability of Ni-based catalysts. In the bibliography, the catalytic activity of zeolite based material for DRE has not been explored, while only two works described the catalytic performance ofOMS based catalysts. The benefits of the incorporation of Ce in SBA-15 structure have been widely described to promote the oxygen surface mobility owing to special redox properties of Ce ( $\text{Ce}^{3+}/\text{Ce}^{4+}$ ) and oxygen vacancy formation. Accordingly, the suitable catalytic performance of Rh/ $\text{CeO}_2$  has been demonstrated due to the interaction between Rh and  $\text{CeO}_2$  and advanced properties of  $\text{CeO}_2$  for DRE.<sup>966,967</sup> Following these leads, in 2009, the catalytic performance of Rh/Ce-SBA-15 catalysts prepared by impregnation of Ce-SBA-15 with different Ce/Si molar ratio issued from direct synthesis was explored.<sup>968</sup> Firstly, the catalytic performance of 5 wt%-Rh, Ni, Co, Pd supported on SBA-15 was checked, revealing the lower catalytic activity of 5wt%Ni/SBA-15 exhibiting the higher catalytic activity of 5wt%Rh-SBA-15. Moreover, a decrease of metal content allowed improving the catalytic performance up to 470% exhibited by 1wt%Rh/SBA-15 in comparison to 5wt%Rh/SBA-15. Therefore, 1wt% Rh/Ce-SBA-15 catalysts with Ce/Si molar ratio ranging 0-1 were prepared. The stability of the ordered mesoporous structure was affected by the incorporation of Ce and could be conserved for Ce/Si up to 1/5. The characterization data showed optimum Rh nanoparticle dispersion and lower particle size, 5-8nm, for Ce/Si=20, probably due to strong interaction metal-metal (Rh-Ce).<sup>969</sup> XPS analysis showed a shift to slightly lower binding energies of Rh ( $3d_{5/2}$ ) and Rh ( $3d_{3/2}$ ) of  $\text{Rh}^0$  with further incorporation of Ce ( $>1/20$ ), indicating the formation of higher Rh particles size (Figure 104), in agreement with the  $\text{H}_2$ -TPR results that showed a shift of reduction peak to higher temperature, attributed to the decrease of the Rh dispersion. The activity over 1wt%Rh/Ce-SBA-15 catalysts increased with Ce/Si ratio from 0 to 1/20 attributed to the improved mobility of surface oxygen species because of the incorporation of Ce being the more suitable Ce/Si molar ratio equal to 1/20. Thus, at 750°C, good catalytic performance was achieved over 1wt%Rh/Ce-SBA-15 (Ce/Si=1/20) with  $\text{H}_2/\text{CO}$  ratio around 1,  $\text{CO}_2$  conversion up to 76% and mole percentage of gas product of 42% for  $\text{H}_2$  and CO, 14% for  $\text{CO}_2$ , over 24h TOS, with  $\text{EtOH}/\text{CO}_2=1$  and  $\text{WHSV}=15594\text{h}^{-1}$ .



**Figure 104.** Rh 3d XP spectra of 1%Rh/Ce-SBA-15 catalysts with different Ce/Si molar ratio. Reprinted with permission from ref.<sup>968</sup> Copyright 2009, Elsevier B.V. All rights reserved.

More recently, the catalytic performance of Ni/KIT-6 prepared by methanol-assisted impregnation method was reported.<sup>970</sup> Characterization results showed that the use of KIT-6 as support enabled improving the dispersion and decreased Ni particles size owing to confinement effect in comparison with Ni/SiO<sub>2</sub>. Therefore, smaller Ni particle sizes allowed preventing the coke formation, and the strong interaction metal/support lowered Ni sintering improving the catalytic stability and activity. Thus, at 550°C, good catalytic performance was achieved over 14wt%Ni/KIT-6 with H<sub>2</sub>/CO ratio around 1.5, EtOH conversion close to 100% and mole composition of gas product of 49% for H<sub>2</sub>, 32% for CO and 19% for CH<sub>4</sub> along 40h TOS, with EtOH/CO<sub>2</sub>=1 and GHSV=40Lg<sub>cat</sub><sup>-1</sup>h<sup>-1</sup>.

### c) Conclusion

The catalytic results showed that almost complete conversion of ethanol can be achieved with almost H<sub>2</sub> theoretical yield, making of DRE a promising technology to produce syngas closing carbon cycle, and requiring solar or nuclear based heat sources in the same way that processes working at high temperature, to ensure carbon neutrality. In the presence of OMS based catalysts good catalytic performance was reached and similar to the best catalytic results achieved in the presence of 2wt%Ir/CeO<sub>2</sub> or 15wt%Cu/Ce<sub>0.8</sub>Zr<sub>0.2</sub>O<sub>2</sub> that exhibited high catalytic stability over 70-90h TOS.<sup>971,972</sup> Since DRE is emerging process valuable mechanism insights are required. Molecular modeling and operando studies will be necessary to the design and ab initio synthesis of efficient and stable advanced catalysts to reach sustainable syngas manufacturing.

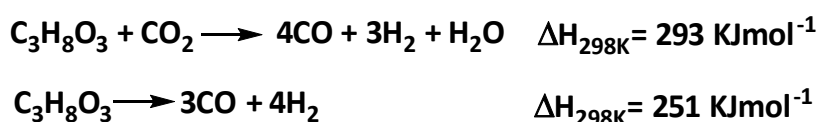
### 6.3.2. *Dry reforming of glycerol (DRG)*

Glycerol is a byproduct of biodiesel production and constitutes promising source for syngas production. Glycerol steam reforming and aqueous phase reforming are routes to produce syngas.<sup>973,974</sup> Nevertheless high H<sub>2</sub>/CO ratio unfavourable for FischerTropsch synthesis along

with high CO<sub>2</sub> production were reached, forcing to disregard this route.<sup>975,976</sup> Thus, dry reforming of glycerol constitutes a promising alternative to produce syngas and solve glycerol crisis converting two wastes into valuable product.

a) Thermodynamics

Following the equations of [Scheme 65](#), 3 moles of H<sub>2</sub> and 4 moles of CO per mole of glycerol can be produced by DRG, while direct glycerol decomposition can produce 4 moles of H<sub>2</sub> and 3 moles of CO per mole of glycerol. Other reactions such as methanation of WGS reaction can take place. From thermodynamic standpoints, complete decomposition of glycerol is very likely. Since CO<sub>2</sub> can be involved in DRG and converted into syngas, a study of CO<sub>2</sub> conversion has to be considered. Therefore, a thermodynamic analysis of DRG for H<sub>2</sub> and syngas synthesis was performed with total Gibbs free energy minimization method and the impact of different reaction parameters were explored.<sup>977</sup> Maximum H<sub>2</sub> and syngas yield are obtained at atmospheric pressure and are influenced by CO<sub>2</sub>/Glycerol ratio. Accordingly up to 7 moles of syngas can be produced per mole of glycerol with CO<sub>2</sub>/glycerol ratio > 3, while H<sub>2</sub> yield is maximum for CO<sub>2</sub>/glycerol ratio < 1. It was observed that syngas yield increased with temperature and CO<sub>2</sub>/glycerol ratio, and optimum reaction conditions are 727°C and CO<sub>2</sub>/glycerol = 1. Under these conditions, 6.4 mol of syngas are produced by mole of glycerol with H<sub>2</sub>/CO = 1 whereas coke deposition is thermodynamically prevented.

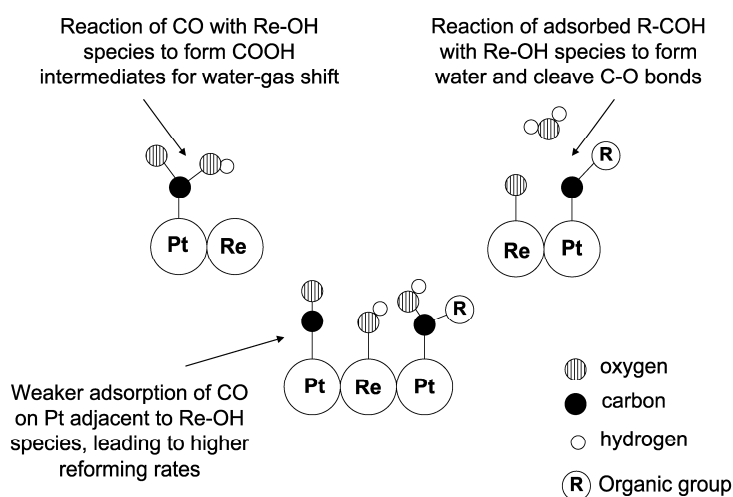


**Scheme 65.** DRG and glycerol decomposition.

b) Catalysts for DRG

Data on dry reforming of glycerol are limited in literature, and we found only one reference exploring the activity of Ni/SBA-15 catalysts.<sup>978</sup> The most used catalysts for GDR, as it occurs for numerous CO<sub>2</sub> conversion process at high temperature, are Ni-based catalyst due to Ni lower price, high catalytic activity and availability. Besides Ni-based catalysts suffer high deactivation due to metal sintering and coke formation, different studies explored the catalytic performance of noble metals since they are more stable against sintering and coke formation at high temperatures.<sup>979</sup> Moreover, the scientific community investigated and demonstrated that the incorporation of second metal strengthens the interactions metal (Ni) /support that lower the physical migration of metal nanoparticles and also establish new interaction metal-metal providing new redox properties such as the doping of Ni-based catalysts with CaO, CeO<sub>2</sub> or La<sub>2</sub>O<sub>3</sub>.<sup>980</sup> Accordingly, the good and outstanding catalytic performance of 3wt% La-promoted

alumina supported 20wt%Ni catalyst, with  $H_2/CO$  lower than 2, was reported.<sup>981</sup> The syngas production was in a first stage attributed to glycerol decomposition pathway and further to RWGS and carbon gasification as described in the literature.<sup>964,982</sup> Good catalyst stability and performance were registered over 72h TOS, at 750°C, with high 90% glycerol conversion and stable  $H_2/CO=1.2-1.7$ , with  $CO_2/Glycerol=5$ . Recently, Re was added to Ni/CaO as promoter for DRG, enhancing  $H_2$  yield and glycerol conversion owing to the formation of acid sites favouring the adsorption of OH groups inducing an increase in the catalytic activity. Also, reaction kinetic and characterization studies of Pt-Re/C catalysts for GDR indicated that the Re improved the rate of glycerol reforming by reducing the binding energy of CO to Pt, leading to lower coverage of the surface and higher accessibility to active sites by reaction intermediates and/or products, and additionally favours WGS reaction and C-O bond cleavage (Figure 105).



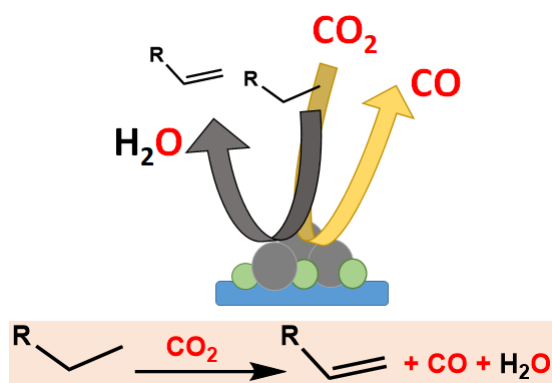
**Figure 105.** Benefits of the incorporation of Re to Pt/C catalysts owing to the formation of Re-OH species for catalytic reforming of oxygenated hydrocarbons. Reprinted with permission from ref.<sup>979</sup>. Copyright 2008, Elsevier Inc. All rights reserved.

Following these leads, 15wt%Ni/SBA-15 and 3wt%Re-15wt%Ni/SBA-15 samples were prepared by impregnation. The addition of Re improved NiO dispersion and allowed decreasing Ni particle size. The study of the catalytic performance of 15wt%Ni/SBA-15 and 3wt%Re-15wt%Ni/SBA-15 revealed higher 57% glycerol conversion and higher 55% hydrogen yield in the presence of 3wt%Re-15wt%Ni/SBA-15, at 700°C, with  $CO_2/glycerol=1$ . The improvement of catalytic activity was attributed to the oxygen storage capacity and mobility of Re that enabled to minimize carbon deposition by gasification of carbon species. A study of reaction parameters showed that  $CO_2/glycerol=1$  was the most suitable ratio while an increase in temperature enhanced competitive methanation and  $CO_2$  hydrogenation. No data about glycerol flow, GHSV nor  $H_2/CO$  were reported that makes difficult the performance evaluation.

### 6.3.3. Conclusion

Dry reforming of ethanol and glycerol, while constitute promising routes to produce syngas, remain emerging technologies that require knowledge and mechanistic insights for the design of efficient and robust catalysts to achieve sustainable syngas manufacturing. In particular to solve the crisis of glycerol as biodiesel by-product and valorize glycerol, the DRG may constitute an alternative route. However, considering the worldwide syngas production and consumption and the urgency in mitigate the CO<sub>2</sub> emissions, the DRG would be an almost marginal alternative. Therefore, considering global syngas production, DRE results more attractive.

## 7 Oxidative dehydrogenation (ODH) of alkanes with CO<sub>2</sub>



**Scheme 66.** Oxidative dehydrogenation of alkanes assisted by CO<sub>2</sub>.

Although there have been great advances in the utilization of CO<sub>2</sub> as building block for chemicals and fuels synthesis, there still exist several inherent drawbacks due to CO<sub>2</sub> inertness and high thermodynamic and kinetic barriers to overcome, requiring of high-energy consumption and green hydrogen production which hinders its industrial implementation. An alternative technological method emerged in the 1990s base of the benefits of the use of CO<sub>2</sub> as soft oxidant and promoters in catalytic processes.<sup>983–985</sup> Back then, the use of CO<sub>2</sub> for dehydrogenation of ethyl benzene allowed reaching higher conversion while H<sub>2</sub>O and CO were new reaction products in addition to H<sub>2</sub> and styrene. These data indicated that reaction underwent an oxidative dehydrogenation pathway in which CO<sub>2</sub> was dissociated into CO and surface oxygen able to abstract hydrogen to form H<sub>2</sub>O (Scheme 66). Thus, CO<sub>2</sub> constantly ensured the lattice oxygen supply and H<sub>2</sub> elimination equilibrium switching (Le Chatelier's principle) via RWGS. Consequently, the use of CO<sub>2</sub> as soft oxidant to perform oxidative dehydrogenation of alkanes present three clear positive benefits respect to catalytic dehydrogenation: enhances equilibrium conversion due to H<sub>2</sub> conversion through RWGS, avoids olefins side reaction due to partial blockage of the active sites by CO<sub>2</sub> adsorption, and improves catalytic life due to coke removal by Boudouard reaction. In addition, CO<sub>2</sub>, the main greenhouse gases, is reduced into CO, a more



valuable chemical. Years ago, the oxidizing capability of different gases for coke gasification was explored and ordered as following:  $O_2$  (105) >  $H_2O$  (3) >  $CO_2$  (1) >  $H_2$  (0.003), illustrating the  $CO_2$  oxidative capacity in addition to heat capability.<sup>986</sup> Thus, the use of  $CO_2$  as soft oxidant may be a new breakthrough in the  $CO_2$  utilization, considering that the global industrial  $CO_2$  use per year is about 230 Mt, while total anthropogenic  $CO_2$  emissions are about 38Gt, this highlights the high demand to convert  $CO_2$ .<sup>987–990</sup>

## 7.1. Introduction

Catalytic dehydrogenation of alkanes constitutes a powerful and widely applied one-step reaction in the industry, which provides hydrogen and olefins that are precursors of a huge variety of industrial products. Nevertheless, catalytic dehydrogenation is thermodynamically limited and highly endothermic and requires high temperature (550–750°C) and low paraffin partial pressure (0.1 MPa).<sup>991</sup> In addition to coke formation because of high temperature, inducing catalyst deactivation and reactor clogging, the higher reactivity of olefins in comparison to alkanes precursors leads to undesired side reactions such as hydrogenolysis, cracking and isomerization. Therefore, different approaches have been explored and the oxidative dehydrogenation using  $CO_2$  as soft oxidant instead of oxygen as alternative emerged and strengthened, because of several advantages from energetic, thermodynamic and kinetic (rate of reaction, higher alkene selectivity) standpoints, such as suppression of the over-oxidation of substrate and product, reduction of carbon deposits and use of  $CO_2$ , the main greenhouse gases. Then, oxidative dehydrogenation of alkanes has been extensively investigated as energy-saving and more environmentally friendly strategy to produce alkenes in the presence of  $MO_x$  supported catalysts mainly with non-precious metals such as Ni, Fe, Co, Cr, La, Cu or V. The catalytic and textural properties of transition and rare earth metal oxides have been widely explored owing to their ability to perform the oxidative dehydrogenation of alkanes.<sup>983,988,990,992–994</sup> The role of redox and acid/base properties play a fundamental role in the adsorption and activation of the reactants, in the dehydrogenation step, and in the regeneration of the oxidation state of the metal oxide catalyst (Figure 106).

### 7.1.1. Mechanistic insights

Efforts have been spent to identify the intermediates of reaction and establish reaction pathways by combination of experimental and computational studies. Likewise, different reaction paths influenced by physicochemical properties were proposed for alkane oxidative dehydrogenation either involving lattice oxygen of metal oxide species further restored by  $CO_2$  reduction, or by combination of simple dehydrogenation and RWGS, although different reaction pathways may be involved in the presence of the same catalyst (Figure 106).

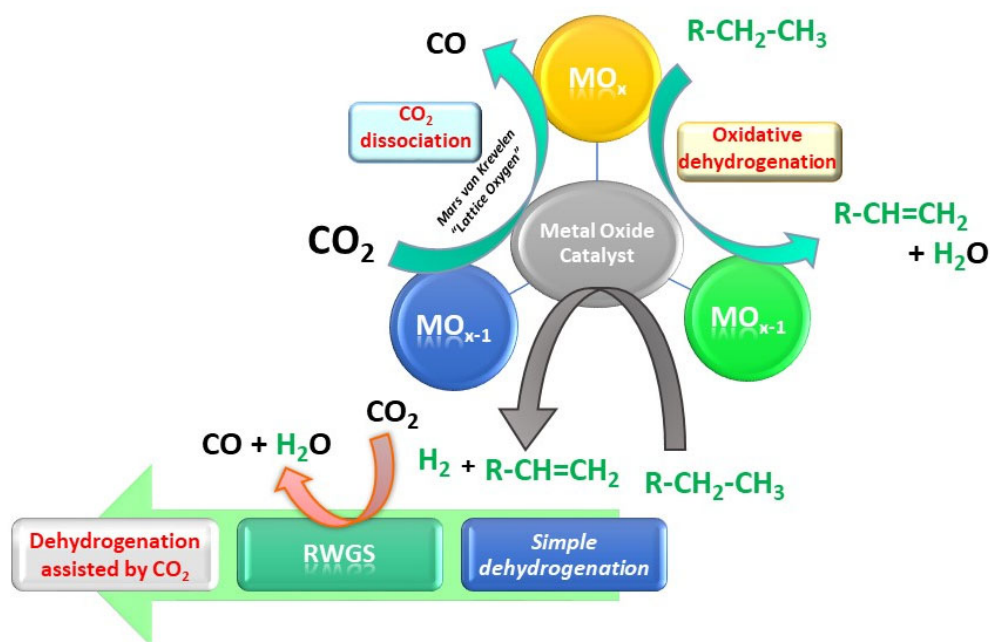
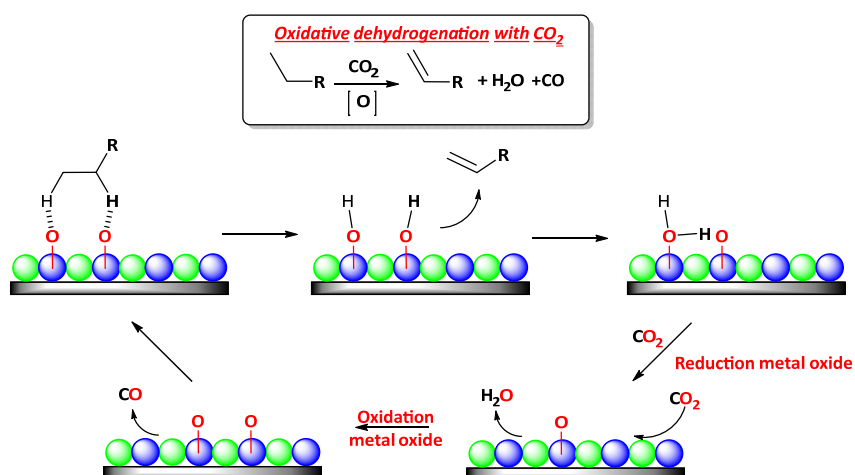


Figure 106. Scheme of different alkane ODH reaction pathways.

### 7.1.2. Role of redox properties

The redox sites of metal oxide catalysts involve the transfer of oxygen atom from metal oxide to the hydrocarbon to complete oxidative dehydrogenation and the production of water. Therefore, the redox cycle is completed when reduced metal oxide is reoxidized by CO<sub>2</sub> and thus CO released. The mechanism is referred as Mars-van-Krevelen mechanism and also redox or regenerative mechanism (Scheme 67).<sup>995–997</sup>

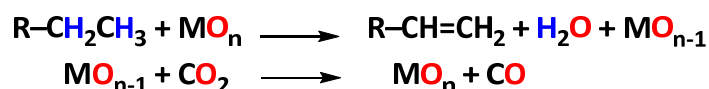


Scheme 67. Role of redox properties of metal oxide catalyst on ODH of alkane mechanism.

### 7.1.3. Role of lattice oxygen

The presence of lattice oxygen in the oxides revealed to play a fundamental role and is closely related with redox properties. Indeed, the oxygen in the network allows the transfer of an oxygen atom from the metal oxide for the abstraction of hydrogen from the alkane and with the

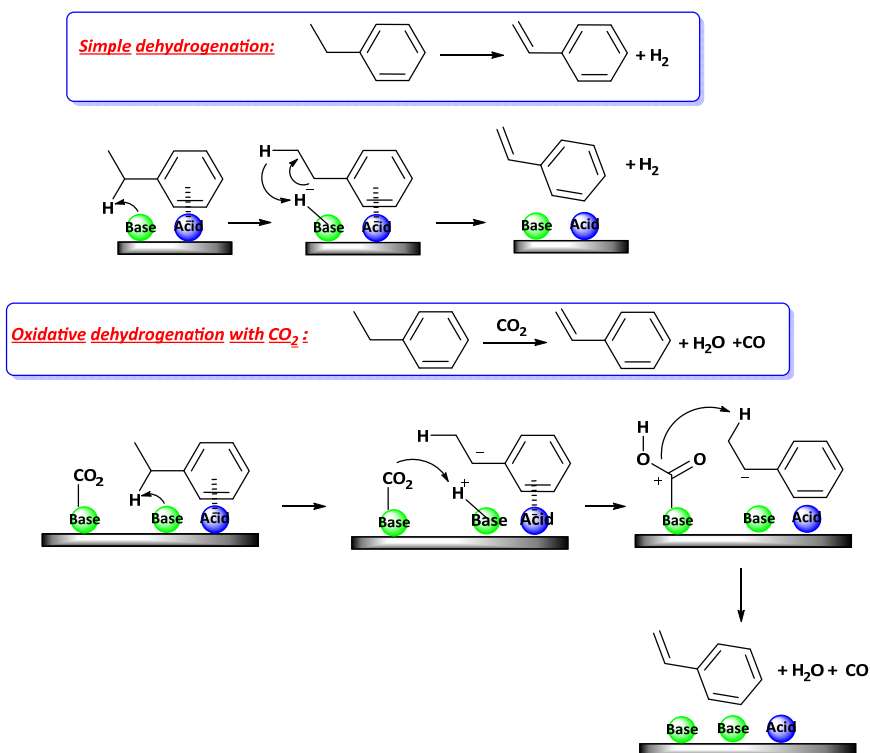
consequent production of water and reduction of the oxidation state of the metal. Therefore, CO<sub>2</sub> contributes to reoxidize the metal and restore the original metal oxidation state and oxygen lattice (Scheme 68).<sup>983,998</sup>



Scheme 68. Role of lattice oxygen and CO<sub>2</sub> on ODH of alkane.

#### 7.1.4. Role of the acid/base sites

The presence of acid/base sites in metal oxide catalysts plays an important role in the alkane and CO<sub>2</sub> adsorption. Indeed acid sites collaborate in the activation of the alkane according with its nature (aromatic cycle) while the basic sites involve the CO<sub>2</sub> activation and hydrogen atom activation/abstraction. Furthermore, the acid/base properties influence the reaction pathway that can partially proceed by simple dehydrogenation and oxidative dehydrogenation (Scheme 69).<sup>999-1001</sup> On the other hand, the excess of acid sites can influence the process selectivity and catalyze side reactions such as cracking, isomerization and condensation.



Scheme 69. Role of acid/base sites on ODH of alkane pathway.

#### 7.1.5. Metal oxide based catalysts for ODH of alkanes

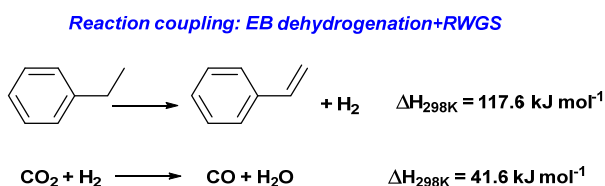
The more widely studied catalytic systems for ODH are chromium, vanadium and iron based catalysts with suitable oxidation states that play a determining role in the catalytic efficiency. VO<sub>x</sub>-materials have been largely used as catalysts for alkanes ODH owing to their activity and selectivity. The interaction metal/support and vanadium loading influenced the dispersion and

stabilization as well as the nature of vanadium species.<sup>990,993,1002–1004</sup> CrO<sub>x</sub>-materials have also exhibited high catalytic activity and selectivity for alkanes ODH owing to the multi-oxidation states of Cr.<sup>993,1005</sup> Actually, redox cycle and Cr active species are still controversial and different pairs have been proposed such as Cr<sup>6+</sup>/Cr<sup>3+</sup> or Cr<sup>3+</sup>/Cr<sup>2+</sup>. Catalytic performance of Cr-based samples is determined by nature and dispersion of chromia active species, in turn influenced by the content and support. The addition of second metals or promoters with specific redox or acid/base properties enable to improve the catalytic performance of the catalyst due to the enhancement in metal oxide dispersion and stability, acid/base and redox properties that influence strongly the ODH pathway.<sup>983,989,1006,1007</sup> The catalytic behavior of the synthesized catalysts also depends on the reaction conditions, and because a high reaction temperature is required, metal sintering and coke deposition induce rapid and severe deactivation, so far, hindering an industrial application. Thus, the research and development of new catalysts for alkanes ODH with CO<sub>2</sub> is a major challenge. In this context, zeolites and OMS due to their versatility in chemical composition, high surface area with moldable pore size and variability in pore system structures, offer opportunities to disperse and stabilize active metal oxides.

## 7.2. Styrene production by ethylbenzene (EB) ODH

The global styrene (ST) market varies with its widespread applications as monomers in the synthesis of synthetic rubber, resins, plastics and mainly polystyrene and several other copolymers production. The worldwide styrene market reached 43.3 B\$ in 2019 corresponding to a production around 20 Mt/year. ST is mainly produced by catalytic dehydrogenation of ethylbenzene (EB) using K-promoted iron oxide catalysts, in presence of excess steam, at 600–700°C and LHSV around 0.43h<sup>-1</sup>.<sup>1008,1009</sup> Due to the endothermic nature of the process ( $\Delta H_{298K}=117.6$  kJmol<sup>-1</sup>), high energy consumption and temperature are required, resulting in coke formation and catalyst deactivation (Scheme 70). Therefore, different approaches have been studied and reaction coupling constitutes an effective approach to improve the equilibrium conversion.<sup>1010,1011</sup> Accordingly, numerous investigations explored the reaction coupling of EB in the presence of CO<sub>2</sub> instead of steam or O<sub>2</sub> combined with RWGS. Therefore, the calculated consumption energy for ST production for the coupling process was 7.9×10<sup>8</sup> J/t versus 6.2×10<sup>9</sup>-7.9×10<sup>9</sup> J/t for current catalytic dehydrogenation. Thus, the oxidative dehydrogenation using CO<sub>2</sub> as soft oxidant as alternative emerged and strengthened because of several advantages from energetic, thermodynamic and kinetic (rate of reaction, higher ST selectivity) standpoints, avoiding the over-oxidation of alkane and consuming CO<sub>2</sub>, the main greenhouse gases.<sup>1012</sup> Hence, the design and development of efficient and robust catalysts is very challengeable, and

thus EB oxidative dehydrogenation has been widely explored as energy-saving and more environmentally friendly strategy to produce ST.



**Scheme 70.** Thermodynamics of ODH of ethane with CO<sub>2</sub> as soft oxidant.

Transition and earth rare metal oxide based catalysts exhibit suitable catalytic activity and have been widely investigated. Fe,<sup>1006</sup> V,<sup>990,1013,1014</sup> Zr,<sup>1015</sup> Ce,<sup>1016,1017</sup> Mn<sup>1018,1019</sup>, Cr<sup>1020,1021</sup> oxides exhibited appropriate catalytic properties to perform the oxidative dehydrogenation with CO<sub>2</sub> of ethylbenzene.<sup>983,990</sup> However, the rapid deactivation of the catalysts is an impediment to the industrial implementation and there is a great interest in the design and development of efficient and robust ODH catalysts. To maximize the dispersion and stabilization of the metallic oxide phase, the great potential of microporous and mesoporous ordered materials as support have been explored due to their high surface area, variability in pores size system, versatility in their framework composition and textural properties, and high thermal and chemical stability.

### 7.2.1. Zeolite-based catalysts for EB ODH

The use of TiO<sub>2</sub>-ZrO<sub>2</sub> binary oxides as catalysts and supports found many applications in catalysis due to their excellent redox properties and oxygen storage capacity as it was illustrated along the present review.<sup>1022</sup> Accordingly, an attempt of preparation and use as catalyst for EB ODH of TiO<sub>2</sub>-ZrO<sub>2</sub> oxides deposited onto mesoporous silicalite-1 (CS-1) was performed. Firstly, metal hydroxide precipitated carbon nanoparticles were prepared by pH controlled precipitation method of metal precursors onto carbon nanoparticles and further used for hydrothermal synthesis of CS-1.<sup>1000</sup> The characterization data showed the XRD pattern typical reflectance of MFI type zeolite while no reflectance of crystalline phase of the TiO<sub>2</sub>-ZrO<sub>2</sub> oxides were detected, indicating that no mixed oxide was occluded on the surface. The registered catalytic performance of TiO<sub>2</sub>-ZrO<sub>2</sub>/CS-1 revealed the better resistance of the supported catalysts, however low catalytic results were achieved, at 650°C, 30% EB conversion and 70-75% ST selectivity were maintained over 9h TOS (Table 14, Entries 18-19). The low selectivity was attributed to higher amount of strong acid and base sites determined by NH<sub>3</sub>-TPD and CO<sub>2</sub>-TPD may be due to the formation of solid solutions (ZrTiO<sub>4</sub>).

The suitable catalytic properties of iron based catalysts for dehydrogenation reaction have been demonstrated.<sup>1008,1023,1024</sup> Accordingly the preparation and use as catalysts of Fe<sub>3</sub>O<sub>4</sub>/ZSM-5 samples with different metal loading for EB ODH were explored.<sup>1025-1027</sup> The catalytic results showed the efficient dispersion of iron oxide over the high ZSM-5 surface area and activity

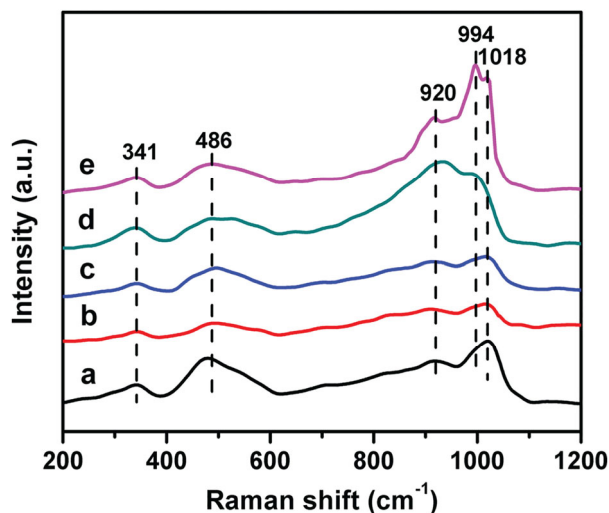
towards CO<sub>2</sub> dissociation into CO and oxygen active species to enable RWGS. This enhanced activity was attributed to oxygen deficiency of supported Fe<sub>3</sub>O<sub>4</sub> and the presence of Fe<sup>2+</sup> species. Nevertheless, at 600°C, low 42% EB conversion and 89% ST selectivity were achieved (Table 14, Entries 20-22). The addition of promoter constitutes an efficient strategy to tune the redox properties and enhance the catalytic activity of metal oxide supported samples.<sup>1028,1029</sup> In this sense, the addition of K has been reported to enhance the rate of carbon gasification from iron oxide catalyst, and extensive studies have determined the formation of potassium monoferrite (KFeO<sub>2</sub>) on the magnetite bulk (Fe<sub>3</sub>O<sub>4</sub>) as the active site for dehydrogenation.<sup>1030–1032</sup> Accordingly, Fe<sub>2</sub>O<sub>3</sub> supported ZSM-5 type chromosilicate (F/CS) samples were prepared following solid-state dispersion method of different γ-Fe<sub>2</sub>O<sub>3</sub> loadings in the structure of K or Na chromosilicate samples, KCS and NCS, respectively.<sup>1033,1034</sup> The catalytic results confirmed the critical role of K as promoter besides Cr, the synergetic effect between both metals to improve the catalytic activity, and with a higher influence than with Na. Moreover, the impacts of the Fe<sub>2</sub>O<sub>3</sub> addition over the catalytic activity depended on the loading and it can be noted that firstly, ST selectivity increased and further decreased. Therefore, at 600°C, highest 92% and 96% ST selectivity for 5% and 10% Fe<sub>2</sub>O<sub>3</sub> loadings over KCS and NCS support, respectively, were reached. Up to 51% ST yield and 96% ST selectivity were achieved over 10wt% Fe<sub>2</sub>O<sub>3</sub>/NCS catalyst. However, the potassium chromosilicate support before washing (KCS<sub>BW</sub>) exhibited the best catalytic performance with 56% ST yield and 96% ST selectivity (Table 14, Entries 23-25). Accordingly, the synergetic effect between Cr and K was considered more effective than synergetic effect between Fe and K. To the contrary, Fe<sub>2</sub>O<sub>3</sub> addition onto NCS revealed the synergetic effect between Fe and Na, promoting catalytic activity with greater magnitude than NCS support. Stability study demonstrated a slight EB conversion decrease from 58 to 56% after the first three runs because of coke deposition that could be recovered after calcination on active sites of the catalyst.

### 7.2.1. OMS-based catalysts for EB ODH

#### a) Monometallic OMS-based catalysts for EB ODH

V-supported catalysts exhibit high activity and selectivity towards styrene formation being the high dispersion and oxidation state (V<sup>5+</sup>) of vanadium species key parameters.<sup>1013,1035</sup> Especially, V-supported on activated carbon,<sup>1036,1037</sup> Al<sub>2</sub>O<sub>3</sub>,<sup>1038,1039</sup> MgO,<sup>1035,1040,1041</sup> at 530-600°C and 0.1MPa allowed reaching high catalytic performance, while the addition of suitable promoters such as Cr, La or Mg showed to promote the activity.<sup>1042</sup> A recent DFT study revealed that ethylbenzene dehydrogenation takes place on the vanadyl oxygen O(1) site of V<sub>2</sub>O<sub>5</sub>(001) surface with the H<sub>2</sub>O formation to H<sub>2</sub> elimination with abstraction of O vacancy of the V<sub>2</sub>O<sub>5</sub>(001) surface.

Nevertheless, because of the high activation energy (3.16eV), CO<sub>2</sub> is not able to properly restore the oxygen vacancy leading to progressive catalyst deactivation.<sup>1043</sup> As the support is key to improve catalyst stability, highly dispersed V supported Al-MCM-41 (V/Al-MCM-41) catalysts were prepared.<sup>1044</sup> The catalytic study for EB ODH showed an increase in catalytic activity with V loading increase up to 6wt% owing to high coverage and dispersion of low polymeric VO<sub>x</sub> species, and further decrease due to V<sub>2</sub>O<sub>5</sub> crystallites formation. UV-Raman spectroscopy for the different samples showed bands at 341 and 914 cm<sup>-1</sup> assigned to the bending mode of the V–O–V bond and the symmetric O–V–O stretching of polymeric vanadia species, the band at 1018 cm<sup>-1</sup> was assigned to the symmetric stretching mode of the V=O bond of the isolated tetrahedral VO<sub>4</sub> species anchored on AlMCM-41, while the band at 996 cm<sup>-1</sup> indicated the formation of V<sub>2</sub>O<sub>5</sub> and increased with V content (Figure 107). Moreover, Al-MCM-41 support showed to improve VO<sub>x</sub> species dispersion in comparison to Si-MCM-41 support and stabilization of V<sup>5+</sup> active species owing to stronger interaction metal-support. The catalyst deactivation was mainly attributed to the reduction of V<sup>5+</sup> into V<sup>3+</sup>, while the coke deposition did not alter catalyst stability. High ST selectivity was reached at 550°C along 20h TOS, with good 58-48% EB conversion (Table 14, Entries 1-2).



**Figure 107.** UV-Raman spectra of VO<sub>x</sub>/Al-MCM-41 samples with different vanadium loading (wt%) (a) 2, (b) 4, (c) 6, (d) 6 and (e) 8. Reprinted with permission from ref.<sup>1044</sup>. Copyright 2019, John Wiley & Sons, Ltd.

Years ago a study of catalytic behavior of VO<sub>x</sub>/Al-MCM-41 revealed similar tendency.<sup>1045</sup> 1.0 mmol/g V loading was determined optimum to the formation of isolated and monolayer polymeric VO<sub>x</sub> species over AlMCM-41. Therefore, 50% ST yield and 97% ST selectivity were reached at 550°C (Table 14, Entry 3). Previously, the high catalytic activity of VO<sub>x</sub>/Si-MCM-41 with 1.5 mmol/g V optimum loading was described,<sup>1046</sup> and similar conclusions were reported. The dispersion and the nature of VO<sub>x</sub> species depended on the V loading. Moreover, two reaction pathways for ethylbenzene dehydrogenation were displayed: direct oxidative

dehydrogenation of EB with CO<sub>2</sub> (40%) and combination of simple dehydrogenation of EB with RWGS. 70% ST yield and 98% ST were obtained at 550°C (Table 14, Entry 4). Interesting catalytic activity of VO<sub>x</sub>/MCM-41 was reported, however low catalytic stability was reached, and no catalyst regeneration and recycling study was performed.

Bimetallic La<sub>2</sub>O<sub>3</sub>-V<sub>2</sub>O<sub>5</sub>/MCM-41 catalysts with different V and 10wt% La content were prepared by impregnation and tested for EB ODH.<sup>1047</sup> The benefits of the addition of a second metal over the V dispersion was shown while the nature of VO<sub>x</sub> species varied with V loading, and the polyvanadate formation occurred for high V content (20wt%). Moreover, the V loading affects the surface acidity. The NH<sub>3</sub>-TPD spectra revealed the presence of VO<sub>4</sub><sup>3-</sup> acid sites in 15V/MCM-41 sample that affects the activity of the catalyst and induces EB and ST cracking. For V loading below 15%, uniform La<sub>2</sub>O<sub>3</sub> and V<sub>2</sub>O<sub>5</sub> dispersion was reached. The key role of La<sub>2</sub>O<sub>3</sub> to effectively lower coke deposition owing to CO<sub>2</sub> adsorption and stabilization into La<sub>2</sub>O<sub>2</sub>CO<sub>3</sub> has been fully described. Moreover, the addition of La<sub>2</sub>O<sub>3</sub> allowed improving the rate of VO<sub>3</sub><sup>2-</sup> oxidation due to the presence of oxygen lattice that can be ensured by CO<sub>2</sub> adsorption and dissociation via La<sub>2</sub>O<sub>2</sub>CO<sub>3</sub>. Then, an enhancement of EB conversion over 10La15V/MCM-41 was observed in comparison to 15V/MCM-41. At 600 °C, high catalytic performance was obtained over 10wt%La-15wt%V/MCM-41 and attributed to the high specific surface area, the large pore volume and optimized La/V ratio. Thus, EB 86.5% conversion and 91% ST selectivity after 4h TOS were achieved and 75% EB conversion was maintained after 12h TOS (Table 14, Entries 5-6). Nevertheless, carbon deposition induced catalyst deactivation. The same group published a similar work reporting the catalytic performance of bimetallic LaVO<sub>x</sub>/SBA-15 samples with different V content showing the importance of the nature of VO<sub>x</sub> species and dispersion controlled by V loading.<sup>1048</sup> The addition of La allowed preventing the carbon deposition and improving catalytic stability. The synergetism between La and V enhanced the catalytic performance of V-catalysts which was maximized over 10wt%La<sub>2</sub>O<sub>3</sub>-15wt%V<sub>2</sub>O<sub>5</sub>/SBA-15 sample owing to the presence of VO<sub>4</sub><sup>3-</sup> active species, achieving 74% ST yield, at 600°C (Table 14, Entries 7-8). The catalyst was regenerated under air calcination at 550°C. Promising catalytic behavior for EB ODH was reported, nevertheless, studies of long-term stability and regeneration of the catalysts are required to evaluate their potential.

Even if the catalytic behavior of Cr-based catalysts for alkane ODH have been widely explored, few examples were reported in the literature using micro- and mesoporous ordered silicates as support for EB ODH. One study investigated the catalytic performance of Cr/MCM-41 catalysts prepared by direct hydrothermal synthesis for EB ODH. The catalytic data showed an increase of the catalytic activity with Cr loading until 1.7wt%.<sup>1021</sup> Specifically, Cr(VI)O<sub>4</sub> in tetrahedral coordination was determined as active monochromate species and reduced to Cr(III)O<sub>6</sub> in



octahedral coordination as inactive polychromate species inducing to the catalyst deactivation. A regeneration study under oxygen allowed recovering the catalytic activity. Mechanistic insights revealed that CO co-formation with ST and H<sub>2</sub> disappearance confirmed that RWGS took place over Cr-MCM-41. It was concluded that ST was produced following two pathways, direct ODH of EB with CO<sub>2</sub> and simple dehydrogenation of EB combined with RWGS. High 70% ST yield and 98% ST were obtained at 550°C (Table 14, Entry 9).

b) Bimetallic OMS-based catalysts for EB ODH

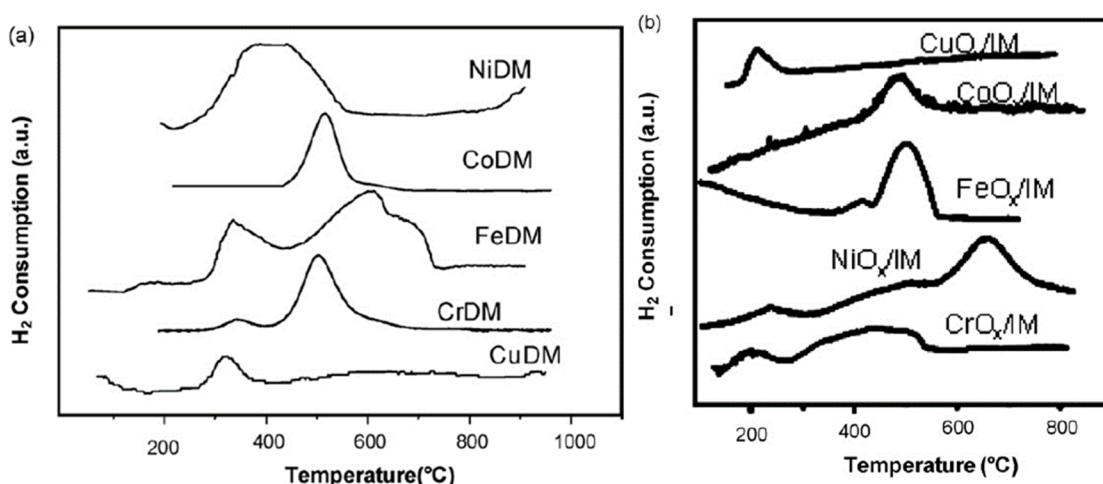
The catalytic performance of bimetallic CoFe<sub>2</sub>O<sub>4</sub>/MCM-41 catalysts prepared by impregnation and compared with Fe<sub>2</sub>O<sub>3</sub>/MCM-41 was recently reported.<sup>1049</sup> The characterization data (XRD, Raman, Mössbauer and XPS) revealed the structural properties and environment of Fe and Co, and the formation of partially inverted Co ferrite where Co<sup>2+</sup> and Fe<sup>3+</sup> occupy both octahedral and tetrahedral positions. The catalytic data demonstrated the superior selectivity and stability of CoFe<sub>2</sub>O<sub>4</sub> phase respect to Fe<sub>2</sub>O<sub>3</sub> owing to high thermal stability of the structure. Mechanistic insights indicated that EB adsorption occurred preferentially over Fe<sup>3+</sup> sites than Co<sup>2+</sup> and preferentially dehydrogenation took place on the octahedral sites in comparison to the tetrahedral sites. 30% ST yield and 99% ST selectivity were maintained at 550°C along 5h TOS (Table 14, Entries 10-11). Low catalytic performance was reached and insufficient data were provided to estimate a production.

The use of CeO<sub>2</sub>-ZrO<sub>2</sub> mixed oxides as catalysts and catalyst supports found many applications owing to their excellent redox properties and oxygen storage capacity as it is discussed in this review.<sup>1050-1052</sup> Therefore, for alkane ODH, the catalytic activity of CeO<sub>2</sub>-ZrO<sub>2</sub> mixed oxides have been widely explored and it was shown that their catalytic performance depended on textural and physicochemical properties being the main drawback the structure stability at high temperature. Therefore, a strategy constitutes in the dispersion and stabilization of CeO<sub>2</sub>-ZrO<sub>2</sub> mixed oxides over a high area support. Following these leads, the catalytic performance of CeO<sub>2</sub>/ZrO<sub>2</sub> pure oxides, mixed oxides and supported mixed oxides on SBA-15 prepared by precipitation, co-precipitation and precipitation-deposition methods was explored.<sup>1053</sup> The characterization data showed that BET surface area of the supported catalyst was lower than original SBA-15 and decreasing with increasing loading due to pore blockage. XRD patterns displayed that SBA-15 structure was mostly maintained with a slight structural ordering decline, whereas no XRD reflections were determined for the supported CeO<sub>2</sub>-ZrO<sub>2</sub> phase suggesting that no crystalline phase of the mixed oxide was formed. The catalytic results revealed an enhancement of catalytic activity due to synergetic effect between Zr and Ce respect to individual bulk oxide but no specific characterization data (H<sub>2</sub>-TPR, CO<sub>2</sub>-TPD, Raman) were

studied. CeO<sub>2</sub>-ZrO<sub>2</sub>/SBA-15 exhibited good and stable catalytic activity, showing the potential of SBA-15 as support, being 65% EB conversion and 93% ST selectivity maintained along 10h TOS, at 650°C (Table 14, Entries 12-14).

c) Effect of preparation method of OMS-based catalysts for EB ODH

It is well known that the preparation method can strongly affect the metal structure and dispersion that in turn influences the catalytic activity and selectivity. Accordingly, M/MCM-41 (M= Co, Cu, Cr, Fe or Ni) following impregnation (IM) and isomorphous substitution (DM) methods were prepared.<sup>1054</sup> Depending on preparation procedure, cationic (Cu<sup>2+</sup>, Co<sup>2+</sup>, and Cr<sup>4+</sup>/Cr<sup>3+</sup>) or metal oxide species were detected in the MCM-41 structure or dispersed on the MCM-41 surface, respectively. H<sub>2</sub>-TPR analysis showed that isomorphically substituted samples were difficult to reduce, excepted Ni- and Fe-containing catalysts, whereas impregnated (MeOx) catalysts possessed easier reducible species (Figure 108). Consequently, the isomorphically substituted catalysts exhibited superior catalytic performance than impregnated series, according to the following activity order: Ni(DM)/MCM-41 > Fe(DM)/MCM-41 > Cr(DM)/MCM-41 > Co(DM)/MCM-41 > Cu(DM)/MCM-41, with modest 52% ST selectivity achieved over Ni(DM)/MCM-41 and maximum 93 and 95% ST selectivity reached over Fe(DM)/MCM-41 and Cr(DM)/MCM-41, respectively, at 550°C (Table 14, Entries 15-17). Moreover, Ni<sup>2+</sup> and Fe<sup>3+</sup> MCM-41 framework, as well as NiO<sub>x</sub> and Fe<sub>2</sub>O<sub>3</sub> extra-framework species were continuously oxidized by CO<sub>2</sub> ensuring the regeneration and availability active sites for EB dehydrogenation. CO<sub>2</sub> plays a vital role in preserving the lattice oxygen on the catalyst surface. Study of deactivation revealed that coke nature influenced the catalytic stability, and polyaromatics formation over Ni<sup>0</sup> active sites was responsible of the catalyst deactivation.



**Figure 108.** H<sub>2</sub>-TPR profiles of isomorphically substituted samples (DM (a)) and impregnated samples (MeOx (b)). Reprinted with permission from ref.<sup>1054</sup>. Copyright 2009, Elsevier B.V. All rights reserved.

### 7.2.2. Conclusion

The use of CO<sub>2</sub> as soft oxidant offers several advantages to ensure and enhance the catalytic activity due to its ability to activate ODH directly promoting EB ODH or by combination of alkane dehydrogenation and RWGS, and thus favouring thermodynamics. The catalytic results showed that high ST selectivity could be reached at good conversion level with OMS based catalysts (V/ and Cr/ MCM-41, La-V/ MCMC-41 and SBA-15) (Figures 109-110). Nevertheless, catalysts lifetime was insufficiently studied to improve the stability and regeneration opportunities. More efforts should be spent to study catalysts robustness and reactor configuration to achieve and maintain high EB yield and selectivity offering SBA-15 support great potential. Despite their better thermal stability and robustness, zeolites because of smaller pore size may present some limitation to efficiently and homogeneously disperse metallic oxide, with high amount of active species and metal loading. Hence, future study should focus on the benefits of hierarchical zeolite application due to its meso- and macroscale secondary porosity, together with microporous primary structure, two-dimensional zeolite nanosheets and core-shell materials to improve the accessibility to the active center and mass transfer. In addition, OMS owing to their large pore structure offer great opportunities to prepare catalysts with high metallic phase dispersion and sintering stability owing to the confinement effect of the mesopores and strong interaction metal/support, combined with thermal stability.

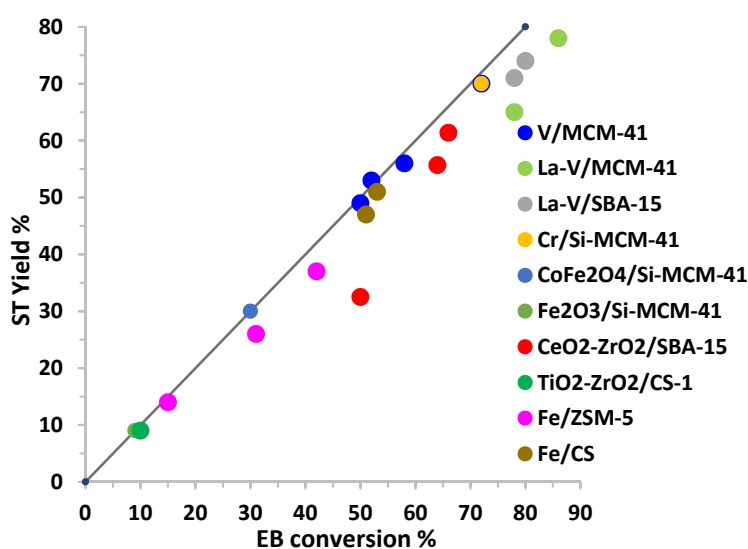
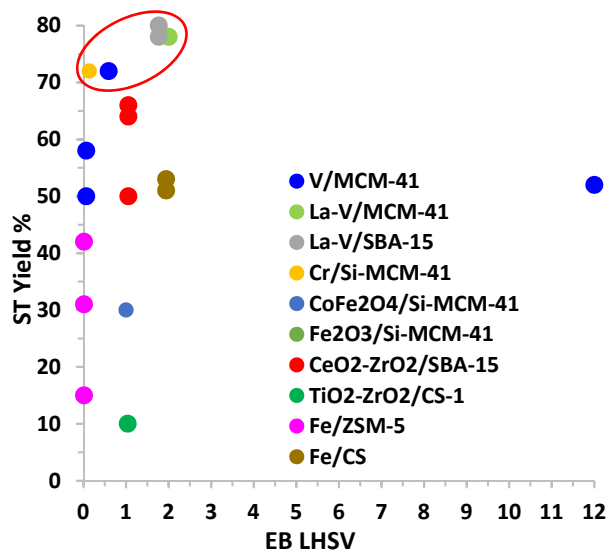


Figure 109. ST yield versus EB conversion in the presence of the different catalysts discussed in this review.



**Figure 110.** ST yield versus EB LHSV in the presence of the different catalysts discussed in this review. The ovoid highlights the best catalytic performance: ST high yield versus EB LHSV.

**Table 14.** Summary of the catalytic performance of the different reviewed catalysts for ethylbenzene ODH.

Entry	Catalysts	Conditions	LHSV <sub>EB</sub> h <sup>-1</sup>	χ <sub>EB</sub> %	ST Yield%	ST Sel.%	Year	Ref
<b>Ordered mesoporous silicates</b>								
<b>● V-based catalyst</b>								
1	6V/Al-MCM-41	0.3g <sub>cat</sub> , CO <sub>2</sub> :EB=15, EB=0.2mLh <sup>-1</sup> , 550°C, 20h	0.666	58-48	56-47	98	2020	1044
2	6V/Si-MCM-41			50-30	49-29	98		
3	5V/Al-MCM-41	0.3g <sub>cat</sub> , CO <sub>2</sub> :EB=20, W/F <sub>EB</sub> =8.8g <sub>cat</sub> h <sup>-1</sup> mol <sup>-1</sup> , 550°C	12	52	53	97	2010	1045
4	5V/Si-MCM-41	0.3g <sub>cat</sub> , CO <sub>2</sub> :EB=20, W/F <sub>EB</sub> =180g <sub>cat</sub> h <sup>-1</sup> mol <sup>-1</sup> , 550°C,	0.59	72	70	98	2009	1046
5	10La15V/MCM-41	0.3g <sub>cat</sub> , EB=2.8mmolh <sup>-1</sup> , CO <sub>2</sub> (14.3 mLmin <sup>-1</sup> ),	0.99	86	78	91	2008	1047
6	10La20V/MCM-41	CO <sub>2</sub> :EB=10, WHSV=1h <sup>-1</sup> 600°C, 5h		78	65	84		
7	10La15V/SBA-15	0.3g <sub>cat</sub> , EB=5mmolh <sup>-1</sup> , CO <sub>2</sub> (15 mLmin <sup>-1</sup> ),	1.769	80(2h)/71(8h)	74(2h)/68(8h)	90-94	2007	1048
8	10La20V/SBA-15	CO <sub>2</sub> :EB=10, 600°C		78(2h)/65(8h)	71(2h)/62(8h)	90-94		
<b>● Cr-based catalyst</b>								
9	Cr/Si-MCM-41 Si/Cr=50	0.15g <sub>cat</sub> , EB=0.6mLmin <sup>-1</sup> , GHSV=6800mLg <sup>-1</sup> h <sup>-1</sup> , CO <sub>2</sub> (30 mLmin <sup>-1</sup> ), Ar (10 mLmin <sup>-1</sup> ), 550°C, 0.5h	0.137	72	70	98	2005	1021
<b>● Fe-based catalyst</b>								
10	CoFe <sub>2</sub> O <sub>4</sub> /Si-MCM-41	0.06g <sub>cat</sub> , CO <sub>2</sub> :EB=30, CO <sub>2</sub> +N <sub>2</sub> (30 mLmin <sup>-1</sup> ),	-	30	30	99	2019	1049
11	Fe <sub>2</sub> O <sub>3</sub> /Si-MCM-41	550°C, 5h		9-5	9-5	99		
<b>● CeO<sub>2</sub>-ZrO<sub>2</sub>-based catalyst</b>								
12	CeO <sub>2</sub> -ZrO <sub>2</sub> /SBA-15 25CeO <sub>2</sub> -25ZrO <sub>2</sub>	600°C, 1g <sub>cat</sub> , EB=9.8mmolh <sup>-1</sup> , CO <sub>2</sub> :EB=5.1, W/F=16.73ghmol <sup>-1</sup> ,	1.054	~50(1h)		~65(1h)	2007	1053
13	CeO <sub>2</sub> -ZrO <sub>2</sub> /SBA-15	650°C		~66-63(10h)		~93(10h)		
14	CeO <sub>2</sub> -ZrO <sub>2</sub> /SBA-15	650°C, without CO <sub>2</sub>		~64-60(10h)		~87-82(10h)		
<b>● Preparation method</b>								
15	Fe(DM)/Si-MCM-41	0.1g <sub>cat</sub> , CO <sub>2</sub> :EB=30, 550°C, 3h		Activity, 10 <sup>3</sup> mmolg <sup>-1</sup> h <sup>-1</sup> : 42.6		95	2010	1054
16	Cr(DM)/Si-MCM-41			27.3		93		
17	Ni(DM)/Si-MCM-41			66.2		52		
<b>Zeolite</b>								
18	TiO <sub>2</sub> -ZrO <sub>2</sub> /CS-1	600°C	1.04	10		90	2009	1000
19		650°C		30		70-75		
		1g <sub>cat</sub> , EB=9.8mmolh <sup>-1</sup> , CO <sub>2</sub> :EB= N <sub>2</sub> :EB =5.1, W/F=16.73ghmol <sup>-1</sup>						
20	1.5Fe/ZSM-5	600°C, 0.03g <sub>cat</sub> , CO <sub>2</sub> :EB=80, CO <sub>2</sub> :H <sub>2</sub> =30,	0.012	31	26	84	2002	1002
21	5Fe/ZSM-5	LHSV=1h <sup>-1</sup>		42	37	89		1004
22	5Fe <sub>2</sub> O <sub>3</sub> /ZSM-5			15	14	96		
23	KCS <sub>BW</sub>	2g <sub>cat</sub> , 600°C, CO <sub>2</sub> (30 mLmin <sup>-1</sup> ), EB =36.64	1.94	58.5	56	96	2017	1033
24	5Fe <sub>2</sub> O <sub>3</sub> /KCS	mmol/h <sup>-1</sup>		51	47	92		
25	10Fe <sub>2</sub> O <sub>3</sub> /NCS			53	51	96		

\* Metal content is given in wt%. χ=conversion

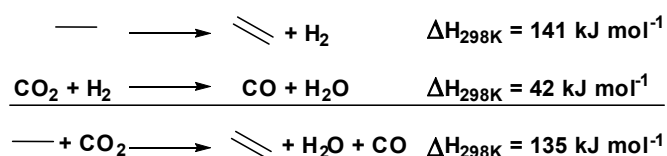
### 7.3. Ethylene production by ethane ODH

#### 7.3.1. Introduction

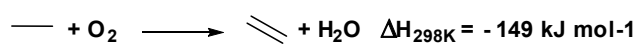
Ethylene is a major chemical building block of worldwide production. Moreover, it is also the largest olefin of the markets, derived from petroleum, and used as feedstock for the commercial production of intermediates and polymers such as ethylene oxide, ethylene dichloride, ethyl benzene, polyethylene, etc. The ethylene global production amounted to 191.5 Mt in 2019, is expected to increase up to 283 Mt in 2024. Ethylene is mainly produced by steam cracking of hydrocarbons like natural gas and naphtha at high temperature, with strong drawbacks such as high energy consumption, rapid coke formation and CO<sub>2</sub> emissions.<sup>1055–1057</sup> Thus different alternative processes for ethylene production have been explored such as ethanol dehydration based on biomass and sustainable feedstock or the oxidative dehydrogenation (ODH) of ethane.<sup>1058,1059</sup> In the last decade, the ODH of alkanes strengthened since offers several advantages from kinetics and environmental standpoints.<sup>1060</sup> Dehydrogenation is an endothermic process that in presence of oxygen becomes exothermic, since produced H<sub>2</sub> is removed by oxidation into water and the equilibrium shifted (Scheme 71). However, the flammability of ethane, exothermicity of the reaction, over-oxidation of ethylene, the hazardous use of pure oxygen and probable hotspots formation hampered the industrial implementation. Therefore, the use of CO<sub>2</sub> as mild oxidant constitutes an alternative to produce ethylene and consumes anthropogenic CO<sub>2</sub> and lengthens catalyst life minimizing coke deposition. Nevertheless, the lack of efficient and robust catalysts delayed the industrial application being the industry requirement an ethylene productivity > 1g<sub>C<sub>2</sub>H<sub>4</sub></sub>g<sub>cat</sub><sup>-1</sup>h<sup>-1</sup>, at temperature as low as possible.<sup>1059,1061</sup>

#### Ethane oxidative dehydrogenation

##### \* CO<sub>2</sub> as mild oxidant (Ethane dehydrogenation+RWGS)



##### \* O<sub>2</sub> as oxidant



Scheme 71. Thermodynamics of ODH of ethane with CO<sub>2</sub> as soft oxidant.

#### 7.3.2. Zeolites based catalysts for ethane ODH

##### a) Cr/zeolite-based catalysts for ethane ODH

Years ago, the catalytic activity of different transition metal oxides (Cr, V, Ga) supported on protonic zeolites prepared by impregnation was explored.<sup>1062,1063</sup> The surface acidity of zeolite play a crucial in chemical transformation, and for the ethane ODH the following activity order was obtained: Cr/H-ZSM-

5(Si/Al=850) > Cr/H-ZSM-5(Si/Al=95) > Cr/H-ZSM-5(Si/Al=45) > Cr/H-ZSM-5(Si/Al=15). These results showed the impact of Si/Al ratio and acid properties over the nature of Cr active species. The initial rate of ethylene formation was 1.6 times higher over Cr/H-ZSM-5(Si/Al=850) than over Cr/SiO<sub>2</sub> while Cr/H-ZSM-5 catalysts, with lower Si/Al ratio, exhibited low activity. On the other hand, Ga and V /ZSM-5(Si/Al=850) showed low activity for ethane ODH. TPR-spectra showed the presence of reduction peak at high temperature (~450°C) assigned to high oxidation state Cr species (Cr(VI)) with a key role in dehydrogenation activity. The authors also claimed the CO<sub>2</sub> importance in the re-oxidation of Cr<sup>3+</sup> species into Cr<sup>6+</sup> active species and in the removing coke from the catalytic surface, thus prolonging the catalyst life. At 650°C, the maximum rate of formation of ethylene was 0.516 mmol<sub>cat</sub><sup>-1</sup>min<sup>-1</sup> with 28% and 90% ethylene yield and selectivity (Table 15, Entry 45). More recently, a series of submicron Cr/ZSM-5-supported samples were prepared by impregnation of ZSM-5 with submicron size and their catalytic and textural properties were explored.<sup>1064</sup> XPS study allowed analyzing the two oxidation states of Cr species, and the deconvolution of the Cr<sub>2p2/3</sub> spectra enabled obtaining two bands at 576.5 and 579.5 eV, assigned to Cr<sup>3+</sup> and Cr<sup>6+</sup>, respectively, and determining a decreasing Cr<sup>6+</sup>/Cr<sup>3+</sup> ratio when Si/Al increased and Na content decreased. These results showed the importance of zeolite framework composition and sodium presence on the nature of chromium species. The catalyst stability increased with Si/Al ratio while Na samples exhibited superior catalytic performance than protonic one. It has been widely described that the nature of chromium oxide is crucial and that crystalline Cr<sub>2</sub>O<sub>3</sub> exhibit low activity while oligomeric chromium species are more active than isolated ones. Therefore the difference in activity for Cr/NaZSM-5 and Cr/HZSM-5 was attributed to the presence of dispersed Cr(VI) species in the form of polymeric chromates and monochromates in Cr/NaZSM-5 and to the presence of crystalline Cr<sub>2</sub>O<sub>3</sub> in Cr/HZSM-5, determined by laser Raman spectroscopy. An optimum in Cr close to 3wt% was found. The best catalytic performance was achieved over 3wt%Cr/NaZSM-5(Si/Al=160), at 650°C, with initial 65% ethane conversion and 49% ethylene yield and good catalytic stability with practically constant 46% ethylene yield over 50h TOS (Table 15, Entries 46-48). A recent work reported an attempt of CO<sub>2</sub> capture and utilization for ethane ODH in two stages, by combining in a fixed-bed reactor a physically mixed adsorbent and catalyst, composed by a double K-Ca salt and a Cr-impregnated H-ZSM-5 zeolite.<sup>988</sup> CO<sub>2</sub> adsorption study revealed that K-Ca exhibited the highest CO<sub>2</sub> uptake (5.2 mmol/g) while characterization-activity results of Cr/H-ZSM-5 samples revealed an optimum 10 wt% Cr loading, with highest TOF number and lowest Cr surface density. The combined capture utilization process consisted first of the CO<sub>2</sub> adsorption at 600°C, with 10 % CO<sub>2</sub>/Ar, followed by ethane ODH reaction at 700°C with 5 % C<sub>2</sub>H<sub>6</sub>/Ar. With GHSV= 5000 mL/g h, (K-Ca)/(Cr10/HZSM-5) ratio of 1, 25 % ethane conversion of 25 %, 88 % and 22 % ethylene selectivity and yield and 14 % CO<sub>2</sub>

conversion were achieved. Nevertheless, catalytic stability and adsorption studies revealed a constant deactivation of the catalyst and decrease of CO<sub>2</sub> adsorption capacity due to adsorbents particles sintering and reduction of Cr active species (Cr<sup>6+</sup>) (Table 15, Entry 50).

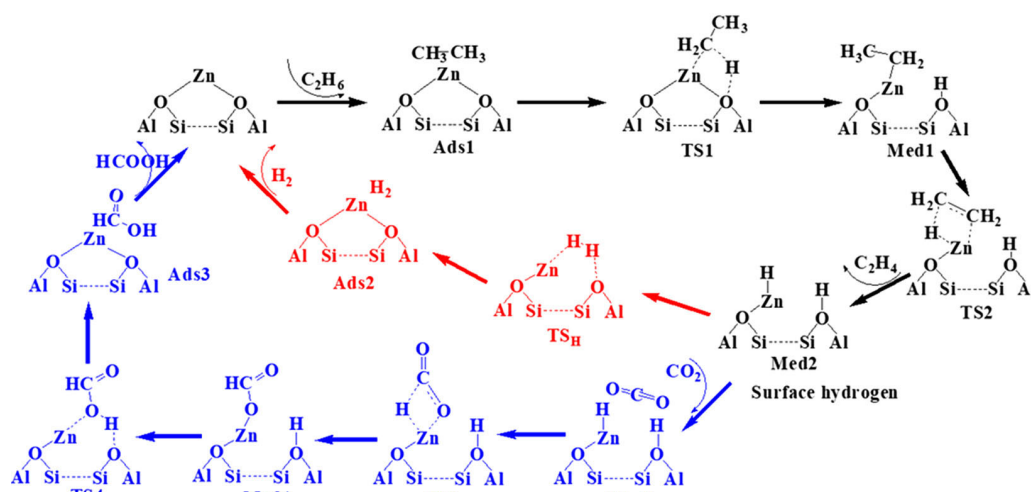
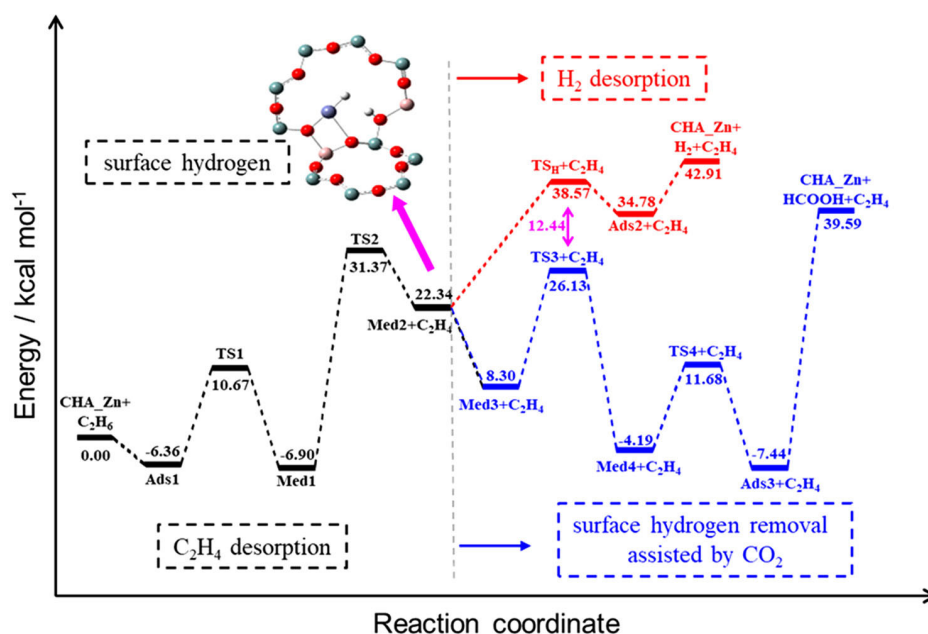
Recently, a series of 5wt%Cr/clinoptilolite samples were prepared by impregnation. Therefore, the benefits of post-synthesis treatment with NH<sub>4</sub>NO<sub>3</sub> and/or HNO<sub>3</sub> over the textural and catalytic properties of Cr-Clinoptilolite samples were explored. Different treatments were applied to natural clinoptilolite zeolite (CLT-R) with NH<sub>4</sub>NO<sub>3</sub> (CLT-A), with (CLT-A) and with NH<sub>4</sub>NO<sub>3</sub>+HNO<sub>3</sub> (CLT-IA).<sup>1065</sup> The catalytic and characterization data revealed that clinoptilolite treatments constituted an efficient and attractive strategy to provide Cr-supported clinoptilolite catalysts with higher surface area and lower particles size owing to cation exchange and dealumination, leading to higher dispersion and smaller particle size of Cr. Moreover, a decrease in surface acidity was observed due to dealumination and resulted favourable to ethylene desorption, and promoting ethylene selectivity. Therefore, the benefits of acid treatment coupled with NH<sub>4</sub>NO<sub>3</sub> treatment were shown and, at 700°C, the better catalytic results were obtained over 5wt%Cr/CLT-IA with 39% ethylene yield and 99% ethylene selectivity, over 5h TOS (Table 15, Entries 50-53).

#### b) Zn/zeolite-based catalysts for ethane ODH

The catalytic behavior of highly dispersed Zn-based SSZ-13 (NaS50) zeolite with different Zn content was explored for ethane ODH.<sup>1066</sup> The catalytic data revealed that conversion was correlated with Zn loading, indicating that Zn constituted the single active site of the catalyst. The catalytic activity of different structure Zn-based zeolites was compared and the superior 2.9wt%Zn/NaS50 catalytic performance was stood out. The following activity order was established, NaS50 > NaZSM-5 > MCM-22 > NaY, interestingly opposite with size of pore diameter order SSZ-13 (0.38 Å) < ZSM-5 and MCM-22 (0.55 Å) < Y(0.78 Å), indicating that zeolites with a small pore opening favoured CO<sub>2</sub> diffusion and adsorption. Then, DFT and operando studies were performed to determine the role of CO<sub>2</sub> in the dehydrogenation of C<sub>2</sub>H<sub>6</sub> over Zn catalysts, considering two type of active sites based on EXAFS data, [Zn–O–Zn]<sup>2+</sup> and Zn<sup>2+</sup>, corresponding to zinc oxide and zinc ion located on SSZ-13 zeolite. The proposed C<sub>2</sub>H<sub>6</sub> dehydrogenation mechanism involves two parts that are the C<sub>2</sub>H<sub>6</sub> activation and C<sub>2</sub>H<sub>4</sub> desorption, and hydrogen desorption. Thus, C<sub>2</sub>H<sub>6</sub> dehydrogenation involves the first C-H cleavage leading to the formation of Brønsted acid zinc hydroxyl group (ZnOH) while the second C-H bond cleavage leads to the formation of Zn-H. Therefore the elimination of hydrogen was envisioned by H<sub>2</sub> desorption, the most energy demanding step over both of considered active sites, or by CO<sub>2</sub> addition on the Zn-H moiety to form Zn-COOH with further formic acid desorption that constitutes a lower energy demanding step (Figure 111). However, operando dual-beam Fourier transform infrared spectrometry



results revealed that ethane ODH mechanism is similar regardless of the presence of CO<sub>2</sub> or not, although stretching vibration in the region 2385-2296 cm<sup>-1</sup> typical of HCOO<sup>-</sup> was recorded in the presence of CO<sub>2</sub>, supporting the DFT calculations and the formation of formic acid to remove hydrogen. A catalytic stability test, over 200 min, revealed good and stable 0.9wt% Zn/Na50 catalytic performance, with 30% ethane conversion and 95-98% ethylene selectivity, while 2.9wt%Zn/Na50 suffered deactivation due to carbon deposition (Table 15, Entries 54-55).



**Figure 111.** Energy profiles for ethane ODH on Zn<sup>2+</sup>, without and with CO<sub>2</sub> as a soft oxidant. Reprinted with permission from ref.<sup>1066</sup>. Copyright 2021, American Chemical Society.

### 7.3.1. OMS-based catalysts for ethane ODH

#### a) Cr/OMS-based catalysts for ethane ODH

Even though several catalytic system based on transition metal oxide were explored, silica-supported chromia revealed to be the more suitable ethane ODH catalyst with CO<sub>2</sub>, with up to 56% ethane

conversion and 93% ethylene selectivity at 650°C.<sup>1067</sup> Nevertheless, the catalytic performance remained insufficient for commercial application,<sup>1068</sup> and the chromium dispersion and stability represent the bottleneck to maximize the catalytic activity and life.<sup>1069–1071</sup> Chromium oxide based materials constitute promising catalysts for ethane ODH and the chromium species nature and dispersion are of paramount importance. Cr<sup>6+</sup> was determined as the most active species, and optimum and uniform dispersion as monolayer coverage allows avoiding the formation of polymeric species, which are less active and selective. Therefore, the use of OMS and zeolites as support, owing to their surface area, thermal stability and versatility in framework composition, offer great opportunities to reach maximum chromia dispersion and stabilization to the design and development of efficient and robust ODH catalysts. The impact of preparation method over the metal dispersion and particle size has been widely reported since in turn affects the catalytic properties of the prepared catalyst. Accordingly, the importance of the sequence addition of chromium and silica precursors over the textural and catalytic properties of Cr/MCM-41 materials with different Cr-loading was explored, indicating Cr-TEOS or TEOS-Cr the addition order of the precursors.<sup>1072</sup> TEM results revealed that TEOS-Cr addition order provided mesoporous silica with very small nanoparticles size while SEM study indicated higher CrO<sub>x</sub> species dispersion with maximum Cr<sup>6+</sup>/Cr<sup>3+</sup> ratio obtained for 8wt%Cr/MCM-41-Cr-TEOS sample. In concordance with characterization data, the best catalytic performance was achieved over 8wt%Cr/MCM-41-Cr-TEOS sample with 58% ethane conversion and 53% ethylene yield at 700°C (Table 15, Entries 1-7). Previously, a study of catalytic performance of Cr/MCM-41 catalysts with different Cr content, prepared by impregnation method, revealed that optimum 8wt% chromium content allowed reaching higher chromium species dispersion with monolayer coverage on MCM-41, smallest particle size and high surface area and optimum redox properties.<sup>1073</sup> Similar results were reached and 56% ethane conversion and 94% ethylene selectivity were obtained over 8wt%Cr/MCM-41, at 700°C (Table 15, Entries 8-11). Earlier the catalytic activity of Cr/MCM-41 for ethane ODH was reported.<sup>1074,1075</sup> Characterization study determined the partial framework insertion of Cr into MCM-41 and Cr dispersion on support MCM-41 surface, while Cr<sup>6+</sup> and Cr<sup>3+</sup> were determined as the catalytic active site. The ethane ODH involving the reduction of Cr<sup>6+</sup> sites by ethane dehydrogenation and the reoxidation of Cr<sup>3+</sup> by surface oxygen species issued from CO<sub>2</sub> dissociation or by CO<sub>2</sub>. The best catalytic performance was achieved over 5wt%Cr/MCM-41 catalyst with 43% ethane conversion and 87% ethylene selectivity at 700°C (Table 15, Entries 12-14).

The benefits of sulfate modification of silica support have been reported for the preparation of active ODH Cr-based catalysts.<sup>1067</sup> The surface acidity has been reported as key parameter to activate alkane and strongly influenced the catalytic performance of ODH catalysts, and the sulfatation showed to

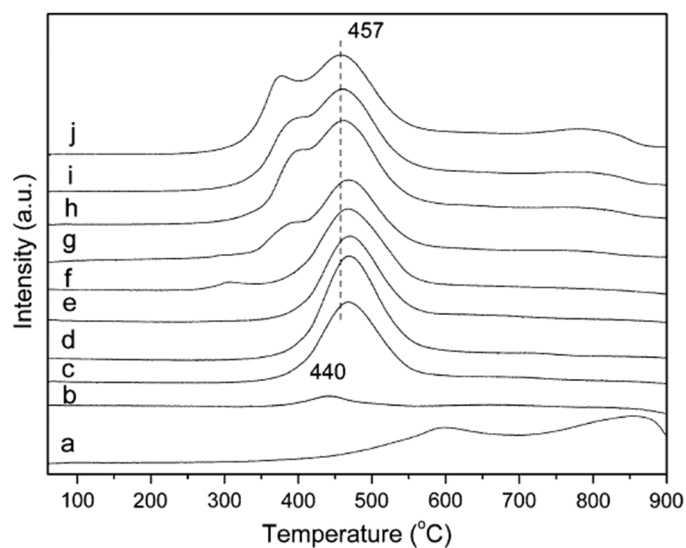
enhance the catalytic activity of Cr/SiO<sub>2</sub> catalyst but inducing a slight decrease in ethylene selectivity. Accordingly, a chromium sulfate modified SBA-15 material with 6% sulfate and 5% Cr (5wt%Cr/S-SBA-15) was prepared by impregnation.<sup>1076</sup> TEM images indicated that sulfation induced a higher and homogeneous dispersion of Cr species in monolayer and with smaller particle size, while XPS and Raman spectra revealed an increase of Cr<sup>6+</sup>/Cr<sup>3+</sup> ratio after sulfate modification which drastically influenced the catalytic activity. The TPR profile showed a shift of the reduction peak towards higher temperature, attributed to stronger interaction between Cr species and SBA-15, leading to higher dispersion. Consequently, the catalytic performance was higher over 5wt%Cr/S-SBA-15 in terms of conversion and selectivity but remained lower than 5wt%Cr/SiO<sub>2</sub> where 56% ethane conversion and 93% ethylene selectivity were achieved at 650°C.<sup>1067</sup> At 650°C, 61% ethane conversion and 82% ethylene selectivity were reached over 5wt%Cr/S-SBA-15, while 45% ethane conversion and 77% ethylene selectivity were reached over 5wt%Cr/SBA-15 (Table 15, Entries 15-17). A study of catalytic stability revealed good stability over 16h TOS with loss of 12 points of ethylene yield.

*i) Bimetallic OMS based-catalysts for ethane ODH*

In the recent decades, and as it was mentioned many times in this review, the preparation of bimetallic and multi-metallic catalysts received much attention to uniformly and highly disperse metallic active phase by establishing strong interactions metal/metal and metal/support due to electronic effects, improving metal stability against physical migration, and to enhance the catalytic activity. Following these leads, recently the synergetic effect of the addition of a second metal oxide (Co, Ce, Zn, Nb, V, and Mo) to Cr-MCM-41 sample, over the textural, physicochemical and catalytic properties, was investigated.<sup>1077</sup> Accordingly MCM-41-supported bimetallic oxides containing Ce, Co, and Zn were prepared following one-pot synthesis, while samples containing Mo, V and Nb were prepared following a two steps synthesis (hydrothermal+impregnation). The mesoporous structure of MCM-41 and high BET surface area were maintained after the incorporation of both metal oxides. H<sub>2</sub>-TPR profiles showed different reduction peaks than Cr-monometallic sample attributed to interaction metal/metal, and revealed an increase in the Cr<sup>6+</sup> concentration for 4wt%Cr-4wt%Ce/MCM41 while higher temperature reduction peaks were registered for 4wt%Cr-4wt%Mo/MCM41 and 4wt%Cr-4wt%V/MCM-41 which could imply a worse reducibility of chromium. The catalytic activity of Cr-based catalysts is related to the amount of Cr<sup>6+</sup> species and the characterization study indicated that incorporation of Ce or Co improved the reducibility of Cr<sup>6+</sup> owing to the redox properties of CeO<sub>2</sub> and Co<sub>3</sub>O<sub>4</sub>. Therefore, the catalytic activity could be correlated with amount of redox sites and dispersion of the metallic phase, and Cr-Ce/MCM-41 and Cr-Co/MCM-41 samples exhibited the higher catalytic activity while Cr-V/MCM-41 and Cr-Mo/MCM-41 displayed lower activity and selectivity to ethylene, and the highest

ethylene selectivity and lower activity were reached over Cr-Zn/MCM-41 and Cr-Nb/MCM-41 (Table 15, Entries 18-23). The highest catalytic performance was reached over 4wt%Cr-4wt%Ce/MCM-41 with 37.9% ethane conversion and 35.1% ethylene yield. In addition to medium catalytic results, the catalyst showed constant deactivation over 8h TOS. The same group studied the impact of the addition of different TiO<sub>2</sub> loading over the catalytic and textural properties of 8wt%Cr-Ti/MCM-41 samples.<sup>1078</sup> MCM-41 samples were firstly modified with TiO<sub>2</sub> addition prior to Cr loading. The synergetic effect between both metal allowed improving Cr dispersion, and Cr<sup>6+</sup> concentration and enhancing metal-support interaction. TPR profiles registered two reduction peaks corresponding to the reduction of Cr<sup>6+</sup> species dispersed on the  $\alpha$ -Cr<sub>2</sub>O<sub>3</sub> surfaces at low temperature, and Cr<sup>6+</sup> species interacting with the framework of siliceous support at higher temperature. An optimum in Cr<sup>6+</sup> amount interacting with the support was observed for 1.9 wt%Ti, which exhibits high Cr dispersion, predicting optimized catalytic activity and stability. Therefore, the best catalytic results were reached over 8wt%Cr-1.9wt%Ti/MCM41 with 52% ethane conversion and 48% ethylene yield at 700°C (Table 15, Entries 24-27). Nevertheless, a constant decrease of the catalytic performance was observed over 8h TOS (Table 15, Entry 28). In the same way, a series Cr/Ce-MCM-41 samples was prepared by first adding CeO<sub>2</sub> and then Cr loading.<sup>1079</sup> Moreover, the benefits of utilization of plasma energy for the catalyst preparation (Cr/Ce-MCM-41(Si/Ce=25)-p) over their morphological and catalytic features were observed. TEM analysis evidenced the alteration of MCM-41 structure when an excess of ceria was used leading to structure deterioration (Si/Ce>25). The incorporation of ceria allowed enhancing the dispersion of Cr while the plasma treatment further improved the distribution and uniformity of nanoparticles in the narrow range of 7.4-22 nm. The authors claimed that the synergistic effect of ceria incorporation and plasma treatment strengthened the interaction between Cr/MCM-41 preventing the migration of Cr particles and controlling the size of Cr ensemble. Therefore, the best catalytic performance was achieved over Cr/Ce-MCM-41(Si/Ce=25)-p with 62% ethylene yield and 64% ethane conversion, at 700°C (Table 15, Entries 29-32). A comparison of catalytic reported data is difficult because of the difference and lack of details of reaction conditions. Therefore, it is not possible to determine ethylene productivity. Despite, Cr/Ce-MCM-41(Si/Ce=25)-p exhibited high catalytic performance and stability and offers great potential for the development of an industrial catalyst. A similar study was reported using SBA-15 as support in which Cr-Ce/SBA-15 samples with different Ce loading were prepared by co-impregnation.<sup>1069</sup> The characterization study showed the improvement of Cr dispersion due to the incorporation of Ce with the preservation of the SBA-15 structure. The TPR profiles registered three reduction peaks, at 457°C corresponding to the reduction of Cr<sup>6+</sup> species, and at 378 and 799°C to reduction of surface ceria oxide (Figure 112). The comparison of H<sub>2</sub>-TPR profiles of 5Cr-Ce/SBA-15 and

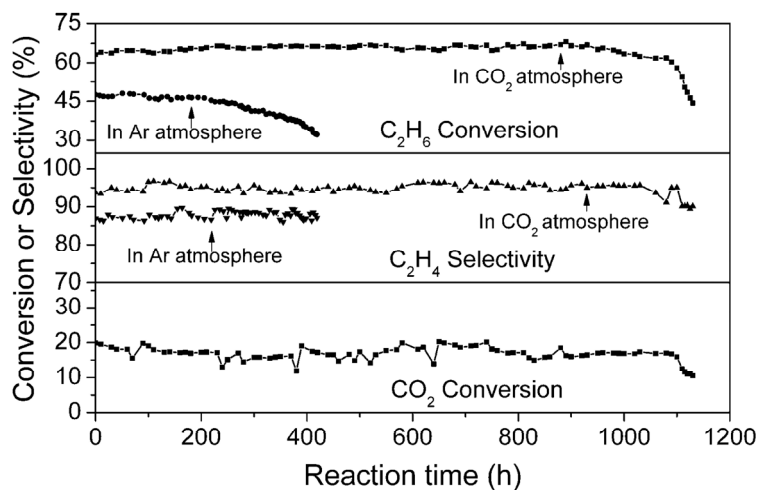
10Ce/SBA-15 samples indicated that Ce reduction temperature decreased due to interaction Ce/Cr that modify the redox ability of Ce species. The H<sub>2</sub> consumption increased with Ce loading to reach a maximum for 5Cr-10Ce/SBA-15 sample corresponding to maximum amount of Cr<sup>6+</sup> species. Therefore, the catalytic activity varied with Ce content, was optimum for 10wt%, and good catalytic performance was displayed over 5wt%Cr–10wt%Ce/SBA-15, with 55% ethane conversion and 96% ethylene selectivity at 700°C (Table 15, Entries 33-36). The catalyst showed constant catalytic activity deactivation with TOS, registering a conversion decrease from 55% until 45% and could not be fully recovered after thermal treatment under CO<sub>2</sub>.



**Figure 112.** H<sub>2</sub>-TPR profiles of SBA-15 samples: (a) 10Ce/SBA-15; (b) bulk Cr<sub>2</sub>O<sub>3</sub>; (c) 2.5Cr/SBA-15; (d) 5Cr/SBA-15; (e) 7.5Cr/SBA-15; (f) 10Cr/SBA-15; (g) 5Cr-5Ce/SBA-15; (h) 5Cr-7.5Ce/SBA-15; (i) 5Cr-10Ce/SBA-15; (j) 5Cr-15Ce/SBA-15. Reprinted with permission from ref.<sup>1069</sup>. Copyright 2008, Springer Science Business Media, LLC.

Years ago, the study and development of monolithic catalyst revealed several advantages of these composites, such as low-pressure drop, high heat and mass transfer rates and minimum axial dispersion owing to their unified structure in a single block. To take advantages of monolithic catalyst features, monolithic Cr/SBA-15/Al<sub>2</sub>O<sub>3</sub>/FeCrAl catalysts were prepared using FeCrAl foils with honeycomb structure as support and SBA-15/Al<sub>2</sub>O<sub>3</sub> as washcoat.<sup>1080</sup> Then, different Cr contents catalysts were prepared by impregnation. H<sub>2</sub>-TPR profiles depict two Cr<sup>6+</sup> reduction peaks at 374-397°C and 510°C, corresponding to soluble Cr<sup>6+</sup> species (isolated chromates on the surface) and to the grafted Cr<sup>6+</sup> species on the silica surface, respectively. XPS spectra of Cr<sub>2p</sub> over fresh and used 5% Cr/SBA-15/Al<sub>2</sub>O<sub>3</sub>/FeCrAl monolithic catalysts showed the presence of two Cr species, Cr<sup>3+</sup> and Cr<sup>6+</sup>, with higher Cr<sup>6+</sup>/Cr<sup>3+</sup> ratio in the fresh catalyst than in the spent one. Catalytic data registered at 750°C showed that ethylene yield increased with Cr loading up to 5% and further decreased accordingly with Cr<sup>6+</sup>/Cr<sup>3+</sup> ratio and the nature of chromium species (Table 15, Entries 37-40). A stability test showed the high

catalytic stability of 5wt%Cr/SBA-15/Al<sub>2</sub>O<sub>3</sub>/FeCrAl over a period of 1100h TOS. Ethane conversion and ethylene selectivity remained practically constant along 1100h and around 66% and 95%, respectively (Figure 113). This work constitutes the best catalytic test reported for ethane ODH.

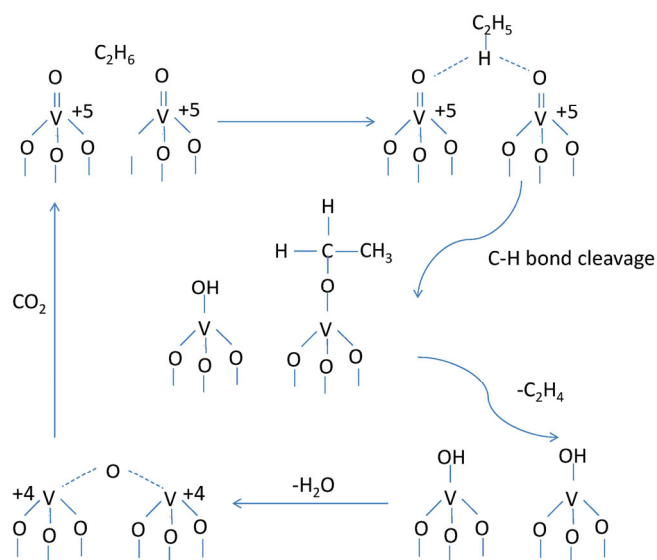


**Figure 113.** Catalytic performance of 5wt% Cr/SBA-15/Al<sub>2</sub>O<sub>3</sub>/FeCrAl catalyst for ethane ODH maintained over 1100h. Reprinted with permission from ref. <sup>1080</sup>. Copyright 2008, American Chemical Society.

#### b) V/OMS-based catalysts for ethane ODH

V-supported catalysts exhibited high activity and selectivity for ethane ODH,<sup>1081,1082</sup> and the high vanadium dispersion, loading and support play a key role in the nature of vanadium species and activity. The most active species are monomeric V<sup>5+</sup> while vanadate dimeric or oligomeric structures can coexist at higher V-loadings.<sup>1083</sup> The nature of the support through the establishment of strong interactions could influence the metal dispersion and stability. As well as, basic supports favour the formation of stable vanadium mixed oxides, while acid supports contribute to high dispersion of vanadium species avoiding the formation of polymeric species. Therefore, a recent study reported the influence of the introduction of different metal into MCM-41 framework on the nature of vanadium species, activity and stability of ODH catalysts.<sup>1084</sup> Thus a series of VO<sub>x</sub>/MCM-41, VO<sub>x</sub>/Mg-MCM-41, VO<sub>x</sub>/Mg-Al-MCM-41 and VO<sub>x</sub>/Mg-Zr-MCM-41 were prepared. The incorporation of different metal (Mg, Al, Zr) affected the catalytic activity, the structural and textural properties (crystallinity, particle size, dispersion) and acid/base properties. XRD patterns showed that the high surface area of MCM-41 enable high dispersion of vanadium and no peak of crystalline V<sub>2</sub>O<sub>5</sub> was registered. The incorporation of Mg and Zr into VO<sub>x</sub>/Mg-Zr-MCM-41 sample led to the formation of MgO and tetragonal phase of zirconia. Moreover, the framework substitution of larger diameter cation such as Zr<sup>4+</sup> and Mg<sup>2+</sup> by smaller Si<sup>4+</sup> induced modifications of bond length of M–O–Si and then led to the MCM-41 structure deformation. FESEM and EDX analysis revealed improved V dispersion on the VO<sub>x</sub>/Mg-Zr-MCM-41 sample attributed to the surface acidity due to framework zirconia. The surface acidity is

determinant for alkane activation, and greater the acidity, higher the ethane conversion. Thus the framework incorporation of Mg, Al and Zr produced different samples with different acid strengths and so different catalytic behaviors. Accordingly, from NH<sub>3</sub>-TPD, the following order of acidity was obtained: VO<sub>x</sub>/MCM-41 < VO<sub>x</sub>/Mg-MCM-41 < VO<sub>x</sub>/Mg-Al-MCM-41 < VO<sub>x</sub>/Mg-Zr-MCM-41. UV-Vis diffuse reflectance spectra allowed determining two types of vanadium oxo-species, one dimensional oligomeric and two-dimensional polymeric units in octahedral coordination. The best catalytic performance for ethane ODH was observed for the VO<sub>x</sub>/Mg-Zr-MCM-41, which contained only oligomeric tetrahedral vanadium species with higher dispersion and the higher amount of acid sites. Thus, at 700°C, 55% ethane conversion and 43% ethylene yield with a productivity of 0.48 g<sub>C<sub>2</sub>H<sub>4</sub></sub>g<sub>cat</sub><sup>-1</sup>h<sup>-1</sup> and good catalytic stability over 10h TOS were reached over VO<sub>x</sub>/Mg-Zr-MCM-41 (Table 15, Entries 41-44). Additionally, a mechanism based on catalytic, characterization studies and literature data was proposed following mars-van-krevelen mechanism (Figure 114).



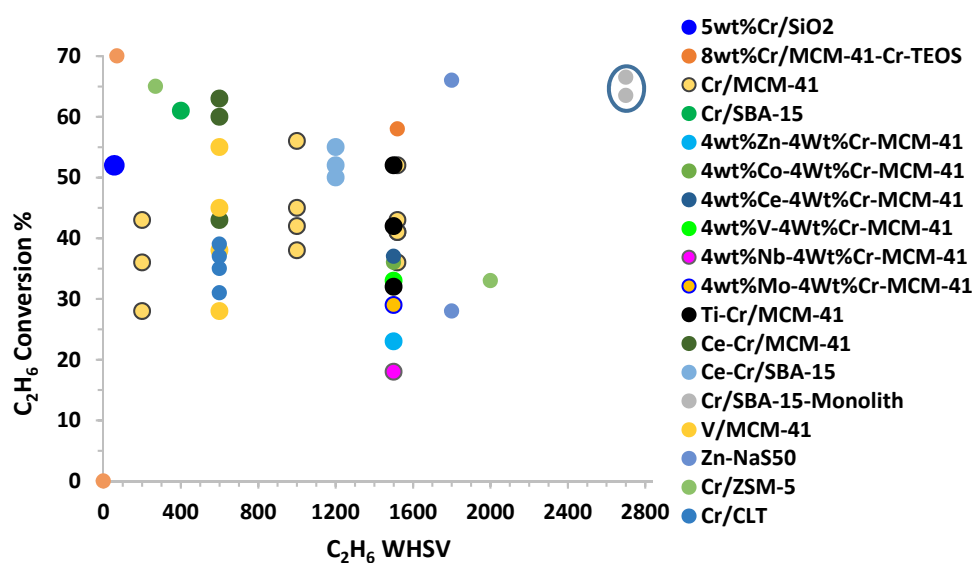
**Figure 114.** Proposed ethane ODH mechanism over Vanadium MCM-41-based catalysts. Reprinted with permission from ref. <sup>1084</sup>. Copyright 2017, Elsevier Inc. All rights reserved.

### 7.3.2. Conclusion

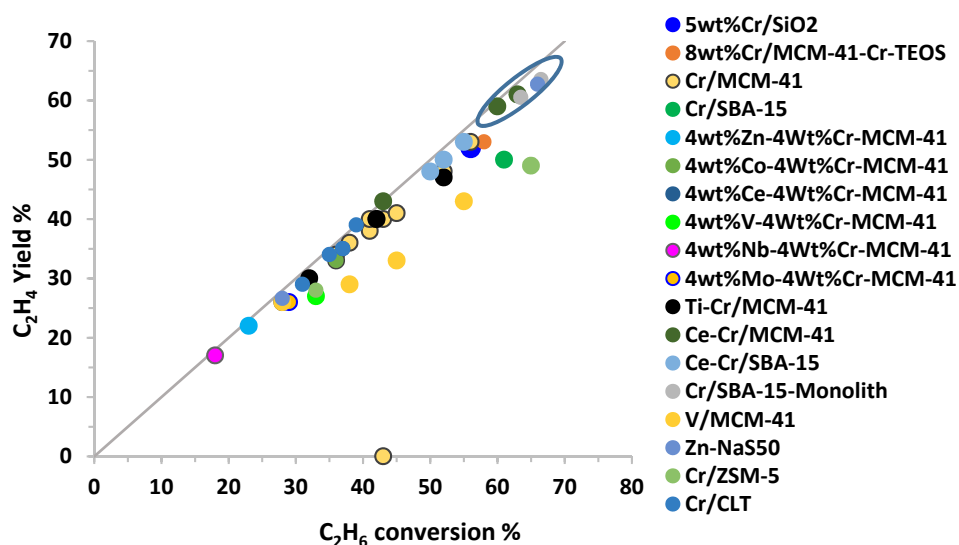
Most of the reported catalysts for ethane ODH are CrO<sub>x</sub>-based, implying severe limitations due to the carcinogenicity of chromium species (Cr<sup>6+</sup>) and severe control and measures in the catalyst preparation, use and elimination. Therefore, alternative should be deeply considered. Besides, the catalytic performance of 5wt%Cr/SBA-15/Al<sub>2</sub>O<sub>3</sub>/FeCrAl over 1100h reached goals of production and catalyst stability with good 63% ethylene yield, highlighting the potential of SBA-15 as support. Actually, the catalyst success will depend on catalysts and operation costs, catalysts stability and coke deposition besides the catalytic performances and features. The use of zeolite as support due to pore size feature is limited since high metal active content required to exhibited high catalytic activity owing

to the presence of large amount of active sites, and achieve high productivity, leads to decreased surface area and pores blockage. Therefore, the preparation of hierarchical zeolite-based ODH catalysts, due to their meso- and macroscale secondary porosity, together with the microporous primary structure and two-dimensional zeolite nanosheets based ODH catalysts, should allow the preparation of zeolitic catalysts with high content of metal species with improved catalytic activity and mass transfer.

In the Figures 115-116  $C_2H_6$  conversion and  $C_2H_4$  yield are plotted versus  $C_2H_6$  WHSV and conversion, respectively, highlighting the catalytic performance of 5wt%Cr/SBA-15/ $Al_2O_3$ /FeCrAl monolithic and Ce-Cr/MCM-41 catalysts.



**Figure 115.** Ethylene yield versus ethane conversion in the presence of the different catalysts discussed in this review. The ovoid highlights the best catalytic performance: high  $C_2H_6$  conversion versus  $C_2H_6$  WHSV.





**Figure 116.** Ethane conversion versus ethane WHSV in the presence of the different catalysts discussed in this review. The ovoid highlights the best catalytic performance: high C<sub>2</sub>H<sub>6</sub> yield versus high C<sub>2</sub>H<sub>6</sub> conversion.

**Table 15.** Summary of the catalytic performance of the different reviewed catalysts for ethane ODH.

Entry	Catalysts	Conditions	GHSV <sub>C<sub>2</sub>H<sub>6</sub></sub> mlg <sub>cat</sub> <sup>-1</sup> h <sup>-1</sup>	χ <sub>C<sub>2</sub>H<sub>6</sub></sub> %	Ethylene Yield%	Ethylene Sel. %	Year	Ref
<b>OMS based catalysts</b>								
<b>● Cr-based catalysts</b>								
<b><u>Monometallic</u></b>								
1	5wt%Cr/SiO <sub>2</sub>	1 g <sub>cat</sub> , 0.1 MPa, 700°C, 6 mlmin <sup>-1</sup> C <sub>2</sub> H <sub>6</sub> , 30 mlmin <sup>-1</sup> CO <sub>2</sub> , 24 mlmin <sup>-1</sup> N <sub>2</sub> , GHSV=3.6 Lg <sup>-1</sup> h <sup>-1</sup> , TOS=1h	360	56	52	93	1999	1067
2	8Cr/MCM-41-Cr-TEOS	0.3 g <sub>cat</sub> , 0.1 MPa, 7.5 mlmin <sup>-1</sup> C <sub>2</sub> H <sub>6</sub> , 37.5 mlmin <sup>-1</sup> CO <sub>2</sub> , and 30 mlmin <sup>-1</sup> N <sub>2</sub> , 700°C, GHSV=15 Lg <sup>-1</sup> h <sup>-1</sup> , TOS=1h	1500	58	53		2019	1072
3	8Cr/MCM-41-TEOS-Cr			43	40			
4	8Cr/MCM-41(impr.)			41	38			
5	5Cr/MCM-41-Cr-TEOS			36	34			
6	10Cr/MCM-41-Cr-TEOS	TOS=10h		52	48			
7	8Cr/MCM-41-Cr-TEOS			41	40			
8	2Cr/MCM-41	0.5 g <sub>cat</sub> , 0.1 MPa, 700°C, GHSV = 9000 h <sup>-1</sup> , C <sub>2</sub> H <sub>6</sub> :CO <sub>2</sub> :N <sub>2</sub> = 10:50:40,	900	38	36		2016	1073
9	5Cr/MCM-41			42	40			
10	8Cr/MCM-41			56	53			
11	11Cr/MCM-41			45	41			
12	3Cr/MCM-41	0.1 MPa, 700°C, GHSV=4000 h <sup>-1</sup> , 5 mlmin <sup>-1</sup> C <sub>2</sub> H <sub>6</sub> , 10 mlmin <sup>-1</sup> CO <sub>2</sub> , 85 mlmin <sup>-1</sup> Ar, TOS=20 min	200	36	33	90	2005	1074
13	5Cr/MCM-41			43	37.5	87		
14	8Cr/MCM-41			28	26	91		
15	5Cr/SBA-15	0.5 g <sub>cat</sub> , 9 mlmin <sup>-1</sup> C <sub>2</sub> H <sub>6</sub> , 54 mlmin <sup>-1</sup> CO <sub>2</sub> , 27 mlmin <sup>-1</sup> He, 0.1 MPa, 650°C, GHSV=10.8 Lg <sup>-1</sup> h <sup>-1</sup> , TOS=1h	1080	61 (1h)	50 (1h)	82 (1h)	2017	1076
16				56 (16h)	40 (16h)	71 (16h)		
17	5Cr/SBA-15			45 (1h)	36.5 (1h)	77 (1h)		
<b><u>Bimetallic</u></b>								
18	4Zn-4Cr-MCM-41	0.3 g <sub>cat</sub> , 0.1 MPa, 7.5 mlmin <sup>-1</sup> C <sub>2</sub> H <sub>6</sub> , 37.5 mlmin <sup>-1</sup> CO <sub>2</sub> , and 30 mlmin <sup>-1</sup> N <sub>2</sub> , 700°C, GHSV=15 Lg <sup>-1</sup> h <sup>-1</sup> , TOS=1h	1500	23	22		2020	1077
19	4Co-4Cr-MCM-41			36	33			
20	4Ce-4Cr-MCM-41			37	35			
21	4V-4Cr-MCM-41			33	27			
22	4Nb-4Cr-MCM-41			18	17			
23	4Mo-4Cr-MCM-41			29	26			
24	0Ti-8Cr-MCM-41	0.3 g <sub>cat</sub> , 0.1 MPa, 7.5 mlmin <sup>-1</sup> C <sub>2</sub> H <sub>6</sub> , 37.5 mlmin <sup>-1</sup> CO <sub>2</sub> , and 30 mlmin <sup>-1</sup> N <sub>2</sub> , 700°C, TOS=1h	1500	42	41		2019	1078
25	1.9Ti-8Cr-MCM-41			52	47			
26	3.75Ti-8Cr-MCM-41	TOS=8h		42	40			
27	11.5Ti-8Cr-MCM-41	GHSV=15 Lg <sup>-1</sup> h <sup>-1</sup> ,		32	30			
28	1.9Ti-8Cr-MCM-41			37	36			
29	Cr/MCM-41	0.5 g <sub>cat</sub> , 0.1 MPa, C <sub>2</sub> H <sub>6</sub> :CO <sub>2</sub> :N <sub>2</sub> =1:4:5, GHSV=6000h <sup>-1</sup> , 700°C, TOS=1h	600	41	40		2019	1079
30	7Cr/Ce-MCM-41(Si/Ce=50)			43	43			

31	7Cr/Ce-MCM-41(Si/Ce=25)			60	59			
32	7Cr/Ce-MCM-41(Si/Ce=25)-p			63	61			
33	5Cr/SBA-15	0.2 g <sub>cat</sub> , 0.1 MPa, GHSV=3.6 Lg <sup>-1</sup> h <sup>-1</sup> , V <sub>CO2</sub> or	900	46	44	95	2008	1069
34	5Cr-7.5Ce/SBA-15	Ar/V <sub>C2H6</sub> =3; 700°C, TOS=0.5h		50	48	96		
35	5Cr-10Ce/SBA-15			55	53	96		
36	5Cr-15Ce/SBA-15			52	50	95.5		
37	2.5Cr/SBA-15/Al <sub>2</sub> O <sub>3</sub> /FeCrAl	GHSV=5.4 Lg <sup>-1</sup> h <sup>-1</sup> , V <sub>CO2</sub> or Ar/V <sub>C2H6</sub> =2, 750°C,	1800	60	58	95	2008	1080
38	5Cr/SBA-15/Al <sub>2</sub> O <sub>3</sub> /FeCrAl	TOS=1h		66.5	63.5	95		
39	7.5Cr/SBA-15/Al <sub>2</sub> O <sub>3</sub> /FeCrAl			63.5	60.5	95		
40	5Cr/SBA-15/Al <sub>2</sub> O <sub>3</sub> /FeCrAl	TOS=1100h		~66	~63	~95		
<b>● V-based catalyst</b>								
41	5VO <sub>x</sub> /MCM-41	0.5 g <sub>cat</sub> , 0.1 MPa, C <sub>2</sub> H <sub>6</sub> :CO <sub>2</sub> :N <sub>2</sub> =1:5:4,	600	28	26		2018	1084
42	5VO <sub>x</sub> /Mg-MCM-41	GHSV=6000h <sup>-1</sup> , 700°C, TOS=1h		38	29			
43	5VO <sub>x</sub> /Mg-Al-MCM-41			45	33			
44	5VO <sub>x</sub> /Mg-Zr-MCM-41			55	43			
<b>Zeolite based catalysts</b>								
45	5Cr/H-ZSM-5(Si/Al=950)	0.3 g <sub>cat</sub> , C <sub>2</sub> H <sub>6</sub> = 10 mLmin <sup>-1</sup> , CO <sub>2</sub> =90 mLmin <sup>-1</sup> , 650°C, TOS=6h, GHSV=20 Lg <sup>-1</sup> h <sup>-1</sup> ,	2000	33	28	86	2002	1063
46	3Cr/NaZSM-5(Si/Al=160)	0.2 g <sub>cat</sub> , F <sub>T</sub> =30 mLmin <sup>-1</sup> ,	270	65 (0.16h)	49 (0.16h)	75 (0.16h)	2015	1064
47		C <sub>2</sub> H <sub>6</sub> :CO <sub>2</sub> :N <sub>2</sub> =3:15:82, 650°C, TOS=50h,		61 (6h)	48 (6h)	79 (6h)		
48		GHSV=9 Lg <sup>-1</sup> h <sup>-1</sup> ,		66-54	49-49	75-86		
49	(K-Ca)/(Cr10/HZSM-5)	10 % CO <sub>2</sub> /Ar (600 °C ), 5 % C <sub>2</sub> H <sub>6</sub> /Ar (700°C), GHSV=5 Lg <sup>-1</sup> h <sup>-1</sup>	250	25	22	88	2020	988
50	5Cr/CLT-R	0.5 g <sub>cat</sub> , F <sub>C2H6</sub> = 5 mLmin <sup>-1</sup> ,	600	31	29	97	2015	1065
51	5Cr/CLT-A	C <sub>2</sub> H <sub>6</sub> :CO <sub>2</sub> :N <sub>2</sub> =1:5:4, 700°C, TOS=5h,		37	35	98		
52	5Cr/CLT-I	GHSV=6 Lg <sup>-1</sup> h <sup>-1</sup> ,		35	34	98		
53	5Cr/CLT-IA			39	39	99		
54	0.9Zn/NaS50	0.1 MPa, CO <sub>2</sub> :C <sub>2</sub> H <sub>6</sub> =1, GHSV=3.6 Lh <sup>-1</sup> g <sub>cat</sub> <sup>-1</sup> ,	1800	28-26		95-98	2021	1066
55	2.9Zn/NaS50	650°C, TOS=3.3h		66-50		-		

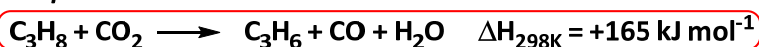
\* Metal content is given in wt%.  $\chi$ =conversion

### 7.3.1. Propylene production by propane ODH

### 7.3.2. Introduction

Propylene is a valuable platform molecule to the production of a large number of chemical commodities (propylene oxide, acrylic acid, acrylonitrile, isopropanol, cumene, butyraldehyde) and polymers. The propylene global production in 2020 was 108 Mt and is expected to reach 128 Mt by 2027, and the current industrial production is based on catalytic propane dehydrogenation.<sup>991,1085</sup> From thermodynamic standpoints (Scheme 72), propane ODH with CO<sub>2</sub> involves different competitive endothermic reactions and mainly propane dry reforming which thermodynamically less constrained than ethane and methane dry reforming.<sup>1086</sup> Other reaction such cracking, propylene and propane decomposition take place readily. On the other hand, since propane ODH is a reaction with volume increase due to process stoichiometry, the co-feeding of inert gas is favourable to propane conversion enhancement, decreasing propylene production. Therefore, the challenge lies in developing a selective catalyst to promote propane ODH and kinetically suppress propane dry reforming. RWGS favours the equilibrium shifting whereas reverse Boudouard reaction improves catalyst life. In addition, efficient separation method are required for CO<sub>2</sub> and CO separation.<sup>1087</sup>

#### Propane ODH



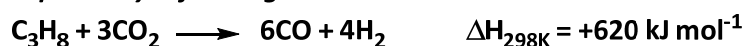
#### Propane dehydrogenation



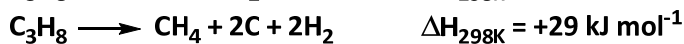
#### RWGS



#### Propane dry reforming



#### Propane decomposition



#### Propane cracking



#### Propylene decomposition



#### Reverse Boudouard reaction



**Scheme 72.** Thermodynamics of oxidative dehydrogenation of propane with CO<sub>2</sub> as soft oxidant and simultaneous processes.

R

Recent reviews deal with the oxidative dehydrogenation of propane with soft oxidants such as CO<sub>2</sub>, NO<sub>x</sub> and S-containing compounds using solid catalysts.<sup>993,1002,1087</sup> The extensive report

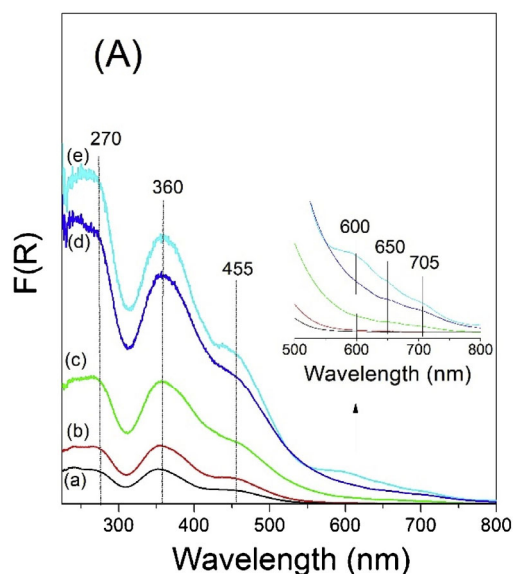
carefully analyzed and described the impact of metal oxide nature (redox ( $\text{CrO}_x$ ,  $\text{VO}_x$ ), non-redox ( $\text{Ga}_2\text{O}_3$ )), morphology and dispersion, support, addition of promoters and method preparation. For propane ODH with  $\text{CO}_2$ ,  $\text{CrO}_x$ -based catalysts revealed exhibiting higher propylene selectivity at higher propane conversion level than other metal oxide based catalysts playing key role redox cycles,  $\text{CrO}_x$  species nature and dispersion, and the textural and chemical properties of the support.<sup>1002</sup> The use of  $\text{CO}_2$  as soft oxidant presents some benefits as it allows completing redox cycles, shifting equilibrium due to  $\text{H}_2$  removal by RWGS, improving catalyst life by coke elimination through reverse Boudouard reaction and enhancing propylene selectivity due to competitive adsorption with  $\text{CO}_2$  favouring propylene desorption. Still efforts are required to elucidate reaction mechanism, improve the stability and regeneration of the catalysts, and to design efficient, robust and selective catalysts towards C-H bond rather than C-C bond activation, using metallic oxide-based catalysts free of Cr due to its carcinogenicity. The acid/base properties constitute a crucial parameter not only because affecting the active metallic phase dispersion but also because different reactants with different adsorption properties are involved. Indeed,  $\text{CO}_2$  adsorption and activation are favoured onto basic sites while propane and  $\text{H}_2$  preferably adsorb on acidic sites, while undesired reaction such as cracking, isomerization and oligomerization can take place. Thus a balance in acidity and basicity surface should be exist.

### 7.3.3. Zeolites-based catalysts for propane ODH

#### a) Effect of surface acidity over catalytic properties for propane ODH

Cr/ZSM-5 catalyst with high Si/Al ratio of 240 were firstly reported for propane dehydrogenation in 2011.<sup>1088</sup> The catalytic study displayed the effect of the ZSM-5 crystallite size on the catalytic activity. Hence, laser Raman spectroscopy allowed determining the nature of Cr species, and  $\text{Cr}^{\text{VI}}$  species (monochromates) were shown to be responsible of catalytic activity of Cr-supported catalysts in alkane oxidative dehydrogenation with  $\text{CO}_2$ . The best catalytic performance was reached over the 3wt%Cr/ZSM-5-S with 0.4  $\mu\text{m}$  crystal size than over 3wt%Cr/ZSM-5-L with 2  $\mu\text{m}$  crystal size due to the presence of higher amount of  $\text{Cr}^{\text{VI}}$  species. Good catalytic data were registered over 3wt%Cr/ZSM-5-S, with 48% propane conversion and 86% propylene selectivity, after 0.16 h TOS, at 550°C (Table 16, Entry 1). The surface acidity is a key parameter to selectively adsorb and active the reactants, and different strategies can be followed to modify the acidity of zeolite by dealumination using acid treatment or by steaming at high temperature. Accordingly, a serie of Cr/Si and Al-Beta samples were prepared with different Cr loading by impregnation using AlBeta sample with Si/Al=17 and dealuminated SiBeta with Si/Al=1000.<sup>1089,1090</sup> The catalytic behavior for propane ODH revealed the negative effect of the

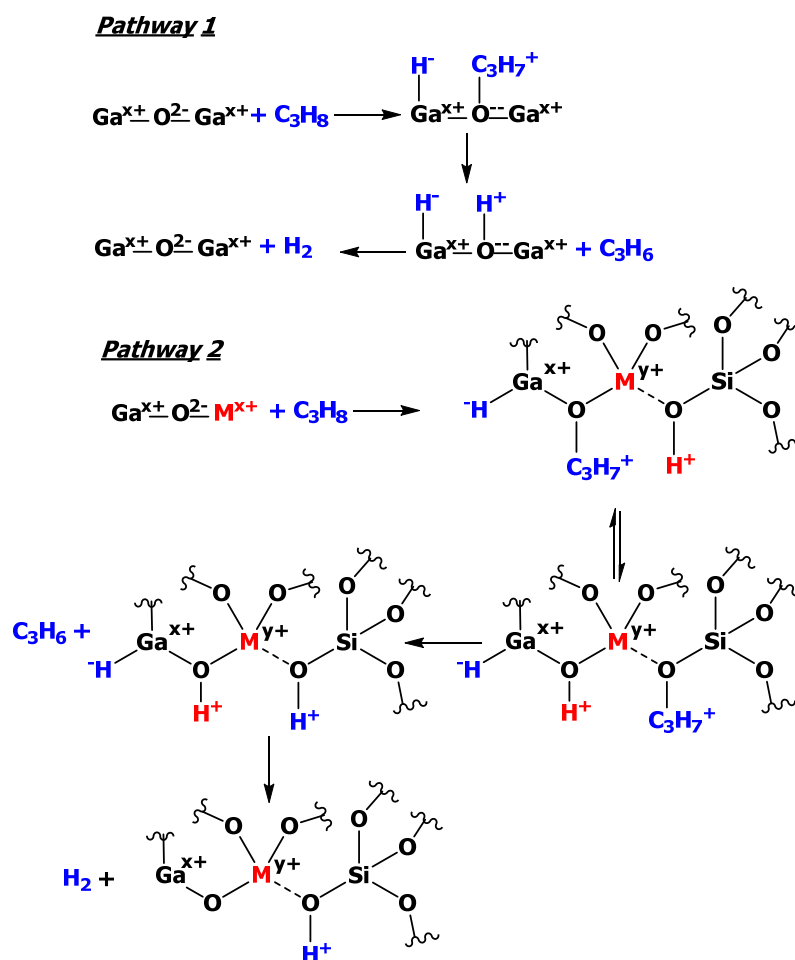
presence of Al over the catalytic activity of 2wt%Cr/AlBeta achieving low 4.5% propane conversion and 2% propylene yield, at 550°C, attributed to higher surface acidity. In contrast, good catalytic performance was registered for the dealuminated samples showing the benefit of dealumination over the catalytic properties. For the Cr/SiBeta catalysts series, an increase in the catalytic performance was noted with Cr content up to 2 wt% according to the number of Cr redox species and further decrease. Indeed, quantitative results of H<sub>2</sub>-TPR determined that in the H<sub>2</sub> volume consumption/Cr<sub>total content</sub> ratio existed a maximum, with a drastic decrease for higher Cr content in the range 2-7wt%, suggesting that Cr is mainly present as non redox Cr species in the form of Cr<sub>2</sub>O<sub>3</sub> amorphous and crystalline as it was supported by UV-V diffuse reflectance spectroscopy spectra illustrating two peaks at 270nm and 360nm assigned to charge transfer of Cr<sup>6+</sup>-O<sup>2-</sup> transition of monochromate species onto the support (Figure 117). Maximum 87% propylene selectivity and 25% propane conversion were maintained over 6h TOS at 450°C (Table 16, Entries 2-5).



**Figure 117.** UV-vis DRS spectra recorded at room temperature for Cr/BA samples: (a) 0.5CrSiBEA, (b) 1CrSiBEA, (c) 2CrSiBEA, (d) 5CrSiBEA and (e) 7CrSiBEA. Reprinted with permission from ref.<sup>1090</sup>. Copyright 2019, Elsevier Ltd. All rights reserved.

Another strategy to modify and weaken the acid properties of zeolite is the isomorphous substitution of Al by another metal such as boron. Therefore, Cr/silicalite-1 and Cr/H[B]MFI (incorporating Boron) were prepared and further treated by steaming (Cr/H[B]MFI-st).<sup>1091</sup> H<sub>2</sub>-TPR spectra revealed that no reduction peak of Cr<sup>6+</sup> into Cr<sup>3+</sup> was observed for Cr/silicalite-1 and Cr/H[B]MFI-st, while it was detected for Boron containing sample (Cr/H[B]MFI). The presence of boron allowed the formation of some Cr<sup>6+</sup> species readily reduced into Cr<sup>3+</sup> by H<sub>2</sub> and also by steaming treatment. Then, steaming treatment enabled the auto-reduction of Cr<sup>6+</sup> into Cr<sup>3+</sup> located near to boron to counterbalance the framework negative charge. The comparison of the catalytic performance revealed that Cr/H[B]MFI exhibited higher catalytic activity and stability

than Cr/silicalite-1. The propane conversion over Cr/H[B]MFI decreased rapidly from 50% until 20% in 2h while this was around 10% over Cr/silicalite-1. When the catalytic performance of Cr/H[B]MFI-st and Cr/H[B]MFI samples were compared along 70h TOS, a constant decrease of propane conversion from 30 to 7% was recorded over Cr/H[B]MFI along 60h TOS, while ~13% propane conversion remained stable over Cr/H[B]MFI-st. These results were attributed to the weakened Brønsted acidity because of steaming treatment and the differences in the nature of Cr species, the  $\text{Cr}^{3+}/\text{Cr}^{6+}$  ratio and the formation of polychromates (Table 16, Entries 6-8). Dealumination strategy by steaming of HZSM-5 zeolite to optimize acid properties of  $\text{Ga}_2\text{O}_3/\text{HZSM-5}$  was also used to improve the catalytic performance of  $\text{Ga}_2\text{O}_3/\text{HZSM-5}$  catalyst.<sup>1092</sup>  $\text{NH}_3$ -TPD study showed only one desorption peak with small area at 264°C attributed to low Al framework content for HZSM-5 zeolite, while after gallium oxide incorporation, a second peak at 465°C was recorded, indicating that some strong acid sites are formed. After steaming and dealumination, acidity was drastically weakened. The excess of loss acidity was attributed to the loss of interaction of  $\text{Ga}_2\text{O}_3$  with the support due to the absence of Al. Hence, the catalytic performance of  $\text{Ga}_2\text{O}_3/\text{HZSM-5}$  samples varied with Si/Al ratio, and propane conversion order was  $\text{Ga}_2\text{O}_3/\text{HZSM-5}(700) \gg \text{Ga}_2\text{O}_3/\text{HZSM-5}(650) > \text{Ga}_2\text{O}_3/\text{HZSM-5}(750) \sim \text{Ga}_2\text{O}_3/\text{HZSM-5}(600) > \text{Ga}_2\text{O}_3/\text{HZSM-5} \sim \text{Ga}_2\text{O}_3/\text{HZSM-5}(800) \sim \text{Ga}_2\text{O}_3/\text{silicalite}$ . Therefore, the catalytic performance was maximum over  $\text{Ga}_2\text{O}_3/\text{HZSM-5}(700)$ , 22% propene yield, and remained stable over 100h (Table 16, Entries 12-13). Catalyst stability increased with increasing Si/Al ratio because of coke deposition lowered. As previous published, the proposed mechanism for propane ODH over  $\text{Ga}_2\text{O}_3$  supported catalysts should follow heterolytic dissociation pathway, where the presence of Brønsted acid sites in zeolite should promote the dehydrogenation reaction (Figure 118).<sup>1093</sup> On the other hand the role of  $\text{CO}_2$  was explored, and a control of  $\text{CO}_2$  and CO concentration for propane ODH allowed determining that CO production was twice  $\text{CO}_2$  conversion, leading to assume that  $\text{CO}_2$  mainly participates in the Boudouard reaction and coke gasification.



**Figure 118.** Ethane ODH mechanism on gallium oxide supported catalysts adapted from ref.<sup>1092,1093</sup>

The introduction of phosphorous in the zeolite by impregnation constitutes another strategy to modify acid properties of zeolite because of the formation of weaker Brønsted acid sites in addition to the thermal stability improvement.<sup>1094–1097</sup> Thus, the same group prepared a series of Ga<sub>2</sub>O<sub>3</sub>/P-HZSM-5 samples with different P percentages (Ga<sub>2</sub>O<sub>3</sub>/P-HZSM-5(n)) and studied the catalytic performance for propane ODH.<sup>1098</sup> The catalytic results revealed that the phosphorus incorporation allowed improving the catalytic performance of the pristine Ga<sub>2</sub>O<sub>3</sub>/HZSM-5, and the best catalytic performance were achieved over Ga<sub>2</sub>O<sub>3</sub>/P-HZSM-5(1.5) with 22% propane conversion and 19% propylene yield after stabilization (Table 16, Entries 14-16). A constant catalytic performance decrease was observed over TOS to reach a steady state after 50h. The propene yield firstly increased with P loading, until 1.5% and further decreased. This trend was attributed to the decrease of the amount of strong acid sites that favour side reactions and to the increase of the amount of weak acid sites which should play a minor role in the propane ODH process.

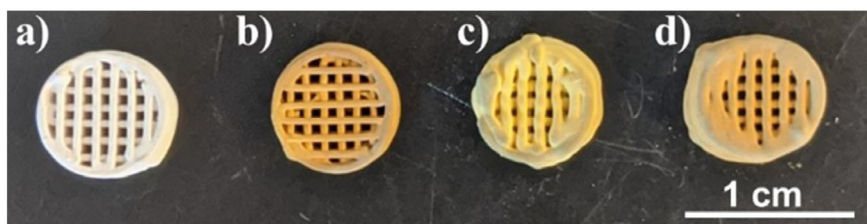
The influence of Si/Al molar ratio for ZnO/HZSM-5 samples prepared from different Si/Al ratio in the synthesis gel using NaAlO<sub>2</sub> as Al source, confirmed that high amount of acid sites



decreased the catalytic activity and stability due to side reactions.<sup>1099</sup> Therefore an increase in catalyst stability with increasing the Si/Al ratio was observed and ascribed to the decrease in surface acidity supported by NH<sub>3</sub>-TPD and FT-IR of pyridine adsorption spectra. The role of CO<sub>2</sub> was also studied varying CO<sub>2</sub> partial pressure, and confirming the benefits of the use of CO<sub>2</sub> to convert H<sub>2</sub> into water through RWGS reaction and so promoting propane ODH, also fomenting coke gasification, while higher partial pressure induced catalyst deactivation due to competitive adsorption of CO<sub>2</sub> and propane over the catalytic surface. Therefore, the best catalytic performance was achieved over ZnO/HZSM-5 with Si/Al ratio=160, with 41.5% propane conversion, 26% propylene yield and higher catalytic stability over 3h TOS (Table 16, Entries 9-11).

b) Effect of preparation method over the catalytic properties for propane ODH

3D-printing technology constitutes a new tool to prepare materials with tuned monolithic properties (surface area, channel size, chemical composition and loading) which is not possible by extrusion. 3D-printing has been successfully used to prepare adsorbents catalyst monoliths such as zeolites, aminosilicates, and MOFs.<sup>1100-1105</sup> Following these leads, a series of Ga, V, and Zr H-ZSM-5 monolithic catalysts with high metal oxide contents were prepared by 3D printing technology (Figure 119).<sup>1106</sup> Characterization of the textural properties revealed that homogeneous distribution of metal oxides was reached for all samples and based on the H<sub>2</sub>-TPR results, V<sup>3+</sup>, V<sup>4+</sup>, V<sup>5+</sup>, Ga<sup>2+</sup> and Zr<sup>4+</sup> species were formed, demonstrating the variety of peaks assigned to the different oxidation states of vanadium and thus, the redox properties of the prepared samples. The NH<sub>3</sub>-TPD profiles of 3D-printed catalyst monoliths revealed the presence of acid sites with different strengths accordingly to the presence of gallium oxide, vanadium oxide and also zirconium oxide while high-strength acid sites formation due to ZrV<sub>2</sub>O<sub>7</sub> superstructures were also detected. In summary, 15V-15Zr@ZSM-5 and 15Ga-15V@ZSM-5 had a higher amounts of strong acid sites, while 15V-15Zr@ZSM-5 and 15Ga-15Zr@ZSM-5 had weaker acid sites. 15Ga-15V-15Zr@ZSM-5 contained low-, medium-, and high- strength acid in agreement with the mixture of three metal oxides. The best catalytic performance was obtained over 15wt%V-15wt%Zr@ZSM-5 with ~38% propane conversion and 90% propylene selectivity remaining stable over 6 h TOS, at 550°C, although all of the monoliths tested exhibited good catalytic performance and stability (Table 16, Entries 17-20). These results demonstrated the applicability of 3D printing technology for preparing active propane ODH catalysts.



**Figure 119.** Photographs of (a) 15Ga-15Zr@ZSM-5, (b) 15Ga-15V@ZSM-5, (c) 15V-15Zr@ZSM-5, and (d) 10Ga-10V-10Zr@ZSM-5 monoliths. Reprinted with permission from ref.<sup>1106</sup>. Copyright 2020, Elsevier B.V. All rights reserved.

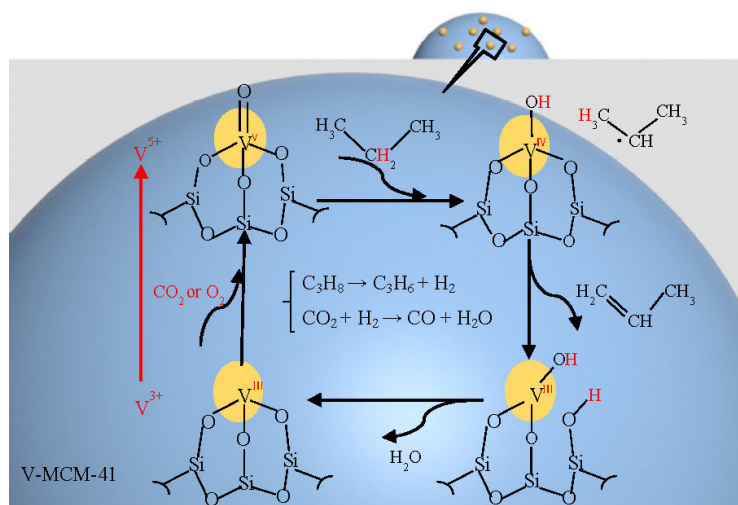
#### 7.3.4. OMS-based catalysts for propane ODH

The dispersion and stability of metal species is key and determine the catalytic activity and can be influenced by the metal/support interaction, acid/base and textural properties. Thus, for the design and development of efficient and robust propane ODH catalysts, ordered mesoporous materials such as SBA-15 and MCM-41 constitute great candidates to deposit metal oxides despite their lower thermal stability in comparison to zeolites.

##### a) V/OMS-based catalysts for propane ODH

As aforementioned, the preparation method and vanadia content allow controlling the nature of vanadia species while the carrier can play an important role. The surface  $\text{VO}_x$  active species are present in sub-monolayer coverage with surface areas close to  $300\text{m}^2\text{g}^{-1}$  and containing 8 V atoms/ $\text{nm}^2$  for various support, except for  $\text{SiO}_2$  because of lower interaction metal/support with 2.5 V atoms/ $\text{nm}^2$ .<sup>1107</sup> Recently, a series of V-MCM-41 catalysts were prepared by hydrothermal synthesis,<sup>1108</sup> and low amounts of V species were introduced into MCM-41 framework while conserving high specific surface area and ordered mesoporous structure. High dispersion of V active species (monomeric and dimeric) was achieved, however due to high vanadium content an increase in the number of acid sites, weak and strong were detected, as well as the formation of  $\text{V}_2\text{O}_5$  crystallites. Laser Raman spectroscopy allowed stating the formation of bulk  $\text{V}_2\text{O}_5$  at high V loading to which the decrease in catalytic activity for propane ODH was attributed. Owing to higher dispersion of  $\text{VO}_4^{3-}$ , 6.8wt%V-MCM-41 exhibited the best catalytic performance. An increase of  $\text{CO}_2/\text{C}_3\text{H}_8$  ratio, from 1:1 up to 5:1, allowed improving propane conversion from 35 to 45%, whereas propene selectivity did not suffered substantial change. Thus, maximum 45% propane conversion and 92% propylene selectivity were reached at  $600^\circ\text{C}$  with suitable  $\text{CO}_2/\text{C}_3\text{H}_8=4:1$  (Table 16, Entries 21-23). A reaction mechanism was proposed involving in a first step, the H abstraction by O of O=V group from propane secondary C atom, and in a second step, H abstraction occurs by the O of the V–O–Si bond, yielding two hydroxyl groups whose dehydration produces water and the formation of oxygen vacancy, being propene released. Along these two steps, vanadyl group is reduced from  $\text{V}^{\text{V}}$  into  $\text{V}^{\text{III}}$  and finally re-oxidized by  $\text{CO}_2$ , restoring V=O group and oxygen lattice (Figure 120). Good catalytic activity was reported but

over short 2h TOS. A study of catalyst recycling revealed that the regeneration of the catalyst over 4 cycles was possible owing to oxidative treatment, being the deactivation due to the reduction V active sites and coke deposition.

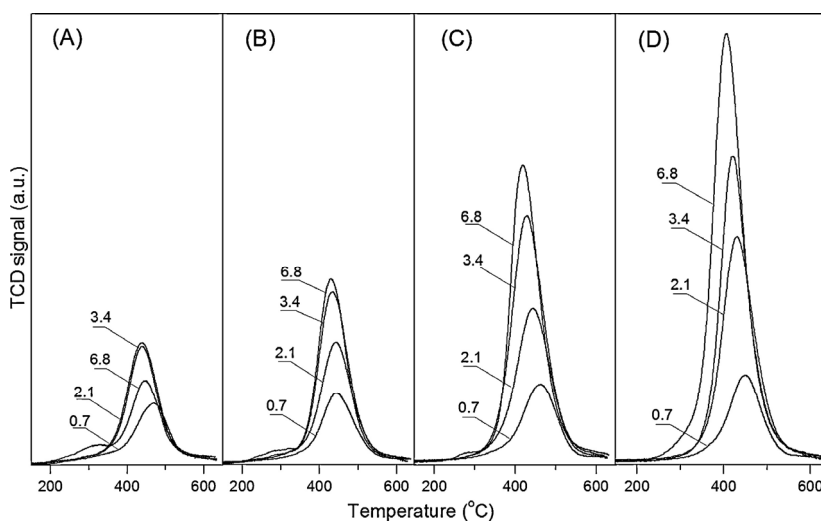


**Figure 120.** Reaction and regeneration cycle mechanism for the propane ODH over V-MCM-41 catalysts. Reprinted with permission from ref.<sup>1108</sup>. Copyright 2018, Dalian Institute of Chemical Physics, the Chinese Academy of Sciences. Published by Elsevier B.V. All rights reserved.

#### b) Cr/OMS-based catalysts for propane ODH

The catalytic activity and selectivity of supported chromia materials for the alkane dehydrogenation have been studied for many years, being key parameters the dispersion and formation of monochromates active species. Years ago, it was demonstrated that the MCM-41 ordered mesoporous structure and its high surface area allow high dispersion and amount of  $\text{Cr}^{6+}$  active species achieving similar catalytic performance than  $\text{Cr}/\text{SiO}_2$  for propane ODH (Table 15, Entries 24-25).<sup>1109</sup> Previously,  $\text{Cr}/\text{MCM-41}$  materials were successfully prepared by direct hydrothermal (DHT) and template-ion exchange (TIE) methods without destroying the mesoporous structure of MCM-41 for  $\text{Si}/\text{Cr}$  ratio  $> 25$ . Difference in chromium species were observed, and for samples prepared by DHT ( $\text{Cr}/\text{MCM-41}(\text{DHT})$ ), monochromate species were formed while for samples prepared by TIE method ( $\text{Cr}/\text{MCM-41}(\text{TIE})$ ), large amount of polychromate species were formed besides monochromate species.<sup>1110</sup> Nevertheless, both samples exhibited similar catalytic performance with 92% propylene oxide selectivity and 28% and 29% propane conversion over 3wt% $\text{Cr}/\text{MCM-41}(\text{DHT})$  and 3wt% $\text{Cr}/\text{MCM-41}(\text{TIE})$  catalysts, respectively, at 550°C (Table 16, Entries 26-27). However, no data of catalytic stability was done. Later, four series of Cr supported catalysts with different Cr content (0.7-13.7wt%) over MCM-41, amorphous silica and mesoporous silica with cubic (SBA-1) and hexagonal phase (SBA-15) were prepared by impregnation and tested for propane ODH.<sup>1111-1113</sup> Higher dispersion of chromium species was achieved over mesoporous supports owing to their high surface area,

implying a higher content of Cr<sup>6+</sup> for mesoporous materials. The nature of chromium species varied with Cr content, and Cr<sup>6+</sup> species directly anchored are mainly formed at low Cr content, whereas at higher content Cr<sub>2</sub>O<sub>3</sub> particles are produced. Despite, amount of Cr<sup>6+</sup> species depends on the support and specifically of surface area. For MCM-41 series, an optimum 6.8wt% Cr content was determined reaching 40% propane conversion and 88.5% propylene selectivity at 550°C (Table 16, Entries 28-31).<sup>1113</sup> Optimum Cr species dispersion was demonstrated as crucial parameter to promote propane ODH and depended on the presence of Cr<sup>6+</sup> species as precursors of Cr active species formed by a different redox cycle of Cr<sup>2+</sup>/Cr<sup>3+</sup> in contrast to mainly described redox cycle of Cr<sup>3+</sup>/Cr<sup>6+</sup>.



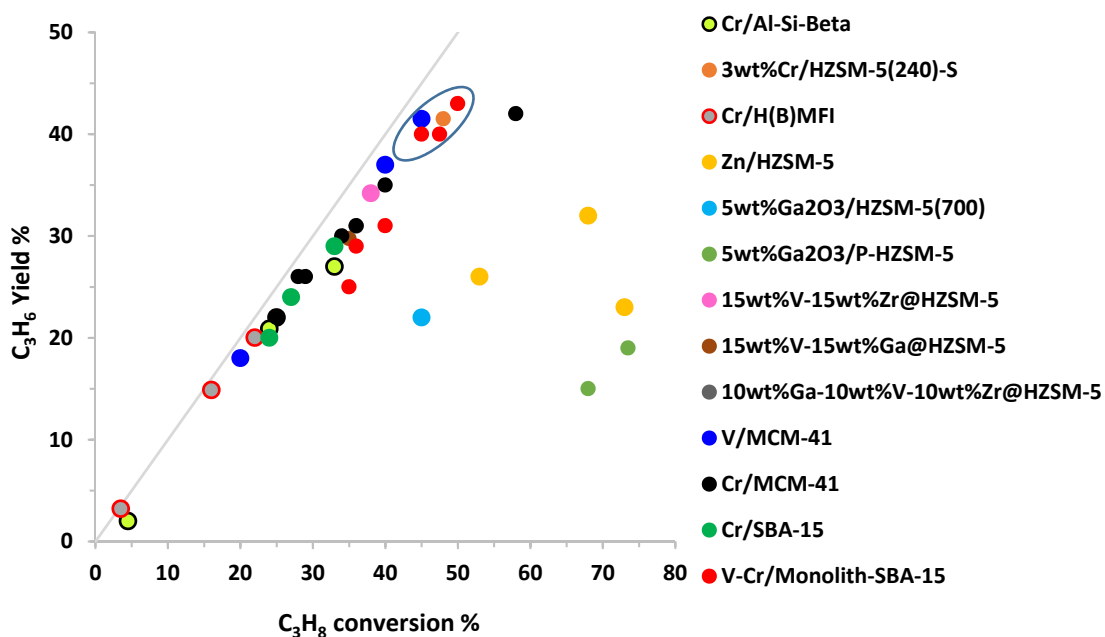
**Figure 121.** H<sub>2</sub>-TPR profiles of four samples series with different Cr contents, SiO<sub>2</sub>-p (A), SiO<sub>2</sub>-a (B), SBA-15 (C) and SBA-1 (D) catalysts series. 0.7, 2.1, 3.4 and 6.8 mean wt% of Cr. Reprinted with permission from ref.<sup>1111</sup>. Copyright 2011, Elsevier B.V. All rights reserved.

In the same way, the catalytic behavior of Cr supported on silica, SBA-1 and SBA-15 with different Cr loading was recently compared.<sup>1111,1112</sup> Similar conclusion were reported, being the catalytic activity dependent on the Cr<sup>6+</sup> amount and dispersion in monolayer coverage controlled by Cr content and support surface area (Figure 121). Moreover, Cr<sup>6+</sup> species were determined as precursors of Cr<sup>3+</sup> and Cr<sup>2+</sup> active species for the propane dehydrogenation and formed Cr<sup>2+</sup>/Cr<sup>3+</sup> redox cycle earlier proposed.<sup>1113,1114</sup> Moderate catalytic performance after 10min TOS at 550°C were obtained over 3.4wt%/SBA-1 and 3.4wt%/SBA-15, reaching 33 and 27% propane conversion, and 88 and 89% propylene selectivity, respectively (Table 16, Entries 31-32).<sup>1112</sup> Earlier, the catalytic properties of Cr/SBA-15 catalyst for propane ODH was yet reported.<sup>1115</sup> 2wt%Cr/SBA-15 exhibited the better catalytic performance than other Cr-supported catalysts due to high Cr species dispersion, reaching low 24% propane conversion and 84% propylene selectivity, at 650°C, over 6h TOS (Table 16, Entry 33). The preparation and use for propane ODH of monolithic V-Cr/SBA-15/Al<sub>2</sub>O<sub>3</sub>/FeCrAl catalysts, using FeCrAl foils as support and SBA-15/Al<sub>2</sub>O<sub>3</sub> as washcoat and V-Cr/SBA-15 as active phase, was described with 10wt%V and 0-

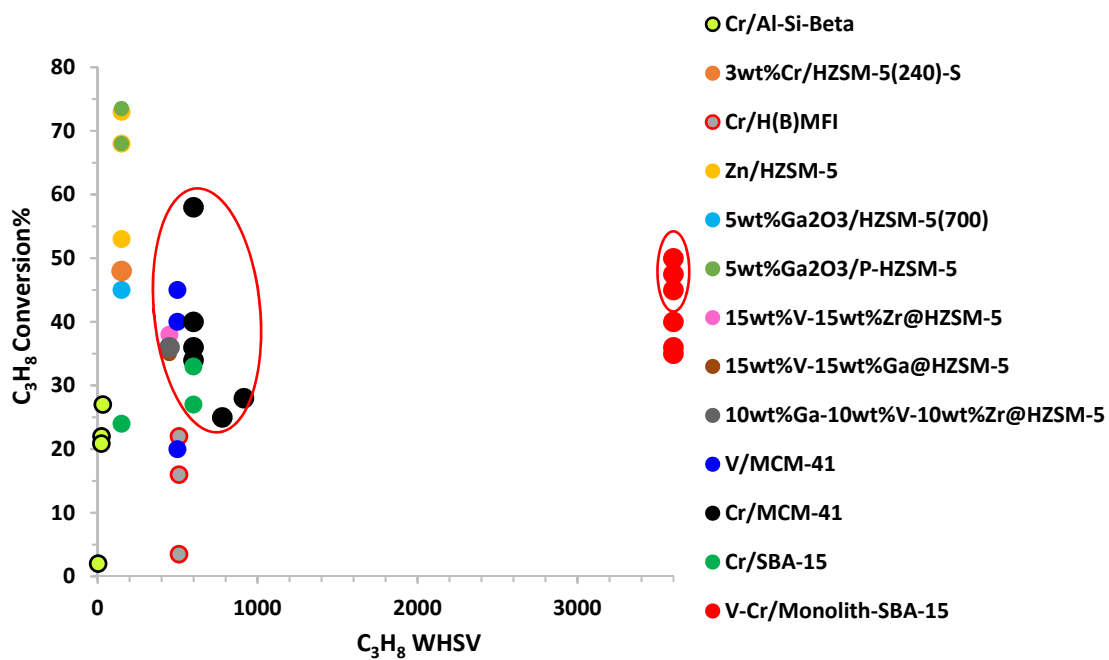
12.5wt%Cr contents.<sup>1116</sup> The SBA-15 mesoporous structure was conserved after the vanadium and chromium impregnation, and  $V^{5+}$  tetrahedral species were determined as the main active species, with high dispersion and enhanced redox properties, owing to strong interaction V-Cr. The incorporation of Cr allowed increasing the redox capacities of V and a lower temperature shift of the V reduction peak was observed from the TPR profiles. Optimum catalytic performance was reached over 10wt%V-10wt%Cr/SBA-15/ $Al_2O_3$ /FeCrAl sample, with good 43% propane conversion and 86% propylene selectivity at 650°C (Table 16, Entries 34-39).

### 7.3.5. Conclusion

Propane ODH with  $CO_2$  is an attractive approach to produce propylene showing different advantages such as shifting of equilibrium owing to combination with RWGS, completion of redox cycle with  $CO_2$  participation, and improvement of catalytic life due to coke elimination through reverse Boudouard reaction. However, many unknowns still remain to elucidate such as redox cycle and involved species, mechanism, competitive adsorption between  $CO_2$ , alkane and alkene and, above all, to investigate the stability, reuse and regeneration of catalysts in order to give industrial application a chance. Therefore, computational modeling and in situ spectroscopy studies will be fundamental tools for the rational design of efficient and stable ODH catalysts. The Figures 122-123 depict a graphical comparison of the different catalytic performance of the propane ODH catalysts to evaluate the productivity or selectivity of the process. High catalytic data were reached, with high propane conversion up to 42%, and propylene selectivity up to 92% with rapid deactivation of the catalyst (V or Cr/MCM-41), while monolithic V-Cr/SBA-15 based catalysts exhibited the best catalytic performance. For industrial application, the propylene productivity is a benchmark as well the propylene selectivity is of paramount importance. To compare the catalysts life additional studies are required since each process has a specific state-of-the-art technology, an optimized reactor system including catalyst regeneration cycles, and the reaction time can be short with catalyst regeneration intervals allowing continuous use for years.<sup>991</sup> For example the CATOFIN® process, widely applied technology, alternates incessantly dehydrogenation, regeneration, and purge stages with a few minutes of duration for each stage, in a multiple reactor beds to ensure constant propylene production (Figure 124).<sup>1117</sup>



**Figure 122.** Propylene yield versus propane conversion in the presence of the different catalysts discussed in this review. The ovoid highlights the best catalytic performance: high  $C_3H_8$  yield versus high  $C_3H_8$  conversion.



**Figure 123.** Propane conversion versus propane WHSV in the presence of the different catalysts discussed in this review. The ovoid highlights the best catalytic performance: high  $C_3H_8$  conversion versus  $C_3H_8$  WHSV.

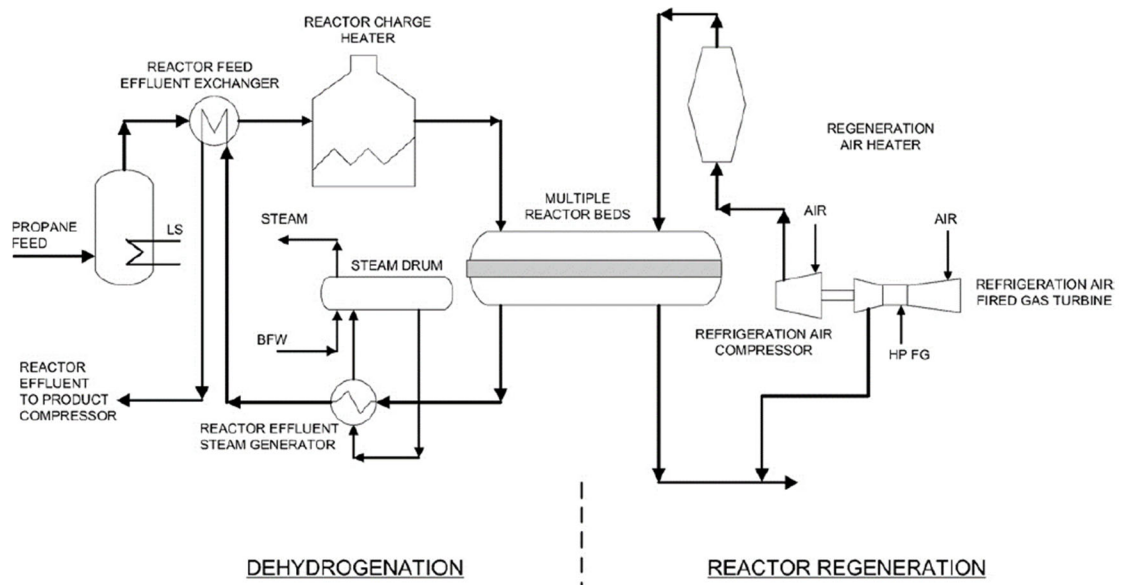


Figure 124. Process flow diagram of the Catofin propane process. Reprinted with permission from ref.<sup>1118</sup>. Copyright.

**Table 16.** Summary of the catalytic performance of the different reviewed catalysts for propane ODH.

Entry	Catalysts	Conditions	GHSV <sub>C<sub>3</sub>H<sub>8</sub></sub> ml <sub>cat</sub> <sup>-1</sup> h <sup>-1</sup>	χ <sub>C<sub>3</sub>H<sub>8</sub></sub> %	C <sub>3</sub> H <sub>6</sub> Yield%	C <sub>3</sub> H <sub>6</sub> Sel.%	Year	Ref
<b>Zeolite-based catalysts</b>								
1	3Cr/HZSM-5(240)-S	0.2 g <sub>cat</sub> , FT=20 mLmin <sup>-1</sup> , 600°C, C <sub>3</sub> H <sub>8</sub> :CO <sub>2</sub> :N <sub>2</sub> =2.5:5:92.5, TOS=0.16h (8h)	150	48 (30)	41.5 (27.5)	86 (92)	2011	1088
2	2%Cr/SiBeta	0.2 g <sub>cat</sub> , F <sub>C<sub>3</sub>H<sub>8</sub></sub> = 2mLmin <sup>-1</sup> ,	600	25	22	87	2020	1090
3	7Cr/SiBeta	C <sub>3</sub> H <sub>8</sub> :CO <sub>2</sub> :He=1:5:9, 550°C, TOS=0.16h		33	27	82		
4	2Cr/AlBeta			4.5	2	45		
5	2Cr/SiBeta	TOS=4h		24-11		87-92		
6	Cr/Silicalite-1	0.1 g <sub>cat</sub> , WHSV <sub>Total</sub> =7.5 gg <sub>cat</sub> <sup>-1</sup> h <sup>-1</sup> ,	510	3.5		92	2011	1091
7	Cr/H[B]MFI	C <sub>3</sub> H <sub>8</sub> :CO <sub>2</sub> :N <sub>2</sub> =15:15:70, 600°C		22		91		
8	Cr/H[B]MFIst			16		93		
9	Zn/HZSM(120)	0.2 g <sub>cat</sub> , FT=20 mLmin <sup>-1</sup> ,	150	73 (27)	23 (20.5)	32 (55)	2009	1099
10	Zn/HZSM(160)	C <sub>3</sub> H <sub>8</sub> :CO <sub>2</sub> :N <sub>2</sub> =2.5:5:92.5, 600°C,		68 (41.5)	32 (26)	47 (62)		
11	Zn/HZSM(201)	TOS=1h (30h)		53 (29)	26 (18)	49.5 (62)		
	5Ga <sub>2</sub> O <sub>3</sub> /HZSM-5(700)	0.2 g <sub>cat</sub> , FT=20 mLmin <sup>-1</sup> , 600°C, C <sub>3</sub> H <sub>8</sub> :CO <sub>2</sub> :N <sub>2</sub> =2.5:5:92.5, TOS=1h,	150	55	15		2007	1092
12		TOS=30-100h		45	22			
14	5Ga <sub>2</sub> O <sub>3</sub> /P-HZSM-5(1)	0.2 g <sub>cat</sub> , FT=20 mLmin <sup>-1</sup> , 600°C,	150	94 (17.5)	13 (10)	14.5 (57)	2008	1098
15	5Ga <sub>2</sub> O <sub>3</sub> /P-HZSM-5(1.5)	C <sub>3</sub> H <sub>8</sub> :CO <sub>2</sub> :N <sub>2</sub> =2.5:5:92.5, TOS=0.5h (50h)		73.5 (22)	19 (12)	27.5 (56.5)		
16	5Ga <sub>2</sub> O <sub>3</sub> /P-HZSM-5(2)			68 (18.5)	15 (9)	22.5 (51)		
17	15V-15Zr@HZSM-5	0.2 g <sub>cat</sub> , F <sub>C<sub>3</sub>H<sub>8</sub></sub> = 1.5mLmin <sup>-1</sup> ,	450	~38		~90	2020	1106
18	15V-15Ga@HZSM-5	C <sub>3</sub> H <sub>8</sub> :CO <sub>2</sub> :He=2.5:5:87.5, 550°C, TOS=6h		~35		~85		
19	15Ga-15Zr@HZSM-5			~35		~65		
20	10Ga-10V-10Zr@HZSM-5			~36		~86		
<b>OMS-based catalysts</b>								
21	4.8V/MCM-41	0.2 g <sub>cat</sub> , F <sub>Total</sub> = 15mLmin <sup>-1</sup> ,	500	20 (20)	~18	92	2018	1108
22	6.8V/MCM-41	C <sub>3</sub> H <sub>8</sub> :CO <sub>2</sub> :Ar=1:4:4, 600°C, TOS=0.5h (2h)		45 (35)	~41.5 (32)	92		
23	8.8V/MCM-41			40 (30)	~37 (27.5)	92		
24	5Cr/MCM-41	0.2 g <sub>cat</sub> , WHSV <sub>Total</sub> = 2800h <sup>-1</sup> ,	780	25	22	89	2005	1109
25	5Cr/SiO <sub>2</sub>	C <sub>3</sub> H <sub>8</sub> :CO <sub>2</sub> =1:3.6, 650°C, TOS=5 min		27	23	85		
26	3Cr/MCM-41(DHT)	0.4 g <sub>cat</sub> , F <sub>Total</sub> = 50mLmin <sup>-1</sup> ,	915	28	26	92	2003	1110
27	3Cr/MCM-41(TIE)	C <sub>3</sub> H <sub>8</sub> :CO <sub>2</sub> =1:5.6, 550°C		29	26	92		
28	3.4Cr/MCM-41	0.4 g <sub>cat</sub> , F <sub>Total</sub> = 30mLmin <sup>-1</sup> , C <sub>3</sub> H <sub>8</sub> :CO <sub>2</sub> =1:5,	600	36	31	89	2008	1113
29	6.8Cr/MCM-41	TOS=0.17h, 550°C		40	35	88.5		
30	13.7Cr/MCM-41			34	30	89		
31	6.8Cr/MCM-41			58	42	72.5		



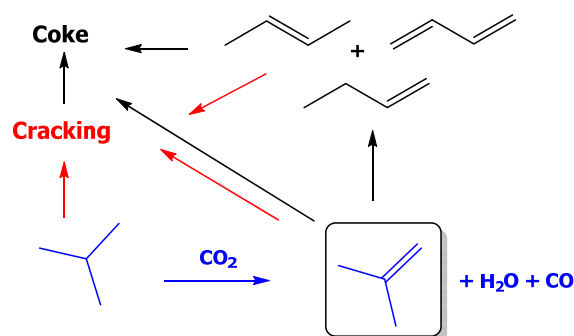
32	3.4Cr/SBA-1	0.2 g <sub>cat</sub> , F <sub>Total</sub> = 30mLmin <sup>-1</sup> ,	600	33	29	88	2011	1111
33	3.4Cr/SBA-15	C <sub>3</sub> H <sub>8</sub> :CO <sub>2</sub> :He=1:5:9, TOS=0.17h, 550°C		27	24	89		
34	2Cr/SBA-15	0.2 g <sub>cat</sub> , 550°C, F <sub>Total</sub> = 20mLmin <sup>-1</sup> ,	150	24	20	84	2002	1112
		C <sub>3</sub> H <sub>8</sub> :CO <sub>2</sub> :N <sub>2</sub> =2.5:5:92.5 TOS=6h,						
35	7.5V/SBA-15/Al <sub>2</sub> O <sub>3</sub> /FeCrAl	650°C, WHSV <sub>Total</sub> = 14400mLg <sup>-1</sup> min <sup>-1</sup> ,	3600	36	29	80	2011	1116
36	10V/SBA-15/Al <sub>2</sub> O <sub>3</sub> /FeCrAl	C <sub>3</sub> H <sub>8</sub> :CO <sub>2</sub> =1:3 TOS=0.17h		40	31	77.5		
37	15V/SBA-15/Al <sub>2</sub> O <sub>3</sub> /FeCrAl			35	25	71.5		
38	10V-7.5Cr/SBA-15/Al <sub>2</sub> O <sub>3</sub> /FeCrAl			45	40	89		
39	10V-10Cr/SBA-15/Al <sub>2</sub> O <sub>3</sub> /FeCrAl			50	43	86		
40	10V-12.5Cr/SBA-15/Al <sub>2</sub> O <sub>3</sub> /FeCrAl			47.5	40	84		

\* Metal content is given in wt%.  $\chi$ =conversion

## 7.4. Isobutene production by isobutane ODH

### 7.4.1. Introduction

Isobutene constitutes an important chemical building block to produce polyisobutene, methyl tert-butyl ether, butyl rubber, and methyl acrylates. Nowadays, the two main methods to produce isobutene based on fossil source are naphtha steam cracking and fluidized catalytic cracking, which cannot fully supply the increasing demand. Thus, catalytic dehydrogenation of isobutane represents a potential and alternative route to produce isobutene.<sup>991,1119,1120</sup> However, isobutane dehydrogenation raises limitations such as thermodynamic equilibrium, high-energy consumption, and severe catalyst deactivation. Over  $\text{CrO}_x/\text{Al}_2\text{O}_3$  commercial catalyst, at  $560^\circ\text{C}$ , 55% isobutene conversion and up to 93.5 % isobutene selectivity can be achieved.<sup>1121</sup> As aforementioned, oxidative dehydrogenation using  $\text{O}_2$  results attractive because of exothermic but limited selectivity is reached due to side reactions and deep oxidation of products. Therefore, oxidative dehydrogenation with  $\text{CO}_2$  becomes an attractive approach scarcely explored in the presence of zeolite and OMS based catalysts (Scheme 73).

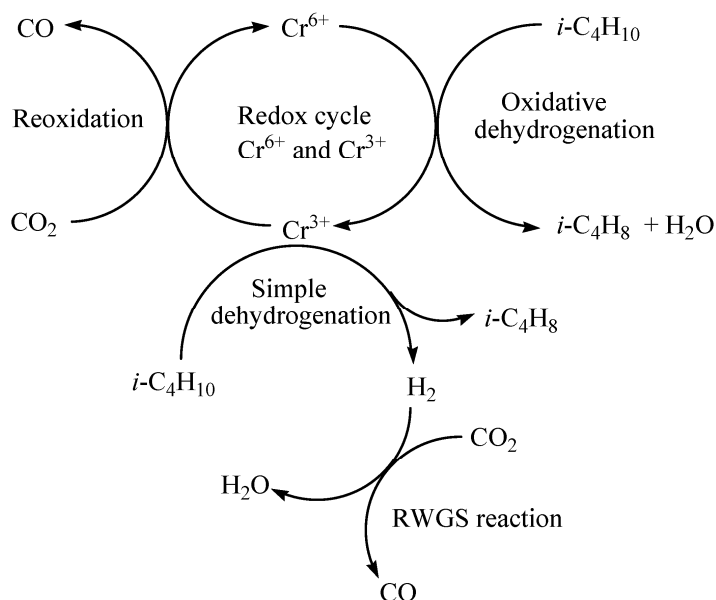


Scheme 73. Oxidative dehydrogenation of isobutane with  $\text{CO}_2$ .

### 7.4.2. OMS- and zeolite-based catalysts for isobutane ODH

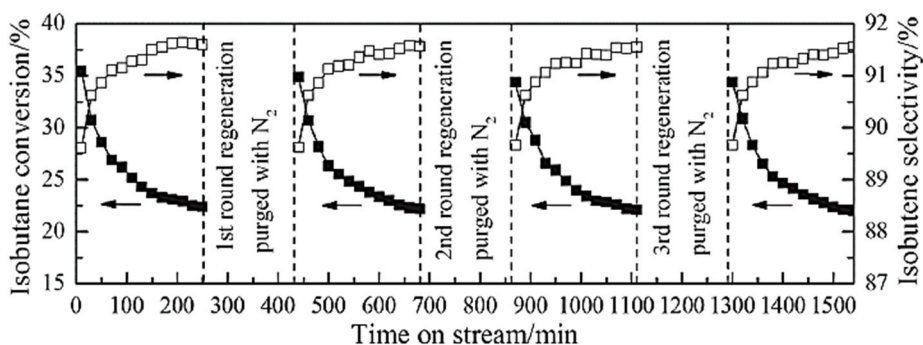
As before reviewed, vanadium and chromium metal oxides supported materials, are the most widely used and studied catalysts for alkanes oxidative dehydrogenation with  $\text{CO}_2$  despite of their toxicity. In line, a series of Cr-supported Silicalite-1 samples were prepared by impregnation, tested for isobutene ODH with  $\text{CO}_2$ , and compared to the catalytic performance of Cr/SBA-15 sample.<sup>1115</sup> A combination mechanism of simple isobutane dehydrogenation with the RWGS was proposed, following redox mechanism assisted by  $\text{CO}_2$  involving  $\text{Cr}^{6+}/\text{Cr}^{3+}$  redox cycle (Figure 125).  $\text{H}_2$ -TPR data revealed higher  $\text{Cr}^{6+}$  amount over 3wt%Cr/Silicalite-1 than 3wt%Cr/SBA-15 owing to better dispersion attributed to abundant nest silanol groups present in silicalite-1 zeolite. A comparison of catalytic performance 3wt%Cr/Silicate-1 and 3wt%Cr/SBA-15 revealed that higher isobutene conversion was achieved on 3wt%Cr/Silicate-1 owing to higher amount of Cr active species, while higher selectivity was reached over 3wt%Cr/SBA-15 attributed to the lower acidity of SBA-15 sample. The characterization of spent catalysts showed

that coke was more easily burnt off over 3wt%Cr/Silicate-1 while higher ratio  $\text{Cr}^{6+}/\text{Cr}^{3+}$  was also determined indicating that Cr species interacting with nest silanols were more easily re-oxidized by  $\text{CO}_2$  during ODH process. Moreover, XRD pattern suggested degradation of SBA-15 ordered hexagonal structure. Thus, at  $570^\circ\text{C}$ , maximum 36.5 % isobutane conversion with 71% isobutene selectivity over 3wt%Cr/Silicalite-1 were reached (Table 17, Entries 1-3).



**Figure 125.** Proposed reaction mechanism of isobutane ODH with  $\text{CO}_2$  over Cr/Silicalite-1 catalysts. Reprinted with permission from ref.<sup>1115</sup>. Copyright 2019, MDPI.

Previously, a series of 3wt%Cr/SBA-15 samples doped with different amount of Ce (1-5wt%) were prepared by impregnation and their catalytic behavior studied for isobutene ODH with  $\text{CO}_2$ .<sup>1122</sup> The benefits of the incorporation of a second metal have been demonstrated throughout this review owing to the establishment of new interactions metal/metal and metal/support improving active metal phase dispersion and stabilization. In line, the incorporation of ceria to the 3wt%Cr/SBA sample allowed enhancing the  $\text{Cr}^{6+}$  species amount attributed to the improved Cr species dispersion owing to ceria incorporation. Thus, the maximum catalytic performance was registered over 3wt%Cr-3wt%Ce/SBA-15 sample, with 35.5% isobutane conversion and 90% isobutene selectivity at  $570^\circ\text{C}$ , 10min TOS (Table 17, Entries 4-8). The highest activity of 3wt%Cr-3wt%Ce/SBA-15 catalyst was attributed to highest reducibility of Cr species determined by  $\text{H}_2$ -TPR. A study of regeneration and recycling by calcination in air, showed that over 3wt%Cr-3wt%Ce/SBA-15 sample, for the first run, isobutene conversion decreased from 35.5% to 22.5% after 4h TOS and that the original activity could be almost fully restored by calcination and for four runs, owing to the removal of coke and reoxidation of  $\text{Cr}^{3+}$  to  $\text{Cr}^{6+}$  active species (Figure 126).



**Figure 126.** Conversion and selectivity versus TOS over 3wt%Cr-3wt%Ce/SBA-15 catalyst for isobutene ODH for 4 cycles. (■) conversion, (□) selectivity. Reprinted with permission from ref.<sup>1122</sup>. Copyright 2017, SIOC, CAS, Shanghai, & WILEY-VCH Verlag GmbH & Co. KGaA, Weinheim.

The good catalytic performance of a series of VO<sub>x</sub>/SBA-15 with different V loading (1-11wt%) prepared by impregnation for isobutane ODH was also demonstrated.<sup>1123</sup> The catalytic and characterization data revealed that catalytic activity was dependent on dispersion and amount of vanadium species. NH<sub>3</sub>-TPD profiles displayed that acid sites formation was due to vanadia incorporation, and that 7wt%V/SBA-15 exhibited lower acidity than 7wt%V/MCM-41. Maximum catalytic performance was achieved over 7wt%V/SBA-15, reaching 41% isobutane conversion and 85% isobutene selectivity due to highest reducibility and amount of dispersed vanadium species determined by H<sub>2</sub>-TPR and Raman spectroscopy (Table 17, Entries 9-11). Comparison of catalytic performance of 7wt%V/SBA-15 and 7wt%V/MCM-41 showed that lower selectivity was achieved over 7wt%V/MCM-41 due to higher acidity, while lower conversion was attributed to lower amount of VO<sub>x</sub> active species. A study of catalyst recycle and regeneration, for four consecutive uses and for 4h TOS, showed that catalytic performance was recovered after calcination owing to coke removal and Cr species oxidation.

#### 7.4.3. Conclusion

Isobutane ODH with CO<sub>2</sub> constitutes an attractive approach to produce isobutene showing different advantages respect to catalytic dehydrogenation. In comparison to propane ODH, fewer papers have been reported in the literature but the isobutene yield and selectivity are high. Moreover, as currently it occurs for catalytic dehydrogenation, the study and development of new catalysts and technologies suitable for propane ODH will be valid and applicable to isobutene ODH.

#### 7.5. Conclusion

Alkane ODH with CO<sub>2</sub> as soft oxidation is an interesting approach with many advantages respect to catalytic dehydrogenation or ODH with oxygen, promoting ODH directly or combining alkane dehydrogenation and RWGS with global favoured thermodynamics and improved catalysts life owing to reverse Boudouard reaction. However, many unknowns remain to elucidate such as

redox cycle and involved species, mechanism, competitive adsorption between CO<sub>2</sub>, alkane and alkene and, desorption of the product and specially the stability, reuse and regeneration of catalysts for commercialization. To achieve required knowledge and understanding, computational modeling and in situ spectroscopy studies will be essential tools for the rational design of efficient and stable ODH catalysts. Good catalytic results were achieved in the presence of OMS-based catalysts that should stimulate and drive the scientific community and industry to explore their potential up to the last step of commercial application. Moreover, to overcome the limitation of microporosity of zeolite, the benefits of the development of catalysts based on hierarchical zeolites and two-dimensional zeolite nanosheets to promote physical isolation and protection of particles as well as mass transfer should be explored.

**Table 17.** Summary of the catalytic performance of the different reviewed catalysts for isobutane ODH.

Entry	Catalysts	Conditions	GHSV <sub>C<sub>4</sub>H<sub>10</sub></sub> mlg <sub>cat</sub> <sup>-1</sup> h <sup>-1</sup>	χ <sub>C<sub>4</sub>H<sub>10</sub></sub> %	C <sub>4</sub> H <sub>8</sub> Yield%	C <sub>4</sub> H <sub>8</sub> Sel.%	Year	Ref
1	2Cr/Silicalite-1	0.1 g <sub>cat</sub> , 570°C, F <sub>Total</sub> = 5.8mLmin <sup>-1</sup> ,	1740	33 (25)		72.5(78)	2019	1115
2	3Cr/Silicalite-1	C <sub>4</sub> H <sub>10</sub> :CO <sub>2</sub> =1:1 TOS=0.17 (6h)		36.5 (28)		71 (75)		
3	7Cr/Silicalite-1			36 (28)		70 (70.5)		
4	3Cr/SBA-15			34 (21)		75 (77)		
5	3Cr/SBA-15	0.5 g <sub>cat</sub> , 570°C, F <sub>Total</sub> = 19.3mLmin <sup>-1</sup>	390	27 (16.5)	24 (15)	90 (90)	2017	1122
6	3Cr-1Ce/SBA-15	<sup>1</sup> , C <sub>4</sub> H <sub>10</sub> :CO <sub>2</sub> =1:5 TOS=0.17 (4h)		33 (20.5)	30 (19)	90 (91.5)		
7	3Cr-3Ce/SBA-15			35.5 (22.5)	32 (20.5)	89.5 (91.5)		
8	3Cr-5Ce/SBA-15			34.5 (21)	31 (19.5)	90 (91.5)		
9	5V/SBA-15	0.5 g <sub>cat</sub> , 570°C, F <sub>Total</sub> = 19.3mLmin <sup>-1</sup>	390	35 (21)	30 (19.5)	86 (90)	2016	1123
10	7V/SBA-15	<sup>1</sup> , C <sub>4</sub> H <sub>10</sub> :CO <sub>2</sub> =1:5, TOS=0.17 (4h)		41 (23)	34.5 (20.5)	85 (89)		
11	11V/SBA-15			37.5 (20)	31.5 (18)	84 (88.5)		

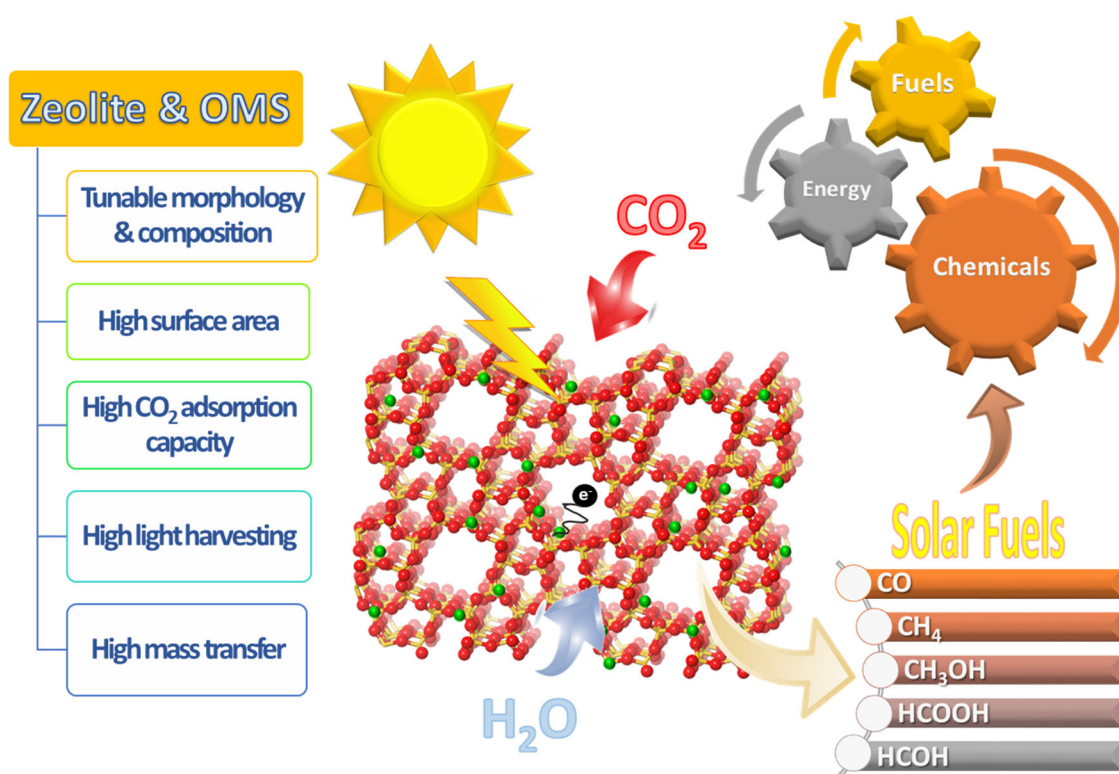
\* Metal content is given in wt%. χ=conversion

## ***C Electro and photocatalytic conversion of CO<sub>2</sub>***

The use of solar energy to CO<sub>2</sub> conversion into chemicals and fuels has received great attention in the last 30 years. Indeed, electro- and photo-reduction reactions offer great potential to produce fuels molecules such as CO, CH<sub>4</sub>, HCOOH, HCHO, MeOH and EtOH, using solar energy directly or indirectly. In photocatalysis, also called artificial photosynthesis, the electrons come from the excitons of semiconductor photocatalysts by means of photonic excitation, whereas in electrocatalysis the electrons come from an external electric field which, in turn, can be supplied by photovoltaic solar cells, i.e. indirectly using solar energy.

### *1            Electroreduction of CO<sub>2</sub>*

Electrocatalytic CO<sub>2</sub> reduction is a very attractive CO<sub>2</sub> conversion due to its ambient reaction conditions and simplicity of device fabrication. However, there are several challenges, such as low CO<sub>2</sub> solubility, high CO<sub>2</sub> activation energy, low energy efficiency and low selectivity of the process. But the main drawbacks that are the low stability of the electrodes and their deactivation in less than 100 h, restrict their commercialization (metal poisoning, agglomeration of the active centers),<sup>1124</sup> while the low selectivity of the process requires costly separation steps and energy consumption.<sup>1125</sup> The low efficiency of solar to chemical energy conversion is due to the difficulties in fulfilling all the requirements: high catalytic activity at the electrode surface, sufficient passivation of the electrode surface (limiting the recombination of carriers), formation of a high energy barrier at the semiconductor/solution interface, and proximity of energy levels between the semiconductor and the reactants to minimize energy loss in interfacial reactions. In the last decades, the large number of investigations on electrocatalysts, reaction conditions and devices for CO<sub>2</sub> electroreduction have allowed to develop the knowledge and to improve the catalytic performance of electrocatalysts. The current understanding of the reaction mechanism requires further exploration involving theoretical calculations and in situ characterization techniques to monitor the variations in the electronic structure of the active sites and to detect metastable intermediates. Therefore, research should not be limited to the development of excellent electrocatalysts, but to an overall understanding of the electrolysis system. So far, the design and development of electrocatalysts, due to multiple requirements and complexity to improve their efficiency and stability, have not considered the use of zeolite and OMS probably due to their intrinsic properties and capabilities to generate and transfer electrons (potential, Faradaic efficiency, energy efficiency), and it is reasonable to consider that future research will focus on other approaches.

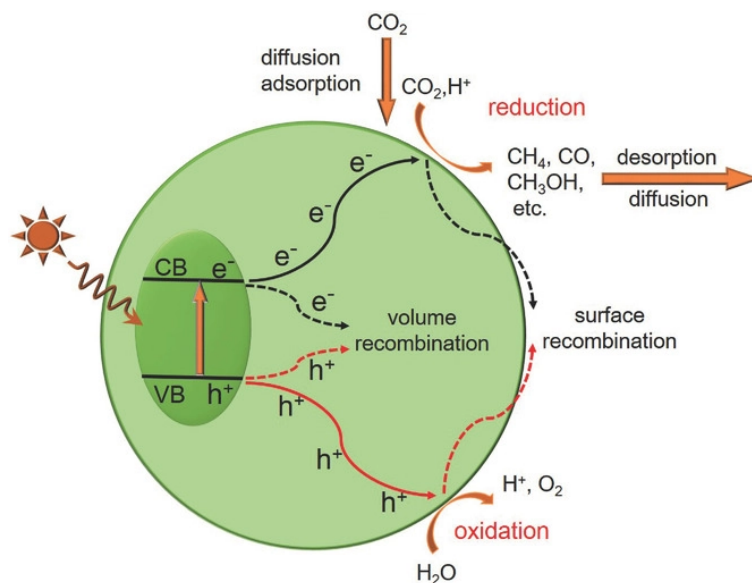


**Figure 127.** Photoreduction of CO<sub>2</sub> to solar fuels.

### 2.1. Fundamentals of photocatalytic CO<sub>2</sub> reduction

Photoreduction of CO<sub>2</sub> is a very attractive strategy for the conversion of carbon dioxide into fuels, making possible a circular economy (Figure 127). Photoreduction of CO<sub>2</sub> is not a selective process and several products are obtained simultaneously. The physicochemical properties of the photocatalyst are determinant for the development of an efficient process and to be able to control the different stages of light absorption, charge separation and migration, adsorption of reactants (CO<sub>2</sub> and H<sub>2</sub>O), activation and conversion (redox surface reactions) and desorption of the products (Figure 128).





**Figure 128.** Different steps involved in the photocatalytic reduction of  $\text{CO}_2$  over a semiconductor photocatalyst. Reprinted with permission from ref.<sup>1126</sup> Copyright 2017, Jinghua Wu et al. Published by WILEY-VCH Verlag GmbH & Co. KGaA, Weinheim.

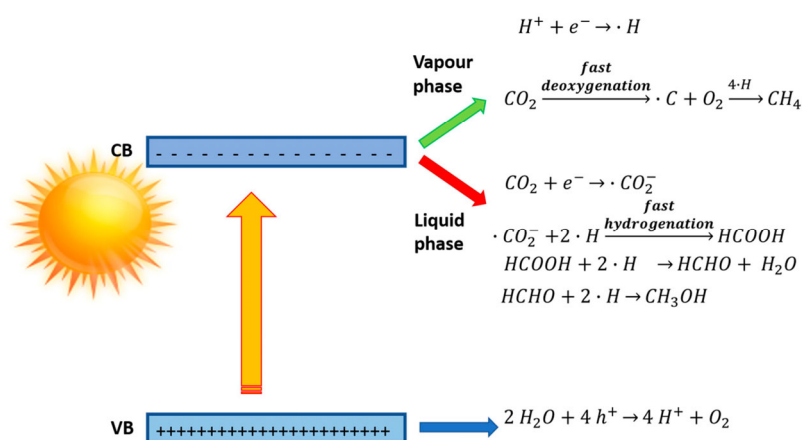
The photocatalytic reduction of  $\text{CO}_2$  requires high energy to break the C=O bond and form the C-H bond, along with the participation of a high number of electrons (2, 4, 6, 8, 10, 12 or more electrons) to produce CO, HCOOH,  $\text{CH}_4$ , HCHO, MeOH and others (Table 18). Then, the high redox potential for an electron transfer to  $\text{CO}_2$  is -1.9 eV due to the linear geometry of the  $\text{CO}_2$  molecule and the energy requirement to bend and inject an electron into its orbitals. Although the redox potential is lower than the conduction band (CB) of most semiconductors, some photocatalysts can adsorb  $\text{CO}_2$  and bend the configuration of the molecule. Thus,  $\text{CO}_2$  can have a lower LUMO level that allows electron transfer. To compare, the thermocatalytic reduction of  $\text{CO}_2$  requires elevated temperatures and pressures, while photocatalysis occurs at room temperature and ambient pressure under solar irradiation, and requires an efficient semiconductor. The photoreduction of  $\text{CO}_2$  constitutes a very attractive technology to produce fuel under atmospheric conditions and at lost energy costs. Thereby, the photocatalytic properties of semiconductors have received much attention in recent decades. Among the main semiconductor photocatalysts used ( $\text{MgO}$ ,  $\text{Ga}_2\text{O}_3$ ,  $\text{ZnO}$ ,  $\text{CdS}$ ,  $\text{GaP}$ ,  $\text{SiC}$ ,  $\text{WO}_3$ ,  $\text{Fe}_2\text{O}_3$ ,  $\text{ZrO}_2$ ),<sup>1126,1127</sup>  $\text{TiO}_2$ -based photocatalysts are preferred due to  $\text{TiO}_2$  availability, cheap and the appropriate band-gap.<sup>1128</sup> Moreover, these materials can be doped with metal such as Pt, Cu, Ag, Fe, Co, and Ni to limit the charge recombination and favoring the photocatalytic process.<sup>1129</sup> Different strategies have been explored such as co-catalyst deposition, defect creation, increasing the specific surface area in order to increase the number of active sites to obtain an efficient photocatalyst with good charge separation, fast charge transfer, high absorption of the solar spectrum, low cost and high stability.<sup>1130</sup>

Upon irradiation, electrons from valence band (VB) are excited to conduction band (CB) leaving vacancies (“holes”) in the valence band. Therefore, the electrons and holes produced can be involved in a photocatalytic reaction (Figures 128 and 129). The photoreduction requires a reductant and the normally preferred one is water owing to its richness, non-toxicity, and effectiveness. The main problem with the use of water as a hydrogen donor and holes quencher is that water competes to absorb electrons in the conduction band to generate hydrogen. In addition, this hydrogen is generally formed in higher yields than CO<sub>2</sub> photoreduction products. Other reductants such as trimethylamine (amines) or Na<sub>2</sub>S capable of consuming the photogenerated holes during the photocatalytic reduction of CO<sub>2</sub> are also used, especially in gas phase, conferring structural stability to the photocatalysts.<sup>1131</sup>

**Table 18.** Standard electrochemical potentials for CO<sub>2</sub> reduction in water at pH~7.

Equation	CO <sub>2</sub> reduction in water	Redox potentials (V)
1	$\text{CO}_2 + \text{e}^- \rightarrow \text{CO}_2^-$	-1.9
2	$\text{CO}_2 + 2\text{H}^+ + 2\text{e}^- \rightarrow \text{HCOOH}$	-0.61
3	$\text{CO}_2 + 2\text{H}^+ + 2\text{e}^- \rightarrow \text{CO} + \text{H}_2\text{O}$	-0.53
4	$2\text{CO}_2 + 12\text{H}^+ + 12\text{e}^- \rightarrow \text{C}_2\text{H}_4 + 4\text{H}_2\text{O}$	-0.34
5	$\text{CO}_2 + 4\text{H}^+ + 4\text{e}^- \rightarrow \text{HCHO} + \text{H}_2\text{O}$	-0.48
6	$\text{CO}_2 + 6\text{H}^+ + 6\text{e}^- \rightarrow \text{CH}_3\text{OH} + \text{H}_2\text{O}$	-0.38
7	$\text{CO}_2 + 8\text{H}^+ + 8\text{e}^- \rightarrow \text{CH}_4 + 2\text{H}_2\text{O}$	-0.24
8	$2\text{H}^+ + 2\text{e}^- \rightarrow \text{H}_2$	-0.41

The reaction medium is another parameter that drastically affects the reaction pathway and selectivity of the photoreduction process. Gas phase reaction through rapid vapor phase deoxygenation leads to selectivity towards methane, while liquid phase reaction through rapid dehydrogenation of water leads to HCOOH, HCOH and CH<sub>3</sub>OH (Figure 109).<sup>1132</sup>



**Figure 129.** Different reaction pathway and selectivity in vapor or liquid phase (conduction (CB) and valence (VB) bands). Reprinted with permission from ref.<sup>1132</sup> Copyright 2017, MDPI.

Up to now, efficiency of photoreduction of CO<sub>2</sub> is less than 1%, and it has been estimated that efficiency of 10% or higher is necessary for economic feasibility.<sup>1133</sup> Accumulation and rigorous interpretation of results based on knowledge and trial/error is a way to the development of efficient photocatalysts but the development of fundamental knowledge is crucial. However, the lack of understanding of the factors controlling product distribution requires systematic studies and understanding of the parameters driving this distribution, such as kinetics, thermodynamics, surface adsorption and activation of CO<sub>2</sub>, determination of active species that allow high reduction potential of photogenerated electrons and simultaneous electron and proton transfer. Undoubtedly, computational chemistry and design of materials will be fundamental to progress in understanding the material properties and reaction mechanism.

A large variety of photocatalytic systems with or without co-catalyst or Z-scheme component compositions for CO<sub>2</sub> photoreduction have been explored. Nevertheless, only few studies focused on the development of zeolite- and OMS- based photocatalysts have been reported. A recent review summarized the recent developments and future prospects of the application of zeolite-based photocatalysts for CO<sub>2</sub> photoreduction.<sup>1134</sup> Herein, the main advances and contribution of zeolite- and OMS- based photocatalysts for the photoreduction of CO<sub>2</sub> to produce fuels are discussed. However, although it is a very attractive process due to its technological and experimental characteristics, the efficiency is too low even with the best photocatalyst to be considered for commercialization.

## 2.2. Photocatalysts for the reduction of CO<sub>2</sub>

### 2.2.1. Zeolite-based catalysts for the photoreduction of CO<sub>2</sub>

#### a) TiO<sub>2</sub>/zeolite-based photocatalysts for the reduction of CO<sub>2</sub>

Zeolites are used as catalysts in numerous chemical processes due to their high specific surface area, pore structures, stability, Lewis and Brønsted acid and base properties, ability to host organic and metal complexes, nanoparticles and metal oxides, high CO<sub>2</sub> uptake capacity<sup>1135</sup> and ability to stabilize radical cations and trap electrons.<sup>1136,1137</sup> All these properties can be tuned to obtain zeolites with superior CO<sub>2</sub> adsorption and activation ability. Unfortunately, the application of zeolites as photocatalysts for CO<sub>2</sub> photoreduction has been rather disregarded probably because it was assumed that the "ideal zeolite" was a good insulator<sup>1138</sup> so research has focused on the development of semiconductors for CO<sub>2</sub> photoreduction. The photoactivity of zeolite is related to the possible photoexcitation of the (M<sup>n+</sup>-O<sup>2-</sup>) to (M<sup>(n-1)+</sup>-O<sup>-</sup>)\* pair. Thus, different approaches have been explored to introduce substituted or anchored heteroatoms into zeolite structures to enhance their photocatalytic properties. Moreover, zeolites provide oxygen defects that promote better charge separation while OH groups favor the proton and

charge transport. These physicochemical properties of zeolites make them attractive supports for the design and synthesis of photocatalysts with different active centers specific for competitive adsorption/desorption of CO<sub>2</sub>, CO, H<sub>2</sub>O and CH<sub>4</sub> and redox reactions.

Several semiconductor photocatalysts have been extensively studied for the photoreduction of CO<sub>2</sub> such as ZnO, TiO<sub>2</sub>, Fe<sub>2</sub>O<sub>3</sub>, graphitic carbon nitride (g-C<sub>3</sub>N<sub>4</sub>) and Cu<sub>2</sub>O. Among them, the adsorption, photoinduced activation and reduction of CO<sub>2</sub> to CH<sub>4</sub> have been extensively studied and demonstrated on TiO<sub>2</sub> surfaces.<sup>1139</sup> Therefore, several studies of zeolite-based photocatalysts have focused on the incorporation of TiO<sub>2</sub> in either bulk form, highly dispersed nanoparticles, wall-embedded complexes or isomorphic substitution (tetrahedrally coordinated).

A study of dispersion of TiO<sub>2</sub> within Y zeolite cavities and framework, prepared following an ion-exchange method and hydrothermal synthesis (ex-Ti-oxide/Y-zeolite and Ti-oxide/Y-zeolites), showed the photocatalytic activity for the reduction of CO<sub>2</sub> with H<sub>2</sub>O to produce CH<sub>4</sub> and CH<sub>3</sub>OH.<sup>1140</sup> Characterization data indicated that TiO<sub>2</sub> species were highly dispersed within the zeolite cavities and were present in tetrahedral coordination. The photocatalytic performance for the formation of CH<sub>4</sub> and CH<sub>3</sub>OH indicated that selectivities strongly depend on the type of catalyst. Thus, over ex-Ti-oxide/Y-zeolite, a high activity and selectivity to CH<sub>3</sub>OH was registered, while CH<sub>4</sub> was the main product over bulk TiO<sub>2</sub> and Ti-oxide/Y-zeolite (Table 19, Entries 1-2). The changes in the photocatalytic performance were attributed to the higher TiO<sub>2</sub> dispersion and charge transfer excited state of the highly dispersed titanium oxide in the ex-Ti-oxide/Y-zeolite sample.

In 2001, the photocatalytic activity of Ti-Beta zeolites in hydroxide and fluoride medium for the reduction of CO<sub>2</sub> was described.<sup>1141</sup> The higher hydrophilicity of the sample synthesized in hydroxide medium (Ti-Beta(OH)) allowed higher efficiency in the quenching of the photoluminescence in the presence of H<sub>2</sub>O. Ti-Beta(OH) exhibited higher photocatalytic activity than Ti-Beta(F) attributed to the higher concentration of photoexcited active sites, (Ti<sup>3+</sup>-O)\*, while higher CH<sub>3</sub>OH selectivity was reached over Ti-Beta(F) photocatalyst. These results revealed the key role of hydrophilic-hydrophobic properties that promote proton and charge transfer as well as adsorption of water on the reactivity and selectivity for the photoreduction of CO<sub>2</sub> (Table 19, Entries 4-6).

b) Organic semiconductor/Zeolite-based photocatalyst for the reduction of CO<sub>2</sub>

Another approach to improve the photocatalytic properties of zeolite-based material is the incorporation of organic semiconductors, such as polythiophene (PT). Then, the preparation of the photocatalyst Na-ZSM-5-PT by chemical oxidative polymerization of thiophene for reduction

of CO<sub>2</sub> to formic and acetic acid was described.<sup>1142</sup> The advantage of a PT/zeolite photocatalyst is the absorption of the radiation at wavelengths  $\leq 650$  nm, invading the infrared region and enabling the use of a wider range of wavelengths for the photoreduction of CO<sub>2</sub> (Table 19, Entry 16). In line, an advanced photocatalyst was prepared combining the photocatalytic properties of TS-1 nanosheets with ones of a semiconductor (graphitic carbon nitride (CN)) to enhance light absorption, especially for visible light. Thus, TS-1 nanosheets were hybridized with hydroxylated CN nanosheets to form a 2D/2D hCN/TS-1 Z-scheme nanocomposite that exhibited higher photocatalytic activity than the pristine TS-1 nanosheets (Table 19, Entries 6-7). The photocatalytic performance increased with the increasing loaded amount of CN up to 10wt%, to reach the maximum owing to optimum charge separation due to strengthened interfacial interaction favorable to charge transfer.

c) Effect of the morphology over the activity of Zeolite-based photocatalysts for the reduction of CO<sub>2</sub>

The microporous nature of zeolite can hinder mass transfer and hamper the catalytic reaction. To this end, the use of zeolite nanosheets with thicknesses of a few nanometers and the introduction of a hierarchical porous structure and the introduction of macropores for the design of novel zeolite-based photocatalysts would be valuable strategies for future developments. Accordingly, the preparation of two-dimensional (2D) TS-1 nanosheets was reported to take advantage of not only the larger surface area but also to reduce the charge transfer distance for CO<sub>2</sub> photoreduction exhibiting higher photocatalytic performance for the reduction of CO<sub>2</sub> than 3D sample (Table 19, Entry 8).<sup>1143</sup> Following the same approach, the synthesis and photocatalytic performance of zeolite SAPO-5 nanosheets for the photoreduction of CO<sub>2</sub> was reported.<sup>1144</sup> The photocatalytic study revealed that SAPO-5 ultrathin nanosheets exhibited six times higher photocatalytic activity than SAPO-5 microrods for CH<sub>4</sub> formation and higher than other standard zeolites. The results were attributing to the higher amount of exposed Al atoms owing to the morphology of nanosheets that enhances not only the CO<sub>2</sub> adsorption capacity but also the excited state electrons capture and transfer. In addition, the nanosheets morphology allowed the improvement for the mass transfer process. All these improved physicochemical properties enabled longer excited state lifetime on SAPO-5 nanosheets and led to higher photoactivity for the reduction of CO<sub>2</sub> (Table 19, Entries 14-15).

d) Effect of metallic doping over the activity of zeolite-based photocatalysts for the reduction of CO<sub>2</sub>

As stated above, the possible photoexcitation of the (M<sup>n+</sup>-O<sub>2</sub><sup>-</sup>) to (M<sup>(n-1)+</sup>-O<sup>-</sup>)\* pair is responsible for the photocatalytic activity of zeolites. Therefore, different strategies have been followed to introduce heteroatoms into zeolite structures and to enhance their photocatalytic activity.

Hence, the introduction of efficient electron scavengers such as noble metals such as Au, Pd or Ag that is relatively inexpensive, allows to improve the photocatalytic performance. Titanosilicate-1 (TS-1) is an important zeolite with isomorphic substitution of  $Ti^{IV}$  species in the MFI zeolite framework, which has long been applied to various photocatalytic and oxidation reactions.<sup>1145,1146</sup> The photocatalytic activity of zeolitic titanosilicate has been explored in various studies and the activity of Ti-O species was reported to be higher than that of Ti species octahedrally coordinated of bulk  $TiO_2$  nanoparticles for  $CO_2$  photoreduction.<sup>1134,1141,1146</sup> Therefore, in addition to the benefits of the pore system, large surface area and the possible modifications of redox and acid/base properties with functional components, different strategies have been followed to improve the photocatalytic activity of these materials, such as the deposition of metal clusters and metal oxide clusters, metal nanoparticles and metal oxide nanoparticles and polymeric semiconductor nanoparticles. Moreover, the presence of high number of silanol groups confers high hydrophobicity to the surface of TS-1 that favors proton and charge transfer as well as adsorption of water.<sup>1147</sup> The synthesis of Ag and  $TiO_2$  nanoparticles co-loaded zeolite TS-1 (Ag- $TiO_2$ /TS-1) by the ion-exchange and in-situ photodeposition method in successive steps was recently reported for its use as photocatalyst for the reduction of  $CO_2$ .<sup>1148</sup> XPS and EPR analyses revealed that Ag- $TiO_2$ /TS-1 nanocomposite exhibits higher amount of  $Ti^{3+}$  defects and oxygen vacancies, allowing better visible light adsorption and separation efficiency of the photogenerated charges. The high photocatalytic activity was attributed to the properties of TS-1, to the highly exposed reduction planes {101} of  $TiO_2$  and to the uniformly dispersed Ag nanoparticles. The TS-1 high surface area and rich defects enabled the high dispersion of active species and molecular adsorption of  $CO_2$ , as well as to accelerate charge separation by hole and electron trapping. Over 1Ag-16.9 $TiO_2$ /TS-1, 3.16 for CO and 0.47  $\mu mol g^{-1} h^{-1}$  high production rate for CO and  $CH_4$  under visible light irradiation, were reached and maintained along three cycles (Table 19, Entry 7).

The photocatalytic activity of ex-Ti-oxide/Y-zeolite catalyst was enhanced by the addition of Pt to promote the charge separation favoring  $CH_4$  over  $CH_3OH$  formation (Table 19, Entry 3).

Also, the photocatalytic performance of a TS-1 nanosheets hybridized material with a semiconductor (graphitic carbon nitride (CN)), hCN/TS-1, was improved by the deposition of Ag nanoparticles. The hCN/TS-1 composite selectively decorated with Ag nanoparticles (Ag/hCN/TS-1) exhibited a high surface area and a 2D/2D heterojunction, improving the visible light absorption, charge separation and photocatalytic efficiency. The content (wt%) of CN and Ag were optimized and the 1.5Ag/hCN10/TS-1 composite displayed the best catalytic performance for  $CO_2$  photoreduction, and the yield in the presence of 1.5Ag/hCN10/TS-1 was approximately 7 times higher than that of pristine TS-1 (Table 19, Entry 10). In this zeolite-based

composite photocatalyst the charge transfer was achieved under visible light irradiation ( $\lambda < 390$  nm). The electrons photogenerated by TS-1 combined with the holes of CN allowed a prolonged excitation of the photoelectron lifetime, which was transferred to the Ag nanoparticles enabling a higher efficiency for the photoreduction of CO<sub>2</sub>.

The incorporation of other hetero-elements has been also reported.<sup>1149</sup> The iron-containing zeolite HZSM-5 photocatalyst was used to prepare a Ti-HZSM-5 hybrid material by the sol-gel method. The characterization study revealed that Ti species were highly dispersed in lower coordination state on the surface of HZSM-5 zeolite. The pristine HZSM-5 sample contains 0.03 wt% Fe which is tetrahedrally coordinated within the silica framework<sup>1150</sup> so the subsequent deposition of Ti species leads to the coexistence of Ti and Fe species on the surface of HZSM-5. Simultaneous photoexcitation under ultraviolet light allows the combination of two nearby excited states ((Fe<sup>2+</sup>-O<sup>-</sup>)<sup>\*</sup> and (Ti<sup>3+</sup>-O<sup>-</sup>)<sup>\*</sup>) that induce an increase of the excited electron concentration and an acceleration of the electron transfer rate over Ti-HZSM-5, as evidenced by the higher photocurrent response of the 0.99Ti-HZSM-5 sample, attributed to a higher efficiency of the separation of the photogenerated electron-hole pairs (Table 19, Entry 11).

The preparation of a series of FeO<sub>x</sub>/ZSM-5 composites with different Fe content for the photoreduction of CO<sub>2</sub> to CO and aldehyde was described.<sup>1151</sup> The unique interaction between the FeO<sub>x</sub> and the ZSM-5 support leads to a large dispersion of FeO<sub>x</sub> which generates alternative way to separate and migrate charge carriers and avoiding the recombination of photogenerated electron-hole pairs. Consequently, the lifetime of charge carriers was prolonged. The photocatalytic results revealed that an increasing Fe content allowed reaching a maximum for CO<sub>2</sub> conversion rate corresponding to 3wt% FeO<sub>x</sub>, with a further decrease. Therefore, over 3FeO<sub>x</sub>/ZSM-5 photocatalyst, maximum 17.6  $\mu\text{mol g}^{-1}\text{h}^{-1}$  high conversion rate of CO<sub>2</sub> with a high aldehyde selectivity (43.1%) were reached (Table 19, Entry 12).

In fact, the photocatalytic properties of zeolite has been associated to the presence of impurities in the sample such as Fe due to the presence of (Fe<sup>3+</sup>-O<sup>2-</sup>)/(Fe<sup>2+</sup>-O<sup>-</sup>)<sup>\*</sup> pair.<sup>1134,1152</sup> Thereby, the photocatalytic activity of commercial HZSM-5 zeolite for the photoreduction of CO<sub>2</sub> with H<sub>2</sub>O at room temperature has been explored.<sup>1138</sup> Under UV-light irradiation, Fe-O species act as excited (Fe<sup>2+</sup>-O<sup>-</sup>)<sup>\*</sup> photoactive sites for the CO<sub>2</sub> reduction reaction. The photocatalytic results revealed that the activity for CO production varied with the source of various zeolites. The highest 3.32  $\mu\text{mol g}^{-1}\text{h}^{-1}$  CO production rate was achieved over the HZSM-5 sample CO<sub>2</sub> (Table 19, Entry 13).

### 2.2.2. Conclusion

The Table 19 summarizes the main results obtained for CO<sub>2</sub> photoreduction in the presence of zeolites-based photocatalysts. The productivity and fuel production cannot be compared exactly

due to the variability in reaction conditions and reaction system configurations, but a general view can be given. The main drawbacks are the narrow absorption range of visible light together with low photoconversion efficiency, which limits the application of these photocatalytic systems. Compared to the study of semiconductor photocatalysts, the study of zeolite-based photocatalysts has been quite disregarded. The unique properties of microporous zeolites make them a viable photocatalytic alternative to sophisticated chemical and semiconductor processes. Their microstructures have a high surface area that favors a higher light uptake, a high CO<sub>2</sub> adsorption capacity and physicochemical and adsorption/desorption properties that allow the activation of the molecules, providing them with high reaction rate and photocatalytic activity. The synthesis and application of hierarchical zeolites to the development of photocatalysts should enable the enhancement of the unique properties of zeolites and counteract mass transport limitations. Hierarchical zeolites possess meso- and macroscale secondary porosity along with microporous primary structures. These materials then exhibit the conventional properties of zeolites with enhanced diffusion of molecules to solve the mass transport limitation. It is hoped that a combination of molecular simulation and machine learning techniques can be applied to the design of zeolite photocatalysts leading to an in-depth understanding of zeolite-based photocatalysts necessary for future research and development of the photoreduction of CO<sub>2</sub>.



**Table 19.** Catalytic activity of zeolite-based photocatalysts for reduction of CO<sub>2</sub>.

Entry	Photocatalyst	Reaction conditions	Main Products	Yield	Year	Ref
1	ex-Ti-oxide/Y-zeolite	Hg lamp ( $\lambda > 280$ nm), 50°C, H <sub>2</sub> O vapors	CH <sub>4</sub> /CH <sub>3</sub> COOH	7.5/5 $\mu\text{molg}_{\text{TiO}_2}^{-1}\text{h}^{-1}$	1998	1140
2	Ti-oxide/Y-zeolite		CH <sub>4</sub> /CH <sub>3</sub> COOH	5/0.25 $\mu\text{molg}_{\text{TiO}_2}^{-1}\text{h}^{-1}$	1998	1140
3	Pt/ex-Ti-oxide/Y-zeolite		CH <sub>4</sub> /CH <sub>3</sub> COOH	12.5/1 $\mu\text{molg}_{\text{TiO}_2}^{-1}\text{h}^{-1}$	1998	1140
4	Ti-Beta(F)	100W Hg lamp ( $\lambda > 250$ nm), 50°C, H <sub>2</sub> O vapors	CH <sub>4</sub> /CH <sub>3</sub> OH	0.8/0.6 $\mu\text{molg}^{-1}\text{h}^{-1}$	2001	1141
5	Ti-Beta(OH)		CH <sub>4</sub> /CH <sub>3</sub> OH	5.8/0.6 $\mu\text{molg}^{-1}\text{h}^{-1}$	2001	1141
6	TS-1	Hg lamp ( $\lambda = 280$ nm), H <sub>2</sub> (0.1 MPa)	CH <sub>4</sub>	3.5 $\mu\text{molg}^{-1}\text{h}^{-1}$	2001	1141
7	1Ag-16.9TiO <sub>2</sub> /TS-1	300W Xe lamp, H <sub>2</sub> O vapors	CO/CH <sub>4</sub>	3.16/0.47 $\mu\text{molg}^{-1}\text{h}^{-1}$	2021	1148
8	TS1 nanosheets	300W Xe lamp, 0.1 MPa, H <sub>2</sub> O vapors	CO/CH <sub>4</sub>	4/1.5 $\mu\text{molg}^{-1}$	2020	1143
9	hCN10/TS-1		CO/CH <sub>4</sub>	14/8 $\mu\text{molg}^{-1}$	2020	1143
10	1.5Ag/hCN10/TS-1		CO/CH <sub>4</sub>	25.5/15 $\mu\text{molg}^{-1}$	2020	1143
11	1Ti(0.03Fe)-ZSM-5	300 W Xe lamp, RT, aqueous solution	CO	2.1 $\mu\text{molg}^{-1}\text{h}^{-1}$	2017	1149
12	3FeO <sub>x</sub> /ZSM-5		HCOH	7.6 $\mu\text{molg}^{-1}\text{h}^{-1}$	2020	1151
13	ZSM-5	4W fluorescent UV light tubes ( $\lambda = 254$ nm), H <sub>2</sub> O vapors	CO	3.32 $\mu\text{molg}^{-1}\text{h}^{-1}$	2016	1138
14	SAPO-5 nanosheets	2x4W lamp ( $\lambda = 254$ nm), RT, H <sub>2</sub> O vapors	CH <sub>4</sub>	0.4 $\mu\text{molg}^{-1}\text{h}^{-1}$	2016	1144
15	SAPO-5 microrods		CH <sub>4</sub>	0.07 $\mu\text{molg}^{-1}\text{h}^{-1}$	2016	1144
16	PT/ZSM-5	150W Halogen lamp (60Wm <sup>-2</sup> ), aqueous solution	HCOOH/CH <sub>3</sub> COOH	12.6/166 $\mu\text{molg}^{-1}$	2019	1142

RT: room temperature

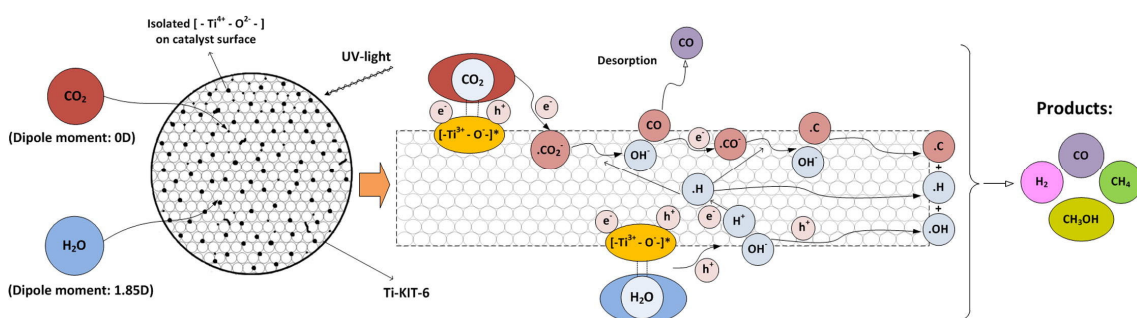
### 2.2.3. OMS-based catalysts for the photoreduction of CO<sub>2</sub>

The photoconversion process involves three crucial steps: the light adsorption on the surface of photocatalyst to produce electron-hole, the photogeneration carrier transport, and the oxidation-reduction reactions. The use of OMS based materials owing to their high surface area and their ability to support and host metallic nanoparticles and metal oxides, organometallic complexes and organic molecules to form specific active species allow improving the photocatalytic conversion of CO<sub>2</sub> of the pristine materials.

#### a) TiO<sub>2</sub>/OMS-based photocatalysts for the reduction of CO<sub>2</sub>

In 1998, the photocatalytic activity of Titanium oxide species embedded within the framework of OMS Ti-MCM-41 and Ti-MCM-48 prepared by a hydrothermal synthesis was explored for the reduction of CO<sub>2</sub> with H<sub>2</sub>O at 55°C to produce CH<sub>4</sub> and CH<sub>3</sub>OH in the gas phase.<sup>1153</sup> The characterization study indicated that Ti species were highly dispersed within the zeolite framework and in tetrahedral coordination. The photocatalytic reaction rate and selectivity showed to be dependent on the type of catalyst. Over Ti-containing OMS and zeolite type catalysts higher amount of CH<sub>3</sub>OH was produced while CH<sub>4</sub> was the main product over bulk TiO<sub>2</sub>. These results were attributed to the charge transfer photoexcited state of the highly dispersed titanium oxide species (Ti<sup>3+</sup>-O)\* (Table 20, Entry 1). The same trend was observed for the photocatalytic reduction of CO<sub>2</sub> over Ti-FSM-16. The CH<sub>3</sub>OH production was related to the local structure of the Ti-oxide species and the photocatalytic activity attributed to the charge transfer excited state dispersed tetrahedrally coordinated Ti-oxide species (Ti<sup>3+</sup>-O)\* (Table 20, Entry 2).<sup>1154</sup> More recently, the photoreduction of CO<sub>2</sub> was studied in the presence optimized Ti-mesoporous silica, Ti-SBA-15 and Ti-KIT-6, with different Si/Ti ratios.<sup>1155</sup> Photocatalytic study revealed that the Ti-KIT-6-calcined with Si/Ti = 100 exhibited the best photocatalytic performance for the reduction of CO<sub>2</sub> with water in the gas phase which was attributed to the higher accessibility to the active sites together with the lower number of TiO<sub>2</sub> agglomerates and higher number of isolated Ti species determined by UV-Vis, TEM and XPS analyses. The concentrations of OH groups was found to play a key role due to the competitive adsorption of CO<sub>2</sub> and H<sub>2</sub>O on the catalyst surface that influences the process selectivity towards CH<sub>4</sub> or CH<sub>3</sub>OH. The higher concentrations of the OH groups, detected from the FT-IR spectra for Ti-KIT-6-calcined with Si/Ti = 100, controls the adsorption properties and the reaction pathway (Table 20, Entry 3). Therefore, CH<sub>4</sub> formation increased with H<sub>2</sub>O adsorption increasing due to the greater hydrophilicity of the material. An appropriate way to boost activation of inert CO<sub>2</sub> molecule is its adsorption on the surface of any semiconductor to lower its energy barrier.<sup>1156</sup> Therefore, a mechanism starting with the CO<sub>2</sub> and H<sub>2</sub>O adsorption on isolated tetrahedrally

coordinated  $Ti^{4+}$  centers was proposed (Figure 130). The UV light absorption enables charge-transfer excited states  $(Ti^{3+}-O)^*$  with the photogenerated electron and hole localized on neighboring atoms responsible of higher lifetime of the excited  $Ti^{3+}-O^-$  ( $54 \mu s$ )<sup>1157</sup> in comparison to bulk  $TiO_2$  powder (nanosecond order). The interaction of  $CO_2$  and  $H_2O$  on the  $(Ti^{3+}-O)^*$  photoexcited active sites leads to the formation of intermediates species and finally to C, H and OH radicals further combined to generate  $CH_4$ ,  $H_2$  and  $CH_3OH$ . The source and intensity of the UV light and the  $H_2O/CO_2$  ratios are the key factors influencing the photoactivity of the catalyst, the main drawback of this system being that the sunlight is not short enough.



**Figure 130.** Reaction mechanism for the photocatalytic reduction of  $CO_2$  with  $H_2O$  vapor over Ti-KIT-6 photocatalyst. Reprinted with permission from ref.<sup>1155</sup> Copyright 2014 Elsevier B.V. All rights reserved.

b) Addition of a co-catalyst to  $TiO_2/OMS$ -based photocatalysts for the reduction of  $CO_2$

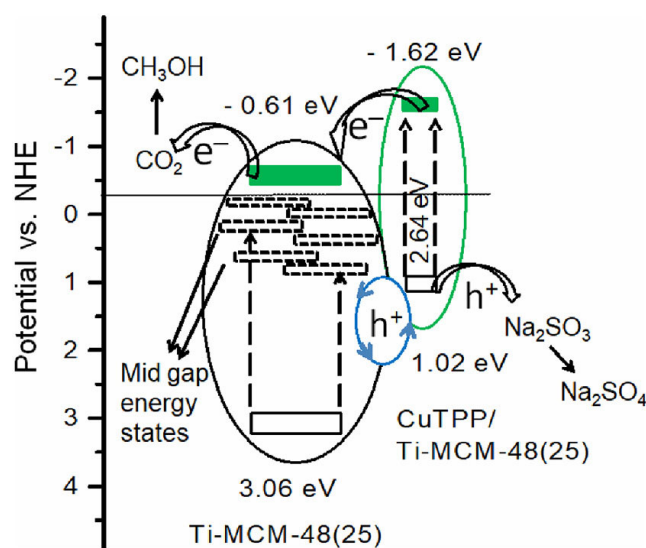
Different strategies have been developed to modify the acid/base properties of the photocatalyst surface in order to enhance the  $CO_2$  adsorption capacity, to promote the separation of photogenerated electron-hole pairs ( $e^-/h^+$ ) and to inhibit recombination such as the deposition or anchoring of organic and inorganic species.

i) *Effect of metallic doping over the photocatalytic activity for the reduction of  $CO_2$*

A series of  $TiO_2/SBA-15$  and  $Cu/TiO_2/SBA-15$  photocatalysts were synthesized by sol-gel route and used for the photoreduction of  $CO_2$  to methanol.<sup>1158</sup> The amount of  $TiO_2$  loading was shown to affect the crystallize size and the mesoporous structure of the catalyst, and an optimum of 45 wt%  $TiO_2$  with crystalline size  $\sim 5.5$  nm was defined. The addition of Cu as co-catalyst to trap photogenerated electrons and inhibit recombination electron-hole pairs ( $e^-/h^+$ ) allowed to enhance the catalytic activity. Therefore, over 2wt% $Cu/TiO_2/SBA-15$  catalyst, high photocatalytic activity was achieved with  $627 \mu mol g^{-1} h^{-1}$  methanol productivity (Table 20, Entry 4).

The effects of Cu-porphyrin (CuTPP) impregnation over the photocalytic properties of Ti-MCM-48 materials for the photoreduction of  $CO_2$  to  $CH_3OH$  was recently explored.<sup>1159</sup> The results showed that  $85.88 \mu mol g^{-1} L^{-1} CH_3OH$  productivity was reached over Ti-MCM 48 (Ti/Si=25) owing to the presence of excess of  $Ti^{3+}$  sites and mid gap energy states enabling the transfer of

photoexcited electrons from the  $\text{Ti}^{3+}$  sites selectively to the adsorbed  $\text{CO}_2$  molecules. Moreover, the impregnation of CuTPP (1.1wt%) enhanced methanol yield up to  $297 \mu\text{mol}\cdot\text{g}^{-1}\text{L}^{-1}$  (Table 20, Entry 5-6). The photoluminescence study confirmed the charge quenching due to the electron transition from the CuTPP to Ti-MCM-48 material. The interaction between CuTPP and Ti sites of Ti-MCM-48 was responsible for the increase in the amount of  $\text{Ti}^{3+}$  sites due to the effective interfacial charge transfer. A mechanism for the charge separation/transportation in heterojunctions and photoreduction of  $\text{CO}_2$  to  $\text{CH}_3\text{OH}$  over CuTPP/Ti-MCM-48 was proposed under visible light irradiation (Figure 131).



**Figure 131.** Proposed charge transfer mechanism for  $\text{CO}_2$  reduction to  $\text{CH}_3\text{OH}$  over CuTPP/Ti-MCM-48. Reprinted with permission from ref.<sup>1159</sup> Copyright 2018, Elsevier B.V. All rights reserved.

The photoactivity and selectivity of MgO/Ti-MCM-41 sample was also improved when the surface was decorated by Pt nanoparticles, reaching to  $8835 \text{ ppmg}^{-1}\text{h}^{-1}$   $\text{CH}_4$  productivity and 93%  $\text{CH}_4$  selectivity.<sup>1160</sup> These results were attributed to the rapid transfer of photogenerated electrons from molecular sieve to the cocatalyst (Pt) which favored the separation rate of the photogenerated electron and hole pairs and avoid their combination. When Pd was loaded, 94% CO selectivity was achieved (Table 20, Entries 8-9).

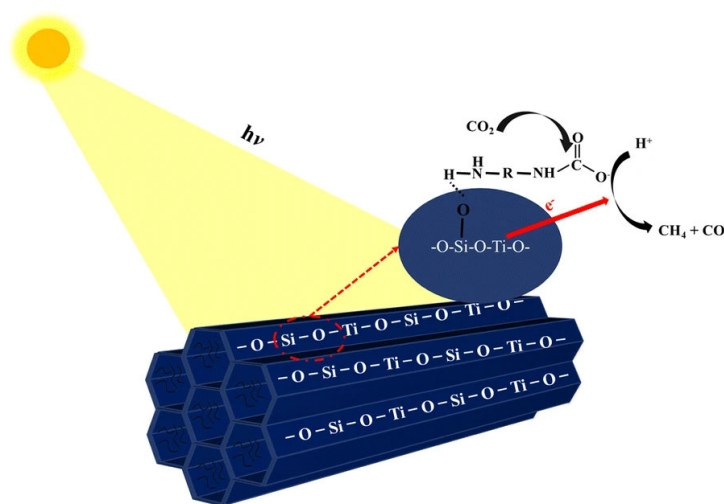
ii) *Effect of alkaline and earth metallic doping over the photocatalytic activity for the reduction of  $\text{CO}_2$*

A study of the effects of the modifications of the surface acidity and active sites by impregnation with basic-earth metal oxides and noble metal nanoparticles of Ti-MCM-41 samples prepared with different molar ratio of Si/Ti was developed for the reduction of  $\text{CO}_2$ .<sup>1160</sup> The modified Ti-MCM-41 samples were used as photocatalysts for the reduction of  $\text{CO}_2$  to  $\text{CH}_4$  and CO. Over Ti-MCM-41 (Si/Ti=10),  $93 \text{ ppmg}^{-1}\text{h}^{-1}$   $\text{CH}_4$  production and 29%  $\text{CH}_4$  selectivity were achieved, while the impregnation of MgO to Ti-MCM-41 increased the photoreduction activity by 1.5 times with 42%  $\text{CH}_4$  selectivity (Table 20, Entry 7). A study of Ca doping of Ti-MCM-41 effects was previously

described for the photoreduction of  $\text{CO}_2$  to  $\text{CH}_4$ .<sup>1161</sup> The Ca doping allowed to improve  $\text{CO}_2$  absorption and the reported catalytic performance of  $\text{Ca}/\text{Ti}_x\text{SiMCM-41}$  was superior to that of the  $\text{Ca}/\text{Ti}_x\text{SiO}_2$  nano-sized material.  $\text{CaO}$  is able to trap and release electrons in the conduction band of  $\text{TiO}_2$  and exhibits a high  $\text{CO}_2$  adsorption capacity, which improves the photoreduction of  $\text{CO}_2$ . On the other hand, the photoexcited electrons in CB can be efficiently accepted and transferred to the absorbed  $\text{CO}_2$  in  $\text{CaO}$ , so  $\text{Ca}/\text{Ti}_x\text{SiMCM-41}$  acts as an efficient reducing agent. Positive holes in CV can be trapped by  $\text{OH}$  or  $\text{H}_2\text{O}$  species. These processes promote the separation of photogenerated electron-hole pairs ( $e^-/h^+$ ), inhibit recombination and favor  $\text{CO}_2$  reduction. Nevertheless, an excess of Ti reduces the photoactivity probably due to the establishment of charge recombination centers within the semiconductor structure. Then  $\text{CH}_4$  was produced over  $\text{Ca}(10\text{wt\%})/\text{Ti}_{35}\text{Si}_{65}\text{MCM-41}$  catalyst at  $82.0 \mu\text{mol g}_{\text{cat}}^{-1}\text{L}^{-1}$  after 8 h TOS (Table 20, Entry 10). These results showed that modifications of surface acidity and active sites allowed controlling the selectivity and efficiency of the  $\text{CO}_2$  reduction process.

iii) *Effect of amines doping over the photocatalytic activity for the reduction of  $\text{CO}_2$*

The benefits of tetraethylenepentamine (TEPA) impregnated on Ti-MCM-41 sample over the photocatalytic activity was investigated for  $\text{CO}_2$  reduction to  $\text{CH}_4$ . The photocatalytic results showed that the presence of TEPA allowed to improve the adsorption and activation of  $\text{CO}_2$ . For a 1% TEPA content optimum dispersion of amino group was obtained and  $232 \text{ ppm g}^{-1}\text{h}^{-1}$   $\text{CH}_4$  productivity was reached (Figure 132) (Table 20, Entry 11). However, high impregnation amount of TEPA caused the blockage of the channel hampered  $\text{CO}_2$  conversion.<sup>1162</sup>



**Figure 132.** Proposed photocatalytic mechanism for  $\text{CO}_2$  reduction TEPA/Ti-MCM-41. Reprinted with permission from ref. <sup>1162</sup> Copyright 2020, Springer Nature B.V.

The photoreduction of  $\text{CO}_2$  was also studied in the liquid phase in the presence of monoethanolamine (MEA) over Ti-MCM-41 to produce methane.<sup>1163</sup> Monoethanolamine was used for both reductant and adsorption properties towards  $\text{CO}_2$ . The results indicated that this

novel method opens the possibility of integrating the most mature CO<sub>2</sub> capture process of MEA absorption and the CO<sub>2</sub> photocatalytic reduction process into one process. Ti-MCM-41 exhibited higher photocatalytic performance than commercial TiO<sub>2</sub>, and over Ti-MCM-41, 62.42 μmol<sub>g<sub>cat</sub></sub><sup>-1</sup> CH<sub>4</sub> productivity was reached under UV light that limits the application of this process (Table 20, Entry 12).

c) Perovskite/OMS-based photocatalysts for the reduction of CO<sub>2</sub>

A MCM-41@CBB (Cs<sub>3</sub>Bi<sub>2</sub>Br<sub>9</sub>) composite has been prepared following a facile and effective impregnation method to confine Cs<sub>3</sub>Bi<sub>2</sub>Br<sub>9</sub> nanoparticles (lead-free halide perovskite) in MCM-41 molecular sieve.<sup>1164</sup> This MCM-41 @CBB has exhibited a good photocatalytic performance for the reduction of CO<sub>2</sub> to CO under visible light irradiation with 17.24 μmol·g<sup>-1</sup>h<sup>-1</sup>. This result was attributed to the space-confined growth of CBB in MCM-41, which promotes the carrier lifetime meaningfully, which is favorable for electron-hole pair separation and subsequent transfer. Other composite were prepared using SBA-3, SBA-15 and MCM-48 as support. The photocatalytic study revealed that these photocatalysts exhibited activities 2.97-13.4 fold higher than that of pure CBB, with 25.4, 23.7 and 5.62 μmol·g<sup>-1</sup>h<sup>-1</sup> CO productivities, over SBA-3@CBB, SBA-15@CBB and MCM-48@CBB, respectively. CO selectivity was close to 78% for CBB and almost 100% for molecular sieve photocatalysts@CBB (Table 20, Entries 13-16). Moreover, these results are comparable with those reported for many lead halide perovskites, and among the best of the lead-free perovskites. This work demonstrated that the space-confined growth of CBB in molecular sieve constitutes an excellent strategy to improve the photocatalytic CO<sub>2</sub> reduction performance and stability of lead-free perovskite.

d) CoO/OMS-based photocatalysts for the reduction of CO<sub>2</sub>

The benefits of CoO nanoparticles deposition on SBA-15 over the photocatalytic performance was explored.<sup>1165</sup> High photocatalytic activity was observed for the reduction of CO<sub>2</sub> to CO with 83% CO selectivity and CO production rate of 25 626 μmol h<sup>-1</sup> g<sup>-1</sup>. The results were attributed to enhanced dispersion and stability of the CoO NPs and the presence of hydroxyl groups on the surface, absorption capacity of SBA-15 support (Table 20, Entry 17).

#### 2.2.4. Conclusion

The Table 20 summarizes the main results obtained for CO<sub>2</sub> photoreduction in the presence of OMS-based photocatalysts. The productivity and fuel performance cannot be compared exactly due to the change in reaction conditions and reactor configuration and catalyst preparation procedure, but a general view can be given. In general, the main drawbacks are the narrow absorption range of visible light together with low photoconversion efficiency (yield), which limits the application of these photocatalytic systems.

### 2.2.5. Conclusion

The main drawbacks for the photoreduction of CO<sub>2</sub> to simple fuel molecule are the narrow absorption range of visible light together with low photoconversion efficiency, which limits the application of these photocatalytic systems. In comparison to the large number of studies reported for semiconductor photocatalysts, the study of zeolite-based photocatalysts has been quite disregarded. This fact has been attributed to the insulator property of zeolite. Nevertheless, the photocatalytic activity of zeolite associated to the possible photoexcitation of the (M<sup>n+</sup>-O<sup>2-</sup>) to (M<sup>(n-1)+</sup>-O<sup>-</sup>)\* pair as well as the the key role of hydrophilic-hydrophobic properties governed by the presence of silanol groups to promote proton and charge transfer and water adsorption, have been fully recognized and demonstrated. Moreover, the unique properties of zeolites and OMS make them a viable photocatalytic alternative to sophisticated chemical and semiconductor processes. Their porous structures have a high surface area that favors a higher light uptake, a high CO<sub>2</sub> adsorption capacity and tunable physicochemical and adsorption/desorption properties that allow the activation of the molecules, providing them with high reaction rate and photocatalytic activity. Moreover, the synthesis and application of hierarchical zeolites to the development of photocatalysts should enable the enhancement of the unique properties of zeolites and counteract mass transport limitations.

A combination of molecular simulation, machine learning techniques and in situ spectroscopy should help to determine the reaction mechanism and find the active sites that work to finally establish the structure-activity/selectivity relationship. This understanding is necessary for the rational design of zeolite and OMS-based photocatalysts for the reduction of CO<sub>2</sub>.

**Table 20.** Catalytic activity of OMS-based photocatalysts for reduction of CO<sub>2</sub>.

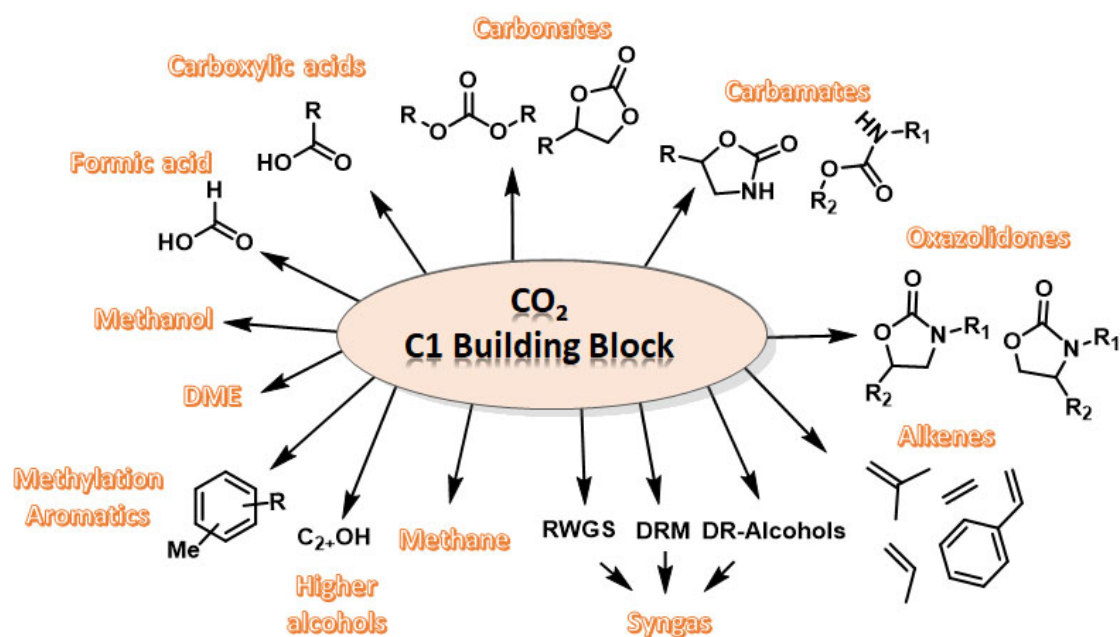
Entry	Photocatalyst	Reaction conditions	Main Products	Yield	Year	Ref
1	Ti-MCM-41	Hg lamp ( $\lambda > 280$ nm), 55°C.	CH <sub>4</sub> /42°C.	2.8/1.5 $\mu\text{molg}_{\text{TiO}_2}^{-1}\text{h}^{-1}$	1998	1153
2	Ti-FSM-16	100 W Hg lamp, 50°C.	CH <sub>4</sub> /CH <sub>3</sub> OH	260/60 $\mu\text{molg}^{-1}\text{h}^{-1}$	2001	1154
3	Ti-KIT-6	UV lamp (300 W), water vapors	CO/CH <sub>4</sub>	18.6/6.7 $\mu\text{molg}^{-1}\text{h}^{-1}$	2015	1155
4	Cu/TiO <sub>2</sub> /SBA-15	400W metal halide lamp, 0.1N NaOH solution, 42°C.	CH <sub>3</sub> OH	627 mmolg <sup>-1</sup> h <sup>-1</sup>	2009	1158
5	Ti-MCM-48	Solution: 0.1M NaOH/0.1M Na <sub>2</sub> SO <sub>3</sub> , Xe lamp (33 mWcm <sup>-2</sup> ), 25°C.	CH <sub>3</sub> OH	85 $\mu\text{molg}^{-1}\text{L}^{-1}$	2018	1159
6	CuTPP/Ti-MCM-48		CH <sub>3</sub> OH	297 $\mu\text{molg}^{-1}\text{h}^{-1}$	2018	1159
	Ti-MCM-41	600W Hg lamp, 30°C, water solution	CH <sub>4</sub>	93 ppm g <sup>-1</sup> h <sup>-1</sup>	2019	1160
7	MgO/Ti-MCM-41		CH <sub>4</sub>	139 ppm g <sup>-1</sup> h <sup>-1</sup>	2019	1160
8	Pt/MgO/Ti-MCM-41		CH <sub>4</sub>	8835 ppm g <sup>-1</sup> h <sup>-1</sup>	2019	1160
9	Pd/MgO/Ti-MCM-41		CO	1623 ppm g <sup>-1</sup> h <sup>-1</sup>	2019	1160
10	Ca/Ti-MCM-41	Hg lamp (6Wcm <sup>-2</sup> ); $\lambda = 365$ nm, 30°C, 0.1 MPa, H <sub>2</sub> O/CO <sub>2</sub> =2, 0.2g cat.	CH <sub>4</sub>	82 $\mu\text{molg}^{-1}\text{L}^{-1}$	2015	1161
11	TEPA/Ti-MCM-41	600W Hg lamp, 30°C, water solution	CH <sub>4</sub>	232 ppm g <sup>-1</sup> h <sup>-1</sup>	2020	1162
12	Ti-MCM-41	9W and 254 nm of a UVC lamp	CH <sub>4</sub>	62.42 $\mu\text{molg}^{-1}\text{h}^{-1}$	2014	1163
13	MCM-41@CBB	300 W Xe lamp equipped with 420 nm cut-off filter ( $\lambda > 420$ nm, 350 mWcm <sup>-2</sup> ), 25°C, 0.1 MPa	CO	17.24 $\mu\text{molg}^{-1}\text{h}^{-1}$	2022	1164
14	SBA-3@CBB		CO	25.4 $\mu\text{molg}^{-1}\text{h}^{-1}$	2022	1164
15	SBA-15@CBB		CO	23.7 $\mu\text{molg}^{-1}\text{h}^{-1}$	2022	1164
16	MCM-48@CBB		CO	5.62 $\mu\text{molg}^{-1}\text{h}^{-1}$	2022	1164
17	Co/SBA-15	TEOA/CH <sub>3</sub> CN/H <sub>2</sub> O (v/v, 1:2:1), ambient conditions, white LED lamp	CO	25 626 $\mu\text{molh}^{-1}\text{g}^{-1}$	2019	1165

TEOA=triethanolamine, TEP=tetraethylenepentamine



## D Summary and perspectives.

The use of CO<sub>2</sub> as a C1 building block to mitigate CO<sub>2</sub> emissions and at the same time produce sustainable chemicals or fuels is a challenging and promising alternative to meet the global demand for chemicals and energy. In this review, we have collected the different reactions involving zeolite and OMS based catalysts to convert CO<sub>2</sub> into valuable chemicals and fuels (Figure 133). Their flexibility in the composition and structure, features as support and/or host of metal, metalorgano-complex, organo-catalyst as well as robustness were highlighted exhibiting the great potential of zeolite and OMS catalysts to boost CO<sub>2</sub> chemical conversion. Today, the use of CO<sub>2</sub> as a building block still requires a lot of effort, fundamental knowledge and insights to understand the mechanisms, determine the intermediate species and the active centres for each stage. The stability of CO<sub>2</sub> and the high activation energy barrier to overcome thermodynamic equilibrium, requiring high energy consumption, are the main impediments and bottleneck to commercialisation that keep these processes still in the laboratory research stage.



**Figure 133** Scheme of CO<sub>2</sub> conversion to valuable chemicals and fuels using zeolite- and OMS- based catalysts discussed in this review.

From environmentally standpoints, the design of reactor and energy efficiency is key and heat will be based on renewable (wind, water, sun) or nuclear energy sources to minimize carbon footprint and meet carbon neutrality. Moreover, the high temperature use enhances the formation of undesirable products making crucial the design and development of efficient and selective catalysts. For the CO<sub>2</sub> conversion heterogeneous catalysts are attractive and preferred for industrial implementation due to their catalytic features such as activity, robustness, efficiency, recovery and recycling, easy handling making them economically advantageous,

environmentally friendly minimizing wastes. To enable CO<sub>2</sub> conversion, efficient and high-throughput CO<sub>2</sub> capture technologies with adequate purity, probably located at point sources, will first have to be available. In the same way, for hydrogenation process, H<sub>2</sub> will be available and green. Despite these barriers, CO<sub>2</sub> constitutes an indisputable and necessary source of carbon to produce the chemicals and fuels that our society requires and on which it depends.

In the present review, we revise and examine the zeolite and OMS based materials activity and opportunities to convert CO<sub>2</sub> into valuable chemicals and fuels. We summarise the main advances, limitations and the major challenges to be overcome in order to successfully convert anthropogenic CO<sub>2</sub>. The synthesis of cyclic carbonates by cycloaddition of CO<sub>2</sub> and epoxides in the presence of advanced multifunctional catalysts based on zeolites and OMS has been extensively studied, and the main issues are low catalyst stability and few recycling opportunities, as well as the use of co-catalysts and harsh operating conditions that hinder the feasibility of this transformation. However, we can highlight the catalytic performance of zeolite and OMS containing the structure directing agent as active sites for catalyzing the cycloaddition with interesting opportunities for stability and recycling, and limited catalyst cost. The cycloaddition constitutes an attractive and important approach since involves a high-energy three membered ring substrate, being 100% atom economy reaction. Moreover, the use of CO<sub>2</sub> constitutes a great opportunity to substitute toxic carbonylating agents such as phosgene and derivatives. Nevertheless, the inertness and stability of CO<sub>2</sub> proved to be the major impediments. On other hand, marginal routes have been explored to produce cyclic carbonates such as olefin oxidative carboxylation and CO<sub>2</sub> carbonylation of diols that received low consideration. On the other hand, the synthesis of dialkyl-carbonates is thermodynamically limited and received poor attention as it is the case of the preparation of acyclic carbamates or 2-oxazolidinones.

The synthesis of carboxylic acid such as acetic acid by reaction between CH<sub>4</sub> and CO<sub>2</sub>, and propanoic acid by reaction between ethane and CO<sub>2</sub> are practically impossible from industrial perspective because of high energetic barriers. Respect to the synthesis of formic acid, the few references found in the bibliography evidence that CO<sub>2</sub> hydrogenation using zeolite and OMS based catalysts has been insufficiently explored besides the requirement of novel and efficient catalytic system for the very challenging production of formic acid as potential way to chemically store hydrogen.

The direct hydrogenation of CO<sub>2</sub> in methanol to industrial production is still an immature process and still requires improvement of the catalytic performance in terms of activity, stability and MeOH selectivity. For future study, the adsorption properties (hydrophobicity) of the surface should be considered while exhaustive and comprehensive studies of active species and

intermediates of reaction will be required for a successful ab initio design of an efficient and robust catalyst, taking into account thermodynamics since the reaction is feasible from low temperature. Considering the morphology, topology, thermal stability, hydrophobic/hydrophilic, acid/base and redox properties of zeolites and OMS materials, greater consideration should focus on these materials when designing new catalysts.

The direct transformation of CO<sub>2</sub> into DME is an attractive route considering the environmental and economic issues involved. Nevertheless, the developed catalysts exhibited limited DME selectivity because of high CO production, in addition to the drastic deactivation catalyst due to water production. Nonetheless, the catalytic performance of La-Cu-ZnO-Al<sub>2</sub>O<sub>3</sub>/HZSM-5 and Cu-ZnO-Al<sub>2</sub>O<sub>3</sub>/HZSM-5 due to the good DME selectivity and productivity were highlighted. However, the direct transformation of CO<sub>2</sub> into DME remained still an immature technology from an industrial perspective and studies taking into account catalyst stability and regeneration step should be performed.

Among CO<sub>2</sub> hydrogenation reactions, CO<sub>2</sub> methanation is the most favoured reaction from thermodynamics. The activation of CO<sub>2</sub> is of paramount importance to reach high methanation activity at lower reaction temperature constituting crucial parameters, the oxygen mobility and basic properties of the support, as well as the hydrophobicity of the catalytic surface to limit the water adsorption and inhibitory effect. Between the different based zeolite and OMS based catalysts herein reported, USY based catalysts exhibited great potential owing to improved stability provided by post synthesis treatments. From commercial and industrial perspectives, several catalytic processes and reactors technology are available that should be transferred to CO<sub>2</sub> methanation as high conversion and CH<sub>4</sub> selectivity closed to 100% are reached at laboratory scale. However, the viability for large scale CO<sub>2</sub> fixation also depends on readily availability and price of CO<sub>2</sub> and H<sub>2</sub> issued from waste and/or renewables sources in order to develop sustainable process, based on heat produced from renewable or nuclear energy to move towards zero carbon footprint.

CO<sub>2</sub> hydrogenation to C<sub>2+</sub>OH is an attractive process to obtain new building blocks molecules and energy carrier. Although this process has been widely studied in the last decades, few works focused on the development of catalysts based on zeolites or OMS besides the benefits of confinement effect, nanoparticle stabilization by electronic features and shape-selectivity (reactant, product, transition state). The best yield has been achieved over RhFeLi/TiO<sub>2</sub> catalyst with 4.91% C<sub>2+</sub>OH yield, maximum 100% ethanol selectivity on the organic product basis has been reached over Cu@Na-Beta catalyst. The main challenge is to improve C<sub>2+</sub>OH yield and selectivity. To this end, ab initio design of the catalysts, introducing the necessary active sites, rationalised and simulated by computational chemistry, can be a decisive tool. Zeolites and OMS

based catalysts constitute good candidate for the development of selective and stable catalysts for CO<sub>2</sub> hydrogenation to C<sub>2+</sub>OH, and have been so far under-considered.

CO<sub>2</sub> hydrogenation to gasoline, olefins and aromatics offers new opportunities to convert CO<sub>2</sub> into value-added products and pave a path to the CO<sub>2</sub> circularity. In the last decade, significant advances in the development of tandem catalysts based on metal oxides and zeolites have been made for the selective hydrogenation of CO<sub>2</sub> to lower olefins (C<sub>2</sub>-C<sub>4</sub>), gasoline (C<sub>5</sub>-C<sub>11</sub>) and aromatics (C<sub>6</sub>-C<sub>8</sub>) of wide interest for the chemical industry. The high activity of heterogeneous catalyst is usually attribute to the synergy between the active sites and the support and/or the promoter. Improvement of process selectivity are still required and challenging and should avoid expensive separation step. Thus, new studies for the specific modifications of zeolite morphology such as pore-size tuning and the poisoning of external acid sites, should allow controlling the hydrocarbon product selectivity. Undoubtedly, the future tandem catalyst for direct hydrogenation of CO<sub>2</sub> to C<sub>2+</sub> will be based on zeolite-type material.

The CO<sub>2</sub> transformation into syngas constitutes a winning approach towards the sustainable production of chemicals and fuels towards carbon neutral society. Further syngas conversion into MeOH or through Fischer Tropsch process constitute direct routes to the production of fuels and chemicals through technologies already explored, developed and implemented. Accordingly, the production of CO from RWGS is challengeable because of its huge interest as building block. Numerous studies investigated RWGS process but new efforts are still required to determine the reaction mechanism and achieve comprehensive knowledge about the nature of active sites to finally establish structure-activity/selectivity relationship. In the present review, we recompiled few works revealing that the potential of zeolites and OMS materials has been scarcely considered and undervalued. These studies described important strategies to maximize CO selectivity and CO<sub>2</sub> conversion, to enhance metal-support interaction and stability, to improve CO<sub>2</sub> adsorption/activation and fast and easy CO desorption, which are determinant for the design of new RWGS catalysts. Future studies of catalytic stability and deactivation are also essential for the RWGS development and implementation. Much efforts have to be devoted to a greater knowledge and understanding of RWGS and a final push is needed to move from laboratory studies to the industrial scale, where zeolites and OMS based materials should play a more relevant role.

The catalytic DRM into syngas (H<sub>2</sub>+CO) enables the simultaneous mitigation of two main greenhouse gases, CH<sub>4</sub> and CO<sub>2</sub>, is 100% atom efficiency process and provides a highly regarded H<sub>2</sub>/CO ratio of 1 for further industrial conversion. However, in practice DRM requires high energy extra consumption due to endothermicity, inducing fast catalyst deactivation, which compromises its industrial implementation as environmental-friendly method to date.

Therefore, the design of robust and efficient catalyst at “low temperature” is topical and very challenging. On the other hand, the viability of the technology depends on the capture and availability of both CO<sub>2</sub> and CH<sub>4</sub>, which cannot be of fossil source. The present review illustrates the high activity of Ni-based zeolites and OMS catalysts despite the deactivation due to Ni sintering and coke deposition that in turn may block access to the active sites and plug the reactor in long-term tests. The use of high surface area support and bi- or multi metal-doping constitute the main strategies to enhance the metal-support interaction and match suitable acid-base and redox properties. Zeolites and OMS offered great opportunities for the design and development of robust and efficient DRM catalyst but the catalytic performance remained far from an industrial application. The studies requires long-term stability test and catalytic regeneration step while the operating temperature is very high (>750°C), with catalytic performance close to thermodynamic equilibrium. From materials standpoints, the small pore size system of zeolites compared to mesoporous materials may be a weakness to reach a high dispersion of small metal nanoparticles and probably more prone to pore blockage. A large collection of references shows the potential of SBA-15 as support, which makes SBA-15 a great candidate to the development of DRM catalyst owing to high surface area, confinement effect of mesoporous structure and thermal stability that should allow achieving high Ni nanoparticles dispersion and stability using optimum preparation method and suitable metallic promoters. Furthermore, the design of DRM reactor alternating cycles of reaction and catalysts regeneration should be key. On the other hand, the combination of POM and DRM processes offers opportunities to overcome the main limitation of energetic cost taking advantage of the POM exothermicity, although POM + DRM route has been insufficiently explored, and less in the presence of zeolite and OMS catalysts.

Other route based on renewable feedstock to produce syngas is the dry reforming (DR) of alcohols issued from bio-resources such as bio-ethanol and glycerol issued from biodiesel, and to effectively close carbon cycle providing valuable chemicals and using the main greenhouse gas, mitigating the effect of anthropogenic CO<sub>2</sub>. Besides, dry reforming of ethanol and glycerol are emerging technologies that require knowledge and mechanistic insights to the design of efficient catalysts, and reach sustainable syngas manufacturing, and additionally to solve the crisis of glycerol as biodiesel byproduct. However, from the point of view of global syngas production and consumption, and the urgency to mitigate CO<sub>2</sub> emissions, the DRG would constitute an almost marginal alternative and DRE results more promising and attractive approach.

As alternative to catalytic dehydrogenation, oxidative dehydrogenation using CO<sub>2</sub> as soft oxidant emerged and strengthened due to several advantages from energetic, thermodynamic and

kinetic (rate of reaction, higher alkene selectivity) standpoints, suppressing substrate and product over-oxidation, reducing carbon deposits and consuming CO<sub>2</sub>, the main greenhouse gas. Then, oxidative dehydrogenation of alkanes has been extensively investigated as energy-saving and more environmentally friendly strategy to produce alkenes. The use of CO<sub>2</sub> as soft oxidant for alkanes ODH involves several advantages to ensure and enhance the catalytic activity due to its ability to activate ODH directly promoting alkane ODH or by combination of alkane dehydrogenation and RWGS, and thus favouring thermodynamics. In this review, the collected results for EB ODH revealed that high ST selectivity was reached at good conversion level. Nevertheless, the lifetime of the catalysts has been insufficiently studied and future studies devote more efforts to study the robustness of catalysts and reactor configurations to achieve and maintain high EB yield and selectivity over a long operating time, combining reaction and regeneration stages. SBA-15 exhibits great potential in contrast to zeolite that despite its better thermal stability and robustness, presents limitation to efficiently and homogeneously disperse high amount of metallic oxide due to the diffusion restrictions and the blockage of pores. Regarding ethane ODH, most of the catalysts are CrO<sub>x</sub>-based, implying severe limitations due to the carcinogenicity of chromium species and hazardous catalyst preparation, use and elimination. Besides, 5wt%Cr/SBA-15/Al<sub>2</sub>O<sub>3</sub>/FeCrAl catalytic performance allowed reaching interesting goals of production and catalyst stability with good 63% ethylene yield, over 1100h highlighting the potential of SBA-15 as support. Actually, the catalyst success will depend on catalyst and operation costs, catalyst stability besides the catalytic performances and features. Propane ODH with CO<sub>2</sub> was also reviewed and good catalytic data were reached, although propane selectivity and productivity must be further improved.

The main drawbacks for the photoreduction of CO<sub>2</sub> to simple fuel molecule are the narrow absorption range of visible light together with low photoconversion efficiency, which limits the application of these photocatalytic systems. The photocatalytic activity of zeolite associated to the possible photoexcitation of the (M<sup>n+</sup>-O<sup>2-</sup>) to (M<sup>(n-1)+</sup>-O<sup>-</sup>)\* pair as well as the the key role of hydrophilic-hydrophobic properties governed by the presence of silanol groups to promote proton and charge transfer and water adsorption, have been fully recognized and demonstrated. Moreover, the unique properties of zeolites and OMS make them a viable photocatalytic alternative to sophisticated chemical and semiconductor processes. Their adjustable porous structures have a high surface area that favors a higher light harvesting, a high CO<sub>2</sub> adsorption capacity and tunable physicochemical and adsorption/desorption properties that allow the activation of the molecules, providing them with high reaction rate and photocatalytic activity. Moreover, the future synthesis and application of hierarchical zeolites to the development of photocatalysts should be a new breakthrough to improve mass transfer and ensure their

development. Future research based on a combination of molecular simulation, machine learning techniques and in situ spectroscopy should help to determine the reaction mechanism and find the active sites that work to finally establish the structure-activity/selectivity relationship. This understanding is necessary for the rational design of zeolite and OMS-based photocatalysts for the reduction of CO<sub>2</sub>.

In the present review, we have analyzed the current state of the art in the zeolite and OMS based materials activity and opportunities to convert CO<sub>2</sub> into valuable chemicals essential for our daily lives, and to pave the way towards reducing carbon footprint. The development of efficient and competitive CO<sub>2</sub> capture and green H<sub>2</sub> technologies are essential to move towards CO<sub>2</sub> conversion, while the potential of zeolite and OMS based materials should be part of the success. Hence, we hope that this review will be a useful contribution to the scientific community and will constitute a new stimulus for the use of zeolite and OMS based materials, and the development of new processes and technologies to boost the conversion of CO<sub>2</sub> into chemicals and fuels.

## E References

- 1 J. Stephenson, K. Newman and S. Mayhew, *J Public Heal.*, 2010, **32**, 150–156.
- 2 <https://www.co2.earth>, *CO2 - Earth*.
- 3 K. M. K. Yu, I. Curcic, J. Gabriel and S. C. E. Tsang, *ChemSusChem*, 2008, **1**, 893–899.
- 4 R. Martín and A. W. Kleij, *ChemSusChem*, 2011, **4**, 1259–1263.
- 5 A. S. Lindsey and H. Jeskey, *Chem. Rev.*, 1957, **57**, 583–620.
- 6 J. Artz, T. E. Müller, K. Thenert, J. Kleinekorte, R. Meys, A. Sternberg, A. Bardow and W. Leitner, *Chem. Rev.*, 2018, **118**, 434–504.
- 7 E. Catizzone, G. Bonura, M. Migliori, F. Frusteri and G. Giordano, *Molecules*, 2017, **23**, 31.
- 8 C. Federsel, R. Jackstell and M. Beller, *Angew. Chemie Int. Ed.*, 2010, **49**, 6254–6257.
- 9 N. Hazari, N. Iwasawa and K. H. Hopmann, *Organometallics*, 2020, **39**, 1457–1460.
- 10 Y. Sun, Z. Lin, S. H. Peng, V. Sage and Z. Sun, *J. Nanosci. Nanotechnol.*, 2019, **19**, 3097–3109.
- 11 A. Dokania, A. Ramirez, A. Bavykina and J. Gascon, *ACS Energy Lett.*, 2019, **4**, 167–176.
- 12 J. W. Maina, C. Pozo-Gonzalo, L. Kong, J. Schütz, M. Hill and L. F. Dumée, *Mater. Horizons*, 2017, **4**, 345–361.
- 13 H. He, J. A. Perman, G. Zhu and S. Ma, *Small*, 2016, **12**, 6309–6324.
- 14 M. Aresta, A. Dibenedetto and A. Angelini, *Chem Rev*, 2014, **114**, 1709–1742.
- 15 W.-L. Dai, S.-L. Luo, S.-F. Yin and C.-T. Au, *Appl. Catal. A Gen.*, 2009, **366**, 2–12.
- 16 M. Ding, R. W. Flaig, H. L. Jiang and O. M. Yaghi, *Chem Soc Rev*, 2019, **48**, 2783–2828.
- 17 IUPAC, <https://goldbook.iupac.org/terms/view/C00876>.
- 18 Y. Shi, S. Hou, X. Qiu and B. Zhao, *Top Curr Chem*, 2020, **378**, 11.
- 19 J. C. Tan and A. K. Cheetham, *Chem. Soc. Rev.*, 2011, **40**, 1059–1080.
- 20 K. W. Chapman, G. J. Halder and P. J. Chupas, *J. Am. Chem. Soc.*, 2009, **131**, 17546–17547.
- 21 A. J. Howarth, Y. Liu, P. Li, Z. Li, T. C. Wang, J. T. Hupp and O. K. Farha, *Nat. Rev. Mater.*, 2016, **1**, 15018.
- 22 M. Colilla and M. Vallet-Regí, in *Comprehensive Biomaterials II*, Elsevier, 2017, pp. 644–685.
- 23 N. A. Mokri, O. Pei Ching, H. Mukhtar and C. Thiam Leng, *J. Phys. Sci.*, 2019, **30**, 145–168.
- 24 S. Cejka, Jiri; Corma, Avelino; Zones, Ed., *Zeolites And Catalysis: Synthesis, Reactions And Applications, Volume 2*, Wiley-VCH Verlag GmbH & Co. KGaA, Weinheim, Germany, 2010.
- 25 M. Mishra and S. K. Jain, *Proc. Natl. Acad. Sci. India Sect. B - Biol. Sci.*, 2011, **81**, 250–259.
- 26 B. M. Weckhuysen and J. Yu, *Chem. Soc. Rev.*, 2015, **44**, 7022–7024.
- 27 A. Quindimil, U. De-La-Torre, B. Pereda-Ayo, J. A. González-Marcos and J. R. González-Velasco, *Appl. Catal. B Environ.*, 2018, **238**, 393–403.
- 28 L. B. Baerlocher, C., and McCusker, Database of Zeolite Structures, <http://www.iza-structure.org/databases/>.
- 29 Y. Li, L. Li and J. Yu, *Chem*, 2017, **3**, 928–949.
- 30 M. E. Davis, C. Saldarriaga, C. Montes, J. Garces and C. Crowdert, *Nature*, 1988, **331**, 698–699.
- 31 J.-L. Paillaud, B. Harbuzaru, J. Patarin and N. Bats, *Science (80-. )*, 2004, **304**, 990 LP – 992.
- 32 J. Jiang, Y. Yun, X. Zou, J. L. Jorda and A. Corma, *Chem. Sci.*, 2015, **6**, 480–485.
- 33 A. Corma, M. J. Díaz-Cabañas, J. Jiang, M. Afeworki, D. L. Dorset, S. L. Soled and K. G. Strohmaier, *Proc. Natl. Acad. Sci. U. S. A.*, 2010, **107**, 13997–14002.
- 34 B. J. Schoeman, J. Sterte and J.-E. Otterstedt, *J. Chem. Soc. Chem. Commun.*, 1993, 994–995.
- 35 L. Tosheva and V. P. Valtchev, *Chem. Mater.*, 2005, **17**, 2494–2513.
- 36 R. Martínez-Franco, C. Paris, M. E. Martínez-Armero, C. Martínez, M. Moliner and A. Corma, *Chem. Sci.*, 2016, **7**, 102–108.
- 37 E. Koohsaryan and M. Anbia, *Chinese J. Catal.*, 2016, **37**, 447–467.
- 38 L. Wang, Z. Zhang, C. Yin, Z. Shan and F.-S. Xiao, *Microporous Mesoporous Mater.*, 2010, **131**, 58–67.
- 39 R. Bai, Y. Song, Y. Li and J. Yu, *Trends Chem.*, 2019, **1**, 601–611.
- 40 Y. Tao, H. Kanoh, L. Abrams and K. Kaneko, *Chem. Rev.*, 2006, **106**, 896–910.
- 41 E. Leclercq, A. Finiels and C. Moreau, *J. Am. Oil Chem. Soc.*, 2001, **78**, 1161–1165.
- 42 P. Concepción-Heydorn, C. Jia, D. Herein, N. Pfänder, H. . Karge and F. . Jentoft, *J. Mol. Catal. A Chem.*, 2000, **162**, 227–246.
- 43 A. Corma, S. Iborra, S. Miquel and J. Primo, *J. Catal.*, 1998, **173**, 315–321.
- 44 M. J. Climent, A. Corma, S. Iborra and J. Primo, *J. Catal.*, 1995, **151**, 60–66.
- 45 G. Sastre and A. Corma, *Chem. Phys. Lett.*, 1999, **302**, 447–453.
- 46 M. Boronat, P. Concepcion, A. Corma, M. Renz and S. Valencia, *J. Catal.*, 2005, **234**, 111–118.
- 47 L. Liu and A. Corma, *Trends Chem.*, 2020, **2**, 383–400.
- 48 M. Moliner, J. E. Gabay, C. E. Kliewer, R. T. Carr, J. Guzman, G. L. Casty, P. Serna and A. Corma, *J. Am. Chem. Soc.*, 2016, **138**, 15743–15750.
- 49 Q. Sun, N. Wang, T. Zhang, R. Bai, A. Mayoral, P. Zhang, Q. Zhang, O. Terasaki and J. Yu, *Angew. Chemie Int. Ed.*, 2019, **58**, 18570–18576.
- 50 L. Liu, M. Lopez-Haro, C. W. Lopes, C. Li, P. Concepcion, L. Simonelli, J. J. Calvino and A. Corma, *Nat. Mater.*, 2019, **18**, 866–873.
- 51 L. Liu, M. Lopez-Haro, D. M. Meira, P. Concepcion, J. J. Calvino and A. Corma, *Angew. Chemie Int. Ed.*, 2020,



- 59, 15695–15702.
- 52 M. Shamzhy, M. Opanasenko, P. Concepción and A. Martínez, *Chem. Soc. Rev.*, 2019, **48**, 1095–1149.
- 53 J. Xu, Q. Wang and F. Deng, *Acc. Chem. Res.*, 2019, **52**, 2179–2189.
- 54 L.-H. Chen, M.-H. Sun, Z. Wang, W. Yang, Z. Xie and B.-L. Su, *Chem. Rev.*, 2020, **120**, 11194–11294.
- 55 D. Kerstens, B. Smeyers, J. Van Waeyenberg, Q. Zhang, J. Yu and B. F. Sels, *Adv. Mater.*, 2020, **32**, 2004690.
- 56 D. P. Serrano, J. M. Escola and P. Pizarro, *Chem. Soc. Rev.*, 2013, **42**, 4004–4035.
- 57 A. Feliczak-Guzik, *Microporous Mesoporous Mater.*, 2018, **259**, 33–45.
- 58 A. Corma, *Chem. Rev.*, 1997, **97**, 2373–2420.
- 59 A. Taguchi and F. Schüth, *Microporous Mesoporous Mater.*, 2005, **77**, 1–45.
- 60 X. S. Zhao, G. Q. Lu and G. J. Millar, *Ind. Eng. Chem. Res.*, 1996, **35**, 2075–2090.
- 61 D. Kumar, K. Schumacher, C. du Fresne von Hohenesche, M. Grün and K. . Unger, *Colloids Surfaces A Physicochem. Eng. Asp.*, 2001, **187–188**, 109–116.
- 62 C. T. Kresge, M. E. Leonowicz, W. J. Roth, J. C. Vartuli and J. S. Beck, *Nature*, 1992, **359**, 710–712.
- 63 D. Zhao, J. Feng, Q. Huo, N. Melosh, G. H. Fredrickson, B. F. Chmelka and G. D. Stucky, *Science (80-. )*, 1998, **279**, 548.
- 64 W. J. J. Stevens, K. Lebeau, M. Mertens, G. Van Tendeloo, P. Cool and E. F. Vansant, *J. Phys. Chem. B*, 2006, **110**, 9183–9187.
- 65 D. Zhao, Q. Huo, J. Feng, B. F. Chmelka and G. D. Stucky, *J. Am. Chem. Soc.*, 1998, **120**, 6024–6036.
- 66 A. Corma, M. T. Navarro, L. Nemeth and M. Renz, *Chem. Commun.*, 2001, 2190–2191.
- 67 T. Blasco, A. Corma, M. T. Navarro and J. P. Pariente, *J. Catal.*, 1995, **156**, 65–74.
- 68 N. Igarashi, K. Hashimoto and T. Tatsumi, *Microporous Mesoporous Mater.*, 2007, **104**, 269–280.
- 69 A. Corma, M. T. Navarro and J. P. Pariente, *J. Chem. Soc. Chem. Commun.*, 1994, 147–148.
- 70 D. E. De Vos, M. Dams, B. F. Sels and P. A. Jacobs, *Chem. Rev.*, 2002, **102**, 3615–3640.
- 71 A. Sayari and S. Hamoudi, *Chem. Mater.*, 2001, **13**, 3151–3168.
- 72 F. Kleitz, *Handb. Heterog. Catal.*, 2008, 178–219.
- 73 A. H. Yonli, I. Gener and S. Mignard, *Microporous Mesoporous Mater.*, 2010, **132**, 37–42.
- 74 J. Zhu, X. Meng and F. Xiao, *Front. Chem. Sci. Eng.*, 2013, **7**, 233–248.
- 75 D. P. Sahoo, D. Rath, B. Nanda and K. M. Parida, *RSC Adv.*, 2015, **5**, 83707–83724.
- 76 C.-H. Yu, C.-H. Huang and C.-S. Tan, *Aerosol Air Qual. Res.*, 2012, **12**, 745–769.
- 77 H. Zhao, J. Hu, J. Wang, L. Zhou and H. Liu, *Acta Physico-Chimica Sin.*, 2007, **23**, 801–806.
- 78 F. Chang, J. Zhou, P. Chen, Y. Chen, H. Jia, S. M. I. Saad, Y. Gao, X. Cao and T. Zheng, *Asia-Pacific J. Chem. Eng.*, 2013, **8**, 618–626.
- 79 T. G. Oliveira, M. J. B. Souza, A. C. F. Coriolano, A. M. G. Pedrosa and A. S. Araujo, *Pet. Sci. Technol.*, 2018, **36**, 1977–1982.
- 80 G. Tian, C. Zhang and F. Wei, *Nanoscale Horizons*, , DOI:10.1039/D2NH00307D.
- 81 W. Zhou, K. Cheng, J. Kang, C. Zhou, V. Subramanian, Q. Zhang and Y. Wang, *Chem. Soc. Rev.*, 2019, **48**, 3193–3228.
- 82 N. J. Azhari, N. Nurdini, S. Mardiana, T. Ilmi, A. T. N. Fajar, I. G. B. N. Makertihartha, Subagjo and G. T. M. Kadja, *J. CO2 Util.*, 2022, **59**, 101969.
- 83 M. G. Sibi, D. Verma and J. Kim, *Catal. Rev.*, 2022, 1–60.
- 84 W. Li, H. Wang, X. Jiang, J. Zhu, Z. Liu, X. Guo and C. Song, *RSC Adv.*, 2018, **8**, 7651–7669.
- 85 H. Zhao, C. Zeng and N. Tsubaki, *Resour. Chem. Mater.*, 2022, **1**, 230–248.
- 86 Q. Zhang, J. Yu and A. Corma, *Adv. Mater.*, 2020, **n/a**, 2002927.
- 87 D. Wang, Z. Xie, M. D. Porosoff and J. G. Chen, *Chem*, , DOI:10.1016/j.chempr.2021.02.024.
- 88 W. Zhou, K. Cheng, J. Kang, C. Zhou, V. Subramanian, Q. Zhang and Y. Wang, *Chem. Soc. Rev.*, 2019, **48**, 3193–3228.
- 89 H. Yang, C. Zhang, P. Gao, H. Wang, X. Li, L. Zhong, W. Wei and Y. Sun, *Catal. Sci. Technol.*, 2017, **7**, 4580–4598.
- 90 K. Shukla and V. C. Srivastava, *RSC Adv.*, 2016, **6**, 32624–32645.
- 91 S. Huang, B. Yan, S. Wang and X. Ma, *Chem. Soc. Rev.*, 2015, **44**, 3079–3116.
- 92 T. Tabanelli, D. Bonincontri, S. Albonetti and F. Cavani, in *Horizons in Sustainable Industrial Chemistry and Catalysis*, eds. S. Albonetti, S. Perathoner and E. A. B. T.-S. in S. S. and C. Quadrelli, Elsevier, 2019, vol. 178, pp. 125–144.
- 93 R. H. Heyn, in *Carbon Dioxide Utilisation*, eds. P. Styring, E. A. Quadrelli and K. B. T.-C. D. U. Armstrong, Elsevier, Amsterdam, 2015, pp. 97–113.
- 94 H. Zhang and M. W. Grinstaff, *J. Am. Chem. Soc.*, 2013, **135**, 6806–6809.
- 95 R. Bernini, E. Mincione, M. Barontini, F. Crisante, G. Fabrizi and A. Gambacorta, *Tetrahedron*, 2007, **63**, 6895–6900.
- 96 J. H. Park, J. Y. Jeon, J. J. Lee, Y. Jang, J. K. Varghese and B. Y. Lee, *Macromolecules*, 2013, **46**, 3301–3308.
- 97 E. J. C. Lopes, A. P. C. Ribeiro and L. M. D. R. S. Martins, *Catalysts*, 2020, **10**, 479.
- 98 E. National Academies of Sciences and Medicine, *Gaseous Carbon Waste Streams Utilization: Status and Research Needs*, The National Academies Press, Washington, DC, 2019.
- 99 A. S. Pensado, A. A. H. Pádua, M. J. P. Comuñas and J. Fernández, *J. Phys. Chem. B*, 2008, **112**, 5563–5574.

- 100 A. Dibenedetto and A. Angelini, in *CO Chemistry*, eds. M. Aresta and R. B. T.-A. in I. C. van Eldik, Academic Press, 2014, vol. 66, pp. 25–81.
- 101 E. Leino, P. Mäki-Arvela, V. Eta, D. Y. Murzin, T. Salmi and J.-P. Mikkola, *Appl. Catal. A Gen.*, 2010, **383**, 1–13.
- 102 E. Alper, O. Y. Orhan and O. Yuksel Orhan, *Petroleum*, 2017, **3**, 109–126.
- 103 H. Zhou and X. Lu, *Sci. China Chem.*, 2017, **60**, 904–911.
- 104 C. Calabrese, F. Giacalone and C. Aprile, *Catalysts*, 2019, **9**, 325.
- 105 G. Fiorani, W. Guo and A. W. Kleij, *Green Chem.*, 2015, **17**, 1375–1389.
- 106 V. Caló, A. Nacci, A. Monopoli and A. Fanizzi, *Org. Lett.*, 2002, **4**, 2561–2563.
- 107 M. North, R. Pasquale and C. Young, *Green Chem.*, 2010, **12**, 1514–1539.
- 108 M. Aresta, *J. Mol. Catal. A Chem.*, 2003, **204–205**, 245–252.
- 109 A.-A. G. Shaikh and S. Sivaram, *Chem. Rev.*, 1996, **96**, 951–976.
- 110 M. Sathish, K. J. Sreeram, J. Raghava Rao and B. Unni Nair, *ACS Sustain. Chem. Eng.*, 2016, **4**, 1032–1040.
- 111 A. L. Michan, B. S. Parimalam, M. Leskes, R. N. Kerber, T. Yoon, C. P. Grey and B. L. Lucht, *Chem. Mater.*, 2016, **28**, 8149–8159.
- 112 N. Yadav, F. Seidi, D. Crespy and V. D’Elia, *ChemSusChem*, 2019, **12**, 724–754.
- 113 J. H. Clements, *Ind. Eng. Chem. Res.*, 2003, **42**, 663–674.
- 114 S. Foltran, R. Mereau and T. Tassaing, *Catal. Sci. Technol.*, 2014, **4**, 1585–1597.
- 115 Q.-W. Song, Z.-H. Zhou and L.-N. He, *Green Chem.*, 2017, **19**, 3707–3728.
- 116 M. Alves, B. Grignard, R. Mereau, C. Jerome, T. Tassaing and C. Detrembleur, *Catal. Sci. Technol.*, 2017, **7**, 2651–2684.
- 117 H. Büttner, L. Longwitz, J. Steinbauer, C. Wulf and T. Werner, *Top. Curr. Chem.*, 2017, **375**, 50.
- 118 L. C. Kingsland, *Law Contemp. Probl.*, 1948, **13**, 354.
- 119 B. Chatelet, L. Joucla, J.-P. Dutasta, A. Martinez, K. C. Szeto and V. Dufaud, *J. Am. Chem. Soc.*, 2013, **135**, 5348–5351.
- 120 Y. Wu, Y. Zhao, R. Li, B. Yu, Y. Chen, X. Liu, C. Wu, X. Luo and Z. Liu, *ACS Catal.*, 2017, **7**, 6251–6255.
- 121 N. Liu, Y.-F. Xie, C. Wang, S.-J. Li, D. Wei, M. Li and B. Dai, *ACS Catal.*, 2018, **8**, 9945–9957.
- 122 M. E. Wilhelm, M. H. Anthofer, R. M. Reich, V. D’Elia, J.-M. Basset, W. A. Herrmann, M. Cokoja and F. E. Kühn, *Catal. Sci. Technol.*, 2014, **4**, 1638–1643.
- 123 J. Li, D. Jia, Z. Guo, Y. Liu, Y. Lyu, Y. Zhou and J. Wang, *Green Chem.*, 2017, **19**, 2675–2686.
- 124 M. Liu, X. Wang, Y. Jiang, J. Sun and M. Arai, *Catal. Rev.*, 2019, **61**, 214–269.
- 125 K. Kiatkittipong, M. A. A. Mohamad Shukri, W. Kiatkittipong, J. W. Lim, P. L. Show, M. K. Lam and S. Assabumrungrat, *Processes*, 2020, **8**, 548.
- 126 V. D’Elia, J. D. A. Pelletier and J.-M. Basset, *ChemCatChem*, 2015, **7**, 1906–1917.
- 127 H. Jing, S. K. Edulji, J. M. Gibbs, C. L. Stern, H. Zhou and S. T. Nguyen, *Inorg. Chem.*, 2004, **43**, 4315–4327.
- 128 Y. Du, D.-L. Kong, H.-Y. Wang, F. Cai, J.-S. Tian, J.-Q. Wang and L.-N. He, *J. Mol. Catal. A Chem.*, 2005, **241**, 233–237.
- 129 R. Nomura, A. Ninagawa and H. Matsuda, *J. Org. Chem.*, 1980, **45**, 3735–3738.
- 130 D. Darensbourg, *Coord. Chem. Rev.*, 1996, **153**, 155–174.
- 131 M. Tu and R. J. Davis, *J. Catal.*, 2001, **199**, 85–91.
- 132 D. Barthomeuf\*, *Catal. Rev.*, 1996, **38**, 521–612.
- 133 D. Barthomeuf, eds. G. Öhlmann, H. Pfeifer and R. B. T.-S. in S. S. and C. Fricke, Elsevier, 1991, vol. 65, pp. 157–169.
- 134 A. Corma, *J. Catal.*, 2003, **216**, 298–312.
- 135 E. J. ; B. Dostkocil Shailendra, V. ; Kaye, Brian, G. ; Davis, Robert J., *J. Phys. Chem. B*, 1999, **103**, 6277–6282.
- 136 E. J. Dostkocil, *Microporous mesoporous Mater.*, 2004, **76**, 177–183.
- 137 E. J. Dostkocil, *J. Phys. Chem. B*, 2005, **109**, 2315–2320.
- 138 H. O. Pastore, S. Coluccia and L. Marchese, *Annu. Rev. Mater. Res.*, 2005, **35**, 351–395.
- 139 S. T. Wilson, B. M. Lok, C. A. Messina, T. R. Cannan and E. M. Flanigen, 1982, 1146–1147.
- 140 R. Krishna and J. M. van Baten, *Microporous Mesoporous Mater.*, 2011, **137**, 83–91.
- 141 Z. Bacsik, O. Cheung, P. Vasiliev and N. Hedin, *Appl. Energy*, 2016, **162**, 613–621.
- 142 G. Singh, J. Lee, A. Karakoti, R. Bahadur, J. Yi, D. Zhao, K. AlBahily and A. Vinu, *Chem. Soc. Rev.*, 2020, **49**, 4360–4404.
- 143 Z. Xie, M. Zhu, A. Nambo, J. B. Jasinski and M. A. Carreon, *Dalt. Trans.*, 2013, **42**, 6732–6735.
- 144 Y. Zhou, Y. Jin, M. Wang, W. Zhang, J. Xie, J. Gu, H. Wen, J. Wang and L. Peng, *Chem. – A Eur. J.*, 2015, **21**, 15412–15420.
- 145 H. Wen, J. Xie, Y. Y. Zhou, Y. Y. Zhou and J. Wang, *Catal. Sci. Technol.*, 2019, **9**, 5725–5735.
- 146 S. K. Kang, H. J. Cho, S.-K. Kim, J. W. Lee, S. Y. Park and H. Choi, 2017.
- 147 Q.-N. Zhao, Q.-W. Song, P. Liu, Q.-X. Zhang, J.-H. Gao and K. Zhang, *Chinese J. Chem.*, 2018, **36**, 187–193.
- 148 R. Srivastava, D. Srinivas and P. Ratnasamy, *Catal. Letters*, 2003, **91**, 133–139.
- 149 D. Srinivas, R. Srivastava and P. Ratnasamy, 2006.
- 150 L. Xu, C. Li, K. Zhang and P. Wu, *ACS Catal.*, 2014, **4**, 2959–2968.
- 151 Y. Kubota, Y. Nishizaki, H. Ikeya, M. Saeki, T. Hida, S. Kawazu, M. Yoshida, H. Fujii and Y. Sugi, *Microporous Mesoporous Mater.*, 2004, **70**, 135–149.

- 152 C. G. Li, L. Xu, P. Wu, H. Wu and M. He, *Chem Commun*, 2014, **50**, 15764–15767.
- 153 D. Liu, G. Li, J. Liu, Y. Wei and H. Guo, *ACS Appl. Mater. Interfaces*, 2018, **10**, 22119–22129.
- 154 B. Sarmah, B. Satpati and R. Srivastava, *J. Colloid Interface Sci.*, 2017, **493**, 307–316.
- 155 S. Kumar, K. Prasad, J. M. Gil, A. J. F. N. F. N. Sobral and J. Koh, *Carbohydr. Polym.*, 2018, **198**, 401–406.
- 156 N. Herron, G. D. Stucky and C. A. Tolman, *Inorganica Chim. Acta*, 1985, **100**, 135–140.
- 157 R. Srivastava, D. Srinivas and P. Ratnasamy, *Catal. Letters*, 2003, **89**, 81–85.
- 158 Council of Scientific and Industrial Research, India., 2005, 14pp.
- 159 D. Wöhrle, *Adv. Mater.*, 1993, **5**, 942–943.
- 160 F. Zhang, Y. Xie, P. Liu, F. Hao, Z. Yao and H. Luo, *Catal. Letters*, 2014, **144**, 1894–1899.
- 161 S. Aparicio, M. Atilhan and F. Karadas, *Ind. Eng. Chem. Res.*, 2010, **49**, 9580–9595.
- 162 R. L. Vekariya, *J. Mol. Liq.*, 2017, **227**, 44–60.
- 163 S. Zhang, W. Cheng and J. Ren, *Tetrahedron Lett.*, 2008, **49**, 3588–3591.
- 164 J. Sun, L. Han, W. Cheng, J. Wang, X. Zhang and S. Zhang, *ChemSusChem*, 2011, **4**, 502–507.
- 165 Y. Zhang, S. Yin, S. Luo and C. T. Au, *Ind. Eng. Chem. Res.*, 2012, **51**, 3951–3957.
- 166 B. Sarmah and R. Srivastava, *Ind. Eng. Chem. Res.*, 2017, **56**, 8202–8215.
- 167 L. Guo, X. Jin, X. Wang, L. Yin, Y. Wang and Y.-W. Yang, *Molecules*, 2018, **23**, 2710.
- 168 K. M. K. Yu, I. Curcic, J. Gabriel, H. Morganstewart and S. C. Tsang, *J. Phys. Chem. A*, 2010, **114**, 3863–3872.
- 169 A. Barbarini, R. Maggi, A. Mazzacani, G. Mori, G. Sartori and R. Sartorio, *Tetrahedron Lett.*, 2003, **44**, 2931–2934.
- 170 V. B. Saptal, B. Nanda, K. M. Parida and B. M. Bhanage, *ChemCatChem*, 2017, **9**, 4105–4111.
- 171 L. Jian, W. Ligu, L. Shimin, L. Xueli, S. Feng and D. Youquan, *Chem. Lett.*, 2010, **39**, 1277–1278.
- 172 S. Zhong, L. Liang, M. Liu, B. Liu and J. Sun, *J. CO<sub>2</sub> Util.*, 2015, **9**, 58–65.
- 173 M. Liu, B. Liu, L. Liang, F. Wang, L. Shi and J. Sun, *J. Mol. Catal. A Chem.*, 2016, **418–419**, 78–85.
- 174 M. V Zakharova, F. Kleitz and F.-G. Fontaine, *ChemCatChem*, 2017, **9**, 1886–1890.
- 175 J. M. Kolle and A. Sayari, *J. CO<sub>2</sub> Util.*, 2018, **26**, 564–574.
- 176 M. Zhang, B. Chu, G. Li, J. Xiao, H. Zhang, Y. Peng, B. Li, P. Xie, M. Fan and L. Dong, *Microporous Mesoporous Mater.*, 2019, **274**, 363–372.
- 177 R. Srivastava, D. Srinivas and P. Ratnasamy, *Tetrahedron Lett.*, 2006, **47**, 4213–4217.
- 178 D. Liu, G. Li, H. Guo and J. Liu, *J. Energy Chem.*, 2020, **41**, 52–59.
- 179 S. Udayakumar, S.-W. Park, D.-W. Park and B.-S. Choi, *Catal. Commun.*, 2008, **9**, 1563–1570.
- 180 J. N. Appaturi and F. Adam, *Appl. Catal. B Environ.*, 2013, **136–137**, 150–159.
- 181 F. Adam, J. N. Appaturi and E.-P. Ng, *J. Mol. Catal. A Chem.*, 2014, **386**, 42–48.
- 182 L. Muniandy, F. Adam, N. R. A. Rahman and E.-P. Ng, *Inorg. Chem. Commun.*, 2019, **104**, 1–7.
- 183 M. Borjian Boroujeni, M. S. Laeini, M. T. Nazeri and A. Shaabani, *Catal. Letters*, 2019, **149**, 2089–2097.
- 184 A. B. Sorokin, *Chem. Rev.*, 2013, **113**, 8152–8191.
- 185 E. M. Maya, A. Valverde-González and M. Iglesias, *Molecules*, 2020, **25**, 4598.
- 186 X.-B. Lu, H. Wang and R. He, *J. Mol. Catal. A Chem.*, 2002, **186**, 33–42.
- 187 W. G. Zhou X., Yang X., Yao J., *Acta Chim. Sin. Ed.*, 2010, **68**, 870–874.
- 188 J.-W. Huang and M. Shi, *J. Org. Chem.*, 2003, **68**, 6705–6709.
- 189 N. Kihara, N. Hara and T. Endo, *J. Org. Chem.*, 1993, **58**, 6198–6202.
- 190 L. Zhou, G. Cai, L. Zhang, Y. Luo, H. Zhenhong, W. Eli, Z. He and W. Eli, *Synth. React. Inorganic, Met. Nano-Metal Chem.*, 2014, **44**, 1545–1550.
- 191 W. Cheng, X. Chen, J. Sun, J. Wang and S. Zhang, *Catal. Today*, 2013, **200**, 117–124.
- 192 J. Liu, G. Yang, Y. Liu, D. Wu, X. Hu and Z. Zhang, *Green Chem.*, 2019, **21**, 3834–3838.
- 193 J. Sun, S. Fujita, B. M. Bhanage and M. Arai, *Catal. Today*, 2004, **93–95**, 383–388.
- 194 M. Aresta, A. Dibenedetto and I. Tommasi, *Appl. Organomet. Chem.*, 2000, **14**, 799–802.
- 195 A. Corma, M. Domine, J. A. Gaona, J. L. Jordá, M. T. Navarro, F. Rey, J. Pérez-Pariente, J. Tsuji, B. McCulloch and L. T. Nemeth, *Chem. Commun.*, 1998, 2211–2212.
- 196 A. Corma, M. A. Camblor, P. Esteve, A. Martinez and J. Perezpariente, *J. Catal.*, 1994, **145**, 151–158.
- 197 P. Jiménez-Lozano, I. D. Ivanchikova, O. A. Kholdeeva, J. M. Poblet and J. J. Carbó, *Chem. Commun.*, 2012, **48**, 9266–9268.
- 198 A. Corma, U. Díaz, V. Fornés, J. L. Jordá, M. Domine and F. Rey, *Chem. Commun.*, 1999, 779–780.
- 199 C. Evangelisti, M. Guidotti, C. Tiozzo, R. Psaro, N. Maksimchuk, I. Ivanchikova, A. N. Shmakov and O. Kholdeeva, 2018, **470**, 393–401.
- 200 B. Gu, T. Xu, G. Xu, J. Bai and C. Li, *Microporous Mesoporous Mater.*, 2020, **293**, 109779.
- 201 M. Honda, M. Tamura, K. Nakao, K. Suzuki, Y. Nakagawa and K. Tomishige, *ACS Catal.*, 2014, **4**, 1893–1896.
- 202 J. Hu, J. Ma, Q. Zhu, Q. Qian, H. Han, Q. Mei and B. Han, *Green Chem.*, 2016, **18**, 382–385.
- 203 M. A. Pacheco and C. L. Marshall, *Energy & Fuels*, 1997, **11**, 2–29.
- 204 Y. Cao, H. Cheng, L. Ma, F. Liu and Z. Liu, *Catal. Surv. from Asia*, 2012, **16**, 138–147.
- 205 J. Bian, M. Xiao, S. Wang, X. Wang, Y. Lu and Y. Meng, *Chem. Eng. J.*, 2009, **147**, 287–296.
- 206 T. Sakakura, J.-C. Choi, Y. Saito and T. Sako, *Polyhedron*, 2000, **19**, 573–576.
- 207 R. Srivastava, D. Srinivas and P. Ratnasamy, *J. Catal.*, 2005, **233**, 1–15.
- 208 M. Aresta, A. Dibenedetto, F. Nocito, A. Angelini, B. Gabriele and S. De Negri, *Appl. Catal. A Gen.*, 2010, **387**,

- 113–118.
- 209 K. Tomishige, T. Sakaihorii, Y. Ikeda and K. Fujimoto, *Catal. Letters*, 1999, **58**, 225–229.
- 210 K. Tomishige, Y. Furusawa, Y. Ikeda, M. Asadullah and K. Fujimoto, *Catal. Letters*, 2001, **76**, 71–74.
- 211 Y. Zhou, S. Wang, M. Xiao, D. Han, Y. Lu and Y. Meng, *RSC Adv.*, 2012, **2**, 6831–6837.
- 212 S. Wang, L. Zhao, W. Wang, Y. Zhao, G. Zhang, X. Ma and J. Gong, *Nanoscale*, 2013, **5**, 5582–5588.
- 213 H. Chen, S. Wang, M. Xiao, D. Han, Y. Lu and Y. Meng, *Chinese J. Chem. Eng.*, 2012, **20**, 906–913.
- 214 A. Aouissi, S. S. Al-Deyab, A. Al-Owais and A. Al-Amro, *Int. J. Mol. Sci.*, 2010, **11**, 2770–2779.
- 215 R. C. Wu, T. Xie and M. Li, *Adv. Mater. Res.*, 2011, **418–420**, 38–41.
- 216 S. Fang and K. Fujimoto, *Appl. Catal. A Gen.*, 1996, **142**, L1–L3.
- 217 D. Ballivet-Tkatchenko, J. H. Z. dos Santos, K. Philippot and S. Vasireddy, *Comptes Rendus Chim.*, 2011, **14**, 780–785.
- 218 Q. Cai, C. Jin, B. Lu, H. Tangbo and Y. Shan, *Catal. Letters*, 2005, **103**, 225–228.
- 219 Y. Yoshida, Y. Arai, S. Kado, K. Kunimori and K. Tomishige, *Catal. Today*, 2006, **115**, 95–101.
- 220 W. Wang, S. Wang, X. Ma and J. Gong, *Catal. Today*, 2009, **148**, 323–328.
- 221 A. Dibenedetto, M. Aresta, A. Angelini, J. Ethiraj and B. M. Aresta, *Chem. – A Eur. J.*, 2012, **18**, 10324–10334.
- 222 N. Kumar, E. Leino, P. Mäki-Arvela, A. Aho, M. Källdström, M. Tuominen, P. Laukkanen, K. Eränen, J.-P. Mikkola, T. Salmi and D. Y. Murzin, *Microporous Mesoporous Mater.*, 2012, **152**, 71–77.
- 223 M. Tamura, M. Honda, K. Noro, Y. Nakagawa and K. Tomishige, *J. Catal.*, 2013, **305**, 191–203.
- 224 M. Honda, S. Sonehara, H. Yasuda, Y. Nakagawa and K. Tomishige, *Green Chem.*, 2011, **13**, 3406–3413.
- 225 H. YAO, *J. Catal.*, 1984, **86**, 254–265.
- 226 M. Y. Zhang, H. Wang and W. G. Gao, *Adv. Mater. Res.*, 2012, **535–537**, 2139–2142.
- 227 X. Hu, C. Zhao, Q. Guan, X. Hu, W. Li and J. Chen, *Inorg. Chem. Front.*, 2019, **6**, 1799–1812.
- 228 A. H. Tamboli, A. A. Chaugule and H. Kim, *Chem. Eng. J.*, 2017, **323**, 530–544.
- 229 K. Tomishige and K. Kunimori, *Appl. Catal. A Gen.*, 2002, **237**, 103–109.
- 230 Y. Pu, K. Xuan, F. Wang, A. Li, N. Zhao and F. Xiao, *RSC Adv.*, 2018, **8**, 27216–27226.
- 231 A. H. Tamboli, A. A. Chaugule, S. W. Gosavi and H. Kim, *Fuel*, 2018, **216**, 245–254.
- 232 T. Sakakura, Y. Saito, M. Okano, J.-C. Choi and T. Sako, *J. Org. Chem.*, 1998, **63**, 7095–7096.
- 233 V. Eta, P. Mäki-Arvela, A.-R. Leino, K. Kordás, T. Salmi, D. Y. Murzin and J.-P. Mikkola, *Ind. Eng. Chem. Res.*, 2010, **49**, 9609–9617.
- 234 X. Zhang, D. Jia, J. Zhang and Y. Sun, *Catal. Letters*, 2014, **144**, 2144–2150.
- 235 T. Chang, M. Tamura, Y. Nakagawa, N. Fukaya, J.-C. Choi, T. Mishima, S. Matsumoto, S. Hamura and K. Tomishige, *Green Chem.*, 2020, **22**, 7321–7327.
- 236 J. Struger, J. Grabuski, S. Cagampan, E. Sverko and C. Marvin, *Bull. Environ. Contam. Toxicol.*, 2016, **96**, 423–431.
- 237 T. R. Fukuto, *Environ. Health Perspect.*, 1990, **87**, 245–254.
- 238 A. K. Ghosh and M. Brindisi, *J. Med. Chem.*, 2015, **58**, 2895–2940.
- 239 D. Chaturvedi, *Tetrahedron*, 2012, **68**, 15–45.
- 240 P. Adams, F. A. Baron, V. I. Synthesis, K. Alky and F. A. Baron, .
- 241 W. Schilling and S. Das, *ChemSusChem*, DOI:10.1002/cssc.202002073.
- 242 A. Isidro-Llobet, M. Álvarez and F. Albericio, *Chem. Rev.*, 2009, **109**, 2455–2504.
- 243 J. Savolainen, J. Leppänen, M. Forsberg, H. Taipale, T. Nevalainen, J. Huuskonen, J. Gynther, P. T. Mannisto and T. Jarvinen, *Life Sci.*, 2000, **67**, 205–216.
- 244 S. O. Thorberg, S. Berg, J. Lundstroem, B. Pettersson, A. Wijkstroem, D. Sanchez, P. Lindberg and J. L. G. Nilsson, *J. Med. Chem.*, 1987, **30**, 2008–2012.
- 245 L. Ufarté, E. Laville, S. Duquesne, D. Morgavi, P. Robe, C. Klopp, A. Rizzo, S. Pizzut-Serin and G. Potocki-Veronese, *PLoS One*, 2017, **12**, e0189201–e0189201.
- 246 R. K. Pandey, S. P. Dagade, M. K. Dongare and P. Kumar, *Synth. Commun.*, 2003, **33**, 4019–4027.
- 247 V. P. Raje, R. P. Bhat and S. D. Samant, *Tetrahedron Lett.*, 2005, **46**, 835–837.
- 248 J.-G. Kim and D. O. Jang, *Tetrahedron Lett.*, 2009, **50**, 2688–2692.
- 249 S. Ozaki, *Chem. Rev.*, 1972, **72**, 457–496.
- 250 G. Tegge, *Starch - Stärke*, 1991, **43**, 79.
- 251 G. Yuan, C. Qi, W. Wu and H. Jiang, *Curr. Opin. Green Sustain. Chem.*, 2017, **3**, 22–27.
- 252 M. Tamura, M. Honda, Y. Nakagawa and K. Tomishige, *J. Chem. Technol. Biotechnol.*, 2014, **89**, 19–33.
- 253 T. V. Q. Nguyen, W.-J. Yoo and S. Kobayashi, *Angew. Chemie Int. Ed.*, 2015, **54**, 9209–9212.
- 254 W. Guo, V. Laserna, J. Rintjema and A. W. Kleij, *Adv. Synth. Catal.*, 2016, **358**, 1602–1607.
- 255 Q. Zhang, H.-Y. Yuan, N. Fukaya, H. Yasuda and J.-C. Choi, *ChemSusChem*, 2017, **10**, 1501–1508.
- 256 S. L. Peterson, S. M. Stucka and C. J. Dinsmore, *Org. Lett.*, 2010, **12**, 1340–1343.
- 257 W.-Z. Zhang, X. Ren and X.-B. Lu, *Chinese J. Chem.*, 2015, **33**, 610–613.
- 258 W. Xiong, C. Qi, H. He, L. Ouyang, M. Zhang and H. Jiang, *Angew. Chemie*, 2015, **127**, 3127–3130.
- 259 D. Riemer, P. Hirapara and S. Das, *ChemSusChem*, 2016, **9**, 1916–1920.
- 260 T. Krawczyk, K. Jasiak, A. Kokolus and S. Baj, *Catal. Letters*, 2016, **146**, 1163–1168.
- 261 W. McGhee and D. Riley, *J. Org. Chem.*, 1995, **60**, 6205–6207.
- 262 R. N. Salvatore, S. Il Shin, A. S. Nagle and K. W. Jung, *J. Org. Chem.*, 2001, **66**, 1035–1037.

- 263 M. Yoshida, N. Hara and S. Okuyama, *Chem. Commun.*, 2000, 151–152.
- 264 E. Vessally, R. Mohammadi, A. Hosseinian, L. Edjlali and M. Babazadeh, *J. CO<sub>2</sub> Util.*, 2018, **24**, 361–368.
- 265 K. N. Singh, *Synth. Commun.*, 2007, **37**, 2651–2654.
- 266 D. Chaturvedi and S. Ray, *Monatshefte für Chemie / Chem. Mon.*, 2006, **137**, 201–206.
- 267 I. Dindarloo Inaloo and S. Majnooni, *New J. Chem.*, 2019, **43**, 11275–11281.
- 268 R. Srivastava, D. Srinivas and P. Ratnasamy, *Appl. Catal. A Gen.*, 2005, **289**, 128–134.
- 269 R. Srivastava, M. D. Manju, D. Srinivas and P. Ratnasamy, *Catal. Letters*, 2004, **97**, 41–47.
- 270 M. M. Heravi and V. Zadsirjan, *Tetrahedron: Asymmetry*, 2013, **24**, 1149–1188.
- 271 N. Kudo, M. Taniguchi, S. Furuta, K. Sato, T. Endo and T. Honma, *J. Agric. Food Chem.*, 1998, **46**, 5305–5312.
- 272 M. Zhou, X. Zheng, Y. Wang, D. Yuan and Y. Yao, *ChemCatChem*, 2019, **11**, 5783–5787.
- 273 R. A. Fairhurst, R. Ch, P. Furet, T. F. R. Clive, O. Gb, F. Ch, F. Hans, R. Alec, F. Riehen, O. Gb, F. Ch, F. Hans, P. Furet and T. Fr, .
- 274 U. N. Riain and A. P. MacGowan, in *Antibiotic and Chemotherapy*, eds. R. G. Finch, D. Greenwood, S. R. Norrby and R. J. B. T.-A. and C. (Ninth E. Whitley, Elsevier, London, 2010, pp. 301–305.
- 275 G. G. Zhanel, C. Shroeder, L. Vercaigne, A. S. Gin, J. Embil and D. J. Hoban, *Can. J. Infect. Dis.*, 2001, **12**, 379–390.
- 276 D. J. Diekema and R. N. Jones, *Drugs*, 2000, **59**, 7–16.
- 277 E. Y. Klein, T. P. Van Boeckel, E. M. Martinez, S. Pant, S. Gandra, S. A. Levin, H. Goossens and R. Laxminarayan, *Proc. Natl. Acad. Sci.*, 2018, **115**, E3463 LP-E3470.
- 278 L. Gzara, A. Chagnes, B. Carré, M. Dhahbi and D. Lemordant, *J. Power Sources*, 2006, **156**, 634–644.
- 279 European Patent, 2004, 1–15.
- 280 B. M. Trost and A. R. Sudhakar, 1988, 7933–7935.
- 281 F. W. Hartner, in *Comprehensive Heterocyclic Chemistry II*, eds. A. R. Katritzky, C. W. Rees and E. F. V. B. T.-C. H. C. I. I. Scriven, Elsevier, Oxford, 1996, pp. 261–318.
- 282 C. Beattie and M. North, *RSC Adv.*, 2014, **4**, 31345–31352.
- 283 P. Wang, J. Qin, D. Yuan, Y. Wang and Y. Yao, *ChemCatChem*, 2015, **7**, 1145–1151.
- 284 S. Pulla, C. M. Felton, P. Ramidi, Y. Gartia, N. Ali, U. B. Nasini and A. Ghosh, *J. CO<sub>2</sub> Util.*, 2013, **2**, 49–57.
- 285 S. Arshadi, E. Vessally, A. Hosseinian, S. Soleimani-amiri and L. Edjlali, *J. CO<sub>2</sub> Util.*, 2017, **21**, 108–118.
- 286 S. Arshadi, E. Vessally, M. Sobati, A. Hosseinian and A. Bekhradnia, *J. CO<sub>2</sub> Util.*, 2017, **19**, 120–129.
- 287 E. Vessally, A. Hosseinian, L. Edjlali, M. Babazadeh and K. Didehban, *Mini. Rev. Org. Chem.*, 2018, **15**, 315–323.
- 288 S. Farshbaf, L. Z. Fekri, M. Nikpassand, R. Mohammadi and E. Vessally, *J. CO<sub>2</sub> Util.*, 2018, **25**, 194–204.
- 289 K. Tominaga and Y. Sasaki, *Synlett*, 2002, **2002**, 0307–0309.
- 290 S. S. Islam, S. Biswas, R. Ali Molla, N. Yasmin and S. M. Islam, *ChemNanoMat*, 2020, **6**, 1386–1397.
- 291 M. Chen, Q. Wu, C. Lin, J. Zhang, J. Zhao, J. Chen and Y. Xu, *ACS Appl. Mater. Interfaces*, 2020, **12**, 40236–40247.
- 292 S. Ghosh, S. Riyajuddin, S. Sarkar, K. Ghosh and S. M. Islam, *ChemNanoMat*, 2020, **6**, 160–172.
- 293 X.-F. Liu, M.-Y. Wang and L.-N. He, *Curr. Org. Chem.*, 2017, **21**, 698–707.
- 294 S. Ghosh, T. S. Khan, A. Ghosh, A. H. Chowdhury, M. A. Haider, A. Khan and S. M. Islam, *ACS Sustain. Chem. Eng.*, 2020, **8**, 5495–5513.
- 295 A. Helal, K. E. Cordova, M. E. Arafat, M. Usman and Z. H. Yamani, *Inorg. Chem. Front.*, 2020, **7**, 3571–3577.
- 296 D. Zhao, X.-H. Liu, C. Zhu, Y.-S. Kang, P. Wang, Z. Shi, Y. Lu and W.-Y. Sun, *ChemCatChem*, 2017, **9**, 4598–4606.
- 297 G. S. Singh, eds. E. F. V Scriven and C. A. B. T.-A. in H. C. Ramsden, Academic Press, 2019, vol. 129, pp. 245–335.
- 298 J. Seayad, A. M. Seayad, J. K. P. Ng and C. L. L. Chai, *ChemCatChem*, 2012, **4**, 774–777.
- 299 R. A. Watile, D. B. Bagal, K. M. Deshmukh, K. P. Dhake and B. M. Bhanage, *J. Mol. Catal. A Chem.*, 2011, **351**, 196–203.
- 300 P. Ramidi, P. Munshi, Y. Gartia, S. Pulla, A. S. Biris, A. Paul and A. Ghosh, *Chem. Phys. Lett.*, 2011, **512**, 273–277.
- 301 M. T. Hancock and A. R. Pinhas, *Tetrahedron Lett.*, 2003, **44**, 5457–5460.
- 302 C. S. Park, M. S. Kim, T. B. Sim, D. K. Pyun, C. H. Lee, D. Choi, W. K. Lee, J.-W. Chang and H.-J. Ha, *J. Org. Chem.*, 2003, **68**, 43–49.
- 303 J. R. Wallace, D. L. Lieberman, M. T. Hancock and A. R. Pinhas, *J. Chem. Educ.*, 2005, **82**, 1229.
- 304 Y. Du, Y. Wu, A.-H. Liu and L.-N. He, *J. Org. Chem.*, 2008, **73**, 4709–4712.
- 305 Y. Wu, L.-N. He, Y. Du, J.-Q. Wang, C.-X. Miao and W. Li, *Tetrahedron*, 2009, **65**, 6204–6210.
- 306 P. Tascedda and E. Duñach, *Chem. Commun.*, 2000, 449–450.
- 307 A. W. Miller and S. T. Nguyen, *Org. Lett.*, 2004, **6**, 2301–2304.
- 308 F. Fontana, C. C. Chen and V. K. Aggarwal, *Org. Lett.*, 2011, **13**, 3454–3457.
- 309 U. R. Seo and Y. K. Chung, *Green Chem.*, 2017, **19**, 803–808.
- 310 D. B. Nale, S. Rana, K. Parida and B. M. Bhanage, *Appl. Catal. A Gen.*, 2014, **469**, 340–349.
- 311 H. Zhou, Y. M. Wang, W. Z. Zhang, J. P. Qu and X. B. Lu, *Green Chem.*, 2011, **13**, 644–650.
- 312 G. E. María, P. M. Teresa, P. Cecilia, L.-E. Alejandro, B. Mercedes, M. Manuel and C. Avelino, *Science (80-. )*, 2017, **355**, 1051–1054.

- 313 A. Corma, *Angew. Chemie Int. Ed.*, 2016, **55**, 6112–6113.
- 314 J.-Y. Li, Q.-W. Song, K. Zhang and P. Liu, *Molecules*, 2019, **24**, 182.
- 315 Q.-W. Song and L.-N. He, eds. P. Tundo, L.-N. He, E. Lokteva and C. Mota, Springer International Publishing, Cham, 2016, pp. 435–453.
- 316 J. Michel, J.-J. Toulmé, J. Vercauteren and S. Moreau, *Nucleic Acids Res.*, 1996, **24**, 1127–1135.
- 317 Y. P. Patil, P. J. Tambade, S. R. Jagtap and B. M. Bhanage, *Green Chem. Lett. Rev.*, 2008, **1**, 127–132.
- 318 H. Akgun, D. Us Yilmaz, R. Cetin Atalay and D. Gozen, *Lett. Drug Des. Discov.*, 2015, **13**, 64–76.
- 319 E. Vessally, S. Soleimani-Amiri, A. Hosseinian, L. Edjlali and M. Babazadeh, *J. CO2 Util.*, 2017, **21**, 342–352.
- 320 M. Michman, S. Patai and Y. Wiesel, *Org. Prep. Proced. Int.*, 1978, **10**, 13–16.
- 321 *Org. Synth.*, 1937, **17**, 16.
- 322 M. Khalifa, A. N. Osman, M. G. Ibrahim, A. el Rahman, E. Ossman and M. A. Ismail, *Pharmazie*, 1982, **37**, 115–7.
- 323 D. B. Nale, S. Rana, K. Parida and B. M. Bhanage, *Catal. Sci. Technol.*, 2014, **4**, 1608–1614.
- 324 E. M. Wilcox, M. R. Gogate, J. J. Spivey and G. W. Roberts, in *Natural Gas Conversion VI*, eds. E. Iglesia, J. J. Spivey and T. H. B. T.-S. in S. S. and C. Fleisch, Elsevier, 2001, vol. 136, pp. 259–264.
- 325 W. Huang, K.-C. Xie, J.-P. Wang, Z.-H. Gao, L.-H. Yin and Q.-M. Zhu, *J. Catal.*, 2001, **201**, 100–104.
- 326 E. M. Wilcox, G. W. Roberts and J. J. Spivey, *Catal. Today*, 2003, **88**, 83–90.
- 327 Y.-H. Ding, W. Huang and Y.-G. Wang, *Fuel Process. Technol.*, 2007, **88**, 319–324.
- 328 C. Coperet, *Chem. Rev.*, 2010, **110**, 656–680.
- 329 A. M. Rabie, M. A. Betiha and S.-E. Park, *Appl. Catal. B Environ.*, 2017, **215**, 50–59.
- 330 A. A. Gabrienko, S. S. Arzumanov, M. V Luzgin, A. G. Stepanov and V. N. Parmon, *J. Phys. Chem. C*, 2015, **119**, 24910–24918.
- 331 A. A. Gabrienko, S. S. Arzumanov, A. V Toktarev, I. G. Danilova, I. P. Prosvirin, V. V Kriventsov, V. I. Zaikovskii, D. Freude and A. G. Stepanov, *ACS Catal.*, 2017, **7**, 1818–1830.
- 332 A. C. Rosenzweig, C. A. Frederick, S. J. Lippard and P. Nordlund, *Nature*, 1993, **366**, 537–543.
- 333 M. Bordeaux, A. Galarneau and J. Drone, *Angew. Chemie Int. Ed.*, 2012, **51**, 10712–10723.
- 334 R. Balasubramanian, S. M. Smith, S. Rawat, L. A. Yatsunyk, T. L. Stemmler and A. C. Rosenzweig, *Nature*, 2010, **465**, 115–119.
- 335 S. I. Chan, Y.-J. Lu, P. Nagababu, S. Maji, M.-C. Hung, M. M. Lee, I.-J. Hsu, P. D. Minh, J. C.-H. Lai, K. Y. Ng, S. Ramalingam, S. S.-F. Yu and M. K. Chan, *Angew. Chemie Int. Ed.*, 2013, **52**, 3731–3735.
- 336 S. Grundner, M. A. C. Markovits, G. Li, M. Tromp, E. A. Pidko, E. J. M. Hensen, A. Jentys, M. Sanchez-Sanchez and J. A. Lercher, *Nat. Commun.*, 2015, **6**, 7546.
- 337 S. Wang, S. Guo, Y. Luo, Z. Qin, Y. Chen, M. Dong, J. Li, W. Fan and J. Wang, *Catal. Sci. Technol.*, 2019, **9**, 6613–6626.
- 338 N. V Beznis, A. N. C. van Laak, B. M. Weckhuysen and J. H. Bitter, *Microporous Mesoporous Mater.*, 2011, **138**, 176–183.
- 339 W. Panjan, J. Sirijaraensre, C. Warakulwit, P. Pantu and J. Limtrakul, *Phys Chem Chem Phys*, 2012, **14**, 16588–16594.
- 340 P. Zhang, X. Yang, X. Hou, J. Mi, Z. Yuan, J. Huang and C. Stampfl, *Catal. Sci. Technol.*, 2019, **9**, 6297–6307.
- 341 G. Li, P. Vassilev, M. Sanchez-Sanchez, J. A. Lercher, E. J. M. Hensen and E. A. Pidko, *J. Catal.*, 2016, **338**, 305–312.
- 342 M. H. Groothaert, P. J. Smeets, B. F. Sels, P. A. Jacobs and R. A. Schoonheydt, *J. Am. Chem. Soc.*, 2005, **127**, 1394–1395.
- 343 D. Palagin, A. J. Knorpp, A. B. Pinar, M. Ranocchiari and J. A. van Bokhoven, *Nanoscale*, 2017, **9**, 1144–1153.
- 344 B. D. Montejo-Valencia, Y. J. Pagán-Torres, M. M. Martínez-Lñesta and M. C. Curet-Arana, *ACS Catal.*, 2017, **7**, 6719–6728.
- 345 J. F. Wu, S. M. Yu, W. D. Wang, Y. X. Fan, S. Bai, C. W. Zhang, Q. Gao, J. Huang and W. Wang, *J Am Chem Soc*, 2013, **135**, 13567–13573.
- 346 Y. G. Kolyagin, I. I. Ivanova, V. V Ordonsky, A. Gedeon and Y. A. Pirogov, *J. Phys. Chem. C*, 2008, **112**, 20065–20069.
- 347 M. V. Luzgin, V. A. Rogov, S. S. Arzumanov, A. V. Toktarev, A. G. Stepanov and V. N. Parmon, *Angew. Chemie Int. Ed.*, 2008, **47**, 4559–4562.
- 348 R. E. Mulvey, *Organometallics*, 2006, **25**, 1060–1075.
- 349 W. Bertleff, M. Roeper and X. Sava, in *Ullmann's Encyclopedia of Industrial Chemistry*, Wiley-VCH Verlag GmbH & Co. KGaA, Weinheim, Germany, 2007.
- 350 A. Itadani, H. Torigoe, T. Yumura, T. Ohkubo, H. Kobayashi and Y. Kuroda, *J. Phys. Chem. C*, 2012, **116**, 10680–10691.
- 351 G. Caeiro, R. H. Carvalho, X. Wang, M. A. N. D. A. Lemos, F. Lemos, M. Guisnet and F. Ramôa Ribeiro, *J. Mol. Catal. A Chem.*, 2006, **255**, 131–158.
- 352 W. Sangthong, M. Probst and J. Limtrakul, *Chemphyschem*, 2014, **15**, 514–520.
- 353 L. M. Gandía, G. Arzamendi and P. M. Diéguez, in *Renewable Hydrogen Technologies*, eds. L. M. Gandía, G. Arzamendi and P. M. B. T.-R. H. T. Diéguez, Elsevier, Amsterdam, 2013, pp. 1–17.
- 354 X. Xiaoding and J. A. Moulijn, *Energy & Fuels*, 1996, **10**, 305–325.

- 355 X. Xiaoding, J. A. Moulijn, J. Ducamp, A. Bengaouer, P. Baurens, I. Fechete, P. Turek and F. Garin, *Comptes Rendus Chim.*, 1996, **21**, 427–469.
- 356 A. Behr, *Bull. des Sociétés Chim. Belges*, 2010, **94**, 671–683.
- 357 T. Herskovitz, *Organometallics*, 1983, **2**, 201–202.
- 358 X. Xiaoding, J. A. Moulijn, J. Ducamp, A. Bengaouer, P. Baurens, I. Fechete, P. Turek and F. Garin, *Energy & Fuels*, 1996, **10**, 305–325.
- 359 W. Reutemann and H. Kieczka, *Ullmann's Encycl. Ind. Chem.*, 2000.
- 360 M. Grasmann and G. Laurency, *Energy Environ. Sci.*, 2012, **5**, 8171–8181.
- 361 G. Centi and S. Perathoner, *Catal. Today*, 2009, **148**, 191–205.
- 362 S. Moret, P. J. Dyson and G. Laurency, *Nat. Commun.*, 2014, **5**, 4017.
- 363 Formic Acid Market - Growth, Trends, COVID-19 Impact, and Forecasts (2022 - 2027), <https://www.mordorintelligence.com/industry-reports/formic-acid-market>.
- 364 C. A. Huff and M. S. Sanford, *ACS Catal.*, 2013, **3**, 2412–2416.
- 365 S. Oldenhof, J. I. van der Vlugt and J. N. H. Reek, *Catal. Sci. Technol.*, 2016, **6**, 404–408.
- 366 N. Onishi, S. Xu, Y. Manaka, Y. Suna, W.-H. Wang, J. T. Muckerman, E. Fujita and Y. Himeda, *Inorg. Chem.*, 2015, **54**, 5114–5123.
- 367 G. H. Gunasekar, K. Park, K.-D. Jung and S. Yoon, *Inorg. Chem. Front.*, 2016, **3**, 882–895.
- 368 D. A. Bulushev and J. R. H. Ross, *Catal. Rev.*, 2018, **60**, 566–593.
- 369 R. Tanaka, M. Yamashita and K. Nozaki, *J. Am. Chem. Soc.*, 2009, **131**, 14168–14169.
- 370 G. A. Filonenko, R. van Putten, E. N. Schulpen, E. J. M. Hensen and E. A. Pidko, *ChemCatChem*, 2014, **6**, 1526–1530.
- 371 A. Álvarez, A. Bansode, A. Urakawa, A. V. Bavykina, T. A. Wezendonk, M. Makkee, J. Gascon and F. Kapteijn, *Chem. Rev.*, 2017, **117**, 9804–9838.
- 372 W.-H. Wang, X. Feng and M. Bao, *Transformation of Carbon Dioxide to Formic Acid and Methanol*, Springer Singapore, Singapore, 2018.
- 373 N. Yan and K. Philippot, *Curr. Opin. Chem. Eng.*, 2018, **20**, 86–92.
- 374 M. W. Farlow and H. Adkins, *J. Am. Chem. Soc.*, 1935, **57**, 2222–2223.
- 375 T. Wang, D. Ren, Z. Huo, Z. Song, F. Jin, M. Chen and L. Chen, *Green Chem.*, 2017, **19**, 716–721.
- 376 C. J. Stalder, S. Chao, D. P. Summers and M. S. Wrighton, *J. Am. Chem. Soc.*, 1983, **105**, 6318–6320.
- 377 D. Preti, C. Resta, S. Squarzialupi and G. Fachinetti, *Angew. Chemie Int. Ed.*, 2011, **50**, 12551–12554.
- 378 A. White, *MRS Bull.*, 2012, **37**, 715–716.
- 379 J. J. de Pablo, B. Jones, C. L. Kovacs, V. Ozolins and A. P. Ramirez, *Curr. Opin. Solid State Mater. Sci.*, 2014, **18**, 99–117.
- 380 M. Moliner, Y. Roman-Leshkov and A. Corma, *Acc Chem Res*, 2019, **52**, 2971–2980.
- 381 Z. Jensen, E. Kim, S. Kwon, T. Z. H. Gani, Y. Román-Leshkov, M. Moliner, A. Corma and E. Olivetti, *ACS Cent. Sci.*, 2019, **5**, 892–899.
- 382 E. M. Gallego, M. T. Portilla, C. Paris, A. León-Escamilla, M. Boronat, M. Moliner and A. Corma, *Science (80-. J.)*, 2017, **355**, 1051 LP – 1054.
- 383 L. Wu, T. Guo and T. Li, *iScience*, 2021, **24**, 102398.
- 384 A. W. Thornton, D. A. Winkler, M. S. Liu, M. Haranczyk and D. F. Kennedy, *RSC Adv.*, 2015, **5**, 44361–44370.
- 385 W. Thongnuam, T. Maihom, S. Choomwattana, Y. Injongkol, B. Boekfa, P. Treesukol and J. Limtrakul, *Phys Chem Phys*, 2018, **20**, 25179–25185.
- 386 F. Li and B. C. Gates, *J. Phys. Chem. C*, 2007, **111**, 262–267.
- 387 A. Uzun and B. C. Gates, *J. Am. Chem. Soc.*, 2009, **131**, 15887–15894.
- 388 B. M. Szyja, D. Smykowski, J. Szczygieł, E. J. M. Hensen and E. A. Pidko, *ChemCatChem*, 2016, **8**, 2500–2507.
- 389 K. Park, G. H. Gunasekar, S.-H. Kim, H. Park, S. Kim, K. Park, K.-D. Jung and S. Yoon, *Green Chem.*, 2020, **22**, 1639–1649.
- 390 G. H. Gunasekar, J. Shin, K.-D. Jung, K. Park and S. Yoon, *ACS Catal.*, 2018, **8**, 4346–4353.
- 391 G. H. Gunasekar, K.-D. Jung and S. Yoon, *Inorg. Chem.*, 2019, **58**, 3717–3723.
- 392 Y.-M. Yu, J.-H. Fei, Y.-P. Zhang and X.-M. Zheng, *Chinese J. Chem.*, 2006, **24**, 840–844.
- 393 V. Srivastava, *Catal. Letters*, 2016, **146**, 2630–2640.
- 394 Globaldata, Production capacity of methanol worldwide in 2018 and 2030, [www.statista.com/statistics/1065891/global-methanol-production-capacity/](http://www.statista.com/statistics/1065891/global-methanol-production-capacity/).
- 395 G. A. Olah, A. Goepfert and G. K. S. Prakash, *Beyond Oil and Gas: The Methanol Economy*, Wiley, Weinheim, Germany, 2009.
- 396 A. M. El-Zeftawy, *J. King Saud Univ. - Eng. Sci.*, 1995, **7**, 209–254.
- 397 W. H. Green, T. Supervisor, W. K. Cheng, T. Reader, M. Dahleh and R. Abeyaratne, 2017.
- 398 K. Atsonios, K. D. Panopoulos and E. Kakaras, *Int. J. Hydrogen Energy*, 2016, **41**, 2202–2214.
- 399 V. Van Speybroeck, K. De Wispelaere, J. Van der Mynsbrugge, M. Vandichel, K. Hemelsoet and M. Waroquier, *Chem. Soc. Rev.*, 2014, **43**, 7326–7357.
- 400 D. Chen, K. Moljord and A. Holmen, *Microporous Mesoporous Mater.*, 2012, **164**, 239–250.
- 401 Z. Li, J. Martínez-Triguero, P. Concepción, J. Yu and A. Corma, *Phys. Chem. Chem. Phys.*, 2013, **15**, 14670–14680.

402 K. Lu, J. Huang, L. Ren, C. Li, Y. Guan, B. Hu, H. Xu, J. Jiang, Y. Ma and P. Wu, *Angew. Chemie Int. Ed.*, 2020, **59**, 6258–6262.

403 C. Li, C. Paris, J. Martínez-Triguero, M. Boronat, M. Moliner and A. Corma, *Nat. Catal.*, 2018, **1**, 547–554.

404 H. Bateni and C. Able, *Catal. Ind.*, 2019, **11**, 7–33.

405 H. J. Venvik and J. Yang, *Catal. Today*, 2017, **285**, 135–146.

406 I. Yarulina, A. D. Chowdhury, F. Meirer, B. M. Weckhuysen and J. Gascon, *Nat. Catal.*, 2018, **1**, 398–411.

407 M. Pérez-Fortes, J. C. Schöneberger, A. Boulamanti and E. Tzimas, *Appl. Energy*, 2016, **161**, 718–732.

408 J. Ott, V. Gronemann, F. Pontzen, E. Fiedler, G. Grossmann, D. B. Kersebohm, G. Weiss and C. Witte, *Ullmann's Encycl. Ind. Chem.*, 2012.

409 G. H. Graaf and J. G. M. Winkelman, *Ind. Eng. Chem. Res.*, 2016, **55**, 5854–5864.

410 K. M. V. Bussche and G. F. Froment, *J. Catal.*, 1996, **161**, 1–10.

411 P. A. Taylor, P. B. Rasmussen and I. Chorkendorff, *J. Chem. Soc. Faraday Trans.*, 1995, **91**, 1267–1269.

412 J. Yoshihara and C. T. Campbell, *J. Catal.*, 1996, **161**, 776–782.

413 J. Szanyi and D. W. Goodman, *Catal. Letters*, 1991, **10**, 383–390.

414 M. Bowker; R. A. Hadden; H. Houghton; J. Hyland; K. Waugh., *J. Catal.*, 1988, **109**, 263–273.

415 I. A. Fisher and A. T. Bell, *J. Catal.*, 1997, **172**, 222–237.

416 Y.-F. Zhao, Y. Yang, C. Mims, C. H. F. Peden, J. Li and D. Mei, *J. Catal.*, 2011, **281**, 199–211.

417 Q.-L. Tang, Q.-J. Hong and Z.-P. Liu, *J. Catal.*, 2009, **263**, 114–122.

418 X. Jiang, X. Nie, X. Guo, C. Song and J. G. Chen, *Chem. Rev.*, , DOI:10.1021/acs.chemrev.9b00723.

419 A. J. Medford, A. C. Lausche, F. Abild-Pedersen, B. Temel, N. C. Schjødt, J. K. Nørskov and F. Studt, *Top. Catal.*, 2014, **57**, 135–142.

420 S. Kuld, M. Thorhauge, H. Falsig, C. F. Elkjær, S. Helveg, I. Chorkendorff and J. Sehested, *Science (80-. )*, 2016, **352**, 969 LP – 974.

421 W. F. Maier, *Angew. Chemie*, 1990, **102**, 965–966.

422 W. Ding, Y. Liu, F. Wang, S. Zhou, A. Chen, Y. Yang and W. Fang, *RSC Adv.*, 2014, **4**, 30677–30682.

423 S. Dang, H. Yang, P. Gao, H. Wang, X. Li, W. Wei and Y. Sun, *Catal. Today*, 2019, **330**, 61–75.

424 A. Karelovic and P. Ruiz, *Catal. Sci. Technol.*, 2015, **5**, 869–881.

425 X. Dong, F. Li, N. Zhao, F. Xiao, J. Wang and Y. Tan, *Appl. Catal. B Environ.*, 2016, **191**, 8–17.

426 J. Nakamura, I. Nakamura, T. Uchijima, Y. Kanai, T. Watanabe, M. Saito and T. Fujitani, *J. Catal.*, 1996, **160**, 65–75.

427 M. Lachowska and J. Skrzypek, *React. Kinet. Catal. Lett.*, 2004, **83**, 269–273.

428 F. Arena, G. Italiano, K. Barbera, G. Bonura, L. Spadaro and F. Frusteri, *Catal. Today*, 2009, **143**, 80–85.

429 B. Liang, J. Ma, X. Su, C. Yang, H. Duan, H. Zhou, S. Deng, L. Li and Y. Huang, *Ind. Eng. Chem. Res.*, 2019, **58**, 9030–9037.

430 Q. Sun, Y.-L. Zhang, H.-Y. Chen, J.-F. Deng, D. Wu and S.-Y. Chen, *J. Catal.*, 1997, **167**, 92–105.

431 H. Tian, X. Li, L. Zeng and J. Gong, *ACS Catal.*, 2015, **5**, 4959–4977.

432 P. Gao, F. Li, N. Zhao, F. Xiao, W. Wei, L. Zhong and Y. Sun, *Appl. Catal. A Gen.*, 2013, **468**, 442–452.

433 R. Ladera, F. J. Pérez-Alonso, J. M. González-Carballo, M. Ojeda, S. Rojas and J. L. G. Fierro, *Appl. Catal. B Environ.*, 2013, **142–143**, 241–248.

434 H. Ren, C.-H. Xu, H.-Y. Zhao, Y.-X. Wang, J. Liu and J.-Y. Liu, *J. Ind. Eng. Chem.*, 2015, **28**, 261–267.

435 X. Guo, D. Mao, G. Lu, S. Wang and G. Wu, *J. Mol. Catal. A Chem.*, 2011, **345**, 60–68.

436 K. Chen, H. Fang, S. Wu, X. Liu, J. Zheng, S. Zhou, X. Duan, Y. Zhuang, S. Chi Edman Tsang and Y. Yuan, *Appl. Catal. B Environ.*, 2019, **251**, 119–129.

437 A. M. Hengne, K. D. Bhatte, S. Ould-Chikh, Y. Saih, J. M. Basset and K.-W. Huang, *ChemCatChem*, 2018, **10**, 1360–1369.

438 S. Tasfy, N. A. M. Zabidi, M. S. Shaharun and D. Subbarao, *Int. J. Nanotechnol.*, 2017, **14**, 410.

439 N. A. M. Zabidi, S. Tasfy and M. S. Shaharun, *AIP Conf. Proc.*, 2016, **1787**, 30009.

440 A. Atakan, P. Mäkie, F. Söderlind, J. Keraudy, E. M. Björk and M. Odén, *Phys. Chem. Chem. Phys.*, 2017, **19**, 19139–19149.

441 A. Atakan, E. Erdtman, P. Mäkie, L. Ojamäe and M. Odén, *J. Catal.*, 2018, **362**, 55–64.

442 A. Atakan, J. Keraudy, P. Mäkie, C. Hultheberg, E. M. Björk and M. Odén, *J. Colloid Interface Sci.*, 2019, **546**, 163–173.

443 M. Mureddu, F. Ferrara and A. Pettinau, *Appl. Catal. B Environ.*, 2019, **258**, 117941.

444 G. Bonura, M. Cordaro, C. Cannilla, F. Arena and F. Frusteri, *Appl. Catal. B Environ.*, 2014, **152–153**, 152–161.

445 X. Guo, D. Mao, G. Lu, S. Wang and G. Wu, *J. Catal.*, 2010, **271**, 178–185.

446 M. K. Koh, M. Khavarian, S. P. Chai and A. R. Mohamed, *Int. J. Hydrogen Energy*, 2018, **43**, 9334–9342.

447 S.-C. Yang, S. H. Pang, T. P. Sulmonetti, W.-N. Su, J.-F. Lee, B.-J. Hwang and C. W. Jones, *ACS Catal.*, 2018, **8**, 12056–12066.

448 D. L. Chiavassa, J. Barrandeguy, A. L. Bonivardi and M. A. Baltanás, *Catal. Today*, 2008, **133–135**, 780–786.

449 S. E. Collins, D. L. Chiavassa, A. L. Bonivardi and M. A. Baltanás, *Catal. Letters*, 2005, **103**, 83–88.

450 A. Gotti and R. Prins, *J. Catal.*, 1998, **175**, 302–311.

451 N. Koizumi, X. Jiang, J. Kugai and C. Song, *Catal. Today*, 2012, **194**, 16–24.

452 X. Jiang, N. Koizumi, X. Guo and C. Song, *Appl. Catal. B Environ.*, 2015, **170–171**, 173–185.



453 H. Jiang, J. Lin, X. Wu, W. Wang, Y. Chen and M. Zhang, *J. CO2 Util.*, 2020, **36**, 33–39.

454 H. Sakurai and M. Haruta, *Catal. Today*, 1996, **29**, 361–365.

455 Y. Li, W. Na, H. Wang and W. Gao, *J. Porous Mater.*, 2017, **24**, 591–599.

456 H. Lei, N. RF, W. GQ and H. ZY, *Fuel*, 2015, **154**, 161–166.

457 B. Chan and L. Radom, *J. Am. Chem. Soc.*, 2008, **130**, 9790–9799.

458 B. Chan and L. Radom, *J. Am. Chem. Soc.*, 2006, **128**, 5322–5323.

459 K. K. Bando, H. Arakawa and N. Ichikuni, *Catal. Letters*, 1999, **60**, 125–132.

460 K. Kitamura Bando, K. Soga, K. Kunimori, N. Ichikuni, K. Okabe, H. Kusama, K. Sayama and H. Arakawa, *Appl. Catal. A Gen.*, 1998, **173**, 47–60.

461 K. Kitamura Bando, K. Soga, K. Kunimori and H. Arakawa, *Appl. Catal. A Gen.*, 1998, **175**, 67–81.

462 K. K. Bando, K. Soga, K. Kunimori, N. Ichikuni, K. Asakura, K. Okabe, H. Kusama, K. Sayama and H. Arakawa, in *Advances in Chemical Conversions for Mitigating Carbon Dioxide*, eds. T. Inui, M. Anpo, K. Izui, S. Yanagida and T. B. T.-S. in S. S. and C. Yamaguchi, Elsevier, 1998, vol. 114, pp. 455–458.

463 1999.

464 J. Gorbe, J. Lasobras, E. Francés, J. Herguido, M. Menéndez, I. Kumakiri and H. Kita, *Sep. Purif. Technol.*, 2018, **200**, 164–168.

465 G. Barbieri, G. Marigliano, G. Golemme and E. Drioli, *Chem. Eng. J.*, 2002, **85**, 53–59.

466 F. Gallucci, L. Paturzo and A. Basile, *Chem. Eng. Process. Process Intensif.*, 2004, **43**, 1029–1036.

467 T. Van Tran, N. Le-Phuc, T. H. Nguyen, T. T. Dang, P. T. Ngo and D. A. Nguyen, *Int. J. Chem. React. Eng.*, 2018, **16**, 20170046.

468 J. Zhong, X. Yang, Z. Wu, B. Liang, Y. Huang and T. Zhang, *Chem. Soc. Rev.*, 2020, **49**, 1385–1413.

469 E. A. Quadrelli, G. Centi, J.-L. Duplan and S. Perathoner, *ChemSusChem*, 2011, **4**, 1194–1215.

470 P. J. . Tijm, F. . Waller and D. . Brown, *Appl. Catal. A Gen.*, 2001, **221**, 275–282.

471 US 2013/0237618 A1, 2013, 1.

472 US2002151758A1, 2002.

473 T.-C. Tsai, *Appl. Catal. A Gen.*, 1999, **181**, 355–398.

474 M. T. Ashraf, R. Chebbi and N. A. Darwish, *Ind. Eng. Chem. Res.*, 2013, **52**, 13730–13737.

475 A. K. Aboul-Gheit, S. A. Hanafy, A. A. Aboul-Enein and S. A. Ghoneim, *J. Taiwan Inst. Chem. Eng.*, 2011, **42**, 860–867.

476 D. Vanvu, M. Miyamoto, N. Nishiyama, Y. Egashira and K. Ueyama, *J. Catal.*, 2006, **243**, 389–394.

477 Y.-G. Li, W.-H. Xie and S. Yong, *Appl. Catal. A Gen.*, 1997, **150**, 231–242.

478 S. Faramawy, *Pet. Sci. Technol.*, 1999, **17**, 249–271.

479 G. Mirth, J. Cejka and J. A. Lercher, *J. Catal.*, 1993, **139**, 24–33.

480 J. Breen, R. Burch, M. Kulkarni, P. Collier and S. Golunski, *J. Am. Chem. Soc.*, 2005, **127**, 5020–5021.

481 J. L. Sotelo, M. A. Uguina, J. L. Valverde and D. P. Serrano, *Ind. Eng. Chem. Res.*, 1993, **32**, 2548–2554.

482 M. M.-J. Li and S. C. E. Tsang, *Catal. Sci. Technol.*, 2018, **8**, 3450–3464.

483 S. G. Jadhav, P. D. Vaidya, B. M. Bhanage and J. B. Joshi, *Chem. Eng. Res. Des.*, 2014, **92**, 2557–2567.

484 K. W. Ting, H. Kamakura, S. S. Poly, T. Toyao, S. M. A. Hakim Siddiki, Z. Maeno, K. Matsushita and K. Shimizu, *ChemCatChem*, 2020, **12**, 2215–2220.

485 J. Zuo, W. Chen, J. Liu, X. Duan, L. Ye and Y. Yuan, *Sci. Adv.*, 2020, **6**, eaba5433.

486 European Alternative Fuels Observatory, BioDME, [www.eafo.eu/alternative-fuels/advanced-biofuels/BioDME](http://www.eafo.eu/alternative-fuels/advanced-biofuels/BioDME).

487 T. A. Semelsberger, R. L. Borup and H. L. Greene, *J. Power Sources*, 2006, **156**, 497–511.

488 P. Nieuwenhuis and P. Wells, in *The Automotive Industry and the Environment*, eds. P. Nieuwenhuis and P. B. T.-T. A. I. and the E. Wells, Elsevier, 2003, pp. 73–86.

489 G. A. Olah, A. Goepfert and G. K. S. Prakash, *J. Org. Chem.*, 2009, **74**, 487–498.

490 C. Arcoumanis, C. Bae, R. Crookes and E. Kinoshita, *Fuel*, 2008, **87**, 1014–1030.

491 P. Makoś, E. Słupek, J. Sobczak, D. Zabrocki, J. Hupka and A. Rogala, *E3S Web Conf.*, 2019, **116**, 00048.

492 S. P. Srivastava and J. Hancsók, *Fuels and Fuel-Additives*, John Wiley & Sons, Inc, Hoboken, NJ, 2014.

493 A. Lerner, M. J. Brear, J. S. Lacey, R. L. Gordon and P. A. Webley, *Fuel*, 2018, **220**, 871–878.

494 L. Jie, L. Shenghua, L. Yi, W. Yanju, L. Guangle and Z. Zan, *Energy & Fuels*, 2010, **24**, 2465–2469.

495 E. S. Yoon and C. Han, in *10th International Symposium on Process Systems Engineering: Part A*, eds. R. M. de Brito Alves, C. A. O. do Nascimento and E. C. B. T.-C. A. C. E. Biscaia, Elsevier, 2009, vol. 27, pp. 169–175.

496 A. Molino, V. Larocca, S. Chianese and D. Musmarra, *Energies*, 2018, **11**, 811.

497 V. Dieterich, A. Buttler, A. Hanel, H. Spliethoff and S. Fendt, *Energy Environ. Sci.*, DOI:10.1039/D0EE01187H.

498 K. L. Ng, D. Chadwick and B. A. Toseland, *Chem. Eng. Sci.*, 1999, **54**, 3587–3592.

499 B. C. Gates and L. N. Johanson, *AIChE J.*, 1971, **17**, 981–983.

500 S. Hosseininejad, A. Afacan and R. E. Hayes, *Chem. Eng. Res. Des.*, 2012, **90**, 825–833.

501 G. Pop, G. Bozga, R. Ganea and N. Natu, *Ind. Eng. Chem. Res.*, 2009, **48**, 7065–7071.

502 D. Masih, S. Rohani, J. N. Kondo and T. Tatsumi, *Appl. Catal. B Environ.*, 2017, **217**, 247–255.

503 A. Brunetti, M. Migliori, D. Cozza, E. Catizzone, G. Giordano and G. Barbieri, *ACS Sustain. Chem. Eng.*, 2020, **8**, 10471–10479.

504 J. J. Spivey, *Chem. Eng. Commun.*, 1991, **110**, 123–142.

505 A. I. Osman and J. K. Abu-Dahrieh, *Catal. Letters*, 2018, **148**, 1236–1245.

506 M. Matzen and Y. Demirel, *J. Clean. Prod.*, 2016, **139**, 1068–1077.

507 J. Ereña, R. Garoña, J. M. Arandes, A. T. Aguayo and J. Bilbao, *Catal. Today*, 2005, **107–108**, 467–473.

508 G. Bonura, M. Migliori, L. Frusteri, C. Cannilla, E. Catizzone, G. Giordano and F. Frusteri, *J. CO<sub>2</sub> Util.*, 2018, **24**, 398–406.

509 G. Bonura, F. Frusteri, C. Cannilla, G. Drago Ferrante, A. Aloise, E. Catizzone, M. Migliori and G. Giordano, *Catal. Today*, 2016, **277**, 48–54.

510 M.-H. Zhang, Z.-M. Liu, G.-D. Lin and H.-B. Zhang, *Appl. Catal. A Gen.*, 2013, **451**, 28–35.

511 X. An, Y.-Z. Zuo, Q. Zhang, D. Wang and J.-F. Wang, *Ind. Eng. Chem. Res.*, 2008, **47**, 6547–6554.

512 S. Wang, D. Mao, X. Guo, G. Wu and G. Lu, *Catal. Commun.*, 2009, **10**, 1367–1370.

513 A. Swapnesh, V. C. Srivastava and I. D. Mall, *Chem. Eng. Technol.*, 2014, **37**, 1765–1777.

514 E. Catizzone, A. Aloise, M. Migliori and G. Giordano, *Appl. Catal. A Gen.*, 2015, **502**, 215–220.

515 M. Xu, J. H. Lunsford, D. W. Goodman and A. Bhattacharyya, *Appl. Catal. A Gen.*, 1997, **149**, 289–301.

516 W.-H. Chen, B.-J. Lin, H.-M. Lee and M.-H. Huang, *Appl. Energy*, 2012, **98**, 92–101.

517 X. He and L. Liu, *IOP Conf. Ser. Earth Environ. Sci.*, 2017, **100**, 012078.

518 G. Bonura, M. Cordaro, L. Spadaro, C. Cannilla, F. Arena and F. Frusteri, *Appl. Catal. B Environ.*, 2013, **140–141**, 16–24.

519 J. Toyir, P. R. de la Piscina, J. L. G. Fierro and N. Homs, *Appl. Catal. B Environ.*, 2001, **29**, 207–215.

520 L. Zhang, Y. Zhang and S. Chen, *Appl. Catal. A Gen.*, 2012, **415–416**, 118–123.

521 Y. Zhao, J. Chen and J. Zhang, *J. Nat. Gas Chem.*, 2007, **16**, 389–392.

522 H. Ham, S. W. Baek, C.-H. Shin and J. W. Bae, *ACS Catal.*, 2019, **9**, 679–690.

523 Y. Zhang, D. Li, S. Zhang, K. Wang and J. Wu, *RSC Adv.*, 2014, **4**, 16391–16396.

524 G.-X. Qi, J.-H. Fei, X.-M. Zheng and Z.-Y. Hou, *Catal. Letters*, 2001, **72**, 121–124.

525 L. Yao, X. Shen, Y. Pan and Z. Peng, *Energy & Fuels*, 2020, acs.energyfuels.Oc01256.

526 F. Zha, H. Tian, J. Yan and Y. Chang, *Appl. Surf. Sci.*, 2013, **285**, 945–951.

527 S. Ren, W. R. Shoemaker, X. Wang, Z. Shang, N. Klinghoffer, S. Li, M. Yu, X. He, T. A. White and X. Liang, *Fuel*, 2019, **239**, 1125–1133.

528 H. Ham, N. T. Xuan, H. S. Jung, J. Kim, H.-S. Roh and J. W. Bae, *Catal. Today*, 2021, **369**, 112–122.

529 R. Liu, H. Tian, A. Yang, F. Zha, J. Ding and Y. Chang, *Appl. Surf. Sci.*, 2015, **345**, 1–9.

530 Q. Li, C. Xin and P. Lian, *Pet. Sci. Technol.*, 2012, **30**, 2187–2195.

531 W. Gao, H. Wang, Y. Wang, W. Guo and M. Jia, *J. Rare Earths*, 2013, **31**, 470–476.

532 Y. Zhang, Y. Zhou, H. Liu, Y. Wang, Y. Xu and P. Wu, *Appl. Catal. A Gen.*, 2007, **333**, 202–210.

533 R. Bouarab, O. Cherifi and A. Auroux, *Thermochim. Acta*, 2005, **434**, 69–73.

534 G. Bonura, M. Cordaro, C. Cannilla, A. Mezzapica, L. Spadaro, F. Arena and F. Frusteri, *Catal. Today*, 2014, **228**, 51–57.

535 F. Frusteri, G. Bonura, C. Cannilla, G. Drago Ferrante, A. Aloise, E. Catizzone, M. Migliori and G. Giordano, *Appl. Catal. B Environ.*, 2015, **176–177**, 522–531.

536 F. Frusteri, M. Cordaro, C. Cannilla and G. Bonura, *Appl. Catal. B Environ.*, 2015, **162**, 57–65.

537 L. Li, D. Mao, J. Xiao, L. Li, X. Guo and J. Yu, *Chem. Eng. Res. Des.*, 2016, **111**, 100–108.

538 Q. Sheng, R.-P. Ye, W. Gong, X. Shi, B. Xu, M. Argyle, H. Adidharma and M. Fan, *J. Environ. Sci.*, 2020, **92**, 106–117.

539 A. Ramirez, A. Dutta Chowdhury, A. Dokania, P. Cnudde, M. Caglayan, I. Yarulina, E. Abou-Hamad, L. Gevers, S. Ould-Chikh, K. De Wispelaere, V. van Speybroeck and J. Gascon, *ACS Catal.*, 2019, **9**, 6320–6334.

540 L. Liu and A. Corma, *Nat. Rev. Mater.*, 2021, **6**, 244–263.

541 G. Bonura, C. Cannilla, L. Frusteri, A. Mezzapica and F. Frusteri, *Catal. Today*, 2017, **281**, 337–344.

542 L. Frusteri, G. Bonura, C. Cannilla, S. Todaro, G. Giordano, M. Migliori and F. Frusteri, *Pet. Chem.*, 2020, **60**, 508–515.

543 G. Bonura, C. Cannilla, L. Frusteri, E. Catizzone, S. Todaro, M. Migliori, G. Giordano and F. Frusteri, *Catal. Today*, 2020, **345**, 175–182.

544 I. Miletto, E. Catizzone, G. Bonura, C. Ivaldi, M. Migliori, E. Gianotti, L. Marchese, F. Frusteri and G. Giordano, *Materials (Basel)*, 2018, **11**, 2275.

545 J. B. Miller, S. E. Rankin and E. I. Ko, *J. Catal.*, 1994, **148**, 673–682.

546 K. Galatsis, Y. X. Li, W. Wlodarski, E. Comini, G. Sberveglieri, C. Cantalini, S. Santucci and M. Passacantando, *Sensors Actuators B Chem.*, 2002, **83**, 276–280.

547 S. Abate, C. Mebrahtu, E. Giglio, F. Deorsola, S. Bensaid, S. Perathoner, R. Pirone and G. Centi, *Ind. Eng. Chem. Res.*, 2016, **55**, 4451–4460.

548 C. Mebrahtu, S. Abate, S. Perathoner, S. Chen and G. Centi, *Catal. Today*, 2018, **304**, 181–189.

549 Y. Zhang, D. Li, Y. Zhang, Y. Cao, S. Zhang, K. Wang, F. Ding and J. Wu, *Catal. Commun.*, 2014, **55**, 49–52.

550 K. Sun, W. Lu, M. Wang and X. Xu, *Catal. Commun.*, 2004, **5**, 367–370.

551 T. D. Rao, T. Karthik and S. Asthana, *J. Rare Earths*, 2013, **31**, 370–375.

552 K. Wang, X. Wang and B. Ren, 2017, **23**, 49–56.

553 G. Bonura, C. Cannilla, L. Frusteri and F. Frusteri, *Appl. Catal. A Gen.*, 2017, **544**, 21–29.

554 Z. Qin, T. Su, H. Ji, Y. Jiang, R. Liu and J. Chen, *AIChE J.*, 2015, **61**, 1613–1627.

555 Y. Yang, M. G. White and P. Liu, *J. Phys. Chem. C*, 2012, **116**, 248–256.

556 M. Behrens, F. Studt, I. Kasatkin, S. Kühl, M. Hävecker, F. Abild-Pedersen, S. Zander, F. Girgsdies, P. Kurr, B.-L. Kniep, M. Tovar, R. W. Fischer, J. K. Nørskov and R. Schlögl, *Science (80- )*, 2012, **336**, 893 LP – 897.

557 H. Bahruji, M. Bowker, W. Jones, J. Hayward, J. Ruiz Esquius, D. J. Morgan and G. J. Hutchings, *Faraday Discuss.*, 2017, **197**, 309–324.

558 H. Bahruji, J. R. Esquius, M. Bowker, G. Hutchings, R. D. Armstrong and W. Jones, *Top. Catal.*, 2018, **61**, 144–153.

559 H. Bahruji, R. D. Armstrong, J. Ruiz Esquius, W. Jones, M. Bowker and G. J. Hutchings, *Ind. Eng. Chem. Res.*, 2018, **57**, 6821–6829.

560 H. Yasuda, T. Sato and Y. Yoshimura, *Catal. Today*, 1999, **50**, 63–71.

561 Y. Ma, Q. Ge, W. Li and H. Xu, *Appl. Catal. B Environ.*, 2009, **90**, 99–104.

562 R. Chu, C. Song, W. Hou, X. Meng, Z. Miao, X. Li, G. Wu, Y. Wan and L. Bai, *J. Taiwan Inst. Chem. Eng.*, 2017, **80**, 1041–1047.

563 BP, Statistical Review of World Energy., <https://www.bp.com/en/global/corporate/energy-economics/statistical-review-of-world-energy.html>.

564 B. C. Brodie, *Proc. R. Soc. London*, 1873, **21**, 245–247.

565 Sabatier Paul, *C. R. Acad. Sci*, 1902, **134**, 689–91.

566 P. Frontera, A. Macario, M. Ferraro and P. Antonucci, *Catalysts*, 2017, **7**, 59.

567 F. N. A. A., J. A. A., R. A. F. A., H. H. U. and H. I., *J. Energy Saf. Technol.*, , DOI:10.11113/jest.v2n2.51.

568 L. Kiewidt and J. Thöming, *Chem. Eng. Sci.*, 2015, **132**, 59–71.

569 I. Hussain, A. A. Jalil, N. S. Hassan, H. U. Hambali and N. W. C. Jusoh, *Chem. Eng. Sci.*, 2020, **228**, 115978.

570 J. Gorre, F. Ortloff and C. van Leeuwen, *Appl. Energy*, 2019, **253**, 113594.

571 M. David, C. Ocampo-Martínez and R. Sánchez-Peña, *J. Energy Storage*, 2019, **23**, 392–403.

572 M. Carmo, D. L. Fritz, J. Mergel and D. Stolten, *Int. J. Hydrogen Energy*, 2013, **38**, 4901–4934.

573 J. Gao, Y. Wang, Y. Ping, D. Hu, G. Xu, F. Gu and F. Su, *RSC Adv.*, 2012, **2**, 2358–2368.

574 A. Beuls, C. Swalus, M. Jacquemin, G. Heyen, A. Karelavic and P. Ruiz, *Appl. Catal. B Environ.*, 2012, **113–114**, 2–10.

575 F. Ocampo, B. Louis and A.-C. Roger, *Appl. Catal. A Gen.*, 2009, **369**, 90–96.

576 C. V Miguel, M. A. Soria, A. Mendes and L. M. Madeira, *J. Nat. Gas Sci. Eng.*, 2015, **22**, 1–8.

577 X. Su, J. Xu, B. Liang, H. Duan, B. Hou and Y. Huang, *J. Energy Chem.*, 2016, **25**, 553–565.

578 C. Mebrahtu, F. Krebs, S. Abate, S. Perathoner, G. Centi and R. Palkovits, in *Horizons in Sustainable Industrial Chemistry and Catalysis*, eds. S. Albonetti, S. Perathoner and E. A. B. T.-S. in S. S. and C. Quadrelli, Elsevier, 2019, vol. 178, pp. 85–103.

579 H. Chen, Y. Mu, Y. Shao, S. Chansai, S. Xu, C. E. Stere, H. Xiang, R. Zhang, Y. Jiao, C. Hardacre and X. Fan, *Catal. Sci. Technol.*, 2019, **9**, 4135–4145.

580 J. L. Falconer, *J. Catal.*, 1980, **62**, 280–285.

581 E. Zagli, *J. Catal.*, 1981, **69**, 1–8.

582 A. Karelavic and P. Ruiz, *J. Catal.*, 2013, **301**, 141–153.

583 S. Sharma, Z. Hu, P. Zhang, E. W. McFarland and H. Metiu, *J. Catal.*, 2011, **278**, 297–309.

584 E. Jwa, S. B. Lee, H. W. Lee and Y. S. Mok, *Fuel Process. Technol.*, 2013, **108**, 89–93.

585 E. Kok, J. Scott, N. Cant and D. Trimm, *Catal. Today*, 2011, **164**, 297–301.

586 M. Iglesias G., C. de Vries, M. Claeys and G. Schaub, *Catal. Today*, 2015, **242**, 184–192.

587 M. A. A. Aziz, A. A. Jalil, S. Triwahyono and A. Ahmad, *Green Chem.*, 2015, **17**, 2647–2663.

588 B. Hammer and J. K. Nørskov, in *Impact of Surface Science on Catalysis*, Academic Press, 2000, vol. 45, pp. 71–129.

589 M. A. Vannice, *Catal. Rev.*, 1976, **14**, 153–191.

590 F. Solymosi and A. Erdöhelyi, *J. Mol. Catal.*, 1980, **8**, 471–474.

591 G. A. Mills and F. W. Steffgen, *Catal. Rev.*, 1974, **8**, 159–210.

592 C. Liang, Z. Ye, D. Dong, S. Zhang, Q. Liu, G. Chen, C. Li, Y. Wang and X. Hu, *Fuel*, 2019, **254**, 115654.

593 M. M. Jaffar, M. A. Nahil and P. T. Williams, *Energy Technol.*, 2019, **7**, 1900795.

594 G. Garbarino, P. Riani, L. Magistri and G. Busca, *Int. J. Hydrogen Energy*, 2014, **39**, 11557–11565.

595 H. Takano, Y. Kirihata, K. Izumiya, N. Kumagai, H. Habazaki and K. Hashimoto, *Appl. Surf. Sci.*, 2016, **388**, 653–663.

596 H. Muroyama, Y. Tsuda, T. Asakoshi, H. Masitah, T. Okanishi, T. Matsui and K. Eguchi, *J. Catal.*, 2016, **343**, 178–184.

597 X. Guo, A. Traitangwong, M. Hu, C. Zuo, V. Meeyoo, Z. Peng and C. Li, *Energy & Fuels*, 2018, **32**, 3681–3689.

598 G. Du, S. Lim, Y. Yang, C. Wang, L. Pfefferle and G. Haller, *J. Catal.*, 2007, **249**, 370–379.

599 C. H. Bartholomew, *Catal. Rev.*, 1982, **24**, 67–112.

600 A. Petala and P. Panagiotopoulou, *Appl. Catal. B Environ.*, 2018, **224**, 919–927.

601 G. Garbarino, D. Bellotti, P. Riani, L. Magistri and G. Busca, *Int. J. Hydrogen Energy*, 2015, **40**, 9171–9182.

602 F. Solymosi, A. Erdöhelyi and M. Kocsis, *J. Chem. Soc. Faraday Trans. 1 Phys. Chem. Condens. Phases*, 1981, **77**, 1003–1012.

603 G. D. Weatherbee and C. H. Bartholomew, *J. Catal.*, 1984, **87**, 352–362.

- 604 S. Scirè, C. Crisafulli, R. Maggiore, S. Minicò and S. Galvagno, *Catal. Letters*, 1998, **51**, 41–45.
- 605 J. Cored, A. García-Ortiz, S. Iborra, M. J. Climent, L. Liu, C.-H. Chuang, T.-S. Chan, C. Escudero, P. Concepción and A. Corma, *J. Am. Chem. Soc.*, 2019, **141**, 19304–19311.
- 606 S. Hwang, J. Lee, U. G. Hong, J. H. Baik, D. J. Koh, H. Lim and I. K. Song, *J. Ind. Eng. Chem.*, 2013, **19**, 698–703.
- 607 D. C. Upham, A. R. Derk, S. Sharma, H. Metiu and E. W. McFarland, *Catal. Sci. Technol.*, 2015, **5**, 1783–1791.
- 608 J. Xu, X. Su, H. Duan, B. Hou, Q. Lin, X. Liu, X. Pan, G. Pei, H. Geng, Y. Huang and T. Zhang, *J. Catal.*, 2016, **333**, 227–237.
- 609 Q. Pan, J. Peng, S. Wang and S. Wang, *Catal. Sci. Technol.*, 2014, **4**, 502–509.
- 610 M. A. A. Aziz, A. A. Jalil, S. Triwahyono and S. M. Sidik, *Appl. Catal. A Gen.*, 2014, **486**, 115–122.
- 611 S. Rönsch, J. Schneider, S. Matthischke, M. Schlüter, M. Götz, J. Lefebvre, P. Prabhakaran and S. Bajohr, *Fuel*, 2016, **166**, 276–296.
- 612 C. Liang, L. Zhang, Y. Zheng, S. Zhang, Q. Liu, G. Gao, D. Dong, Y. Wang, L. Xu and X. Hu, *Fuel*, 2020, **262**, 116521.
- 613 S. Tada and R. Kikuchi, *Catal. Sci. Technol.*, 2015, **5**, 3061–3070.
- 614 E. F. Sousa-Aguiar, in *Zeolites and Zeolite-Like Materials*, eds. B. F. Sels and L. M. B. T.-Z. and Z.-L. M. Kustov, Elsevier, Amsterdam, 2016, pp. 265–282.
- 615 A. Corma, in *Zeolites: Facts, Figures, Future Part A - Proceedings of the 8th International Zeolite Conference*, eds. P. A. Jacobs and R. A. B. T.-S. in S. S. and C. van Santen, Elsevier, 1989, vol. 49, pp. 49–67.
- 616 T. Franken and A. Heel, *J. CO<sub>2</sub> Util.*, 2020, **39**, 101175.
- 617 R. Delmelle, R. B. Duarte, T. Franken, D. Burnat, L. Holzer, A. Borgschulte and A. Heel, *Int. J. Hydrogen Energy*, 2016, **41**, 20185–20191.
- 618 N. P. Davidova, M. L. Valcheva and D. M. Shopov, in *Structure and Reactivity of Modified Zeolites*, eds. P. A. Jacobs, N. I. Jaeger, P. Jírů, V. B. Kazansky and G. B. T.-S. in S. S. and C. Schulz-Ekloff, Elsevier, 1984, vol. 18, pp. 353–360.
- 619 A. Martínez, E. Peris and G. Sastre, *Catal. Today*, 2005, **107–108**, 676–684.
- 620 A. H. Yonli, I. Gener and S. Mignard, *Microporous Mesoporous Mater.*, 2010, **132**, 37–42.
- 621 M. C. Bacariza, I. Graça, J. M. Lopes and C. Henriques, *Microporous Mesoporous Mater.*, 2018, **267**, 9–19.
- 622 R. A. Hubble, J. Y. Lim and J. S. Dennis, *Faraday Discuss.*, 2016, **192**, 529–544.
- 623 J. Yang Lim, J. McGregor, A. J. Sederman and J. S. Dennis, *Chem. Eng. Sci.*, 2016, **141**, 28–45.
- 624 J. F. da Costa-Serra, C. Cerdá-Moreno and A. Chica, *Appl. Sci.*, 2020, **10**, 5131.
- 625 I. Rossetti, M. Compagnoni, E. Finocchio, G. Ramis, A. Di Michele, A. Zucchini and S. Dzwigaj, *Int. J. Hydrogen Energy*, 2016, **41**, 16878–16889.
- 626 H. Yang, L. Xu, M. Chen, C. Lv, Y. Cui, X. Wen, C. Wu, B. Yang, Z. Miao, X. Hu and Q. Shou, *Microporous Mesoporous Mater.*, 2020, **302**, 110250.
- 627 M. C. Bacariza, M. Biset-Peiró, I. Graça, J. Guilera, J. Morante, J. M. Lopes, T. Andreu and C. Henriques, *J. CO<sub>2</sub> Util.*, 2018, **26**, 202–211.
- 628 M. C. Bacariza, I. Graça, J. M. Lopes and C. Henriques, *ChemCatChem*, 2018, **10**, 2773–2781.
- 629 M. C. Bacariza, R. Bértolo, I. Graça, J. M. Lopes and C. Henriques, *J. CO<sub>2</sub> Util.*, 2017, **21**, 280–291.
- 630 K. S. Walton, M. B. Abney and M. Douglas LeVan, *Microporous Mesoporous Mater.*, 2006, **91**, 78–84.
- 631 E. Díaz, E. Muñoz, A. Vega and S. Ordóñez, *Ind. Eng. Chem. Res.*, 2008, **47**, 412–418.
- 632 P. A. S. Moura, D. P. Bezerra, E. Vilarrosa-García, M. Bastos-Neto and D. C. S. Azevedo, *Adsorption*, 2016, **22**, 71–80.
- 633 J. Juan-Juan, M. Román-Martínez and M. Illán-Gómez, *Appl. Catal. A Gen.*, 2004, **264**, 169–174.
- 634 B. Coughlan and M. A. Keane, *Zeolites*, 1991, **11**, 2–11.
- 635 L. Liu, D. M. Meira, R. Arenal, P. Concepcion, A. V Puga and A. Corma, *ACS Catal.*, 2019, **9**, 10626–10639.
- 636 M. C. Bacariza, M. Maleval, I. Graça, J. M. Lopes and C. Henriques, *Microporous Mesoporous Mater.*, 2019, **274**, 102–112.
- 637 B. Rotenberg, J.-P. Morel, V. Marry, P. Turq and N. Morel-Desrosiers, *Geochim. Cosmochim. Acta*, 2009, **73**, 4034–4044.
- 638 Q. Pan, J. Peng, T. Sun, S. Wang and S. Wang, *Catal. Commun.*, 2014, **45**, 74–78.
- 639 I. Graça, L. V. González, M. C. Bacariza, A. Fernandes, C. Henriques, J. M. Lopes and M. F. Ribeiro, *Appl. Catal. B Environ.*, 2014, **147**, 101–110.
- 640 M. C. Bacariza, I. Graça, A. Westermann, M. F. Ribeiro, J. M. Lopes and C. Henriques, *Top. Catal.*, 2016, **59**, 314–325.
- 641 L. Wei, W. Haije, N. Kumar, J. Peltonen, M. Peurla, H. Grenman and W. de Jong, *Catal. Today*, 2021, **362**, 35–46.
- 642 N. Czuma, K. Zarębska, M. Motak, M. E. Gálvez and P. Da Costa, *Fuel*, 2020, **267**, 117139.
- 643 Y. Chen, B. Qiu, Y. Liu and Y. Zhang, *Appl. Catal. B Environ.*, 2020, **269**, 118801.
- 644 F. Goodarzi, L. Kang, F. R. Wang, F. Joensen, S. Kegnaes and J. Mielby, *ChemCatChem*, 2018, **10**, 1566–1570.
- 645 W. Wei and G. Jinlong, *Front. Chem. Sci. Eng.*, 2011, **5**, 2–10.
- 646 W. Wang, S. Wang, X. Ma and J. Gong, *Chem. Soc. Rev.*, 2011, **40**, 3703–3727.
- 647 F. Wang, S. He, H. Chen, B. Wang, L. Zheng, M. Wei, D. G. Evans and X. Duan, *J. Am. Chem. Soc.*, 2016, **138**, 6298–6305.

- 648 J. Huang, X. Li, X. Wang, X. Fang, H. Wang and X. Xu, *J. CO2 Util.*, 2019, **33**, 55–63.
- 649 G. Zhi, X. Guo, Y. Wang, G. Jin and X. Guo, *Catal. Commun.*, 2011, **16**, 56–59.
- 650 G. Garbarino, C. Wang, T. Cavattoni, E. Finocchio, P. Riani, M. Flytzani-Stephanopoulos and G. Busca, *Appl. Catal. B Environ.*, 2019, **248**, 286–297.
- 651 M. Guo and G. Lu, *RSC Adv.*, 2014, **4**, 58171–58177.
- 652 U. De-La-Torre, A. Quindimil, J. González-Velasco, D. Lozano-Castelló, B. Pereda-Ayo, J. González-Marcos, A. Bueno-López, A. Davó-Quiñonero and V. Alcalde-Santiago, *ChemCatChem*, DOI:10.1002/cctc.201801585.
- 653 I. Sreedhar, Y. Varun, S. A. Singh, A. Venugopal and B. M. Reddy, *Catal. Sci. Technol.*, 2019, **9**, 4478–4504.
- 654 L. Atzori, M. G. Cutrufello, D. Meloni, R. Monaci, C. Cannas, D. Gazzoli, M. F. Sini, P. Deiana and E. Rombi, *Int. J. Hydrogen Energy*, 2017, **42**, 20689–20702.
- 655 A. Trovarelli, *Catal. Rev.*, 1996, **38**, 439–520.
- 656 B. Murugan and A. V Ramaswamy, *J. Am. Chem. Soc.*, 2007, **129**, 3062–3063.
- 657 J. A. Farmer and C. T. Campbell, *Science (80- )*, 2010, **329**, 933 LP – 936.
- 658 L. Wei, N. Kumar, W. Haije, J. Peltonen, M. Peurla, H. Grénman and W. de Jong, *Mol. Catal.*, 2020, **494**, 111115.
- 659 F. Wang, S. He, H. Chen, B. Wang, L. Zheng, M. Wei, D. G. Evans and X. Duan, *J. Am. Chem. Soc.*, 2016, **138**, 6298–6305.
- 660 A. Westermann, B. Azambre, M. C. Bacariza, I. Graça, M. F. Ribeiro, J. M. Lopes and C. Henriques, *Appl. Catal. B Environ.*, 2015, **174–175**, 120–125.
- 661 R. Zhang, H. Chen, Y. Mu, S. Chansai, X. Ou, C. Hardacre, Y. Jiao and X. Fan, *AIChE J.*, 2020, **n/a**, e17007.
- 662 F. Azzolina-Jury and F. Thibault-Starzyk, *Top. Catal.*, 2017, **60**, 1709–1721.
- 663 Q. Bi, X. Huang, G. Yin, T. Chen, X. Du, J. Cai, J. Xu, Z. Liu, Y. Han and F. Huang, *ChemCatChem*, 2019, **11**, 1295–1302.
- 664 A. Westermann, B. Azambre, M. C. Bacariza, I. Graça, M. F. Ribeiro, J. M. Lopes and C. Henriques, *Catal. Today*, 2017, **283**, 74–81.
- 665 R. Zhang, A. Wei, M. Zhu, X. Wu, H. Wang, X. Zhu and Q. Ge, *J. CO2 Util.*, 2021, **52**, 101678.
- 666 J. Li, C. Ma, S. Zhu, F. Yu, B. Dai and D. Yang, *Nanomaterials*, 2019, **9**, 1428.
- 667 K. Zhang, G. Zhang, X. Liu, A. N. Phan and K. Luo, *Ind. Eng. Chem. Res.*, 2017, **56**, 3204–3216.
- 668 W. Hua, L. Jin, X. He, J. Liu and H. Hu, *Catal. Commun.*, 2010, **11**, 968–972.
- 669 Y. Li, Z. Wei and Y. Wang, *Front. Chem. Sci. Eng.*, 2014, **8**, 133–140.
- 670 Z. Fan, K. Sun, N. Rui, B. Zhao and C. Liu, *J. Energy Chem.*, 2015, **24**, 655–659.
- 671 F. Azzolina-Jury, D. Bento, C. Henriques and F. Thibault-Starzyk, *J. CO2 Util.*, 2017, **22**, 97–109.
- 672 J. Zhang, Z. Xin, X. Meng and M. Tao, *Fuel*, 2013, **109**, 693–701.
- 673 D. Liu, R. Lau, A. Borgna and Y. Yang, *Appl. Catal. A Gen.*, 2009, **358**, 110–118.
- 674 S. Corthals, J. Van Nederkassel, J. Geboers, H. De Winne, J. Van Noyen, B. Moens, B. Sels and P. Jacobs, *Catal. Today*, 2008, **138**, 28–32.
- 675 D. Li, L. Zeng, X. Li, X. Wang, H. Ma, S. Assabumrungrat and J. Gong, *Appl. Catal. B Environ.*, 2015, **176–177**, 532–541.
- 676 X. Wang, L. Zhu, Y. Liu and S. Wang, *Sci. Total Environ.*, 2018, **625**, 686–695.
- 677 C. Wu, L. Dong, J. Onwudili, P. T. Williams and J. Huang, *ACS Sustain. Chem. Eng.*, 2013, **1**, 1083–1091.
- 678 M. C. Bacariza, I. Graça, S. S. Bebiano, J. M. Lopes and C. Henriques, *Chem. Eng. Sci.*, 2018, **175**, 72–83.
- 679 J. Ashok, S. Pati, P. Hongmanorom, Z. Tianxi, C. Junmei and S. Kawi, *Catal. Today*, 2020, **356**, 471–489.
- 680 E. Christensen, J. Yanowitz, M. Ratcliff and R. L. McCormick, *Energy & Fuels*, 2011, **25**, 4723–4733.
- 681 F. Zeng, C. Mebrahtu, X. Xi, L. Liao, J. Ren, J. Xie, H. J. Heeres and R. Palkovits, *Appl. Catal. B Environ.*, 2021, **291**, 120073.
- 682 S. Zhang, Z. Wu, X. Liu, K. Hua, Z. Shao, B. Wei, C. Huang, H. Wang and Y. Sun, *Top. Catal.*, 2021, **64**, 371–394.
- 683 R. A. Dagle, A. D. Winkelman, K. K. Ramasamy, V. Lebarbier Dagle and R. S. Weber, *Ind. Eng. Chem. Res.*, 2020, **59**, 4843–4853.
- 684 H. T. Abdulrazaq and T. J. Schwartz, eds. A. Basile, A. Iulianelli, F. Dalena and T. N. B. T.-E. Veziroğlu, Elsevier, 2019, pp. 3–24.
- 685 F. A. E., P. R. J., T. B. T., J. A. D., O. Michael and K. D. M., *Science (80- )*, 2006, **311**, 506–508.
- 686 T. Walther and J. M. François, *Biotechnol. Adv.*, 2016, **34**, 984–996.
- 687 P. Dürre, *Ann. N. Y. Acad. Sci.*, 2008, **1125**, 353–362.
- 688 D. Pimentel and T. W. Patzek, *Nat. Resour. Res.*, 2005, **14**, 65–76.
- 689 H. T. Luk, C. Mondelli, D. C. Ferré, J. A. Stewart and J. Pérez-Ramírez, *Chem. Soc. Rev.*, 2017, **46**, 1358–1426.
- 690 S. Gehrman and N. Tenhumberg, *Chemie Ing. Tech.*, 2020, **92**, 1444–1458.
- 691 C. K. Rofer-DePoorter, *Chem. Rev.*, 1981, **81**, 447–474.
- 692 R. A. van Santen, A. J. Markvoort, I. A. W. Filot, M. M. Ghouri and E. J. M. Hensen, *Phys. Chem. Chem. Phys.*, 2013, **15**, 17038–17063.
- 693 C. Yang, R. Mu, G. Wang, J. Song, H. Tian, Z.-J. Zhao and J. Gong, *Chem. Sci.*, 2019, **10**, 3161–3167.
- 694 L. Wang, L. Wang, J. Zhang, X. Liu, H. Wang, W. Zhang, Q. Yang, J. Ma, X. Dong, S. J. Yoo, J.-G. Kim, X. Meng and F.-S. Xiao, *Angew. Chemie Int. Ed.*, 2018, **57**, 6104–6108.
- 695 F. Zhang, W. Zhou, X. Xiong, Y. Wang, K. Cheng, J. Kang, Q. Zhang and Y. Wang, *J. Phys. Chem. C*, 2021, **125**,

- 24429–24439.
- 696 T. Chen, J. Su, Z. Zhang, C. Cao, X. Wang, R. Si, X. Liu, B. Shi, J. Xu and Y.-F. Han, *ACS Catal.*, 2018, **8**, 8606–8617.
- 697 M. Ao, G. H. Pham, J. Sunarso, M. O. Tade and S. Liu, *ACS Catal.*, 2018, **8**, 7025–7050.
- 698 Y. Liu, F. Göeltl, I. Ro, M. R. Ball, C. Sener, I. B. Aragão, D. Zanchet, G. W. Huber, M. Mavrikakis and J. A. Dumesic, *ACS Catal.*, 2017, **7**, 4550–4563.
- 699 C. Wang, J. Zhang, G. Qin, L. Wang, E. Zuidema, Q. Yang, S. Dang, C. Yang, J. Xiao, X. Meng, C. Mesters and F.-S. Xiao, *Chem*, 2020, **6**, 646–657.
- 700 V. Schwartz, A. Campos, A. Egbebi, J. J. Spivey and S. H. Overbury, *ACS Catal.*, 2011, **1**, 1298–1306.
- 701 G. van der Lee, B. Schuller, H. Post, T. L. F. Favre and V. Ponec, *J. Catal.*, 1986, **98**, 522–529.
- 702 G. Prieto, P. Concepción, A. Martínez and E. Mendoza, *J. Catal.*, 2011, **280**, 274–288.
- 703 H.-Y. Luo, P.-Z. Lin, S.-B. Xie, H.-W. Zhou, C.-H. Xu, S.-Y. Huang, L.-W. Lin, D.-B. Liang, P.-L. Yin and Q. Xin, *J. Mol. Catal. A Chem.*, 1997, **122**, 115–123.
- 704 H. Kusama, K. Okabe, K. Sayama and H. Arakawa, *Catal. Today*, 1996, **28**, 261–266.
- 705 H. Wang, L. Wang and F.-S. Xiao, *ACS Cent. Sci.*, 2020, **6**, 1685–1697.
- 706 Y. Wang, C. Wang, L. Wang, L. Wang and F.-S. Xiao, *Acc. Chem. Res.*, 2021, **54**, 2579–2590.
- 707 L. Liu, U. Díaz, R. Arenal, G. Agostini, P. Concepción and A. Corma, *Nat. Mater.*, 2017, **16**, 132–138.
- 708 S. Li, H. Guo, C. Luo, H. Zhang, L. Xiong, X. Chen and L. Ma, *Catal. Letters*, 2013, **143**, 345–355.
- 709 L. Ding, T. Shi, J. Gu, Y. Cui, Z. Zhang, C. Yang, T. Chen, M. Lin, P. Wang, N. Xue, L. Peng, X. Guo, Y. Zhu, Z. Chen and W. Ding, *Chem*, 2020, **6**, 2673–2689.
- 710 G. Wang, R. Luo, C. Yang, J. Song, C. Xiong, H. Tian, Z.-J. Zhao, R. Mu and J. Gong, *Sci. China Chem.*, 2019, **62**, 1710–1719.
- 711 L. Torrente-Murciano, D. Mattia, M. D. Jones and P. K. Plucinski, *J. CO<sub>2</sub> Util.*, 2014, **6**, 34–39.
- 712 A. Tavakoli, M. Sohrabi and A. Kargari, *Chem. Eng. J.*, 2008, **136**, 358–363.
- 713 A. Noreen, M. Li, Y. Fu, C. C. Amoo, J. Wang, E. Maturura, C. Du, R. Yang, C. Xing and J. Sun, *ACS Catal.*, 2020, **10**, 14186–14194.
- 714 P. del Campo, C. Martínez and A. Corma, *Chem. Soc. Rev.*, 2021, **50**, 8511–8595.
- 715 C. Martínez and A. Corma, *Coord. Chem. Rev.*, 2011, **255**, 1558–1580.
- 716 M. Aresta, A. Dibenedetto and A. Angelini, *Chem. Rev.*, 2014, **114**, 1709–1742.
- 717 C. Panzone, R. Philippe, A. Chappaz, P. Fongarland and A. Bengaouer, *J. CO<sub>2</sub> Util.*, 2020, **38**, 314–347.
- 718 D. D. Suppiah, W. M. A. W. Daud and M. R. Johan, *Energy & Fuels*, 2021, **35**, 17261–17278.
- 719 J. Wei, Q. Ge, R. Yao, Z. Wen, C. Fang, L. Guo, H. Xu and J. Sun, *Nat. Commun.*, 2017, **8**, 15174.
- 720 J. Chen, T. Liang, J. Li, S. Wang, Z. Qin, P. Wang, L. Huang, W. Fan and J. Wang, *ACS Catal.*, 2016, **6**, 2299–2313.
- 721 P. Gao, S. Li, X. Bu, S. Dang, Z. Liu, H. Wang, L. Zhong, M. Qiu, C. Yang, J. Cai, W. Wei and Y. Sun, *Nat. Chem.*, 2017, **9**, 1019–1024.
- 722 M. Fujiwara, R. Kieffer, H. Ando and Y. Souma, *Appl. Catal. A Gen.*, 1995, **121**, 113–124.
- 723 M. Fujiwara, T. Satake, K. Shiokawa and H. Sakurai, *Appl. Catal. B Environ.*, 2015, **179**, 37–43.
- 724 O. Martin, A. J. Martín, C. Mondelli, S. Mitchell, T. F. Segawa, R. Hauert, C. Drouilly, D. Curulla-Ferré and J. Pérez-Ramírez, *Angew. Chemie Int. Ed.*, 2016, **55**, 6261–6265.
- 725 Z. Li, J. Wang, Y. Qu, H. Liu, C. Tang, S. Miao, Z. Feng, H. An and C. Li, *ACS Catal.*, 2017, **7**, 8544–8548.
- 726 P. Gao, S. Dang, S. Li, X. Bu, Z. Liu, M. Qiu, C. Yang, H. Wang, L. Zhong, Y. Han, Q. Liu, W. Wei and Y. Sun, *ACS Catal.*, 2018, **8**, 571–578.
- 727 X. Liu, M. Wang, C. Zhou, W. Zhou, K. Cheng, J. Kang, Q. Zhang, W. Deng and Y. Wang, *Chem. Commun.*, 2018, **54**, 140–143.
- 728 Y. Ni, Z. Chen, Y. Fu, Y. Liu, W. Zhu and Z. Liu, *Nat. Commun.*, 2018, **9**, 3457.
- 729 K. Cheng, W. Zhou, J. Kang, S. He, S. Shi, Q. Zhang, Y. Pan, W. Wen and Y. Wang, *Chem*, 2017, **3**, 334–347.
- 730 T. Wang, C. Yang, P. Gao, S. Zhou, S. Li, H. Wang and Y. Sun, *Appl. Catal. B Environ.*, 2021, **286**, 119929.
- 731 Z. Li, Y. Qu, J. Wang, H. Liu, M. Li, S. Miao and C. Li, *Joule*, 2019, **3**, 570–583.
- 732 X. Zhang, A. Zhang, X. Jiang, J. Zhu, J. Liu, J. Li, G. Zhang, C. Song and X. Guo, *J. CO<sub>2</sub> Util.*, 2019, **29**, 140–145.
- 733 Q. Xin, H. Guo, Y. Wang, L. Xiao, W. Wang and W. Wu, *J. Environ. Chem. Eng.*, 2022, **10**, 108032.
- 734 Z. Mei, N. Zhang, S. Ouyang, Y. Zhang, T. Kako and J. Ye, *Sci. Technol. Adv. Mater.*, 2012, **13**, 055001.
- 735 P. Zhang, L. Tan, G. Yang and N. Tsubaki, *Chem. Sci.*, 2017, **8**, 7941–7946.
- 736 Y. Wang, L. Tan, M. Tan, P. Zhang, Y. Fang, Y. Yoneyama, G. Yang and N. Tsubaki, *ACS Catal.*, 2019, **9**, 895–901.
- 737 Y. Wang, W. Gao, S. Kazumi, H. Li, G. Yang and N. Tsubaki, *Chemistry (Easton)*, 2019, **25**, 5149–5153.
- 738 W. Gao, L. Guo, Q. Wu, C. Wang, X. Guo, Y. He, P. Zhang, G. Yang, G. Liu, J. Wu and N. Tsubaki, *Appl. Catal. B Environ.*, 2022, **303**, 120906.
- 739 R. P. Ye, J. Ding, W. Gong, M. D. Argyle, Q. Zhong, Y. Wang, C. K. Russell, Z. Xu, A. G. Russell, Q. Li, M. Fan and Y. G. Yao, *Nat Commun*, 2019, **10**, 5698.
- 740 W. Liu, S. Cheng, H. S. Malhi, X. Gao, Z. Zhang and W. Tu, *Catalysts*, 2022, **12**, 1432.
- 741 L. Guo, J. Li, Y. Cui, R. Kosol, Y. Zeng, G. Liu, J. Wu, T. Zhao, G. Yang, L. Shao, P. Zhan, J. Chen and N. Tsubaki, *Chem. Commun.*, 2020, **56**, 9372–9375.

742 R. Kosol, L. Guo, N. Kodama, P. Zhang, P. Reubroycharoen, T. Vitidsant, A. Taguchi, T. Abe, J. Chen, G. Yang, Y. Yoneyama and N. Tsubaki, *Catal. Commun.*, 2021, **149**, 106216.

743 J. Zhang, S. Lu, X. Su, S. Fan, Q. Ma and T. Zhao, *J. CO<sub>2</sub> Util.*, 2015, **12**, 95–100.

744 J. Liang, L. Guo, W. Gao, C. Wang, X. Guo, Y. He, G. Yang and N. Tsubaki, *Ind. Eng. Chem. Res.*, 2022, **61**, 10336–10346.

745 Y. Xu, C. Shi, B. Liu, T. Wang, J. Zheng, W. Li, D. Liu and X. Liu, *Catal. Sci. Technol.*, 2019, **9**, 593–610.

746 M. Peacock, J. Paterson, L. Reed, S. Davies, S. Carter, A. Coe and J. Clarkson, *Top. Catal.*, 2020, **63**, 328–339.

747 G. Leonzio, *J. CO<sub>2</sub> Util.*, 2018, **27**, 326–354.

748 X. Su, X. Yang, B. Zhao and Y. Huang, *J. Energy Chem.*, 2017, **26**, 854–867.

749 P. Kaiser, R. B. Unde, C. Kern and A. Jess, *Chemie Ing. Tech.*, 2013, **85**, 489–499.

750 M. Zhu, Q. Ge and X. Zhu, *Trans. Tianjin Univ.*, 2020, **26**, 172–187.

751 L. Zhang, L. Chen, S. Xia, C. Wang and F. Sun, *Entropy*, 2018, **20**, 415.

752 O.-S. Joo, K.-D. Jung, I. Moon, A. Y. Rozovskii, G. I. Lin, S.-H. Han and S.-J. Uhm, *Ind. Eng. Chem. Res.*, 1999, **38**, 1808–1812.

753 2012, 2012.

754 O.-S. Joo, K.-D. Jung and J. Yonsoo, in *Carbon Dioxide Utilization for Global Sustainability*, eds. S.-E. Park, J.-S. Chang and K.-W. B. T.-S. in S. S. and C. Lee, Elsevier, 2004, vol. 153, pp. 67–72.

755 L. F. Bobadilla, J. L. Santos, S. Ivanova, J. A. Odriozola and A. Urakawa, *ACS Catal.*, 2018, **8**, 7455–7467.

756 A. Goguet, F. C. Meunier, D. Tibiletti, J. P. Breen and R. Burch, *J. Phys. Chem. B*, 2004, **108**, 20240–20246.

757 J. A. Rodriguez, P. Liu, D. J. Stacchiola, S. D. Senanayake, M. G. White and J. G. Chen, *ACS Catal.*, 2015, **5**, 6696–6706.

758 C.-S. Chen, W.-H. Cheng and S.-S. Lin, *Catal. Letters*, 2000, **68**, 45–48.

759 M. J. L. Ginés, A. J. Marchi and C. R. Apesteguía, *Appl. Catal. A Gen.*, 1997, **154**, 155–171.

760 Y. A. Daza and J. N. Kuhn, *RSC Adv.*, 2016, **6**, 49675–49691.

761 D. S. Newsome, *Catal. Rev.*, 1980, **21**, 275–318.

762 Y. Zhuang, R. Currie, K. B. McAuley and D. S. A. Simakov, *Appl. Catal. A Gen.*, 2019, **575**, 74–86.

763 M. D. Porosoff, B. Yan and J. G. Chen, *Energy Environ. Sci.*, 2016, **9**, 62–73.

764 J. A. Rodriguez, J. Evans, L. Feria, A. B. Vidal, P. Liu, K. Nakamura and F. Illas, *J. Catal.*, 2013, **307**, 162–169.

765 C.-S. Chen, W.-H. Cheng and S.-S. Lin, *Appl. Catal. A Gen.*, 2003, **238**, 55–67.

766 S. I. Fujita, M. Usui and N. Takezawa, *J. Catal.*, 1992, **134**, 220–225.

767 S. Saeidi, S. Najari, F. Fazlollahi, M. K. Nikoo, F. Sefidkon, J. J. Klemeš and L. L. Baxter, *Renew. Sustain. Energy Rev.*, 2017, **80**, 1292–1311.

768 Y.-J. Han, J. M. Kim and G. D. Stucky, *Chem. Mater.*, 2000, **12**, 2068–2069.

769 C. Yang, P. Liu, Y. Ho, C. Chiu and K. Chao, *Chem. Mater.*, 2003, **15**, 275–280.

770 B. Lu and K. Kawamoto, *RSC Adv.*, 2012, **2**, 6800–6805.

771 B. Lu and K. Kawamoto, *J. Environ. Chem. Eng.*, 2013, **1**, 300–309.

772 B. Lu and K. Kawamoto, *Catal. Sci. Technol.*, 2014, **4**, 4313–4321.

773 R. Merkache, I. Fechete, M. Maamache, M. Bernard, P. Turek, K. Al-Dalama and F. Garin, *Appl. Catal. A Gen.*, 2015, **504**, 672–681.

774 H. Yuan, X. Zhu, J. Han, H. Wang and Q. Ge, *J. CO<sub>2</sub> Util.*, 2018, **26**, 8–18.

775 A. G. Kharaji, A. Shariati and M. A. Takassi, *Chinese J. Chem. Eng.*, 2013, **21**, 1007–1014.

776 Y. Han, C. Fang, X. Ji, J. Wei, Q. Ge and J. Sun, *ACS Catal.*, 2020, **10**, 12098–12108.

777 B. Lu, Y. Ju, T. Abe and K. Kawamoto, *Inorg. Chem. Front.*, 2015, **2**, 741–748.

778 J. Adanez, A. Abad, F. Garcia-Labiano, P. Gayan and L. F. de Diego, *Prog. Energy Combust. Sci.*, 2012, **38**, 215–282.

779 Y. A. Daza, R. A. Kent, M. M. Yung and J. N. Kuhn, *Ind. Eng. Chem. Res.*, 2014, **53**, 5828–5837.

780 M. Wenzel, L. Rihko-Struckmann and K. Sundmacher, *Chem. Eng. J.*, 2018, **336**, 278–296.

781 D. Maiti, B. J. Hare, Y. A. Daza, A. E. Ramos, J. N. Kuhn and V. R. Bhethanabotla, *Energy Environ. Sci.*, 2018, **11**, 648–659.

782 B. J. Hare, D. Maiti, S. Ramani, A. E. Ramos, V. R. Bhethanabotla and J. N. Kuhn, *Catal. Today*, 2019, **323**, 225–232.

783 Y. A. Daza, D. Maiti, R. A. Kent, V. R. Bhethanabotla and J. N. Kuhn, *Catal. Today*, 2015, **258**, 691–698.

784 S. Carter, A. Selcuk, R. J. Chater, J. Kajda, J. A. Kilner and B. C. H. Steele, *Solid State Ionics*, 1992, **53–56**, 597–605.

785 D. Maiti, Y. A. Daza, M. M. Yung, J. N. Kuhn and V. R. Bhethanabotla, *J. Mater. Chem. A*, 2016, **4**, 5137–5148.

786 X. Zhu, K. Li, L. Neal and F. Li, *ACS Catal.*, 2018, **8**, 8213–8236.

787 J. C. Brower, B. J. Hare, V. R. Bhethanabotla and J. N. Kuhn, *ChemCatChem*, 2020, **12**, 6317–6328.

788 C. Li, A. Vidal-Moya, P. J. Miguel, J. Dedecek, M. Boronat and A. Corma, *ACS Catal.*, 2018, **8**, 7688–7697.

789 C. Wang, E. Guan, L. Wang, X. Chu, Z. Wu, J. Zhang, Z. Yang, Y. Jiang, L. Zhang, X. Meng, B. C. Gates and F. S. Xiao, *J Am Chem Soc*, 2019, **141**, 8482–8488.

790 J. Zhang, L. Wang, B. Zhang, H. Zhao, U. Kolb, Y. Zhu, L. Liu, Y. Han, G. Wang, C. Wang, D. S. Su, B. C. Gates and F.-S. Xiao, *Nat. Catal.*, 2018, **1**, 540–546.

791 A. Okemoto, M. R. Harada, T. Ishizaka, N. Hiyoshi and K. Sato, *Appl. Catal. A Gen.*, 2020, **592**, 117415.

- 792 X. Yang, X. Su, X. Chen, H. Duan, B. Liang, Q. Liu, X. Liu, Y. Ren, Y. Huang and T. Zhang, *Appl. Catal. B Environ.*, 2017, **216**, 95–105.
- 793 K. K. Bando, N. Ichikuni, K. Soga, K. Kunimori, H. Arakawa and K. Asakura, *J. Catal.*, 2000, **194**, 91–104.
- 794 A. M. Gadalla and B. Bower, *Chem. Eng. Sci.*, 1988, **43**, 3049–3062.
- 795 H. Stull, Daniel R.; Prophet, *JANAF thermochemical tables*, Washington., 1971.
- 796 S. Wang, G. Q. (Max) Lu and G. J. Millar, *Energy & Fuels*, 1996, **10**, 896–904.
- 797 Z. Bian, S. Das, M. H. Wai, P. Hongmanorom and S. Kawi, *ChemPhysChem*, 2017, **18**, 3117–3134.
- 798 A. Takano, T. Tagawa and S. Goto, *J. Chem. Eng. JAPAN*, 1994, **27**, 727–731.
- 799 N. R. Dibbern, H. C.; Olesen, P.; Rostrup-Nielsen, J. R.; Tottrup, P. B. and Udengaard, *Hydrocarb. Process (United States)*.
- 800 J. H. Edwards and A. M. Maitra, *Fuel Process. Technol.*, 1995, **42**, 269–289.
- 801 A. Shamsi and C. D. Johnson, *Catal. Today*, 2003, **84**, 17–25.
- 802 K. Tomishige, Y. Himeno, Y. Matsuo, Y. Yoshinaga and K. Fujimoto, *Ind. Eng. Chem. Res.*, 2000, **39**, 1891–1897.
- 803 E. Akpan, Y. Sun, P. Kumar, H. Ibrahim, A. Aboudheir and R. Idem, *Chem. Eng. Sci.*, 2007, **62**, 4012–4024.
- 804 Y. Kathiraser, U. Oemar, E. T. Saw, Z. Li and S. Kawi, *Chem. Eng. J.*, 2015, **278**, 62–78.
- 805 N. Ivanova, V. Gugleva, M. Dobрева, I. Pehlivanov, S. Stefanov and V. Andonova, *Intech*, 2016, **i**, 13.
- 806 A. T. Ashcroft, A. K. Cheetham, M. L. H. Green and P. D. F. Vernon, *Nature*, 1991, **352**, 225–226.
- 807 M. C. J. Bradford and M. A. Vannice, *Catal. Rev.*, 1999, **41**, 1–42.
- 808 D. Pakhare and J. Spivey, *Chem. Soc. Rev.*, 2014, **43**, 7813–7837.
- 809 J.-H. Kim, D. J. Suh, T.-J. Park and K.-L. Kim, *Appl. Catal. A Gen.*, 2000, **197**, 191–200.
- 810 D. Chen, K. Christensen, E. Ochoa-Fernandez, Z. Yu, B. Totdal, N. Latorre, A. Monzon and A. Holmen, *J. Catal.*, 2005, **229**, 82–96.
- 811 J. A. Lercher, J. H. Bitter, W. Hally, W. Niessen and K. Seshan, in *11th International Congress On Catalysis - 40th Anniversary*, eds. J. W. Hightower, W. Nicholas Delgass, E. Iglesia and A. T. B. T.-S. in S. S. and C. Bell, Elsevier, 1996, vol. 101, pp. 463–472.
- 812 S. Tang, L. Ji, J. Lin, H. C. Zeng, K. L. Tan and K. Li, *J. Catal.*, 2000, **194**, 424–430.
- 813 S. Wang, *Appl. Catal. B Environ.*, 1998, **16**, 269–277.
- 814 S. Natesakhawat, R. Watson, X. Wang and U. Ozkan, *J. Catal.*, 2005, **234**, 496–508.
- 815 M.-S. Fan, A. Z. Abdullah and S. Bhatia, *ChemCatChem*, 2009, **1**, 192–208.
- 816 Z. Cheng, Q. Wu, J. Li and Q. Zhu, *Catal. Today*, 1996, **30**, 147–155.
- 817 L. Xu, H. Song and L. Chou, *Appl. Catal. B Environ.*, 2011, **108–109**, 177–190.
- 818 S. Liu, L. Guan, J. Li, N. Zhao, W. Wei and Y. Sun, *Fuel*, 2008, **87**, 2477–2481.
- 819 K. Tomishige, O. Yamazaki, Y. Chen, K. Yokoyama, X. Li and K. Fujimoto, *Catal. Today*, 1998, **45**, 35–39.
- 820 A. Effendi, K. Hellgardt, Z.-G. Zhang and T. Yoshida, *Catal. Commun.*, 2003, **4**, 203–207.
- 821 Z. Hou, *Appl. Catal. A Gen.*, 2003, **253**, 381–387.
- 822 A. Luengnaruemitchai and A. Kaengsilalai, *Chem. Eng. J.*, 2008, **144**, 96–102.
- 823 D. Halliche, O. Cherifi and A. Auroux, *Thermochim. Acta*, 2005, **434**, 125–131.
- 824 A. H. Fakeeha, W. U. Khan, A. S. Al-Fatesh and A. E. Abasaeed, *Chinese J. Catal.*, 2013, **34**, 764–768.
- 825 H. Inque, N. Hatanaka, K. Kiden, S. Murata and M. Nomura Omura, *J. Japan Pet. Inst.*, 2002, **45**, 314–320.
- 826 G. Moradi, F. Khezeli and H. Hemmati, *J. Nat. Gas Sci. Eng.*, 2016, **33**, 657–665.
- 827 H. Xu, B. W. Zeiger and K. S. Suslick, *Chem. Soc. Rev.*, 2013, **42**, 2555–2567.
- 828 Z. Li, T. Zhuang, J. Dong, L. Wang, J. Xia, H. Wang, X. Cui and Z. Wang, *Ultrason. Sonochem.*, 2021, **71**, 105384.
- 829 A. B. Patil and B. M. Bhanage, in *Handbook of Nanoparticles*, Springer International Publishing, Cham, 2016, pp. 143–166.
- 830 Y. Vafaeian, M. Haghighi and S. Aghamohammadi, *Energy Convers. Manag.*, 2013, **76**, 1093–1103.
- 831 M. H. Amin, S. Putla, S. Bee Abd Hamid and S. K. Bhargava, *Appl. Catal. A Gen.*, 2015, **492**, 160–168.
- 832 S. Wang and G. . (Max) Lu, *Appl. Catal. B Environ.*, 1998, **19**, 267–277.
- 833 J. Li, D. Wang, G. Zhou, Y. Xue, C. Li and T. Cheng, *Ind. Eng. Chem. Res.*, 2011, **50**, 10955–10961.
- 834 K. Asami, X. Li, K. Fujimoto, Y. Koyama, A. Sakurama, N. Kometani and Y. Yonezawa, *Catal. Today*, 2003, **84**, 27–31.
- 835 J. Zhang, H. Wang and A. K. Dalai, *Ind. Eng. Chem. Res.*, 2009, **48**, 677–684.
- 836 J. Zhang, H. Wang and A. Dalai, *J. Catal.*, 2007, **249**, 300–310.
- 837 Z. Hou and T. Yashima, *Catal. Letters*, 2003, **89**, 193–197.
- 838 M. Nowosielska, W. K. Jozwiak and J. Rynkowski, *Catal. Letters*, 2008, **128**, 83.
- 839 C. Crisafulli, S. Scirè, S. Minicò and L. Solarino, *Appl. Catal. A Gen.*, 2002, **225**, 1–9.
- 840 H. Wang, Z. Li and S. Tian, *React. Kinet. Catal. Lett.*, 2004, **83**, 245–252.
- 841 J. Estephane, S. Aouad, S. Hany, B. El Khoury, C. Gennequin, H. El Zakhem, J. El Nakat, A. Aboukaïs and E. Abi Aad, *Int. J. Hydrogen Energy*, 2015, **40**, 9201–9208.
- 842 A. Koh, L. Chen, W. Keeleong, B. Johnson, T. Khimiyak and J. Lin, *Int. J. Hydrogen Energy*, 2007, **32**, 725–730.
- 843 I. Luisetto, S. Tuti and E. Di Bartolomeo, *Int. J. Hydrogen Energy*, 2012, **37**, 15992–15999.
- 844 V. M. Gonzalez-delaCruz, R. Pereñiguez, F. Ternero, J. P. Holgado and A. Caballero, *J. Phys. Chem. C*, 2012, **116**, 2919–2926.



- 845 P. Djinić, I. G. Osojnik Črnivec, B. Erjavec and A. Pintar, *Appl. Catal. B Environ.*, 2012, **125**, 259–270.
- 846 L. Chen, Q. Zhu and R. Wu, *Int. J. Hydrogen Energy*, 2011, **36**, 2128–2136.
- 847 A. J. Najfach, C. B. Almquist and R. E. Edelmann, *Catal. Today*, 2021, **369**, 31–47.
- 848 F. Rahmani, M. Haghighi, Y. Vafaeian and P. Estifaeae, *J. Power Sources*, 2014, **272**, 816–827.
- 849 B. . Liu and C. . Au, *Appl. Catal. A Gen.*, 2003, **244**, 181–195.
- 850 J. B. Wang, S.-Z. Hsiao and T.-J. Huang, *Appl. Catal. A Gen.*, 2003, **246**, 197–211.
- 851 Z. Zhang and X. E. Verykios, *Appl. Catal. A Gen.*, 1996, **138**, 109–133.
- 852 W. D. Zhang, B. S. Liu, C. Zhu and Y. L. Tian, *Appl. Catal. A Gen.*, 2005, **292**, 138–143.
- 853 V. A. Tsipouriari and X. E. Verykios, *J. Catal.*, 1999, **187**, 85–94.
- 854 L. Tian, X. H. Zhao, B. S. Liu and W. D. Zhang, *Energy & Fuels*, 2009, **23**, 607–612.
- 855 P. Djinić, J. Batista and A. Pintar, *Int. J. Hydrogen Energy*, 2012, **37**, 2699–2707.
- 856 R. Wang, X. HY, L. XB, G. QJ and L. WZ, *Appl. Catal. A Gen.*, 2006, **305**, 204–210.
- 857 N. Gao, M. Cheng, C. Quan and Y. Zheng, *Fuel*, 2020, **273**, 117702.
- 858 G. Xu, K. Shi, Y. Gao, H. Xu and Y. Wei, *J. Mol. Catal. A Chem.*, 1999, **147**, 47–54.
- 859 M. Usman, W. M. A. Wan Daud and H. F. Abbas, *Renew. Sustain. Energy Rev.*, 2015, **45**, 710–744.
- 860 M. Tang, L. Xu and M. Fan, *Int. J. Hydrogen Energy*, 2014, **39**, 15482–15496.
- 861 K. Dossoumov, D. K. Churina, G. Y. Yergaziyeva, L. K. Myltykbayeva and E. Z. Ermeshev, *Int. J. Chem. Eng. Appl.*, 2016, **7**, 1–5.
- 862 B. Pawelec, S. Damyanova, K. Arishtirova, J. L. G. Fierro and L. Petrov, *Appl. Catal. A Gen.*, 2007, **323**, 188–201.
- 863 J.-S. Chang, S.-E. Park, J. W. Yoo and J.-N. Park, *J. Catal.*, 2000, **195**, 1–11.
- 864 Y. K. Chang, Jong-San; Park, Sang-Eon; Roh, Hyun-Seog; Park, *Bull. Korean Chem. Soc.*, 1998, **19**, 809–812.
- 865 J. Chang, S. Park and H. Chon, *Appl. Catal. A Gen.*, 1996, **145**, 111–124.
- 866 H. U. Hambali, A. A. Jalil, A. A. Abdulrasheed, T. J. Siang, T. A. T. Abdullah, A. Ahmad and D.-V. N. Vo, *Int. J. Energy Res.*, 2020, **44**, 5696–5712.
- 867 G. Yang, J. He, Y. Yoneyama, Y. Tan, Y. Han and N. Tsubaki, *Res. Chem. Intermed.*, 2008, **34**, 771–779.
- 868 J. Bao, J. He, Y. Zhang, Y. Yoneyama and N. Tsubaki, *Angew. Chemie*, 2008, **120**, 359–362.
- 869 M. Javed, S. Cheng, G. Zhang, P. Dai, Y. Cao, C. Lu, R. Yang, C. Xing and S. Shan, *Fuel*, 2018, **215**, 226–231.
- 870 C. Dai, A. Zhang, C. Song and X. Guo, ed. C. B. T.-A. in C. Song, Academic Press, 2018, vol. 63, pp. 75–115.
- 871 J. Bao and N. Tsubaki, *Chem. Rec.*, 2018, **18**, 4–19.
- 872 B. Han, C. C. Amoo, G. Zhang, S. Cheng, B. Mazonde, M. Javed, X. Gai, C. Lu, R. Yang and C. Xing, *Energy Technol.*, 2019, **7**, 1801033.
- 873 B. Bonelli, L. Forni, A. Aloise, J. B. Nagy, G. Fornasari, E. Garrone, A. Gedeon, G. Giordano and F. Trifirò, *Microporous Mesoporous Mater.*, 2007, **101**, 153–160.
- 874 R. de Ruiter, A. P. M. Kentgens, J. Grootendorst, J. C. Jansen and H. van Bekkum, *Zeolites*, 1993, **13**, 128–138.
- 875 P. Frontera, A. Macario, A. Aloise, F. Crea, P. L. Antonucci, J. B. Nagy, F. Frusteri and G. Giordano, *Catal. Today*, 2012, **179**, 52–60.
- 876 P. Frontera, A. Aloise, A. Macario, F. Crea, P. L. Antonucci, G. Giordano and J. B. Nagy, *Res. Chem. Intermed.*, 2011, **37**, 267–279.
- 877 R. Vovk, Evgeny; Zhou, Xiaohong; Liu, Zebang; Guan, Cairu; Yang, Yong; Kong, Wenbo; Si, *258th ACS Natl. Meet. Expo.*
- 878 S. N. Miskan, R. S. M. Zaki, M. B. Bahari, H. D. Setiabudi and R. Jusoh, *Mater. Today Proc.*, , DOI:10.1016/j.matpr.2021.08.310.
- 879 H. U. Hambali, A. A. Jalil, A. A. Abdulrasheed, T. J. Siang and D.-V. N. Vo, *J. Energy Inst.*, 2020, **93**, 1535–1543.
- 880 L. Liu, M. Lopez-Haro, C. W. Lopes, D. M. Meira, P. Concepcion, J. J. Calvino and A. Corma, *J. Catal.*, 2020, **391**, 11–24.
- 881 L. Liu, M. Lopez-Haro, J. A. Perez-Omil, M. Boronat, J. J. Calvino and A. Corma, *Nat. Commun.*, 2022, **13**, 821.
- 882 D. Farrusseng and A. Tuel, *New J. Chem.*, 2016, **40**, 3933–3949.
- 883 C. Pagis, A. R. Morgado Prates, D. Farrusseng, N. Bats and A. Tuel, *Chem. Mater.*, 2016, **28**, 5205–5223.
- 884 C. Dai, S. Zhang, A. Zhang, C. Song, C. Shi and X. Guo, *J. Mater. Chem. A*, 2015, **3**, 16461–16468.
- 885 T. Kobayashi, T. Furuya, H. Fujitsuka and T. Tago, *Chem. Eng. J.*, 2019, **377**, 120203.
- 886 R. Amin, X. Chang and B. Liu, *Ind. Eng. Chem. Res.*, 2017, **56**, 7445–7453.
- 887 L. A. Kolahalam, I. V. Kasi Viswanath, B. S. Diwakar, B. Govindh, V. Reddy and Y. L. N. Murthy, *Mater. Today Proc.*, 2019, **18**, 2182–2190.
- 888 S. S. Su and I. Chang, eds. D. Brabazon, E. Pellicer, F. Zivic, J. Sort, M. Dolores Baró, N. Grujovic and K.-L. Choy, Springer International Publishing, Cham, 2018, pp. 15–29.
- 889 A. Gedanken, *Ultrason. Sonochem.*, 2004, **11**, 47–55.
- 890 Q. Chen, J. Li and Y. Li, *J. Phys. D: Appl. Phys.*, , DOI:10.1088/0022-3727/48/42/424005.
- 891 S. Dąbrowska, T. Chudoba, J. Wojnarowicz and W. Łojkowski, *Crystals*, 2018, **8**, 379.
- 892 M. Abdollahifar, M. Haghighi and M. Sharifi, *Energy Convers. Manag.*, 2015, **103**, 1101–1112.
- 893 J. Estephane, M. Ayoub, K. Safieh, M.-N. Kaydouh, S. Casale and H. El Zakhem, *Comptes Rendus Chim.*, 2015, **18**, 277–282.
- 894 H. Jeong, K. I. Kim, D. Kim and I. K. Song, *J. Mol. Catal. A Chem.*, 2006, **246**, 43–48.

- 895 C. Thunyaratchatanon, A. Luengnaruemitchai, J. Jitjamnong, N. Chollacoop, S.-Y. Chen and Y. Yoshimura, *Energy & Fuels*, 2018, **32**, 9744–9755.
- 896 P. Frontera, A. Aloise, A. Macario, P. L. Antonucci, F. Crea, G. Giordano and J. B. Nagy, *Top. Catal.*, 2010, **53**, 265–272.
- 897 A. S. de Jesus, M. L. Maloncy and M. S. Batista, *React. Kinet. Mech. Catal.*, 2017, **122**, 501–511.
- 898 A. N. Pinheiro, A. Valentini, J. M. Sasaki and A. C. Oliveira, in *Zeolites and related materials: Trends, targets and challenges*, eds. A. Gédéon, P. Massiani and F. B. T.-S. in S. S. and C. Babonneau, Elsevier, 2008, vol. 174, pp. 205–208.
- 899 A. N. Pinheiro, A. Valentini, J. M. Sasaki and A. C. Oliveira, *Appl. Catal. A Gen.*, 2009, **355**, 156–168.
- 900 Y. Zeng, X. Zhu, D. Mei, B. Ashford and X. Tu, *Catal. Today*, 2015, **256**, 80–87.
- 901 D. Ray, D. Nepak, S. Janampelli, P. Goshal and C. Subrahmanyam, *Energy Technol.*, 2019, **7**, 1801008.
- 902 K.-S. Nguyen, Hoang Hai; Kim, in *CTSI-Cleantech*, 2014, pp. 422–425.
- 903 H. H. Nguyen and K.-S. Kim, *Catal. Today*, 2015, **256**, 88–95.
- 904 N. Hadian and M. Rezaei, *Fuel*, 2013, **113**, 571–579.
- 905 N. A. S. Amin and T. C. Yaw, *Int. J. Hydrogen Energy*, 2007, **32**, 1789–1798.
- 906 B. Nematollahi, M. Rezaei and M. Khajenoori, *Int. J. Hydrogen Energy*, 2011, **36**, 2969–2978.
- 907 M. J. Ledoux and C. Pham-Huu, *CATTECH*, 2001, **5**, 226–246.
- 908 Q. Wei, G. Yang, X. Gao, N. Yamane, P. Zhang, G. Liu and N. Tsubaki, *Chem. Eng. J.*, 2017, **327**, 465–473.
- 909 T. S. Phan, A. R. Sane, B. Rêgo de Vasconcelos, A. Nzihou, P. Sharrock, D. Grouset and D. Pham Minh, *Appl. Catal. B Environ.*, 2018, **224**, 310–321.
- 910 K. Takanahe, K. Nagaoka, K. Nariai and K. Aika, *J. Catal.*, 2005, **232**, 268–275.
- 911 C. Wang, N. Sun, N. Zhao, W. Wei and Y. Zhao, *Catal. Today*, 2017, **281**, 268–275.
- 912 A. G. Dedov, A. S. Loktev, I. E. Mukhin, A. A. Karavaev, S. I. Tyumenova, A. E. Baranchikov, V. K. Ivanov, K. I. Maslakov, M. A. Bykov and I. I. Moiseev, *Pet. Chem.*, 2018, **58**, 203–213.
- 913 M. H. Amin, *Catalysts*, 2020, **10**, 51.
- 914 H. Drobna, M. Kout, A. Sořtysek, V. M. González-Delacruz, A. Caballero and L. Čapek, *React. Kinet. Mech. Catal.*, 2017, **121**, 255–274.
- 915 M. Zhang, S. Ji, L. Hu, F. Yin, C. Li and H. Liu, *Chinese J. Catal.*, 2006, **27**, 777–781.
- 916 K. S. Park, J. M. Cho, Y. M. Park, J. H. Kwon, J. S. Yu, H. E. Jeong, J. W. Choung and J. W. Bae, *Catal. Today*, 2022, **388–389**, 224–230.
- 917 T. Xie, L. Shi, J. Zhang and D. Zhang, *Chem. Commun.*, 2014, **50**, 7250–7253.
- 918 X. Zhang, L. Zhang, H. Peng, X. You, C. Peng, X. Xu, W. Liu, X. Fang, Z. Wang, N. Zhang and X. Wang, *Appl. Catal. B Environ.*, 2018, **224**, 488–499.
- 919 N. Abdullah, N. Ainirazali, C. C. Chong, H. A. Razak, H. D. Setiabudi, A. A. Jalil and D.-V. N. Vo, *Int. J. Hydrogen Energy*, 2020, **45**, 18426–18439.
- 920 Q. Zhang, J. Wang, P. Ning, T. Zhang, M. Wang, K. Long and J. Huang, *Korean J. Chem. Eng.*, 2017, **34**, 2823–2831.
- 921 M. E. Gálvez, A. Albarazi and P. Da Costa, *Appl. Catal. A Gen.*, 2015, **504**, 143–150.
- 922 Q. Zhang, K. Long, J. Wang, T. Zhang, Z. Song and Q. Lin, *Int. J. Hydrogen Energy*, 2017, **42**, 14103–14114.
- 923 Q. Zhang, M. Wang, T. Zhang, Y. Wang, X. Tang and P. Ning, *RSC Adv.*, 2015, **5**, 94016–94024.
- 924 N. Ainirazali, N. A. N. AbGhazab, H. D. Setiabudi and C. S. Yee, *Indian J. Sci. Technol.*, 2017, **10**, 1–5.
- 925 N. Wang, W. Chu, T. Zhang and X. S. Zhao, *Int. J. Hydrogen Energy*, 2012, **37**, 19–30.
- 926 C. C. T. and P. C. H. F., *Science (80-. )*, 2005, **309**, 713–714.
- 927 E. Friedrich, F. Stefano, Z. Ling, M. Tiziano, A. Cristina, F. Paolo, C. Giovanni and R. Renzo, *Science (80-. )*, 2005, **309**, 752–755.
- 928 O. Omoregbe, H. T. Danh, S. Z. Abidin, H. D. Setiabudi, B. Abdullah, K. B. Vu and D.-V. N. Vo, *Procedia Eng.*, 2016, **148**, 1388–1395.
- 929 U. Oemar, Y. Kathiraser, L. Mo, X. K. Ho and S. Kawi, *Catal. Sci. Technol.*, 2016, **6**, 1173–1186.
- 930 Z. Taherian, M. Yousefpour, M. Tajally and B. Khoshandam, *Int. J. Hydrogen Energy*, 2017, **42**, 24811–24822.
- 931 W. C. Conner and J. L. Falconer, *Chem. Rev.*, 1995, **95**, 759–788.
- 932 B. Erdogan, H. Arbag and N. Yasyerli, *Int. J. Hydrogen Energy*, 2018, **43**, 1396–1405.
- 933 T. Huang, W. Huang, J. Huang and P. Ji, *Energy Sources, Part A Recover. Util. Environ. Eff.*, 2015, **37**, 510–517.
- 934 H. Wu, H. Liu, W. Yang and D. He, *Catal. Sci. Technol.*, 2016, **6**, 5631–5646.
- 935 M. Chotirach, S. Tungasmita, D. Nuntasri Tungasmita and S. Tantayanon, *Int. J. Hydrogen Energy*, 2018, **43**, 21322–21332.
- 936 A. P. E. York, J. B. Claridge, A. J. Brungs, S. Chi Tsang and M. L. H. Green, *Chem. Commun.*, 1997, 39–40.
- 937 J. Cheng and W. Huang, *Fuel Process. Technol.*, 2010, **91**, 185–193.
- 938 J. Huang, T. Huang, L. Liu, W. Huang and R. Ma, *Energy Sources, Part A Recover. Util. Environ. Eff.*, 2011, **33**, 2249–2256.
- 939 W.-J. Cai, L.-P. Qian, B. Yue and H.-Y. He, *Chinese Chem. Lett.*, 2014, **25**, 1411–1415.
- 940 A. Albarazi, P. Beaunier and P. Da Costa, *Int. J. Hydrogen Energy*, 2013, **38**, 127–139.
- 941 A. Albarazi, M. E. Gálvez and P. Da Costa, *Catal. Commun.*, 2015, **59**, 108–112.
- 942 J. Huang, R. Ma, Z. Gao, C. Shen and W. Huang, *Chinese J. Catal.*, 2012, **33**, 637–644.

- 943 J. Huang, R. Ma, T. Huang, A. Zhang and W. Huang, *J. Nat. Gas Chem.*, 2011, **20**, 465–470.
- 944 A. S. Al-Fatesh, Y. Arafat, A. A. Ibrahim, H. Atia, A. H. Fakeeha, U. Armbruster, A. E. Abasaeed and F. Frusteri, *Appl. Catal. A Gen.*, 2018, **567**, 102–111.
- 945 N. Wang, X. Yu, K. Shen, W. Chu and W. Qian, *Int. J. Hydrogen Energy*, 2013, **38**, 9718–9731.
- 946 H. Zhang, M. Li, P. Xiao, D. Liu and C. J. Zou, *Chem. Eng. Technol.*, 2013, **36**, n/a-n/a.
- 947 D. Xu, W. Li, Q. Ge and H. Xu, *Fuel Process. Technol.*, 2005, **86**, 995–1006.
- 948 C. C. Chong, S. N. Bukhari, Y. W. Cheng, H. D. Setiabudi, A. A. Jalil and C. Phalakornkule, *Appl. Catal. A Gen.*, 2019, **584**, 117174.
- 949 C. C. Chong, Y. W. Cheng, H. D. Setiabudi, N. Ainirazali, D.-V. N. Vo and B. Abdullah, *Int. J. Hydrogen Energy*, 2020, **45**, 8507–8525.
- 950 M. N. Kaydouh, N. El Hassan, A. Davidson, S. Casale, H. El Zakhem and P. Massiani, *Microporous Mesoporous Mater.*, 2016, **220**, 99–109.
- 951 J. Tian, H. Li, X. Zeng, Z. Wang, J. Huang and C. Zhao, *Chinese J. Catal.*, 2019, **40**, 1395–1404.
- 952 A. Al-Fatesh, A. Ibrahim, J. Abu-Dahrieh, A. Al-Awadi, A. El-Toni, A. Fakeeha and A. Abasaeed, *Catalysts*, 2018, **8**, 229.
- 953 A. S. Al-Fatesh, H. Atia, J. K. Abu-Dahrieh, A. A. Ibrahim, R. Eckelt, U. Armbruster, A. E. Abasaeed and A. H. Fakeeha, *Int. J. Hydrogen Energy*, 2019, **44**, 20770–20781.
- 954 D. Liu, X. Y. Quek, W. N. E. Cheo, R. Lau, A. Borgna and Y. Yang, *J. Catal.*, 2009, **266**, 380–390.
- 955 A. S. Al-Fatesh, Hanan atia, A. A. Ibrahim, A. H. Fakeeha, S. K. Singh, N. K. Labhsetwar, H. Shaikh and S. O. Qasim, *Renew. Energy*, 2019, **140**, 658–667.
- 956 S. Yasyerli, S. Filizgok, H. Arbag, N. Yasyerli and G. Dogu, *Int. J. Hydrogen Energy*, 2011, **36**, 4863–4874.
- 957 H. Arbag, S. Yasyerli, N. Yasyerli and G. Dogu, *Int. J. Hydrogen Energy*, 2010, **35**, 2296–2304.
- 958 S. Damyanova, B. Pawelec, K. Arishtirova, J. L. G. Fierro, C. Sener and T. Dogu, *Appl. Catal. B Environ.*, 2009, **92**, 250–261.
- 959 Z. Taherian, A. Khataee and Y. Orooji, *Renew. Sustain. Energy Rev.*, 2020, **134**, 110130.
- 960 J. Yu, J. A. Odriozola and T. R. Reina, *Catalysts*, 2019, **9**, 1015.
- 961 W. Wang and Y. Wang, *Int. J. Hydrogen Energy*, 2009, **34**, 5382–5389.
- 962 M. B. Bahari, B. C. Goo, T. L. M. Pham, T. J. Siang, H. T. Danh, N. Ainirazali and D.-V. N. Vo, *Procedia Eng.*, 2016, **148**, 654–661.
- 963 M. B. Bahari, N. H. H. Phuc, B. Abdullah, F. Alenazey and D.-V. N. Vo, *J. Environ. Chem. Eng.*, 2016, **4**, 4830–4838.
- 964 M. A. A. Aziz, H. D. Setiabudi, L. P. Teh, N. H. R. Annuar and A. A. Jalil, *J. Taiwan Inst. Chem. Eng.*, 2019, **101**, 139–158.
- 965 S. Bac, S. Keskin and A. K. Avci, *Sustain. Energy Fuels*, 2020, **4**, 1029–1047.
- 966 S. Zhao, W. Cai, Y. Li, H. Yu, S. Zhang and L. Cui, *J. Saudi Chem. Soc.*, 2018, **22**, 58–65.
- 967 A. M. da Silva, K. R. de Souza, G. Jacobs, U. M. Graham, B. H. Davis, L. V Mattos and F. B. Noronha, *Appl. Catal. B Environ.*, 2011, **102**, 94–109.
- 968 X. Wu and S. Kawi, *Catal. Today*, 2009, **148**, 251–259.
- 969 Y. N. Palai, K. Anjali, A. Sakthivel, M. Ahmed, D. Sharma and S. K. Badamali, *Catal. Letters*, 2018, **148**, 465–473.
- 970 Y. Wei, W. Cai, S. Deng, Z. Li, H. Yu, S. Zhang, Z. Yu, L. Cui and F. Qu, *Renew. Energy*, 2020, **145**, 1507–1516.
- 971 D. Cao, W. Cai, Y. Li, C. Li, H. Yu, S. Zhang and F. Qu, *Catal. Letters*, 2017, **147**, 2929–2939.
- 972 T. Hou, Y. Lei, S. Zhang, J. Zhang and W. Cai, *J. Rare Earths*, 2015, **33**, 42–45.
- 973 P. D. Vaidya and A. E. Rodrigues, *Chem. Eng. Technol.*, 2009, **32**, 1463–1469.
- 974 A. Fasolini, D. Cespi, T. Tabanelli, R. Cucciniello and F. Cavani, *Catalysts*, 2019, **9**, 722.
- 975 A. G. Adeniyi and J. O. Ighalo, *Chem. Pap.*, 2019, **73**, 2619–2635.
- 976 N. D. Charisiou, K. Polychronopoulou, A. Asif and M. A. Goula, *Surf. Coatings Technol.*, 2018, **352**, 92–111.
- 977 X. Wang, M. Li, M. Wang, H. Wang, S. Li, S. Wang and X. Ma, *Fuel*, 2009, **88**, 2148–2153.
- 978 N. A. Roslan, N. N. Mohd Arif, J. L. Jaspin, N. A. Mohamed Razali and S. Zainal Abidin, *Energy Sources, Part A Recover. Util. Environ. Eff.*, 2019, 1–13.
- 979 E. L. Kunkes, D. A. Simonetti, J. A. Dumesic, W. D. Pyrz, L. E. Murillo, J. G. Chen and D. J. Buttrey, *J. Catal.*, 2008, **260**, 164–177.
- 980 Z.-Y. Huang, C.-H. Xu, J. Meng, C.-F. Zheng, H.-W. Xiao, J. Chen and Y.-X. Zhang, *J. Environ. Chem. Eng.*, 2014, **2**, 598–604.
- 981 K. W. Siew, H. C. Lee, J. Gimbut, S. Y. Chin, M. R. Khan, Y. H. Taufiq-Yap and C. K. Cheng, *Renew. Energy*, 2015, **74**, 441–447.
- 982 P. P. Florez-Rodriguez, A. J. Pamphile-Adrián and F. B. Passos, *Catal. Today*, 2014, **237**, 38–46.
- 983 M. B. Ansari and S.-E. Park, *Energy Environ. Sci.*, 2012, **5**, 9419–9437.
- 984 M. Sugino, H. Shimada, T. Turuda, H. Miura, N. Ikenaga and T. Suzuki, *Appl. Catal. A Gen.*, 1995, **121**, 125–137.
- 985 J.-S. Chang, S.-E. Park and M. S. Park, *Chem. Lett.*, 1997, **26**, 1123–1124.
- 986 J. B. Bartholomew, C.H.; Butt, *Catalyst Deactivation*, Elsevier Science, Amsterdam, Elsevier., 1991.
- 987 D. Monforti-Ferrario, F ; Muntean, M ; Vignati, E ; Crippa, M ; Solazzo, E ; Schaaf, E ; Olivier, J.G.J ; Guizz1.

- Monforti-Ferrario, F ; Muntean, M ; Vignati, E ; Crippa, M ; Solazzo, E ; Schaaf, E ; Olivier, J.G.J ; Guizzardi, D. Fossil CO<sub>2</sub> and GHG emission, *Fossil CO<sub>2</sub> and GHG emissions of all world countries*, 2020.
- 988 A. Al-Mamoori, S. Lawson, A. A. Rownaghi and F. Rezaei, *Appl. Catal. B Environ.*, 2020, **278**, 119329.
- 989 G. Li, C. Liu, X. Cui, Y. Yang and F. Shi, *Green Chem.*, 2021, **23**, 689–707.
- 990 D. Mukherjee, S.-E. Park and B. M. Reddy, *J. CO<sub>2</sub> Util.*, 2016, **16**, 301–312.
- 991 J. J. H. B. Sattler, J. Ruiz-Martinez, E. Santillan-Jimenez and B. M. Weckhuysen, *Chem. Rev.*, 2014, **114**, 10613–10653.
- 992 D. Chen, A. Holmen, Z. Sui and X. Zhou, *Chinese J. Catal.*, 2014, **35**, 824–841.
- 993 M. A. Atanga, F. Rezaei, A. Jawad, M. Fitch and A. A. Rownaghi, *Appl. Catal. B Environ.*, 2018, **220**, 429–445.
- 994 S.-E. Park and J. S. Yoo, in *Carbon Dioxide Utilization for Global Sustainability*, eds. S.-E. Park, J.-S. Chang and K.-W. B. T.-S. in S. S. and C. Lee, Elsevier, 2004, vol. 153, pp. 303–314.
- 995 C. Doornkamp and V. Ponec, *J. Mol. Catal. A Chem.*, 2000, **162**, 19–32.
- 996 W. Qi, P. Yan and D. S. Su, *Acc. Chem. Res.*, 2018, **51**, 640–648.
- 997 K. Toko, K. Ito, H. Saito, Y. Hosono, K. Murakami, S. Misaki, T. Higo, S. Ogo, H. Tsuneki, S. Maeda, K. Hashimoto, H. Nakai and Y. Sekine, *J. Phys. Chem. C*, 2020, **124**, 10462–10469.
- 998 A. Guerrero-Ruiz, I. Rodríguez-Ramos, P. Ferreira-Aparicio and J. C. Volta, *Catal. Letters*, 1997, **45**, 113–118.
- 999 S. Sato, M. Ohhara, T. Sodesawa and F. Nozaki, *Appl. Catal.*, 1988, **37**, 207–215.
- 1000 N. Jiang, D.-S. Han and S.-E. Park, *Catal. Today*, 2009, **141**, 344–348.
- 1001 D. R. Burri, K.-M. Choi, S.-C. Han, A. Burri and S.-E. Park, *J. Mol. Catal. A Chem.*, 2007, **269**, 58–63.
- 1002 X. Jiang, L. Sharma, V. Fung, S. J. Park, C. W. Jones, B. G. Sumpter, J. Baltrusaitis and Z. Wu, *ACS Catal.*, 2021, **11**, 2182–2234.
- 1003 C. A. Carrero, R. Schloegl, I. E. Wachs and R. Schomaecker, *ACS Catal.*, 2014, **4**, 3357–3380.
- 1004 S. Rostom and H. de Lasa, *Catalysts*, 2020, **10**, 418.
- 1005 T. A. Bugrova, V. V. Dutov, V. A. Svetlichnyi, V. Cortés Corberán and G. V. Mamontov, *Catal. Today*, 2019, **333**, 71–80.
- 1006 I. Kainthla, J. T. Bhanushali, R. S. Keri and B. M. Nagaraja, *Catal. Sci. Technol.*, 2015, **5**, 5062–5076.
- 1007 A. Qiao, V. N. Kalevaru, J. Radnik and A. Martin, *Catal. Today*, 2016, **264**, 144–151.
- 1008 F. Cavani and F. Trifirò, *Appl. Catal. A Gen.*, 1995, **133**, 219–239.
- 1009 V. R. B. Gurram, S. S. Enumula, K. S. Koppadi, R. R. Chada, D. R. Burri and S. R. R. Kamaraju, *Catal. Commun.*, 2019, **118**, 1–4.
- 1010 A. Sun, Z. Qin and J. Wang, *Appl. Catal. A Gen.*, 2002, **234**, 179–189.
- 1011 G. Towler and S. Lynn, *Chem. Eng. Sci.*, 1994, **49**, 2585–2591.
- 1012 Z.-W. Liu, C. Wang, W.-B. Fan, Z.-T. Liu, Q.-Q. Hao, X. Long, J. Lu, J.-G. Wang, Z.-F. Qin and D. S. Su, *ChemSusChem*, 2011, **4**, 341–345.
- 1013 I. Kainthla, G. V. Ramesh Babu, J. T. Bhanushali, R. S. Keri, K. S. Rama Rao and B. M. Nagaraja, *New J. Chem.*, 2017, **41**, 4173–4181.
- 1014 M. A. Betiha, A. M. Rabie, A. M. Elfadly and F. Z. Yehia, *Microporous Mesoporous Mater.*, 2016, **222**, 44–54.
- 1015 N. Jiang, A. Burri and S.-E. Park, *Chinese J. Catal.*, 2016, **37**, 3–15.
- 1016 L. Zhang, Z. Wu, N. C. Nelson, A. D. Sadow, I. I. Slowing and S. H. Overbury, *ACS Catal.*, 2015, **5**, 6426–6435.
- 1017 M. Kovacevic, S. Agarwal, B. L. Mojet, J. G. van Ommen and L. Lefferts, *Appl. Catal. A Gen.*, 2015, **505**, 354–364.
- 1018 K. Ren, J. Song, Y.-H. Song, H. Wang, Z. Liu, Z.-T. Liu, J. Jiang and Z.-W. Liu, *J. CO<sub>2</sub> Util.*, 2017, **22**, 63–70.
- 1019 S. Wang and Z. H. Zhu, *Energy & Fuels*, 2004, **18**, 1126–1139.
- 1020 T. Badstube, H. Papp, R. Dziembaj and P. Kustrowski, *Appl. Catal. A Gen.*, 2000, **204**, 153–165.
- 1021 Y. Ohishi, T. Kawabata, T. Shishido, K. Takaki, Q. Zhang, Y. Wang and K. Takehira, *J. Mol. Catal. A Chem.*, 2005, **230**, 49–58.
- 1022 B. M. Reddy and A. Khan, *Catal. Rev.*, 2005, **47**, 257–296.
- 1023 M. Saito, H. Kimura, N. Mimura, J. Wu and K. Murata, *Appl. Catal. A Gen.*, 2003, **239**, 71–77.
- 1024 Y. Sekine, R. Watanabe, M. Matsukata and E. Kikuchi, *Catal. Letters*, 2008, **125**, 215–219.
- 1025 M. S. Park, J.-S. Chang, D. S. Kim and S.-E. Park, *Res. Chem. Intermed.*, 2002, **28**, 461–469.
- 1026 J. S. Chang, J. Noh, S. E. Park, W. Y. Kim and C. W. Lee, *Bull. Korean Chem. Soc.*, 1998, **19**, 1342–1346.
- 1027 J.-S. Chang, S.-E. Park, W. Y. Kim, M. Anpo and H. Yamashita, in *Advances in Chemical Conversions for Mitigating Carbon Dioxide*, eds. T. Inui, M. Anpo, K. Izui, S. Yanagida and T. B. T.-S. in S. S. and C. Yamaguchi, Elsevier, 1998, vol. 114, pp. 387–390.
- 1028 J. Matsui, T. Sodesawa and F. Nozaki, *Appl. Catal.*, 1990, **67**, 179–188.
- 1029 T. Hirano, *Appl. Catal.*, 1986, **26**, 81–90.
- 1030 S. C. Ndlela and B. H. Shanks, *Ind. Eng. Chem. Res.*, 2006, **45**, 7427–7434.
- 1031 M. Muhler, *J. Catal.*, 1990, **126**, 339–360.
- 1032 G. Ketteler, W. Ranke and R. Schlögl, *J. Catal.*, 2002, **212**, 104–111.
- 1033 M. Khatamian, M. S. Oskoui and E. Sadeghi, *J. Phys. Chem. C*, 2017, **121**, 6650–6661.
- 1034 E. Sadeghi, M. S. Oskoui, M. Khatamian and A. H. Ghassemi, *Mod. Res. Catal.*, 2016, **05**, 75–84.
- 1035 Y. Sakurai, T. Suzuki, K. Nakagawa, N. Ikenaga, H. Aota and T. Suzuki, *J. Catal.*, 2002, **209**, 16–24.
- 1036 Y. Sakurai, T. Suzuki, N. Ikenaga and T. Suzuki, *Appl. Catal. A Gen.*, 2000, **192**, 281–288.

- 1037 C. Nederlof, F. Kapteijn and M. Makkee, *Appl. Catal. A Gen.*, 2012, **417–418**, 163–173.
- 1038 A. Sun, Z. Qin, S. Chen and J. Wang, *Catal. Today*, 2004, **93–95**, 273–279.
- 1039 S. Chen, Z. Qin, X. Xu and J. Wang, *Appl. Catal. A Gen.*, 2006, **302**, 185–192.
- 1040 S. Jarczewski, M. Drozdek, P. Michorczyk, C. Cuadrado-Collados, J. Gandara-Loe, J. Silvestre-Albero, L. Lityńska-Dobrzyńska and P. Kuśtrowski, *Appl. Surf. Sci.*, 2020, **504**, 144336.
- 1041 A. Corma, J. M. L. Nieto and N. Paredes, *Appl. Catal. A Gen.*, 1993, **104**, 161–174.
- 1042 D.-Y. Hong, V. P. Vislovskiy, Y. K. Hwang, S. H. Jhung and J.-S. Chang, *Catal. Today*, 2008, **131**, 140–145.
- 1043 H. Fan, J. Feng, X. Li, Y. Guo, W. Li and K. Xie, *Chem. Eng. Sci.*, 2015, **135**, 403–411.
- 1044 S. Chen, Z. Xu, D. Tan, D. Pan, X. Cui, Y. Qiao and R. Li, *Appl. Organomet. Chem.*, 2020, **34**, 1–10.
- 1045 Z. Li, K. Su, B. Cheng, D. Shen and Y. Zhou, *Catal. Letters*, 2010, **135**, 135–140.
- 1046 Y. Qiao, C. Miao, Y. Yue, Z. Xie, W. Yang, W. Hua and Z. Gao, *Microporous Mesoporous Mater.*, 2009, **119**, 150–157.
- 1047 B. S. Liu, R. Z. Chang, L. Jiang, W. Liu and C. T. Au, *J. Phys. Chem. C*, 2008, **112**, 15490–15501.
- 1048 B. S. Liu, G. Rui, R. Z. Chang and C. T. Au, *Appl. Catal. A Gen.*, 2008, **335**, 88–94.
- 1049 M. da Costa Borges Soares, F. F. Barbosa, M. A. M. Torres, A. Valentini, A. dos Reis Albuquerque, J. R. Sambrano, S. B. C. Pergher, N. Essayem and T. P. Braga, *Catal. Sci. Technol.*, 2019, **9**, 2469–2484.
- 1050 R. Di Monte and J. Kašpar, *Catal. Today*, 2005, **100**, 27–35.
- 1051 A. Chen, Y. Zhou, N. Ta, Y. Li and W. Shen, *Catal. Sci. Technol.*, 2015, **5**, 4184–4192.
- 1052 O. Irún, S.-A. Sadosche, J. Lasobras, J. Soler, E. Francés, J. Herguido and M. Menéndez, *Catal. Today*, 2013, **203**, 53–59.
- 1053 D. R. Burri, K.-M. Choi, J.-H. Lee, D.-S. Han and S.-E. Park, *Catal. Commun.*, 2007, **8**, 43–48.
- 1054 A. H. de Moraes Batista, F. F. de Sousa, S. B. Honorato, A. P. Ayala, J. M. Filho, F. W. de Sousa, A. N. Pinheiro, J. C. S. de Araujo, R. F. Nascimento and A. Valentini, *J. Mol. Catal. A Chem.*, 2010, **315**, 86–98.
- 1055 Y. Gao, L. Neal, D. Ding, W. Wu, C. Baroi, A. M. Gaffney and F. Li, *ACS Catal.*, 2019, **9**, 8592–8621.
- 1056 H. Zimmermann and R. Walzl, in *Ullmann's Encyclopedia of Industrial Chemistry*, Wiley-VCH Verlag GmbH & Co. KGaA, Weinheim, Germany, 2009.
- 1057 K. Y. Grace Chan, F. Inal and S. Senkan, *Ind. Eng. Chem. Res.*, 1998, **37**, 901–907.
- 1058 C. A. Gärtner, A. C. van Veen and J. A. Lercher, *ChemCatChem*, 2013, **5**, 3196–3217.
- 1059 F. Cavani, N. Ballarini and A. Cericola, *Catal. Today*, 2007, **127**, 113–131.
- 1060 S. Najari, S. Saeidi, P. Concepcion, D. D. Dionysiou, S. K. Bhargava, A. F. Lee and K. Wilson, *Chem. Soc. Rev.*, 2021, **50**, 4564–4605.
- 1061 L. Čapek, J. Adam, T. Grygar, R. Bulánek, L. Vradman, G. Košová-Kučerová, P. Čičmanec and P. Knotek, *Appl. Catal. A Gen.*, 2008, **342**, 99–106.
- 1062 N. Mimura, M. Okamoto, H. Yamashita, S. T. Oyama and K. Murata, *J. Phys. Chem. B*, 2006, **110**, 21764–21770.
- 1063 N. Mimura, I. Takahara, M. Inaba, M. Okamoto and K. Murata, *Catal. Commun.*, 2002, **3**, 257–262.
- 1064 Y. Cheng, F. Zhang, Y. Zhang, C. Miao, W. Hua, Y. Yue and Z. Gao, *Chinese J. Catal.*, 2015, **36**, 1242–1248.
- 1065 F. Rahmani, M. Haghighi and M. Amini, *J. Ind. Eng. Chem.*, 2015, **31**, 142–155.
- 1066 J. Liu, N. He, Z. Z. Zhang, J. Yang, X. Jiang, J. Su, M. Shu, R. Si, G. Xiong, H. H. Xie, G. Vilé, Z. Z. Zhang, J. Su, M. Shu, R. Si, G. Xiong, H. H. Xie and G. Vilé, *ACS Catal.*, 2021, **11**, 2819–2830.
- 1067 W. SB, K. Murata, T. Hayakawa, S. Hamakawa and K. Suzuki, *Catal. Letters*, 1999, **63**, 59–64.
- 1068 S. Wang, K. Murata, T. Hayakawa, S. Hamakawa and K. Suzuki, *Appl. Catal. A Gen.*, 2000, **196**, 1–8.
- 1069 X. Shi, S. Ji and K. Wang, *Catal. Letters*, 2008, **125**, 331–339.
- 1070 A. S. Al-Awadi, S. M. Al-Zahrani, A. M. El-Toni and A. E. Abasaeed, *Catalysts*, 2020, **10**, 97.
- 1071 X. Ge, M. Zhu and J. Shen, *React. Kinet. Catal. Lett.*, 2002, **77**, 103–108.
- 1072 A. S. Al-Awadi, A. M. El-Toni, M. Alhoshan, A. Khan, J. P. Labis, A. Al-Fatesh, A. E. Abasaeed and S. M. Al-Zahrani, *Ceram. Int.*, 2019, **45**, 1125–1134.
- 1073 E. Asghari, M. Haghighi and F. Rahmani, *J. Mol. Catal. A Chem.*, 2016, **418–419**, 115–124.
- 1074 Y. Li, X. He, S. Wu, K. Zhang, G. Zhou, J. Liu, K. Zhen, T. Wu and T. Cheng, *J. Nat. Gas Chem.*, 2005, **14**, 207–212.
- 1075 Y.-L. Bi, V. C. Corberán, H. Zhuang and K.-J. Zhen, in *Carbon Dioxide Utilization for Global Sustainability*, eds. S.-E. Park, J.-S. Chang and K.-W. B. T.-S. in S. S. and C. Lee, Elsevier, 2004, vol. 153, pp. 343–346.
- 1076 P. Thirumala Bai, S. Srinath, K. Uppendar, T. V Sagar, N. Lingaiah, K. S. Rama Rao and P. S. Sai Prasad, *Appl. Petrochemical Res.*, 2017, **7**, 107–118.
- 1077 A. S. Al-Awadi, A. M. El-Toni, M. Alhoshan, A. Khan, M. A. Shar, A. E. Abasaeed and S. M. Al-Zahrani, *Crystals*, 2019, **10**, 7.
- 1078 A. S. Al-Awadi, A. M. El-Toni, S. M. Al-Zahrani, A. E. Abasaeed, M. Alhoshan, A. Khan, J. P. Labis and A. Al-Fatesh, *Appl. Catal. A Gen.*, 2019, **584**, 117114.
- 1079 S. Asghari, M. Haghighi and P. Taghavinezhad, *Microporous Mesoporous Mater.*, 2019, **279**, 165–177.
- 1080 X. Shi, S. Ji, K. Wang and C. Li, *Energy & Fuels*, 2008, **22**, 3631–3638.
- 1081 A. H. Elbadawi, M. S. Osman, S. A. Razzak and M. M. Hossain, *J. Taiwan Inst. Chem. Eng.*, 2016, **61**, 106–116.
- 1082 L. Čapek, R. Bulánek, J. Adam, L. Smoláková, H. Sheng-Yang and P. Čičmanec, *Catal. Today*, 2009, **141**, 282–287.

- 1083 T. Grygar, L. Čapek, J. Adam and V. Machovič, *J. Electroanal. Chem.*, 2009, **633**, 127–136.
- 1084 P. Taghaviniazad, M. Haghighi and R. Alizadeh, *Microporous Mesoporous Mater.*, 2018, **261**, 63–78.
- 1085 *Global Propylene Industry*, 2020.
- 1086 E. Gomez, S. Kattel, B. Yan, S. Yao, P. Liu and J. G. Chen, *Nat. Commun.*, 2018, **9**, 1398.
- 1087 T. Otroshchenko, G. Jiang, V. A. Kondratenko, U. Rodemerck and E. V. Kondratenko, *Chem. Soc. Rev.*, 2021, **50**, 473–527.
- 1088 F. Zhang, R. Wu, Y. Yue, W. Yang, S. Gu, C. Miao, W. Hua and Z. Gao, *Microporous Mesoporous Mater.*, 2011, **145**, 194–199.
- 1089 J. Janas, J. Gurgul, R. P. Socha, J. Kowalska, K. Nowinska, T. Shishido, M. Che and S. Dzwigaj, *J. Phys. Chem. C*, 2009, **113**, 13273–13281.
- 1090 P. Michorczyk, K. Zeńczak-Tomera, B. Michorczyk, A. Węgrzyniak, M. Basta, Y. Millot, L. Valentin and S. Dzwigaj, *J. CO<sub>2</sub> Util.*, 2020, **36**, 54–63.
- 1091 Q. Zhu, M. Takiguchi, T. Setoyama, T. Yokoi, J. N. Kondo and T. Tatsumi, *Catal. Letters*, 2011, **141**, 670–677.
- 1092 B.-J. Xu, B. Zheng, W.-M. Hua, Y.-H. Yue and Z. Gao, in *From Zeolites to Porous MOF Materials - The 40th Anniversary of International Zeolite Conference*, eds. R. Xu, Z. Gao, J. Chen and W. B. T.-S. in S. S. and C. Yan, Elsevier, 2007, vol. 170, pp. 1072–1079.
- 1093 P. Meriaudeau and C. Naccache, *J. Mol. Catal.*, 1990, **59**, L31–L36.
- 1094 P. Tynjälä and T. T. Pakkanen, *Microporous Mesoporous Mater.*, 1998, **20**, 363–369.
- 1095 J. Vedrine, *J. Catal.*, 1982, **73**, 147–160.
- 1096 M. Briend, A. Lamy, S. Dzwigaj and D. Barthomeuf, in *Zeolite Chemistry and Catalysis*, eds. P. A. Jacobs, N. I. Jaeger, L. Kubelková and B. B. T.-S. in S. S. and C. Wichterlov', Elsevier, 1991, vol. 69, pp. 313–320.
- 1097 T. Blasco, A. Corma and J. Martínez-Triguero, *J. Catal.*, 2006, **237**, 267–277.
- 1098 Y. Ren, W. Hua, Y. Yue and Z. Gao, *React. Kinet. Catal. Lett.*, 2008, **95**, 113–122.
- 1099 Y. Ren, F. Zhang, W. Hua, Y. Yue and Z. Gao, *Catal. Today*, 2009, **148**, 316–322.
- 1100 S. Lawson, Q. Al-Naddaf, A. Krishnamurthy, M. St. Amour, C. Griffin, A. A. Rownaghi, J. C. Knox and F. Rezaei, *ACS Appl. Mater. Interfaces*, 2018, **10**, 19076–19086.
- 1101 A. Zhakeyev, P. Wang, L. Zhang, W. Shu, H. Wang and J. Xuan, *Adv. Sci.*, 2017, **4**, 1700187.
- 1102 X. Li, F. Rezaei and A. A. Rownaghi, *React. Chem. Eng.*, 2018, **3**, 733–746.
- 1103 H. Thakkar, S. Lawson, A. A. Rownaghi and F. Rezaei, *Chem. Eng. J.*, 2018, **348**, 109–116.
- 1104 H. Thakkar, S. Eastman, A. Al-Mamoori, A. Hajari, A. A. Rownaghi and F. Rezaei, *ACS Appl. Mater. Interfaces*, 2017, **9**, 7489–7498.
- 1105 A. Soliman, N. AlAmoodi, G. N. Karanikolos, C. C. Doumanidis and K. Polychronopoulou, *Nanomaterials*, 2020, **10**, 2198.
- 1106 A. Farsad, S. Lawson, F. Rezaei and A. A. Rownaghi, *Catal. Today*, 2021, **374**, 173–184.
- 1107 I. E. Wachs and B. M. Weckhuysen, *Appl. Catal. A Gen.*, 1997, **157**, 67–90.
- 1108 Z.-F. Han, X.-L. Xue, J.-M. Wu, W.-Z. Lang and Y.-J. Guo, *Chinese J. Catal.*, 2018, **39**, 1099–1109.
- 1109 X. Ge, H. Zou, J. Wang and J. Shen, *React. Kinet. Catal. Lett.*, 2005, **85**, 253–260.
- 1110 Y. Wang, Y. Ohishi, T. Shishido, Q. Zhang, W. Yang, Q. Guo, H. Wan and K. Takehira, *J. Catal.*, 2003, **220**, 347–357.
- 1111 P. Michorczyk, J. Ogonowski and K. Zeńczak, *J. Mol. Catal. A Chem.*, 2011, **349**, 1–12.
- 1112 X. Zhang, Y. Yue and Z. Gao, *Catal. Letters*, 2002, **83**, 19–25.
- 1113 P. Michorczyk, J. Ogonowski, P. Kuśtrowski and L. Chmielarz, *Appl. Catal. A Gen.*, 2008, **349**, 62–69.
- 1114 N. Ikenaga, T. Tsuruda, K. Senma, T. Yamaguchi, Y. Sakurai and T. Suzuki, *Ind. Eng. Chem. Res.*, 2000, **39**, 1228–1234.
- 1115 Y. Luo, C. Miao, Y. Yue, W. Yang, W. Hua and Z. Gao, *Catalysts*, 2019, **9**, 1040.
- 1116 H. J. Zhang, Z. G. Jia and S. F. Ji, *Adv. Mater. Res.*, 2011, **287–290**, 1671–1674.
- 1117 S. Chen, X. Chang, G. Sun, T. Zhang, Y. Xu, Y. Wang, C. Pei and J. Gong, *Chem. Soc. Rev.*, 2021, **50**, 3315–3354.
- 1118 W. Won, K. S. Lee, S. Lee and C. Jung, *Comput. Chem. Eng.*, 2010, **34**, 508–517.
- 1119 G. R. Kotelnikov, R. K. Mikhailov and A. P. Troitskii, *Chem. Technol. Fuels Oils*, 1988, **24**, 49–52.
- 1120 R. A. Buyanov and N. A. Pakhomov, *Kinet. Catal.*, 2001, **42**, 64–75.
- 1121 B. M. Weckhuysen and R. A. Schoonheydt, *Catal. Today*, 1999, **51**, 223–232.
- 1122 C. Wei, F. Xue, C. Miao, Y. Yue, W. Yang, W. Hua and Z. Gao, *Chinese J. Chem.*, 2017, **35**, 1619–1626.
- 1123 C. Wei, F. Xue, C. Miao, Y. Yue, W. Yang, W. Hua and Z. Gao, *Catalysts*, 2016, **6**, 171.
- 1124 Z. Sun, T. Ma, H. Tao, Q. Fan and B. Han, *Chem*, 2017, **3**, 560–587.
- 1125 Y. Ling, Q. Ma, Y. Yu and B. Zhang, *Trans. Tianjin Univ.*, 2021, **27**, 180–200.
- 1126 J. Wu, Y. Huang, W. Ye and Y. Li, *Adv. Sci.*, 2017, **4**, 1700194.
- 1127 S. N. Habisreutinger, L. Schmidt-Mende and J. K. Stolarczyk, *Angew. Chemie Int. Ed.*, 2013, **52**, 7372–7408.
- 1128 A. Nikokavoura and C. Trapalis, *Appl. Surf. Sci.*, 2017, **391**, 149–174.
- 1129 Ž. Kovačič, B. Likozar and M. Huš, *ACS Catal.*, 2020, **10**, 14984–15007.
- 1130 Ștefan Neațu, J. Maciá-Agulló and H. Garcia, *Int. J. Mol. Sci.*, 2014, **15**, 5246–5262.
- 1131 K. Li, B. Peng and T. Peng, *ACS Catal.*, 2016, **6**, 7485–7527.
- 1132 A. Olivo, E. Ghedini, M. Signoretto, M. Compagnoni and I. Rossetti, *Energies*, 2017, **10**, 1394.
- 1133 Hiragond, Ali, Sorcar and In, *Catalysts*, 2019, **9**, 370.

- 1134 A.-Y. Lo and F. Taghipour, *Appl. Mater. Today*, 2021, **23**, 101042.
- 1135 M. M. Zagho, M. K. Hassan, M. Khraisheh, M. A. A. Al-Maadeed and S. Nazarenko, *Chem. Eng. J. Adv.*, 2021, **6**, 100091.
- 1136 J. K. Thomas, *Chem. Rev.*, 1993, **93**, 301–320.
- 1137 S. Hashimoto, *J. Photochem. Photobiol. C Photochem. Rev.*, 2003, **4**, 19–49.
- 1138 Y. Tong, Y. Zhang, N. Tong, Z. Zhang, Y. Wang, X. Zhang, S. Zhu, F. Li and X. Wang, *Catal. Sci. Technol.*, 2016, **6**, 7579–7585.
- 1139 X. Chang, T. Wang and J. Gong, *Energy Environ. Sci.*, 2016, **9**, 2177–2196.
- 1140 H. Yamashita, Y. Fujii, Y. Ichihashi, S. G. Zhang, K. Ikeue, D. R. Park, K. Koyano, T. Tatsumi and M. Anpo, *Catal. Today*, 1998, **45**, 221–227.
- 1141 K. Ikeue, H. Yamashita, M. Anpo and T. Takewaki, *J. Phys. Chem. B*, 2001, **105**, 8350–8355.
- 1142 J. Kianička, G. Čík, F. Šeršeň, I. Špánik, R. Sokolík and J. Filo, *Molecules*, 2019, **24**, 992.
- 1143 I. Khan, X. Chu, I. Khan, H. Liu, W. Li, L. Bai and L. Jing, *Mater. Res. Bull.*, 2020, **130**, 110926.
- 1144 S. Zhu, S. Liang, Y. Wang, X. Zhang, F. Li, H. Lin, Z. Zhang and X. Wang, *Appl. Catal. B Environ.*, 2016, **187**, 11–18.
- 1145 M. Taramasso, G. Perego and B. Notari, *US4410501a*, 1983, 1–8.
- 1146 S. Yamagata, M. Nishijo, N. Murao, S. Ohta and I. Mizoguchi, *Zeolites*, 1995, **15**, 490–493.
- 1147 Y. Shiraishi, N. Saito and T. Hirai, *J. Am. Chem. Soc.*, 2005, **127**, 8304–8306.
- 1148 Y. Sun, G. Li, Y. Gong, Z. Sun, H. Yao and X. Zhou, *J. Hazard. Mater.*, 2021, **403**, 124019.
- 1149 Y. Tong, L. Chen, S. Ning, N. Tong, Z. Zhang, H. Lin, F. Li and X. Wang, *Appl. Catal. B Environ.*, 2017, **203**, 725–730.
- 1150 G. Yan, X. Wang, X. Fu and D. Li, *Catal. Today*, 2004, **93–95**, 851–856.
- 1151 X. Zhao, W. Chen, G. Li, G. Feng, S. Li, X. Dong, Y. Song, X. Yu, X. Chen, W. Wei and Y. Sun, *Appl. Catal. A Gen.*, 2020, **595**, 117503.
- 1152 G. Hu, J. Yang, X. Duan, R. Farnood, C. Yang, J. Yang, W. Liu and Q. Liu, *Chem. Eng. J.*, 2021, **417**, 129209.
- 1153 M. Anpo, H. Yamashita, K. Ikeue, Y. Fujii, S. G. Zhang, Y. Ichihashi, D. R. Park, Y. Suzuki, K. Koyano and T. Tatsumi, *Catal. Today*, 1998, **44**, 327–332.
- 1154 K. Ikeue, H. Mukai, H. Yamashita, S. Inagaki, M. Matsuoka and M. Anpo, *J. Synchrotron Radiat.*, 2001, **8**, 640–642.
- 1155 M. Hussain, P. Akhter, N. Russo and G. Saracco, *Chem. Eng. J.*, 2015, **278**, 279–292.
- 1156 V. P. Indrakanti, J. D. Kubicki and H. H. Schobert, *Energy Environ. Sci.*, 2009, **2**, 745.
- 1157 Y. Izumi, *Coord. Chem. Rev.*, 2013, **257**, 171–186.
- 1158 H.-C. Yang, H.-Y. Lin, Y.-S. Chien, J. C.-S. Wu and H.-H. Wu, *Catal. Letters*, 2009, **131**, 381–387.
- 1159 S. Nadeem, A. Mumtaz, M. Mumtaz, M. I. Abdul Mutalib, M. S. Shaharun and B. Abdullah, *J. Mol. Liq.*, 2018, **272**, 656–667.
- 1160 W. Jia, T. Liu, Q. Li and J. Yang, *Catal. Today*, 2019, **335**, 221–227.
- 1161 S. W. Jo, B. S. Kwak, K. M. Kim, J. Y. Do, N.-K. Park, S. O. Ryu, H.-J. Ryu, J.-I. Baek and M. Kang, *Appl. Surf. Sci.*, 2015, **355**, 891–901.
- 1162 W. Jia, Q. Li, L. Zhang, L. Hou, T. Liu, G. Bhavana and J. Yang, *J. Nanoparticle Res.*, 2020, **22**, 288.
- 1163 H.-Y. Wu, H. Bai and J. C. S. Wu, *Ind. Eng. Chem. Res.*, 2014, **53**, 11221–11227.
- 1164 Z. Cui, P. Wang, Y. Wu, X. Liu, G. Chen, P. Gao, Q. Zhang, Z. Wang, Z. Zheng, H. Cheng, Y. Liu, Y. Dai and B. Huang, *Appl. Catal. B Environ.*, 2022, **310**, 121375.
- 1165 Z.-C. Fu, J. T. Moore, F. Liang and W.-F. Fu, *Chem. Commun.*, 2019, **55**, 11523–11526.